Universitat Autònoma de Barcelona

Ru, Co and Ca-based Catalysts for Artificial Photosynthesis

Marcos Gil Sepulcre

Universitat Autònoma de Barcelona

Ru, Co and Cu-based Catalysts for Artificial Photosynthesis

Marcos Gil Sepulcre

Tesi Doctoral

Programa de Doctorat en Química

Dr. Roger Bofill Arasa and Dr. Xavier Sala Román

Departament de Química

Facultat de Ciències

2018

Memòria presentada per aspirar al Grau de Doctor en Química per Marcos Gil Sepulcre

Marcos Gil Sepulcre

Vist i plau

Dr. Roger Bofill Arasa

Departament de Química
Facultat de Ciències
Universitat Autònoma de Barcelona

Dr. Xavier Sala Román

Departament de Química
Facultat de Ciències
Universitat Autònoma de Barcelona

Bellaterra, 15 de Gener de 2018

Acknowledgments/Agradecimientos

In this part, I will express in my native language my acknowledgements to all the people who has walked with me during this travel.

En primer lugar, tengo que agradecer a mis directores de tesis, Roger y Xavi. Sin vosotros nada de esto sería posible. Gracias por estar durante estos cuatro años siempre dispuestos a ayudarme, llueva o nieve. Vuestros consejos (químicos y no tan químicos), vuestro apoyo, y vuestros ánimos han hecho posible que hoy esté donde estoy. No puedo olvidarme de Jordi y Lluís, a pesar de no ser mis directores de tesis, habéis sido una pieza clave dentro del periodo que he pasado en SelOxCat, siempre con buen humor y dispuestos a echar un cable incondicionalmente, gracias.

Aunque no es mi director oficial, quiero agradecer a Toni todo su apoyo durante este largo viaje. Siempre has tenido tiempo para ayudarme en cualquier problema que tuviera y tu puerta ha estado abierta siempre de par en par para lo que necesitara. Gracias por darme la oportunidad de trabajar en uno de los mejores centros del mundo con un grupo de investigación de un nivel excepcional. De manera especial quiero agradecer a Carolina que durante mi última época en el ICIQ me ha aconsejado y ayudado siempre tanto en la química como en las decisiones que tenía que afrontar a diario.

Muy especialmente tengo que atribuir parte de esto a mis compañeros de laboratorio durante todo este tiempo, Jonathan, Rosa, Javi, Lluís, Bing, Hai Jie, Nacho, Nuria y Jordi C. Vosotros habéis sido mi familia adoptiva durante todo el tiempo que he pasado en Barcelona, y habéis hecho que entrara cada mañana al laboratorio siempre con una gran sonrisa en la cara. Tampoco me puedo dejar a toda la planta de Inorgánica, Merche, João, Jose, Dani, Dani H., Quim, Katia, Selene, Jordi B., Jordi, Alba, Natalia. No solo me llevo compañeros de trabajo, sino amigos.

Gracias a todo el mundo que ha estado colaborando de una forma u otra con la química de esta tesis. Particularmente, gracias a todo el equipo técnico de la UAB y ICIQ, los cuales me habéis ayudado siempre que lo he necesitado. Especialmente a gracias a Fernando, que ha estado peleando mano a mano a mi lado en parte de estos proyectos.

No tengo que olvidarme de las personas que ayudaron a que iniciara mi interés por el mundo de la investigación, que empezaron siendo compañeros de trabajo durante el Máster y que con el tiempo se han ido convirtiendo en buenos amigos, siempre

dispuestos a ayudar y a luchar por seguir en contacto a pesar de que las circunstancias nos hayan llevado por caminos diferentes. Muchas gracias a Javi, Eric, Guillermo, Marc, Amparo, Maikel y Alicia. Especialmente tengo que dar las gracias a Andrea, sin lugar a duda, sin tu ayuda sería imposible que hoy estuviera aquí.

A mi grupo de amigos en mi Valencia, Javi, Jero, Àlex y Guillem. Habéis sido todo un pilar básico desde que éramos enanos, hasta ahora, haciendo y enseñándome a tomarme los baches con el mejor humor. Gracias!

No me puedo olvidar de parte de mi grupo de amigos aquí en Tarragona con el cual he compartido infinitos cafés y alguna que otra cerveza. Gracias Funes, Elena, Adirán, Bruna, Víctor, Marta, Vane.

A mi madre, mi padre y mi hermano, no tengo palabras para expresar lo agradecido que estoy de que hayáis estado ahí a mi lado, por apoyarme siempre en mis decisiones os gustaran más o menos, nunca me habéis fallado y esto es un 50% vuestro. No me olvido de mis Abuelos, mis tías y a Elena. Gracias por estar ahí siempre, habéis sido fundamentales en esta aventura.

A todo mi grupo de música, Iván, Carles, Sergio y Ferran, tengo que agradeceros todos los buenos momentos que hemos pasado y pasaremos juntos, conoceros, compartir esas tardes convertidas en noches, los conciertos y en general tocar la guitarra con vosotros, ha sido y sigue siendo una de las mejores experiencias de mi vida.

I have to say thanks to all Nippe's group from the Texas A&M University, Courtney, Corey, Trevor, Soomin and Siyoung. All of you helped me from the exact moment I started my "American experience" until you drove me to Dallas airport for saying me goodbye. Thank you Michael for giving me the opportunity of living one of the biggest experiences in my life.

Finally, I have to acknowledge the research group of Antoni Llobet in ICIQ, Mª José, Chuanjun, Laura, Dooshaye, Marta, Jan, Roc, Asmaul, Abi, Primavera, Natalia and Léonie. It is a great pleasure to work with all of you every day, you make me feel like at home. I also want to specially give my thanks to Pablo and Sergi not only for being amazing lab mates, but also for becoming friends inside and outside the laboratory.

The work performed in the present doctoral thesis has been possible thanks to the funding of:

Institut Català d'Investigación en Química (ICIQ)

Ministerio de Economía y Competitividad. Secretaría de Estado de Investigación, Desarrollo e Innovación through Projects: CTQ2011-26440 and MINECO/FEDER CTQ2015-64261-R

Finally, I would also like to thank the Universitat Autònoma de Barcelona for the pre-doctoral PIF-UAB grant and the ICIQ for a one-year contract.

Graphical Abstracts

Chapter 1. General Introduction

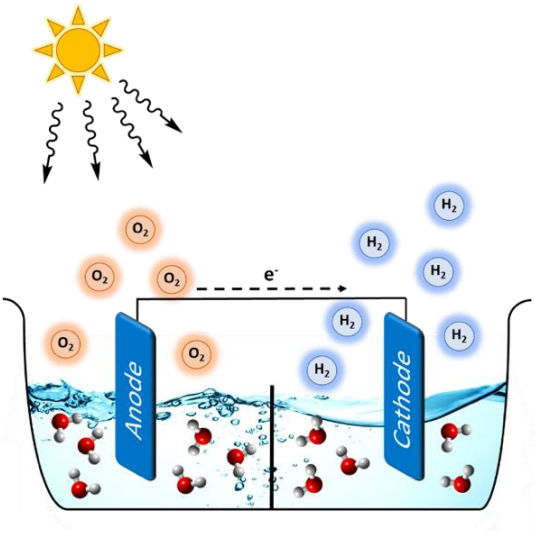

A brief introduction about today's energy situation, natural photosynthesis and its connection to artificial photosynthesis is presented in this chapter. The most significant mechanistic aspects of water oxidation and proton reduction are also introduced. Finally, an analysis of the state-of-the-art of the most relevant catalysts related to this PhD thesis is also presented and the features that control their catalytic performance highlighted.

Chapter 2. Objectives

Chapter 3. Ruthenium Complexes Bearing Pentadentate Ligands: Isomerization processes and Water oxidation catalysis

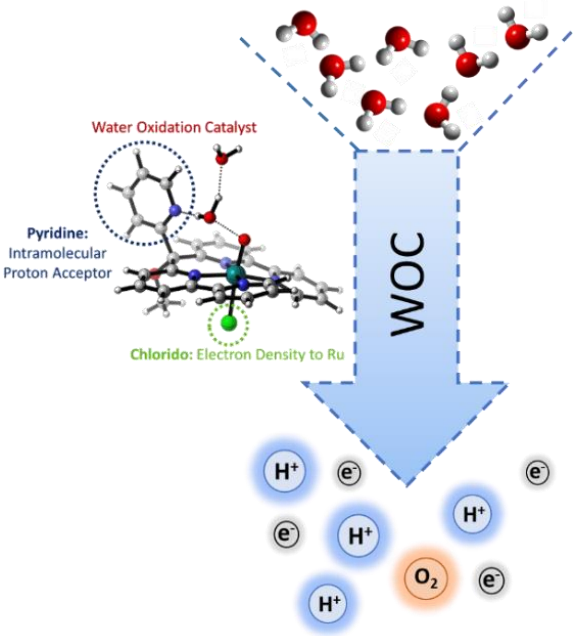

This chapter presents the synthesis and isomeric analysis of a new family of ruthenium complexes containing pentadentate polypyridyl ligands. Their structural and electrochemical characterization is discussed and compared with related Ru complexes. A series of detailed electrochemical, spectroscopic and kinetic studies allows the identification of new species formed after oxidation of the complexes in aqueous solution that proved to be key for further understanding their catalytic behavior in water oxidation.

Chapter 4. Synthesis of New Cu^{II} Complexes Bearing Bipyridyl-diamidate Ligands. Characterization and Water Oxidation Catalysis.

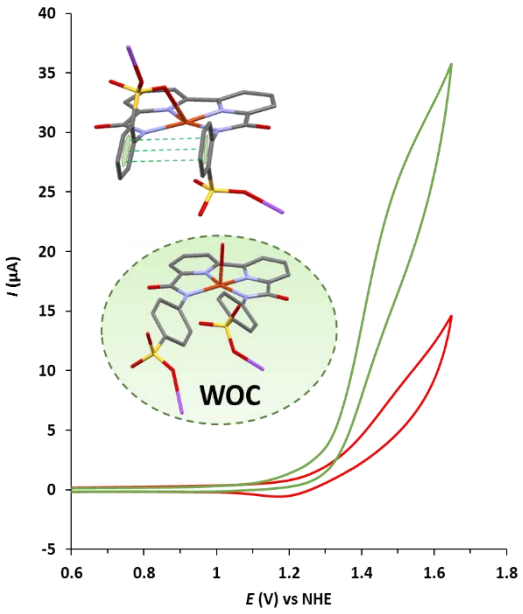

The synthesis of two new ligands containing a bipyridyl framework modified with strong σ-donor amidate groups is presented together with the preparation and characterization of their corresponding Cu^{II} complexes. The catalytic performance of these complexes in water oxidation catalysis is also discussed and their electrochemical properties and catalytic activity are compared with those of well-known copper-based related complexes previously reported in the literature.

Chapter 5. Catalytic H_2 Evolution with CoO, $Co(OH)_2$ and CoO(OH) NPs Generated from a Molecular Polynuclear Co Complex

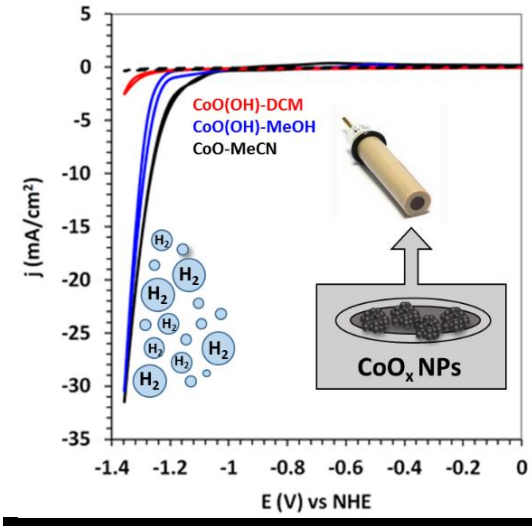

The last chapter presents the electrodeposition onto GC electrodes of Co-derived NPs from a molecular Co complex in different solvents. A thorough characterization of the NPs obtained allows determining the influence of the solvents employed for their synthesis in their size and final chemical nature. Finally, the application in proton reduction catalysis of the prepared cathodes is also reported.

Chapter 6. General Conclusions

Chapter 7. Annexes

Glossary of terms and abbreviations

1D	Monodimensional
2D	Bidimensional
AcO-	Acetate
ATP	Adenosine Triphosphate
b_6f	Cytocrome b_6f complex
bpp^-	3,5-bis(2-pyridyl)pyrazolate
bpy	2,2'-bipyridine
CAN	Cerium Ammonium Nitrate
C_{DL}	Double Layer Capacitance
COSY	Correlation Spectroscopy
CPE	Controlled Potential Electrolysis
C_S	Specific Capacitance
CV	Cyclic Voltammetry
BDD	Boron Doped Diamond
d	doublet
δ	Chemical shift
ΔG_{H^*}	ΔG of hydrogen adsorption
DCM	Dichloromethane
DFT	Density Functional Theory
dmso	Dimethyl sulfoxide
DPV	Differential Pulse Voltammetry
E	Potential
ECSA	Electrochemically Active Surface Area
ε	Extintion Coefficient
E½	Half wave potential
ESI-MS	Electrospray Ionization Mass Spectrometry
FE	Faradaic Efficiency
FOWA	Foot of the Wave Analysis
GC	Glassy Carbon
H2bda	[2,2'-bipyridine]-6,6'-dicarboxylic acid
HER	Hydrogen Evolution Reaction
HEC	Hydrogen Evolution Catalyst
hv	Light
J	Coupling constant
λ	Wavelenght
M	Molar
I	Ionic force
I2M	Bimolecular Interaction Mechanism
i	Current
j	Current density
m/z	Mass-to-Charge ratio
MLCT	Metal to Ligand Charge Transfer
MS	Mass Spectrometry
NADPH	Nicotinamide Adenine Dinucleotide Phosphate
η	Overpotential
n-BuLi	n-Butyllithium
NHC	N-Heterocyclic Carbene

NHE	Normal Hydrogen Electrode
NMR	Nuclear Magnetic Resonance
NOESY	Nuclear Overhauser Spectroscopy
NPs	Nanoparticles
OEC	Oxygen Evolving Center
OXONE	Potassium Peroxymonosulfate
PCET	Proton Coupled Electron Transfer
PEC	Photoelectrochemical cell
PEM	Proton Exchange Membrane
Ph	Phenyl
ppm	Parts per million
ppy	Phenylpyridine
PSI	Photosystem I
PSII	Photosystem II
PT	Proton Transfer
PV	Photovoltaic
py	Pyridine
PY4Im	1,3-bis(bis(2-pyridyl)methyl)imidazol-2-ylidene
RDV	Rotating Disk Voltammetry
RF	Roughness Factor
RT	Room Temperature
S	Surface of the electrode
s	Singlet
SCE	Saturated Calomel Electrode
t	Triplet
$TBAPF_6$	Tetra(N-butyl)ammonium hexafluorophosphate
TEA	Trimethylamine
TOF	Turnover Frequency
TON	Turnover Number
trpy	2,2':6',2''-terpyridine
UV-vis	Ultraviolet-visible Spectroscopy
v	Scan rate
vs.	versus
WNA	Water Nucleophilic attack
WO	Water Oxidation
WOC	Water Oxidation Catalyst

Table of contents

CHAPTER I

General introduction

This chapter has the main objective of providing the motivation for the research presented in this thesis and place the reader in the field of study. General aspects about natural and artificial photosynthesis are presented. The processes involved in a typical water splitting device, water oxidation and hydrogen evolution reactions, are also introduced. Moreover, an analysis of the water oxidation and hydrogen evolution catalysts most relevant for this work are introduced, and the features that control their catalytic performance discussed.

1.1 The energy problem of humanity

Over the past century and especially over the past decades humanity has based the industrial revolution mostly on fossil fuels. Our economic model has relied on consumption of coal, petroleum and gas to satisfy the global energy demand (Figure 1). However, reserves are decreasing at the same time that energy demand continues increasing.[1] Nevertheless, their indiscriminate use is clearly related with the increase of carbon dioxide emissions to the atmosphere that is well known to be the major contribution to greenhouse effect and global warming in our planet.[2]

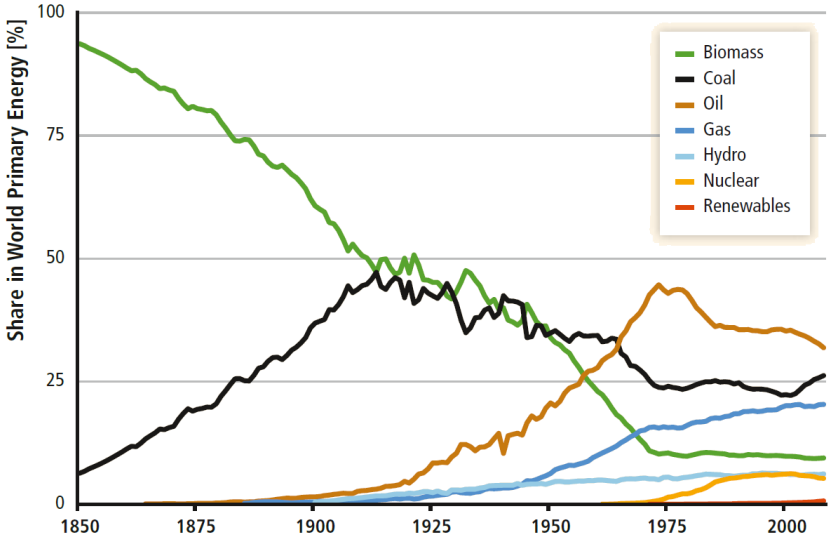

Figure 1. Structural change in world primary energy (in percentages) over the period 1850 – 2008, illustrating the substitution of traditional biomass (mostly non-commercial) by coal and later by oil and gas. The emergence of hydro, nuclear and renewable energy is also shown.[3]

Therefore, it is clear that a new, clean, sustainable and cheap energy source is necessary for supporting a society in continuing growth. Nowadays, approximately 80% of the global energy consumption is satisfied by fossil-based fuels (Figure 2, left). Nuclear plants could be a good alternative due to the low impact on CO_2 production, but they generate radioactive residues that must be stored, and serious problems related with the safety have been made clearly patent (for example nuclear accidents in Chernobyl and Fukushima).

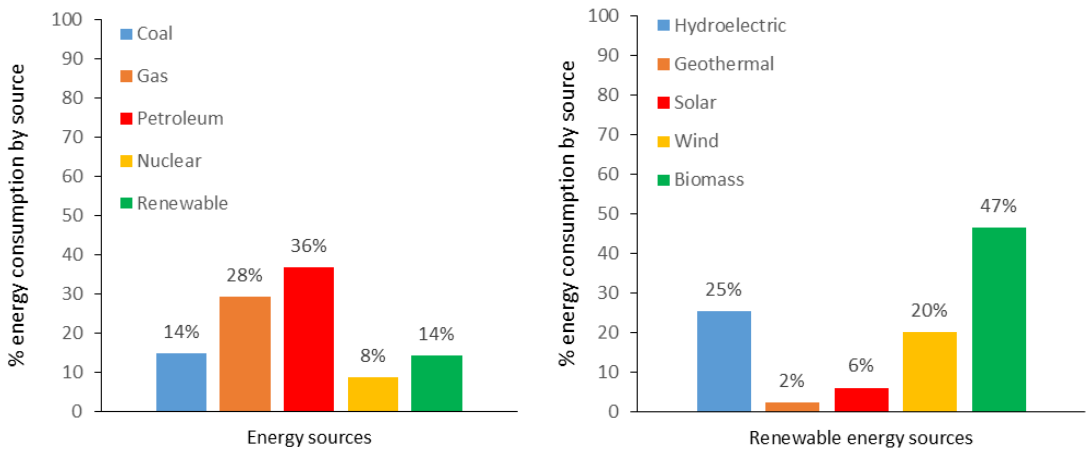

Figure 2: (Left) Percentage of energy consumption by fuel source and (Right) percentage of renewable consumption by type (2016). Source: Annual Energy Review, Energy Information Administration. Department of Energy, US. September, 2016.

Taking into account the criteria mentioned above, renewable resources including biomass, hydroelectric, geothermal, wind power and solar energy are good candidates for replacing fossil fuels as primary energy sources. Particularly interesting and promising in this regard is solar energy, since the earth receives an almost unlimited energy flow from the sun. Despite the fact that one hour of sunlight is comparable to the energy that humankind uses in one year, sunlight only provides 6% of all renewable energies used nowadays, as shown in Figure 2.

Due the fact that solar energy is a clean, abundant, sustainable and safe energy source, many researches have paid attention in this field during the last 50 years.[4] However, so far most of the studies have focused on the direct conversion of solar energy into electricity using solar cells that, due to the inherent problems in the storage and transport of electricity, are strongly dependent on sunlight power stability.[5] In consequence, ulterior transformation of electricity into more useful forms is necessary, such as liquid or gas fuels, which can be easily stored and moved to different places. Plants have been performing a similar process for millions of years, storing the solar energy in the form of chemical bonds thanks to photosynthesis. They are capable to use water, sunlight and CO_2 to form sugars and other carbohydrate molecules, which can be later consumed as fuels for their mitochondrial respiration or used for their growth.

Inspired in photosynthesis, during the last decades the scientific community has been trying to emulate the behavior of green plants by developing artificial photosynthetic

systems. In these schemes, the cleavage of a water molecule by means of sunlight energy to produce electrons, protons and dioxygen is always the starting reaction. The generated current can be used for reducing protons, N_2 or CO_2 and generate H_2 or other useful fuels that can be stored and burned afterwards, producing heat and energy in a clean manner.[6]

1.1.1 Natural photosynthesis

As a general description, the photosynthesis is the process by which green plants, algae and cyanobacteria store the energy from the sun in the form of chemical bonds. In this process, the energy of sunlight is employed to oxidize water into O_2, which is released to the environment as side product, generating a gradient of protons and electrons that are later combined with CO_2 to form biomass in the form of carbohydrates (Equation 1).[7]

$$6CO_2 + 12H_2O \rightarrow C_6H_{12}O_6 + 6O_2 + 6H_2O \qquad \text{Eq. 1}$$

Nature solves the thermodynamic and mechanistic barriers associated with the amount of electrons involved in this process –up to four in the case of water oxidation (WO)- and the number of bonds that must be broken and formed through the catalytic conversion of water to protons and dioxygen in the chloroplasts of the higher green plants, cyanobacteria and algae.[8] The oxidation of water takes place in a series of protein systems, named photosystem II (PSII) and, particularly, in the Oxygen Evolving Centre (OEC), a catalytic cluster responsible of accumulating the four oxidative charges needed. These systems are situated along the thylakoid membrane together with Cytochrome b_6f, photosystem I (PSI) and ATP synthase, which are the responsible of using the released electrons to form NADPH and ATP (Figure 3).

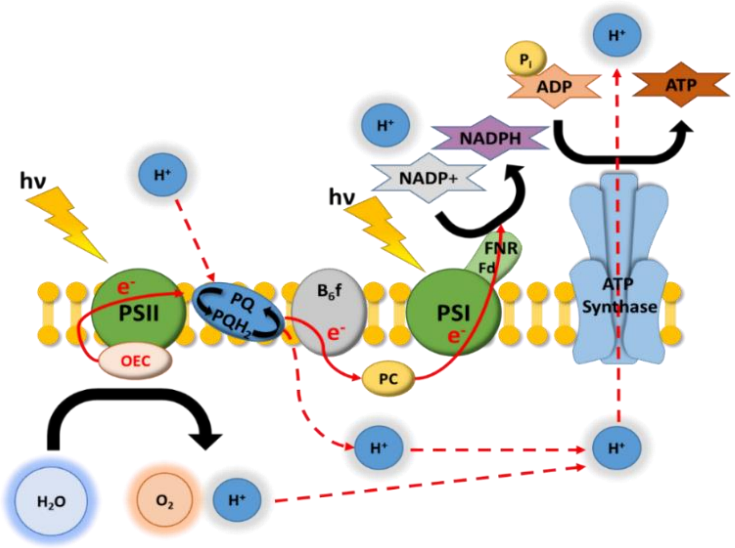

Figure 3. Representation of the electron-proton transport along the thylakoid membrane and the role of the different protein systems involved in this process.

The process of photosynthesis starts with the absorption of sunlight by chlorophyll P680 and other pigments. The excited P680* species induces an electron transfer to pheophytin (pheo), generating a charge separation that generates the high oxidizing species $P680^{\bullet+}$. This species oxidizes a tyrosine residue (Y_z), located between the OEC and the PSII reaction center, which is the responsible of abstracting one electron from the OEC. The above process has to be repeated four times for oxidizing H_2O, since four electrons need to be removed from two water molecules in order to release one oxygen molecule. After water oxidation at the OEC, an electron transport chain brings the released electrons through cytochrome b_6f to PSI. Here is where, with the help of solar energy, reduced NADPH (Nicotinamide Adenine Dinucleotide Phosphate) as a hydrogen carrier is produced from $NADP^+$, as well as the energy vector molecule ATP (Adenosine Triphosphate). Afterwards, NADPH and ATP will be used for fixing atmospheric CO_2 in the stroma of the chloroplast.

Several X-Ray Diffraction (XRD), X-ray Absorption Spectroscopy (XAS) and Differential Functional Theory (DFT) studies have been performed in order to study and determine the structure of the OEC, responsible for the oxidation of water in green plants.[9,10] A X-ray structure resolved at 1.95 Å by Suga *et al.* is shown in Figure 4.[9] The core of the OEC comprises a Mn_4CaO_5 cluster where three Mn atoms and one Ca atom are linked by oxo groups forming a cubane like structure. The Ca and 3 out of the 4 Mn atoms, bridged by oxo species, constitute the cubane structure, whereas a fourth Mn atom

is located outside the cubane and linked to two other Mn atoms of the cubane through a di-μ-oxo bridge. The surrounding area is formed by amino acid residues and water molecules, which provide a coordination framework around the cluster.

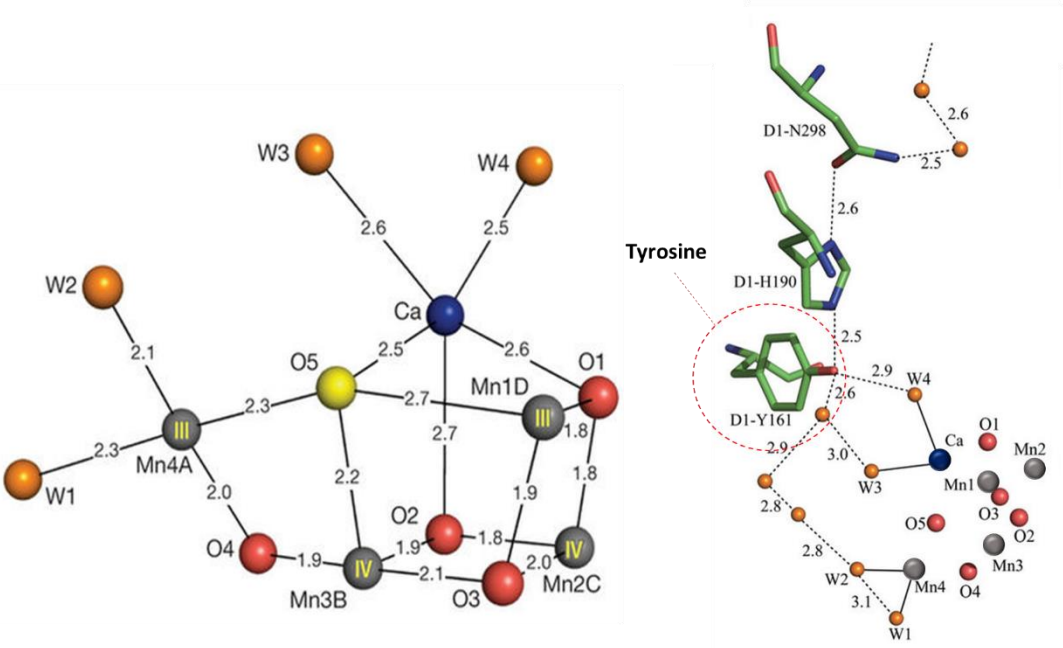

Figure 4. Structure of the Mn_4CaO_5 cluster of the OEC from PSII. (Left) Distances (Å) between metal atoms and oxo bridges or water molecules.[9] (Right) Representation of the environment around tyrosine residue (Y_z, D1-Y161) involved in the oxidation of the Mn_4CaO_5 cluster.[10a] Colour code: Mn, purple; Ca, yellow; O bridge, red; O (H_2O), orange.

1.1.2 Artificial photosynthesis

Inspired by nature, artificial photosynthesis deals with the use of sunlight in order to oxidize water with the aim of using the released H^+ and e^- for reducing either H^+, CO_2 or N_2 into H_2, hydrocarbons or NH_3, and therefore at the end of the day storing the energy of light in the form of chemical bonds.

From the above processes, the splitting of two water molecules to produce hydrogen as energy carrier (so-called water splitting, equation 4), is the result of two coupled half-reactions, the oxidation of the water (equation 2) and the reduction of the generated protons to molecular hydrogen using the released electrons (equation 3). The separate study of both half-reactions allows a rational tuning of specific catalysts for each case as well as the design of a device capable to perform the whole water splitting process.

$$2H_2O \rightarrow O_2 + 4H^+ + 4e^- \quad \text{Eq. 2}$$

$$4H^+ + 4e^- \rightarrow 2H_2 \quad \text{Eq. 3}$$

$$2H_2O \rightarrow O_2 + 2H_2 \quad \text{Eq. 4}$$

During last years, artificial photosynthetic devices have been designed following mainly three different approaches:[11] the generation of photovoltaic electrolyzer cells (PV/Electrolyzer), of photo-electrochemical cells (PECs) and the use of mixed colloid devices (Figure 5).[12]

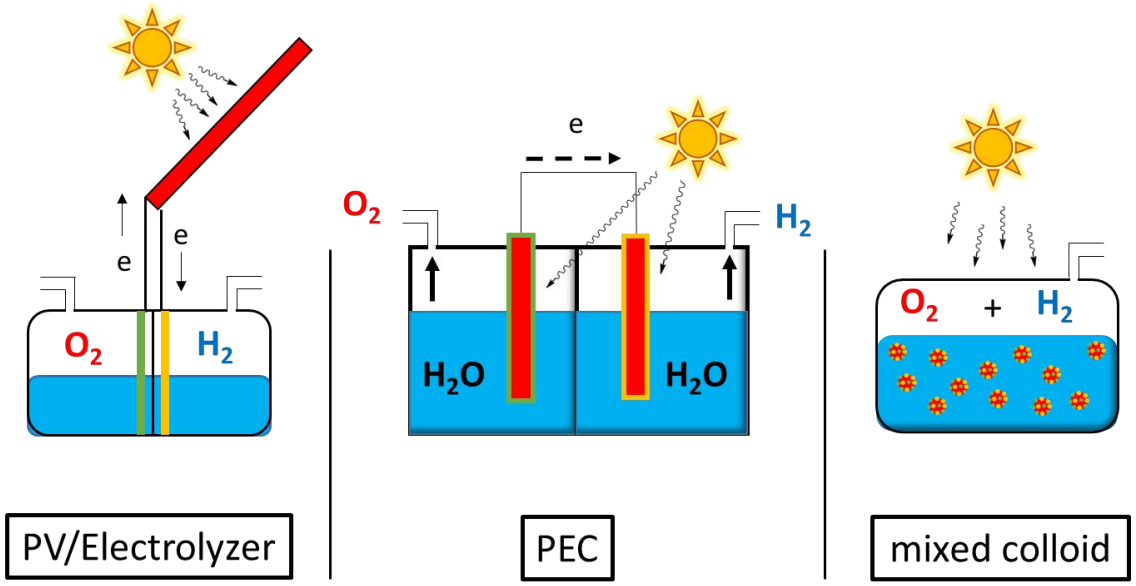

Figure 5. Schematic drawing of three different devices for the light driven water splitting process.

The PV/Electrolyzer design consists in the use of a commercial PV cell as light absorber, which is connected to the catalysts located in the anode and the cathode. Its main advantage is the large amount of PV cells and heterogeneous catalysts that are available. However, one of the main problems for large-scale applications is the high cost of PV cells. An opposite design is found in the mixed colloid cells, where the light absorbers and the catalysts are integrated in single particles and suspended in the electrolyte, building a simple and low-cost water splitting device. However, these systems are currently not competitive enough and still in a proof-of-concept stage, and improvements in terms of stability and solar-to-hydrogen efficiencies are still necessary.[13] Finally, PECs represent a compromise between the efficiency and feasibility of PV/electrolizer cells and the simplicity of mixed colloid cells. These cells consist in

individual photoanodes and photocathodes connected by a solid/ionic-conductor junction (Figure 6).

This design is usually composed by:

1) An anode compartment containing an electrode with:
   - Photosensitive material capable of absorbing photons from sunlight and provoke a charge separation (n-type).
   - A water oxidation catalyst (WOC), based on metal oxides or anchored molecular catalysts.
2) A junction to physically separate both compartments and allow the flow of protons.
3) A cathode compartment containing an electrode with:
   - Photosensitive material (p-type).
   - A hydrogen evolution catalyst (HEC).

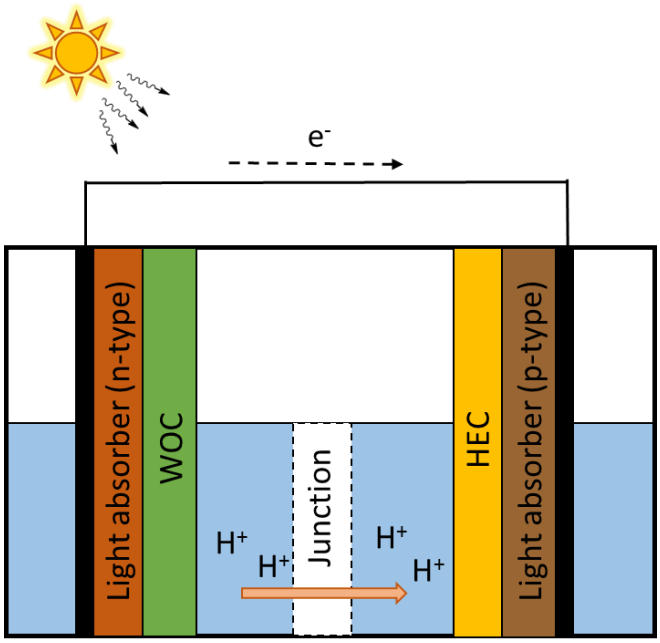

Figure 6. Schematic drawing of a water splitting photo-electrochemical cell (PEC).

The process starts with the absorption of a photon by the photosensitive material, which excites an electron from the valence band to the conduction band creating an electron-hole pair. This is regenerated by the WO catalyst, which accumulates oxidative equivalents. When four oxidative equivalents are accumulated, the WO reaction can take place. At the same time, electrons excited in the cathode by sunlight are used for reducing the protons to hydrogen by the hydrogen evolution catalyst. For avoiding charge

accumulation, the excited electrons of the n-type light absorber must pass through the wire for regenerating the electron-hole pair created in the p-type absorber, and the protons generated go through the conductor junction to the cathode.

In an ideal case, these setups would be used for testing the catalytic water oxidation and hydrogen evolution activities. However, to allow a fast screening of new designed catalysts, both reactions are normally studied independently by using sacrificial electron donors and acceptors. These sacrificial compounds trigger the catalytic reaction, supplying the electron-transfer requirements for these processes, accepting or donating electrons without the need for a full artificial photosynthetic device. The most common sacrificial oxidants are cerium ammonium nitrate (CAN), $[Ru(bpy)_3]^{3+}$, potassium periodate or potassium peroxymonosulfate (OXONE)[14] for water oxidation, and ascorbic acid or trimethylamine (TEA) are the most common sacrificial reductants for the hydrogen evolution reaction (HER).[15] Furthermore, electrochemically-triggered WO and HER processes have also been extensively studied during the last years, providing fast and simple setups for analyzing the catalytic performance of new catalysts.

1.2 Water oxidation catalysis

The oxidation of two molecules of H_2O requires the transfer of four electrons, the breakage of four O-H bonds and the formation of an O-O bond. Thus, because of its mechanistic complexity, this half reaction is currently the bottle-neck process for developing an efficient and sustainable artificial overall water splitting device. Moreover, its unfavorable thermodynamic potential (E^o = 1.23 V vs. NHE at pH = 0)[16] is associated with a high activation barrier for this half-reaction. Thus, a catalyst capable of accumulating four oxidative charges and operating close to the thermodynamic WO potential is necessary. Besides, an ideal WO catalyst must be able to interact with photosensitizing materials and be stable in water at high oxidation states in order to avoid degradation during catalysis.[17]

Several examples of homogeneous and heterogeneous systems have been reported as WOCs. However, due to the work carried out during this PhD Thesis, we will focus our attention in the molecular complexes, which usually are complexes of transition metals such as Cu,[18,19,20,21,22] Fe,[23] Ir,[24] Mn,[25] Co[26,27,28] or Ru.[29,30,31]

1.2.1. Mechanism of water oxidation catalysis

An important factor to consider for the rational design of molecular complexes for water oxidation catalysis is the mechanism that takes place during the formation of O_2. Extensive studies have focused towards elucidating and understanding the different steps involved in this process combining kinetics, ^{18}O labelling and DFT calculations. Basically, two different mechanisms have been proposed for the formation of an O-O bond[32] (Figure 7). The water nucleophilic attack (WNA), in which one molecule of water acts as a nucleophile, attacking an electrophile M-O species, favoring the breakage of the M-O bond and the subsequent formation of an hydroperoxide species, which after a posterior oxidation process releases the oxygen molecule. In contrast, in the bimolecular mechanism (I2M) two M-O units are involved in the formation of the O=O bond. In both cases, the formation of the O=O bond is the rate-determining step of the whole process, and this needs to be taken into consideration during the rational design of new catalysts.

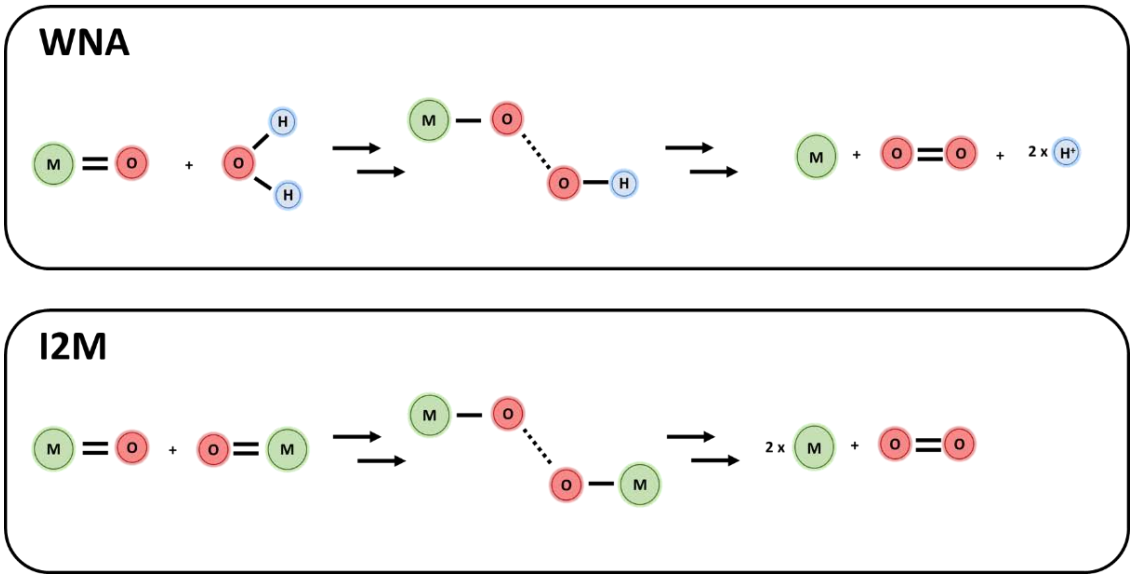

Figure 7. Schematic representation for the two most commonly proposed O-O bond formation pathways in WO catalysis.

Most of the mechanistic knowledge about molecular complexes for WO catalysis comes from studies carried out with Ru complexes.[32a] However, this information can be made extensive to the rest of molecular catalysts based on other transition metals.

1.2.2 Ru-based molecular complexes

Ruthenium is a metal located in the second transition metal series of the Periodic Table. Its electronic configuration [Kr] $4d^7$ $5s^1$ gives access to the widest variety of oxidation states, from (+8) in RuO_4 to (-2) in $[Ru(CO)_4]^{2-}$, which correspond to d^0 and d^{10} electronic configurations, respectively. When combined with polypyridyl ligands, ruthenium complexes are generally stable at high oxidation states and its octahedral geometry allows a tailor-made fine-tuning of their redox potentials. All these properties make ruthenium polypyridyl complexes promising candidates as catalysts for oxidation reactions, including water oxidation as well as the oxidation of other organic and inorganic substrates.[33]

A particularly interesting redox behavior can be found when a water molecule is directly bonded to the metal centre, which allows the possibility to simultaneously exchange electrons and protons giving rise to the proton coupled electron transfer (PCET) effect. This redox behavior was first described in 1970 by Thomas J. Meyer,[34,35] and has been extensively studied for the case of ruthenium aqua complexes. However, it also happens in aqua complexes of other transition metals, facilitating the four electron-transfer necessary for oxidizing water. As shown in Scheme 1, the loss of each electron is linked to the loss of one proton, which is facilitated by the increase of the acidity of the aqua ligand due to its ligation to an acidic transition metal.[36]

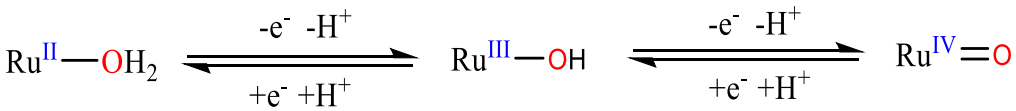

Scheme 1. Schematic representation of the proton coupled electron transfer process in ruthenium aqua complexes.

PCET allows that the total charge of the complex remain constant throughout the process, thus avoiding the formation of high-energy intermediates due to charge accumulation,[37] which translates in a decrease of the necessary potentials to obtain highly oxidized species. On the other hand, the dependence of the $E_{1/2}$ redox potentials with pH follows the Nernst equation; thus, for a one e^-/one proton transfer process the redox potential diminishes 59 mV per pH unit. This dependence is graphically represented in the so-called Pourbaix diagrams.

The effect of PCET in the potentials can be easily observed by comparing the Latimer diagrams for complex $[Ru(bpy)_2(Cl)_2]$ and its analog containing a pyridine (py) and an aqua ligand $[Ru(bpy)_2(py)(OH_2)]^{2+}$ (Scheme 2). In this example, the changes in the electronic content occur in the dπ levels and not in the σ-bonding framework, which explains the coordinative stability after two consecutive oxidation processes for the latter. Thus, for the case of the bis chlorido complex, the first oxidation (Ru^{III}/Ru^{II}) takes place at lower potentials (0 V), and the increase of the total charge of the complex provokes the shift of the second oxidation potential (Ru^{IV}/Ru^{III}) up to 1.7 V. Contrastingly, when one molecule of pyridine and one molecule of water are coordinated to the metal centre, a significant increase in 0.67 V of the oxidation potential for the Ru^{III}/Ru^{II} couple takes place[36,38] and a much smaller increase in potential is observed for the Ru^{IV}/Ru^{III} couple (0.11 V) compared to the 1.7 V increase for the bis chlorido complex. These data make clearly evident the drastic stabilization of the Ru^{IV}=O state in the aqua-containing coordination environment through $d\pi_{Ru}$-$2p\pi_o$ multiple bonding,[39] causing the near overlap of the Ru^{III}/Ru^{II} and Ru^{IV}/Ru^{III} redox couples.

$$\underset{d\pi^4}{cis\text{-}[Ru^{IV}(bpy)_2(Cl)_2]^{2+}} \xrightarrow{1.7\ V} \underset{d\pi^5}{cis\text{-}[Ru^{III}(bpy)_2(Cl)_2]^{+}} \xrightarrow{0.0\ V} \underset{d\pi^6}{cis\text{-}[Ru^{II}(bpy)_2(Cl)_2]^{0}} \quad \textbf{(1)}$$

$$\underset{d\pi^4}{cis\text{-}[Ru^{IV}(bpy)_2(py)(O)]^{2+}} \xrightarrow{0.78\ V} \underset{d\pi^5}{cis\text{-}[Ru^{III}(bpy)_2(py)(OH)]_2^{2+}} \xrightarrow{0.67\ V} \underset{d\pi^6}{cis\text{-}[Ru^{II}(bpy)_2(py)(OH_2)]^{2+}} \quad \textbf{(2)}$$

Scheme 2. Latimer diagram for complexes $[Ru(bpy)_2(Cl)_2]$ (1) and $[Ru(bpy)_2(py)(OH_2)]^{2+}$ (2). Potentials referenced vs. NHE at pH 7.

The properties of molecular complexes are influenced by the ligands. This is clearly manifested in the redox properties of ruthenium polypyridyl complexes, where the Ru^{III}/Ru^{II} and Ru^{IV}/Ru^{III} redox couples are strongly influenced by the ligands surrounding the metal centre. Table 1 shows a variety of complexes and their redox potentials, where the strong ligand effect can be appreciated.[40]

Table 1. Electrochemical properties of Ru-aqua complexes in H_2O at pH=7.0.

Entry	Complex[a]	$E_{1/2}$ (V vs NHE)[b]		
		$Ru^{III/II}$	$Ru^{IV/III}$	$\Delta E_{1/2}$[c]
1	$[Ru(NH_3)(H_2O)]^{2+}$	-0.09	0.59	0.68
2	*cis*-$[Ru(bpy)_2(py)(H_2O)]^{2+}$	0.67	0.78	0.11
3	*cis*-$[Ru(bpy)_2(PPh_3)(H_2O)]^{2+}$	0.74	1.00	0.26
4	$Ru(trpy)(4,4'\text{-}Me_2\text{-}bpy))(H_2O)]^{2+}$	0.71	0.85	0.14
5	$Ru(trpy)(4,4'\text{-}((CO_2Et)_2bpy))(H_2O)]^{2+}$	0.90	1.04	0.14
6	$[Ru(trpy)(bpy)(H_2O)]^{2+}$	0.73	0.86	0.13
7	$[Ru(trpy)(acac)(H_2O)]^{+}$	0.43	0.80	0.37
8	$[Ru(trpy)(C_2O_4)(H_2O)]$	0.40	0.69	0.29

Abbreviations: bpy = 2,2'-bipyridine; py = pyridine, PPh_3 triphenylphosphine; trpy = 2,2';6',2''-terpyridine; acac = acetyl acetomate anion. [b]$E_{1/2}$ values for Ru^{III}-OH/Ru^{II}-OH_2 and Ru^{IV}=O/Ru^{III}-OH. [c]$\Delta E_{1/2} = E_{1/2}{}^{Ru(IV/III)} - E_{1/2}{}^{Ru(III/II)}$.

As can be seen in Table 1, the Ru(III/II) redox couple is strongly affected by the ligands. Thus, in entries 2 to 6 the Ru(II) state is stabilized by Ru dπ- ligand π^* back-bonding interactions thanks to the presence of π electron-rich systems, while in entries 7 and 8 Ru(III) state is clearly stabilized by the electron-donating characteristics of the oxygen-containing ligands, that diminish the necessary potential to reach the Ru(III) state. In the case of the Ru(IV/III) redox couple, this is less sensitive to ligand modifications in comparison with the Ru(III/II) couple. This phenomenon is due to the control on the π-binding properties exerted by the oxo ligand of the Ru^{IV}=O species through a $d\pi_{Ru}$-p_o interaction.

In conclusion, the ability to accumulate high oxidation states in a narrow range of potentials due to PCET and the high moldable redox properties thanks to the potential variability of the ligands make aqua complexes excellent candidates for their application in WO catalysis.

The first molecular complex capable of accumulating four oxidative charges and oxidizing water was reported in the 80s by Meyer and coworkers.[41,42] This was the dinuclear Ru complex *cis,cis*-[(bpy)$_2$(H$_2$O)Ru^{III}(μ-O)Ru(H$_2$O)(bpy)$_2$]$^{4+}$ (**1**) (Chart 1), commonly named as the "blue dimer". These studies shed light on the difficult multielectron oxidation of H_2O to O_2 and proved that was indeed possible. The first studies revealed a moderate catalytic activity, with a 13.2 turnover number (TON) and a 4.2 x 10^{-3} s^{-1} turnover frequency (TOF) when Ce^{IV} was used as sacrificial oxidant.[43] Ulterior extensive kinetic studies[44] and DFT calculations[45] showed that the cause for the low catalytic activity of the "blue dimer" is related to the instability of its μ-oxo bridge, which can breakdown under catalytic conditions, giving rise to inactive monomeric complexes.

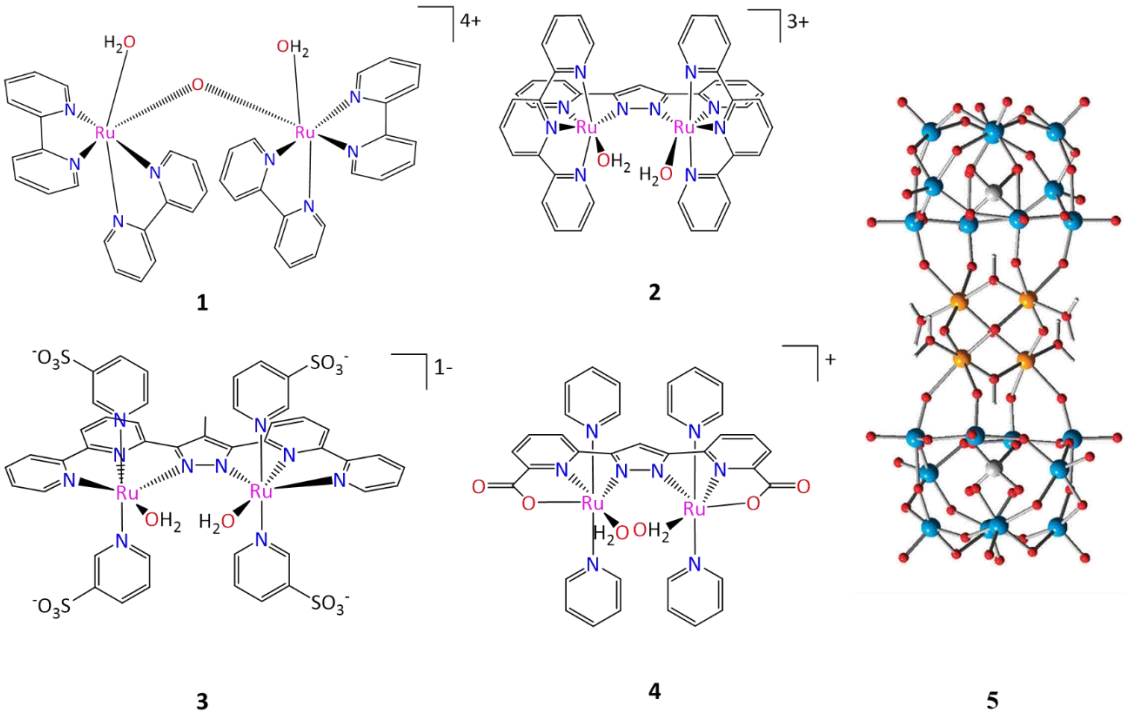

Chart 1. Structures of **1**, **2**, **3**, **4** and **5** able to catalyze the WO reaction. Drawing of the X-ray structure of catalyst **5** has been taken from the corresponding reference.[46] Color code: Ru, yellow; O, red; Si, blue; W, white.

Llobet and co-workers prepared a modification of the blue dimer (complex **2**, Chart 1**)** bearing a more rugged 3,5-bis(2-pyridyl)pyrazolate (bpp$^-$) bridging ligand, where the two Ru-OH$_2$ groups are placed in close proximity favoring their coupling at high oxidation states (I2M mechanism) and a better electronic communication between both metal centres through the conjugated bridge. Despite the TOF was increased by a factor

of 3 (Table 2)[47] complex **2** still showed moderate catalytic performance, with a maximum TON of 17.5, and displayed a relatively low efficiency with respect to the employed sacrificial oxidant (70%). This behavior was attributed to the oxidation of the CH group of the pyrazole moiety present in the bridging ligand. The introduction of an extra methyl group in the pyrazole ring (complex **3**, Chart 1) stabilizes the complex under WO conditions, showing better efficiencies up to 90%.[48] Later on, in 2015 Llobet and Meyer reported a new efficient and rugged Ru dinuclear catalyst for WO (complex **4)**. [49] This complex was also based on the bpp^- framework, incorporating two strongly anionic carboxylic moieties, which allow affording an impressive TOF of 1.4 s^{-1} when Ce^{IV} was used as oxidant.

In order to avoid the degradation of the ligands due to the strong oxidative conditions necessary for WO catalysis, several research groups focused their efforts in the development of polyoxometalates (POMs) as catalysts for this transformation. These systems provide a robust all-inorganic framework environment coordinating the metal core, which makes them promising for applications in WO.[46] A relevant example, $Ru^{IV}_4(\mu\text{-}O)_4(\mu\text{-}OH)_2(H_2O)_4(\gamma\text{-}Si\text{-}W_{10}O_{36})_2]^{10-}$, (see **5** in Chart 1 and Table 2) was independently reported in 2008 by the groups of Bonchio[50] and Hill.[51] The prepared system was able to oxidize water to dioxygen with a 90% efficiency with respect to the added sacrificial oxidant (CAN) and a TOF value of 0.125 s^{-1}, and was also found to be active in neutral conditions using $[Ru(bpy)_3]^{3+}$ as sacrificial oxidant.

An interesting turn in the field of WO occurred in 2005, when Thummel *et al*. reported for the first time that the four-electron transfer necessary for oxidizing water could occur on a single-site metal complex.[52,53] This group published the first family of mononuclear complexes bearing the tridentate polypyridyl ligand 2,6-di(1,8-naphthyridin-2-yl)pyridine capable of catalyzing WO, although with moderate performances (see complexes **6**-**8** in Chart 2 and Table 2). However, it was not until 2008 that Meyer and co-workers reported a thorough mechanistic study that demonstrated the mononuclear nature of the catalysis.[30,54] The proposed catalytic cycle has been later adapted for several catalysts, which are proposed to follow a WNA mechanism.[55,56,57]

Scheme 3 shows a schematic drawing of the proposed WNA mechanism. In this process, the Ru(II)-H_2O species is sequentially oxidized by two sequential $H^+/1e^-$ processes up to Ru(IV)=O at pH 1 (1). An additional one-electron oxidation allows

reaching the Ru(V)=O species (2), which contains a highly electrophilic oxo group able to react with a water molecule, generating the corresponding hydroperoxide species Ru(III)-OOH (3). The formation of this intermediate is accompanied by a two-electron reduction of the metal centre. At this point, an additional oxidation is necessary to activate the catalyst and form Ru(IV)-OO (4), which is the rate-determining step (rds) for this system. In 0.1 M HNO_3, two electrons are transferred to the metal centre from the peroxide bonded ligand, closing the catalytic cycle, while one molecule of oxygen gas is released (5). In 1 M HNO_3 an additional oxidation is necessary to activate the system, reaching Ru(V)-OO (6), which releases oxygen (7) and re-enters in the catalytic cycle as Ru(III)-OH.

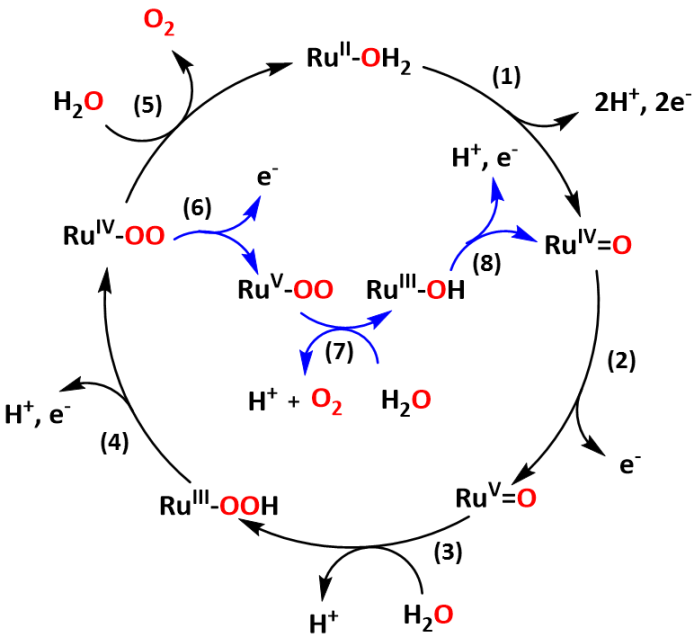

Scheme 3. Schematic drawing of the proposed WNA mechanism for water oxidation by mononuclear Ru complexes in 0.1 M HNO_3.[54] The blue arrows represent the alternative pathway in 1 M HNO_3.

Since then, new Ru mononuclear WO catalysts were synthesized and tested in WO (such as complexes **9-12** shown in Chart 2 and Table 2), although in terms of efficiency and catalytic performance they did not exceed those of the previous dinuclear complexes.[58,59] However, the discovery of single-site water oxidation catalysis offered the possibility of straightforward ligand/complex design, synthesis and characterization and therefore allowed a rapid expansion of the field.

Table 2. Summary of catalytic WO data for dinuclear and mononuclear Ru complexes discussed along the text.

Complex	Conc. Cat (mM)	Ce^{IV} eq.	TOF (s^{-1})[a]	TON	O-O Mechanism	Ref.
1	0.31	100	0.004	13.2	WNA	43
2	1	100	0.014	17.5	I2M	47
3	1	100	0.07	22.6 (211)[b]	WNA	48
4	0.1	100	1.4	-	-	49
5	0.004	400	0.0125	-	WNA	50.60
6	0.067	5000	0.0015	20	WNA	53
7	0.067	5000	0.014	260	WNA	53
8	0.067	5000	0.0033	35	WNA	53
9	0.067	5000	0.00051	320	WNA	58
10	2.9	30	0.00074	7.5	WNA	30.54
11	-	-	-	-	WNA	30.54
12	1	100	0.000052	14	WNA	59
13	0.015	35800	120.4 (303)[c]	8360	I2M	31
14	0.0024	150000	1000	24000	I2M	64
15	0.0024	150000	780	11300	I2M	64
16	0.00093	390000	380	101000	I2M	64
17	0.00093	390000	530	61300	I2M	64
18	-	-	50000[d]	-	WNA	65

[a] Initial turnover frequency. [b] Turnover number when decreasing the concentration of catalyst to 0.1 mM. [c] Maximum turnover number obtained when [Cat.] = 0.21 mM and Ce^{IV}/Cat = 2250/1. [d] TOF_{max} obtained by electrochemical methods using foot of the wave (FOWA) analysis.

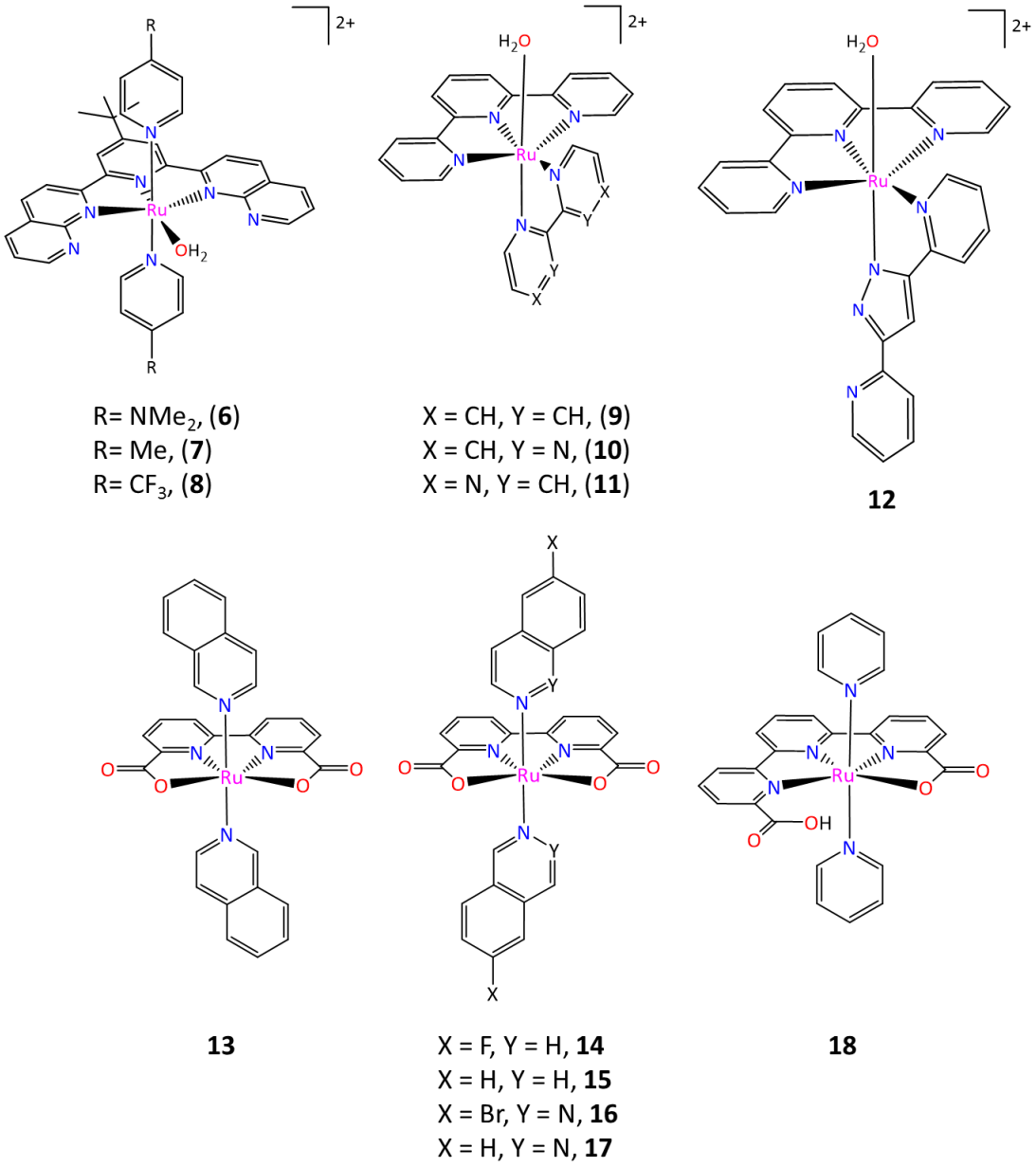

Chart 2. Structure of relevant mononuclear Ru complexes able to perform WO catalysis.

From 2009 onwards Sun and co-workers have reported a series of mononuclear complexes based on the bda^{2-} ligand (H_2bda is [2,2'-bipyridine]-6,6'-dicarboxylic acid).[31,61] From these, complex **13** shown in Chart 2 showed the best catalytic activity reported so far, achieving the impressive TON and TOF values of 8360 and 303 s^{-1}, respectively (Table 2), when triggered with Ce^{IV}. The strong electron-donating ability of the carboxylate moieties present in the bda^{2-} ligand,[62] the expansion to a Ru 7 coordination number[61] during catalysis and the highly efficient bimolecular (I2M) O-O bond formation assisted through π-stacking interactions among the axial ligands[63] are considered the main reasons for this high catalytic performance.

Scheme 4 shows a schematic drawing of the proposed I2M mechanism for mononuclear complexes containing the bda^{2-} ligand. In this particular case, the catalytic cycle starts similarly to that of WNA, reaching a Ru(V)=O species from Ru(II)-H_2O through mainly PCET processes (1-3). Then, the equilibrium between the Ru(V)=O and Ru(IV)=O$^{\bullet}$ species (4) allows the dimerization of the complex, forming the corresponding peroxide intermediate Ru(IV)-O-O-Ru(IV) (5), which is highly favored by π-stacking interactions between the axial pyridyl ligands.[63] The next step is the reductive elimination of the bridging peroxido ligand to form dioxygen (6), which is the rds and closes the catalytic cycle.

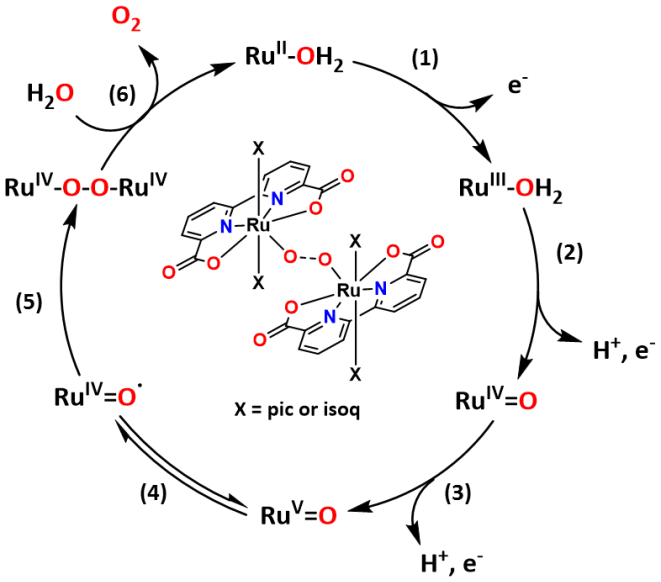

Scheme 4. Schematic drawing of the proposed I2M mechanism for water oxidation for mononuclear complexes **13-17** triggered with Ce^{IV} at pH 1. Abbreviations: pic = 4-Methylpyridine; isoq = Isoquinoline

In a follow up study, Sun *et al.* took advantage of the bda^{2-} framework and tuned the axial ligands, developing a new set of complexes (**14-17**, Chart 2).[64] Still with Ce^{IV} as sacrificial oxidant, a high reaction rate (TOFs of 380-1000 s^{-1}) and elevated TON values (11300-101000) were achieved (Table 2).

Recently, Llobet, Sala and co-workers synthetized and tested a new Ru mononuclear complex based in the ligand tda^{2-} ([2,2′:6′,2″-terpyridine]-6,6″-dicarboxylate), shown as complex **18** in Chart 2.[65] Its catalytic performance was measured by electrochemical methods, achieving the impressive TOF values of 8000 s^{-1} and 50000 s^{-1} at pH 7.0 and 10.0, respectively, according to foot of the wave analysis

(FOWA).[66] This represents the best results ever reported for molecular water oxidation catalysis. The high catalytic activity is mainly assigned to two factors: a) the easy access to high oxidation states and stabilization of a seven coordination environment for Ru, provided by the anionic ligand tda^{2-}, and b) the presence of a pendant base, which acts as a proton acceptor and has a key role during the critical O-O bond formation step. In contrast with the I2M mechanism identified for Ru-bda^{2-} complexes, Ru-tda^{2-} forms the O-O bond through the nucleophilic attack of a water molecule to a M-O species (WNA). Given that this pathway is not affected by the restricted mobility of the catalyst, this fact has been found particularly relevant when targeting to the generation of efficient anodes[67] and photoanodes[68] by grafting this molecular complex at the surface of an electrode material.

1.2.3 Copper-based molecular complexes

Copper-based WO catalysts have lately attracted the attention due to the high abundance and low cost of this metal and the potential simplicity in the synthesis of these systems. Thus, the application of copper-based molecular catalysts for WO is a novel and emerging research area. The first homogeneous copper WOC was $[(bpy)Cu(\mu\text{-}OH)]_2^{2+}$, reported by Mayer *et. al.* in 2012.[18] It was observed that a simple bypiridine copper complex can be assembled giving rise the formation of an active copper dinuclear dimer, which at high pH exhibits an equilibrium with its monomeric $[(bpy)Cu(OH)_2]$ form (**19** in Chart 3), the real responsible for the whole catalytic activity -a high TOF of 100 s^{-1} was achieved at 750 mV overpotential at pH 12.5 (Table 3).

In a follow up study, Meyer and co-workers developed complex **20** (Chart 3), containing a triglycylglycine macrocyclic ligand (H_4TGG), which was able to electrocatalytically oxidize water diminishing the overpotential down to 520 mV at pH 11.[19] This complex displayed stable catalytic activity for at least 5 hours, with moderate TON ~13 and a 99% Faradaic efficiency (Table 3).

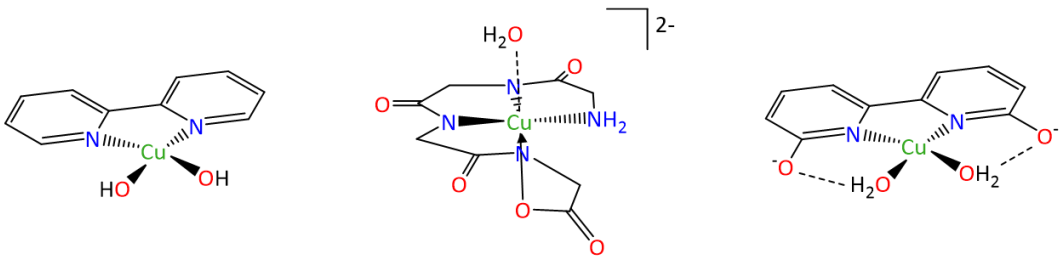

19 **20** **21**

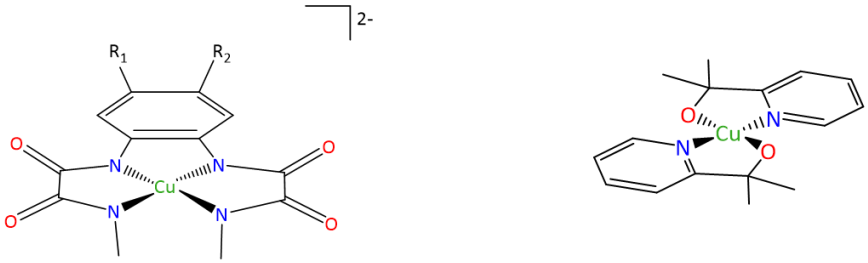

R_1=R_2= H, **22**
R_1=R_2= Me, **23**
R_1= H, R_2= OMe, **24**
R_1=R_2= OMe, **25**

26

Chart 3. Structure of the most relevant molecular copper-based WO catalysts.

Recently, Lin *et. al*. developed a "biomimetic" copper-based WOC (**21** in Chart 3 and Table 3).[20] This work was the first example of the use of non-innocent ligands, which can facilitate the PCET events and influence the catalytic activity of the complex. Subsequently, Llobet and co-workers prepared a new family of Cu complexes (**22**-**25**) capable of oxidizing water containing tetradentate amidate redox active ligands[21] capable of oxidizing water. By exchanging the substituents of the ligand, the overpotential can be drastically reduced until a value of only 170 mV when the phenyl ring is substituted with two methoxy groups (**25**) (Table 3). It is generally accepted that redox-active ligands in all these complexes avoid the problematic formation of Cu(IV)=O/Cu(III)-O$^{\bullet}$ intermediates thanks to the formation of highly electrophilic –OH moieties that avoid the need to reach the Cu(IV) state.[69]

Finally, a robust Cu complex was recently reported by Brudvig and co-workers (**26** in Chart 3), which is capable of oxidizing water over 12 h with only ~20% of catalyst degradation, obtaining a TON above 30.[70] However, this complex operates at much higher overpotential (520-580 mV) compared to complex **25** (Table 3).

Table 3. Summary of catalytic WO data for Cu complexes discussed along the text.

Complex	*pH*	η (V)[a]	TON	k_{obs}, s^{-1}[,b]	Ref.
19	12.5	~750	-	100	18
20	11.0	~650	-	33	19
21	12.4	~540	400	0.4	20
22	11.5	600	1947	3.56	21
23	11.5	400	-	3.58	21
24	11.5	270	-	0.43	21
25	11.5	170	-	0.16	21
26	10.4-13.3	~520-580	~30	~0.7	70

[a] Measured by DPV for complexes **21-24** and from the initial foot of the half-peak potential of electrocatalytic wave (CVs) for the rest. [b] Measured by FOWA in complexes **21-24** and other methodologies for the rest. [d] TOF_{max} obtained by electrochemical methods using foot of the wave (FOWA) analysis.

1.2.4 Other transition metal complexes as WO catalysts

Ru and Cu WO catalysts have been carefully discussed in the previous sections given their central role in this PhD Thesis. However, as mentioned before, other metals have attracted interest in this field due to their high abundance and low prize and/or their high catalytic activity. The following is a short summary of the most representative examples of each relevant transition metal.

1.2.4.1 Iridium

Despite the fact that it is not an earth abundant metal, iridium molecular complexes have gained popularity as WOCs during the last years. The first family of homogeneous iridium WO catalysts was reported by Bernhard *et al* in 2008 (**27a-e** in Chart 4).[71] These new family of complexes bearing cyclometalated phenylpyridine ligands (ppy), achieved catalytic activity for several days, demonstrating the promising future of Ir as WO catalysts.

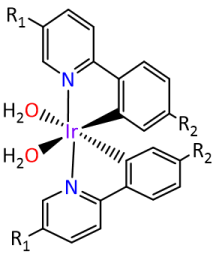

R_1=R_2= H, **27a**
R_1= Me, R_2= H, **27b**
R_1= Me, R_2= Ph, **27c**
R_1= Me, R_2= F, **27d**
R_1= Me, R_2= Cl, **27e**

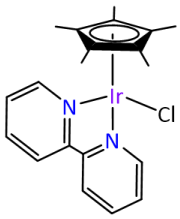

28

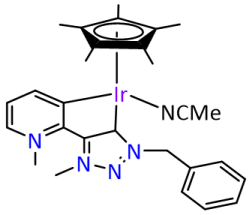

29

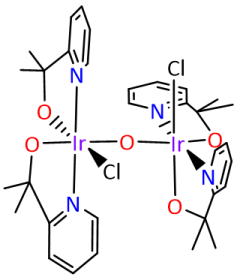

30

Chart 4. Structure of relevant Ir complexes able to perform WO catalysis.

Inspired by the work of Bernhard, Crabtree and co-workers reported a new family of iridium-based WO catalysts containing the pentamethylcyclopentadienyl (Cp*) ligand and cyclometalated N,N-bidentate ligands.[72] The best results were obtained with **28**, which achieved an initial TOF of 0.24 s^{-1} and a TON ~320 at pH 0.87 when Ce(IV) was used as sacrificial oxidant. In a follow up study, Albrecht *et. al*. prepared a wide variety of Ir complexes containing carbene-type ligands, which significantly improved the performance in WO catalysis, obtaining for **29** a TON of ~10000 at pH ~1.[73] Despite the long-term activity obtained with Ir-based complexes, full characterization of the active species is not straightforward due to the partial or complete oxidation of the ligands under the strong oxidizing conditions used,[74] or decomposition forming IrO_x materials.[75] Moreover, several studies indicate that some of these complexes are only the precursors of the real active catalysts.[76] A recent example is the transformation of the precursor [Cp*Ir(pyalk)Cl] in the real active species (**30** in Chart 4). This behavior difficults the understanding of their catalytic performance and the rational design of improved iridium-based WO catalysts.[76]

1.2.4.2 Cobalt

Compared to other first-row transition metals such as manganese and iron, molecular cobalt-based WO catalysts have evolved very fast. Berlinguette *et al.* reported in 2011 the first example of a Co complex which was capable of electrochemically oxidize water *via* a PCET mechanism at a pH range of 7.6-10.3 (**31** in Chart 5).[77] However, the real nature of the active species was further discussed after subsequent

studies, which highlighted how small quantities (1-2%) of free Co(II) ions dissociated from the parent complex are capable of catalyzing the oxidation of water.[78]

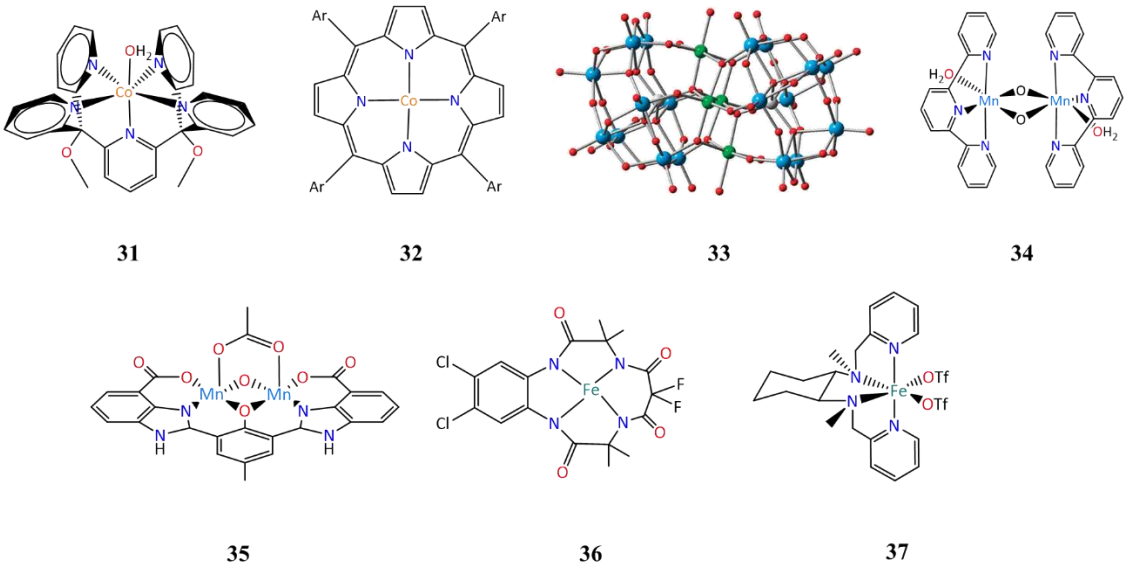

Chart 5. Structure of most relevant Co, Mn and Fe complexes able to perform WO catalysis. Drawing of the X-ray structure of **33** has been taken from the corresponding reference.[46] Color code: Co, green; O, red; Si, blue; W, white.

In follow up studies, a wide variety of Co molecular complexes bearing corroles,[79] porphyrines,[80] salen-base ligands,[81] polyoxometalates,[82,83] and the bpp^- ligand[27] were synthetized and tested in water oxidation catalysis. Despite Co-based molecular complexes show promising activities and are based on a relatively abundant metal, their stability under catalytic conditions and, therefore, the real nature of the active species, have been a matter of debate. A recent example of the instability of these systems has been reported for a Co porphyrin **32** (Chart 5), which was initially described to act in a molecular manner but that recent Synchrotron-based studies have showed the formation of heterogeneous CoO_x as active species.[84] Another example is the Co-based POM **33**, reported in 2010 by Hill *et. al.*, which achieved a good catalytic performance when triggered either electrochemically (E = 1.3 V vs. NHE, pH 8),[82] chemically ($[Ru(bpy)_3]^{3+}$ as sacrificial oxidant),[82] or photocatalitically ($[Ru(bpy)_3]^{2+}$ as photosensitizer).[85] However, ulterior studies showed again that the nature of the real catalyst and the evolution of the POM to cobalt oxide was strongly dependent of the catalytic conditions.[86] Despite the identification of the real active species is not always straightforward in these systems, important progress in the development and application of Co-based POMs in WO catalysis have been made during the last years.[83]

1.2.4.3 Manganese

The use of manganese in WOCs is specially attractive due to the high natural abundance and low cost of this metal and also because this is the metal which catalyzes WO in the OEC of PSII. In 1999 Crabtree developed the first dinuclear manganese complex capable of oxidizing water into molecular oxygen (**34** in Chart 5).[87] In ulterior studies, several manganese-based catalysts have been reported and tested in WO catalysis.[88] However, isotopic labeling studies confirmed that part of the O_2 formed during the catalysis was derived from the sacrificial oxidant. Finally, Åkermark and co-workers reported new manganese molecular complexes bearing imidazole and carboxylate groups, which lower the oxidation potential of the metal complex (**35** in Chart 5).[89] This decrease in the potential allows their compatibility with oxygen-free sacrificial oxidants such as $[Ru(bpy)_3]^{3+}$. To sum up, despite the intrinsic interest in using Mn complexes in WO catalysis, the catalytic performance of the available complexes is in general relatively modest, and often doubts about the origin of the produced oxygen – water or decomposition of the sacrificial oxidant employed – arise.

1.2.4.4 Iron

The low cost, low toxicity and high natural abundance have made iron a promising metal to be used in molecular WO catalysis. In 2010, Bernhard and co-workers reported the first family of iron molecular complexes capable of oxidizing water into oxygen, achieving moderate turnover numbers TOFs (>1.3 s^{-1}) when Ce^{IV} was used as sacrificial oxidant (**36** in Chart 5).[23] Soon afterwards, Lloret-Fillol, Costas *et al.* reported a wide variety of Fe molecular complexes bearing tetradentante ligand frameworks, which catalyzed WO. The best results were reported with complex **37**, which achieved a TON of 360 and a TOF of 0.23 s^{-1} and a TON ~1050 and a TOF of 0.06 s^{-1} when using Ce^{IV} and $NaIO_4$ as sacrificial oxidants, respectively.[90] Again, in the case of iron serious concerns about the real molecular nature of the active species present during the catalytic WO cycle have been reported.[91]

1.3 Hydrogen evolution catalysis

As mentioned previously, the typical water splitting device consists in two half reactions taking place in two different compartments: water oxidation at the anode, which releases four protons, four electrons and one molecule of oxygen, and the hydrogen evolution reaction at the cathode, using the protons and electrons released in the WO reaction, producing H_2, an attractive clean and highly energetic fuel that only produces water as by-product when burnt under O_2 in an electrochemical hydrogen fuel cell.

Analogously to WO, HER requires a cheap, efficient and robust catalyst which operates at low overpotential with respect to the thermodynamic potential (E^o = 0 V vs. NHE at pH = 0).[92] In terms of activity and efficiency, the best catalyst for HER is undoubtedly platinum, which operates near to the thermodynamic potential.[93] However, this non-abundant and expensive metal is not available in high amounts[94] and hampers the future large-scale industrial applications. Nature uses hydrogenases, which are capable of catalyzing the reversible reaction $2H^+ + 2e^- \leftrightarrow H_2$, using mainly Fe and Ni as catalytic sites.[95] Therefore, chemists, inspired by nature, have sought the design of new and effective catalysts for the hydrogen evolution reaction (HER) based in abundant transition metals.

During the last decades, several coordination metal complexes of Ni,[96] Fe,[97] Co[98] and Mo[99] capable of reducing protons into molecular hydrogen have been reported. However, due to the work carried out during this PhD Thesis, we will focus on the use of heterogeneous materials as catalysts for the HER, which have been usually based on Ni, Co, Mo, Fe, Pt or Ru or mixtures of them.

1.3.1 Benchmarking methodology for heterogeneous materials for HER catalysis

During the last decades, efforts have focused in the development of efficient and robust heterogeneous materials for their application in HER. Interestingly, a standard benchmarking protocol for comparing the different catalysts was developed in 2015 by Jaramillo *et al*.[100] In this work, the authors evaluate the WO and HER catalytic activity and stability of a family of noble and non-noble metal materials in strong acid and basic conditions. The benchmarking methodology is depicted in Figure 8, which through the combination of a series of electrochemical techniques allows straightforward, cheap and

preliminary evaluation of the catalytic activity of metals and metal oxides in HER and WO.

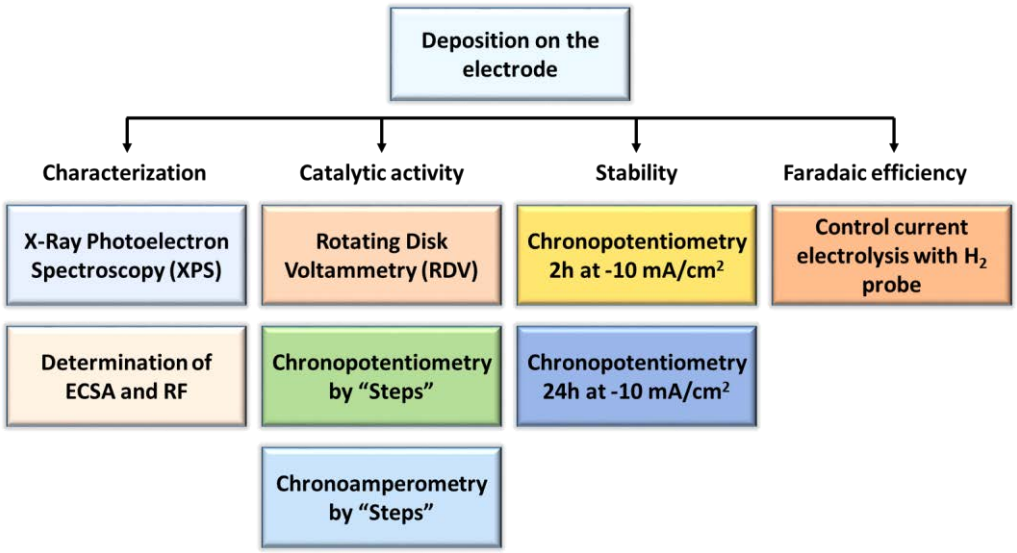

Figure 8. Schematic representation for the benchmarking protocol of heterogeneous catalysts for HER reported by Jaramillo and co-workers.[100]

The characterization of the catalyst is performed by the combination of two different techniques. First, the elemental composition of the material deposited in the electrode is determined by XPS. Second, the Electrochemically Active Surface Area (ECSA) and the so-called Roughness Factor (RF) are estimated by the double-layer capacitance measurement of the system from their cyclic voltammograms (CV) in a non-Faradaic region according to the following equations, where i_c is the current assumed to be due to the double-layer charging, C_{DL} is the double layer capacitance, v is the scan rate, S is the surface of the electrode and C_S is the specific capacitance based on typical values reported for metal electrodes in different aqueous solutions previously reported in the literature.[101]

$$i_c = vC_{DL} \quad \text{Eq. 5}$$

$$ECSA = \frac{C_{DL}}{C_S} \quad \text{Eq. 6}$$

$$RF = \frac{ECSA}{S} \quad \text{Eq. 7}$$

Finally, the catalytic activity of the systems is measured using a combination of Rotating Disk Voltammetry (RDV), controlled current chronopotentiometric experiments by "steps" and controlled potential chronoamperometric experiments by "steps". From these experiments, the benchmarking overpotential (η) necessary to achieve a current density of 10 mA/cm^2, which is the current density expected at the cathode for a 10% efficient solar water- splitting device, is obtained.[101,102]

Furthermore, the stability of active catalysts is evaluated by controlled current chronopotentiometric experiments during 2 h, while their Faradaic Efficiency (FE) can be determined after a controlled potential electrolysis by determining the amount of hydrogen formed using a H_2-sensitive Clark probe.

Figure 9 shows the η measured using this methodology to achieve a 10 mA/cm^2 current density for several metals and metal alloys at acidic and basic pH. The results show that NiMo-(a) and NiMoCo achieved a similar activity than Pt-based catalysts, with overpotentials ($\eta_{10\ \mathrm{mA/cm^2}}$) close to -0.05 V at acidic pH. In case of basic pH values, several non-noble materials showed similar activity than platinum at basic pH, including NiMo-(a), NiMoCo, CoMo, NiMo-(b), NiFe-(a) and NiMoFe-(a), showing a reasonable stability under a constant operating current density of 10 mA/cm^2. However, a larger loading of catalyst (~100 times larger) is still required for achieving similar overpotentials than those of Pt-based cathodes.

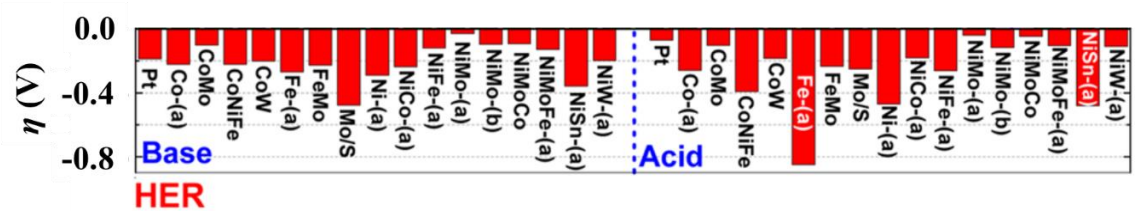

Figure 9. Overpotential necessary to achieve a current density of 10 mA/cm^2 after two hours of controlled current electrolysis for different metal films and alloy films. The measurements in basic conditions were performed at *pH* = 14 and those under acidic conditions at *pH* = 0.[100]

1.3.2 Mechanistic considerations of HER catalysis driven by heterogeneous catalysts

The mechanism generally accepted for HER in basic media is depicted in Figure 10.[103] The first step consists in the so-called Volmer or discharge step, where a single

electron transfer takes place between the heterogeneous catalyst and the water molecules, provoking the adsorption of hydrogen atoms on the surface and the release of OH^- to the media. After the generation of the adsorbed hydrogen atoms, the reaction can proceed by two different pathways, either recombination of two adsorbed hydrogen atoms (Tafel mechanism) or protonation of an adsorbed hydrogen atom coupled with an electron transfer (Heyrovsky mechanism), finally provoking the release of H_2 molecules.

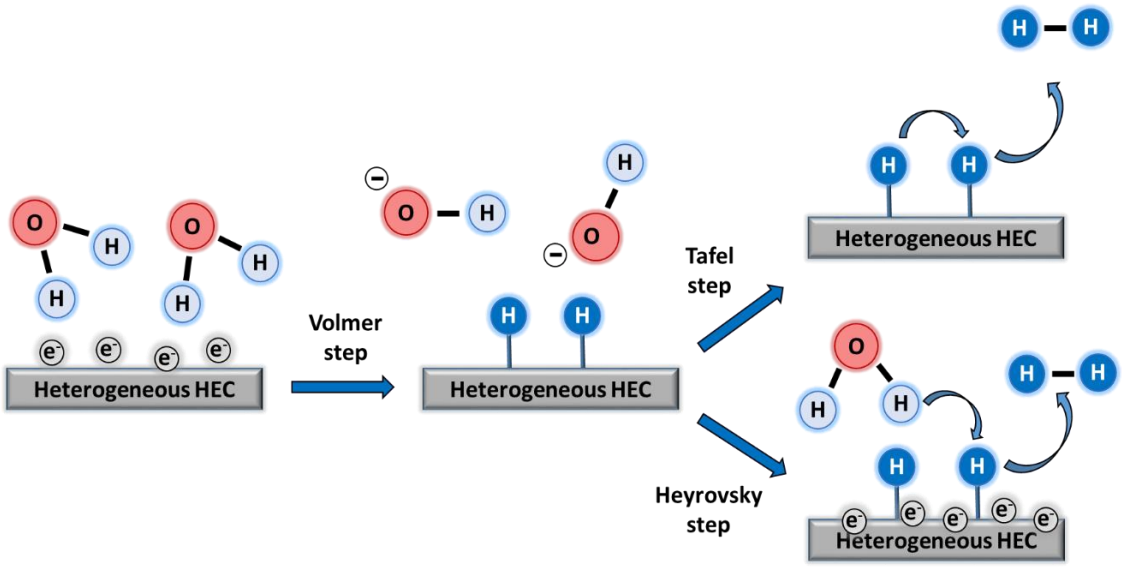

Figure 10. Schematic representation of the Volmer-Tafel and Volmer-Heyrovky mechanisms for heterogeneous catalytic HER in neutral-basic media.

Mechanistic information can be easily extracted from the representation of the overpotential (η) vs. the logarithm of the current density, the so-called Tafel diagrams. A Tafel slope of approximately 100 mV indicates that the discharge (Volmer) step is the rate limitting step. On the other hand, lower values of Tafel slope are characteristic of rate limiting Tafel and Heyrovsky steps.[103,104]

As could be expected, the strength of the metal-adsorbed hydrogen interaction plays a determining role in the catalytic activity of the different materials. The relationship between the logarithm of the exchange current densities (j_0) for HER in acidic media vs. ΔG of hydrogen adsorption (ΔG_{H^*}) is usually represented in the so-called Volcano-type diagrams.[105] Recently, computational studies have provided support for the interpretation of Volcano-type diagrams by calculating ΔG_{H^*} for a number of metal surfaces (Figure 11).[104,106]

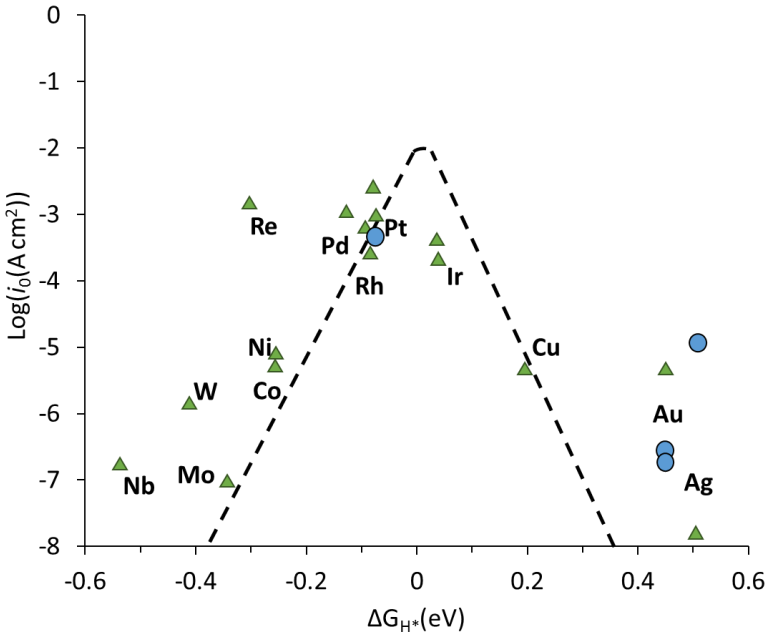

Figure 11. Volcano type diagram for different polycrystalline (▲) and Single-crystal (●) metal surfaces and their electrocatalytic activity towards catalytic HER in acidic media. The log of the experimentally obtained current density (i_0) is plotted versus the calculated free energy for hydrogen adsorption interaction (ΔG_{H^*}) for each metal surface.[104]

The two branches of the volcano curve diagram represented in Figure 11 can be understood in the following way: the metals located in the left branch of the volcano diagram with negative ΔG_{H^*} show strong M-H* interactions, which facilitates the Volmer step but retards the Tafel and Heyrovsky steps. On the other hand, metals situated at the right-hand branch, with large positive ΔG_{H^*}, show weak M-H* interactions, thus favouring the Tafel and Heyrovsky steps but significantly retarding or hampering the Volmer step.[104,106] Thus, a compromise between both tendencies, finding an equilibrium between a favourable adsorption and an easy recombination/protonation step as well, is desirable in order to get a potential fast heterogeneous HER catalyst. As first suggested by Parsons,[107] the optimum value should be around $\Delta G_{H^*} = 0$. The noble metals Rh, Ir and Pt possess a ΔG_{H^*} value close to 0, and therefore high HER catalytic activities are expected. However, we are interested in designing efficient and robust HER catalysts, not entirely constituted by expensive and limited precious metals. Non-noble metals such as Ni, Co, W or Mo, despite a bit far from the center of the volcano plot, have shown to be good candidates for this purpose.

1.3.3 Heterogeneous non-noble HER catalysts

During the last years, some efforts have focused in the combination of Pt with non-noble metals in order to reduce the noble metal loading through the supporting of Pt monolayers on low-cost materials such as Mo_2C[108] or WC[109] or by developing Pt_3Ni nanostructures,[110] obtaining good results in terms of stability and activity towards HER catalysis. However, the final objective is to completely avoid the use of Pt in the cathodes.

Nanoparticulate systems are promising materials as they provide high surface areas with relatively small catalyst loadings[111] and an easy synthesis/characterization compared with films and other heterogeneous materials.[112] These characteristics have converted NPs into a matter of great interest as electrocatalysts for water splitting. An example based on non-noble metals can be found with MoS_2 NPs, which achieves a moderate electrocatalytic activity (0.18 mA/cm^2, at η = -150 mV) at pH 0.24.[113] The catalytic activity for MoS_2 towards HER catalysis has been extensively studied through the design of diverse materials such as mesoporous structures[114] or MoS_2 NPs deposited onto reduced graphene oxide,[115] obtaining higher current densities than 10 mA/cm^2 at overpotentials as low as -150 to 230 mV.

Also, electrocatalytic active Ni-based materials have been reported, such as Ni_2P NPs, showing good activity and stability in acidic aqueous media, with current densities of 20 mA/cm^2 at η = -130 mV at acidic pH and η = -205 mV under basic conditions.[116] More recently, Ni-C-N nanosheets have also been developed and their catalytic activity has been tested, reaching overpotentials as low as -60.9 mV for obtaining 10 mA/cm^2 current densities, close to the ideal overpotential shown by Pt in acidic media, and displaying also long term stability (active after 70 h).[117]

Finally, the mixture of non-noble metals has been also tested electrochemically in HER, including Ni-Mo,[118] Fe-Ni-S (INS)[119] and Ni-Co-S,[120] which display a higher electrocatalytic activity than their monometallic counterparts, showing how combining the properties of two catalytically active metals helps improving the efficiency of the resulting materials.

1.3.3.1 Cobalt nanoparticles as heterogeneous HER catalysts

Due to the low price and significant catalytic activity towards HER catalysis, cobalt-based materials have emerged in the past decades, consolidating their presence in

the field. In particular, as we mentioned before, nanoparticulated materials are promising candidates for this reaction. To date, several examples of electrocatalytically active Co NPs towards HER can be found in the literature. Table 4 summarizes the HER catalytic performances of some Co-derived NP systems.

A clear example of good catalytic performance can be found with CoP NPs, which can be easily synthetized from $[Co_2(CO)_8]$.[121] CoP NPs can be supported on Ti, achieving catalytic currents of 10 mA/cm^2 at relatively low overpotentials (-75 mV), showing high stability in acidic solutions and no evidence of degradation over 24 h of catalysis (entry 1, Table 4).

In order to improve the dispersibility and increase the catalytic surface area, Co and Co/CoO_x NPs have also been immobilized on N-doped carbon structures such as nanotubes[122] and graphitic carbon,[123] achieving 10 mA/cm^2 at η = -314-210 mV (entries 2-4, Table 4), working both at basic and acidic pH values. Moreover, the introduction of these C-based structures improves the electron transfer and mass transport while preventing the aggregation of the NPS, enhancing therefore their stability during catalysis.[124] Other structures, such as nanofibers[125] and nanopolyhedrons[126] bearing cobalt-based NPs have been also reported as HER catalysts, reaching good catalytic performances (entries 5 and 6, Table 4).

Table 4. Summary of HER catalytic data for Co-derived NPs and other Co-based nanomaterials discussed along the text

Entry	System	Overpotential[a] (mV)	pH	Comments	Ref.
1	CoP/Ti	-75	0	CoP NPs supported onto Ti electrodes	121
2	Co@NCNT	-210 -250	0 13	Co NPs emdebbed in N-Doped Carbon Nanotubes	122
3	Co@Co-N-C	-314	13	Co NPs encapsulated inside Co-N-doped carbon	123a
4	Co/CoO@Co–N-C	-280	13	Co NPs inmobilizaed on Co-N-doped carbon	123b
5	Co@CNF	-196	14	Co NPs integrated in carbon nanofibers	125
6	Co-P/NC	-154	14	CoP/Co_2P NPs embedded in N-doped carbon matrices	126
7	Co NPs	-540	7	Co NPs formed by decomposition of a Co complex	128
8	$Co(OH)_2/C_3N_4$	Photocatalysis	-	$Co(OH)_2$ NPs in carbon nitride	130
9	Co-IONR	Photocatalysis	-	Co NPs on α-Fe_2O_3 nanorings	131
10	Co-P	-94	14	Co-P films deposited on GCE	132
11	Co/CoO NWs	-35	14	Co/CoO nanowire array on Ni foam	133
12	CoP/CC	-67	0	CoP nanowire array on carbon cloth	134
13	CoS_2 NWs	-145	0	CoS_2 nanowires supported on a graphite disk	135
14	Tetsubo-like $Co(OH)_2$ NRs	-69	14	$Co(OH)_2$ supported in MECN	136
15	$Co(OH)_2$@PANI HNSs	-65	14	$Co(OH)_2$ supported by Ni foam containing PANI	137

[a] Overpotential necessary to achieve a current density of 10 mA/cm^2. Abbreviations: MECN = macroporous electrically conductive network; PANI = Polyaniline, PPh_3 triphenylphosphine.

The formation of Co NPs from the decomposition of molecular complexes under oxidative or reductive stress must also be taken into account. Several examples can be found in the literature for cobalt-based molecular complexes tested for WO catalysis,[127] but also for HER catalysis. An example of this was reported in 2012 by Savéant *et al.*[128] when testing the HER catalytic activity of the molecular Co complex $[Co(dpg)_3(BF)_2]^+$ (Figure 12). After application of modest cathodic potentials (E = -0.75 V vs. NHE) in MeCN solutions containing $HClO_4$, Co NPs where formed and deposited onto the glassy carbon electrode, which resulted good HER electrocatalysts when placed in a clean pH 7 solution (Figure 12 and entry 7, Table 4). In this scenario, the coordination environment around the metal centre plays a key role in the morphology and degree of dispersion of the formed NPs.[129]

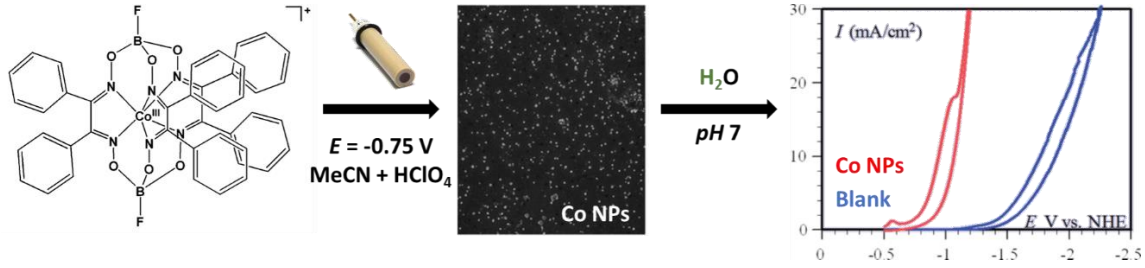

Figure 12. Schematic representation of the degradation of $[Co(dpg)_3(BF)_2]^+$ (Left) under reductive stress forming Co NPs deposited onto the GC working electrode (Center), which are electrocatalytically active in HER at pH 7 (Right).

Co NPs have also been used as co-catalysts implanted on graphitic carbon nitride ($g\text{-}C_3N_4$)[130] and $\alpha\text{-}Fe_2O_3$ nanorings[131] in photocatalytic HER, improving the efficiency of these systems (entries 8 and 9, Table 4).

1.3.3.2 Other cobalt-based materials and nanostructures as HER catalysts

Although cobalt NPs are good candidates for HER catalysis, simple electrodeposited Co-P films deposited onto glassy carbon electrodes are also capable of reducing protons into hydrogen raising catalytic currents of 10 mA/cm^2 at overpotentials of 94 mV under basic conditions (entry 10, Table 4).[132]

In follow up studies, several examples of nanostructurated cobalt-based materials have been reported and their catalytic activity has been tested in HER. These nanomaterials include Co/CoO,[133] CoP,[134] CoS_2 nanowires,[135] $Co(OH)_2$ nanorods[136] and $Co(OH)_2$ nanosheets,[137] which can be grown in different kind of supports such as Ni foam,

carbon cloth or graphite disks, forming 3D electrodes with high surface areas and a clear improvement of their overpotentials (entries 11-15, Table 4).

1.4 References

[1]Armaroli, N.; Balzani, V. *Angew. Chem. Int. Ed.* **2007**, *46*, 52-66.

[2] (a) Karl, T. R.; Trenberth, K. E. *Science* **2003**, *302*, 1719-1723 (b) Omae, I. *Coord. Chem. Rev.* **2012**, *256*, 1384-1405 c) Wang, W.; Wang, S.; Ma, X.; Gong, J.; *Chem. Soc. Rev.* **2011**, *40*, 3703-3727.

[3] Edenhofer, O.; Pichs-Madruga, R.; Sokona, Y.; Farahani, E.; Kadner, S.; Seyboth, K.; Adler, A.; Baum, I.; Brunner, S.; Eickemeier, P.; Kriemann, B.; Savolainen, J.; Schlomer, S.; Von Stechow, C.; Zwickel, T.; Minx, J.C. (eds). *IPCC: Climate Change 2014. Mitigation of Climate Change. Working Group III Contribution to the Fifth Assessment Report of the Intergovernmental Panel on Climate Change.* Cambridge University Press.

[4] Styring, S. *Faraday Discuss.* **2012**, *155*, 357-376.

[5] Karlsson, S.; Boixel, J.; Pellegrin, Y.; Blart, E,; Becker, H.-C,; Odobel, F.; Hammarstrom, L. *Faraday Discuss.* **2012,** *155***,** 233-252.

[6] (a) Hurst, J. K. *Science.* **2010**, *328*, 315-316. (b) Sanderson, K. *Nature*, **2008**, *452*, 400-402.

[7] (a) Nelson, N.; Ben-She, A. *Nat. Rev. Mol. Cell. Biol.* **2004**, *5*, 971-982; (b) McEvoy, J. P.; Brudvig, G. W. *Chem rev.* **2006**, *106*, 4455-4483; (c) Kärkäs M. D.; Verho O.; Johnston E. V.; Åkermark B, Chem. Rev. **2014**, 114, 11863-12001.

[8] Romain, S.; Vigara L.; Llobet, A. *Acc. Chem. Res* **2009**, *42*, 1944-1953.

[9] Suga, M.; Akita, F.; Hirata, K.; Ueno, G.; Murakami, H.; Nakajima, Y.; Shimizu, T.; Yamashita, K.; Yamamoto, M.; Ago, H.; Shen, J.-R. *Nature* **2015**, *517*, 99-103.

[10] (a) Umena, Y.; Kawakami, K.; Shen, J.-R.; Kamiya, N. *Nature* **2011**, *473*, 55-60; (b) Glöckner, C.; Kern, J.; Broser, M.; Zouni, A.; Yachandra, V.; Yano, J. *J. Biol. Chem.* **2013**, *288*, 22607-22620; (c) Blomberg, M. R. A.; Borowski, T.; Himo, F.; Liao, R.-Z.; Siegbahn, P. E. M. *Chem. Rev.* **2014**, *114*, 3601-3658.

[11] Nielander, A. C.; Shaner, M. R.; Papadantonakis, K, M.; Francis, S. A.; Lewis, N. S. *Energy Environ.* Sci. **2015**, *8*, 16–25.

[12] McKone, J. R.; Lewis, N. S.; Gray, H. B.; *Chem. Mater.* **2014**, *26*, 407−414.

[13] Fabian, D. M.; Hu, S.; Singh, N.; Houle, F. A.; Hisatomi, T.; Domen, K.; Osterlohf, F. E.; Ardo, S. *Energy Environ. Sci.* **2015**, *8*, 2825-2850.

[14] Parent, A. R.; Crabtree, R. H.; Brudvig, G. W. *Chem. Soc. Rev.* **2013**, *42*, 2247-2252.

[15] Pellegrin Y.; Odobel F. *C. R. Chimie* **2017**, *20*, 283-295.

[16] Pourbaix, M. *Atlas of Electrochemical Equilibria in Aqueous Solutions*; Pergamon Press: Oxford, 1966.

[17] Inoue, H.; Shimada, T.; Kou, Y.; Nabetani, Y.; Masui, D.; Takagi, S.; Tachibana, H. *ChemSusChem* **2011**, *4*, 173-179.

[18] Barnett, S. M.; Goldberg, K. I.; Mayer, J. M. *Nat. Chem.* **2012**, *4*, 498-502.

[19] Zhang, M.-T.; Chen, Z.; Kang, P.; Meyer, T. J. *J. Am. Chem. Soc.* **2013**, *135*, 2048-2051.

[20] Zhang, T.; Wang, C.; Liu, S.; Wang, J.-L.; Lin, W. *J. Am. Chem. Soc.* **2014**, *136*, 273-281.

[21] Garrido-Barros, P.; Funes-Ardoiz, I.; Drouet, S.; Benet-Buchholz, J.; Maseras, F.; Llobet, A. *J. Am. Chem. Soc.* **2015**, *137*, 6758-6761.

[22] Garrido-Barros, P.; Gimbert-Suriñach C.; Moonshiram D.; Picon A.; Monge P.; Batista V. S.; Llobet A. *J. Am. Chem. Soc.* **2017**, *139*, 12907-12910.

[23] Ellis, W. C.; McDaniel, N. D.; Bernhard, S.; Collins, T. J. *J. Am. Chem. Soc.* **2010**, *132*, 10990-10991.

[24] Hull, J. F.; Balcells, D.; Blakemore, J. D.; Incarvito, C. D.; Eisenstein, O.; Brudvig, G. W.; Crabtree, R. H. *J. Am. Chem. Soc.* **2009**, *131*, 8730-8731.

[25] Cady, C. W.; Crabtree, R. H.; Brudvig, G. W. *Coord. Chem. Rev.* **2008**, *252*, 444-455.

[26] Leung, C.-F.; Ng, S.-M.; Ko, C.-C.; Man, W.-L.; Wu, J.; Chen, L.; Lau, T.-C. *Energy Environ. Sci.* **2012**, *5*, 7903-7907.

[27] Rigsby, M. L.; Mandal, S.; Nam, W.; Spencer, L. C.; Llobet, A.; Stahl, S. S. *Chem. Sci.* **2012**, *3*, 3058-3062.

[28] Gimbert-Suriñach, C.; Moonshiram, D.; Francàs, L.; Planas, N.; Bernales, V.; Bozoglian, F.; Guda, A.; Mognon, L.; López, I.; Hoque, M. A.; Gagliardi, L.; Cramer, C. J.; Llobet, A. *J. Am. Chem. Soc.* **2016**, *138*, 15291-15294.

[29] Bozoglian, F.; Romain, S.; Ertem, M. Z.; Todorova, T. K.; Sens, C.; Mola, J.; Rodriguez, M.; Romero, I.; Benet-Buchholz, J.; Fontrodona, X.; Cramer, C. J.; Gagliardi, L.; Llobet, A. *J. Am. Chem. Soc.* **2009**, *131*, 15176-15187.

[30] Concepcion, J. J.; Jurss, J. W.; Templeton, J. L.; Meyer, T. J. *J. Am. Chem. Soc.* **2008**, *130*, 16462-16463.

[31] Duan, L.; Bozoglian, F.; Mandal, S.; Stewart, B.; Privalov, T.; Llobet, A.; Sun, L. *Nat. Chem.* **2012**, *4*, 418-423.

[32] (a) Sala X.; Maji S.; Bofill R.; Garcia-Antón J.; Escriche L.; Llobet A.; *Acc. Chem. Res.* 2014, *47*, 504-516. (b) Garrido-Barros, P.; Gimbert-Suriñach, C.; Matheu R.; Sala X.; Llobet A.; Chem. Soc. Rev **2017**, *DOI: 10.1039/c7cs00248c.*

[33] (a) Ishizuka, T.; Ohzu, S.; Kojima T.; *Synlett.* **2014**, *25*, 1667-1679; (b) Farrás, P.; Benniston, A. C. *Tetrahedron lett.* **2014**, *55*, 7011-7014; (c) Li, F.; Yu, M.; Jiang, Y.; Huang, F.; Li, Y.; Zhang, B.; Sun, L. *Chem commun*, **2011**, *47*, 8948-8951; (d)Thompson, M. S.; De Giovani, W. F.; Moyer, B. A.; Meyer, T. J. *J. Org. Chem.* **1984**, *25*, 4972-4977; (e) Catalano, V. J.; Heck, R. A.; Immoos, C. E.; Hill, M. G. *Inorg. Chem.* **1998**, *37*, 2150-2157; (f) Che, C-M; Ho, C.; Lau, T-C. *J. Chem. Soc. Dalton Trans.* **1991**, 0, 1901-1907; (g) Che. C-M.; Cheng, K-W.; Chan, M. C. W.; Lau. T-C.; Mak, C-K. *J. Org. Chem.* **2000**, *65*, 7996-8000: (g) Stultz, L. K.; Huynh, H. V.; Binstead, R. A.; Curry, M.; Meyer, T. J. *J. Am. Chem. Soc.* **2000**, *122*, 5984-5996.

[34] Moyer, B. A.; Meyer, T. J. *J. Am. Chem. Soc.* **1978**, *100*, 3601-3603.

[35] Nagle, J. K.; Bernstein, J. S.; Young, R. C.; Meyer, T. J. *Inorg. Chem.* **1981**, *20*, 1760-1764.

[36] Meyer, T.J.; Huynh, M. H. V. *Inorg. Chem.* **2003**, *42*, 8140-8160.

[37] (a) Masllorens, E.; Rodríguez, M.; Romero, I.; Roglans, A.; Parella, T.; Benet-Buchholz, J.; Poyatos, M.; Llobet, A. *J. Am. Chem. Soc.* **2006**, *128*, 5306-5307; (b) Meyer, T. *J. Electrochem. Soc.* **1984**, *131*, 221C-228C.

[38] (a) Moyer, B. A.; Meyer T. J.; *Inorg. Chem.* **1981**, *20*. 436-444; (b) Binstead, R. A.; Moyer, B. A.; Samuels, G.J.; Meyer, T. J. *J. Am. Chem. Soc.* **1981**, *103*, 2897-2899.

[39] Che, C. M.; Yam, V. W. W. *Adv. Inorg. Chem.* **1992**, *39*, 233-325.

[40] Dovletoglou, A.; Adeyemi, S. A.; Meyer, T. J. *Inorg. Chem.* **1996**, *35*, 4120-4127.

[41] Gersten, S. W.; Samuels, G. J.; Meyer, T. J. *J. Am. Chem. Soc.* **1982**, *104*, 4029-4030.

[42] Gilbert, J. A.; Eggleston, D. S.; Murphy, W. R., Jr.; Geselowitz, D. A.; Gersten, S. W.; Hodgson, D. J.; Meyer, T. J. *J. Am. Chem. Soc.* **1985**, *107*, 3855-3864.

[43] (a) Collin, J. P.; Sauvage, J. P. *Inorg. Chem.* **1986**, *25*, 135-141; (b) Nagoshi, K.; Yamashita, S.; Yagi, M.; Kaneko. *J. Mol. Catal. A: Chem.* **1999**, *144*, 71-76.

[44] (a) Cape, J. L.; Hurst, J. K. *J. Am. Chem. Soc.* **2008**, *130*, 827-829; (b) Geselowitz, D.; Meyer, T. J. *Inorg. Chem.* **1990**, *29*, 3894-3896; (c) Chronister, C. W.; Binstead, R. A.; Ni, J.; Meyer, T. J. *Inorg. Chem.* **1997**, *36*, 3814-3815; (d) Binstead, R. A.; Chronister, C. W.; Ni, J.; Hartshorn, C. M.; Meyer, T. J. *J. Am. Chem. Soc.* **2000**, *122*, 8464-8473; (e) Liu, F.; Concepcion, J. J.; Jurss, J. W.; Cardolaccia, T.; Templeton, J. L.; Meyer, T. J. *Inorg. Chem.* **2008**, *47*, 1727-1752; (f) Moonshiram, D.; Alperovich, I.; Concepcion, J. J.; Meyer, T. J.; Pushkar, Y. *Proc. Natl. Acad. Sci. U.S.A.* **2013**, *110*, 3765-3770; (g) Moonshiram, D.; Jurss, J. W.; Concepcion, J. J.; Zakharova, T.; Alperovich, I.; Meyer, T.

J.; Pushkar, Y. *J. Am. Chem. Soc.* **2012**, *134*, 4625-4636; (h) Hurst, J. K.; Zhou, J.; Lei, Y. *Inorg. Chem.* **1992**, *31*, 1010-1017; (i) Lei, Y.; Hurst, J. K. *Inorg. Chim. Acta* **1994**, *226*, 179-185; (j) Yamada, H.; Siems, W. F.; Koike, T.; Hurst, J. K. *J. Am. Chem. Soc.* **2004**, *126*, 9786-9795; (k) Stull, J. A.; Britt, R. D.; McHale, J. L.; Knorr, F. J.; Lymar, S. V.; Hurst, J. K. *J. Am. Chem. Soc.* **2012**, *134*, 19973-19976.

[45] (a) Yang, X.; Baik, M.-H. *J. Am. Chem. Soc.* **2004**, *126*, 13222-13223; (b) Yang, X.; Baik, M.-H. *J. Am. Chem. Soc.* **2006**, *128*, 7476-7485. Batista, E. R.; Martin, R. L. *J. Am. Chem. Soc.* **2007**, *129*, 7224-7225; (c) Jurss, J. W.; Concepcion, J. J.; Butler, J. M.; Omberg, K. M.; Baraldo, L. M.; Graff Thompson, D.; Lebeau, E. L.; Hornstein, B.; Schoonover, J. R.; Jude, H.; Thompson, J. D.; Dattelbaum, D. M.; Rocha, R. C.; Templeton, J. L.; Meyer, T. J. *Inorg. Chem.* **2012**, *51*, 1345-1358.

[46] Sartorel, A.; Bonchi, M.; Campagna, S.; Scadola F. *Chem. Soc. Rev.* **2013**, *42*, 2262-2280.

[47] Sens, C.; Romero, I.; Rodríguez, M.; Llobet, A.; Parella, T.; Benet-Buchholz, J. *J. Am. Chem. Soc.* **2004**, *126*, 7798-7799.

[48] Neudeck, S.; Maji, S.; López, I.; Meyer, S.; Meyer, F.; Llobet, A. *J. Am. Chem. Soc.* **2014**, *136*, 24-27.

[49] Sander, A. C.; Maiji, S.; Francàs L.; Böhnisch, T.; Dechert, S.; Llobet, A.; Meyer, F. *ChemSusChem* **2015**, *8*, 1697-1702.

[50] Sartorel, A.; Carraro, M.; Scorrano, G.; De Zorzi, R.; Geremia, S.; McDaniel, N. D.; Bernhard, S.; Bonchio, M. *J. Am. Chem. Soc.* **2008**, *130*, *5006-5007.*

[51] Geletii, Y. V.; Botar, B.; Kögerler, P.; Hillesheim, D. A.; Musaev, D. G.; Hill, C. L. *Angew. Chem. Int. Ed.* **2008**, *47*, 3896-3899.

[52] Zong, R.; Thummel, R. P. *J. Am. Chem. Soc.* **2005**, *127*, 12802-12803.

[53] Tseng, H.-W.; Zong, R.; Muckerman, J. T.; Thummel, R. *Inorg. Chem*, **2008**, *47*, 11763-11773.

[54] Concepcion, J. J.; Tsai, M. K.; Muckerman, J. T.; Meyer, T. J. *J. Am. Chem. Soc.* **2010**, *132*, 1545-1557.

[55] Cao, R.; Lai, W.; Du, P. *Energy Environ. Sci*. **2012**, *5*, 8134-8157.

[56] Murakami, M.; Hong, D.; Suenobu, T.; Yamaguchi, S.; Ogura, T.; Fukuzumi, S. *J. Am. Chem. Soc.* **2011**, *133*, 11605-11613.

[57] Vigara, L.; Ertem, M. Z.; Planas, N.; Bozoglian, F.; Leidel, N.; Dau, H.; Haumann, M.; Gagliardi, L.; Cramer, C. J.; Llobet, A. *Chem. Sci.* **2012**, *3*, 2576-2586.

[58] Wasylenko, D. J.; Gamesamoorthy, C.; Koivisto, B. D.; Henderson, M. A.; Berlingette, C. P. *Inorg. Chem*. **2010**, *49*, 2202-2209.

[59] Roeser, S.; Farràs, P.; Bozoglian, F.; Mártinez-Belmonte, M.; Benet-Buchholz, J.; Llobet, A. *ChemSusChem*, **2011**, *4*, 197-207.

[60] Sartorel, A.; Miró, P.; Salvadori, E.; Romain, S.; Carraro, M.; Scorrano, G.; Di Valentin, M.; Llobet, A.; Bo, C.; Bonchio, M. *J. Am. Chem. Soc.* **2009**, *131*, 16051-16053.

[61] Duan, L.; Fischer, A.; Xu, Y.; Sun, L. *J. Am. Chem. Soc.* **2009**, *131*, 10397-10399.

[62] Duan, L.; Xu, Y.; Tong, L.; Sun, L. *ChemSusChem* **2011**, *4*, 238-244.

[63] Richmond, C. J.; Matheu, R.; Poater, A.; Falivene, L.; Benet-Buchholz, J. B.; Sala, X.; Cavallo, L.; Llobet, A. *Chem. Eur. J.* **2014**, *20*, 17282-17286.

[64] Wang, L.; Duan, L.; Wang, Y.; Ahlquist, M. S. G.; Sun, L. *Chem. Commun.* **2014**, *50*, 12947-12950.

[65] Matheu, R.; Ertem, M. Z.; Benet-Buchholz, J.; Coronado, E.; Batista, V. S.; Sala, X.; Llobet, A. *J. Am. Chem. Soc.* **2015**, *137*, 10786-10795.

[66] Matheu, R.; Neuveck, S.; Meyer, F.; Sala, X.; Llobet, A. *ChemSusChem*, **2016**, *9*, 3361-3369.

[67] Creus, J.; Matheu, R.; Peñafiel, I.; Moonshiram, D.; Blondeau,P.; Benet-Buchholz, J.; García-Antón, J.; Sala, X.; Godard,C.; Llobet, A. *Angew. Chem. Int. Ed.* **2016**, *55*, 1-6.

[68] Matheu, R.; Moreno-Hernandez I. A.; Sala, X.; Gray, H. B.; Brunschwig, B. S.; Llobet, A.; Lewis, N. S. *J. Am. Chem. Soc.* **2017**, *139*, 11345-11348.

[69] Koepke, S. J.; Light K. M.; VanNatta, P. E.; Wiley, K. M. *J. Am. Chem. Soc.* **2017**, *139*, 8586-8600.

[70] Fisher, K. J.; Materna, K. L.; Mercado, B. Q.; Crabtree, R. H.; Brudvig, G. W. *ACS Catal.* **2017**, *7*, 3384-3387.

[71] McDaniel, N. D.; Coughlin, F. J.; Tinker, L. L.; Bernhard, S. *J. Am. Chem. Soc.* **2008**, *130*, 210-217.

[72] (a) Hull, J. F.; Balcells, D.; Blakemore, J. D.; Incarvito, C. D.; Eisenstein, O.; Brudvig, G. W.; Crabtree, R. H. *J. Am. Chem. Soc.* **2009**, *131*, 8730-.8731; (b) Blakemore, J. D.; Schley, N. D.; Balcells, D.; Hull, J. F.; Olack, G. W.; Incarvito, C. D.; Eisenstein, O.; Brudvig, G. W.; Crabtree, R. H. *J. Am. Chem. Soc.* **2010**, *132*, 16017-16029.

[73] (a) Brewster, T. P.; Blakemore, J. D.; Schley, N. D.; Incarvito, C. D.; Hazari, N.; Brudvig, G. W.; Crabtree, R. H. *Organometallics* **2011**, *30*, 965-973; (b) Lalrempuia, R.; McDaniel, N. D.; Müller-Bunz, H.; Bernhard, S.; Albrecht, M.; *Angew, Chem. Int. Ed.* **2010**, *49*, 9765-9768.

[74] Savini, A.; Belanzoni, P.; Bellachioma G.; Zuccaccia, C.; Zuccaccia, D.; Macchoini, A. *Green. Chem.* **2011**, *13*, 3360-3374.

[75] (a) Schley, N. D.; Blakemore, J. D.; Subbaiyan, N. K.; Incarvito, C. D.; D'Souza, F.; Crabtree, R. H.; Brudvig, G. W. *J. Am. Chem. Soc.* **2011**, *133*, 10473-10481; (b) Grotjahn; D. B.; Brown, D. B.; Martin, J. K.; Marelius, D. C.; Abadian, M.; Tran, H. N.; Kalyuzhny G.; Vecchio, K. S.; Specht, Z. G.; Cortes-Llamas, S. A.; Miranda-Soto, V.; Van Niekerk, C.; Moore, C. E.; Rheingold, A. L. *J. Am. Chem. Soc.* **2011**, *133*, 19024-19027; (c) Blakemorem J. D.; Schley, N. D.; Olack, G. W.; Incarvito, C. D.; Brudvig, G. W.; Crabtree, R. H. *Chem. Sci.* **2011**, *2*, 94-98.

[76] (a) Hintermair, U.; Sheenhan, S. W.; Parent, A. R.; Ess, D. H.; Richens, D. T.; Vaccaro, P. H.; Brudvig, G. W.; Crabtree, R. H. *J. Am. Chem. Soc.* **2013**, *135*, 10837-1051; (b) Thomsen, J. M.; Sheehan, S. W.; Hashmi, S. M.; Campos, J.; Hintermair, U.; Crabtree, R. H.; Brudvig, G. W. *J. Am. Chem. Soc.* **2014**, *136*, 13826–13834; (c) Yang, K. R.; Matula, A. J.; Kwon, G.; Hong, J.; Sheehan, W. S.; Thomsen, J. M.; Brudvig, G. W.; Crabtree, R. H.; Tiede, D. M.; Chen, L. X.; Batista V. S. *J. Am. Chem. Soc.* **2016**, *138*, 5511-5514; (d) Sharninghausen, L. S.; Sinha, S. B.; Shopov, D. Y.; Choi, B.; Mercado, B. Q.; Roy, X.; Balcells, D.; Brudvig, G. W.; Crabtree, R. H. *J. Am. Chem. Soc.* **2016**, *138*, 15917-15926.

[77] Wasylenko, D. L.; Ganesamoorthy, C.; Borau-Garcia, J.; Berlinguette, C. P. *Chem. Commun.* **2011**; *47*, 4249-4251.

[78] Wasylenko, D. J.; Palmer, R. D.; Schott, E.; Berlinguette, C. P. *Chem. Commun.* **2012**, *48*, 2107-2019.

[79] (a) Dogutan, D. K.; McGuire, R., Jr.; Nocera, D. G. *J. Am. Chem. Soc.* **2011**, *133*, 9178-9180; (b) Lei, H.; Han, A.; Li, F.; Zhang, M.; Han, Y.; Du, P.; Lai, W.; Cao, R. *Phys. Chem. Chem. Phys.* **2014**, **16**, 1883-1893.

[80] (a) Wang, D.; Groves, J. T. *Proc. Natl. Acad. Sci. U.S.A.* **2013**, *110*, 15579-15584; (b) Nakazono, T.; Parent, A. R.; Sakai, K. *Chem. Commun.* **2013**, *49*, 6325-6327.

[81] (a) Pizzolato, E.; Natali, M.; Posocco, B.; Montellano López, A.; Bazzan, I.; Di Valentin, M.; Galloni, P.; Conte, V.; Bonchio, M.; Scandola, F.; Sartorel, A. *Chem. Commun.* **2013**, *49*, 9941-9943; (b) Fu, S.; Liu, Y.; Ding, Y.; Du, X.; Song, F.; Xiang, R.; Ma, B. *Chem. Commun.* **2014**, *50*, 2167-2169.

[82] Yin, Q.; Tan, J. M.; Besson, C.; Geletii, Y. V.; Musaev, D. G.; Kuznetsov, A. E.; Luo, Z.; Hardcastle, K. I.; Hill, C. L. *Science* **2010**, *328*, 342-345.

[83] (a) Natali, M.; Bazzan, I.; Goberna-Ferrón, S.; Al-Oweini, R.; Ibrahim, M, Bassil, B. S.; Dau, H.; Scandola, F.; Galán-Mascarós, J. R.; Kortz, U.; Sartorel, A.; Zaharieva, I.; Bonchio, M. *Green Chem.* **2017**, *18*, 2416-2426; (b) Soriano-López, J.; Goberna-Ferrón, S.; Vigara, L.; Carbó, J. J.; Poblet, J. M.; Galán-Mascarós, J. R. *Inorg. Chem*, **2013**, 4753-4755; (c) Bazzan I.; Volpe, A.; Dolbecq, A.; Natali, M.; Sartorel, A.; Mialane, P.; bonchio, M. *Catalysis Today*, **2017**, *290*, 39-50.

[84] Daniel, Q.; Ambre, R. B.; Zhang, B.; Philippe, B.; Chen, H.; Li, F.; Fan, K.; Ahmadi, S.; Rensmo H.; Sun, L. *ACS Catal.* **2017**, *7*, 1143-1149.

[85] Huang, Z.; Luo, Z.; Geletii, Y. V.; Vickers, J. W.; Yin, Q.; Wu, D.; Hou, Y.; Ding, Y.; Song, J.; Musaev, D. G.; Hill, C. L.; Lian, T. *J. Am. Chem. Soc.* **2011**, *133*, 2068-2071.

[86] (a) Stracke, J.J.; Finke, R.G. *J. Am. Chem. Soc.* **2011**, *133*, 14872-14875; (b) Stracke, J.J.; Finke, R.G. *ACS Catal.* **2013**, *3*, 1209-1219; (c) Stracke, J.J.; Finke, R.G. *ACS Catal.* **2014**, *4*, 79-89; (d) Stracke, J.J.; Finke, R.G. *ACS Catal*. **2014**, *4*, 909-933; (e) Vickers, J.W.; Lv, H.; Sumliner, J.M.; Zhu, G.; Luo, Z.; Musaev, D.G.; Geletii, Y.V.; Hill, C.L. *J. Am. Chem. Soc.* **2013**, *135*, 14110-14118; (f) Folkman, S. J.; Finke, R.G. *ACS Catal*. **2017**, *7*, 7-16.

[87] Limburg, J.; Vrettos, J. S.; Liable-Sands, L. M.; Rheingold, A. L.; Crabtree, R. H.; Brudvig, G. W. *Science* **1999**, *283*, 1524-1527.

[88] (a) Limburg, J.; Vrettos, J. S.; Chen, H. Y.; de Paula, J. C.; Crabtree, R. H.; Brudvig, G. W. *J. Am. Chem. Soc.* **2001**, *123*, 423-430; (b) Cady, C. W.; Shinopoulos, K. E.; Crabtree, R. H.; Brudvig, G. W. *Dalton Trans.* **2010**, *39*, 3985-3989; (c) Kurz, P.; Berggren, G.; Anderlund, M. F.; Styring, S. *Dalton Trans.* **2007**, 4258-4261; (d) Berggren, G.; Thapper, A.; Huang, P.; Kurz, P.; Eriksson, L.; Styring, S.; Anderlund, M. F. *Dalton Trans.* **2009**, 10044-10054; (f) Berggren, G.; Thapper, A.; Huang, P.; Eriksson, L.; Styring, S.; Anderlund, M. F. *Inorg. Chem.* **2011**, *50*, 3425-3430; (g) Young, K. J.; Takase, M. K.; Brudvig, G. W. *Inorg. Chem.* **2013**, *52*, 7615-7622.

[89] (a) Karlsson, E. A.; Lee, B.-L.; Åkermark, T.; Johnston, E. V.; Kärkäs, M. D.; Sun, J.; Hansson, Ö.; Bäckvall, J.-E.; Åkermark, B. *Angew. Chem., Int. Ed.* **2011**, *50*, 11715-11718; (b) Arafa, W. A. A.; Kärkäs, M. D.; Lee, B.-L.; Åkermark, T.; Liao, R.-Z.; Berends, H.-M.; Messinger, J.; Siegbahn, P. E. M.; Åkermark, B. *Phys. Chem. Chem. Phys.* **2014**, *16*, 11950-11964.

[90] Fillol, J. L.; Cordolà, Z.; Garcia-Bosch, I.; Gómez, L.; Pla, J. J.; Costas, M. *Nat. Chem.* **2011**, *3*, 807-813.

[91] Hong, D.; Mandal, S.; Yamada, Yusuke.; Lee, Y-M.; Nam, W.; Llobet, A.; Fukuzumi, S. *Inorg. Chem.* **2013**, *52*, 9522-9531.

[92] M. T. Dinh Nguyen, A. Ranjbari, L. Catala, F. Brisset, P. Millet, A. Aukauloo, *Coord. Chem. Rev.* **2012**, *256*, 2435-2444.

[93] (a) Jin, S.; Faber, M. S. Energy. Environ. Sci. 2014, 7, 3519-3519; (b) Zheng, Y.; Jiao, Y.; Jaroniec, M.; Qiao, S. Z. *Angew. Chem. Int. Ed*. **2015**, *54*, 52-65.

[94] Gordon, R. B.; Bertram, M.; Graedel, T. E.; *Proc. Natl. Acad. Sci. USA* **2006**, *103*, 1209-1214.

[95] (a) Lubitz, W.; Reijerse, E. J.; Messinger, J. *Energy Environ. Sci.* **2008**, *1*, 15-31. (b) Fontecilla-Camps, J. C.; Volbeda, A.; Cavazza, C.; Nicolet, Y. *Chem. Rev.* **2007**, *107*, 4273-4303.

[96] (a) Helm, M. L.; Stewart, M. P.; Bullock, R. M.; Rakowski Dubois, M. R.; Dubois, D. L. *Science* **2011**, *833*, 863-866. (b) Wilson, A. D.; Shoemaker, R. K.; Miedaner, A.; Muckerman, J. T.; DuBois, D. L.; Rakowski DuBois, M. R. *Proc. Natl. Acad. Sci. U.S.A.* **2007**, *104*, 6951-6956. (c) Rakowski DuBois, M. R.; DuBois, D. L. *Chem. Soc. Rev.* **2009**, *38*, 62-72.

[97] (a) Bughun, I.; Lexa, D; Savéant, J.-M. *J. Am. Chem. Soc.* **1996**, *118*, 3982-3983. (b) Evans, D. J.; Pickett, C. J. *Chem. Soc. Rev.* **2003**, *32*, 268-275. (c) Capon, J.-F.; Gloaguen, F.; Schollhammer, P.; Talarmin, J. *Coord. Chem. Rev.* **2005**, *249*, 1664-1676.

[98] (a) Artero, V.; Chavarot-Kerlidou, M.; Fontecave, M. *Angew. Chem., Int. Ed.* **2011**, *50*, 7238-7266. (b) Sun, Y.; Bigi, J. P.; Piro, N. A.; Tang, M. L.; Long, J. R.; Chang, C. J. *J. Am. Chem. Soc.* **2011**, *133*, 9212-9215. (c) Lee, C. H.; Dogutan, D. K.; McGuire, R.; Nocera, D. G. *J. Am. Chem. Soc.* **2011**, *133*, 8775-8777. (d) Gimbert-Suriñach, C.; Albero, J.; Stoll, T.; Fortage, J.; Collomb, M-N.; Deronzier, A.; Palomares, E.; Llobet, A. *J. Am. Chem. Soc.* **2014**, *136*, 7655-7661.

[99] (a) Karunadasa, H. L.; Chang, C. J.; Long, J. R. *Nature* **2010**, *464*, 1329-1333. (b) Appel, A. M.; Dubois, D. L.; Rakowski DuBois, M. R. *J. Am. Chem. Soc.* **2005**, 12717-11726.

[100] McCrory, C. C. L.; Jung, S; Ferrer, I. M.; Chatman, S. M.; Peters J. C.; Jaramillo, T. F. *J. Am. Chem. Soc.* **2015**, *137*, 4347–4357.

[101] McCrory, C. C. L.; Jung, S.; Peters, J. C.; Jaramillo, T. F. *J. Am. Chem. Soc.* **2013**, *135*, 16977-16987.

[102] Weber, M. F.; Dignam, M. J.; *J. Electrochem. Soc.* **1984**, *131*, 1258-1265.

[103] Conway, B. E.; Tilak, B. V. *Electrochim. Acta* **2002**, *47*, 3571-3594.

[104] Nørskov, J. K.; Bligaard, T.; Logadottir, A.; Kitchin, J. R.; Chen, J. G.; Pandelov, S.; Stimming U. *J. Electrochem. Soc.* **2005**, *152*, J23-126.

[105] Cook, T. R.; Dogutan, D. K.; Reece, S. Y.; Surendranath, Y.; Teets, T. S.; Nocera, D. G. *Chem. Rev.* **2010**, *110*, 6474-6502.

[106] Greeley, J.; Jaramillo, T. F.; Bonde, J.; Chorkendorff, I.; Nørskov, J. K. *Nat. Mater.* **2006**, *5*, 909-913.

[107] Parsons, R. *Trans. Faraday Soc.* **1958**, *54*, 1053-1063.

[108] Kelly, T. G.; Lee, K. X.; Chen, J. G.; *J. Power Sources*, **2014**, *271*, 76-81.

[109] Esposito, D.V.; Hunt, S.T.; Stottlemyer, A.L.; Dobson, K.D.; McCandless, B.E.; Birkmire, R.W.; Chen, J.G. *Angew. Chem. Int. Ed.* **2010**, *49*, 9859-9862.

[110] Chen, C.; Kang, Y.; Huo, Z.; Zhu, Z.; Huang, W.; Xin, H. L.; Snyder, J. D.; Li, D.; Herron, J. A.; Mavrikakis, M.; Chi, M.; More, K. L.; Li, Y.; Markovic, N. M.; Somorjai, G. A.; Yang, P.; Stamenkovic, V. R. *Science* **2014**, *343*, 1339-1343.

[111] (a) Esswein, A. J.; McMurdo, M. J.; Ross, P. N. Bell, A. T.; Tilley, T. D. *J. Phys. Chem. C*, **2009**, *113*, 15068–15072. (b) Paoli, E. A.; Masini, F; Frydendal, R.; Deiana, D.; Schlaup, C.; Malizia, M; Hansen, T. W.; Horch, S.; Stephens, I. E. L.; Chorkendorff, I. *Chem. Sci.* **2015**, *6*, 190-196.

[112] Sanchez-Sanchez, C. M.; Solla-Gullon, J.; Montiel, V. *Electrohemistry*, **2013**, *11*, 34-70.

[113] Jaramillo, T. F.; Jørgensen, K.P.; Bonde, J.; Nielsen, J.H.; Horch, S.; Chorkendorff, I.; *Science*, **2007**, *317*, 100-102.

[114] Kibsgaard, J.; Chen, Z.; Reinecke, B. N.; Jaramillo, T. F. *Nat. Mater.* **2012**, *1*, 963-969.

[115]Li, Y.; Wang, H.; Xie, L.; Liang, Y.; Hong, G.; Dai, H. *J. Am. Chem. Soc.* **2011**, *133*, 7296-7299.

[116]Popczun, E. J.; McKone, J. R.; Read, C. G.; Biacchi, A. J.; Wiltrout, A. M.; Lewis, N. S.; Schaak, R. E.; *J. Am. Chem. Soc.* **2013**, *135*, 9267-9270.

[117] Yin, J.; Fan, Q.; Li, Y.; Cheng, F.; Zhou, P.; Xi, P.; Sun, S. *J. Am. Chem. Soc.* **2016**, *138*, 14546-14549.

[118] McKone, J. R.; Sadtler, B. F; Werlang, C. A.; Lewis, N. S.; Gray, H. B.; *ACS Catal.* **2013**, *3*, 166-169.

[119] Long, X.; Li, G.; Wang, Z.; Zhu, H. Y.; Zhang, T.; Xiao, S.; Guo, W.; Yang, S.; *J. Am. Chem. Soc.* **2015**, *137*, 11900-11903.

[120] Irshad, A.; Munichandraiah, N.; *ACS Appl. Mater. Interfaces*, **2017**, *9*, 19746-19755.

[121] Popczun, E. J.; Read, C. G.; Roske, C. W.; Lewis, N. S.; Schaak, R. E. *Angew. Chem. Int. Ed.* **2014**, *53*, 5427-5430.

[122] Zhang, E.; Xie, Y; Ci, S.; Jia, J.; Cai, P.; Yi, L.; Wen, Z. *J. Mater. Chem. A*, **2016**, *4*, 17288-17298.

[123] (a) Wang, Y.; Nie, Y.; Ding, W.; Chen, S. G. ; Xiong, K.; Qi, X. Q.; Zhang, Y.; Wang, J.; Wei, Z. D. *Chem. Commun.* **2015**, *51*, 8942-8945; (b) Zhang, X.; Liu, R.; Zang, Y.; Liu, G.; Wang, G.; Zhang, Y.; Zhang H.; Zhao, H. *Chem. Commun.* **2016**, *52*, 5946-5949.

[124] Li, J.; Wang, Y.; Zhou, T.; Zhang, H.; Sun, X.; Tang, J.; Zhang, L.; Al-Enizi, A. M.; Yang, Z.; Zheng, G. *J. Am. Chem. Soc.* **2015**, *137*, 14305-14312.

[125] Su, H.; Wang, H.-H.; Zhang, B.; Wang, K-X.; Li, K-H.; Chen J-S. *Nano Energy*, **2016**, *22*, 79-86.

[126] You, B.; Jiang, N.; Sheng, M.; Gul, S.; Yano, J.; Sun, Y. *Chem. Mater.* **2015**, *27*, 7636-7642.

[127] (a) Hong, D.; Jung, J.; Park, J.; Yamada, Y.; Suenobu, T.; Lee, Y.-M.; Nam, W.; Fukuzumi, S. *Energy Environ. Sci*. **2012**, *5*, 7606-7616; (b) Stracke, J. J.; Finke, R. G. *J. Am. Chem. Soc.* **2011**, *133*, 14872-14875.

[128] Anxolabéhère-Mallart, E.; Costentin, C.; Fournier, M.; Nowak, S.; Robert, M.; Savéant, J.-M. *J. Am. Chem. Soc.* **2012**, *134*, 6104-6107.

[129] (a) Hocking, R. K.; Brimblecombe, R.; Chang, L.-Y.; Singh, A.; Cheah, M. H.; Glover, C.; Casey, W. H.; Spiccia, L. *Nat. Chem.* **2011**, *3*, 461-466; (b) Singh, A.; Hocking, W. H.; Chang, S. L.-Y.; George, B. M.; Fehr, M.; Lips, K.; Schnegg, A. Spiccia, L. *Chem. Mater.* **2013**, *25*, 1098-1108.

[130] Li, Z.; Wu, Y.; Lu, G.; *Appl. Catal, B: Env.* **2016**, *188*, 56-64.

[131] Wender, H.; Gonçalves, R. V.; Dias, C. S. B.; Zapata, M. J. M.; Zagonel, L. F.; Mendonça, E. C.; Teixeira, S. R.; Garcia, F. *Nanoscale*, **2013**, *5*, 9310-9316.

[132] Jiang, N.; You, B.; Sheng, M.; Sun, Y. *Angew. Chem. Int. Ed.* **2015**, *54*, 6251-6254.

[133] Liu, X.; Dong, C.; Dong, W.; Wang, X.; Yuan, X.; Huang, F. *RSC Adv.* **2016**, *6*, 38515-38520.

[134]Tian, J.; Liu, Q.; Asiri, A. M.; Sun, Z. *J. Am. Chem. Soc.* **2014**, *136*, 7587-7590.

[135] Faber, M. S.; Dziedzic, R.; Lukowsky, M. A.; Kaiser, N. S.; Ding, Q.; Jin, S.; *J. Am. Chem. Soc.* **2014**, *136*, 10053-10061.

[136]Tong, X.; Wu, D.; Zhang, C.; Lian, K.; Xiong, D.; Xu, S.; Zhu, Y.; Qi, R.; Huang, R.; Wang, L.; Chu, P. K. *J. Mater. Chem. A*, **2017**, *5*, 2629–2639

[137] Feng, J.-X.; Ding, L.-X.; Ye, S.-H.; He, X.-J.; Xu, H.; Tomg, Y.-X.; Li, G.-R. *Adv. Mater.* **2015**, *27*, 7051-7057.

CHAPTER II

Objectives

According to the state-of-the of the field of artificial photosynthesis presented in Chapter 1, the main objectives of this thesis are exposed in the present chapter.

General

One of the most exiting objectives of the scientific community during the last years has been the design of efficient and robust catalysts for water splitting, where the characterization and understanding of their catalytic pathways plays a key role in their rational design. Therefore, the general aim of this PhD Thesis is the study of the structural, electrochemical and catalytic properties of new homogeneous and heterogeneous WO and HER catalysts based on Ru, Cu and Co. This general aim can be divided into three specific objectives.

Objective 1

During the last decades, Ru aqua complexes have been extensively studied in the field of catalytic WO. In particular, pentadentate ligands from the Py_5 family could be promising candidates for this reaction; their chelate effect provides a robust first coordination sphere while allowing the coordination of one aqua ligand at the sixth coordination position. Thus, the first target of this first project is the synthesis, structural and electrochemical characterization of new mononuclear Ru complexes bearing the **bpy2PYMe** scaffold and its analogs **bpy(bpyMe)PYMe** and **bpy2PYOMe**. The study of the catalytic performance of the prepared complexes towards WO and the unraveling of their mechanistic pathways is also proposed.

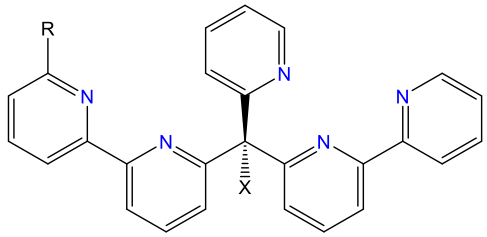

R = H, X = Me; **bpy2PYMe**
R = Me, X = Me; **bpy(bpyMe)PYMe**
R = H, X = OMe; **bpy2PYOMe**

Objective 2

Finding an efficient, cheap and "green" alternative to the noble metal-based molecular catalysts for WO has become one of the main challenges for scientists during the last years in the field of artificial photosynthesis. With this purpose on mind, molecular copper-based complexes have gained interest in this field. On the other hand, it is well known that tetradentate bipyridine-based ligands stabilize the coordination sphere around the copper center forming a square planar geometry, and that negatively charged deprotonated amide groups would have a drastic effect in the redox potential of the Cu^{III}/Cu^{II} couple, thus decreasing the potentials necessary for achieving high oxidation

states. Within this context, the synthesis of two new tetradentate ligands (*p*-L and *o*-L) is envisaged, as well as the preparation and thorough characterization of their corresponding Cu complexes. The aim of this study is to analyze the effect of the relative disposition of the Cu centre and the sulfonate groups onto the electrocatalytic performance of the corresponding complexes in WO and comparison of the latter with other copper-based catalyst reported previously in the literature.

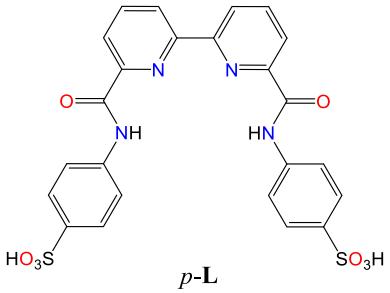

p-**L**

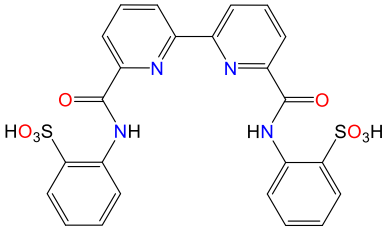

o-**L**

Objective 3

During the past decade, the scientific community have focused its efforts towards developing new catalysts for the Hydrogen Evolution Reaction based on earth-abundant metals. In this field, a large amount of Co-based homogeneous and heterogeneous catalysts have been prepared and extensively studied for this purpose, showing good activities at relatively low overpotentials. Within this scenario, the Co-based multinuclear cluster ($[Co_8Na_4(L)_4(OH)_2(CO_3)_2(py)_{10}](BF_4)_2$) (**1**), reported in 2015 by G. Aromí and co-workers, could be a promising candidate for catalyzing this reaction. Consequently, the third goal of this PhD Thesis is to study the electrochemical behavior and stability of **1** under reductive stress and its electrocatalytic performance towards HER. In case of deactivation and consequent formation of Co-based materials under turnover conditions, the composition, morphology and catalytic activity towards HER of the formed species will be analyzed.

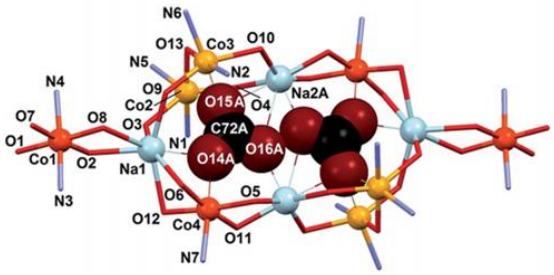

$[Co_8Na_4(L)_4(OH)_2(CO_3)_2(py)_{10}](BF_4)$

CHAPTER III

Ruthenium Complexes Bearing Pentadentate Ligands: Isomerization Processes and Water Oxidation Catalysis.

As presented in Chapter I, Ru polypyridyl complexes are specially interesting for applications in water oxidation catalysis becoming subject of study during the last decades. In this chapter we report the synthesis of a new family of Ru complexes bearing pentadentate polypyridyl ligands and their application in water oxidation catalysis.

In the first subchapter, we focused our attention in the structural and electrochemical characterization of the complexes. The isomerization equilibria over Ru^{II} and Ru^{III} are also studied in detail. Finally, a comparison with other Ru complexes containing pentadentate ligands is also presented.

In the second subchapter, we focus our attention in the reactivity towards water oxidation. Detailed spectroscopic and kinetic studies are reported, which allowed the identification of new species formed after a series of substitution reactions at different oxidation states. The catalytic activity of these complexes is also discussed, showing how the different substitution kinetic constants between the complexes are critical for their catalytic performance.

This chapter consists in the following papers:

Paper A **Gil-Sepulcre, M.**; Axelson, J. C.; Aguiló, J.; Solà-Hernández, L.; Francàs, L.; Poater, A.; Blancafort, L.; Benet-Buchholz, J.; Guirado, G.; Escriche, L.; Llobet, A.; Bofill, R.; Sala. X. *Inorg. Chem.* **2016**, *55*, 11216-11229.

Paper B **Gil-Sepulcre, M.**; Schilling, M.; Böhler, M.; Bozoglian, F; Bachmann, C.; Scherrer, D.; Fox, T.; Spingler, B.; Gimbert-Suriñach, C.; Alberto, R.; Bofill, R.; Sala, X.; Luber, S.; Richmond, C. J.; Llobet A. *ChemSusChem* **2017**, *10*, 4517-4525.

PAPER A: Synthesis and Isomeric Analysis of Ru^{II} Complexes Bearing Pentadentate Scaffolds

Gil-Sepulcre, M.; Axelson, J. C.; Aguiló, J.; Solà-Hernández, L.; Francàs, L.; Poater, A.; Blancafort, L.; Benet-Buchholz, J.; Guirado, G.; Escriche, L.; Llobet, A.; Bofill, R.; Sala. X. *Inorg. Chem.* **2016**, *55*, 11216-11229.

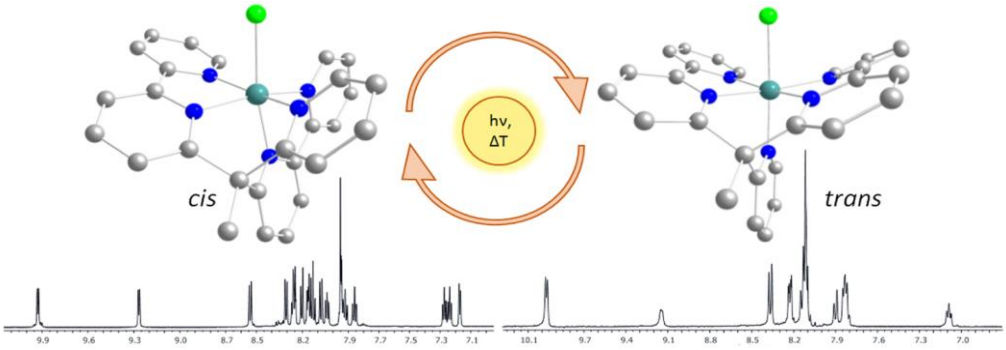

Abstract: A Ru^{II}-pentadentate polypyridyl complex $[Ru^{II}(\kappa\text{-}N^5\text{-bpy2PYMe})Cl]^+$ (**1**$^+$, bpy2PYMe = 1-(2-pyridyl)-1,1-bis(6-2,2'-bipyridyl)ethane) and its aqua derivative $[Ru^{II}(\kappa\text{-}N^5\text{-bpy2PYMe})(H_2O)]^{2+}$ (**2**$^{2+}$) have been synthesized and characterized by experimental and computational methods. In MeOH, **1**$^+$ exists as two isomers in different proportions, *cis* (70%) and *trans* (30%), which are interconverted under thermal and photochemical conditions by a sequence of processes: chlorido decoordination, decoordination/recoordination of a pyridyl group and chlorido recoordination. Under oxidative conditions in dichloromethane, *trans*-**1**$^{2+}$ generates a $[Ru^{III}(\kappa\text{-}N^4\text{-bpy2PYMe})Cl_2]^+$ intermediate after the exchange of a pyridyl ligand by a Cl^- counterion, which explains the *trans*/*cis* isomerization observed when the system is taken back to Ru(II). On the contrary, *cis*-**1**$^{2+}$ is in direct equilibrium with *trans*-**1**$^{2+}$, with absence of the $\kappa\text{-}N^4$-bis-chlorido Ru^{III}-intermediate. All these equilibria have been modeled by DFT calculations. Interestingly, the aqua derivative is obtained as a pure *trans*-$[Ru^{II}(\kappa\text{-}N^5\text{-bpy2PYMe})(H_2O)]^{2+}$ isomer (*trans*-**2**$^{2+}$), while the addition of a methyl substituent to a single bpy of the pentadentate ligand leads to the formation of a single *cis* isomer for both chlorido- and aqua-derivatives, $[Ru^{II}(\kappa\text{-}N^5\text{-bpy(bpyMe)PYMe})Cl]^+$ (**3**$^+$) and $[Ru^{II}(\kappa\text{-}N^5\text{-bpy(bpyMe)PYMe})(H_2O)]^{2+}$ (**4**$^{2+}$), due to the steric constraints imposed by the modified ligand. This system has also been structurally and electrochemically compared to the previously reported $[Ru^{II}(PY5Me_2)X]^{n+}$ system (X=Cl, *n*=1 (**5**$^+$); X=H_2O, *n*=2 (**6**$^{2+}$)), which also contains a $\kappa\text{-}N^5\text{-}Ru^{II}$ coordination environment, and to the newly synthesized $[Ru^{II}(PY4Im)X]^{n+}$ complexes (X=Cl, *n*=1 (**7**$^+$); X=H_2O, *n*=2 (**8**$^{2+}$)), which possess an electron-rich $\kappa\text{-}N^4C\text{-}Ru^{II}$ site due to the replacement of a pyridyl group by an imidazolic carbene.

Introduction

Transition metal complexes containing polypyridyl ligands have been extensively used in catalytic oxidation systems due to their stability and synthetic versatility.[1] Among these, Ru-aqua polypyridyl complexes are particularly interesting because of both their easily accessible high oxidation states through proton-coupled electron transfer (PCET) processes and the inertness of the polypyridyl ligands bonded to the Ru metal center.[2]

Pentadentate ligands that coordinate metals in a square pyramidal fashion are able to both enforce an octahedral geometry around the metal center as well as restrict the metal substitution chemistry to a single coordination site.[3] An archetypical example is the $PY5R_2$ family (PY = pyridine, R = H, Me, OH, OMe, etc., Chart 1), which usually binds the metal ion through one axial and four equatorial positions.[4]

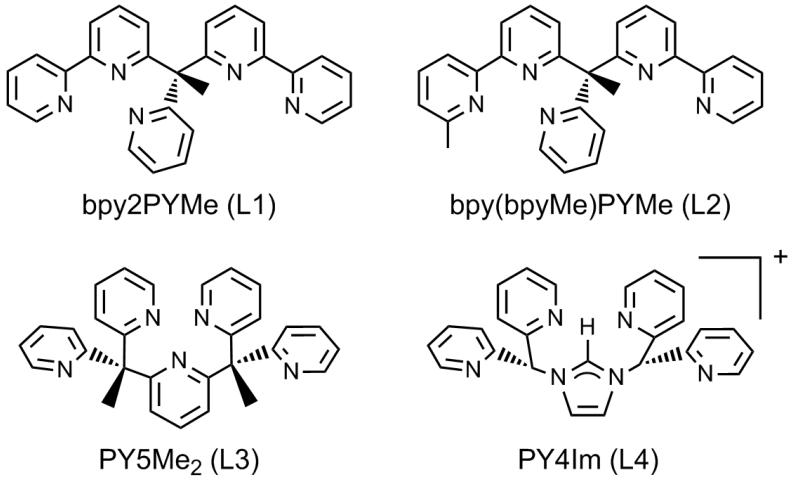

Chart 1. Schematic drawing of the ligands discussed in this work.

Recently, several works have emerged taking advantage of the interesting properties of this scaffold. For instance, Berlinguette *et al.* have reported the first tetravalent Co complex stabilized by proton coupled electron transfer (PCET) processes by employing the $PY5R_2$ ligand (R = H).[5] This pentadentate ligand ensures: (a) one single free coordination site in an octahedral type of geometry to accommodate the aqua ligand, thus allowing PCET processes, (b) a rugged coordination environment non-susceptible to oxidative decomposition, and (c) the stabilization of the coordination site *trans* to the M-O bond, preventing in consequence decomposition via ligand dissociation. Other examples of the $PY5R_2$ family include the $PY5Me_2$ ligand (R = Me),[6] whose Ru^{III}-OH complex has been recently reported by Kojima *et al.* to oxidize substrates such as

hydroquinones in water.[7] In addition, $PY5Me_2$-related compounds containing Co(II)[8] and Mo(II)[9] have been proven to be active in electrocatalytic water reduction. Also, in 2010, Long and co-workers reported a series of first row metal complexes containing the PY4Im ligand, in which the axial pyridine of the $PY5R_2$ scaffold was replaced by a *N*-heterocyclic carbene (NHC) moiety.[10] Finally, the same group reported in 2013 a series of first row metal complexes containing the related pentapyridyl ligand bpy2PYMe, which in the case of Co(II) has been show to be an active catalyst for the proton reduction reaction.[6b,11]

An important issue to be considered during redox catalysis employing polypyridyl transition metal complexes is the potential presence of several isomers due to the flexibility of the polydentate ligand, which can hamper a rational analysis of their behavior.[12] Furthermore, it is also fundamental to assess the stability of a given isomer when the central metal ion experiences the gain or loss of an electron. Within this context, we present the synthesis and isomeric analysis by spectroscopic, electrochemical and theoretical (DFT) methods of two Ru(II) complexes bearing 1-(2-pyridyl)-1,1-bis(6-2,2'-bipyridyl)ethane ligand scaffolds (L1 and L2 in Chart 1), and the comparison of their structural and electronic properties with those of related Ru(II) complexes containing the pentadentate ligands L3 and L4 (Chart 1).

Results and discussion

Synthesis and Characterization of 1(Cl), $2(PF_6)_2$, 3(Cl) and $4(PF_6)_2$.

For the synthesis of bpy2PYMe (L1), the two-step procedure reported by Long and co-workers[11] involved reacting 2-ethylpyridine with MeLi and 6-bromo-2,2'-bipyridine and mixing the isolated intermediate with BuLi and another equivalent of 6-bromo-2,2-bipyridine. However, in this study the route was simplified to a one-pot reaction of 2-ethylpyridine with LDA (lithium diisopropylamide) and 6-bromo-2,2'-bipyridine, obtaining L1 as a yellow oil in 70% yield (a detailed description of the synthesis can be found in the Supplementary Material). The synthetic strategy followed for the preparation of the respective chlorido and aqua complexes **1(Cl)** and **$2(PF_6)_2$** is depicted in Scheme 1 and in the Experimental Section.

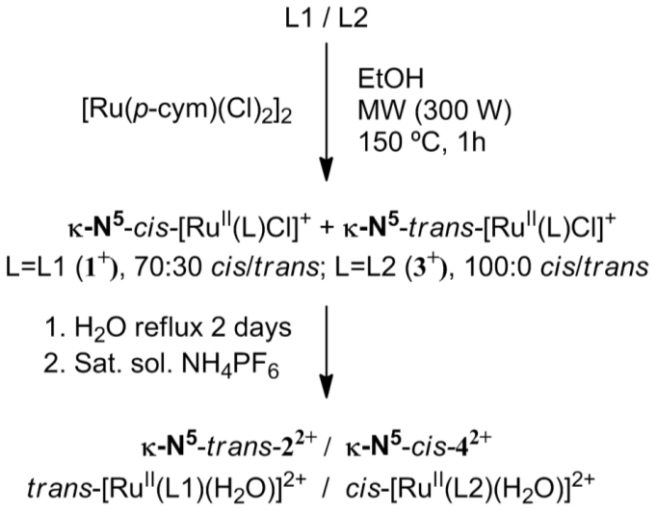

Scheme 1. Synthetic pathway for the preparation of the chlorido complexes $\mathbf{1}^{+}$ and $\mathbf{3}^{+}$ and the aqua complexes $\mathbf{2}^{2+}$ and $\mathbf{4}^{2+}$.

For the synthesis of the chlorido complex $\mathbf{1}^{+}$, the ^{1}H NMR spectrum of the reaction mixture in ethanolic solution showed the presence of two compounds, which could be separated by fractionated precipitation through sequential exposure to EtOH followed by DCM (see the Experimental Section for further details). With this method, two pure isomers were obtained, which have been called *trans*-$\mathbf{1}^{+}$ and *cis*-$\mathbf{1}^{+}$, respectively, depending on whether the pyridyl moiety is positioned *trans* or *cis* with respect the Cl^{-} ligand (Scheme 1 and Figure 1).

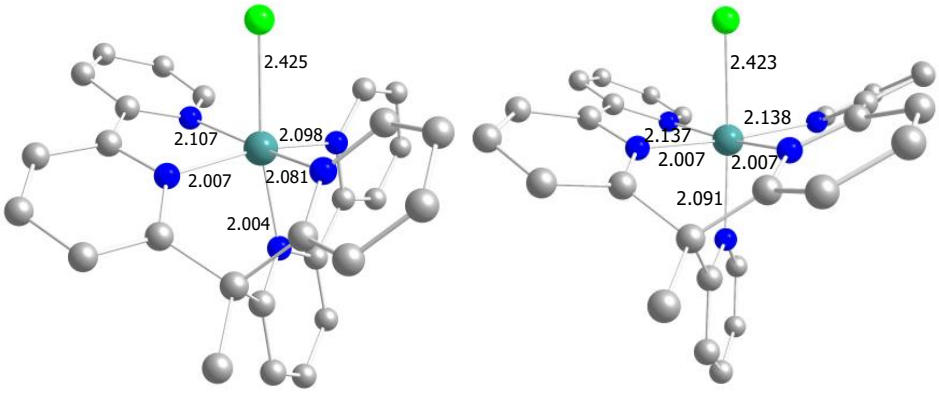

Figure 1. Plot of the DFT calculated structures of *cis*-$\mathbf{1}^{+}$ (left) and *trans*-$\mathbf{1}^{+}$ (right). Atom color code: blue, nitrogen; light green, chlorine; dark green, ruthenium; light grey, carbon. All Ru-X calculated distances (X=Cl, N) are shown in Å. Hydrogen atoms have been omitted for clarity.

The experimentally obtained *cis:trans* ratio is approximately 70:30, and both individual compounds have been characterized by NMR (Figure 2 and Figures S1 and S2), UV-vis spectroscopy (Figure S13) and ESI-TOF and MALDI-TOF MS (Figure S9).

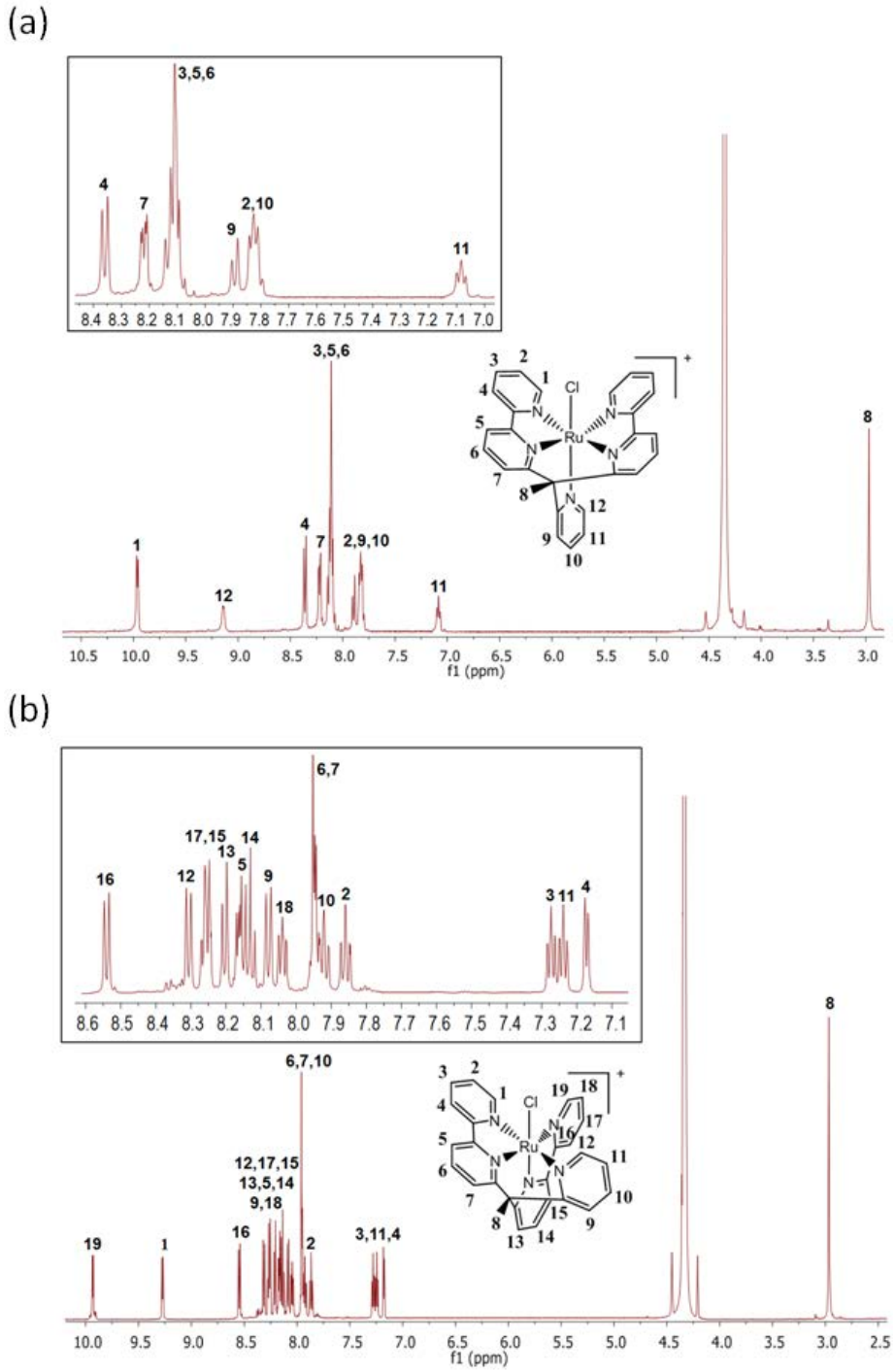

Figure 2. ^{1}H NMR spectra including the assignment of signals for *trans*-**1**$^{+}$ (400 MHz, 298 K, d_3-$MeNO_2$) (a) and *cis*-**1**$^{+}$ (600 MHz, 298 K, d_3-$MeNO_2$) (b). A zoom of the aromatic region is shown in the insets.

The higher symmetry of the *trans* isomer, which belongs to the C_S point group, compared to the C_1 point group of the *cis* isomer can be confirmed in the NMR spectra; whereas the former only shows 12 ^{1}H and 17 ^{13}C resonances (Figure 2a and Figure S1a), the latter displays 19 ^{1}H and 27 ^{13}C resonances (Figure 2b and Figure S2a). The unequivocal assignment of the respective *cis* and *trans* isomers is also clear when observing the integrals of the down-field doublets corresponding to H19, H1 and H16 (1:1:1) and H1 and H12 (2:1), respectively.

Complexes *cis*-**1**$^{+}$ and *trans*-**1**$^{+}$ are both stable in a DCM solution in darkness at RT. However, at 0 °C in the presence of light (100 W incandescent white light bulb) *trans*-**1**$^{+}$ is partially converted into *cis*-**1**$^{+}$ as monitored by NMR. In sharp contrast, *cis*-**1**$^{+}$ remains stable in DCM under irradiation. Interestingly, the behavior of both isomers is completely different in MeOH. In this case both isomers are interconverted under irradiation at 0 °C and under heating (RT or 50 °C) in darkness, with faster interconversion rates observed for the photo-induced case. For example, under irradiation at 0 °C pure *cis*-**1**$^{+}$ is converted into a *cis*-**1**$^{+}$:*trans*-**1**$^{+}$ (73:15) mixture and pure *trans*-**1**$^{+}$ is converted into a *cis*-**1**$^{+}$:*trans*-**1**$^{+}$ (63:19) mixture within 30 hours (Figure S20). Furthermore, an additional minor species has been detected by NMR (12% abundance for the former case and 18% for the latter), in which at least one MeOH solvent molecule is coordinated to the Ru ion.

To obtain additional information regarding the potential mechanism of isomerization between *trans*-**1**$^{+}$ and *cis*-**1**$^{+}$, density functional theory (DFT) calculations[13] in MeOH and DCM were carried out (Figure 3). In both solvents, the calculations tend to show a slightly higher stability of the *cis* isomer by 0.1 kcal/mol in MeOH and by 0.4 kcal/mol in DCM. The isomerization may be understood as a stepwise equilibrium involving three steps: (1) decoordination of the chlorido ligand, (2) isomerization of one pyridyl group in the decoordinated species, and (3) recoordination of the chloride ion (see Figure 3). Light-induced Ru-Cl bond breakage should not be surprising, since breakage of Ru-X bonds (*e.g.* X = N, S, O) in Ru(II)-polypyridyl complexes upon light irradiation has been previously described elsewhere.[14] Interestingly, in our case the DFT calculations have determined that reaching the equilibrium starting from a single form depends on the polarity of the solvent, as has been experimentally observed. In MeOH, the chlorido decoordination step from the *trans*-**1**$^{+}$ and *cis*-**1**$^{+}$ forms costs 12.7 and 13.5 kcal/mol,

respectively, and the barrier involving the ligand isomerization step is 19.7 kcal/mol. Therefore, the isomerization is energetically possible in MeOH at RT, and the equilibrium between the *cis* and *trans* forms can be established. In contrast, in DCM the decoordination, isomerization and decoordination sequence has a barrier of 32.1 kcal/mol due to the lower polarity of the solvent, which disfavors the separation of charges that occurs during this process. Although there is a concerted transition state linking the two isomers of $\mathbf{1}^+$ in DCM, this path is not viable energetically because it has a barrier of 37.4 kcal/mol relative to *trans*-$\mathbf{1}^+$ (see coordinate data sets and absolute energy for DFT optimized complexes in the Supplementary Material). Thus, the *cis* and *trans* isomers are kinetically trapped under these conditions, and no isomerization occurs at RT.

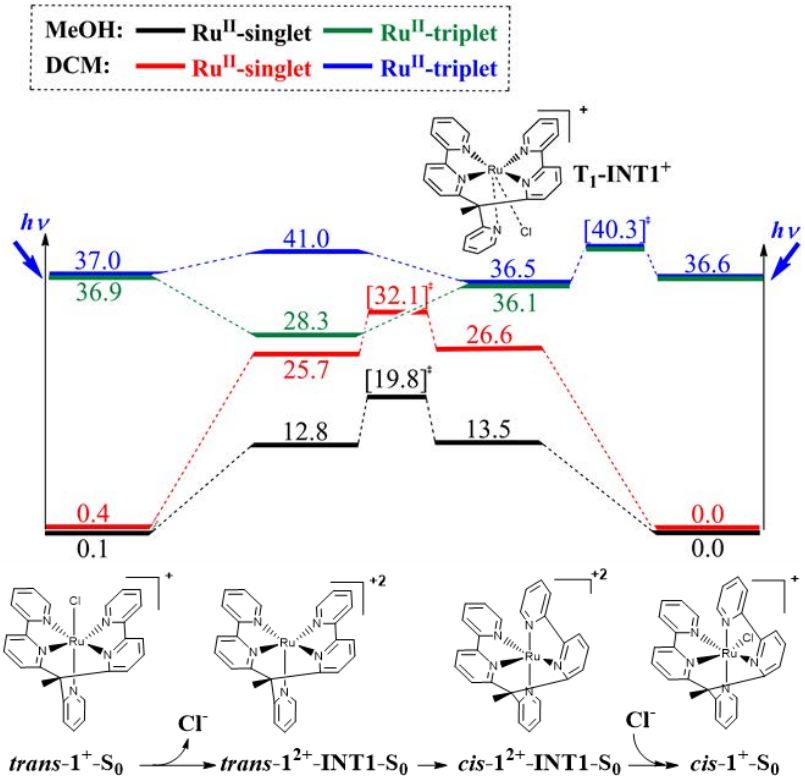

Figure 3. Energy diagram (B3LYPd3/TZVP-D95+~sdd//B3LYPd3/SVP~sdd) for the thermal and photo-induced isomerization processes for $\mathbf{1}^+$ in MeOH and DCM. Red curve denotes the singlet spin surface, and blue curve denotes the triplet spin surface in DCM, whereas black and green curves denote the singlet and triplet spin surfaces in MeOH, respectively. All Gibbs energies are calculated relative to *cis*-$\mathbf{1}^+$ and are reported in kcal/mol (transition state energies in brackets). S_0 = ground state, T_1 = first excited triplet state.

The *cis*-*trans* isomerization in the photo-excited triplet state also follows the chlorido decoordination/recoordination mechanism according to the calculations, which are in agreement with the experimentally observed behavior (Figure 3). Under these conditions, isomerization from the *trans* to the *cis* isomer occurs in both solvents. The calculations show that the chlorido decoordination step is exothermic in MeOH by 8.6 kcal/mol, while it is only slightly endothermic in DCM (by 4.0 kcal/mol). The different endothermicity of the reaction in the ground and excited state explains why *trans*-**1**$^{+}$ is stable in DCM in the dark, but not under irradiation. The situation is different for the triplet-state isomerization in the *cis* to *trans* direction, which occurs only in MeOH. The decoordination reaction starting from *cis*-**1**$^{+}$ follows a stepwise mechanism which goes through an intermediate, **T_1-INT-1**$^{+}$, where the chlorine atom is partially dissociated (Ru-Cl distance of 4.0 Å) and the ligand has a quasi-*trans* conformation. The barrier for this step is low in both solvents (3.7 kcal/mol). At **T_1-INT-1**$^{+}$, the energy gap between the triplet and ground state is small, 5.1 kcal/mol in DCM and 5.6 kcal/mol in MeOH. Therefore, when the molecule is at **T_1-INT-1**$^{+}$, it can decay from the triplet to the ground state instead of completing the dissociation. In the ground state, this is followed by re-association of the chloride ion to the complex and regeneration of the *cis*-**1**$^{+}$ species without isomerization. The calculations suggest that this process will be more favorable in DCM, where the energy gap is smaller, and this might explain why the light-induced isomerization from the *cis* form is suppressed in this solvent, but not in MeOH. Such non-adiabatic processes are common in the photoreactivity of transition metal complexes[15] and organic molecules,[16] and involvement of a singlet/triplet crossing has been previously postulated in the photoisomerization of Ru(II) monoaquo complexes.[17]

The computational results also indicate that the minor species (12-18%) detected in the NMR experiments in MeOH are the trapping products of the decoordinated intermediates. This corresponds to a stepwise replacement of the chlorido ligands by MeOH. The relative energy of the MeOH-coordinated products is 5.2 and 5.9 kcal/mol with respect to *trans*-**1**$^{+}$ and *cis*-**1**$^{+}$, respectively. The alternative structures where MeOH replaces one of the pyridyl ligands instead of a chloride are less favorable energetically; from *trans*-**1**$^{+}$ the cost of dissociating the pyridyl ligand *trans* to Cl^{-} (25.0 kcal/mol, Figure S33) is higher than that of the chloride dissociation, and the concerted substitution of the pyridyl ligand by MeOH is 6.4 kcal/mol even higher in energy.

The electrochemical behavior of the *cis*-**1**$^{+}$ and *trans*-**1**$^{+}$ isomers has also been studied in DCM, a non-coordinating solvent, at different scan rates (Figure 4).

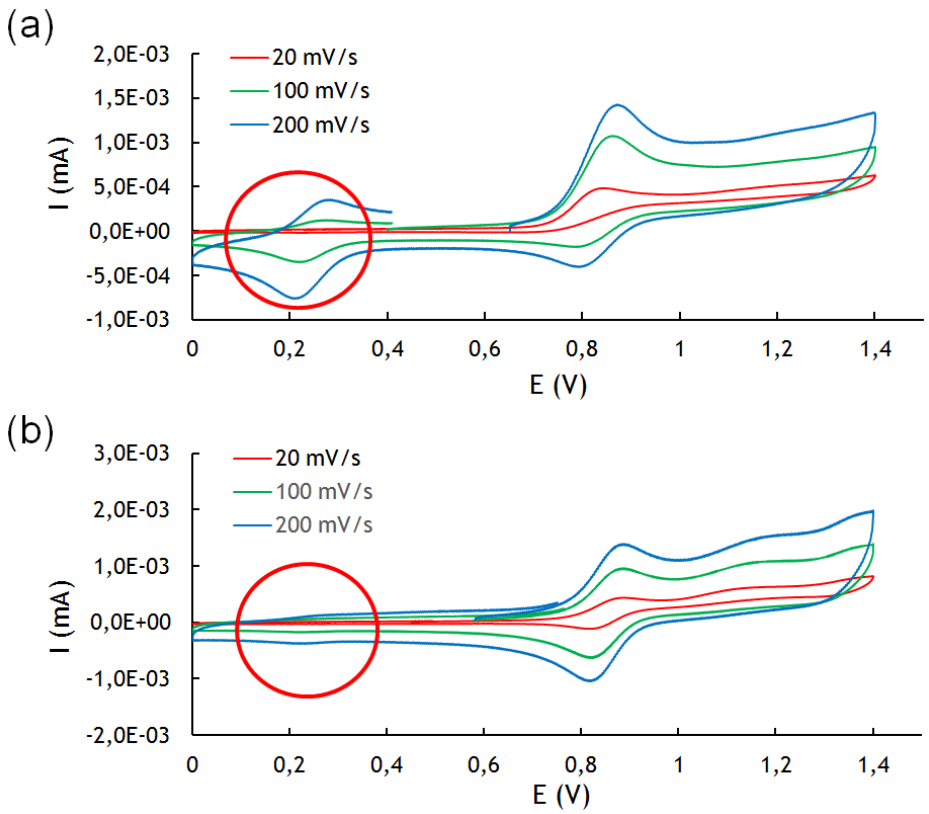

Figure 4. Cyclic voltammogram for *trans*-**1**$^{+}$ (a) and *cis*-**1**$^{+}$ (b) in DCM + 0.1 M n-Bu_4NPF_6 at different scan rates. Glassy carbon electrode is used as working electrode (diameter: 1 mm). The redox potentials are determined *vs.* SCE. Red circle denotes formation of $[Ru^{II/III}(\kappa\text{-}N^4\text{-bpy2PYMe})Cl_2]^{0/+}$ intermediate.

Typical cyclic voltammograms (CVs) for *trans*-**1**$^{+}$ show a one-electron pseudo-reversible wave at 0.829 V *vs.* SCE.[18] In the corresponding cathodic counter scan and in a second scan a new reversible wave appears at 0.241 V *vs.* SCE, indicating the formation of a new electroactive product through a chemical reaction linked to the Ru^{II}/Ru^{III} electron transfer process (Figure 4a and Figure S25, red). A closer look at the CVs reveals that the peak currents are of the same order of magnitude as those expected for a one electron transfer reaction for a diffusing solution species in DCM.[19] The analysis of the peak current values (and their dependence on concentration and scan rate), the peak potential values (and their dependence on concentration) and the potential width values provide a window into the nature of the electrochemical mechanism and the values of the kinetic constants coupled to the electron transfer. Increasing the concentration of *trans*-**1**$^{+}$ results in increases in the peak current value without significant shifts in the peak potential up

0.5 mM, whereas the anodic peak potential shows a dependence with scan rate (ca. 30 mV), which means that the chemical reaction coupled to the electron transfer should be a first order reaction, EC mechanism (Figure S21).[19]

In the case of the *cis*-**1**$^{+}$ isomer, a similar electrochemical behavior is observed: a quasi-reversible one electron oxidation wave appears at 0.851 V, and the same peak detected in solutions of *trans*-**1**$^{+}$ isomer appears again at 0.241 V in the corresponding cathodic counter scan but now with lower associated currents (Figure 4b). The lower cathodic and anodic peak current values obtained for the peak at 0.241 V reflect the higher stability of the oxidized *cis*-**1**$^{2+}$ form in comparison with *trans*-**1**$^{2+}$ (Figure S25, black).

In order to determine the nature of the product formed after the first electron transfer of *trans*-**1**$^{+}$, a controlled potential electrolysis (CPE) at 1.2 V vs. SCE was performed in darkness. After the passage of 1.0 F per mol of complex, the analysis of the oxidized sample by means of CV shows the formation of the electroactive product at 0.241 V (Figure S22). Interestingly, this species is not formed when exchanging the coordinating Cl^{-} counterion in **1**$^{+}$ by the non-coordinating PF_6^{-} ion. The CV of *trans*-[Ru^{II}(bpy2PYMe)Cl](PF_6) in DCM only shows a reversible wave at 0.829 V, with complete absence of the signal of the new species at 0.241 V (Figure S22, c). Therefore, the new species must be formed upon coordination of a Cl^{-} ion to the Ru metal center under oxidative conditions in DCM to generate a [Ru^{III}(κ-N^4-bpy2PYMe)Cl_2]$^{+}$ species (or **κ-N^4-bis-Cl**$^{+}$) after the exchange of a pyridyl ligand by a Cl^{-} counterion. Indeed, this **κ-N^4-bis-Cl**$^{+}$ species shows a Ru^{III}/Ru^{II} potential of 0.241 V *vs.* SCE ([Ru^{III}(bpy2PYMe)Cl_2]$^{+}$/[Ru^{II}(bpy2PYMe)Cl_2] redox pair) by CV, and has been detected by MALDI-TOF MS after a CPE at 1.2 V for 6 h (7.56 F/mol) of a *trans*-**1**$^{+}$ sample. As can be observed in Figure S9a, the higher intensity of the upper MW peaks compared to the parent *cis*-**1**$^{+}$ and *trans*-**1**$^{+}$ compounds is indicative of the presence of the second Cl^{-} atom in the bis-chlorido compound, since total loss of one Cl^{-} ligand and partial loss of the second Cl^{-} ligand is happening. Interestingly, when oxidizing *trans*-**1**$^{+}$ in darkness in DCM (CPE at 1.2 V for 16 h, 4.15 F/mol) and then reducing it back again (CPE at 0 V for 5 h, 1.62 F/mol), a 70:30 mixture of *cis*-**1**$^{+}$: *trans*-**1**$^{+}$ was obtained according to NMR data (Figure S23), which is the same proportion obtained during the synthesis of **1**$^{+}$ (Scheme 1). Consequently, isomerization can also be achieved in non-coordinating solvents (DCM) by bulk electrolysis. Therefore, the **κ-N^4-bis-Cl**$^{+}$ species formed after

oxidation of *trans*-**1**$^{+}$ is in fact an intermediate in the isomerization process that, when reduced back to Ru(II), it may exchange either of the two chloride ligands with the dangling N_{pyr} ligand. If the exchanged Cl^- ion is the same as the one that entered during oxidation, the system will return to the original isomer (*trans*-**1**$^{+}$), whereas if the other is lost, the *cis*-**1**$^{+}$ isomer will be formed. It also became apparent that the [Ru^{II}(κ-N^4-bpy2PYMe)Cl_2] intermediate (**κ-N^4-bis-Cl**) formed upon reduction at potentials lower than 0.241 V is poorly stable, since its detection by MS or NMR has been completely unfruitful.

A detailed analysis of the CV parameters for *trans*-**1**$^{+}$ and *cis*-**1**$^{+}$ at different scan rates allows for the experimental determination of their first order kinetic constants, 1.6 s^{-1} and 0.02 s^{-1}, respectively, by plotting the anodic peak potential *vs.* log *v* (where *v* is scan rate, V s^{-1}) and log [**1**$^{+}$] for both *cis*-**1**$^{+}$ and *trans*-**1**$^{+}$ (Figure S21) according to the following equations (1) and (2).[19]

$$I_p = 0.446\, n\, F\, S\, C^{o}\, \sqrt{\frac{F}{RT}}\sqrt{v}\,\sqrt{D} \quad (1)$$

$$E_p = E^{o} + 0.78\left(\frac{RT}{F}\right) - \left(\frac{RT}{2F}\right)\ln\left(\frac{RT}{Fkv}\right) \quad (2)$$

From this analysis, it can be deduced that the Ru(III)-species *trans*-**1**$^{2+}$ possesses a lower ΔG^0 compared to the *cis*-**1**$^{2+}$ isomer. Thus, the bis-chlorido Ru(III)-intermediate (**κ-N^4-bis-Cl**$^{+}$) is not formed directly after the oxidation of *cis*-**1**$^{+}$ (Figure 4b), but through a previously established equilibrium between *cis*-**1**$^{2+}$ and *trans*-**1**$^{2+}$ (Scheme 2). Hence, in all cases, departing either from *cis*-**1**$^{+}$ or *trans*-**1**$^{+}$, the Ru(III)-bis chlorido intermediate is only formed after the formation of *trans*-**1**$^{2+}$. Finally, the remaining kinetic and thermodynamic parameters have been obtained by individually simulating the experimental CVs recorded at 200 mV/s for both *cis*-**1**$^{+}$ and *trans*-**1**$^{+}$ by an iterative mathematical process using the DigiSim 2.0 CV simulator software[20] (Figure S24) assuming the proposed mechanistic model of Scheme 2 (for further details please refer to the Experimental Section).[21] The dramatic differences between the value of the thermodynamic constant K_1 deduced for Ru(III) and those of K_2 and K_3 deduced for Ru(II) between the **κ-N^4-bis-Cl** and the **κ-N^5-Cl** species is also consistent with the hard-soft acid-base (HSAB) theory and the charge of the central metal ion. Thus, according to the HSAB principle one might expect higher affinity of Ru(II) to bind to N-donor ligands

compared to a chlorido ligand, whereas for Ru(III) the higher charge on the metal makes it more prone to bind to negatively charged ligands.

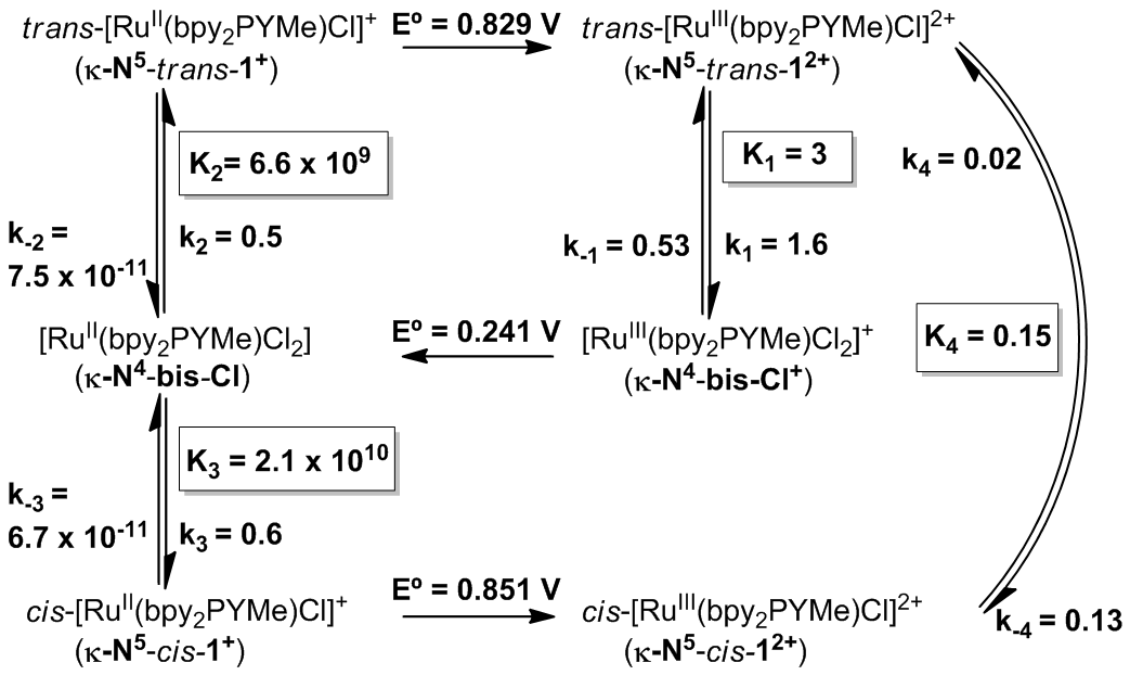

Scheme 2. Proposed isomeric equilibria and kinetic rate constants (k, in s^{-1}) and thermodynamic constants (K, highlighted in boxes) in DCM under oxidative and reductive conditions of *cis*-**1**$^+$ and *trans*-**1**$^+$ complexes.

To obtain more insight into the electrochemical behavior of **1**$^+$, we have modeled the formation of the bis-chlorido intermediates **κ-N^4-bis-Cl** and **κ-N^4-bis-Cl**$^+$ species in DCM by DFT calculations (Figure 5). The **κ-N^4-bis-Cl** species can exist as several possible isomers, of which we have characterized the two most likely to be formed from a structural viewpoint. These two isomers are labeled *trans*-1-INT3-S_0 and *cis*-1-INT3-S_0, where the two chlorido ligands are in *trans* or *cis*, respectively. We postulate that these isomers are formed from *trans*-**1**$^+$ and *cis*-**1**$^+$ after decoordination of the single pyridyl ligand and coordination of the chloride counterion. The barriers for pyridyl decoordination are 25.5 and 26.7 kcal/mol, respectively, and the relative energy of the **κ-N^4-bis-Cl** intermediates INT3 are 9.2 kcal/mol (for *trans*) and 25.1 kcal/mol (for *cis*). From the electrochemical measurements, the relative energy of the **κ-N^4-bis-Cl** intermediate is 14.2 kcal/mol, which suggests that the isomer detected experimentally corresponds to *trans*-INT3, where both chlorido ligands are in axial positions and the electrostatic repulsion between these two ligands is reduced. In Figure 5 we also show a possible isomerization path that interconnects both isomers of INT3. Starting from *trans*-

INT3, it involves decoordination of a chlorido ligand to give *trans*-INT4, rotation of one of the bipyridyl ligands and recoordination of the chloride ion.

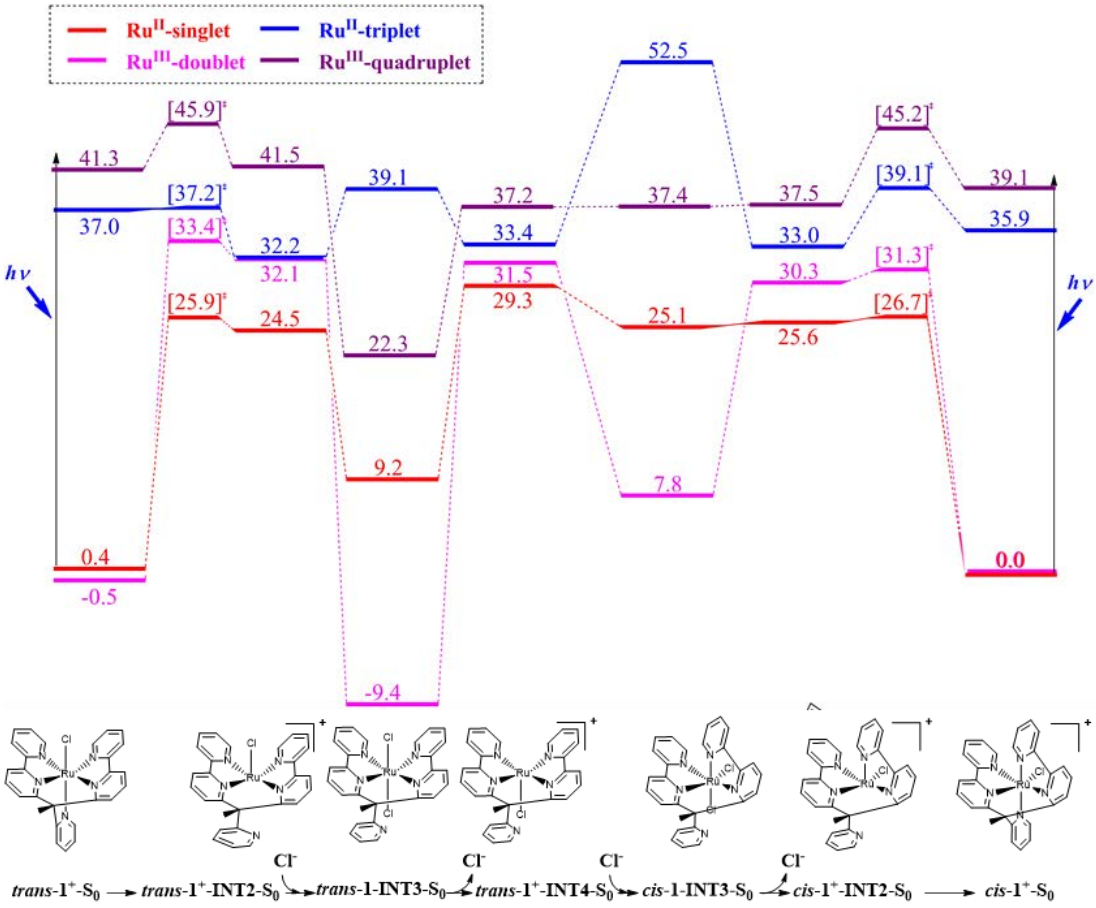

Figure 5. Energy diagram (B3LYPd3/TZVP-D95+~sdd//B3LYPd3/SVP~sdd) for the thermal and photo-induced isomerization processes for $\mathbf{1}^{+}$ and $\mathbf{1}^{2+}$ in DCM in the presence of added chloride ions. Red curve denotes the singlet spin surface, and blue curve denotes the triplet spin surface for Ru^{II}, whereas pink and violet curves denote the doublet and quadruplet spin surfaces for Ru^{III}, respectively. All Gibbs energies are calculated relative to *cis*-$\mathbf{1}^{+}$ or *cis*-$\mathbf{1}^{2+}$ and are reported in kcal/mol (transition state energies in brackets). S_0 = ground state.

With regard to the Ru(III) species, the possible *cis-trans* isomerization pathway involving chlorido decoordination and recoordination is shown in Figures S34 and S35. The decoordination step from *trans*-$\mathbf{1}^{2+}$ in MeOH and DCM has high barriers of 29.1 and 48.9 kcal/mol, respectively, because of the higher charge on the Ru atom, and probably precludes the occurrence of this mechanism for $\mathbf{1}^{2+}$. In consequence, for Ru(III) the isomerization involving the **κ-N⁴-bis-Cl⁺** intermediate is the more favorable path in DCM, since it involves a maximum barrier of 33.9 kcal/mol (Figure 5) compared to the barrier of 48.9 kcal/mol for the chlorido decoordination (Figure S35).

The corresponding aqua complex $\mathbf{2}^{2+}$ was prepared by stirring an aqueous solution of $\mathbf{1}^{+}$ for 2 days under reflux (Scheme 1). In contrast to the chlorido complex $\mathbf{1}^{+}$, $\mathbf{2}^{2+}$ exists in solution as a single *trans*-$\mathbf{2}^{2+}$ isomer according to NMR data (Figure S3), showing very similar spectra to those corresponding to *trans*-$\mathbf{1}^{+}$ given the fact that both molecules possess the same symmetry. The *trans* configuration of $\mathbf{2}^{2+}$ has also been confirmed by X-ray diffraction analysis (see Figure 6a in the Comparative Analysis Section below), and the complex has been further characterized by UV-vis spectroscopy (Figure S15) and ESI-TOF MS (Figure S10, a).

In order to prevent the isomeric equilibrium between the *cis* and *trans*-chlorido forms and to obtain a single *cis*-aqua species to be compared to the *trans*-$\mathbf{2}^{2+}$ species (*e.g.* in catalysis), a methyl substituent was introduced at the 6' position of one of the bpy moieties of bpy2PYMe in order to increase the steric hindrance and disrupt the formation of the *trans* configuration. The new ligand bpy(bpyMe)PYMe (L2, Chart 1) was obtained in a 17% yield following the same one-pot methodology used for the synthesis of bpy2PYMe (L1), the only difference being that 6-bromo-6'-methyl-2,2'-bipyridine was used instead of 6-bromo-2,2'-bipyridine (see Experimental Section for further details). A thorough NMR analysis of L2 can be found in Figure S4, in which the newly added methyl group can be clearly identified at 2.59 ppm in the HMBC spectrum. Concerning the respective chlorido and aqua complexes **3(Cl)** and **4(PF$_6$)$_2$**, the synthetic strategy followed for their preparation is depicted in Scheme 1 and in the Experimental Section.

Complexes **3**(**Cl**) and **4**(**PF$_6$**)$_2$ have been characterized by NMR spectroscopy (Figures S5 and S6, respectively). The presence of 28 ^{13}C NMR resonances for **3**(**Cl**) and **4**(**PF$_6$**)$_2$ and a ^{1}H NMR spectrum that resembles that of *cis*-$\mathbf{1}^{+}$ (although the signals now appear in a narrower range) are effectively an indication of the formation of a single *cis* isomer for both chlorido and aqua compounds. This is a consequence of the steric hindrance provided by the extra methyl group introduced into the original bpy2PYMe ligand (which according to the HMBC NMR spectra in Figures S5i and S6i can be assigned at 3.63 ppm and 3.05 ppm for $\mathbf{3}^{+}$ and $\mathbf{4}^{2+}$, respectively). Moreover, the formation of a pure *cis* isomer for $\mathbf{3}^{+}$ and $\mathbf{4}^{2+}$ has also been confirmed by X-ray diffraction analysis after slow evaporation of an acetone:water solution of **3**(**Cl**) (Figure S17, Table S2 and Experimental Section) and after ether diffusion into an acetone:DCM solution of **4**(**PF$_6$**)$_2$ (see Figure 6b in the Comparative Analysis Section below). All Ru-N distances and N-

Ru-N angles of both complexes logically resemble, and for *cis*-**3**$^{+}$ the Ru-Cl distance (2.456 Å) lies within normal expected values.[7,13d,22]

Additionally, **3**(**Cl**) and **4**(**PF$_6$**)$_2$ have been characterized by ESI-TOF MS, UV-vis and CV/DPV techniques (Figures S10, S14 and S28 in the Supporting Information, respectively), confirming the purity and integrity of the complexes and the expected similar spectroscopic and electrochemical properties to those of their related chlorido and aqua derivatives **1**$^{+}$ and **2**$^{2+}$, respectively. It should be highlighted as well that during the reductive scan of *cis*-**3**$^{+}$ a Ru^{II}-**κ-N^4-bis-Cl** species is formed at potentials near 0.27 V (Figure S22a, black). However, this species cannot isomerize to a hypothetical *trans*-**3**$^{+}$ species when reattaching the unbound N$_{Pyr}$ ligand due to the steric hindrance introduced by the extra methyl group present in L2. We believe this is the reason why no trace of either *trans*-**3**$^{+}$ or *trans*-**4**$^{2+}$ has been detected. Furthermore, DFT calculations for both isomers of system **3** revealed that *cis*-**3**$^{+}$ was 2.7 kcal/mol more stable than *trans*-**3**$^{+}$, in perfect agreement with the experimental data.

Synthesis and Characterization of 5(Cl), 6(OTf)$_2$, 7(Cl) and 8(BF$_4$)$_2$.

The synthetic strategy followed for the preparation of the respective chlorido and aqua complexes **5(Cl)** and **6(OTf)$_2$** bearing the PY5Me$_2$ (L3) ligand differs from the recently published data.[11] and is therefore depicted in Scheme 3 and in the Experimental Section. NMR spectra of **5**$^{+}$and **6**$^{2+}$ were coincident with data published by Kojima *et al.*[7] (for more information please refer to the Experimental Section), and good quality crystals of **6**$^{2+}$ could be obtained and analyzed by X-ray diffraction for the first time (Figures 6c and S18 and Table S4). Also, the electrochemical properties of **5**$^{+}$ have been studied by CV in acetonitrile (Figure S29), exhibiting a unique reversible wave at E^0 = 0.78 V *vs.* SCE (ΔE = 61 mV), corresponding to the Ru^{III}/Ru^{II} process.

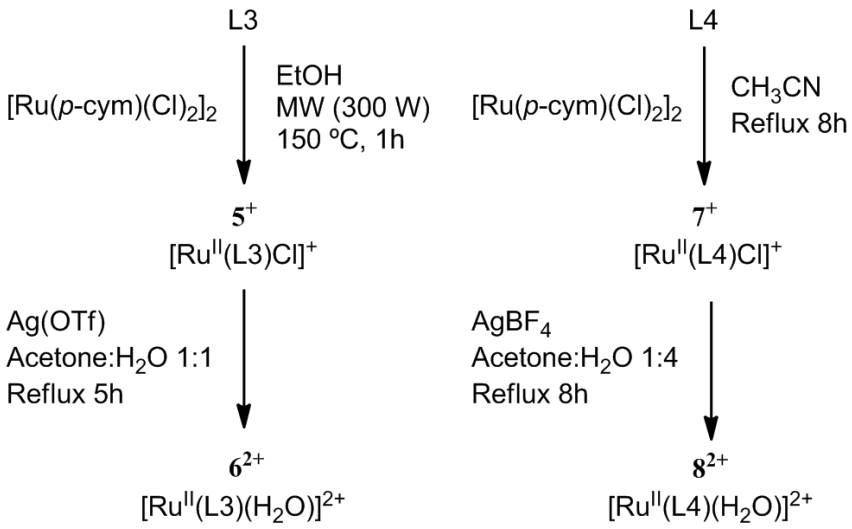

Scheme 3. Synthetic pathway for the preparation of the chlorido complexes $\mathbf{5}^{+}$ and $\mathbf{7}^{+}$ and the aqua complexes $\mathbf{6}^{2+}$ and $\mathbf{8}^{2+}$.

Complexes $\mathbf{7}^{+}$ and $\mathbf{8}^{2+}$, bearing the PY4Im (L4) ligand, were synthesized according to Scheme 3 (further details can be found in the Experimental Section) and have been characterized by ESI-MS (Figures S11 and S12), NMR (Figures S7 and S8), CV and DPV (Figures S30-S32), and UV-vis (Figure S16) techniques. Compound $\mathbf{7}^{+}$ in MeOH shows a unique reversible wave at E^0 = 0.84 V (ΔE = 75 mV) corresponding to the Ru^{III}/Ru^{II} process (Figure S30).

NMR analysis of $\mathbf{7}^{+}$ and $\mathbf{8}^{2+}$ show that both compounds display C2v symmetry in solution, with one symmetry plane passing through the chlorido/oxygen, the C(14) of the central imidazole and the Ru atom and bisecting the C(12)-C(13) bond of the imidazole ring, thus interconverting the two sides of the complex. Moreover, one symmetry plane (perpendicularly bisecting the former) contains the imidazole ring and the Ru and chlorido/aqua groups, hence interconverting the other two pyridine rings. As a result, we expect only 6 ^{1}H resonances, as confirmed in the corresponding ^{1}H NMR spectra (Figures S7a and S8a). It is worth mentioning that the characteristic down-field shift of the doublet corresponding to H1 (9.42 and 9.20 ppm, respectively) is likely due to hydrogen bonding interactions between the protons alpha to the nitrogen atoms of each pyridyl ring and the chlorido/oxygen coordinated to the Ru ion. HMBC and HSQC experiments have played an essential role in unambiguously assigning H12 and H6 singlets as well as all quaternary carbon resonances (Figures S7 and S8). Suitable crystals for X-ray diffraction analysis of

8$(BF_4)_2$ were obtained as well (Figures 6d and S19 and Table S5), the structure of which is compared to those of *trans*-**2**$^{2+}$, *cis*-**4**$^{2+}$ and **6**$^{2+}$ in the next Section.

Structural and Electrochemical Comparative Analysis of the aqua complexes.

Mercury plots of the X-ray crystal structures of *trans*-**2**$^{2+}$, *cis*-**4**$^{2+}$, **6**$^{2+}$ and **8**$^{2+}$ are shown in Figure 6, and the corresponding crystallographic data can be found in Tables S1 and S3-S5, respectively. Table S6 includes a list of selected bond distances and angles for the four aqua complexes, which are in the expected range compared to other Ru(II) polypyridyl complexes.[23] The effect of the higher rigidity of the bpy2PYMe ligand (L1) compared to the more flexible $PY5Me_2$ (L3) and Py4Im (L4) ligands can be seen in the geometry around the Ru(II) atom, as it displays the least ideal octahedral environment of the series (N1-Ru-N2 and O-Ru-N_5 angles –entries 7 and 11- close to 170° and O-Ru-N1 angle –entry 12- close to 80° in *trans*-**2**$^{2+}$, and longer Ru-N1 distance –entry 1- in *trans*-**2**$^{2+}$ compared to **6**$^{2+}$ and **8**$^{2+}$). The distortion from the ideal octahedral geometry is even more pronounced upon introduction of the Me moiety to generate L2 (*cis*-**4**$^{2+}$) due to the steric constraints it imposes. Thus, the N1-Ru-N3 and N2-Ru-N4 angles (entries 9 and 10) are 11° and 5° smaller than for the case of L1 (N1-Ru-N2 angle, entry 7), respectively, and the O-Ru-N1 and O-Ru-N4 angles are 12° and 6° off from 90° (entries 12 and 15 in Table S6, respectively, and Figure 6b).

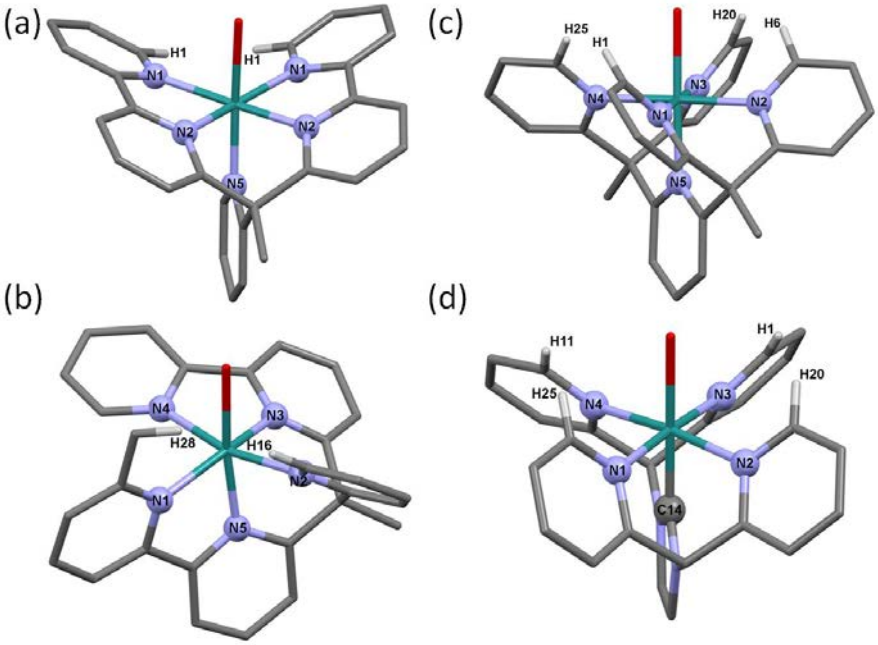

Figure 6. Mercury plot of the X-Ray crystal structures of *trans*-**2**$^{2+}$ (a), *cis*-**4**$^{2+}$ (b), **6**$^{2+}$ (c) and **8**$^{2+}$ (d). Atom color code: blue, nitrogen; red, oxygen; dark green, ruthenium; light grey, carbon. Only the hydrogen atoms closest to the oxygen atoms are shown in white.

The less rigid character of the L3 and L4 scaffolds is reflected in the relative orientation of the 4 equatorial pyridine rings in $\mathbf{6}^{2+}$ and $\mathbf{8}^{2+}$, which are clearly non parallel and show four alpha H atoms within hydrogen bonding distance to the O atom of the aqua ligand (2.6-2.9 Å, Figure 6c-d). On the other hand, for L1 and L2 the existence of a C-C bridge in the bpy ligands precludes any relative rotation of the pyridine rings and impedes the approach of any pyridyl H atoms to the axial O atom. The closest distances for *trans*-$\mathbf{2}^{2+}$ fall in the range of 3.9 Å for O-H1, and 2.8 Å for O-H16 in *cis*-$\mathbf{4}^{2+}$ (Figure 6a-b), all of which are longer than clear O···H bond distances. Exceptionally, one of the hydrogen atoms of the 6' Me substituent in *cis*-$\mathbf{4}^{2+}$ lies within the limit of hydrogen bonding to the O atom (O-H28 distance of 2.6 Å), which is again an indication of the steric constraints imposed by the methylated ligand.

The last significant difference observed between the four structures is the shorter Ru-X_{ax} distance for $\mathbf{8}^{2+}$ (Table S6, entry 3) due to the much stonger σ-donor character of the carbene moiety (C_{ax}) with regards to the pyridyl scaffold present in *trans*-$\mathbf{2}^{2+}$, *cis*-$\mathbf{4}^{2+}$ and $\mathbf{6}^{2+}$. This feature has a dramatic effect in the acidity of the aqua group, which is significantly decreased (see pKa values in Table 1 below). Interestingly, despite the presence of different coordinating atoms in the site *trans* to the aqua group, all Ru-O distances are similar, between 2.1 and 2.2 Å (Table S6, entry 6).

The electrochemical behavior of the aqua-complexes has also been studied in detail at different pHs, therefore allowing the construction of their Pourbaix diagrams (Figure S27), and a global comparison of the redox potentials at pH 7 and the pK_a values of *trans*-$\mathbf{2}^{2+}$, *cis*-$\mathbf{4}^{2+}$, $\mathbf{6}^{2+}$, $\mathbf{8}^{2+}$ and those of the paradigmatic Ru-penta-N-dentate complex[24] $[Ru(trpy)(bpy)(H_2O)]^{2+}$ is presented in Table 1.

Table 1. Redox potentials at pH 7 (in V *vs*. SCE), and pK_a values for the aqua-complexes $\mathbf{2}^{2+}$, $\mathbf{4}^{2+}$, $\mathbf{6}^{2+}$ and $\mathbf{8}^{2+}$ and the related Ru complex $[Ru(trpy)(bpy)(H_2O)]^{2+}$.

Complex	III / II	IV / III	ΔE (mV) [d]	pK_{a1} (Ru^{III})	pK_{a2} (Ru^{II})	Ref.
trans-$\mathbf{2}^{2+}$ [a]	0.56	0.75	190	2.6	11.0	c
cis-$\mathbf{4}^{2+}$ [a]	0.51	---		---	---	c
$\mathbf{6}^{2+}$ [a]	0.38	---		2.7	10.7	c
$\mathbf{6}^{2+}$ [b]	0.46	---		---	11.0	7
$\mathbf{8}^{2+}$ [a]	0.58	0.80	220	5.3	12.7	c
$[Ru(trpy)(bpy)(H_2O)]^{2+}$ [a]	0.49	0.62	130	1.7	9.7	24

[a] In aqueous phosphate buffer pH 7. [b] In Britton-Robinson buffer. [c] This work. [d] $\Delta E = E^{IV/III} - E^{III/II}$.

It is well known that the presence of an aqua group enables a simultaneous removal of electrons and protons (PCET) at relatively low and close potentials since the buildup of high columbic charges is avoided,[25] allowing easy access to high oxidation states necessary for oxidative catalytic transformations. According to the Pourbaix diagrams (Figure S27), slopes of approximately -59 mV per pH unit in the central pH regions indicate the presence of the single PCET processes Ru^{III}-OH/Ru^{II}-OH_2 and Ru^{IV}-O/Ru^{III}-OH.[24] Consequently, the two waves observed at 0.56 V and 0.75 V vs. SCE for *trans*-$\mathbf{2}^{2+}$ and at 0.58 V and 0.80 V for $\mathbf{8}^{2+}$ at pH 7 can be assigned to the Ru^{III}-OH/Ru^{II}-OH_2 and Ru^{IV}-O/Ru^{III}-OH processes, respectively (L1 and L4 have been omitted for clarity), whereas for *cis*-$\mathbf{4}^{2+}$ and $\mathbf{6}^{2+}$ the wave corresponding to the Ru^{III}-OH/Ru^{II}-OH_2 process can be detected at 0.51 V and 0.38 V, respectively (Table 1). Thus, at pH 7 the Ru^{III}/Ru^{II} and Ru^{IV}/Ru^{III} redox processes are separated by 190 mV in *trans*-$\mathbf{2}^{2+}$ and by 220 mV in $\mathbf{8}^{2+}$, while this separation is only of 130 mV in $[Ru^{II}(trpy)(bpy)]^{2+}$. This difference points out the higher stability of the Ru^{III}(OH) species of *trans*-$\mathbf{2}^{2+}$ and even more so for $\mathbf{8}^{2+}$ than in $[Ru^{II}(trpy)(bpy)]^{2+}$, which in the case of $\mathbf{8}^{2+}$ could be due to

hydrogen bonding interactions between the hydroxo group and the hydrogen atoms alpha to the pyridyl nitrogens of the pentadentate ligand (see Figure 6d).

Referring again to the Pourbaix diagrams, the two vertical lines (non-redox processes) allow determination of the pK_{a1} (Ru^{III}-OH_2) and pK_{a2} (Ru^{II}-OH_2) values. Therefore, for *trans*-$\mathbf{2}^{2+}$ these values are 2.6 and 11.0, respectively, which are very similar to those of $\mathbf{6}^{2+}$ (2.7 and 10.7) given the strong resemblance from an electronic viewpoint of L1 and L3. The pK_{a2} value for $\mathbf{6}^{2+}$ differs slightly from the value obtained previously by Kojima *et al.* (11.0),[7] although this difference may be attributed to the different buffers used in both works (Table 1). Finally, the pK_a values of the aqua group for $\mathbf{8}^{2+}$ (5.3 and 12.7 for Ru^{III} and Ru^{II}, respectively) are significantly higher because of the strong σ-donating character of the carbene scaffold present in L4. The decreased acidity of the aqua group in $\mathbf{8}^{2+}$ is also evident when comparing its pK_a values with those of $[Ru(trpy)(bpy)(H_2O)]^{2+}$; the pK_{a1} and pK_{a2} values for the PY4Im complex increase by 3.6 and 3 units, respectively, compared to $[Ru(tpy)(bpy)(H_2O)]^{2+}$, while $\mathbf{2}^{2+}$ and $\mathbf{6}^{2+}$ occupy an intermediate position, with pK_a values only 0.9-1.3 units greater than those of $[Ru(trpy)(bpy)]^{2+}$.

Conclusions

The combined use of spectroscopic, spectrometric, electrochemical and theoretical methods has led to a proposed isomerization mechanism for the **1**$^{+}$ chlorido species and the quantification of the thermodynamic parameters. In MeOH both isomers are interconverted under thermal and photochemical conditions by a sequence of chlorido decoordination, decoordination/recoordination of a pyridyl group and chlorido recoordination. Also, under oxidative conditions in DCM the exchange of a pyridyl group of the ligand by a Cl^{-} counterion in *trans*-**1**$^{2+}$ generates a bis-chlorido intermediate $[Ru^{III}(\kappa\text{-}N^{4}\text{-bpy2PYMe})Cl_2]^{+}$ (**κ-N^{4}-bis-Cl^{+}**), which is essential for the isomerization process observed when the system is reduced back to Ru(II). In contrast, under the same conditions *cis*-**1**$^{2+}$ is in direct equilibrium with *trans*-**1**$^{2+}$, with absence of the **bis-Cl^{+}** intermediate. Interestingly, its aqua derivative exists as a pure single isomer (*trans*-**2**$^{2+}$), while by increasing the steric hindrance of the pentadentate ligand via introduction of a methyl group the isomerization equilibrium is completely inhibited and a single *cis* isomer is obtained (*cis*-**3**$^{+}$/*cis*-**4**$^{2+}$). The electrochemical and structural data of this series of complexes (**1**$^{+}$ to **4**$^{2+}$) has also been compared to those of related Ru pentadentate choro- and aqua-compounds, some of which are reported here for the first time (**7**$^{+}$ and **8**$^{2+}$). This comparison shows how the influence of the chemical and structural characteristics of the pentadentate ligand impacts on the electrochemical and acid-base properties of the resulting Ru(II) complexes**,** which are fundamental for modulating their activity in redox catalysis. In the near future we plan to further extend this study by comparing the capacity of the aqua compounds described as catalysts for redox oxidative transformations.

Experimental section

Materials. All reagents used in the present work were obtained from Aldrich Chemical Co. and were used without further purification. Reagent-grade organic solvents were obtained from Scharlab. $RuCl_3 \cdot 3H_2O$ and $[Ru(p\text{-cymene})(Cl)_2]_2$ were supplied by Alfa Aesar and were used as received. The synthesis of the ligand $PY5Me_2$ was performed following the procedure described in the literature.[26] In order to obtain the bpy2PYMe, bpy(bpyMe)PYMe and PY4Im ligands, some modifications have been introduced to the procedures already published. Thus, for bpy2PYMe[11] and bpy(bpyMe)PYMe we performed a one-pot reaction of 2-ethylpyridine with LDA and 6-bromo-2,2'-bipyridine (as well as 6-bromo-6'-methyl-2,2'-bipyridine for the latter), whereas for PY4Im[10] the silver derivative PY4Im-Ag was obtained by reaction of (PY4Im)Br with Ag_2O in acetonitrile instead of DCM (see Results Section for further details).

All synthetic manipulations were routinely performed under nitrogen or argon atmosphere using Schlenk tubes and vacuum-line techniques.

Instrumentation and Measurements. UV-vis spectroscopy was performed by a HP8453 spectrometer using 1 cm quartz cells. NMR spectroscopy was performed on a Bruker DPX 250 MHz, DPX 360 MHz, DPX 400 MHz or a DPX 600 MHz spectrometer. Samples were run in $CDCl_3$, MeOD, CD_3CN, CD_3NO_2 or acetone-d_6 with internal references. Electrospray ionization mass spectrometry (ESI-MS) experiments were carried out on an HP298s gas chromatography (GC-MS) system from the Servei d'Anàlisi Química of the Universitat Autònoma de Barcelona (SAQ-UAB). MALDI-TOF MS measurements were run on a Bruker MALDI TOF ultrafleXtrem model under reflector mode by depositing on a GrounSteel plate 0.5 μL of a MeOH solution of the complexes. Cyclic voltammetry (CV), differential pulse voltammetry (DPV) and controlled-potential electrolysis (CPE) experiments were performed on a Biologic SP-150 potentiostat, using EC Lab software for data acquisition and data handling. Measurements were made using a three-electrode conical cell equipped with a methanol jacket, which makes it possible to fix the temperature by means of a thermostat. A glassy carbon disk electrode of 1.0 mm diameter (or a carbon graphite rod in the case of CPE) was used as a working electrode, a Pt disk of 1 mm diameter as an auxiliary electrode and an aqueous saturated calomel electrode (SCE) as a reference electrode. All of the potentials are reported versus (SCE) isolated from the working electrode compartment by a salt bridge. The salt solution

of the reference calomel electrode is separated from the electrochemical solution by a salt-bridge capped with a frit, which is made of a ceramic material, allowing ionic conduction between the two solutions and avoiding appreciable contamination. Ideally, the electrolyte solution present in the bridge is the same as the one used for the electrochemical solution, in order to minimize junction potentials. Working electrodes were polished with 0.05 micron Alumina paste washed with distilled water and acetone before each measurement. The complexes were dissolved in acetone, acetonitrile or DCM containing the necessary amount of n-Bu_4NPF_6 ($TBAPF_6$) or $TBABF_4$ as supporting electrolyte to yield 0.1 M ionic strength solutions. CV were recorded at a 100 $mV \cdot s^{-1}$ scan rate, and DPV were recorded using pulse amplitudes of 0.05 V, pulse widths of 0.05 s, sampling widths of 0.02 s, pulse periods of 0.1 s and quite times of 2 s. E^0 values reported in this work were estimated from CV experiments as the average of the oxidative and reductive peak potentials $(E_{p,a} + E_{p,c})/2$. The error associated with the potential values is less than 5 mV. In order to minimize the ohmic drop effects, the electrode used as a working electrode is 1.0 mm diameter and the scan rates investigated were in the range 0.1 – 1 V s^{-1}. Positive feedback iR compensation was used throughout. Typically compensated resistances were 0.5-2.0 kΩ, depending on the electrode location in the electrochemical cell. For the Pourbaix diagrams, CV and DPV of the corresponding aqua complexes were recorded in aqueous phosphate solutions to which small amounts of HCl 0.1 M or NaOH 0.1 M had been added in order to adjust the pH to the desired value. For the controlled-potential electrolysis (CPE) experiments, a 0.68 mM solution of **1**(Cl) in 5 mL DCM, containing 0.1 M of $TBAPF_6$ as supporting electrolyte, was prepared. Oxidative CPE at different potentials vs. SCE was performed using a carbon graphite rod as a working electrode. After the passage of the desired number of Faradays, the electrolysis was stopped, and the mixture was then analyzed by CV. For the light-induced isomerization processes, the dissolved complexes in a N_2 purged schlenk flask were kept at 0 °C (water bath) and irradiated by a 100 W incandescent white light bulb, while for the temperature-driven isomerization processes the water bath was set at 50 °C and the schlenk was covered with aluminium foil.

Computational Details. Density functional theory (DFT) calculations have been carried out with the Gaussian 09 set of programs.[27] For geometry optimizations, the well-established and computationally fast hybrid-GGA functional B3LYP was used,[28] including the D3 dispersion correction of Grimme.[29] The electronic configuration of the molecular systems was described with the standard split-valence basis set with a polarization function of Ahlrichs and co-workers for H, C, N, O, and Cl (SVP keyword in Gaussian).[30] For Ru we used the small-core, quasi-relativistic Stuttgart/Dresden effective core potential, with an associated valence basis set contracted (standard SDD keywords in Gaussian 09).[31,32,33] The geometry optimizations were performed without symmetry constraints, and the characterization of the located stationary points was performed by analytical frequency calculations.

Gibbs energies, ΔG, were built through single point energy calculations on the B3LYP-d3/SVP geometries using the B3LYP-d3 functional and the triple-ζ valence plus polarization on main group atoms (TZVP keyword in Gaussian).[34] Furthermore diffuse basis sets (D95+) have been incorporated for Cl.[35] Solvent effects were included with the PCM model using dichloromethane and methanol as solvents.[36] To these B3LYP-d3/TZVP electronic energies in solvent, zero point energy and thermal and entropic corrections were included from the gas phase frequency calculations at the B3LYP-d3/SVP level of theory.

Synthetic preparations. *[Ru^{II}(bpy2PYMe)Cl]Cl [**1**(Cl)]*. A sample of bpy2PYMe (0.140 mmol) was dissolved in 5 mL of dry ethanol, then 81 mg of [Ru(*p*-cymene)$(Cl)_2]_2$ (0.140 mmol) was added. The mixture was stirred and heated with a microwave (MW, 300 W) at 150 °C during 1 h. After this time the solution was filtrated through celite and the volume was reduced in the rotary evaporator. After addition of ethanol, the *trans*-**1**(Cl) isomer precipitated as a burgundy coloured solid, which was filtered and washed with DCM. Further addition of DCM to the supernatant yielded a burgundy coloured solid (*cis*-**1**(Cl) isomer), which was filtered and washed with Et_2O. Yield: 20 mg (*trans*-**1**(Cl), 24%) and 49 mg (*cis*-**1**(Cl), 60%). ^{1}H NMR *cis*-$\mathbf{1}^+$ (600 MHz, d_3-nitromethane, 298K): δ = 9.93 (d, 1H, J19-18=4.9 Hz, H19), 9.27 (dd, 1H, J1-2=5.7 Hz, J1-3=1.1 Hz, H1), 8.54 (d, 1H, J16-17=7.5 Hz, H16), 8.31 (d, 1H, J12-11=8.0 Hz, H12), 8.26 (m, 2H, H17, H15), 8.21 (d, 1H, J13-14=7.5 Hz, H13), 8.17 (dd, 1H, J5-6=5.5 Hz, J5-7=2.1 Hz, H5), 8.13 (t, 1H, J14-13,15=7.9 Hz, H14), 8.08(d, 1H, J9-10=8.3 Hz, H9), 8.04 (m, 1H, H18), 7.95

(m, 2H, H6, H7), 7.92 (m, 1H, H10), 7.86 (t, 1H, J2-1,3=7.9 Hz, H2), 7.28 (t, 1H, J3-2,4=6.1 Hz, H3), 7.24 (t, 1H, J11-12,10=6.1 Hz, H11), 7.18 (d, 1H, J4-3=5.3 Hz, H4), 2.964 (s, 1H, H8). $^{13}C\{^{1}H\}$ NMR (151 MHz, d_3-nitromethane, 298K): δ = 161.8 (C6), 160.1 (C5), 160.0 (C22), 159.5 (C23), 158.3 (C13), 158.0 (C10), 156.9 (C18, C1), 153.2 (C27), 152.1 (C4), 139.1 (C15), 138.2 (C25) 137.6 (C2), 136.3 (C8), 135.9 (C20), 128.6 (C26), 126.2 (C3), 124.7 (C24), 124.6 (C14), 124.4-124.3 (C9, C16), 123.5 (C17), 123.2 (C21), 122.8 (C13), 122.2 (C7) 59.8 (C11), 21.9 (C12). UV/vis (DCM): λmax, nm (ε, $M^{-1}\cdot cm^{-1}$)= 295 (20517), 355 (5437), 523 (4496). ESI-MS (DCM): *m/z*= 552.1($[M-Cl]^+$). Elemental analysis (% found): C, 55.27; H, 3.67; N, 11.90. Calcd for $C_{27}H_{21}Cl_2N_5Ru$: C, 55.20; H, 3.60; N, 11.92. ^{1}H NMR *trans*-**1**$^+$ (400 MHz, d_3-nitromethane, 298K): δ = 9.96 (d, 2H, J1-2=5.3 Hz, H1), 9.14 (d, 1H, J11-12=4.8 Hz, H12), 8.36 (d, 2H, J4-3=8.0 Hz, H4), 8.22 (dd, 2H, J7-6=6.4 Hz, J7-5=2.4 Hz, H7), 8.12 (m, 6H, H3,H5,H6), 7.90 (d, 1H, J9-10=8.1 Hz, H9), 7.83 (m, 3H, H2, H10), 7.08 (t, 1H, J11-10=6.3 Hz, J11-12=4.9 Hz, H11), 2.97 (s, 3H, H8). $^{13}C\{^{1}H\}$ NMR (100 MHz, d_3-nitromethane, 298K): δ = 161.4 (C10), 160.9 (C6), 160.4 (C5), 157.4 (C17), 154.3 (C1), 140.9 (C13), 139.5 (C15) 139.1 (C3), 137.1 (C7), 126.6 (C2), 125.6 (C14), 124.3 (C16), 123.8 (C4), 122.7 (C8), 122.1 (C9), 60.8 (C11), 21.9 (C12). UV/vis (DCM): λmax, nm (ε, $M^{-1}\cdot cm^{-1}$)= 298 (19198), 390 (4652), 534 (5029). ESI-MS (DCM): *m/z*= 552.1 ($[M-Cl]^+$). Elemental analysis (% found): C, 55.31; H, 3.68; N, 11.88. Calcd for $C_{27}H_{21}Cl_2N_5Ru$: C, 55.20; H, 3.60; N, 11.92.

*$[Ru^{II}(bpy2PYMe)(H_2O)](PF_6)_2$ [**2**$(PF_6)_2$]*. 40 mg (0.06 mmol) of the 3:7 *trans*-**1**$^+$:*cis*-**1**$^+$ mixture obtained in the crude of the synthesis of **1**(Cl) were dissolved in 20 mL of water. The mixture was stirred and heated at 100 °C for 2 days, after which 0.5 mL of a NH_4PF_6 saturated aqueous solution was added. The volume was reduced until a brown precipitate appeared, which was filtered and washed with Et_2O. Yield: 43 mg (76%). ^{1}H NMR (400 MHz, d_6-acetone:D_2O 95:5, 298K): δ = 10.32 (d, 2H, J1-2=5.4 Hz, H1), 9.58 (d, 1H, J12-11=4.7 Hz, H12), 8.84 (d, 2H, J4-3=8.0 Hz, H4), 8.70 (d, 2H, J7-6=7.3 Hz, H7), 8.51 (m, 7H, H3,H5,H6), 8.20 (m, 3H, H2, H9, H10), 7.50 (t, 1H, J11-10=6.4 Hz, J11-12= 4.9 Hz, H11), 3.21 (s, 3H, H8). $^{13}C\{^{1}H\}$ NMR (100 MHz, d_6-acetone:D_2O 95:5, 298K): δ = 159.7 (C10), 159.4 (C6), 158.1 (C5), 157.2 (C13), 156.2 (C17), 154.5 (C1), 140.4 (C15) 140.0 (C3), 138.9 (C7), 127.4 (C2), 126.9 (C14), 124.7 (C16), 124.5 (C4), 123.8 (C8), 122.4 (C9), 59.9 (C11), 21.2 (C12). UV/vis (H_2O): λmax, nm (ε, $M^{-1}\cdot cm^{-1}$)= 371 (3988), 494 (4485). ESI-MS (MeOH): *m/z*= 536.2 ($[M-2PF_6-2H^+]^+$). Elemental

analysis (% found): C, 39.42; H, 2.85; N, 8.51. Calcd for $C_{27}H_{23}F_{12}N_5OP_2Ru$: C, 39.33; H, 2.81; N, 8.49.

bpy(bpyMe)PYMe (L2). For the synthesis of L2 the same methodology used for the synthesis of L1 was employed, except that in the second step (16 h reaction) 6-bromo-6'-methyl-2,2'-bipyridine was used instead of 6-bromo-2,2'-bipyridine. The synthesis of 6-bromo-6'-methyl-2,2'-bipyridine was performed introducing some modifications with respect to the procedure described in the literature.[37] Thus, to a solution of 2-bromo-6-methylpyridine in THF at -65 °C, 1.2 equiv of BuLi in hexanes was added slowly (30 min), and the mixture was stirred for 3 h at -65 °C. Then, 1.2 equiv of Me_3SnCl in THF was added slowly (30 min), and the mixture was then allowed to slowly reach RT (1 h) under an Ar atmosphere and with constant stirring. The reaction was quenched with 10 mL NH_4Cl saturated solution, the mixture was extracted with ethyl acetate and dried with sodium sulfate, filtered and dried by solvent evaporation. The orange liquid obtained corresponds to 2-methyl-6-(trimethylstannyl)pyridine. Then, this stannate derivative was used to perform the coupling reaction with 2,6-dibromopyridine in the presence of LiCl (2 equiv.) and $Pd(PPh_3)_4$ (catalytic amounts) in order to obtain 6-bromo-6'-methyl-2,2'-bipyridine, as described elsewhere.[38] Yield: 17 %. ^{1}H NMR (400 MHz, $CDCl_3$, 298K): δ = 8.62 (m, 2H), 8.30 (m, 2H), 8.26 (d, 1H, J = 7.3 Hz), 8.01 (d, 1H, J = 6.9 Hz), 7.71 (m, 3H), 7.54 (m, 2H), 7,15 (m, 6H), 2.59 (s, 3H), 2.54 (s, 3H). ^{13}C NMR (100 MHz, $CDCl_3$, 298K): δ = 166.5, 165.2, 164.9, 157.5, 156.5, 155.9, 154.9, 154.5, 148.9, 148.7, 136.9, 136.7, 136.7, 136.7, 135.7, 123.9, 123.9, 123.6, 132.5, 123.5, 123.0, 121.3, 121.1, 118.3, 118.3, 118.2, 60.7, 27.7, 24.4. ESI-MS (DCM): *m/z*= 430.2 ($[M+H]^+$). Elemental analysis (% found): C, 78.21; H, 5.44; N, 16.34. Calcd for $C_{28}H_{23}N_5$: C, 78.30; H, 5.40; N, 16.31.

*$[Ru^{II}$(bpy(bpyMe)PYMe)Cl]Cl [**3**(Cl)]*. A sample of bpy(bpyMe)PYMe (0.233 mmol) was dissolved in 5 mL of dry ethanol, then 71 mg of $[Ru(p\text{-cymene})(Cl)_2]_2$ (0.116 mmol) was added. The mixture was stirred and heated with a MW (300 W) at 150 °C for 1 h. After this time the volume was reduced in the rotary evaporator. After addition of MeOH and 0.5 mL of a NH_4PF_6 saturated aqueous solution, *cis*-**3**(Cl) precipitated as a red solid, which was filtered and washed with MeOH and Et_2O. Yield: 112 mg (68%). ^{1}H NMR (400 MHz, d_2-DCM, 298K): δ = 9.40 (d, 1H, J = 6.0 Hz), 8.33 (d, 1H, J = 8.0 Hz), 8.12 (m, 2H), 8.06 (m, 3H), 7.98 (m, 3H), 7.92 (t, 1H, J = 7.6 Hz), 7.83 (m, 3H), 7.31 (t, 1H, J = 6.4 Hz), 7.22 (t, 1H, J = 6.4 Hz), 6.90 (d, 1H, J = 6 Hz), 3.63 (s, 3H), 2.90 (s, 3H).

^{13}C NMR (100 MHz, d_2-DCM, 298K): δ = 165.6, 161.2, 160.1, 159.0, 158.6, 158.6, 157.7, 156.9, 156.1, 150.6, 137.8, 137.3, 136.1, 135.9, 134.6, 128.3, 125.5, 123.2, 122.8, 122.7, 122.1, 122.0, 121.8, 121.7, 120.5, 57.8, 27.6, 21.9. UV/vis (DCM): λmax, nm (ε, $M^{-1}\cdot cm^{-1}$)= 292 (29954), 379 (4787), 502 (5802). ESI-MS (DCM): *m/z*= 566.1 ($[M-Cl]^+$). Elemental analysis (% found): C, 56.01; H, 3.89; N, 11.59. Calcd for $C_{28}H_{23}Cl_2N_5Ru$: C, 55.91; H, 3.85; N, 11.64.

*[Ru^{II}(bpy(bpyMe)PYMe)(H_2O)](PF_6)$_2$ [**4**(PF_6)$_2$]*. 30 mg of **3**(Cl) were dissolved in 12 mL of water. The mixture was stirred and heated at 100 °C for 2 days, after which 0.5 mL of a NH_4PF_6 saturated aqueous solution was added. The volume was reduced until a red precipitate appeared, which was filtered and washed with Et_2O. Yield: 31 mg (86%). ^{1}H NMR (400 MHz, d_6-acetone:D_2O 5:95, 298K): δ = 9.04 (d, 1H, J = 4.8 Hz), 8.27 (t, 2H, J = 7.6 Hz), 8.16 (dd, 1H, J = 6.8, 2.4 Hz), 8.01 (m, 6H), 7.81 (m, 5H), 7.28 (t, 1H, J = 6.4 Hz), 7.19 (t, 1H, J = 6.4 Hz), 7.02 (d, 1H, J = 6 Hz), 3.05 (s, 3H), 2.80 (s, 3H). ^{13}C NMR (100 MHz, d_6-acetone:D_2O 5:95, 298K): δ = 164.2, 161.2, 158.7, 157.9, 157.0, 157.0 156.8, 156.5, 156.0, 151.7, 138.6, 138.2, 138.0, 136.7, 136.3, 128.7, 125.9, 124.2, 124.0, 123.7, 123.0, 122.5, 122.0, 121.4, 121.4, 58.0, 24.9, 20.5. UV/vis (H_2O): λmax, nm (ε, $M^{-1}\cdot cm^{-1}$)= 300 (21271), 354 (6125), 392 (5709), 521 (5203). ESI-MS (DCM): *m/z*= 550.1($[M-2PF_6+2H]^+$). Elemental analysis (% found): C, 40.19; H, 3.03; N, 8.32. Calcd for $C_{28}H_{25}F_{12}N_5OP_2Ru$: C, 40.11; H, 3.01; N, 8.35.

*[Ru^{II}($PY5Me_2$)Cl]Cl [**5**(Cl)]*. A sample of $PY5Me_2$ (0.225 mmol) was dissolved in 5 mL of dry ethanol, then 137 mg of [Ru(*p*-cymene)$(Cl)_2]_2$ (0.225 mmol) was added. The mixture was stirred and heated with a MW (300 W) at 150 °C during 1 h. After this time the volume was reduced in the rotary evaporator. After addition of Et_2O, a yellow solid precipitated, which was filtered and washed with Et_2O. Yield: 103 mg (74%). ^{1}H NMR (400 MHz, DMSO-d_6, 298K) δ = 9.67 (dd, *J* = 5.8, 1.8 Hz, 4H), 8.04 (m, 7H), 7.96 (td, *J* = 7.8, 1.5 Hz, 4H), 7.53 (ddd, *J* = 7.3, 5.8, 1.4 Hz, 4H), 2.76 (s, 6H). Elemental analysis (% found): C, 56.66; H, 4.12; N, 11.31. Calcd for $C_{29}H_{25}Cl_2N_5Ru$: C, 56.59; H, 4.09; N, 11.38.

*[Ru^{II}($PY5Me_2$)(H_2O)](OTf)$_2$ [**6**(OTf)$_2$]*. **5**(Cl) (40 mg, 0.07 mmol) and AgOTf (23 mg, 0.09 mmol) were dissolved in darkness in a flask containing acetone:water (10 mL,

1:1). The resulting solution was stirred and heated under reflux for 5 h. After cooling down to room temperature the solution was filtered to remove the AgCl byproduct. Slow evaporation of the acetone yielded a yellow solid, which was filtered and dried in air. The residue was crystalized by Et_2O diffusion into water. Yield: 40 mg (67%). ^{1}H NMR (400 MHz, DMSO-d_6, 298K) δ = 9.45 (dd, *J* = 5.9, 1.7 Hz, 4H), 8.06 (m, 11H), 7.63 (ddd, *J* = 7.3, 5.7, 1.4 Hz, 4H), 7.52 (s, 2H), 2.78 (s, 6H). Elemental analysis (% found): C, 43.31; H, 3.19; N, 8.11. Calcd for $C_{31}H_{27}F_6N_5O_7S_2Ru$: C, 43.26; H, 3.16; N, 8.14.

PY4Im-Ag (L4). For the synthesis of L4, 2-methylpyridine reacted with 2-fluoropyridine via lithiation in hexanes affording 2-(2-pyridylmethyl)pyridine,[39] which was subsequently brominated to yield bis(2-pyridyl)bromomethane.[40] This precursor was then added to a basic solution containing imidazole to obtain (PY4Im)Br, as previously described by Long and Smith.[10] However, the silver derivative PY4Im-Ag could only be isolated as a pure white powder when (PY4Im)Br reacted with Ag_2O in acetonitrile instead of in CH_2Cl_2.[10]

III

*[Ru^{II}(PY4Im)Cl]Cl [**7**(Cl)]*. [PY4ImAg]Br (0.062 g, 0.202 mmol) and [Ru(*p*-cymene)$(Cl)_2]_2$ (0.062 g, 0.101 mmol) were dissolved in a flask containing acetonitrile (25 mL), and the resulting solution was heated under reflux overnight. After that time a yellow precipitate appeared, which was filtered and dried with diethyl ether. Yield: 94 mg (86%).^{1}H-NMR (400MHz, DMSO-d_6, 298K): δ = 9.42 (d, 4H, J1-2=5.67 Hz, H1), 7.93 (d, 4H, H4), 7.92 (t, 4H, H3), 7.77 (s, 2H, H12), 7.46 (t, 4H, H2), 7.45 (s, 2H, H6). ^{13}C{^{1}H} NMR (100 MHz, DMSO-d_6, 298K): δ = 194.78 (C14), 155.63 (C1), 154.91 (C5), 137.20 (C4), 125.67 (C3), 124.40 (C2), 120.51 (C12), 65.19 (C6). ESI-MS (MeOH): *m/z*= 541.05([M-Cl]$^+$). Elemental analysis (% found): C, 52.10; H, 3.69; N, 14.51. Calcd for $C_{25}H_{21}Cl_2N_6Ru$: C, 52.00; H, 3.67; N, 14.55.

*[Ru^{II}(PY4Im)(H_2O)]$(BF_4)_2$ [**8**$(BF_4)_2$]*. **7**(Cl) (0.060 g, 0.103 mmol) and $AgBF_4$ (0.061 g, 0.309 mmol) were dissolved in darkness in a flask containing acetone:water (10 mL, 1:4). The resulting solution was stirred and heated under reflux overnight. After cooling down to room temperature, the solution was filtered to remove the AgCl byproduct. Slow evaporation of the acetone yielded yellow crystals, which were filtered and dried over air. Yield: 60 mg (84%). ^{1}H-NMR (400 MHz, D2O, 298K): δ = 9.20 (d, 4H, J1-2=5.60 Hz, H1), 7.89 (d, 4H, H4), 7.87 (ddd, 4H, H3), 7.62 (s, 2H, H12), 7.44 (ddd, 4H, J2-3=7.73 Hz, J2-1=5.60 Hz, J2-4=2.12 Hz, H2), 7.13 (s, 2H, H6). ^{13}C{^{1}H}

NMR (100MHz, D2O, 298K): δ = 195.18 (C14), 154.24 (C1), 153.26 (C5), 137.15 (C4), 125.46 (C3), 124.00 (C2), 119.64 (C12), 66.07 (C6). UV/vis (aqueous solution at pH 8, phosphate buffer): λmax, nm (ε, $M^{-1}\cdot cm^{-1}$)= 245 (10270), 360 (6549), 394 (7140). ESI-MS (MeOH): *m/z*= 269.0 ([M-2BF_4-H_2O+MeOH]$^{2+}$). Elemental analysis (% found): C, 43.07; H, 3.35; N, 11.98. Calcd for $C_{25}H_{23}B_2F_8N_6ORu$: C, 43.01; H, 3.32; N, 12.04.

X-ray Crystal Structure Determination. X-ray crystal structure determination was made on a Bruker-Nonius diffractometer equipped with an APPEX II 4K CCD area detector, a FR591 rotating anode with Mo Kα radiation, Montel mirrors as a monochromatic and a Kryoflex low-temperature device (T = -173°C). Full-sphere data collection was used with w and f scans. Programs used were as follows: for data collection, Bruker APPEX II (versions v1.0-22, v2009.1-0 and v2009.1-02); for data reduction, Bruker SAINT (versions V.2.10, V/.60A and V7.60A); for absorption corrections, Bruker SADABS (versions V.2.10, V2008 and V2008/1);[41] and for structure refinement, SHELXTL (versions V6.12 and V6.14)[42] and SQUEEZE[43] implemented in Platon.[44]

Crystals of **2**(**PF_6**)$_2$ have been obtained by slow ether diffusion in an acetone:water solution of the aqua complex. **2**$^{2+}$ crystallizes in a cell in which the asymmetric unit of this structure contains half a molecule of the cationic metal complex, which has C_s symmetry since the Ru ion shows a distorted octahedral symmetry, two half PF_6^- anions and highly disordered acetone molecules. The cationic metal complex is coordinated to an oxygen atom, which likely corresponds to a water molecule in accordance with the number of counteranions and a diamagnetic NMR spectrum. The PF_6^- anions are disordered in different orientations shared with neighboring asymmetric units. In order to avoid the highly disordered acetone molecules the program SQUEEZE[43] was applied leading to a refined model with a R1 value of 4.79 % in which all the solvent molecules were removed. For **3**(**Cl**), crystals have been obtained after slow evaporation of an acetone:water saturated solution of the chlorido complex. The asymmetric unit of this structure contains one molecule of *cis*-**3**$^+$ with distorted octahedral geometry, one Cl^- counterion and seven water molecules, in agreement with a Ru(II) oxidation state. For **4**(**PF_6**)$_2$, crystals have been obtained after slow ether diffusion in an acetone:dichloromethane solution of the aqua complex. The asymmetric unit of this structure contains one molecule of *cis*-**4**$^{2+}$ with distorted octahedral symmetry

coordinated to a water molecule, two PF_6^- anions and one dichloromethane molecule (R1 value of 3.02 %). For **6**(**OTf**)$_2$, crystals have been obtained by slow ether diffusion in an acetone:water solution of the aqua complex, The structure of $\mathbf{6}^{2+}$ is very similar to that observed by Kojima for the corresponding chlorido complex,[7] containing a pseudo-octahedral coordination environment around the metal. Additionally, the triflate counter ions appear above the coordinated water molecule within hydrogen bonding distance, and the axial pyridine is tilted 3° from the Ru-N_{ax} axis, similar to the observed 9° tilt for the Co(II) derivative of Py5Me$_2$.[8] For **8**(**BF$_4$**)$_2$, crystals have been obtained after slow evaporation of an acetone:water saturated solution of the aqua complex. $\mathbf{8}^{2+}$ crystallizes in a cell containing four $[Ru(PY4Im)(H_2O)]^{2+}$ cationic units, sixteen water molecules and eight BF_4^- anions, in agreement with a Ru(II) oxidation state. The asymmetric unit contains one molecule of the cationic complex with a coordinated water molecule, two BF_4^- anions and four non-coordinated water molecules. One of the BF_4^- anions and three of the water molecules are disordered over two positions.

Contribution

Marcos Gil-Sepulcre synthetized and characterized the new compounds, performed the electrochemical and spectroscopic experiments and analyses, and prepared the manuscript.

Acknowledgment

Support form MINECO (CTQ2011-26440, CTQ2014-59832-JIN, CTQ2015-69363-P and CTQ2015-64261-R) is gratefully acknowledged. M.G.-S. is grateful for the award of a PIF doctoral grant from UAB. J.C.A. was supported by NSF-GRF Grant No. DGE-1106400. We deeply thank Jeffrey R. Long for his scientific advice and critical discussion and Selene Gil-Moreno for the help in the obtaining of the crystals of **8**$(BF_4)_2$.

Abbreviations

Bpy, 2,2'-bipyridine; CV, Cyclic Voltammetry; DCE, 1,2-*dichloroethane;* DCM, Dichloromethane; *p*-cym, *p*-cymene; DPV, Differential Pulse Voltammetry; DFT, Density Functional Theory; GC, Gas Chromatography; MS, Mass Spectrometry; Pyr, pyridine; rds, rate determining step; RT, Room Temperature; TS, Transition State.

References

[1] Berardi, S.; Drouet, S.; Francàs, L.; Gimbert-Surinach, C.; Guttentag, M.; Richmond, C.; Stoll, T.; Llobet, A. *Chem. Soc. Rev.* **2014**, *43*, 7501-7519.

[2] Bofill, R.; García-Antón, J.; Escriche, L.; Sala, X.; Llobet, A. *Comprehensive Inorganic Chemistry II* **2013**, *8*, 505-523.

[3] Chantarojsiri, T.; Sun, Y. J.; Long, J. R.; Chang, C. J. *Inorg. Chem.* **2015**, *54*, 5879-5887.

[4] (a) de Vries, M. E.; La Crois, R. M.; Roelfes, G.; Kooijman, H.; Spek, A.; Hage, R.; Feringa, B. L. *Chem. Commun.* **1997**, 1549-1550. (b) Klein Gebbink, R. J. M.; Jonas, R. T.; Goldsmith, C. R.; Stack, T. D. P. *Inorg. Chem.* **2002**, *41*, 4633-4641.

[5] Wasylenko, D. J.; Ganesamoorthy, C.; Borau-Garcia, J.; Berlinguette, C. P. *Chem. Commun.*, **2011**, *47*, 4249-4251.

[6] (a) Goggins, E. M.; Lekich, T. T.; Weare, W. W.; Sommer, R. D.; Ribeiro, M. A.; Pinheiro, C. B. *Eur. J. Inorg. Chem.* **2016**, 1054-1059. (b) Zee, D. Z.; Chantarojsiri, T.; Long, J. R.; Chang, C. J. *Acc. Chem. Res.* **2015**, *48*, 2027-2036. (c) Wu, X. Y.; Huang, T.; Lekich, T. T.; Sommer, R. D.; Weare, W. W. *Inorg. Chem.* **2015**, *54*, 5322-5328. (d) King, A. E.; Nippe, M.; Atanasov, M.; Chantarojsiri, T.; Wray, C. A.; Bill, E.; Neese, F.; Long, J. R.; Chang, C. J. *Inorg. Chem.* **2014**, *53*, 11388-11395. (e) Ghosh, S.; Singh, S. K.; Tewary, S.; Rajaraman, G. *Dalton Trans.* **2013**, *42*, 16490-16493. (f) Feng, X. W.; Liu, J. J.; Harris, T.D.; Hill, S.; Long, J. R. *J. Am. Chem. Soc.* **2012**, *134*, 7521-7529. (g) Zadrozny, J. M.; Freedman, D. E.; Jenkins, D. M.; Harris, T. D.; Iavarone, A. T.; Mathoniere, C.; Clerac, R.; Long, J. R. *Inorg. Chem.* **2010**, *49*, 8886-8896. (h) Freedman, D. E.; Jenkins, D. M.; Long, J. R. *Chem. Commun.* **2009**, 4829-4831. (i) Freedman, D. E.; Jenkins, D. M.; Iavarone, A. T.; Long, J. R. *J. Am. Chem. Soc.* **2008**, *130*, 2884-2885.

[7] Ohzu, S.; Ishizuka, T.; Kotani, H.; Kojima, T. *Chem. Comm.* **2014**, *50*, 15018-15021.

[8] (a) Sun, Y.; Bigi, J. P.; Piro, N.A.; Tang, M. L.; Long, J. R.; Chang, C. J. *J. Am. Chem. Soc.* **2011**, *133*, 9212-9215. (b) Sun, Y.; Sun, Y.; Long, J. R.; Yang, P.; Chang, C. J. *Chem. Sci.*, **2013**, *4*, 118-124.

[9] Karunadasa, H. I.; Chang, C. J.; Long, J. R. *Nature* **2010**, *464*, 1329-1333.

[10] Smith, J. M.; Long, J. R. *Inorg. Chem.* **2010**, *49*, 11223-11230.

[11] Nippe, M.; Khnayzer, R. S.; Panetier, J. A.; Zee, D. Z.; Olaiya, B. S.; Head-Gordon, M.; Chang, C. J.; Castellano, F. N.; Long, J. R. *Chem. Sci.* **2013**, *4*, 3934-3945.

[12] (a) Weisser, F.; Hohloch, S.; Plebst, S.; Schweinfurth, D.; Sarkar, B. *Chem. Eur. J.* **2014**, *20*, 781-793. (b) Weisser, F.; Stevens, H.; Klein, J.; van der Meer, M.; Hohloch, S.; Sarkar, B. *Chem. Eur. J.* **2015**, *21*, 8926-8938.

[13] (a) Francàs, L.; González-Gil, R.; Poater, X. Fontrodona, X.; García-Antón, J.; Sala, X.; Escriche, L.; Llobet, A. *Inorg. Chem.* **2014**, *53*, 8025-8035. (b) Vaquer, L.; Poater, A.; De Tovar, J.; García-Antón, J.; Solà, M.; Llobet, A.; Sala; X. *Inorg. Chem.* **2013**, *52*, 4985-4992. (c) A. Poater, A.; Mola, J.; Gallegos Saliner, A.; Romero, I.; Rodríguez, M.; Llobet, A.; Solà, M. *Chem. Phys. Lett.* **2008**, *458*, 200-204. (d) Mola, J.; Romero, I.; Rodríguez, M.; Bozoglian, F.; Poater, A.; Solà, M.; Parella, T.; Benet-Buchholz, J.; Fontrodona, X.; Llobet, A. *Inorg. Chem.* **2007**, *46*, 10707-10716.

[14] (a) McClure, B. A.; Abrams, E. R.; Rack, J. J. *J. Am. Chem. Soc.* **2010**, *132*, 5428-5436. (b) Sharma, R.; Knoll, J. D.; Martin, P. D.; Podgorski, I.; Turro, C.; Kodanko, J. J. *Inorg. Chem.* **2014**, *53*, 3272-3274.

[15] Santos, A. R.; Escudero, D.; González, L.; Orellana, G. *Chem. Asian J.* **2015**, *10*, 622-629.

[16] Blancafort, L. *ChemPhysChem* **2014**, *15*, 3166-3181.

[17] Ding, L.; Chung, L. W.; Morokuma, K. J. *Chem. Theory Comput.* **2014**, *10*, 668-675.

[18] The ferrocene/ferrocenium couple measured in DCM + 0.1 M of n-Bu4NPF6 is 0.509 (error 0.009) V vs. SCE, which is in agreement with previous studies performed by N. G. Tsierkezos: Tsierkezos, N. G. Cyclic Voltammetric Studies of Ferrocene in Nonaqueous Solvents in the Temperature Range from 248.15 to 298.15 K. *J. Solution Chem.* **2007**, *36*, 289-302.

[19] (a) Savéant, J. M. *Elements of Molecular and Biomolecular Electrochemistry* **2006**, Wiley-Interscience, New York. (b) Bard, A. J. *Electrochemical Methods: Fundamentals and Applications* **2001**, John Wiley & Sons, Inc., New York.

[20] Bott, A. W.; Feldberg, S. W.; Rudolph, M. Fitting Experimental Cyclic Voltammetry Data with Theoretical Simulations Using DigiSim® 2.1. Current Separations **1996,** 15:2.

[21] Estimated errors in the equilibrium and kinetic constants using DigiSim® are less than 10 %.

[22] Mola, J.; Dinoi, C.; Sala, X.; Rodríguez, M.; Romero, I.; Parella, T.; Fontrodona, X.; Llobet, A. *Dalton Trans.* **2011**, *40*, 3640-3646.

[23] (a) Zong, R.; Thummel, R. *J. Am. Chem. Soc.* **2005**, *127*, 12802-12803. (b) Duan, L.; Fischer, A.; Xu, Y.; Sun, L. *J. Am. Chem. Soc.* **2009**, *131*, 10397-10399. (c) Yagi, M.; Tajima, S.; Komi, M.; Yamazaki, H. *Dalton Trans.* **2011**, *40*, 3802-3804.

[24] Takeuchi, K. J.; Thompson, M. S.; Pipes, D. W.; Meyer, T. J. *Inorg. Chem.* **1984**, *23*, 1845-1851.

[25] (a) Huynh, M. H. V.; Meyer, T. J. *Chem. Rev.* **2007**, *107*, 5004-5064. (b) Gagliardi, C. J.; Westlake, B. C.; Kent, C. A.; Paul, J. J.; Papanikolas, J. M.; Meyer, T. J. *Coord. Chem. Rev.* **2010**, *254*, 2459-2471.

[26] Bechlars B.; D'Alessandro, D. M.; Jenkins, D. M.; Iavarone, A. T.; Glover, S. D.; Kubiak, C. P.; Long, J. R. *Nature Chem.* **2010**, 2, 362–368.

[27] *Gaussian 09, Revision D.01*, Frisch, M. J.; Trucks, G. W.; Schlegel, H. B.; Scuseria, G. E.; Robb, M. A.; Cheeseman, J. R.; Scalmani, G.; Barone, V.; Mennucci, B.; Petersson, G. A.; Nakatsuji, H.; Caricato, M.; Li, X.; Hratchian, H. P.; Izmaylov, A. F.; Bloino, J.; Zheng, G.; Sonnenberg, J. L.; Hada, M.; Ehara, M.; Toyota, K.; Fukuda, R.; Hasegawa, J.; Ishida, M.; Nakajima, T.; Honda, Y.; Kitao, O.; Nakai, H.; Vreven, T.; Montgomery, Jr., J. A.; Peralta, J. E.; Ogliaro, F.; Bearpark, M.; Heyd, J. J.; Brothers, E.; Kudin, K. N.; Staroverov, V. N.; Kobayashi, R.; Normand, J.; Raghavachari, K.; Rendell, A.; Burant, J. C.; Iyengar, S. S.; Tomasi, J.; Cossi, M.; Rega, N.; Millam, J. M.; Klene, M.; Knox, J. E.; Cross, J. B.; Bakken, V.; Adamo, C.; Jaramillo, J.; Gomperts, R.; Stratmann, R. E.; Yazyev, O.; Austin, A. J.; Cammi, R.; Pomelli, C.; Ochterski, J. W.; Martin, R. L.; Morokuma, K.; Zakrzewski, V. G.; Voth, G. A.; Salvador, P.; Dannenberg, J. J.; Dapprich, S.; Daniels, A. D.; Farkas, Ö.; Foresman, J. B.; Ortiz, J. V.; Cioslowski, J.; Fox, D. J. Gaussian, Inc., Wallingford CT, **2009**.

[28] (a) Becke, A. D. *J. Chem. Phys.* **1993**, *98*, 5648-5652. (b) Lee, C.; Yang, W.; Parr, R. G. *Phys. Rev. B* **1988**, *37*, 785-789. (c) Stevens, P.; Devlin, F. J.; Chabalowski, C. F.; Frisch, M. J. *J. Phys. Chem.* **1994**, *98*, 11623-11627.

[29] Grimme, S.; Ehrlich, S.; Goerigk, L. *J. Comp. Chem.* **2011**, *32*, 1456-1465.

[30] Schaefer, A.; Horn, H.; Ahlrichs, R. *J. Chem. Phys.* **1992**, *97*, 2571-2577.

[31] Haeusermann, U.; Dolg, M.; Stoll, H.; Preuss, H. *Mol. Phys.* **1993**, *78*, 1211-1224.

[32] Kuechle, W.; Dolg, M.; Stoll, H.; Preuss, H. *J. Chem. Phys.* **1994**, *100*, 7535-7542.

[33] Leininger, T.; Nicklass, A.; Stoll, H.; Dolg, M.; Schwerdtfeger, P. *J. Chem. Phys.* **1996**, *105*, 1052-1059.

[34] Weigend, F.; Ahlrichs, R. *Phys. Chem. Chem. Phys.* **2005**, *7*, 3297-3305.

[35] Dunning Jr, T. H.; Hay, P. J.; in *Modern Theoretical Chemistry*, Ed. Schaefer III, H. F., Vol. 3. Plenum, New York, **1977**, 1-28.

[36] Marenich, A. V.; Cramer, C. J.; Truhlar, D. G. *J. Phys. Chem. B* **2009**, *113*, 6378-6396.

[37] Bianchini, C.; Gatteschi, D.; Giambastiani, G.; Guerrero, I.; Ienco, A.; Laschi, F.; Mealli, C.; Meli, A.; Sorace, L.; Toti, A.; Vizza, F. *Organometallics* **2007**, *26*, 726-739.

[38] Patroniak, V.; Kubicki, M.; Grochowska, A. R.; Grochowska, A. M. *Tetrahedron* **2005**, *61*, 5475–5480.

[39] Dyker, G.; Muth, O. *Eur. J. Org. Chem.* **2004**, 4319-4322.

[40] Vedevnikov, A. N.; Fettinger, J. C.; Mohr, F. *J. Am. Chem. Soc.* **2004**, *126*, 11160-11161.

[41] Blessing, R. H. *Acta Cryst.* **1995**, *A51*, 33-38.

[42] Sheldrick, G. M. *Acta Cryst.* **2008**, A64, 112-122.

[43] (a) Sluis, P. Van der; Spek, A. L. *Acta Cryst.* **1990**, *A46*, 194-201. (b) Spek, A. L. *Acta Cryst.* **2015**, *C71*, 9-18.

[44] Spek, A. L. *J. Appl. Cryst.* **2003**, *36*, 7-13.

Supporting Information

Synthesis and Isomeric Analysis of Ru^{II} Complexes Bearing Pentadentate Scaffolds

Table of Contents

1. Synthesis of the ligand bpy2PYMe

To 24 mL of a -84 °C THF/pentane/ehtylbenzene solution of 2-ethylpyridine, 2.5 mL of a THF solution of LDA (2.0 M) were added with continuous stirring. The mixture was maintained for 1 h at -84 °C and was then warmed till 0°C for an additional hour. After that, the mixture was cooled again to -84 °C and 1.178 g of 6-bromo-2,2'-bipyridine (5.0 mmol), obtained according to the method described elsewhere[1] and dissolved in THF, were added, and the mixture was allowed to slowly reach RT, at which the reaction proceeded during 2 days. After this first step, an identical reaction cycle was repeated to the sample (cooling to -84 °C, addition of LDA, etc.) with the only exception that the reaction at RT of the second aliquot of 6-bromo-2,2'-bipyridine was performed for 16 h. After that, the mixture was quenched with H_2O (10 mL) and extracted with CH_2Cl_2 (3 x 40 mL). After drying the combined organics with $MgSO_4$ and removing the solvent under reduced pressure, the product was purified by column chromatography (silica, 1st, CH_2Cl_2, 2nd EtOAc). A yellow oil was obtained. Yield: 1.458 g (70 %). ^{1}H NMR (400 MHz, $CDCl_3$, 298K): δ 8.67 (m, 3H), 8.33 (d, 2H, J = 7.8 Hz), 8.21 (d, 2H, J = 8.0 Hz), 7.77 (t, 2H, J = 7.5 Hz), 7.73 (t, 2H, J = 8.0 Hz), 7.66 (t, 1H, J = 7.5 Hz), 7.26 (m, 6H), 2.55 (s, 3H).

2. Spectroscopic Characterization

NMR Spectroscopy

(a)

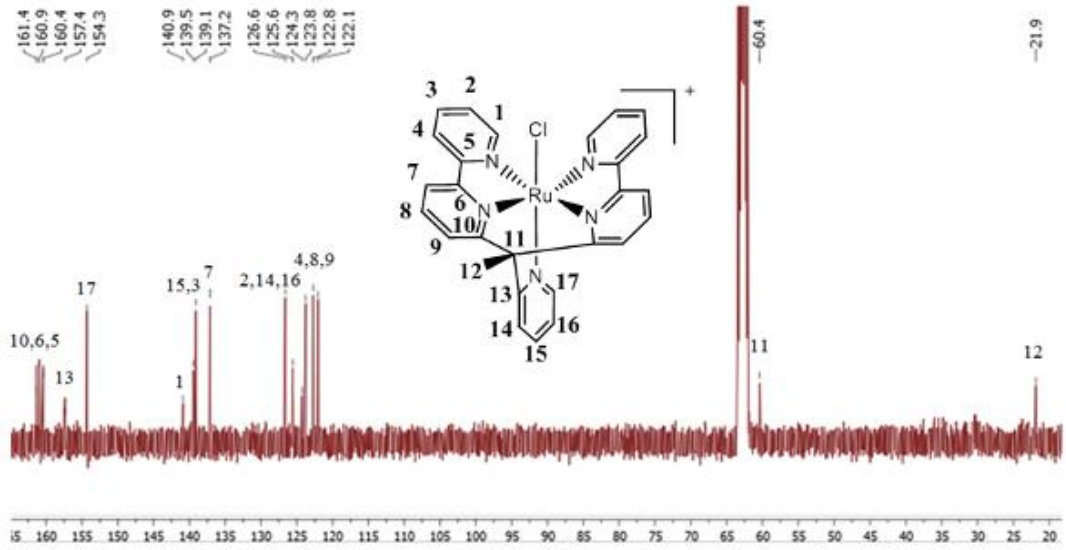

(b)

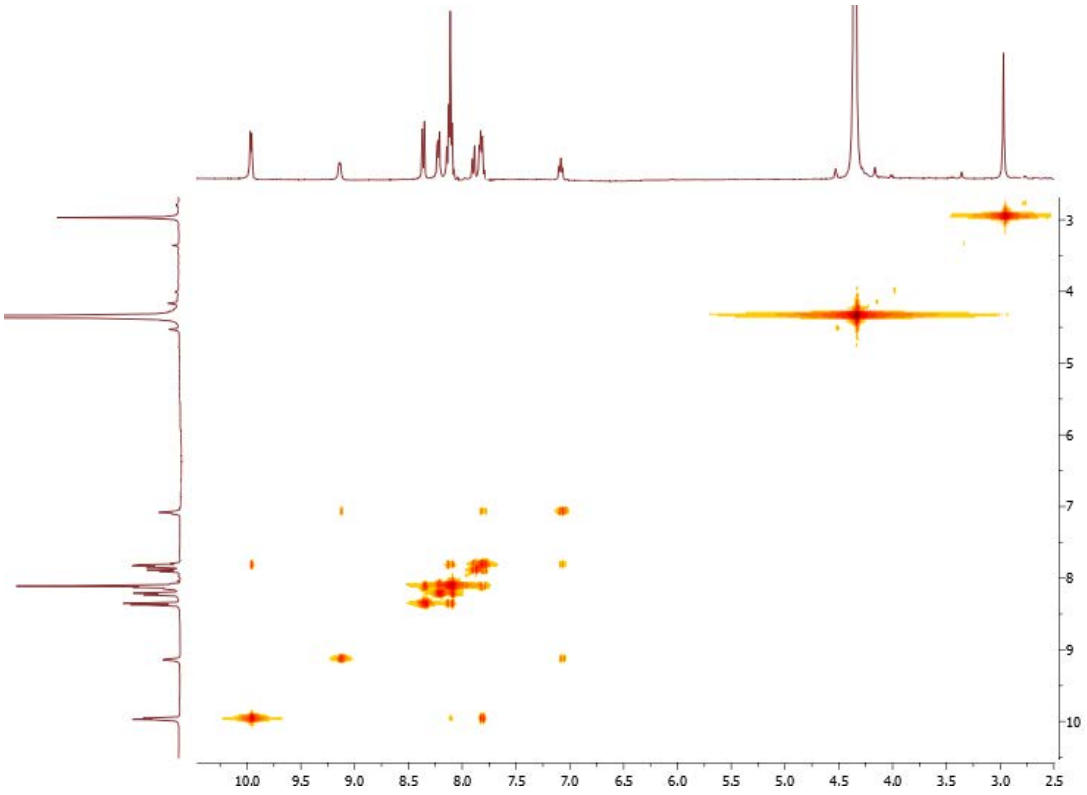
10.0
9.5
9.0
8.5
8.0
7.5
7.0
6.5
6.0
5.5
5.0
4.5
4.0
3.5
3.0
2.5
3
4
5
6
7
8
9
10

(c)

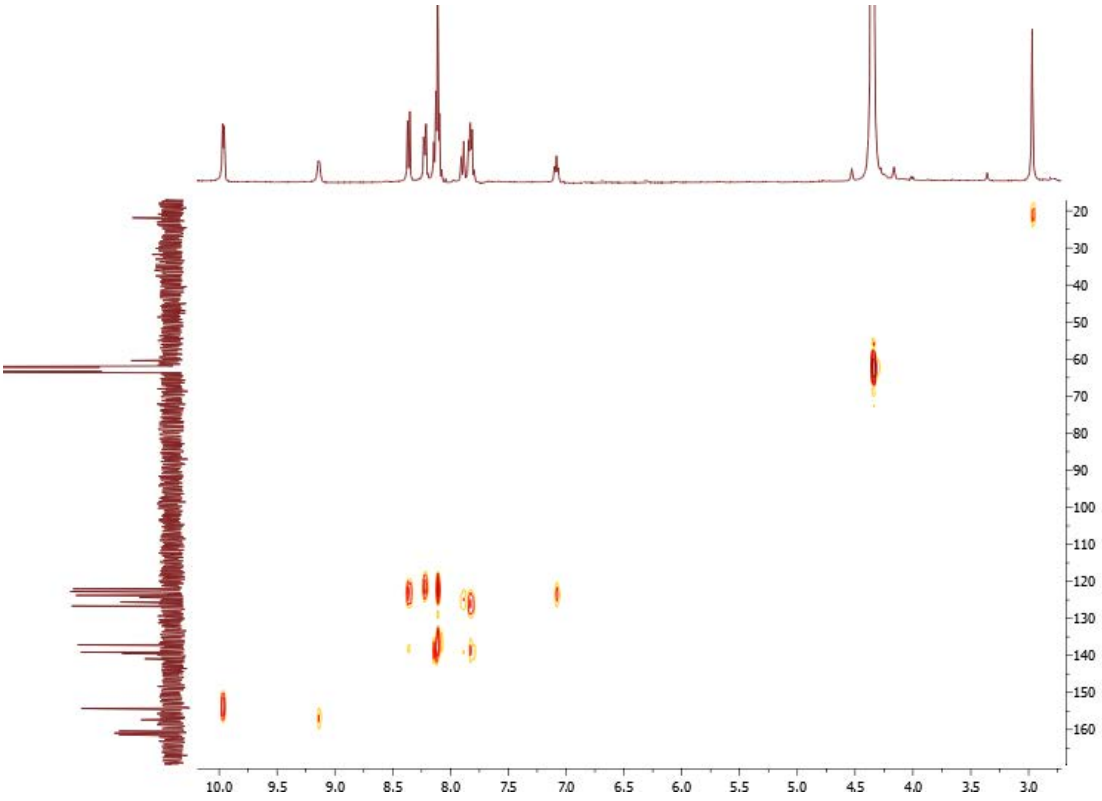
10.0
9.5
9.0
8.5
8.0
7.5
7.0
6.5
6.0
5.5
5.0
4.5
4.0
3.5
3.0
20
30
40
50
60
70
80
90
100
110
120
130
140
150
160

III

(d)

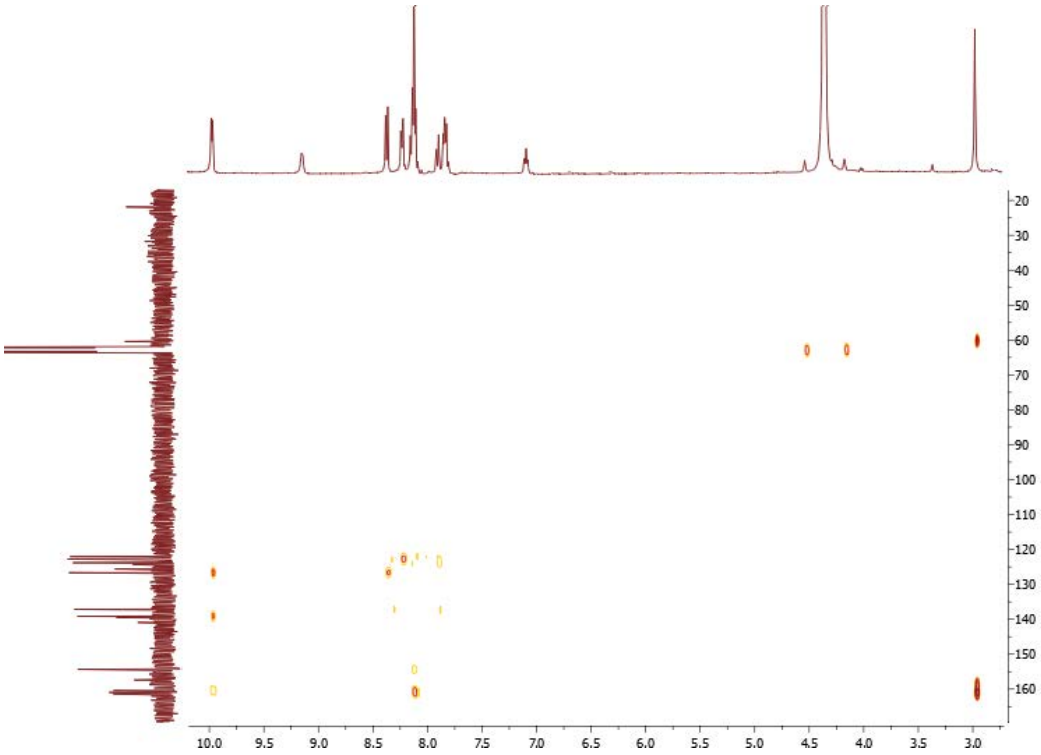

Figure S1. ^{13}C-{^{1}H}-NMR (a) spectra including the assignment of signals, and 2D NMR spectra (400 MHz, 298 K, d_3-$MeNO_2$) for *trans*-**1**$^{+}$: (b) COSY, (c) HSQC NMR and (d) HMBC NMR.

(a)

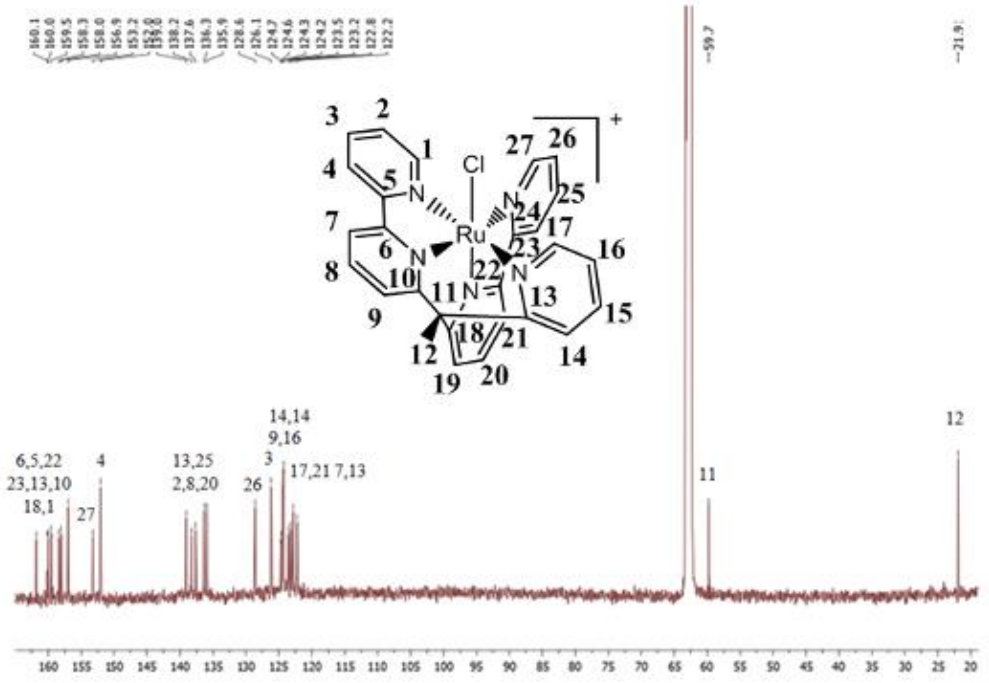

(b)

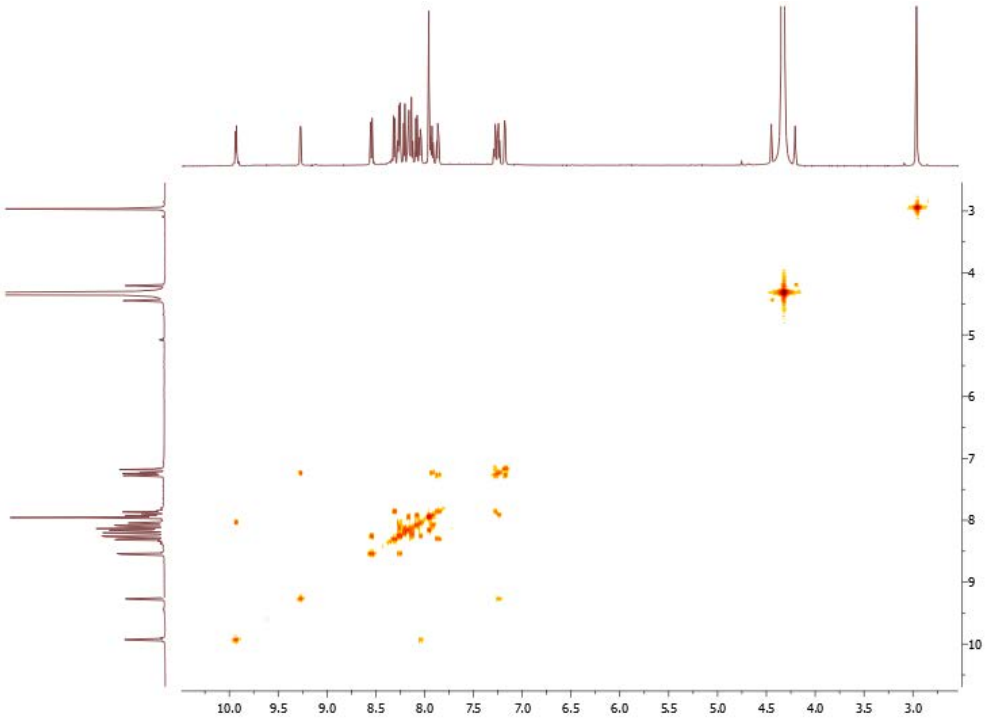
3
4
5
6
7
8
9
10
10.0
9.5
9.0
8.5
8.0
7.5
7.0
6.5
6.0
5.5
5.0
4.5
4.0
3.5
3.0

(c)

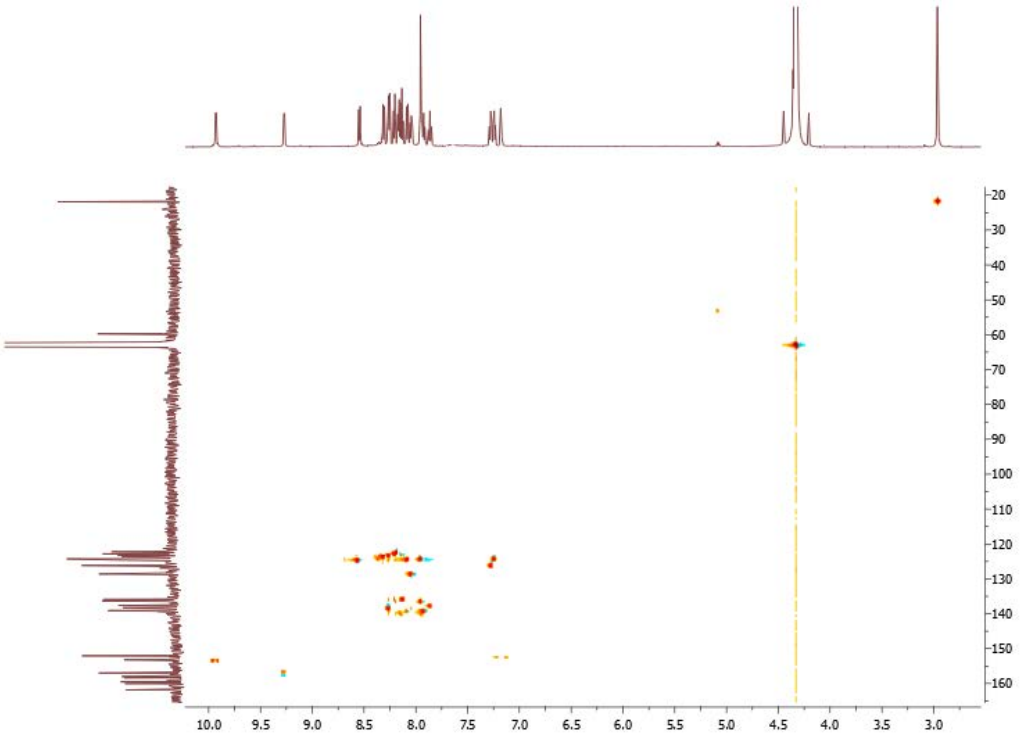
20
30
40
50
60
70
80
90
100
110
120
130
140
150
160
10.0
9.5
9.0
8.5
8.0
7.5
7.0
6.5
6.0
5.5
5.0
4.5
4.0
3.5
3.0

(d)

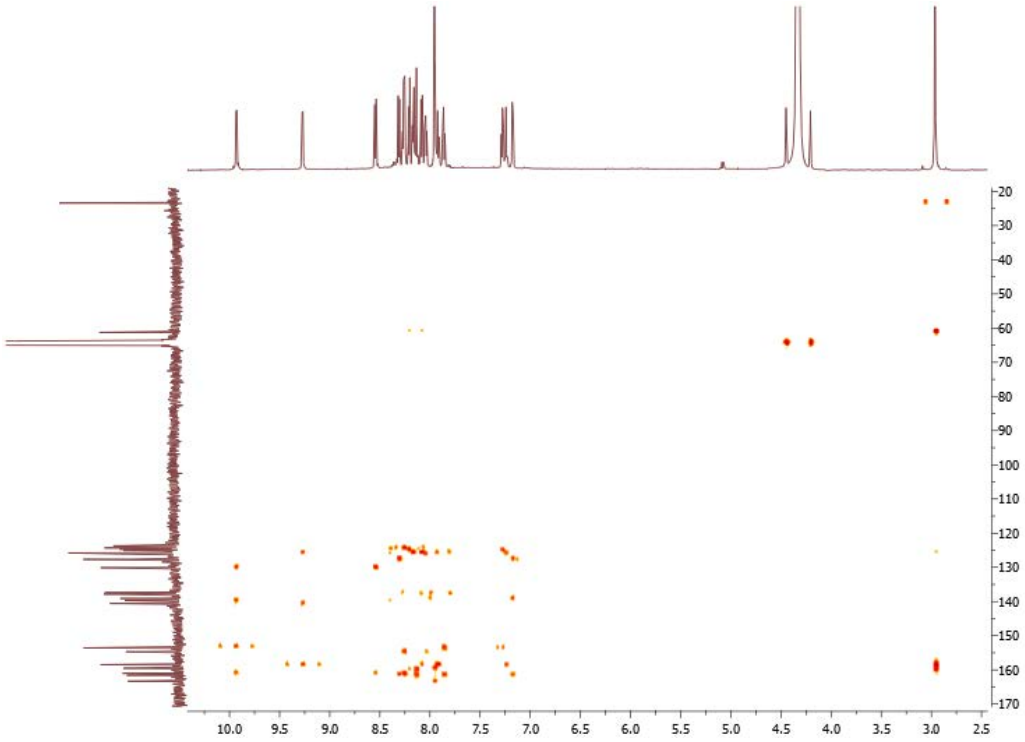

(e)

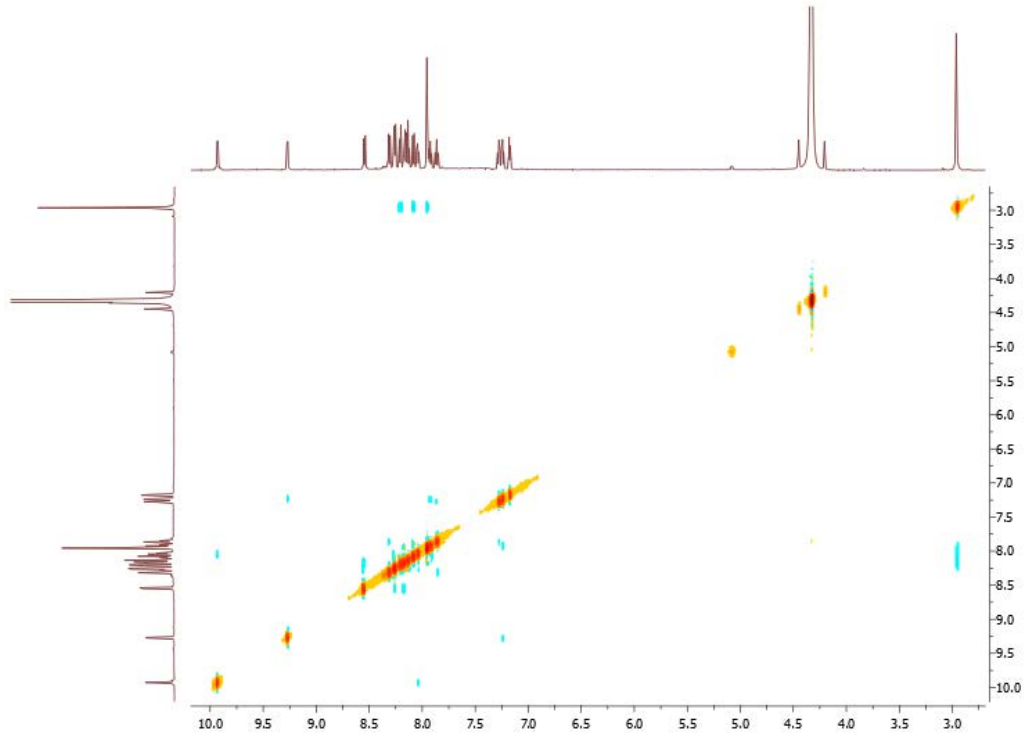

Figure S2. ^{13}C-{^{1}H}-NMR (a) spectra including the assignment of signals, and 2D NMR spectra (600 MHz, 298 K, d_3-$MeNO_2$) for *cis*-**1**$^{+}$: (b) COSY, (c) HSQC NMR, (d) HMBC NMR and (e) NOESY

(a)

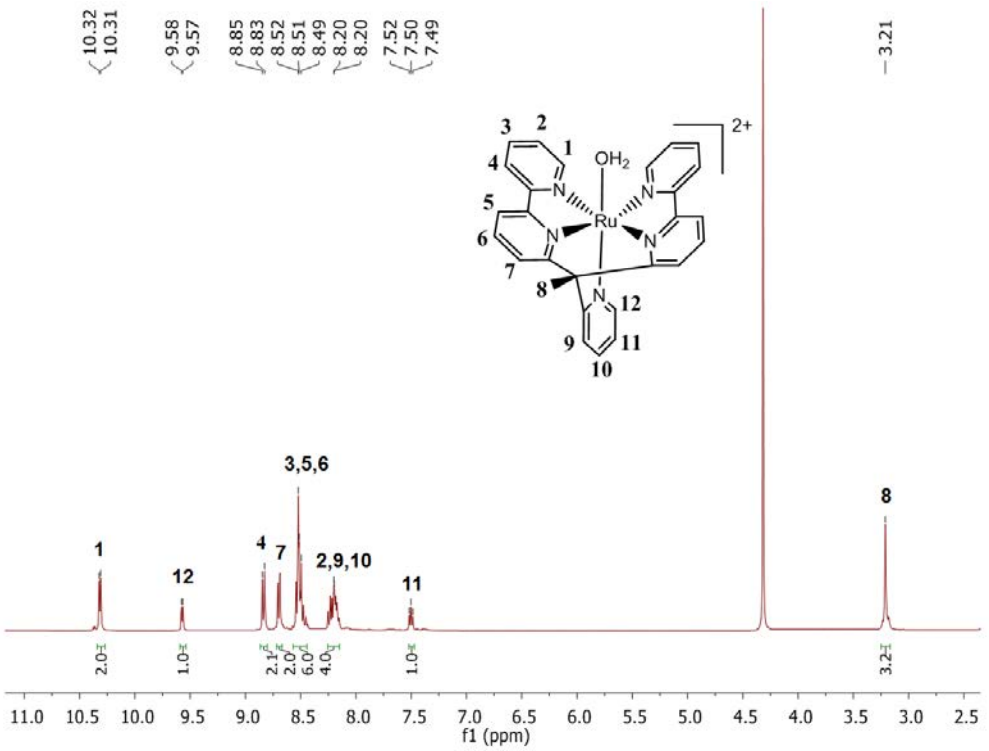
10.32
10.31
9.58
9.57
8.85
8.83
8.52
8.51
8.49
8.20
8.20
7.52
7.50
7.49
3.21
2+
OH2
Ru
3,5,6
8
1
12
4
7
2,9,10
11
2.0
1.0
2.1
2.0
6.0
4.0
1.0
3.2
11.0 10.5 10.0 9.5 9.0 8.5 8.0 7.5 7.0 6.5 6.0 5.5 5.0 4.5 4.0 3.5 3.0 2.5
f1 (ppm)

(b)

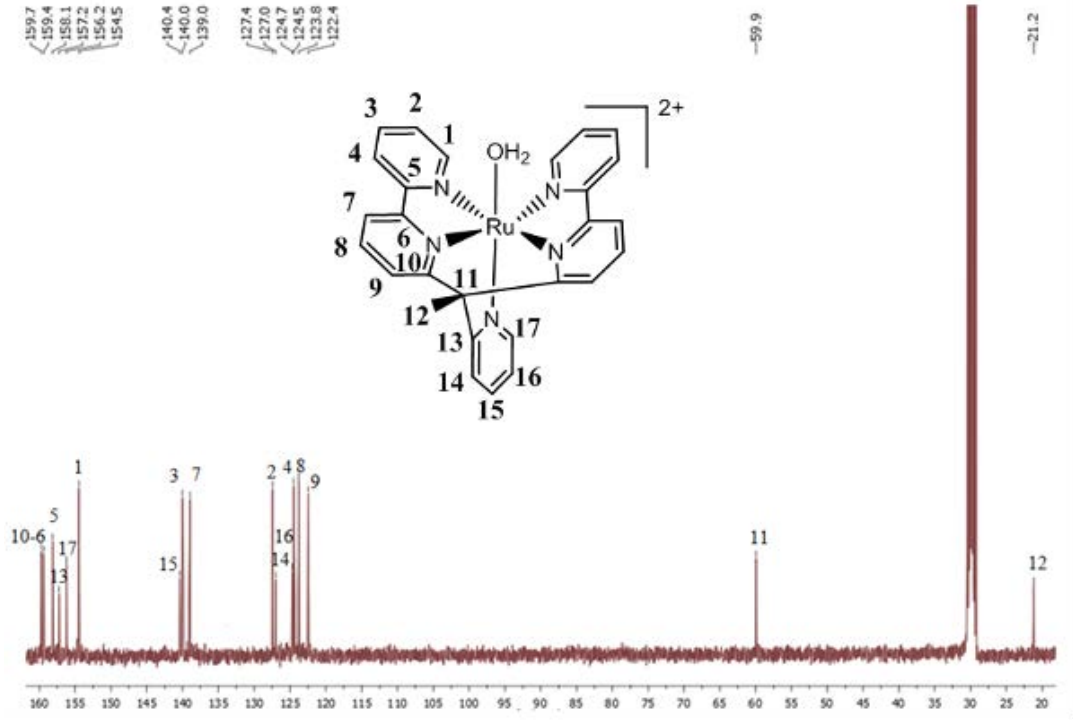
159.7
159.4
158.1
157.2
156.2
154.5
140.4
140.0
139.0
127.4
127.0
124.7
124.5
123.8
122.4
99.9
21.2
2+
OH2
Ru
11
12
160 155 150 145 140 135 130 125 120 115 110 105 100 95 90 85 80 75 70 65 60 55 50 45 40 35 30 25 20

III

(c)

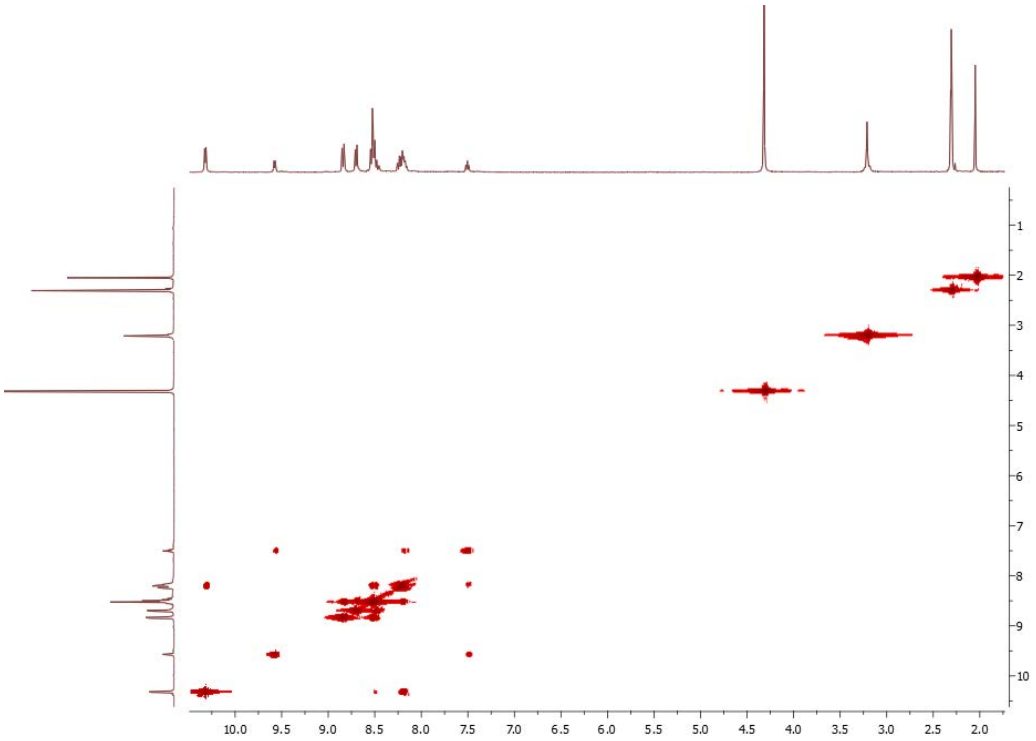
10.0 9.5 9.0 8.5 8.0 7.5 7.0 6.5 6.0 5.5 5.0 4.5 4.0 3.5 3.0 2.5 2.0
1 2 3 4 5 6 7 8 9 10

(d)

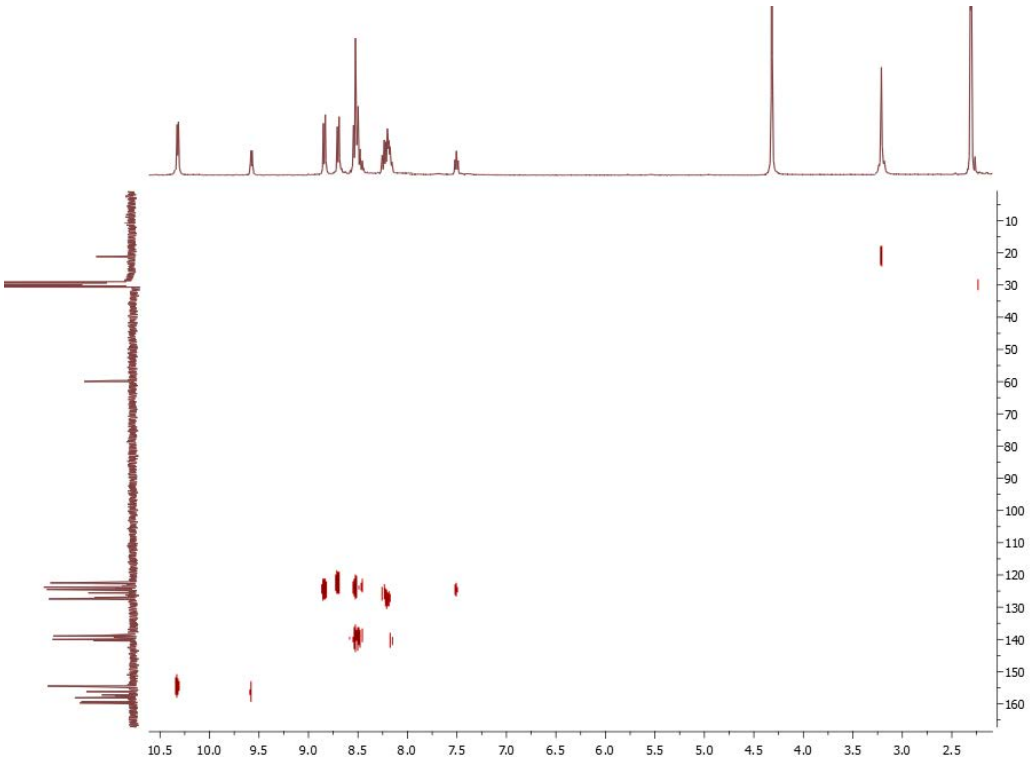
10.5 10.0 9.5 9.0 8.5 8.0 7.5 7.0 6.5 6.0 5.5 5.0 4.5 4.0 3.5 3.0 2.5
10 20 30 40 50 60 70 80 90 100 110 120 130 140 150 160

(e)

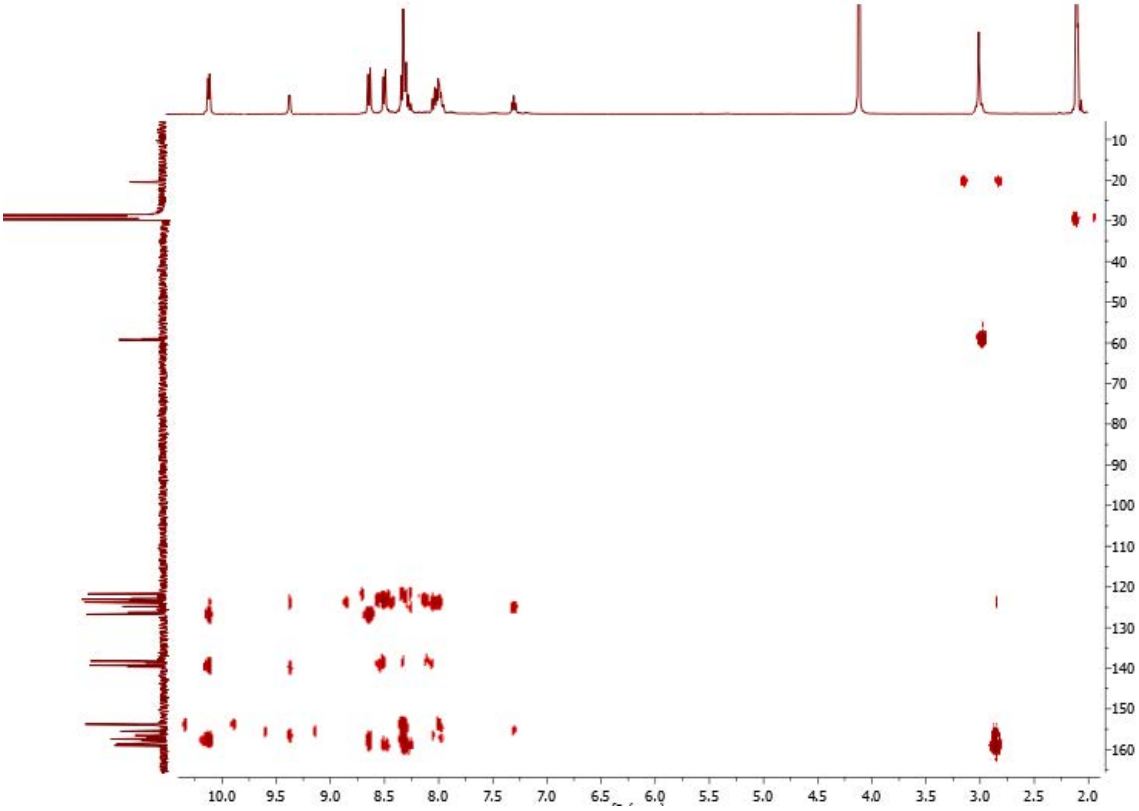

Figure S3. ^{1}H-NMR (a) and ^{13}C-{^{1}H}-NMR (b) spectrum including the assignment of signals, and 2D NMR spectra (400 MHz, 298 K, d_6-acetone:D_2O 95:5) for complex *trans*-**2**$^{2+}$: (c) COSY, (d) HSQC NMR and (e) HMBC NMR.

(a)

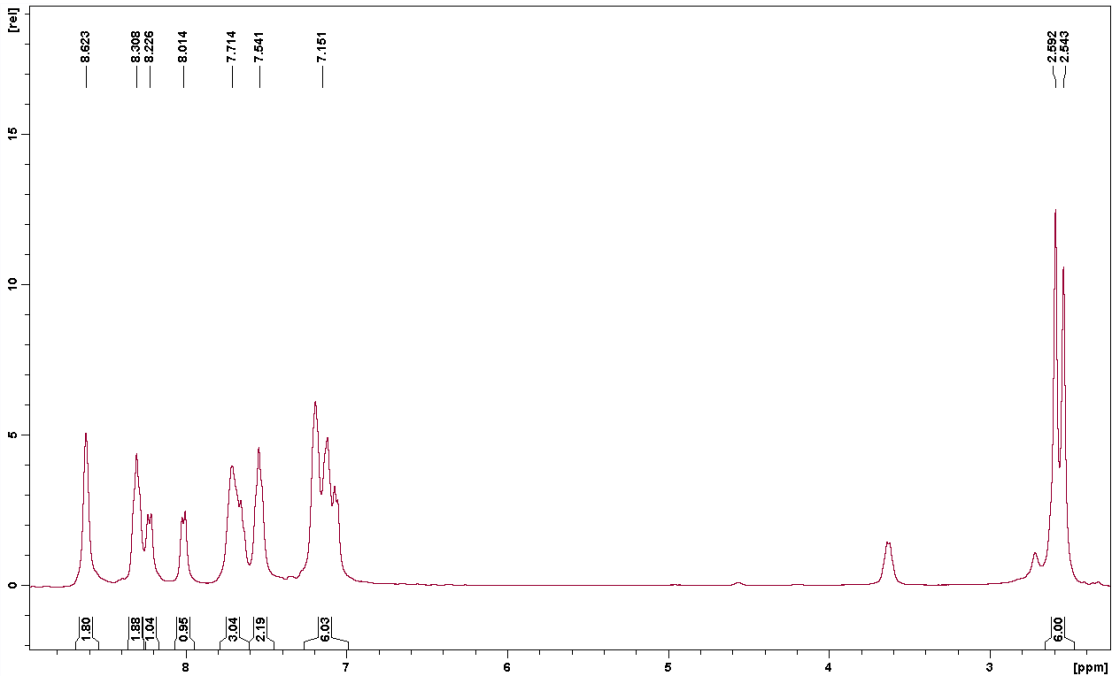

(b)

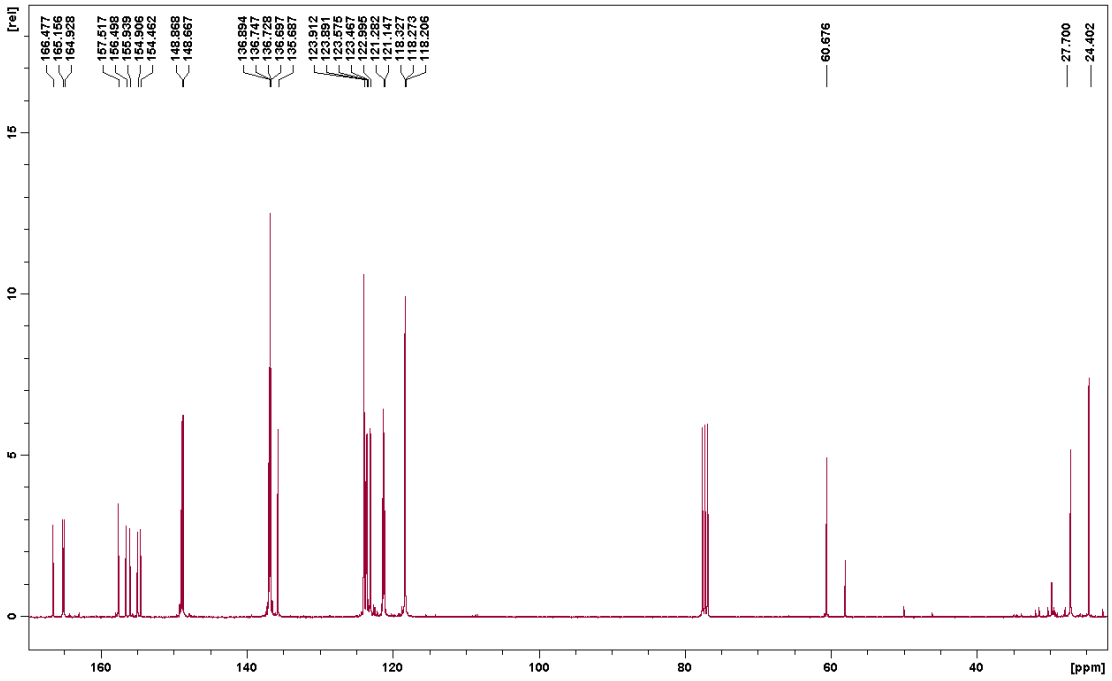
[rel]
166.477
165.156
164.928
157.517
156.498
155.939
154.906
154.462
148.868
148.667
136.894
136.747
136.728
136.697
135.687
123.912
123.891
123.575
123.467
122.995
121.282
121.147
118.327
118.273
118.206
60.676
27.700
24.402
[ppm]

(c)

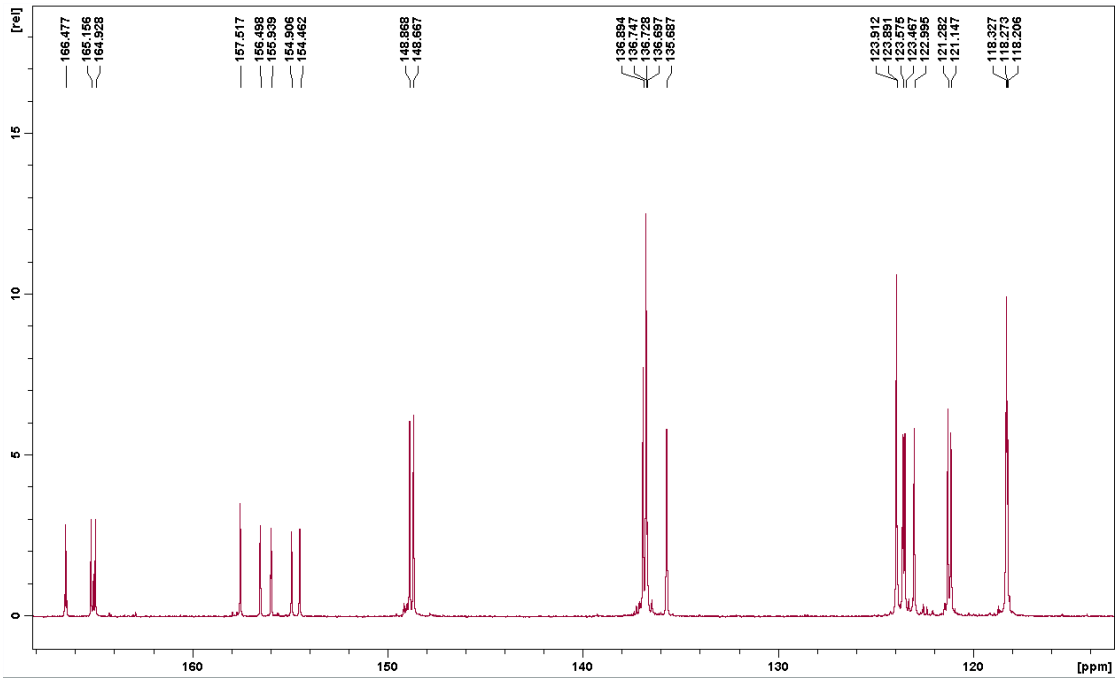
[rel]
166.477
165.156
164.928
157.517
156.498
155.939
154.906
154.462
148.868
148.667
136.894
136.747
136.728
136.697
135.687
123.912
123.891
123.575
123.467
122.995
121.282
121.147
118.327
118.273
118.206
[ppm]

(d)

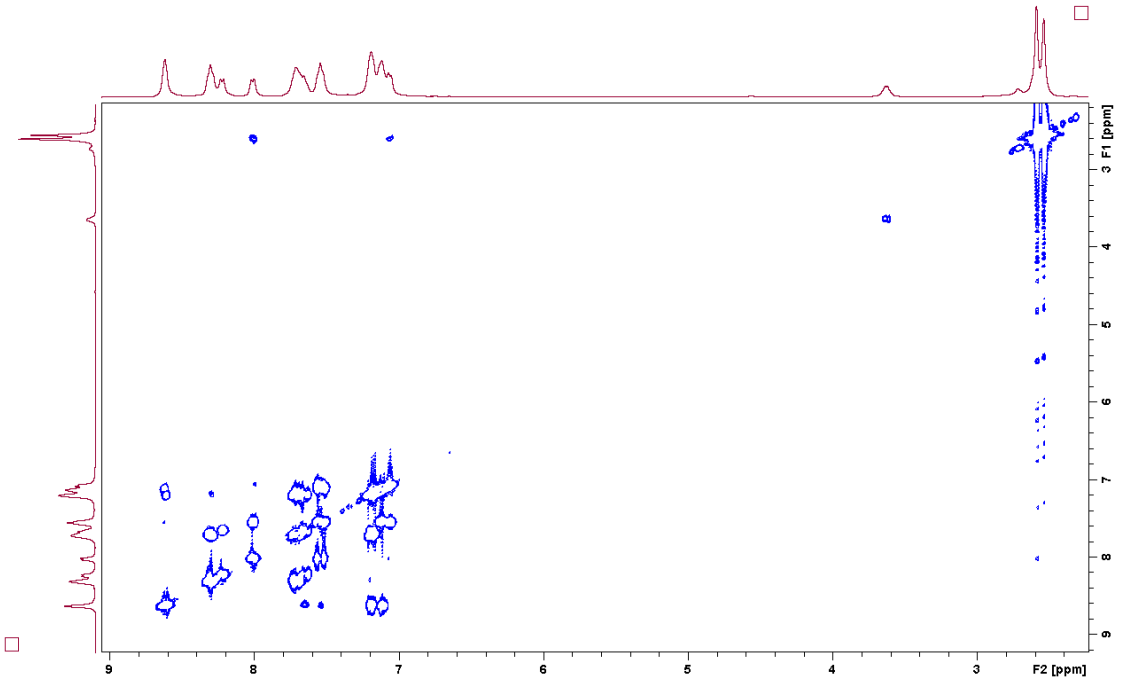

(e)

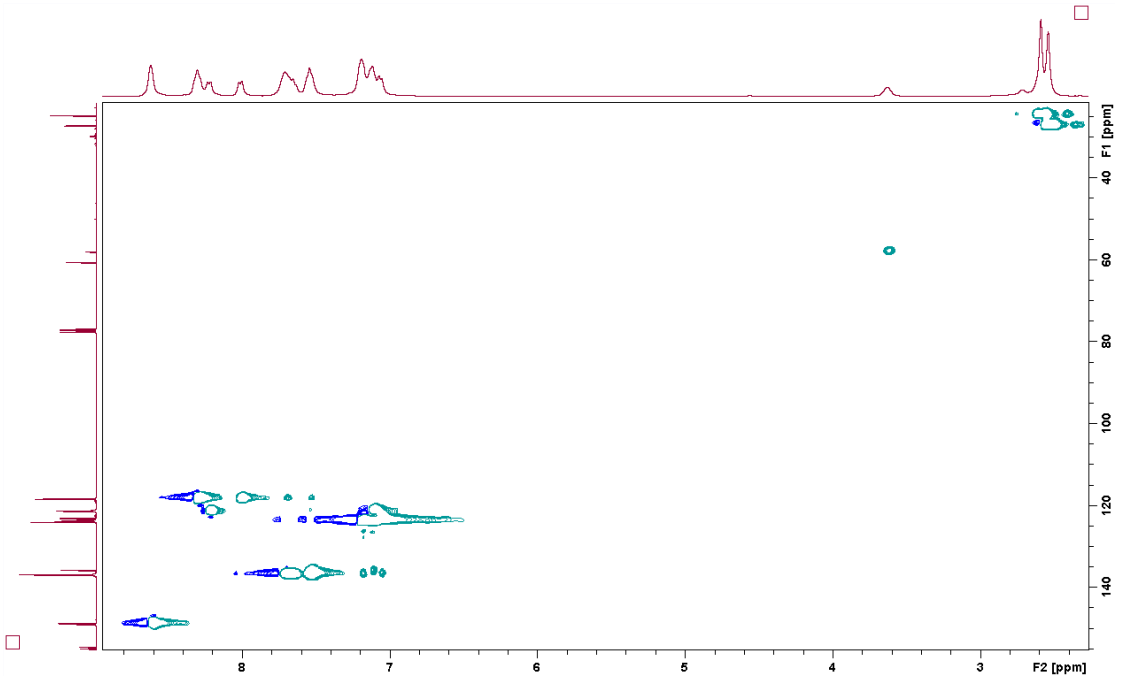

(f)

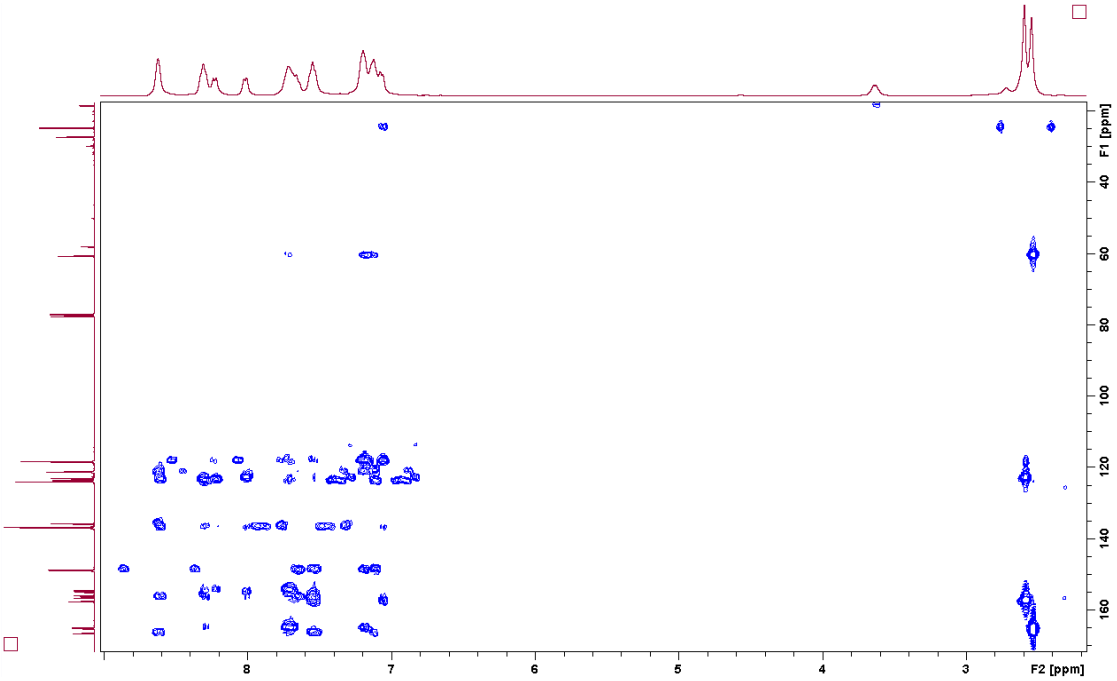

Figure S4. ^{1}H-NMR (a) and ^{13}C-{^{1}H}-NMR spectra (b,c) and 2D NMR spectra (400 MHz, 298 K, $CDCl_3$) for the bpy(bpyMe)PYMe ligand (L2): COSY (d), HSQC NMR (e) and HMBC NMR (f).

(a)

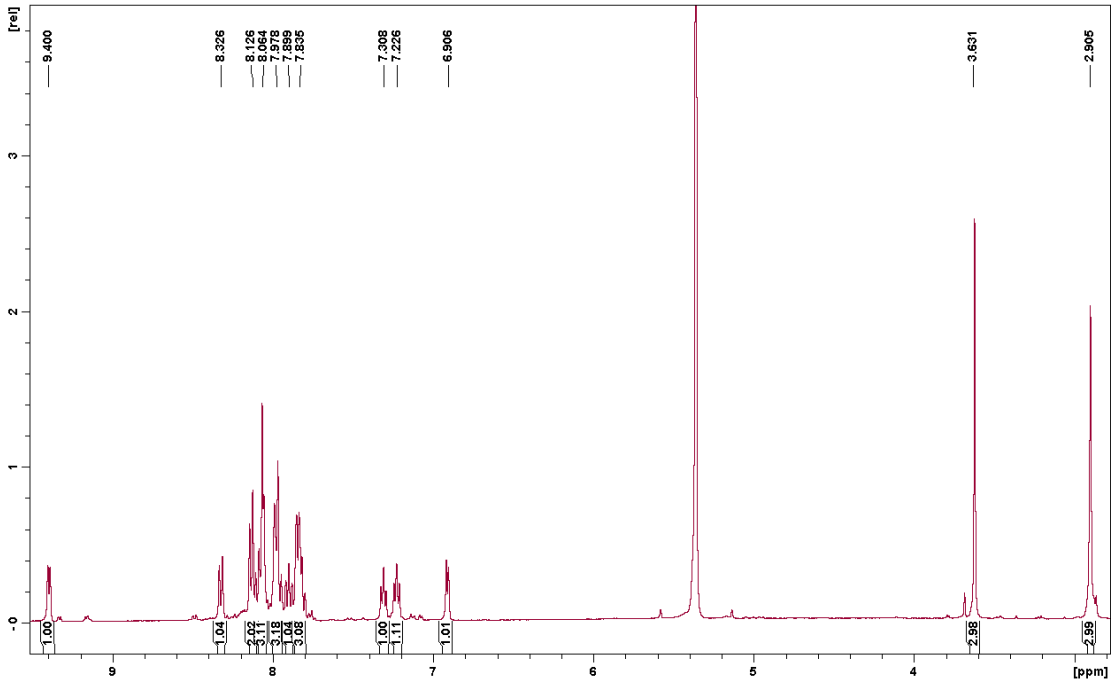

(b)

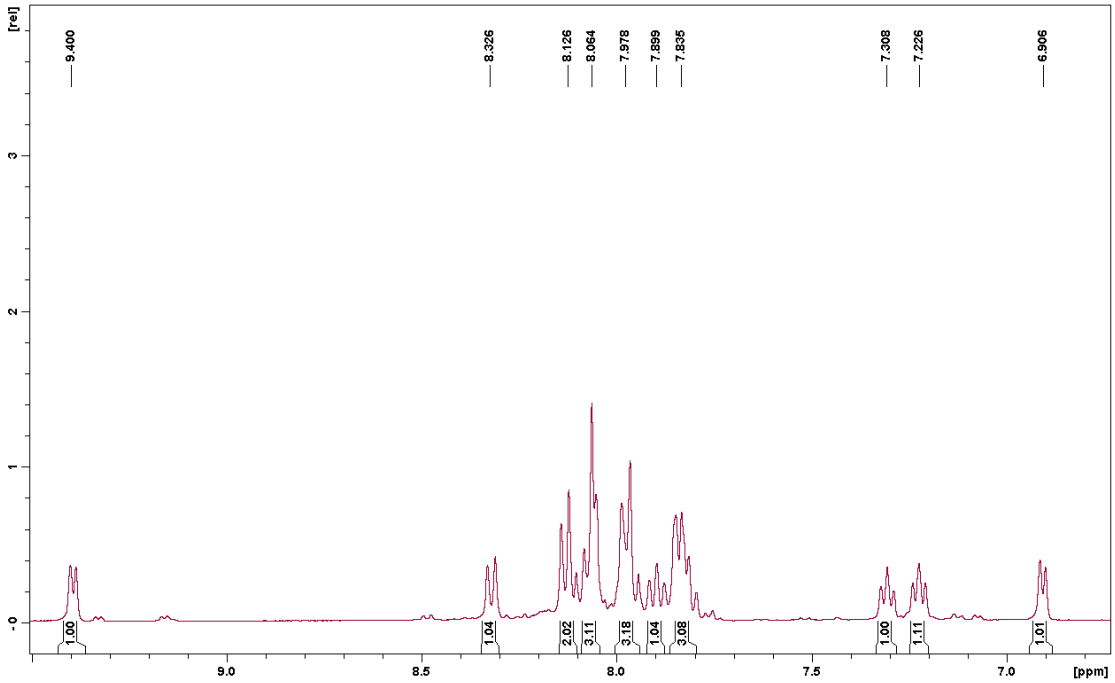
[rel]
9.400
8.326
8.126
8.064
7.978
7.899
7.835
7.308
7.226
6.906
1.00
1.04
2.02
3.11
3.18
1.04
3.08
1.00
1.11
1.01
9.0
8.5
8.0
7.5
7.0
[ppm]

(c)

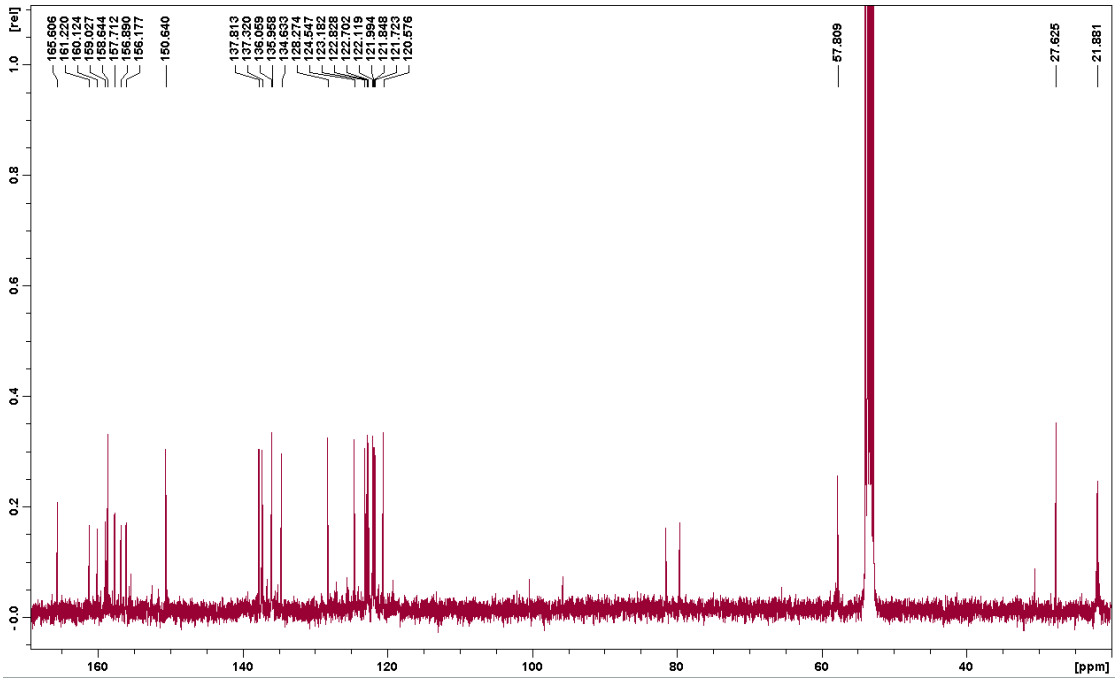
[rel]
165.606
161.220
160.124
159.027
158.944
157.712
156.890
156.177
150.640
137.813
137.320
136.059
135.958
134.853
123.274
123.047
123.182
122.828
122.702
122.119
121.994
121.848
121.723
120.576
57.809
27.625
21.881
160
140
120
100
80
60
40
[ppm]

III

(d)

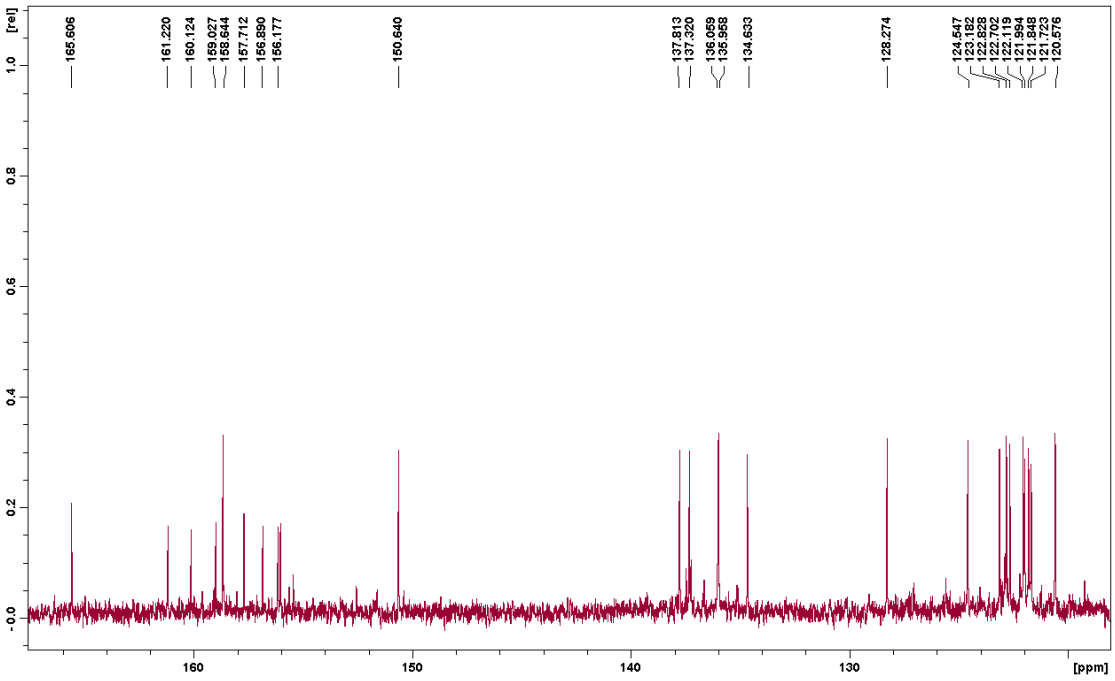
[rel]
1.0
0.8
0.6
0.4
0.2
-0.0
165.606
161.220
160.124
159.027
158.644
157.712
156.890
156.177
150.640
137.813
137.320
136.059
135.988
134.633
128.274
124.547
123.182
122.828
122.702
122.119
121.994
121.848
121.723
120.576
160
150
140
130
[ppm]

(e)

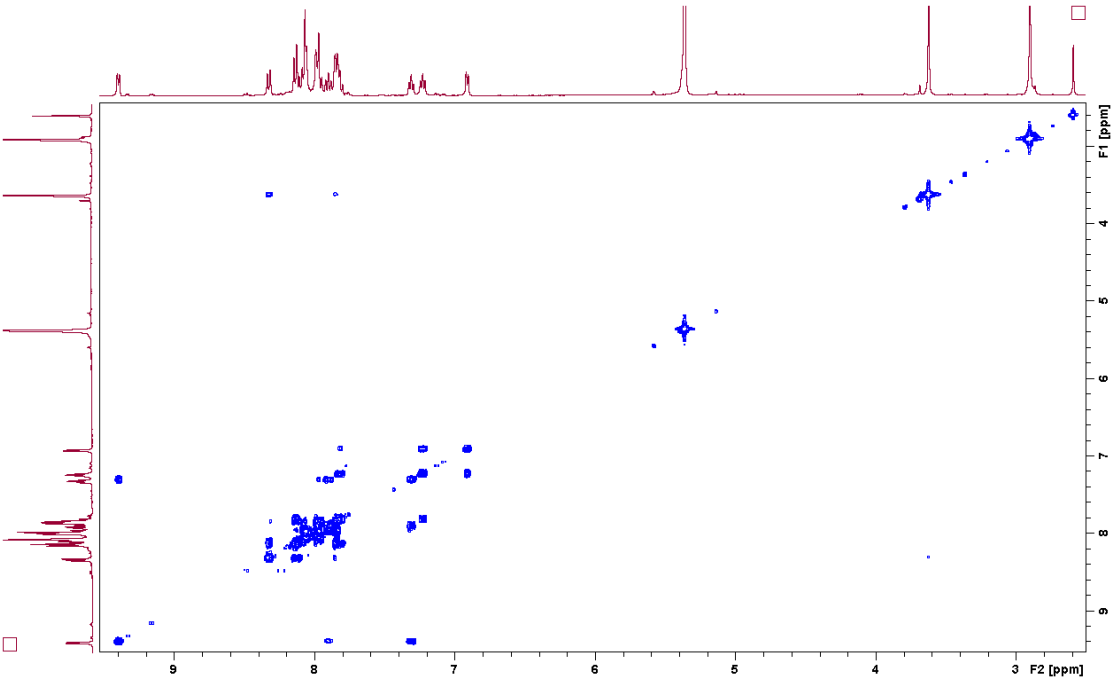
F1 [ppm]
9
8
7
6
5
4
3
F2 [ppm]

(f)

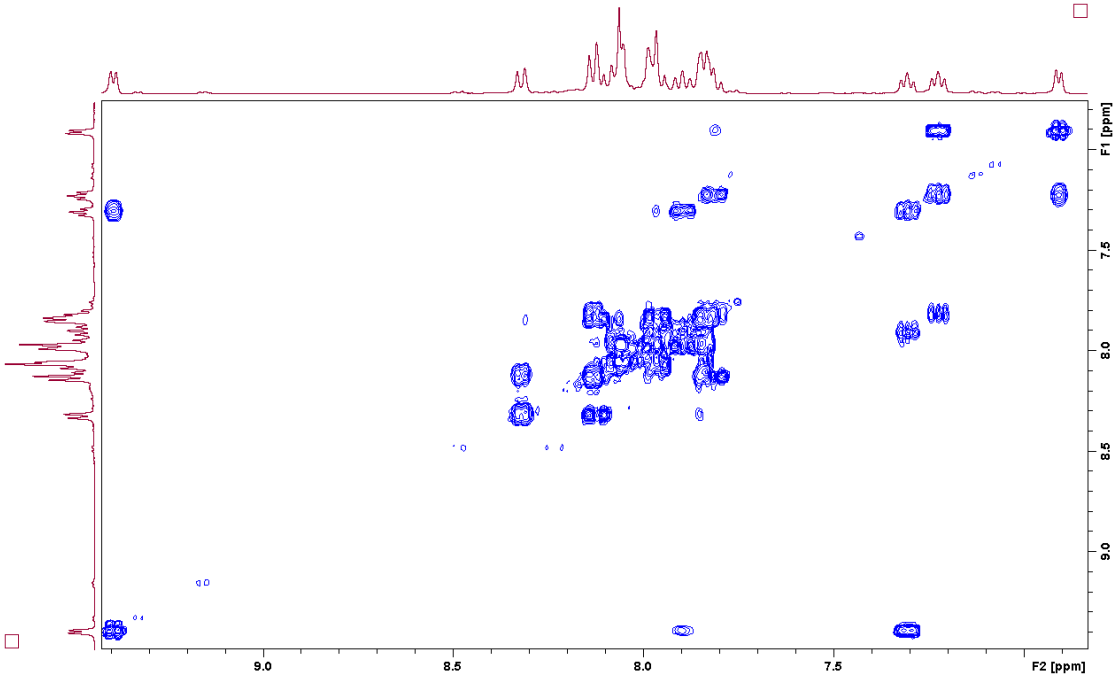
F1 [ppm]
7.5
8.0
8.5
9.0
9.0
8.5
8.0
7.5
F2 [ppm]

(g)

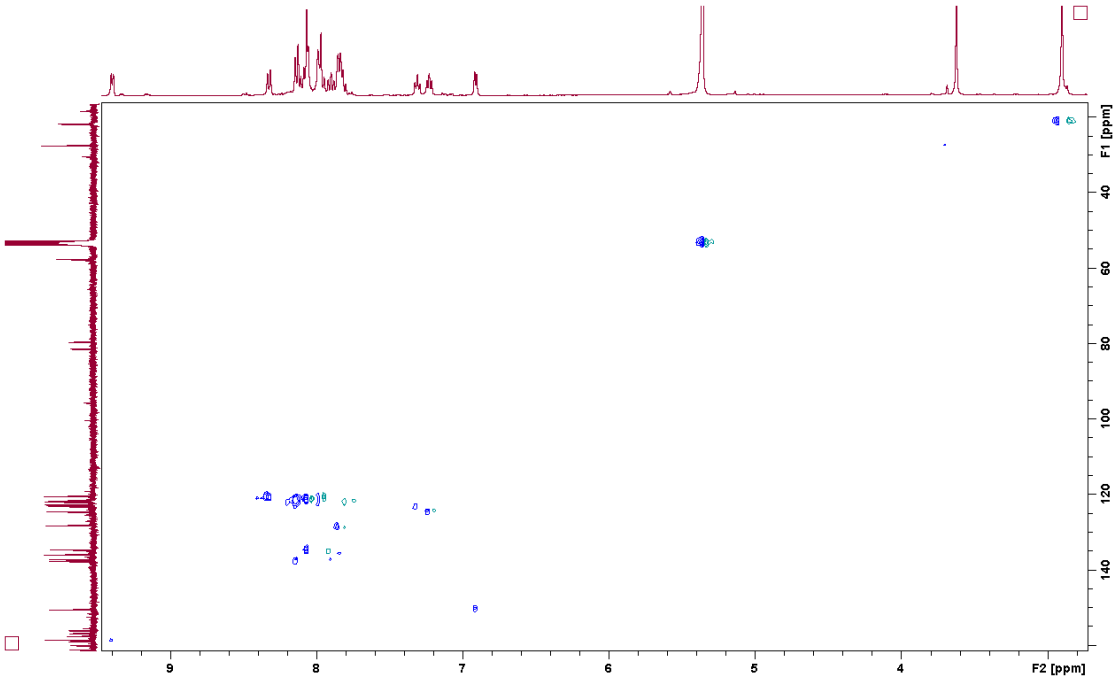
F1 [ppm]
40
60
80
100
120
140
9
8
7
6
5
4
F2 [ppm]

(h)

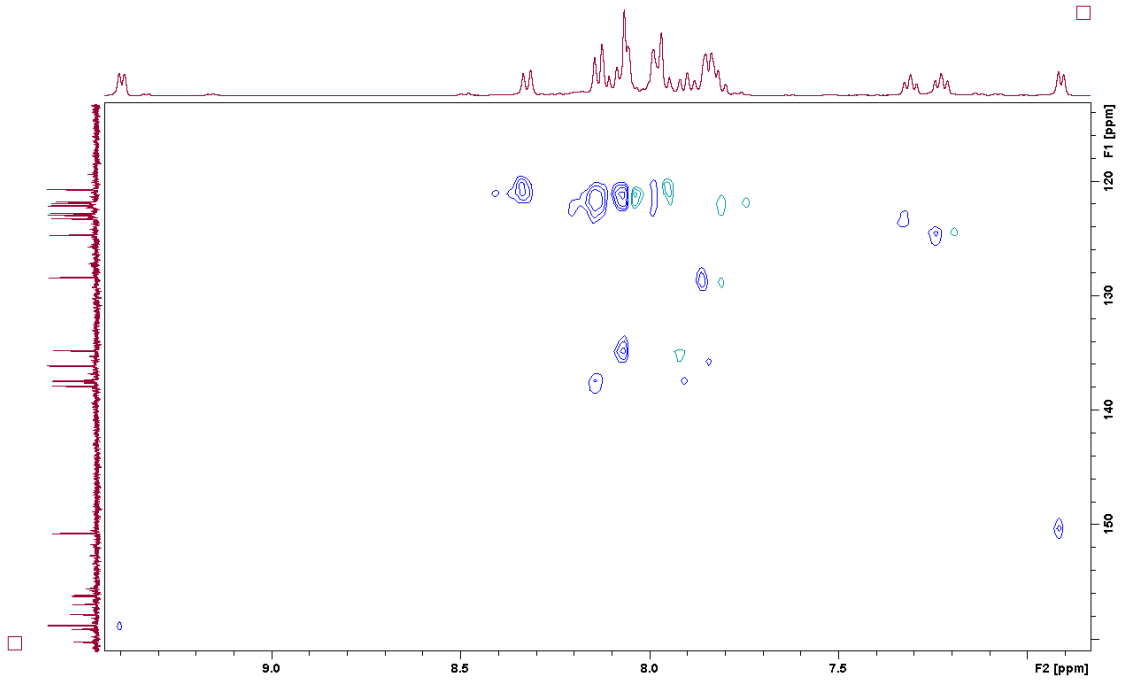
F1 [ppm]
120
130
140
150
9.0
8.5
8.0
7.5
F2 [ppm]

(i)

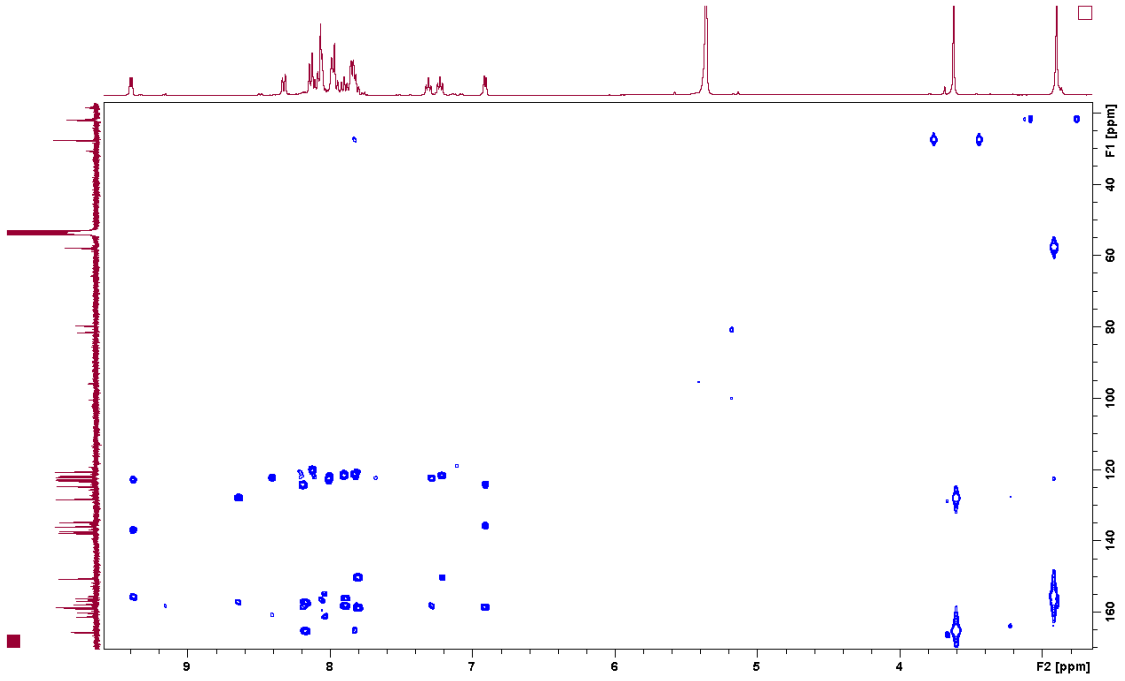
F1 [ppm]
40
60
80
100
120
140
160
9
8
7
6
5
4
F2 [ppm]

(j)

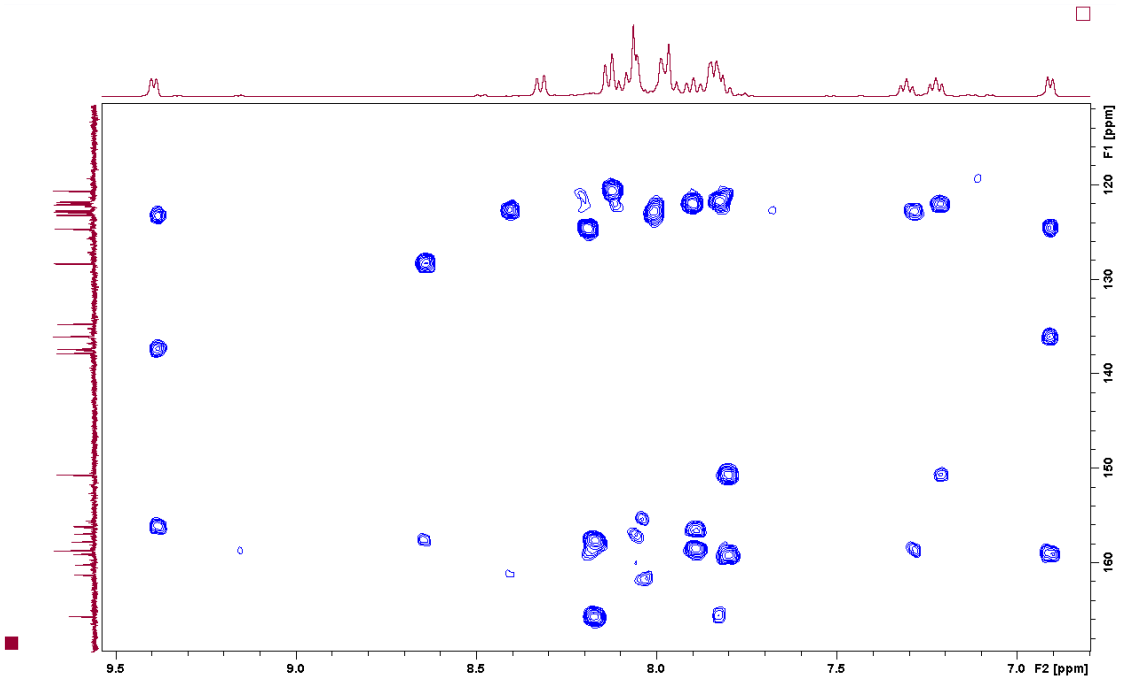

Figure S5. ^{1}H-NMR (a,b) and ^{13}C-{^{1}H}-NMR spectra (c,d) and 2D NMR spectra (400 MHz, 298 K, CD_2Cl_2) for complex *cis*-**3**$^{+}$: COSY (e,f), HSQC NMR (g,h) and HMBC NMR (i,j).

(a)

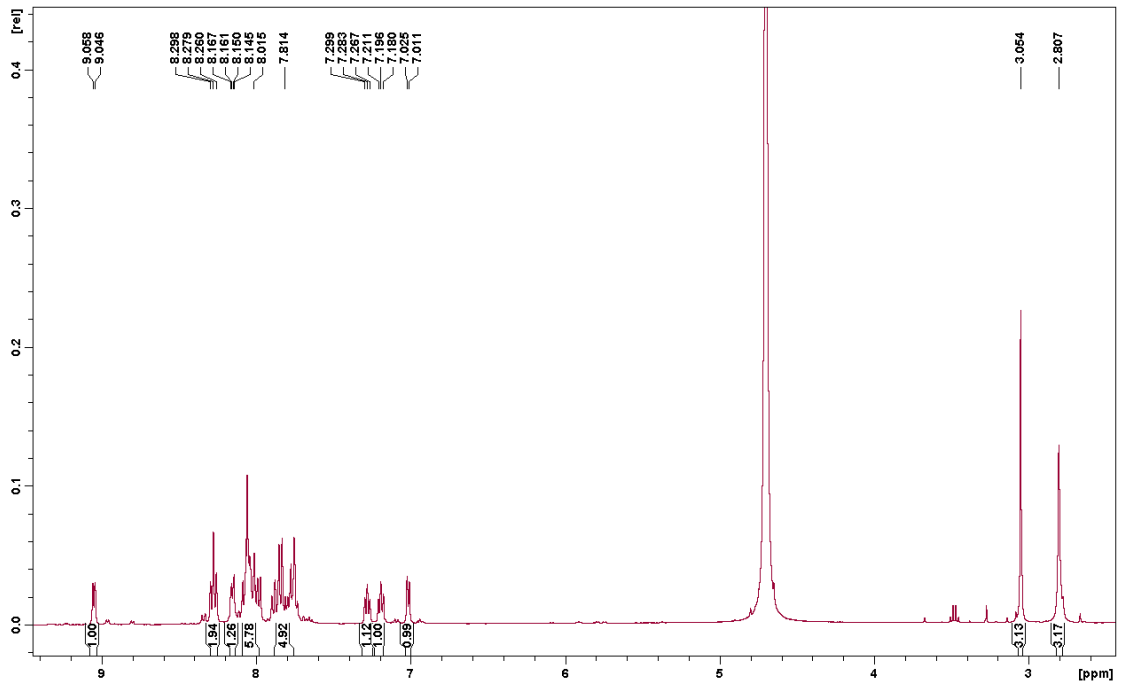

(b)

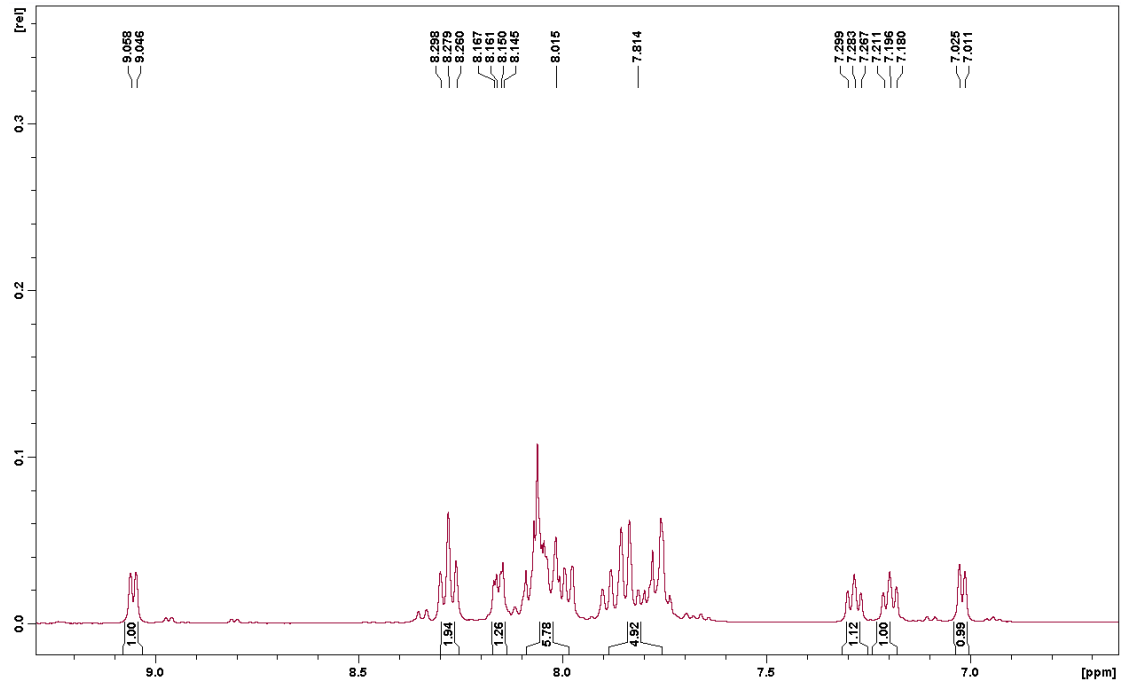
[rel]
9.058
9.046
8.298
8.279
8.260
8.167
8.161
8.150
8.145
8.015
7.814
7.299
7.283
7.267
7.211
7.196
7.180
7.025
7.011
1.00
1.94
1.26
5.78
4.92
1.12
1.00
0.99
[ppm]

(c)

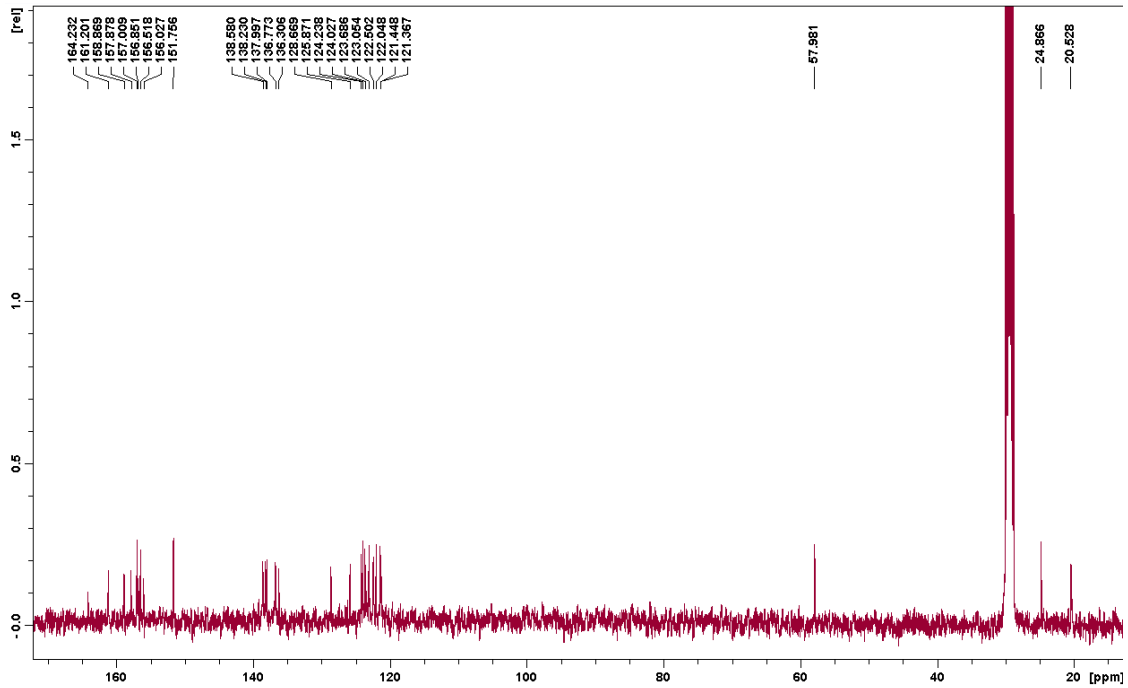
[rel]
164.232
161.201
158.869
157.878
157.009
156.851
156.519
155.027
151.756
138.580
138.230
137.997
136.773
136.306
128.669
125.871
124.238
124.027
123.686
123.054
122.502
122.048
121.448
121.367
57.981
24.866
20.528
[ppm]

(d)

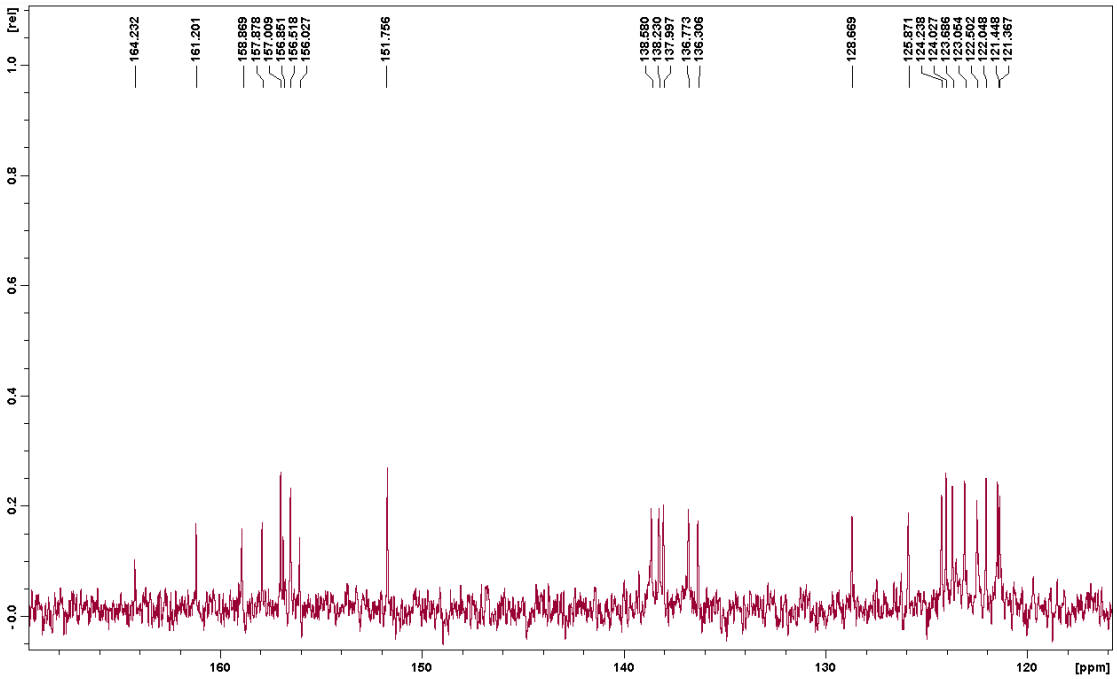
[rel]
1.0
0.8
0.6
0.4
0.2
-0.0
164.232
161.201
158.869
157.878
157.009
156.851
156.518
156.027
151.756
138.590
138.230
137.997
136.773
136.306
128.669
125.871
124.238
124.027
123.686
123.054
122.502
122.048
121.448
121.367
160
150
140
130
120
[ppm]

(e)

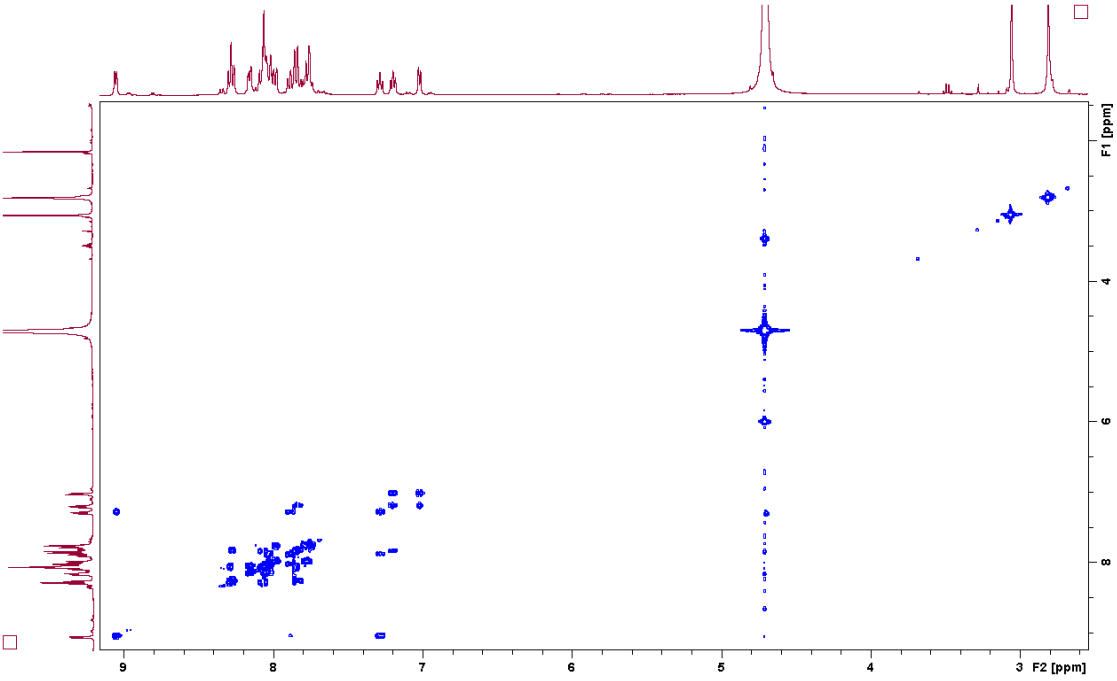
F1 [ppm]
4
6
8
9
8
7
6
5
4
3
F2 [ppm]

III

(f)

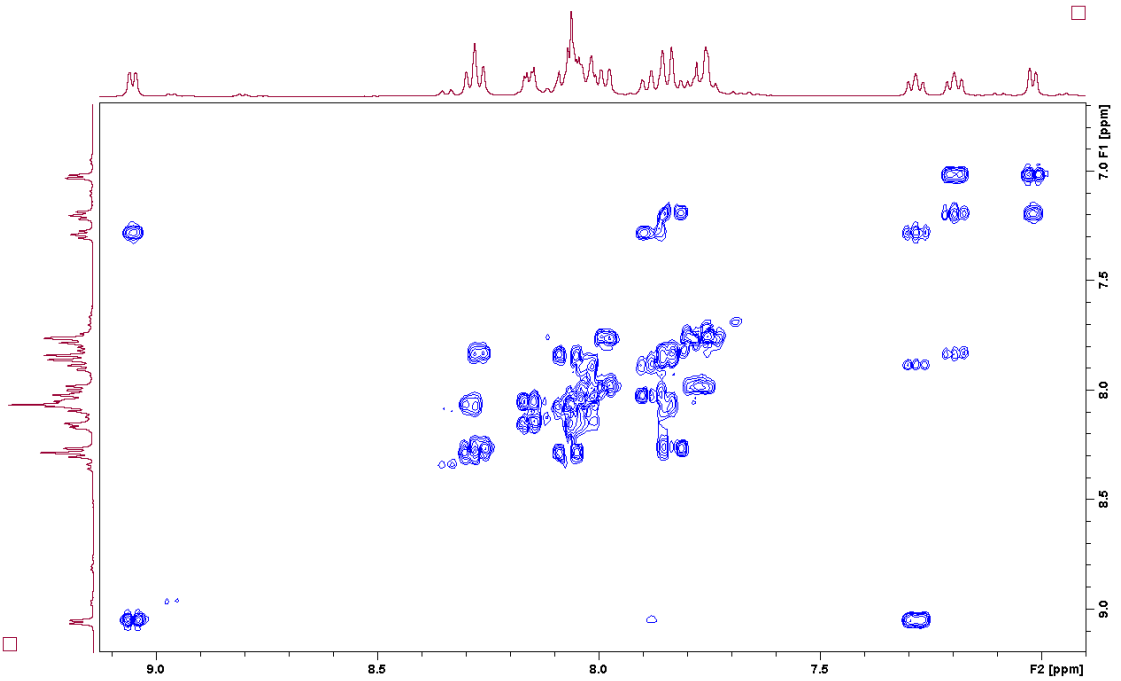
7.0 F1 [ppm]
7.5
8.0
8.5
9.0
9.0
8.5
8.0
7.5
F2 [ppm]

(g)

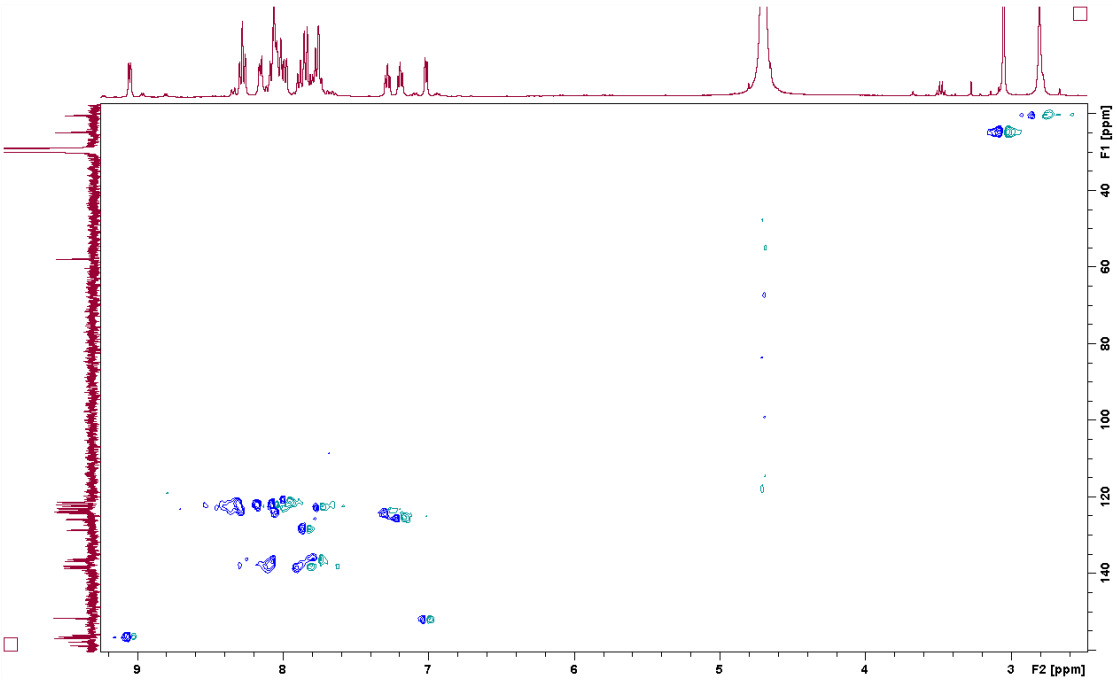
F1 [ppm]
40
60
80
100
120
140
9
8
7
6
5
4
3
F2 [ppm]

(h)

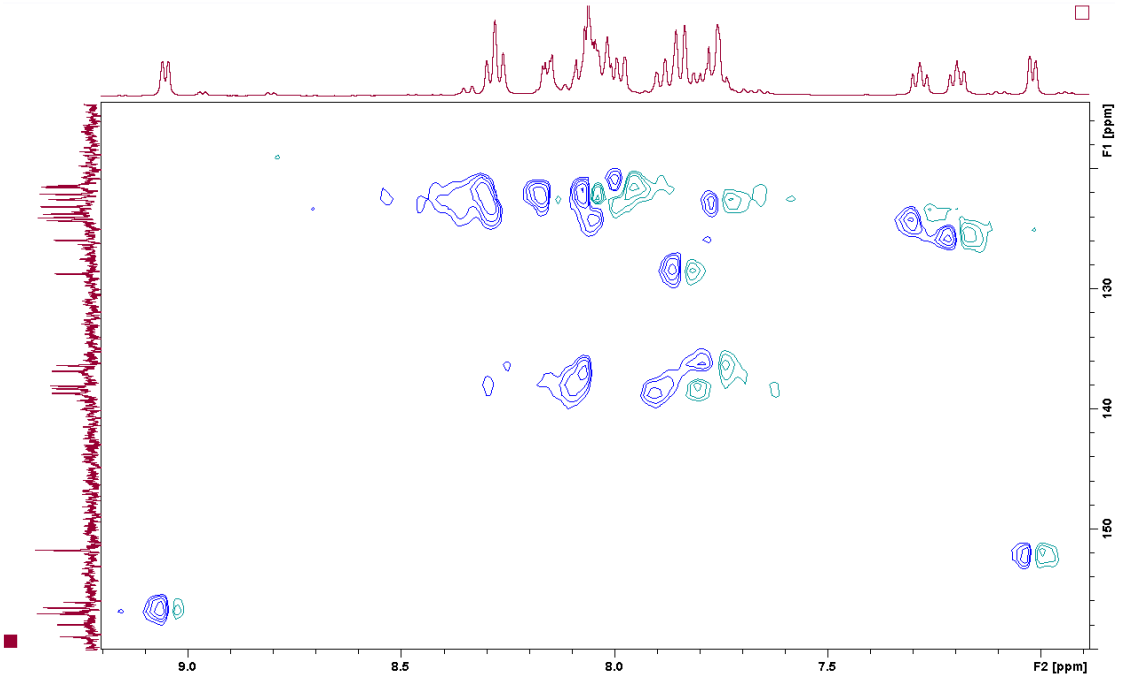
F1 [ppm]
130
140
150
9.0
8.5
8.0
7.5
F2 [ppm]

(i)

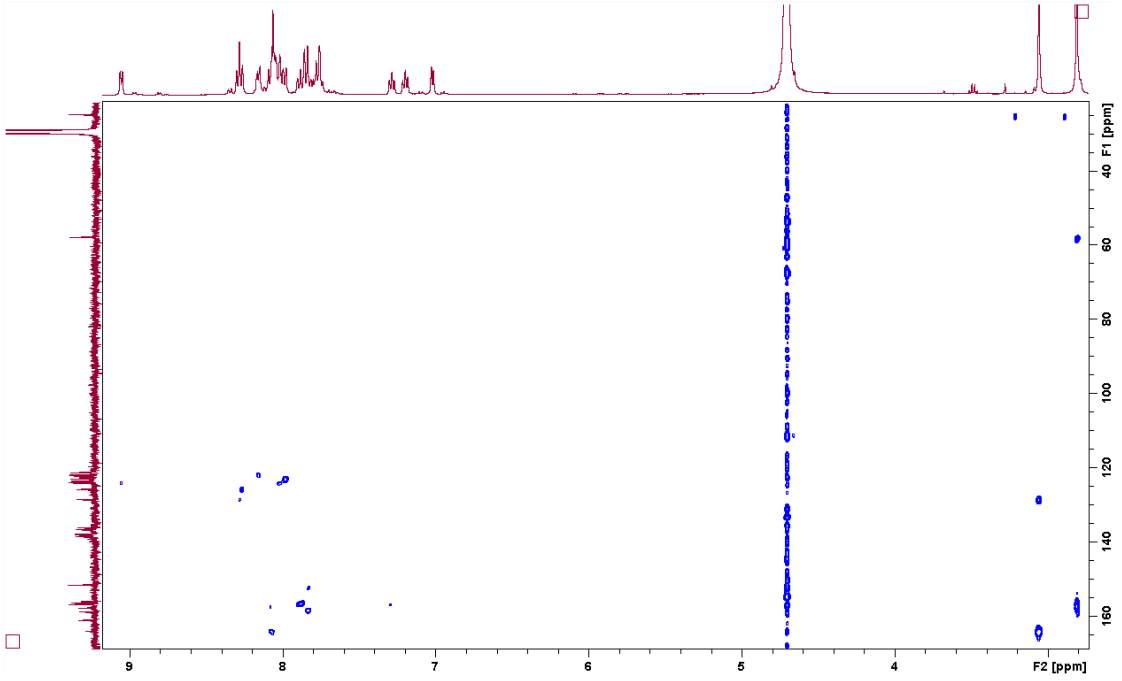
F1 [ppm]
40
60
80
100
120
140
160
9
8
7
6
5
4
F2 [ppm]

(j)

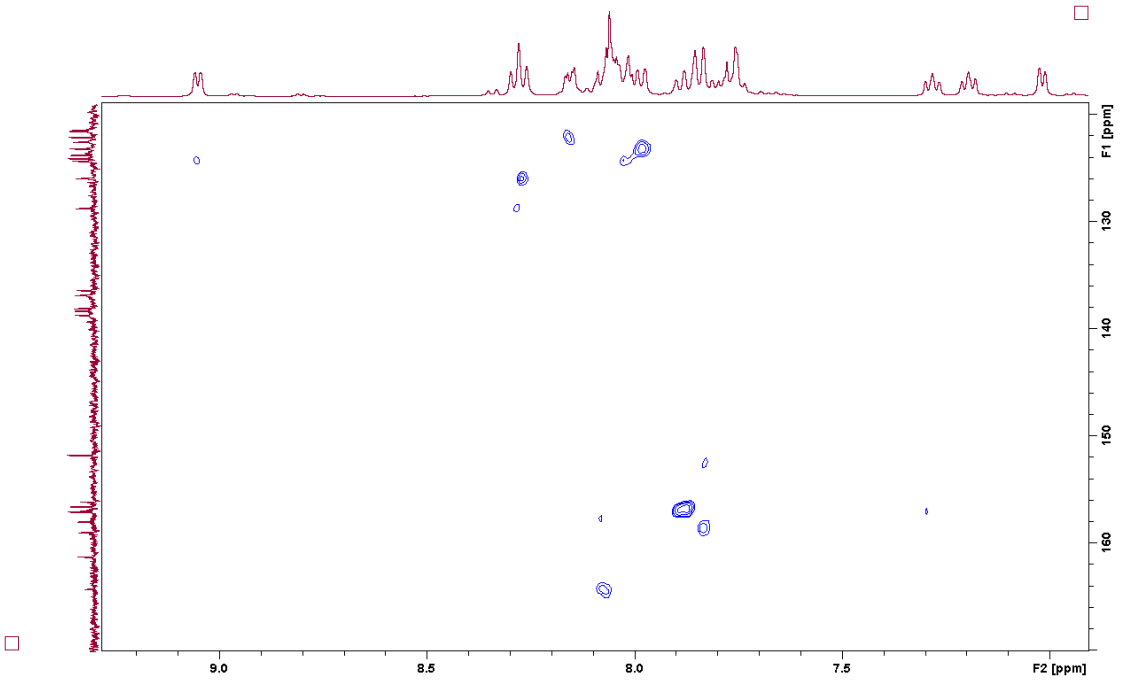

Figure S6. ^{1}H-NMR (a,b) and ^{13}C-{^{1}H}-NMR spectra (c,d) and 2D NMR spectra (400 MHz, 298 K, d_6-acetone:D_2O 5:95) for complex *cis*-**4**$^{2+}$: COSY (e,f), HSQC NMR (g,h) and HMBC NMR (i,j).

a)

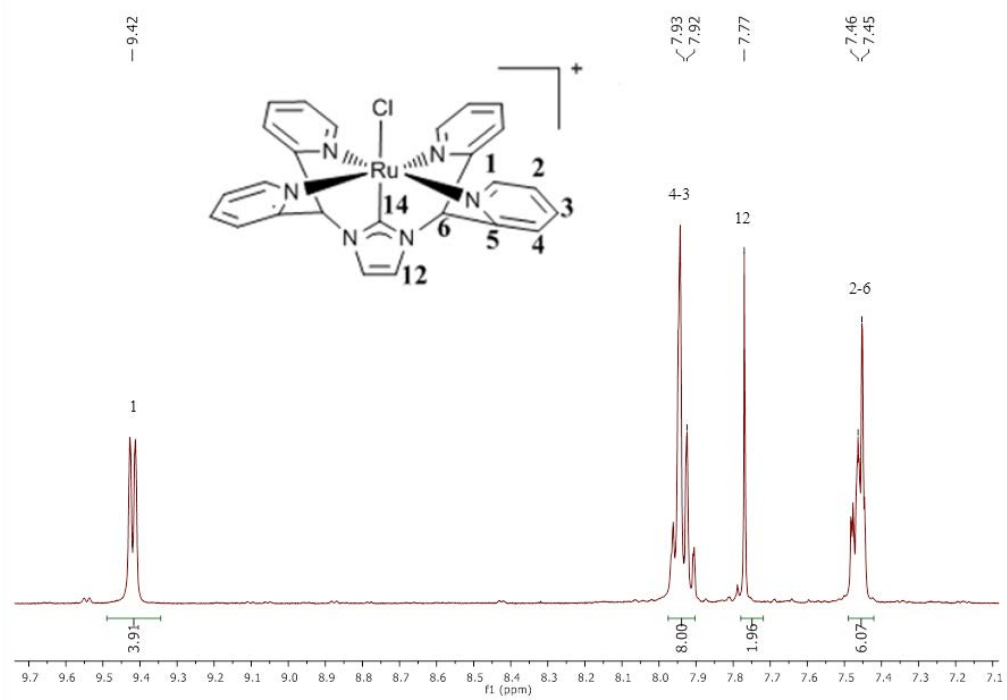

b)

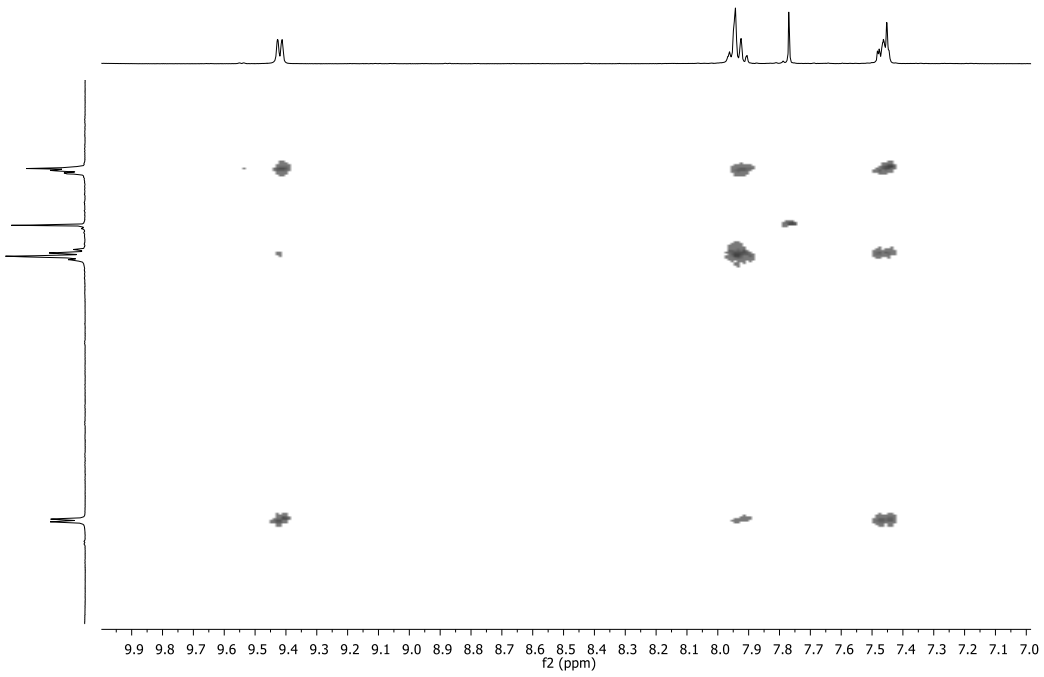
9.9 9.8 9.7 9.6 9.5 9.4 9.3 9.2 9.1 9.0 8.9 8.8 8.7 8.6 8.5 8.4 8.3 8.2 8.1 8.0 7.9 7.8 7.7 7.6 7.5 7.4 7.3 7.2 7.1 7.0
f2 (ppm)

c)

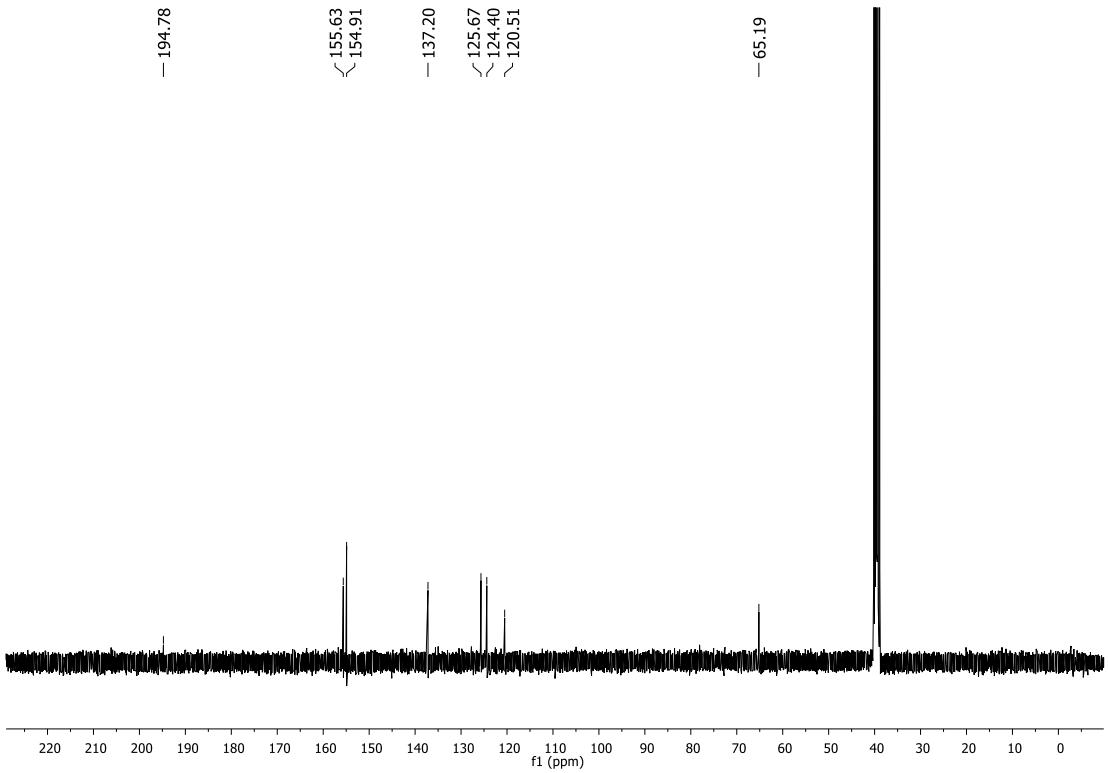
194.78
155.63
154.91
137.20
125.67
124.40
120.51
65.19
220 210 200 190 180 170 160 150 140 130 120 110 100 90 80 70 60 50 40 30 20 10 0
f1 (ppm)

d)

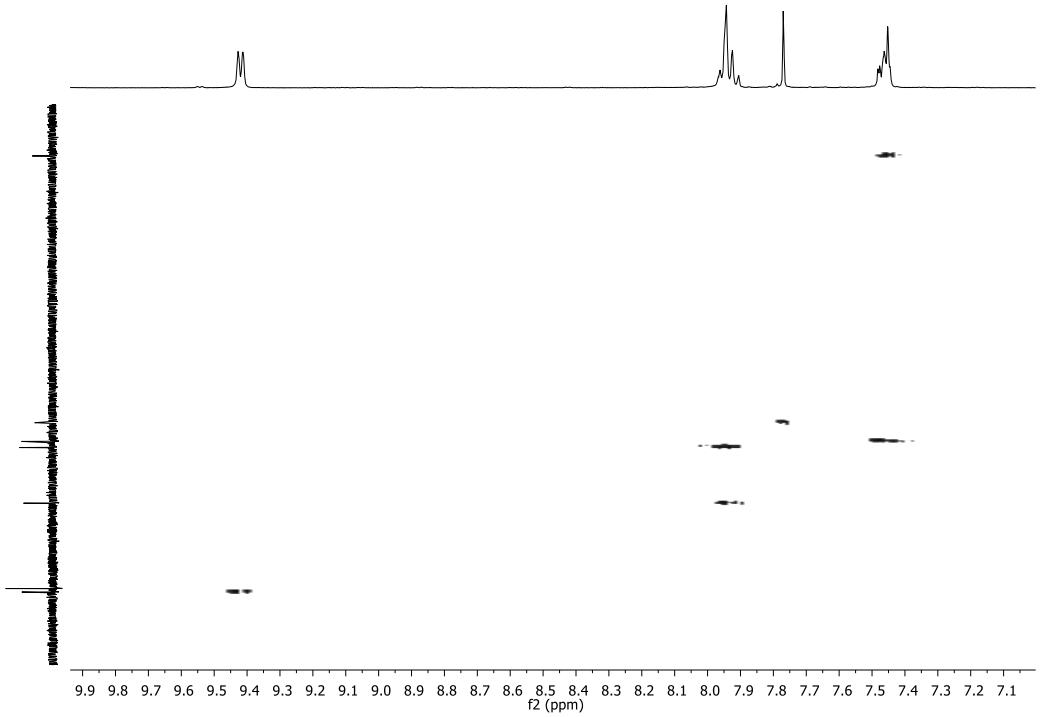

e)

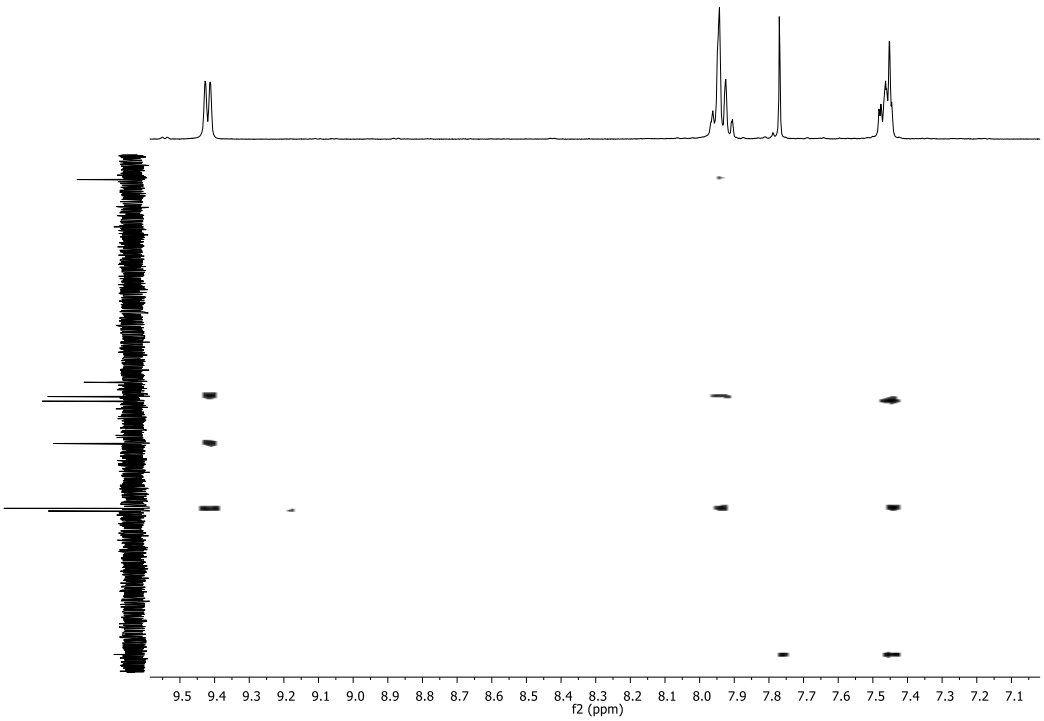

Figure S7. ^{1}H-NMR spectrum including signal assignment (a) and 2D NMR spectra (400 MHz, 298 K, DMSO-d_6) for **7**$^{+}$: (b) COSY, (c) ^{13}C-{^{1}H}-NMR, (d) HSQC NMR (aromatic region) and (e) HMBC NMR (aromatic region).

a)

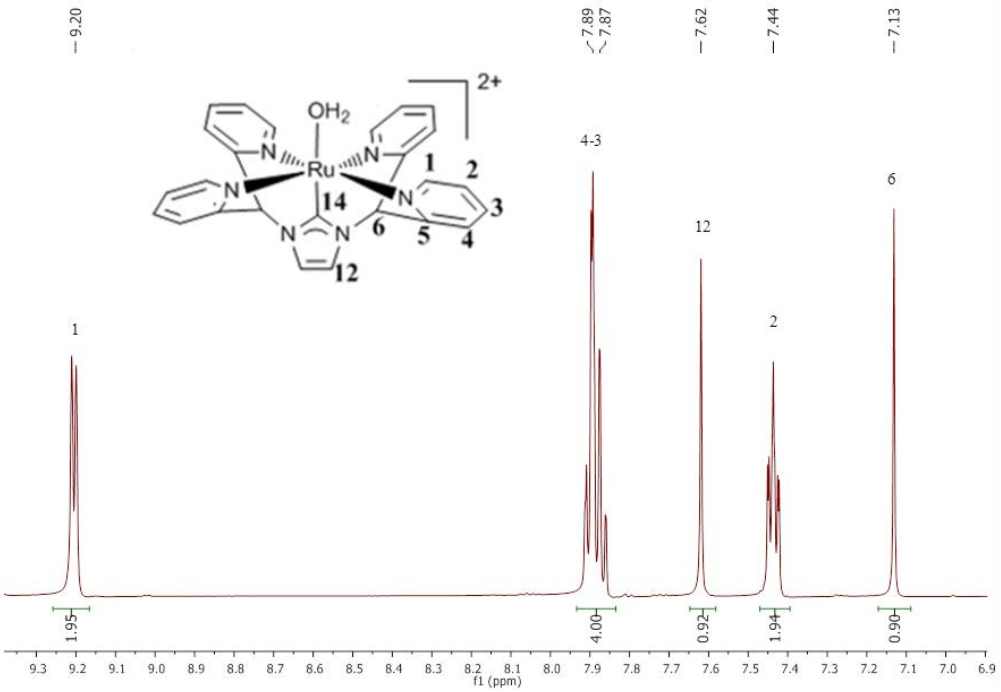
9.20
7.89
7.87
7.62
7.44
7.13
OH2
2+
Ru
N
1
2
3
4
5
6
12
14
4-3
12
6
2
1
1.95
4.00
0.92
1.94
0.90
f1 (ppm)

b)

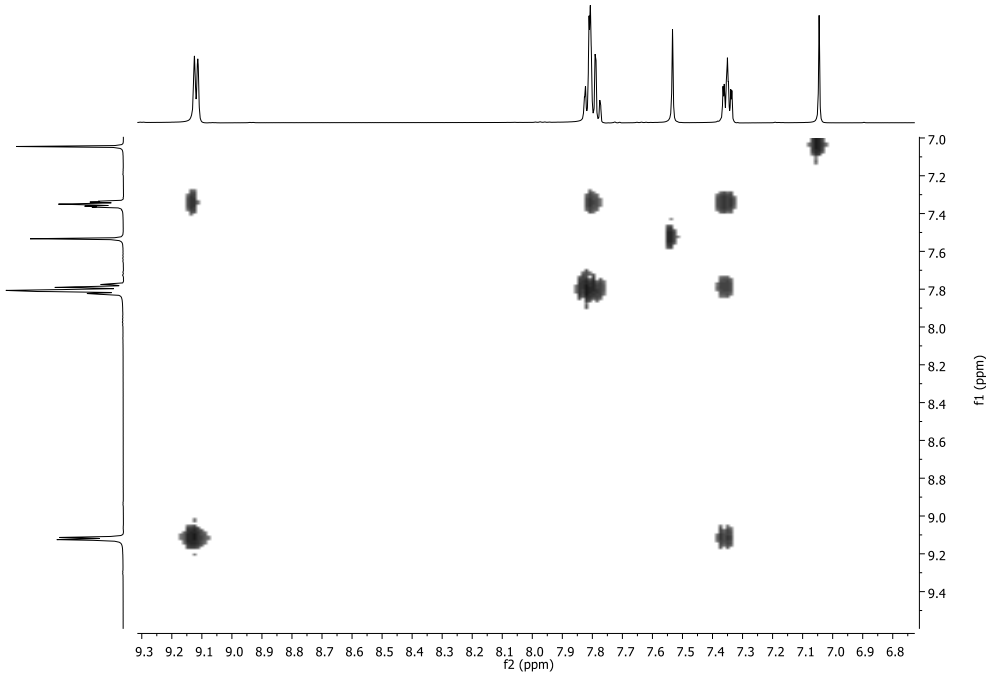
f1 (ppm)
f2 (ppm)

III

c)

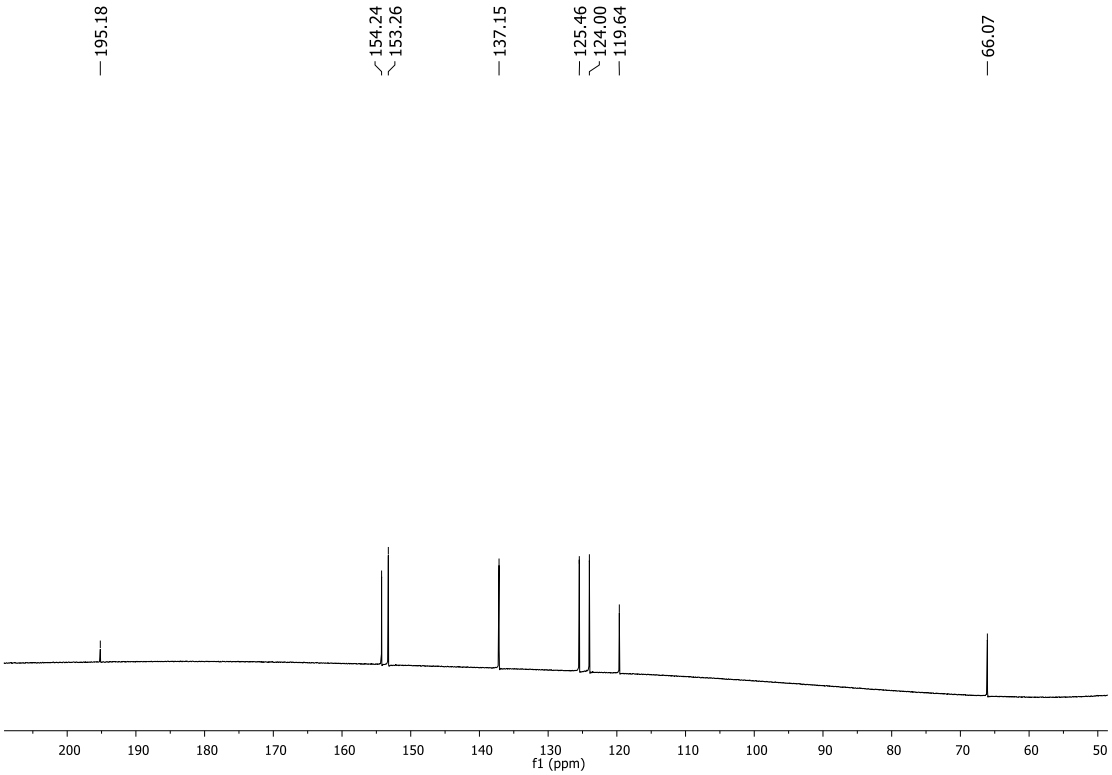
195.18
154.24
153.26
137.15
125.46
124.00
119.64
66.07
200 190 180 170 160 150 140 130 120 110 100 90 80 70 60 50
f1 (ppm)

d)

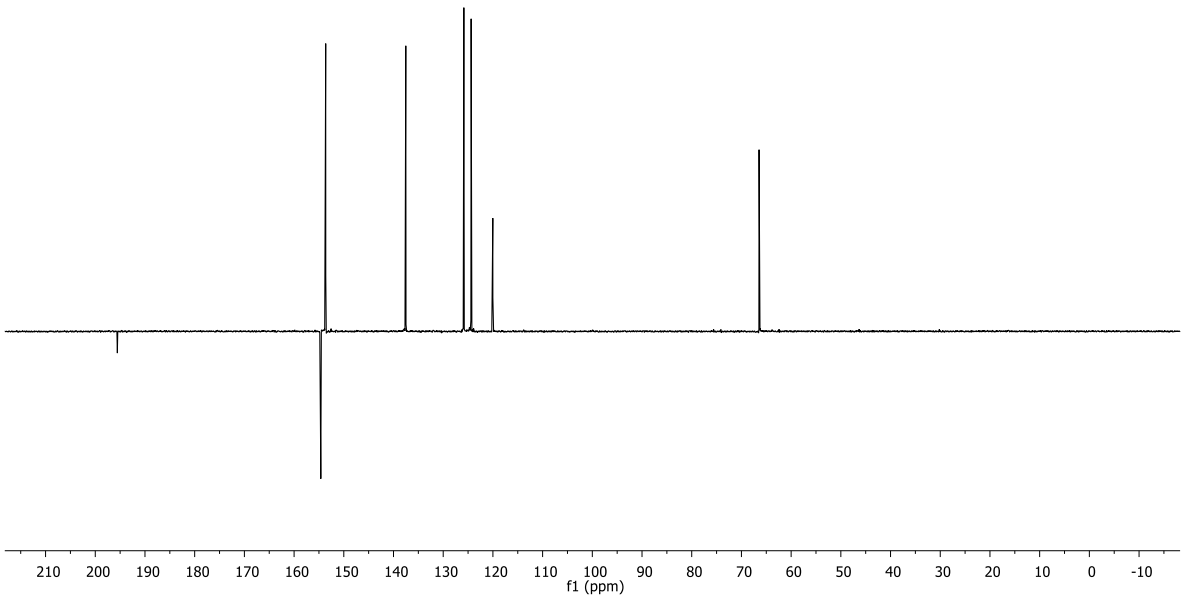
210 200 190 180 170 160 150 140 130 120 110 100 90 80 70 60 50 40 30 20 10 0 -10
f1 (ppm)

e)

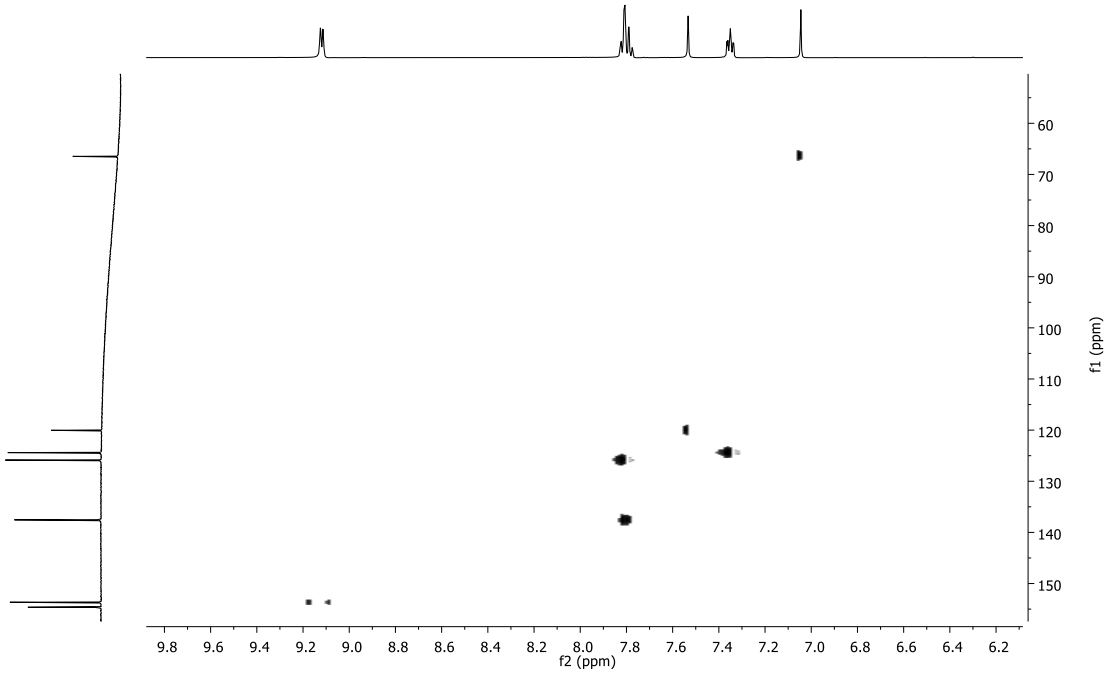

f)

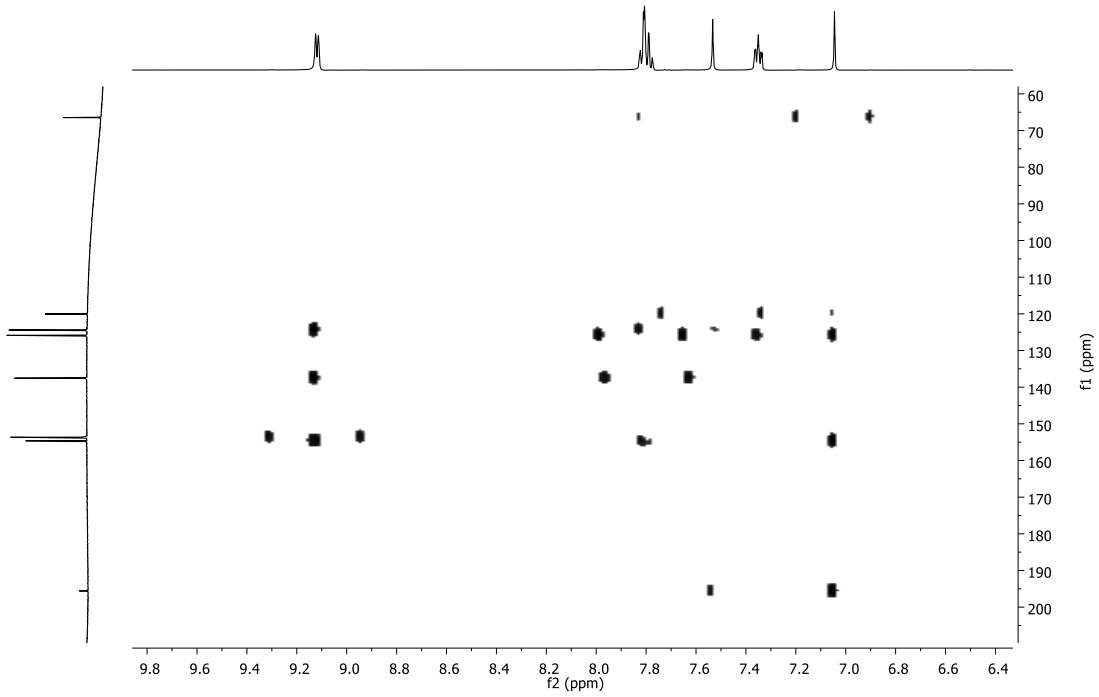

Figure S8. ^{1}H-NMR spectrum including signal assignment (a) and 2D NMR spectra (400 MHz, 298 K, D_2O) for complex $\mathbf{8}^{2+}$: (b) COSY, (c) ^{13}C-{^{1}H}-NMR, (d) ^{13}C-{^{1}H}-DEPTQ135, (e) HSQC NMR (aromatic region) and (f) HMBC NMR (aromatic region).

Mass Spectrometry

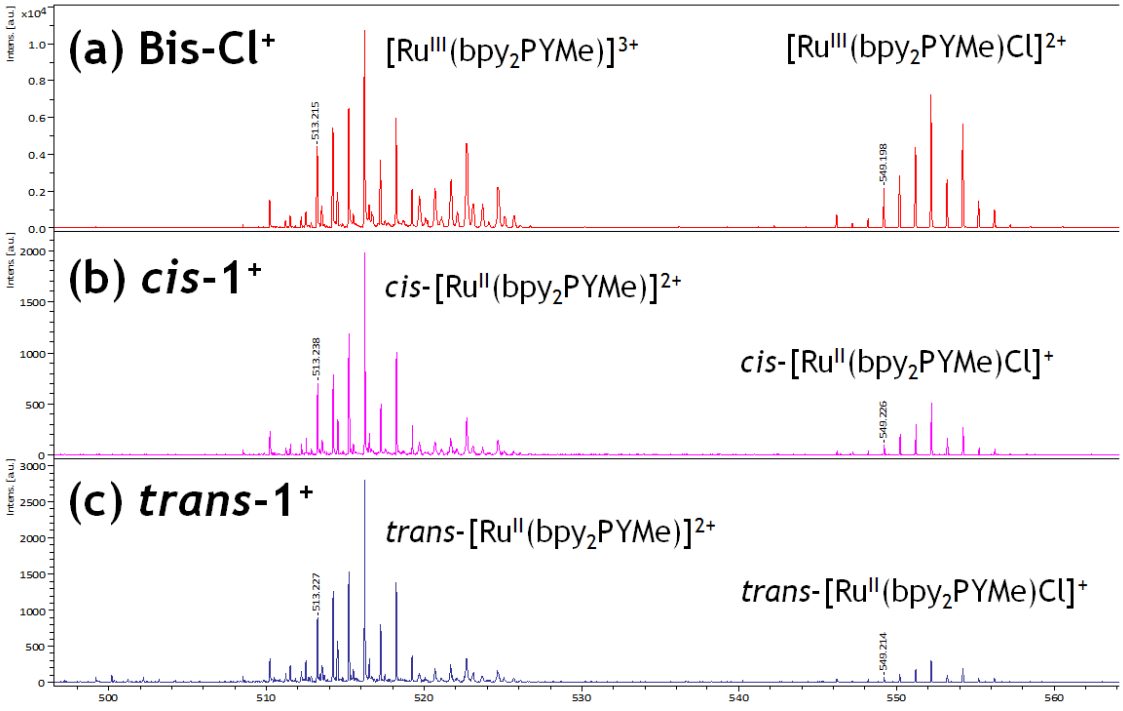

(d)

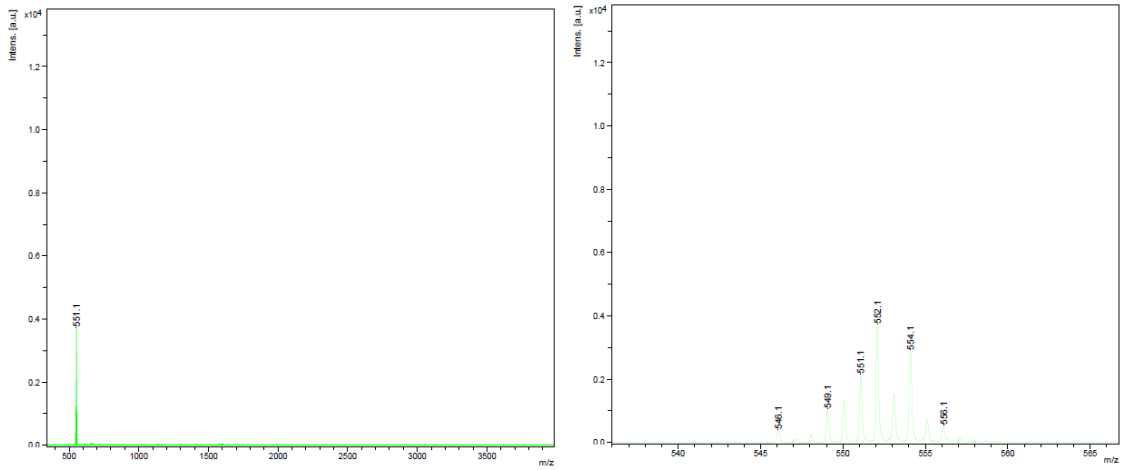

(e)

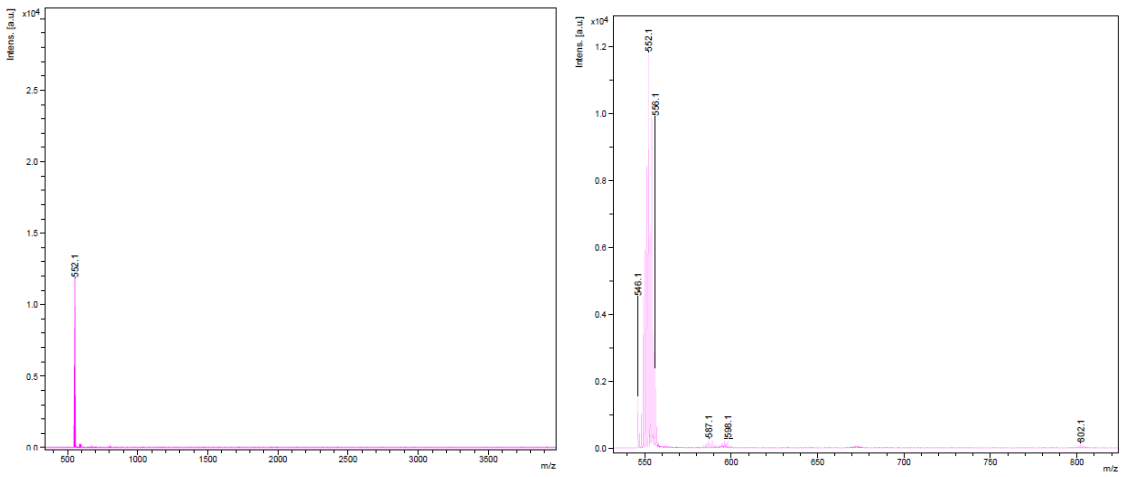

Figure S9. MALDI-TOF MS spectra of **bis-Cl**$^{+}$ (a), *cis*-**1**$^{+}$ (b) and *trans*-**1**$^{+}$ (c) and ESI-TOF MS spectra of *cis*-**1**$^{+}$ (d) and *trans*-**1**$^{+}$ (e) (deconvoluted, left; experimental, right). Note for the case of MALDI-TOF spectra the presence of cationic species without the Cl^{-} ligand probably due to the laser impact.

III

(a)

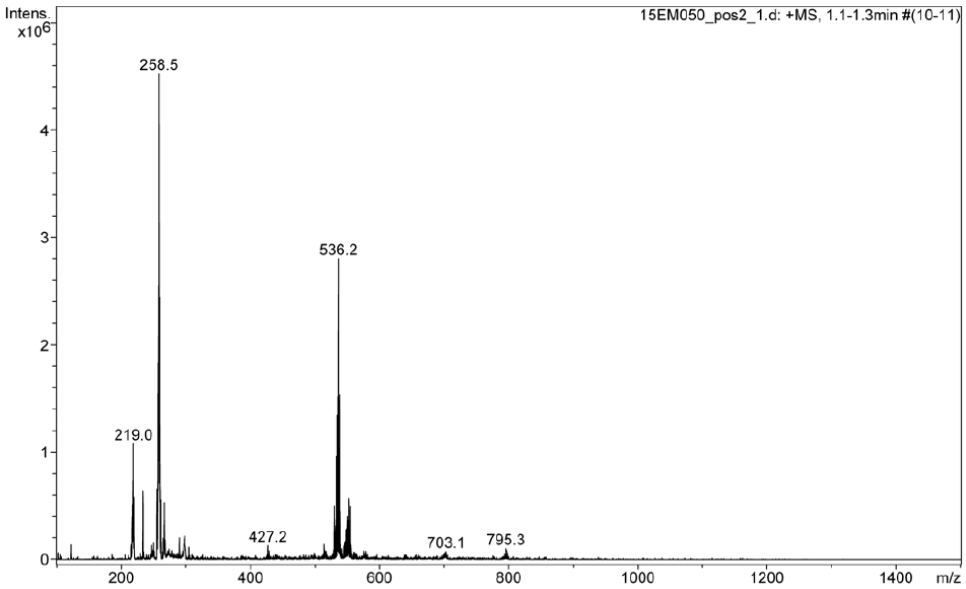

(b)

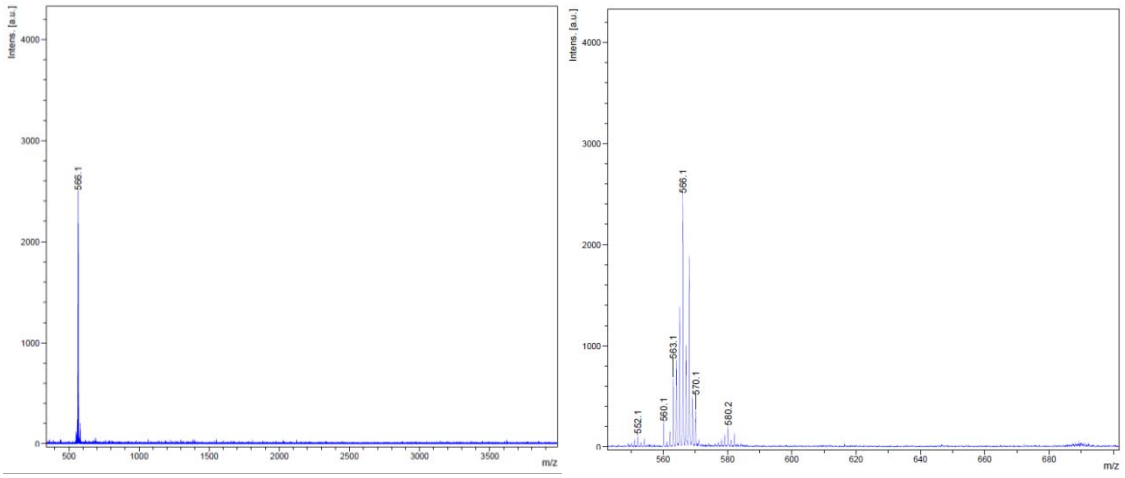

(c)

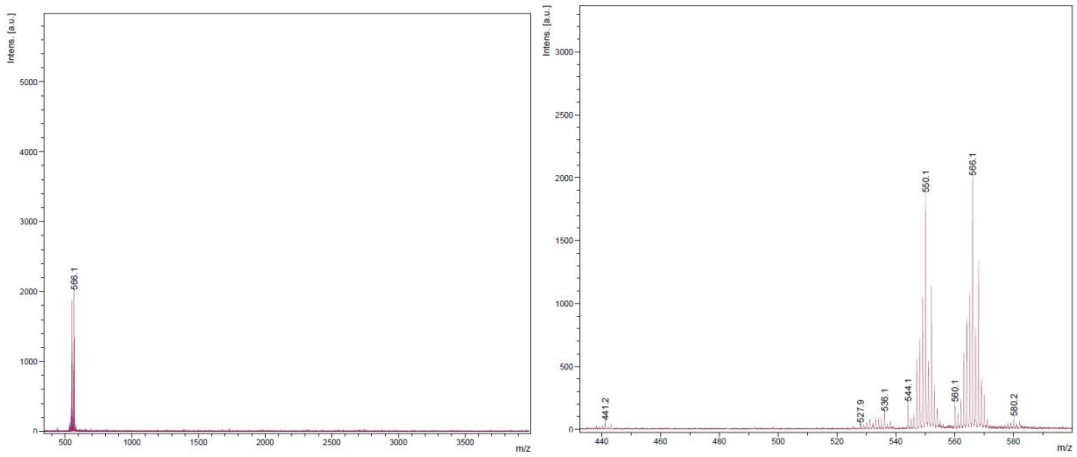

Figure S10. ESI-TOF-MS spectra for complexes **2**$(\mathbf{PF_6})_2$ (a), **3**(**Cl**) (b) (deconvoluted, left; experimental, right) and **4**$(\mathbf{PF_6})_2$ (c) (deconvoluted, left; experimental, right).

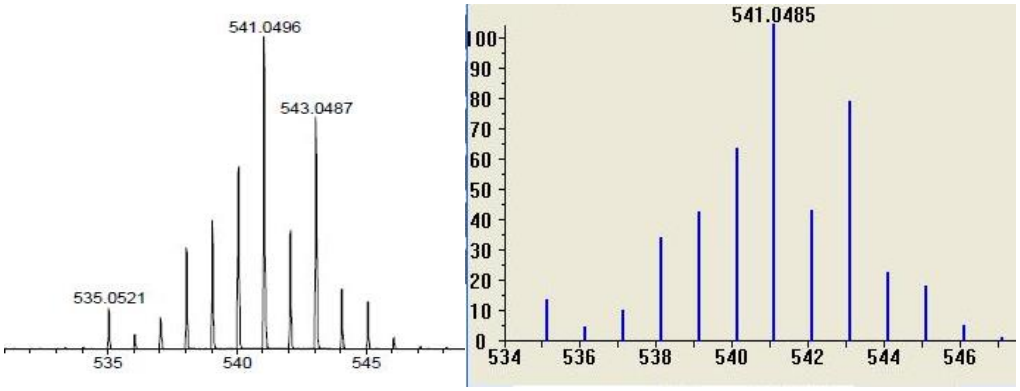

Figure S11. Experimental (left) and theoretical zoom (right) ESI-MS spectra for complex $\mathbf{7}^{+}$.

a)

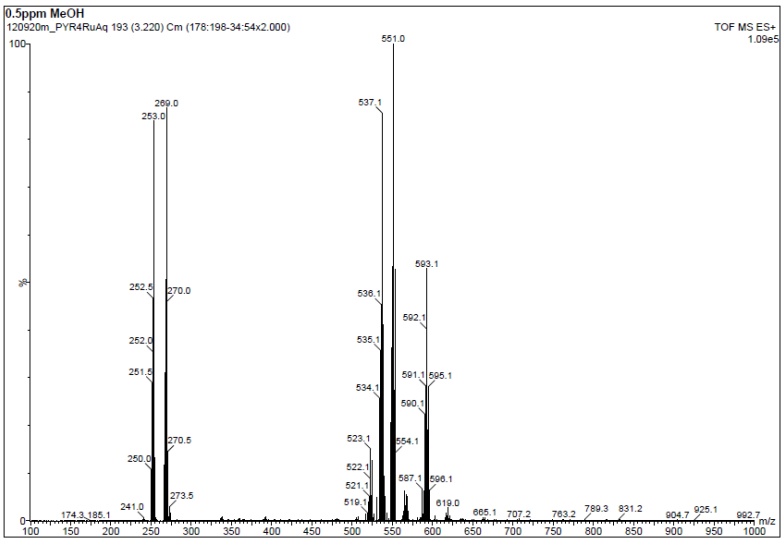

b)

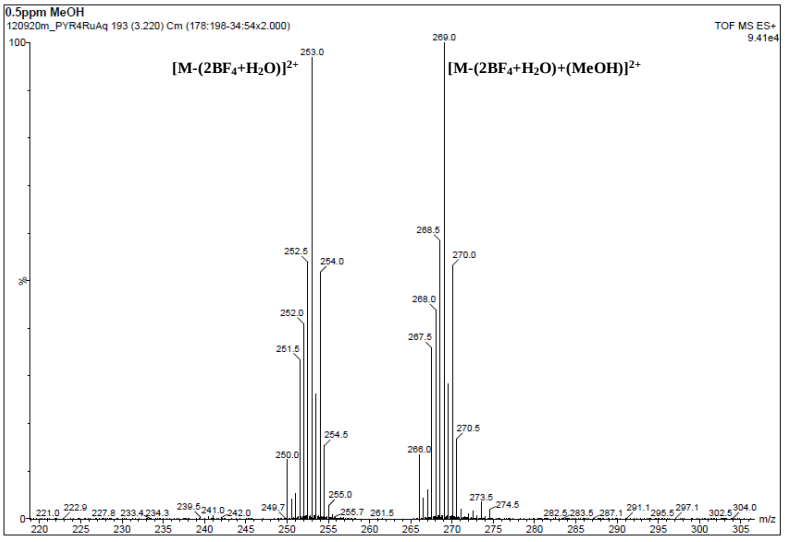

c)

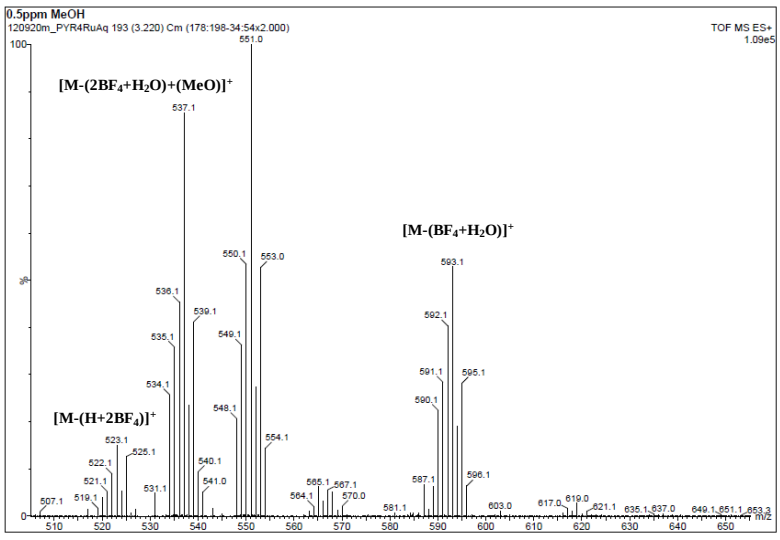

Figure S12. Experimental ESI-MS spectra for complex $\mathbf{8}^{2+}$ (a) and partial zoomed views (b,c).

UV-vis Spectroscopy

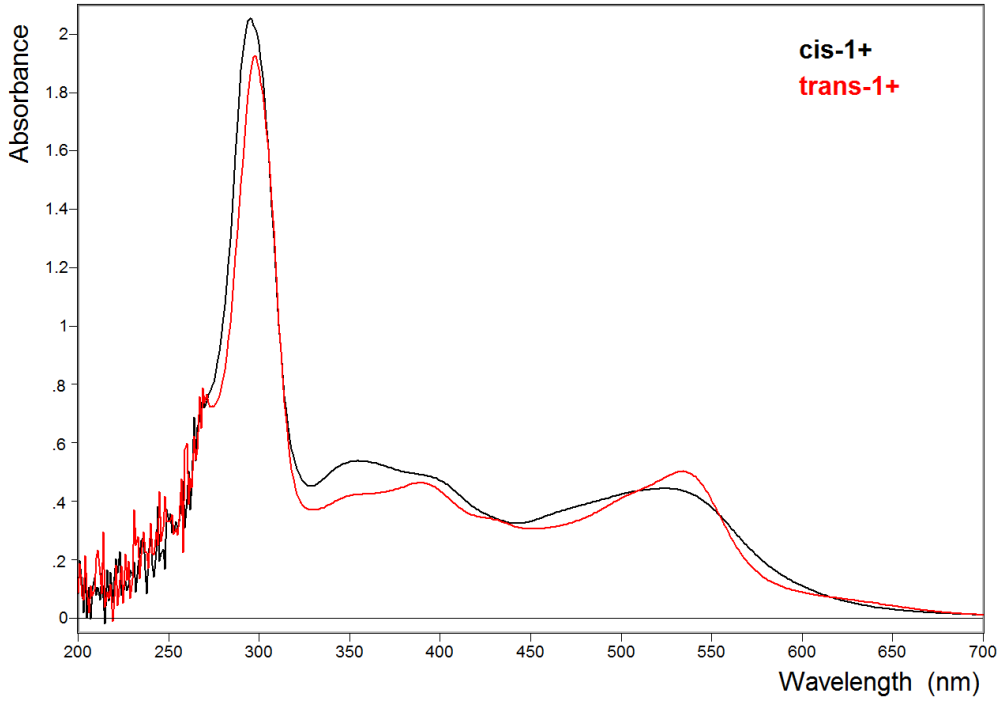

Figure S13. UV-Vis spectra of a $1x10^{-4}$M solution of *cis*-**1**$^{+}$ (black) and of *trans*-**1**$^{+}$ (red) in DCM.

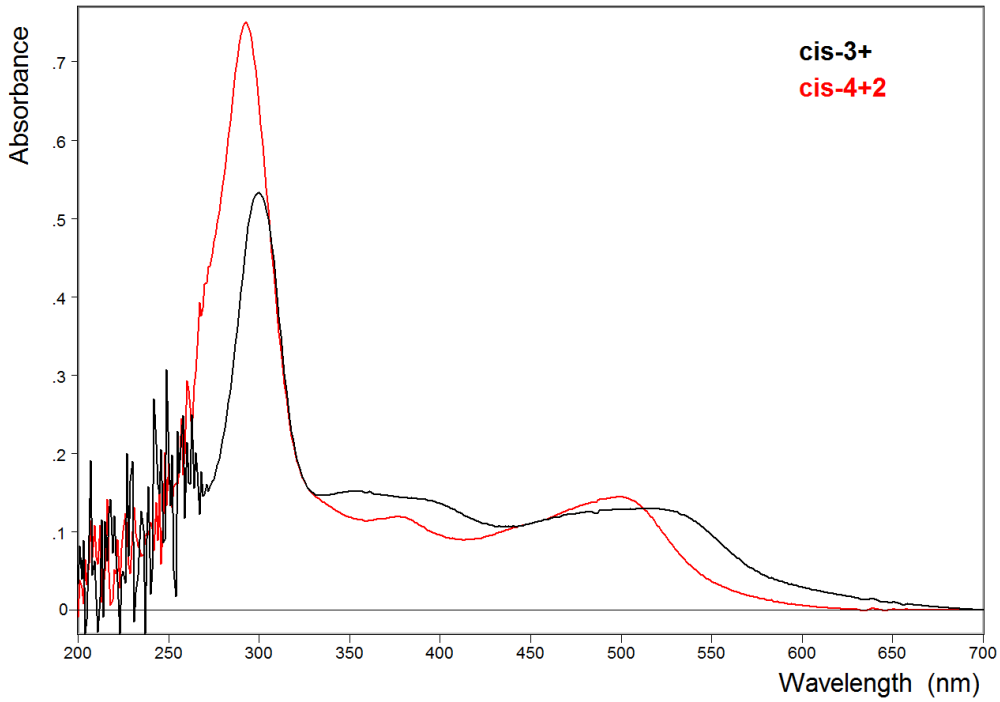

Figure S14. UV-Vis spectra of a $2.5 \cdot 10^{-5}$ M solution of *cis*-**3**$^{+}$ in DCM (black) and of *cis*-**4**$^{2+}$ in water (red).

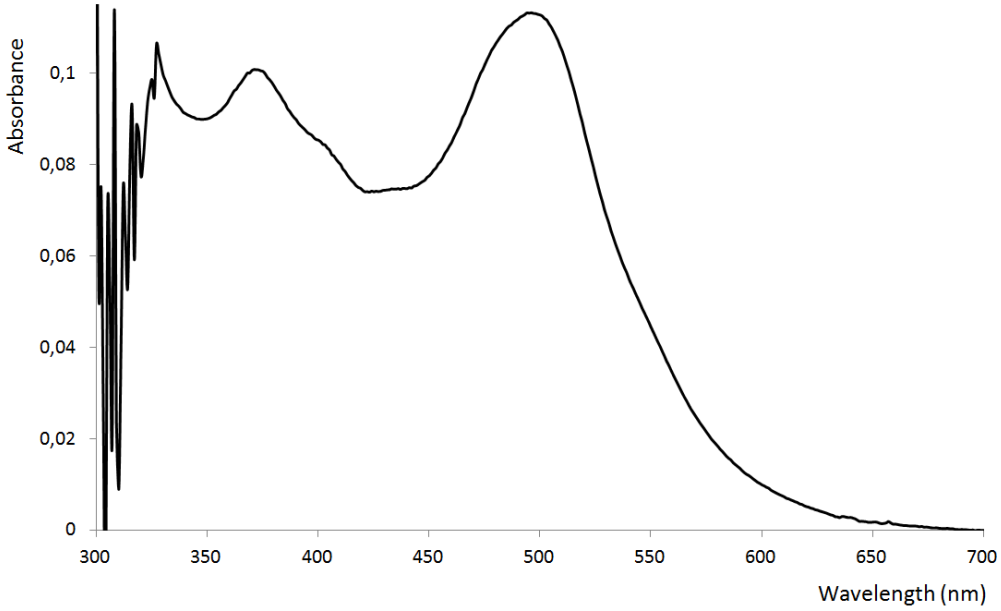

Figure S15. UV-Vis spectra of a $2.5 \cdot 10^{-5}$ M solution of the aqua complex *trans*-$\mathbf{2}^{2+}$ in water.

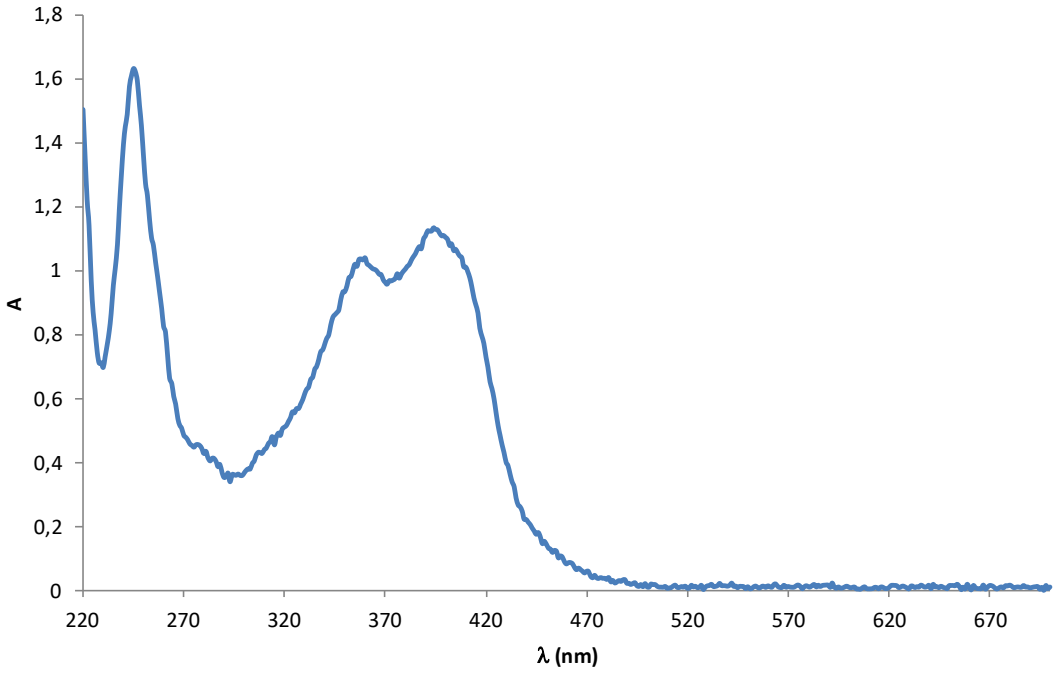

Figure S16. UV-vis spectra for a $1.6 \cdot 10^{-4}$ M solution of $\mathbf{8}^{2+}$ in H_2O at pH 8 (phosphate buffer).

X-Ray Crystallography

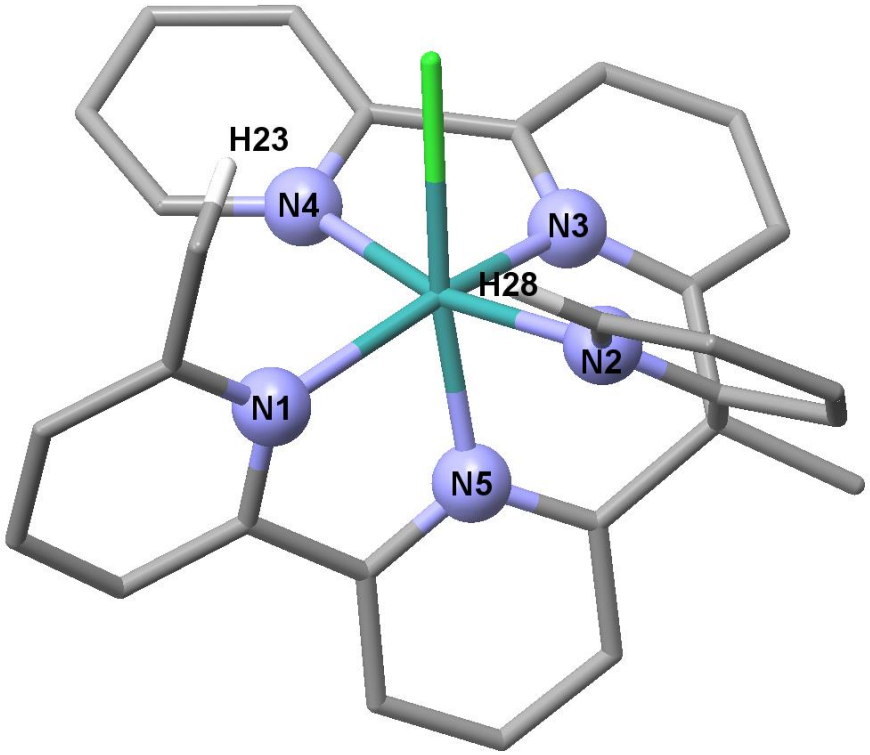

Figure S17. Mercury plot of the X-Ray crystal structure of *cis*-**3**$^{+}$. Atom color code: blue, nitrogen; green, chlorine; dark green, ruthenium; light grey, carbon. Only hydrogen atoms close to the chlorine are shown in white.

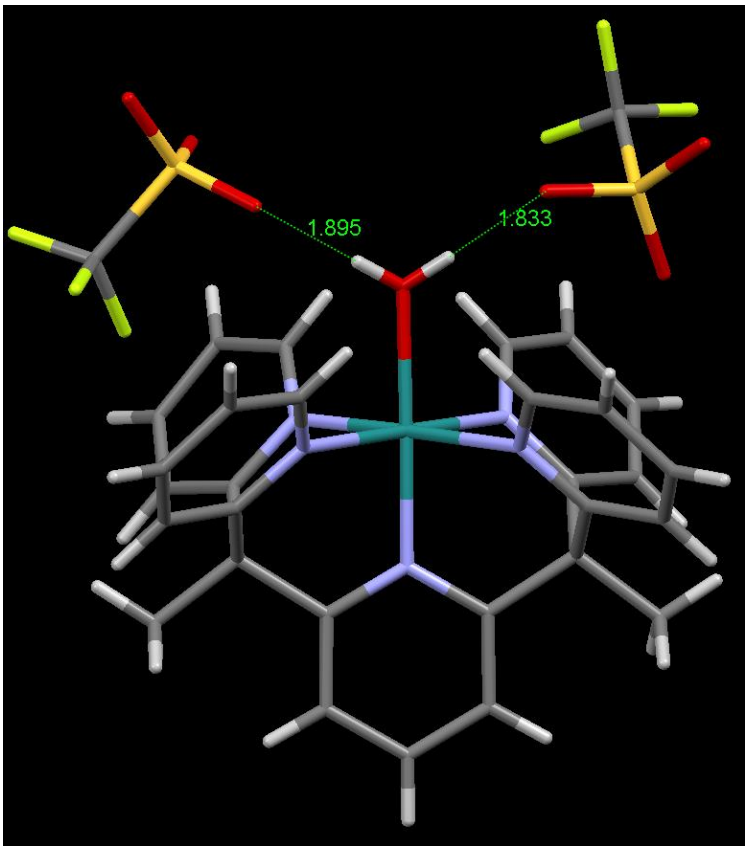

Figure S18. Mercury view of the crystal structure of $\mathbf{6}^{2+}$. Triflate counter ions and O-H distances are shown to demonstrate proximity to the hydrogen atoms of the water molecule. Note that two outer sphere triflate anions are positioned above the coordinated water molecule, each having an oxygen within 1.8-1.9 Å of a hydrogen atom. Consequently, hydrogen bonding occurs that restrains the water molecule in place well enough to identify the hydrogen atoms in the electron density map generated from X-ray diffraction and that also tilts the water molecule out of the plane of the axial pyridine. Atom color code: blue, nitrogen; red, oxygen; dark green, ruthenium; light grey, carbon; white, hydrogen; yellow, sulphur; light green, fluorine.

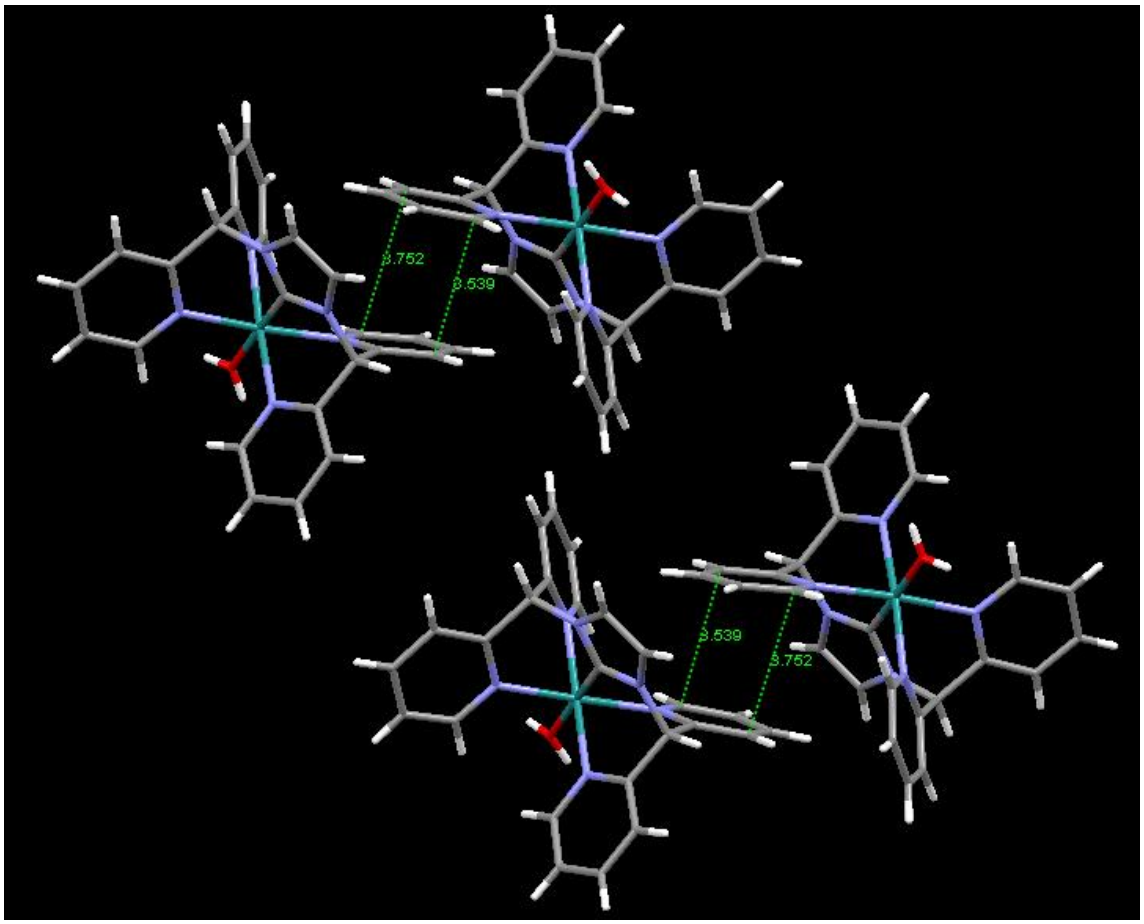

Figure S19. Plot of the unit cell of $\mathbf{8}^{2+}$ containing four $[Ru(PY4Im)(H_2O)]^{2+}$ cationic units and the corresponding distances of the two by two π-stacking interactions *via* a pyridyl group. Atom color code: blue, nitrogen; red, oxygen; dark green, ruthenium; light grey, carbon; white, hydrogen.

Table S1. Crystallographic data for complex *trans*-$\mathbf{2}^{2+}$.

Empirical formula	C13.50 H11.50 F6 N2.50 O0.50 P Ru0.50	
Formula weight	412.26	
Temperature	293(2) K	
Wavelength	0.71073 Å	
Crystal system	Monoclinic	
Space group	$P2_1/m$	
Unit cell dimensions	a = 11.1429(3) Å	α= 90°.
	b = 15.2112(4) Å	β= 111.892(4)°.
	c = 12.5195(4) Å	γ = 90°.
Volume	1968.99(11) $Å^3$	
Z	4	
Density (calculated)	1.391 Mg/m^3	
Absorption coefficient	0.562 mm^{-1}	
F(000)	820	
Crystal size	0.30 x 0.03 x 0.02 mm^3	
Theta range for data collection	1.753 to 33.144°.	
Index ranges	-16<=h<=15, -23<=k<=23, -17<=l<=18	
Reflections collected	30113	
Independent reflections	7275 [R(int) = 0.0442]	
Completeness to theta = 25.242°	99.8 %	
Absorption correction	None	
Refinement method	Full-matrix least-squares on F^2	
Data / restraints / parameters	7275 / 128 / 303	
Goodness-of-fit on F^2	1.045	
Final R indices [I>2sigma(I)]	R1 = 0.0479, wR2 = 0.1427	
R indices (all data)	R1 = 0.0668, wR2 = 0.1574	
Largest diff. peak and hole	1.740 and -0.758 $e.Å^{-3}$	

Table S2. Crystallographic data for complex *cis*-**3**$^{+}$ and list of selected distances and angles (see Figure S23 for atom labeling scheme).

Empirical formula	C28 H32.50 Cl2 N5 O4.75 Ru	
Formula weight	687.06	
Temperature	100(2) K	
Wavelength	0.71073 Å	
Crystal system	Triclinic	
Space group	P-1	
Unit cell dimensions	a = 11.2464(6)Å	α= 89.2684(17)°.
	b = 11.3285(6)Å	β= 71.2816(16)°.
	c = 12.4192(7)Å	γ = 68.8142(16)°.
Volume	1387.72(13) Å^3	
Z	2	
Density (calculated)	1.644 Mg/m^3	
Absorption coefficient	0.806 mm^{-1}	
F(000)	703	
Crystal size	0.25 x 0.15 x 0.03 mm^3	
Theta range for data collection	1.743 to 28.363°.	
Index ranges	-13<=h<=15,-15<=k<=15,0<=l<=16	
Reflections collected	18607	
Independent reflections	18607[R(int) =null]	
Completeness to theta =28.363°	98.299995%	
Absorption correction	Multi-scan	
Max. and min. transmission	0.976 and 0.751	
Refinement method	Full-matrix least-squares on F^2	
Data / restraints / parameters	18607/ 24/ 434	
Goodness-of-fit on F^2	1.027	
Final R indices [I>2sigma(I)]	R1 = 0.0502, wR2 = 0.1190	
R indices (all data)	R1 = 0.0709, wR2 = 0.1320	
Largest diff. peak and hole	0.637 and -1.211 e.Å^{-3}	

Bond distances		**Angles**	
Ru-N1	2.149(3)	N1-Ru-N3	159.11(13
Ru-N2	2.051(3)	N2-Ru-N4	166.73(12
Ru-N5	1.967(3)	Cl-Ru-N5	172.88(10
Ru-N3	1.979(3)	Cl-Ru-N1	106.13(9)
Ru-N4	2.086(3)	Cl-Ru-N2	90.87(9)
Ru-Cl	2.4558(10	Cl-Ru-N3	89.26(9)
Cl-H23	2.520	Cl-Ru-N4	80.85(9)
Cl-H28	3.093		

Table S3. Crystallographic data for complex *cis*-**4**$^{2+}$.

Empirical formula	C29 H27 Cl2 F12 N5 O P2 Ru	
Formula weight	923.46	
Temperature	100(2) K	
Wavelength	0.71073 Å	
Crystal system	Monoclinic	
Space group	P2(1)/c	
Unit cell dimensions	a = 8.0148(2)Å	α= 90°.
	b = 22.2295(6)Å	β=101.1002(8)°.
	c = 18.7377(5)Å	γ= 90°.
Volume	3275.95(15) $Å^3$	
Z	4	
Density (calculated)	1.872 Mg/m^3	
Absorption coefficient	0.844 mm^{-1}	
F(000)	1840	
Crystal size	0.10 x 0.10 x 0.05 mm^3	
Theta range for data collection	1.437 to 30.588°.	
Index ranges	-11<=h<=10,-22<=k<=31,-26<=l<=25	
Reflections collected	46733	
Independent reflections	10036[R(int) = 0.0372]	
Completeness to theta =30.588°	99.6%	
Absorption correction	Multi-scan	
Max. and min. transmission	0.959 and 0.908	
Refinement method	Full-matrix least-squares on F^2	
Data / restraints / parameters	10036/ 2/ 479	
Goodness-of-fit on F^2	1.013	
Final R indices [I>2sigma(I)]	R1 = 0.0302, wR2 = 0.0663	
R indices (all data)	R1 = 0.0431, wR2 = 0.0712	
Largest diff. peak and hole	0.696 and -0.575 $e.Å^{-3}$	

Table S4. Crystallographic data for complex $\mathbf{6}^{2+}$.

Empirical formula	C31 H27 F6 N5 O7 Ru S2	
Formula weight	860.77	
Temperature	100(2) K	
Wavelength	0.71073 Å	
Crystal system	Triclinic	
Space group	P-1	
Unit cell dimensions	a = 11.0219(3) Å	α= 82.2640(10)°
	b = 12.5423(4) Å	β= 88.6300(10)°
	c = 13.0793(4) Å	γ = 66.3630(10)°
Volume	1640.42(9) $Å^3$	
Z	2	
Density (calculated)	1.743 Mg/m^3	
Absorption coefficient	0.696 mm^{-1}	
F(000)	868	
Crystal size	0.22 x 0.13 x 0.04 mm^3	
Theta range for data collection	1.57 to 25.36°.	
Index ranges	-13<=h<=13, -14<=k<=15, -15<=l<=15	
Reflections collected	62994	
Independent reflections	5996 [R(int) = 0.0231]	
Completeness to theta = 25.00°	99.7 %	
Absorption correction	Semi-empirical from equivalents	
Max. and min. transmission	0.9727 and 0.8619	
Refinement method	Full-matrix least-squares on F^2	
Data / restraints / parameters	5996 / 0 / 479	
Goodness-of-fit on F^2	1.053	
Final R indices [I>2sigma(I)]	R1 = 0.0202, wR2 = 0.0484	
R indices (all data)	R1 = 0.0216, wR2 = 0.0496	
Largest diff. peak and hole	0.409 and -0.351 $e.Å^{-3}$	

Table S5. Crystallographic data for complex $\mathbf{8}^{2+}$.

Empirical formula	C25 H30 B2 F8 N6 O5 Ru	
Formula weight	769.24	
Temperature	100(2)K	
Wavelength	0.71073 Å	
Crystal system	Monoclinic	
Space group	P2(1)/n	
Unit cell dimensions	a = 12.7198(12) Å	a= 90.00 °.
	b = 13.6489(16) Å	b = 108.488(5) °.
	c = 18.6702(19) Å	γ = 90.00 °.
Volume	3074.1(6) $Å^3$	
Z	4	
Density (calculated)	1.662 Mg/m^3	
Absorption coefficient	0.605 mm^{-1}	
F(000)	1552	
Crystal size	0.40 x 0.05 x 0.01 mm^3	
Theta range for data collection	1.88 to 32.93 °.	
Index ranges	-19 <=h<=17 ,-20 <=k<=20 ,-28 <=l<=28	
Reflections collected	38867	
Independent reflections	11294 [R(int) = 0.0542]	
Completeness to theta =32.93 °	0.979 %	
Absorption correction	Empirical	
Max. and min. transmission	0.9940 and 0.7938	
Refinement method	Full-matrix least-squares on F^2	
Data / restraints / parameters	11294 / 34 / 487	
Goodness-of-fit on F^2	1.039	
Final R indices [I>2sigma(I)]	R1 = 0.0614 , wR2 = 0.1634	
R indices (all data)	R1 = 0.0920 , wR2 = 0.1900	
Largest diff. peak and hole	2.991 and -2.684 $e.Å^{-3}$	

Table S6. Selected interatomic distances (Å) and angles (°) for the aqua complexes *trans*-$\mathbf{2}^{2+}$, ***cis***-$\mathbf{4}^{2+}$, $\mathbf{6}^{2+}$ and $\mathbf{8}^{2+}$ (atom labeling refers to Figure 6).

Entry	Bond distances	*trans*-$\mathbf{2}^{2+}$	*cis*-$\mathbf{4}^{2+}$	$\mathbf{6}^{2+}$	$\mathbf{8}^{2+}$
1	Ru-N1	2.113(2)	2.1386(15)	2.0846(14)	2.090(3)
2	Ru-N2	1.980(2)	2.0473(15)	2.0624(14)	2.096(3)
3	Ru-X_{ax}[a]	2.011(3)	1.9639(15)	2.0008(14)	1.892(3)
4	Ru-N3	_____	1.9910(15)	2.0688(14)	2.090(3)
5	Ru-N4	_____	2.0850(15)	2.0699(14)	2.085(3)
6	Ru-O	2.135(2)	2.1619(13)	2.1228(13)	2.195(3)
	Angles				
7	N1-Ru-N2	171.01(7)	102.96(6)	82.95(6)	81.51(10)
8	N3-Ru-N4	_____	78.60(6)	82.79(6)	81.41(11)
9	N1-Ru-N3	_____	160.12(6)	177.80(6)	174.36(10)
10	N2-Ru-N4	_____	166.17(6)	177.94(6)	174.14(10)
11	O-Ru-X_{ax}[a]	172.73(9)	171.59(6)	178.13(5)	179.24(12)
12	O-Ru-N1	82.48(6)	102.37(5)	93.23(6)	93.40(11)
13	O-Ru-N2	91.95(7)	88.34(6)	89.97(5)	92.60(10)
14	O-Ru-N3	_____	92.36(6)	88.36(6)	92.07(10)
15	O-Ru-N4	_____	83.54(6)	91.20(5)	93.11(10)

[a] X_{ax} represents either a N5 for *trans*-$\mathbf{2}^{2+}$, *cis*-$\mathbf{4}^{2+}$ and $\mathbf{6}^{2+}$ or a C14 for $\mathbf{8}^{2+}$.

3. Isomerization studies

(a)

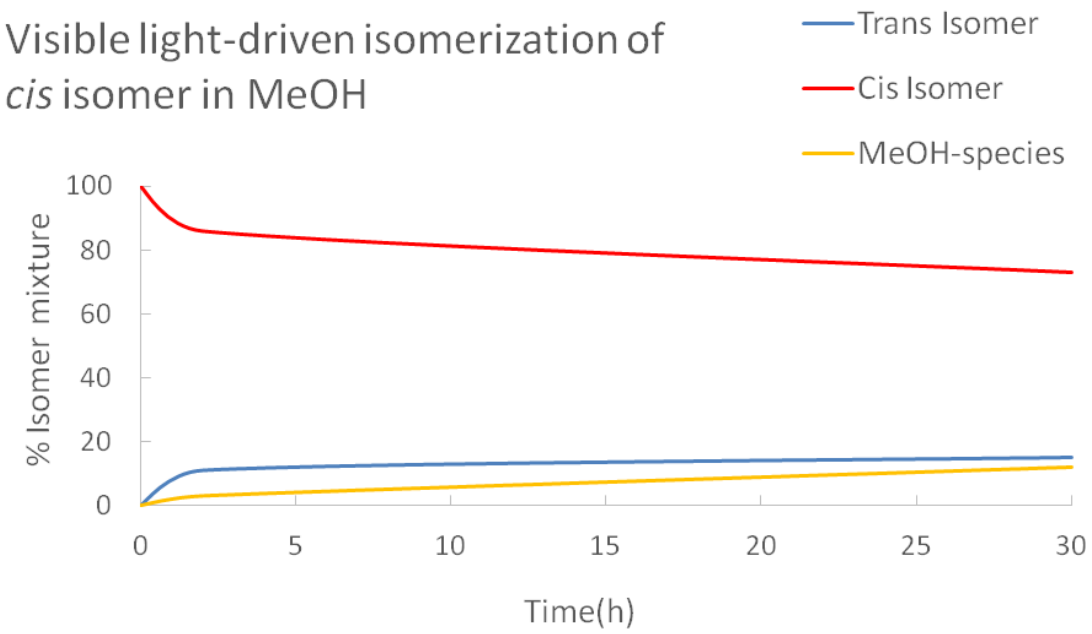

(b)

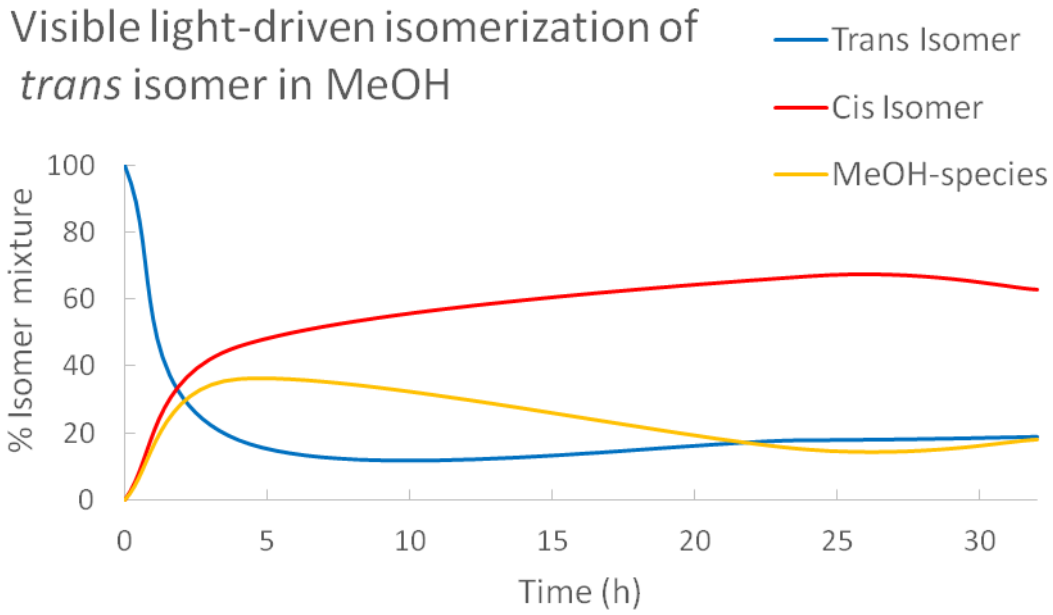

Figure S20. Light-induced isomerization process of *cis*-$\mathbf{1}^{+}$ (a) and of *trans*-$\mathbf{1}^{+}$ (b) in MeOH.

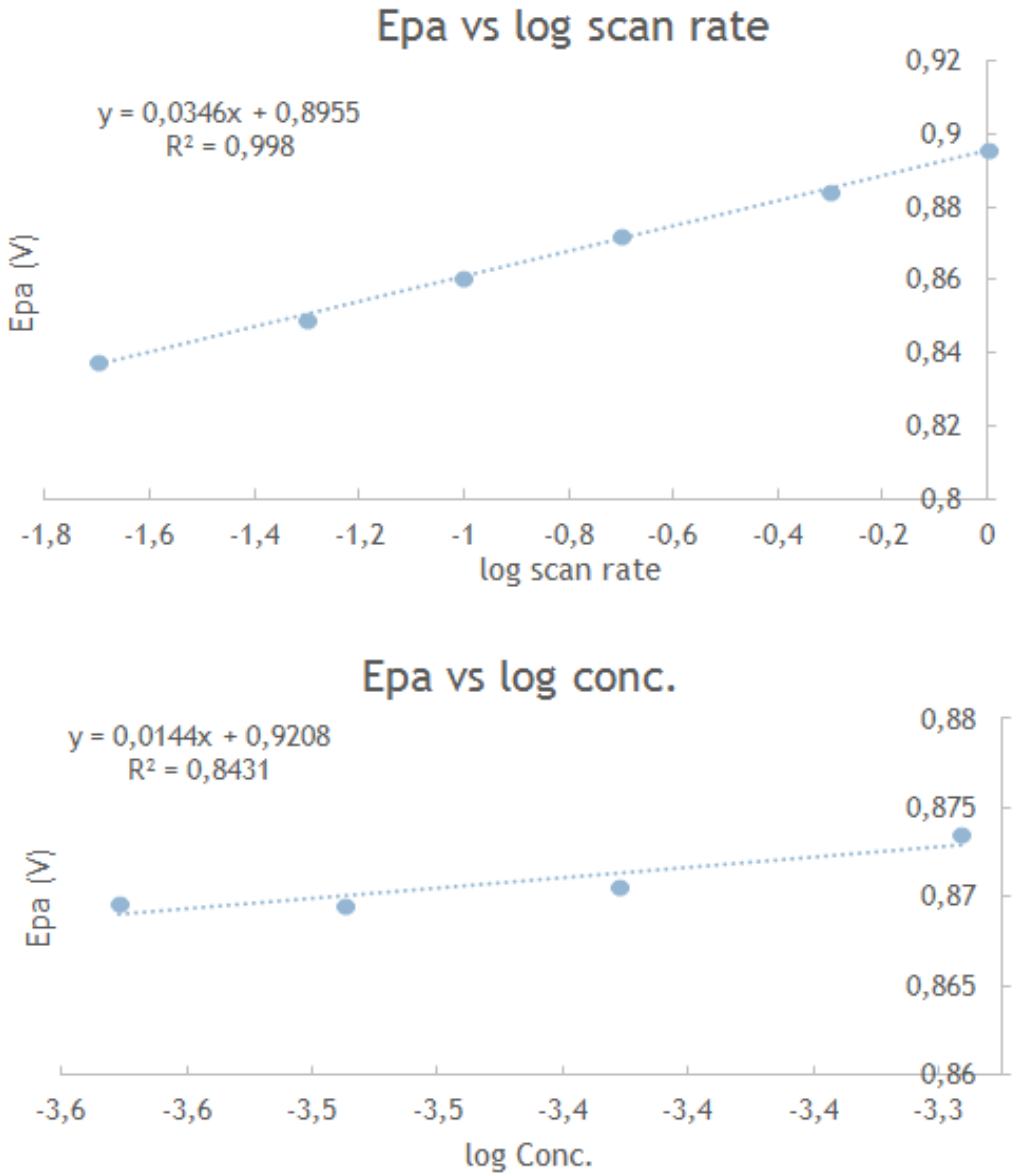

$$E_p = E° + 0.78\left(\frac{RT}{F}\right) - \left(\frac{RT}{2F}\right)\ln\left(\frac{RT}{Fkv}\right)$$

$$I_p = 0.446\, n\, F\, S\, C° \sqrt{\frac{F}{RT}}\sqrt{v}\,\sqrt{D}$$

Figure S21. Plot of the anodic peak potential *vs.* log *v* (*v*=scan rate) and log [*trans*-**1**$^+$].

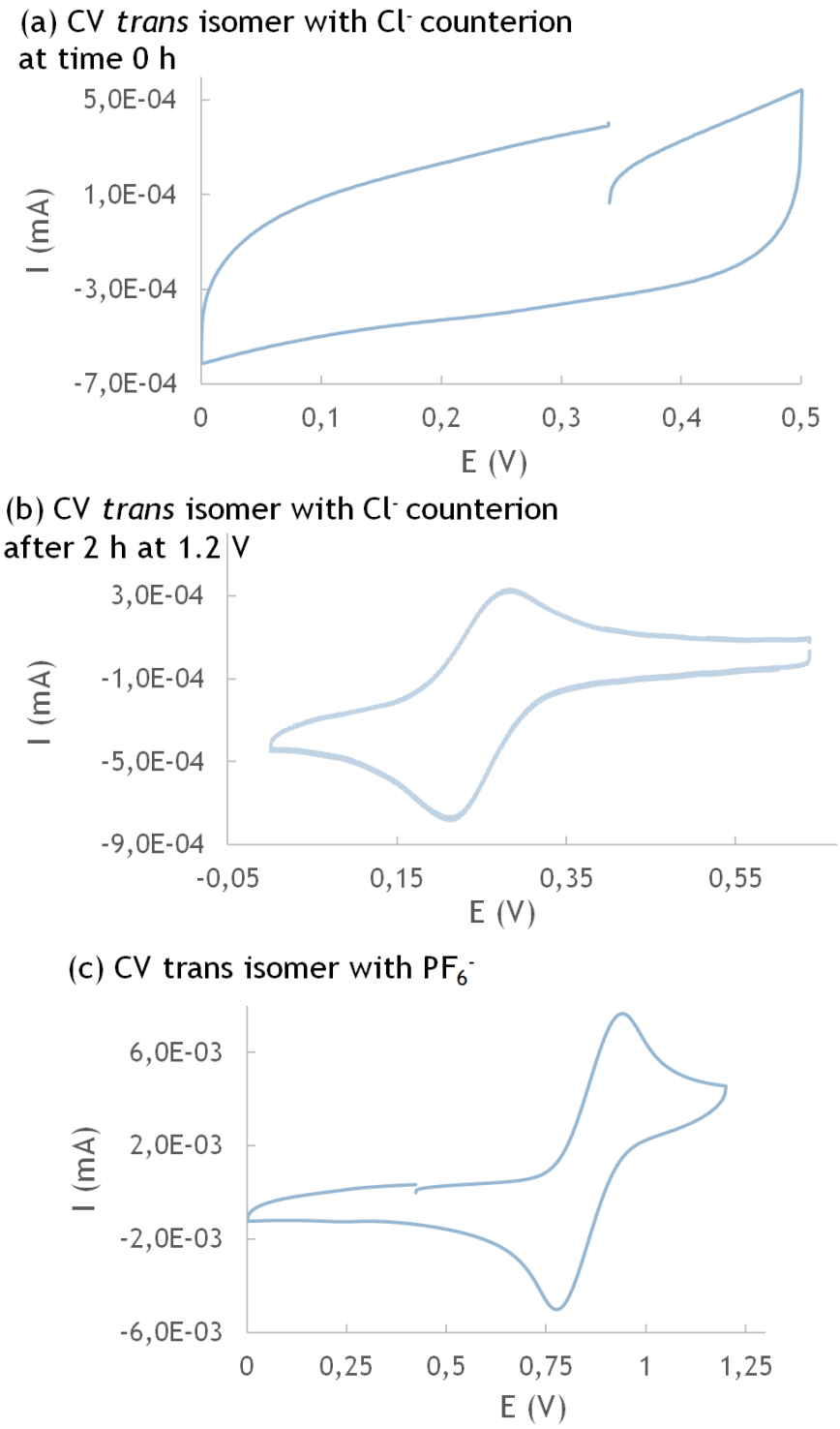

Figure S22. Cyclic voltammogram from 0 to 0.6 V at 100 mV/s in DCM + 0.1 M n-Bu_4NPF_6 for *trans*-**1**$^+$ before (a) and after (b) a CPE at 1.2 V for 2 h (1.0 F/mol), and full scan CV of *trans*-[Ru^{II}(bpy$_2$PYMe)Cl](PF$_6$) (c). Glassy carbon electrode is used as working electrode (diameter: 1 mm). The redox potentials are determined *vs.* SCE.

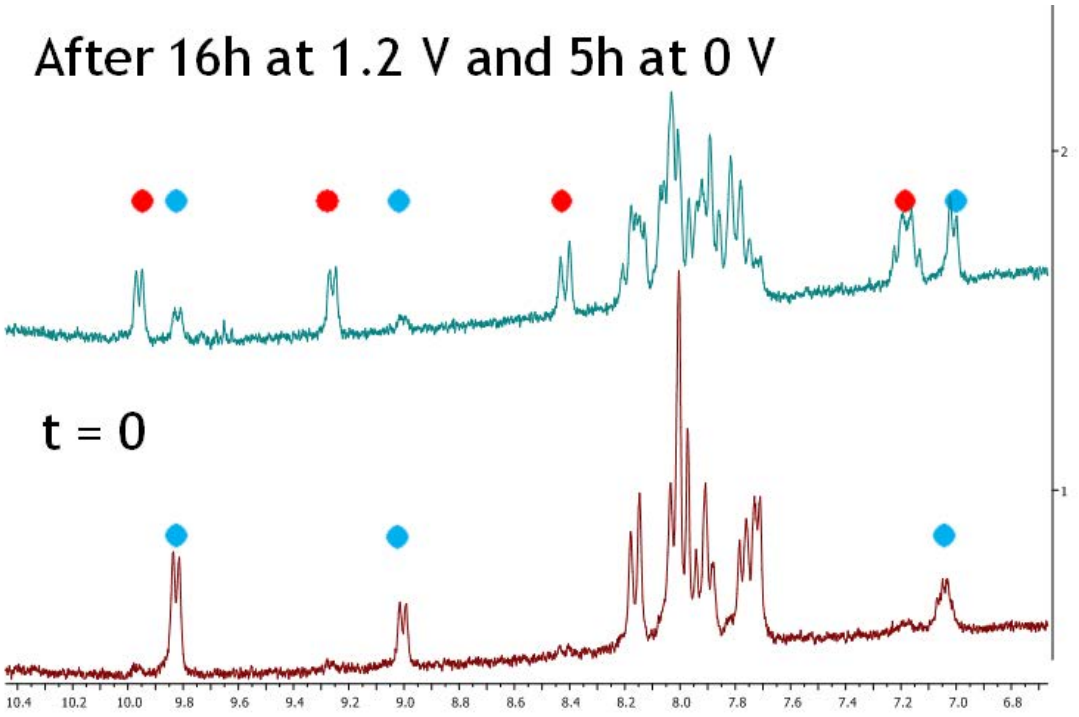

Figure S23. ^{1}H-NMR spectra of *trans*-**1**$^{+}$ before (bottom) and after (top) a CPE at 1.2 V for 16 h (4.15 F/mol) and a CPE at 0 V for 5 h (1.62 F/mol). Signals corresponding to the *trans* isomer are labeled in blue and those corresponding to the *cis* isomer in red.

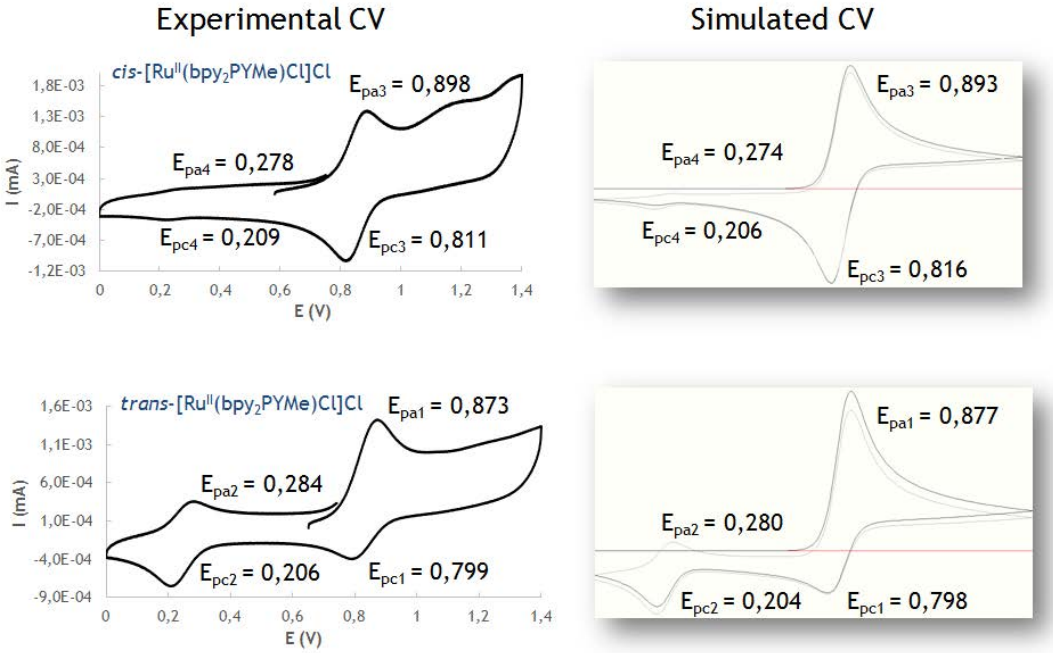

Figure S24. Left: Experimental CV recorded *vs.* SCE in DCM + 0.1 M TBAPF$_6$ at 200 mV/s for *cis*-**1**$^{+}$ (top) and *trans*-**1**$^{+}$ (bottom). Right: Simulated CV obtained by means of *DigiSim 2.0 CV* simulator software using the proposed mechanistic model depicted in Scheme 2.

4. Electrochemistry

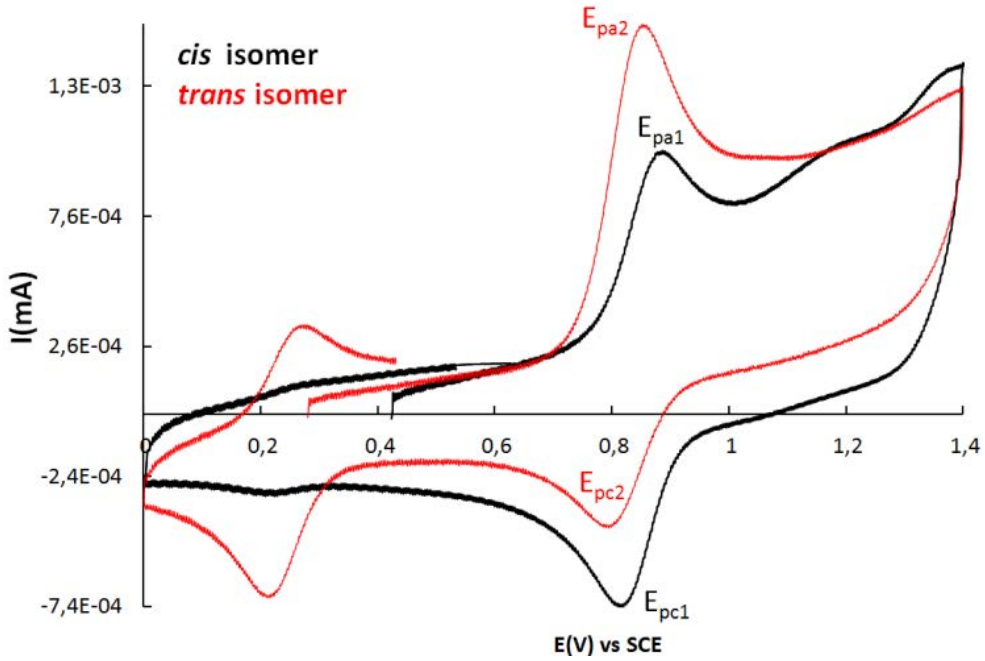

Figure S25. Cyclic voltammogram at 200 mV/s in DCM + 0.1 M n-Bu_4NPF_6 of *cis*-**1**$^+$ (black) and *trans*-**1**$^+$ (red). Glassy carbon electrode is used as working electrode (diameter: 1 mm). The redox potentials are determined vs. SCE.

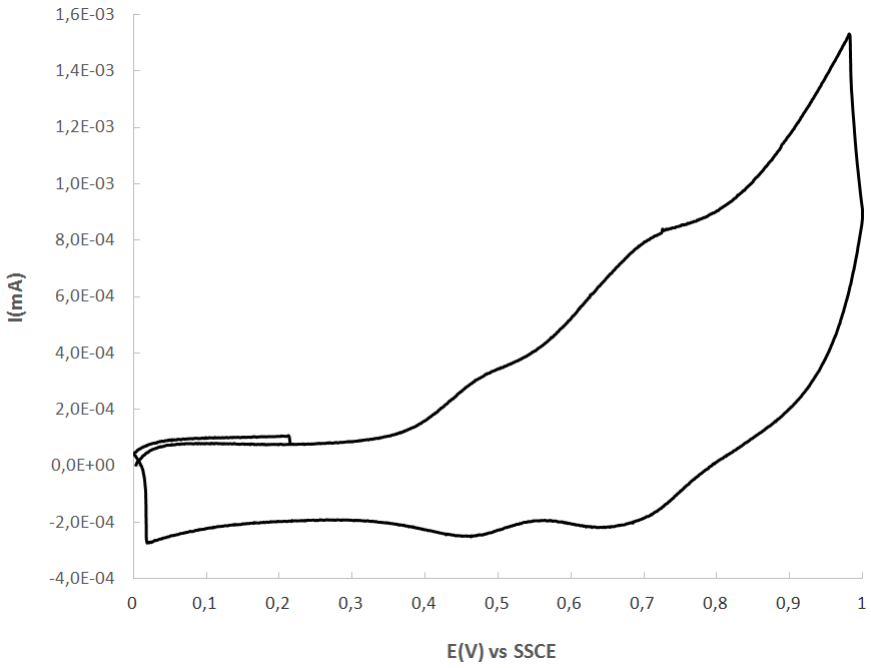

Figure S26. Cyclic voltammogram at 100 mV/s in water pH 7 (phosphate buffer) at 100 mV/s scan rate containing 0.1 M n-Bu_4NPF_6 of *trans*-**2**$^{2+}$. Glassy carbon electrode is used as working electrode and the potential is measured *vs.* SCE.

(a)

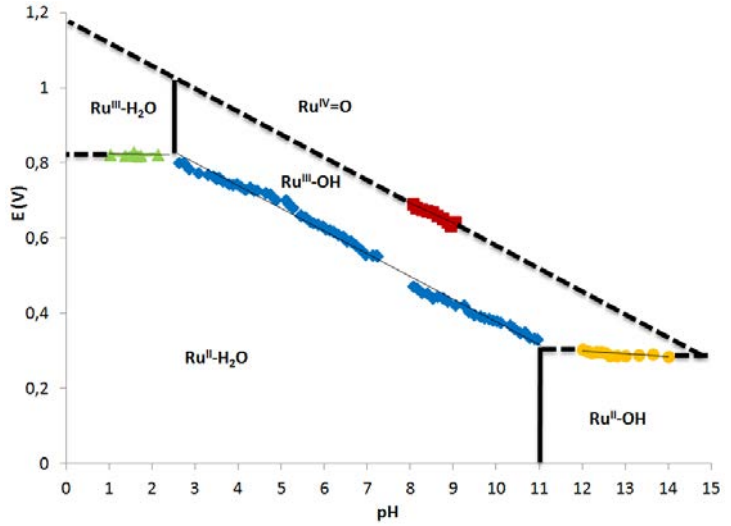

(b)

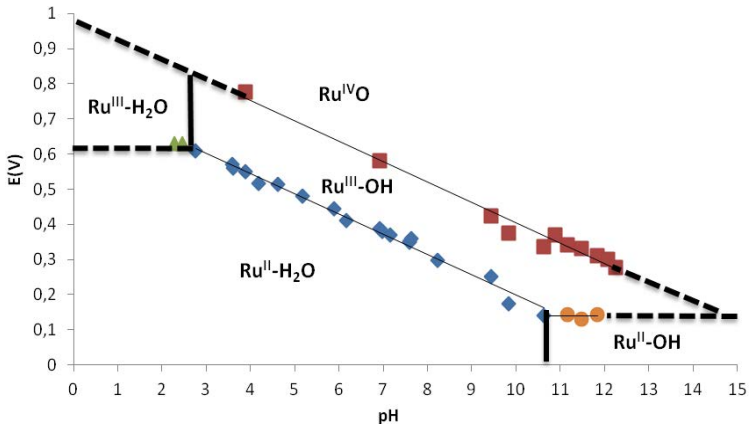

(c)

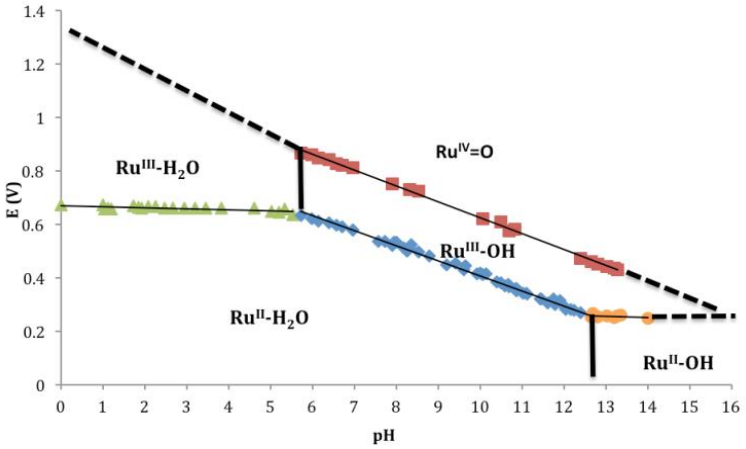

Figure S27. Pourbaix diagram for *trans*-**2**$^{2+}$ (a), **6**$^{2+}$ (b) and **8**$^{2+}$ (c). Continuous lines: experimental data. Dashed lines: hypothetical data. All potentials are referred to SCE.

(a)

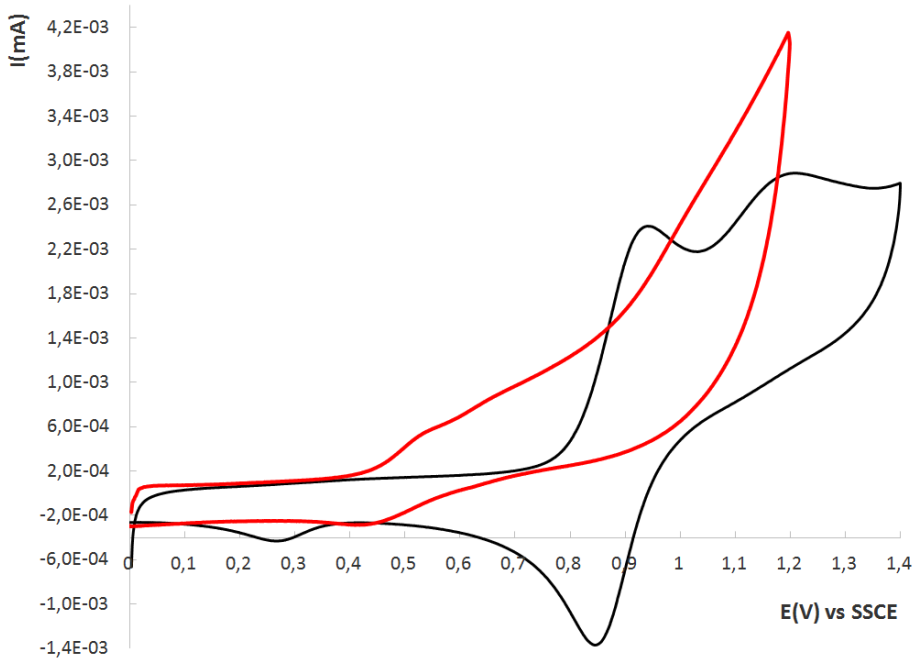

(b)

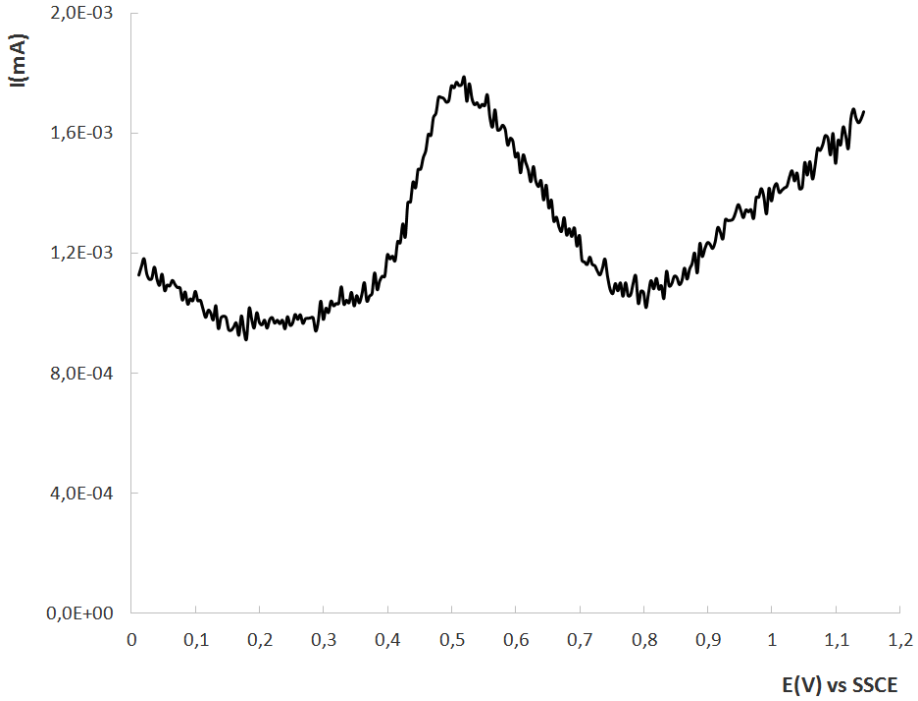

Figure S28. (a) CV of *cis*-$\mathbf{3}^{+}$ in DCM containing 0.1 M n-Bu_4NPF_6 (black) and of *cis*-$\mathbf{4}^{2+}$ in aqueous pH 7 phosphate buffer (red) and (b) DPV of *cis*-$\mathbf{4}^{2+}$ in an aqueous pH 7 phosphate buffer. A glassy carbon electrode has been used as working electrode and the potential has been measured *vs.* SCE at a 100 mV/s scan rate

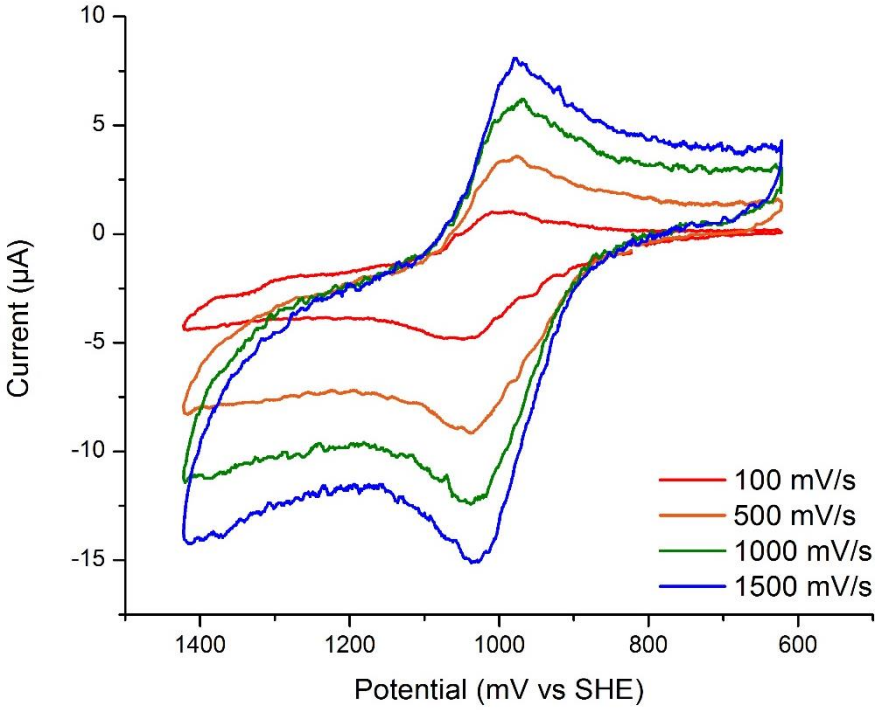

Figure S29. Current vs. potential at varying scan rates for complex $\mathbf{5}^{+}$. E^{0}= 1.020 V *vs.* SHE at 100 mV/s (or 0.78 V *vs.* SCE). The difference in peak potential is 61 mV. Concentration of $\mathbf{5}^{+}$, 1.6 mM; electrode, platinum; electrolyte, 0.1 M tetrabutylammonium hexafluorophosphate in acetonitrile.

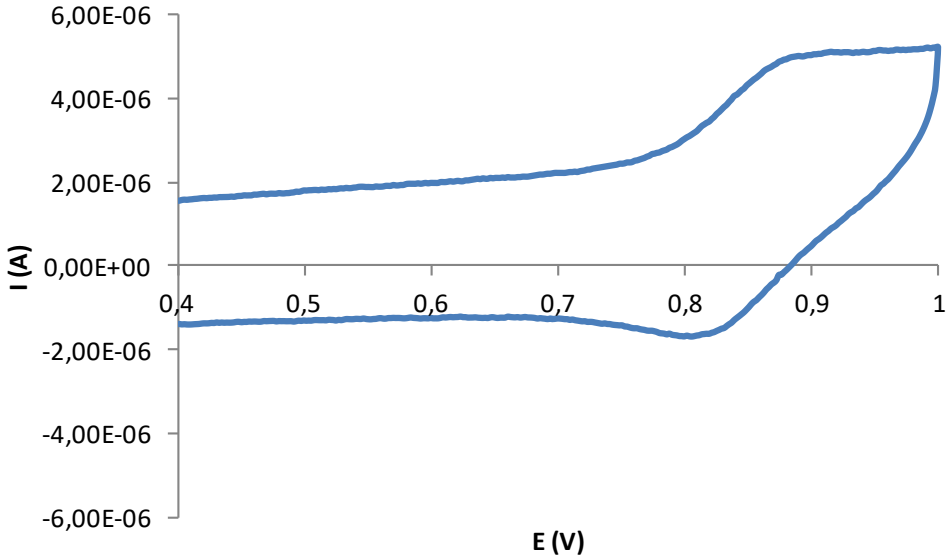

Figure S30. Cyclic voltammogram for $\mathbf{7}^{+}$ in 0.1 M n-Bu_4NPF_6 in methanol at 100 mV/s scan rate. Glassy carbon electrode is used as working electrode and the potential is measured *vs.* SCE.

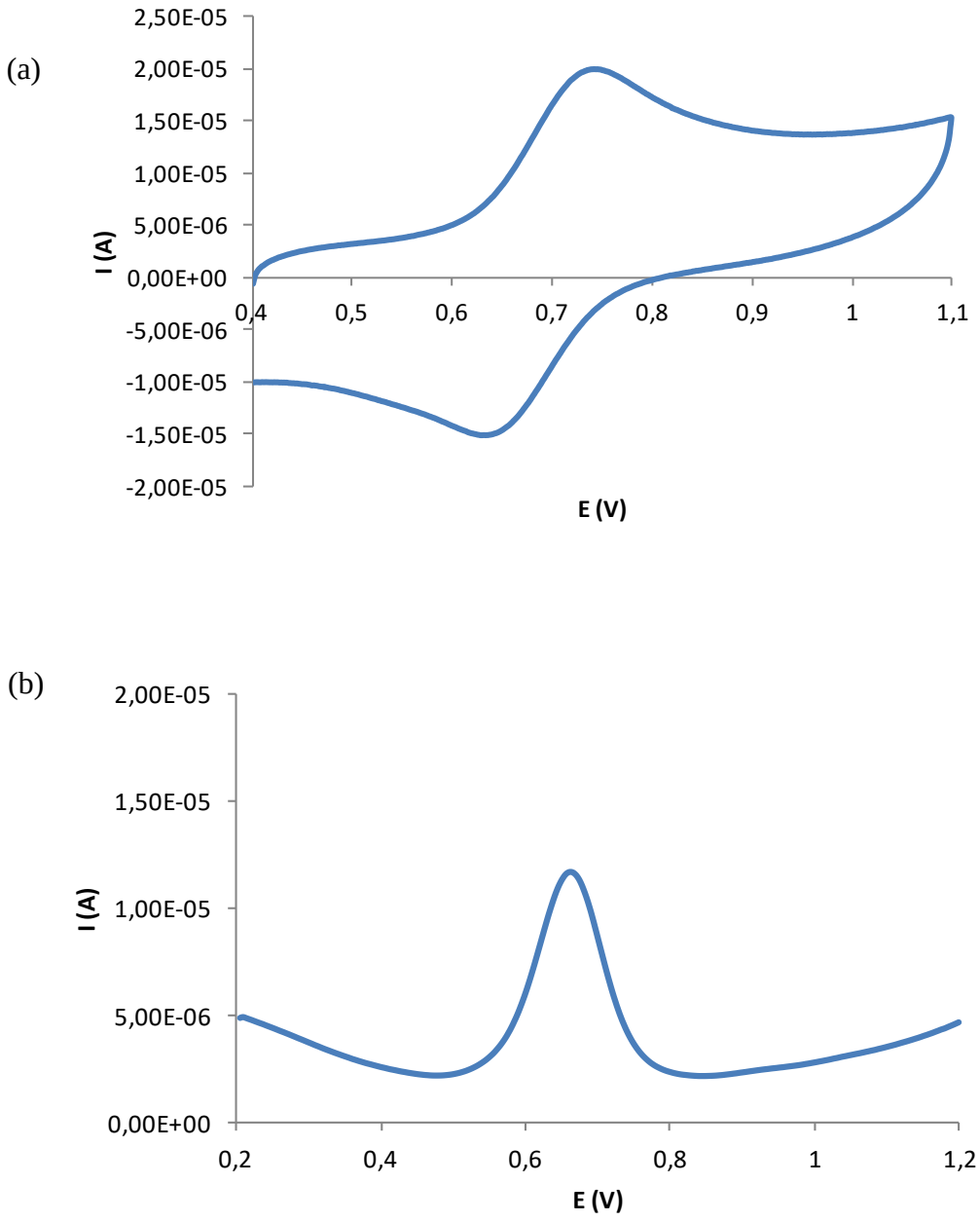

Figure S31. Cyclic voltammogram (a) and differential pulse voltammogram (b) for the aqua complex $\mathbf{8}^{2+}$ in water pH 2 (phosphate buffer) at 100 mV/s scan rate. Glassy carbon electrode is used as working electrode and the potential is measured vs. SCE.

(a)

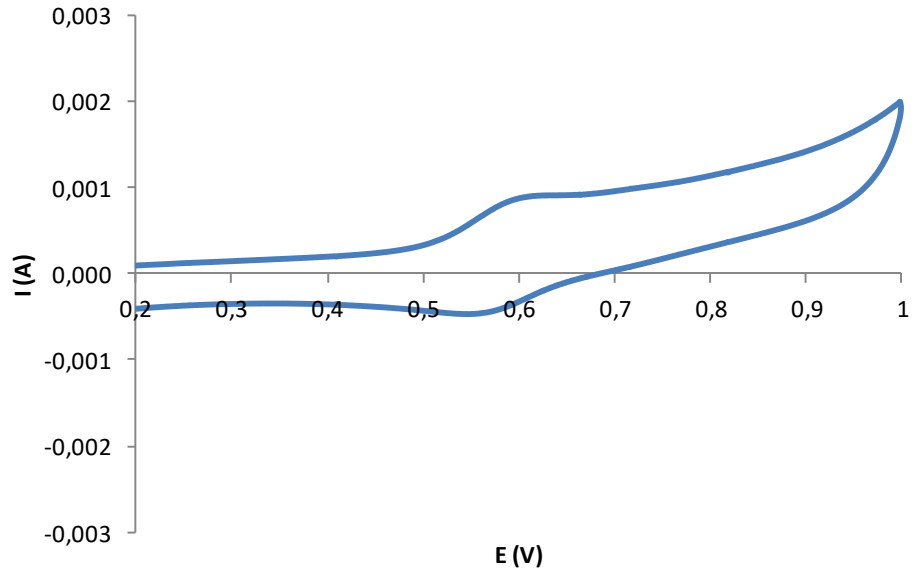

(b)

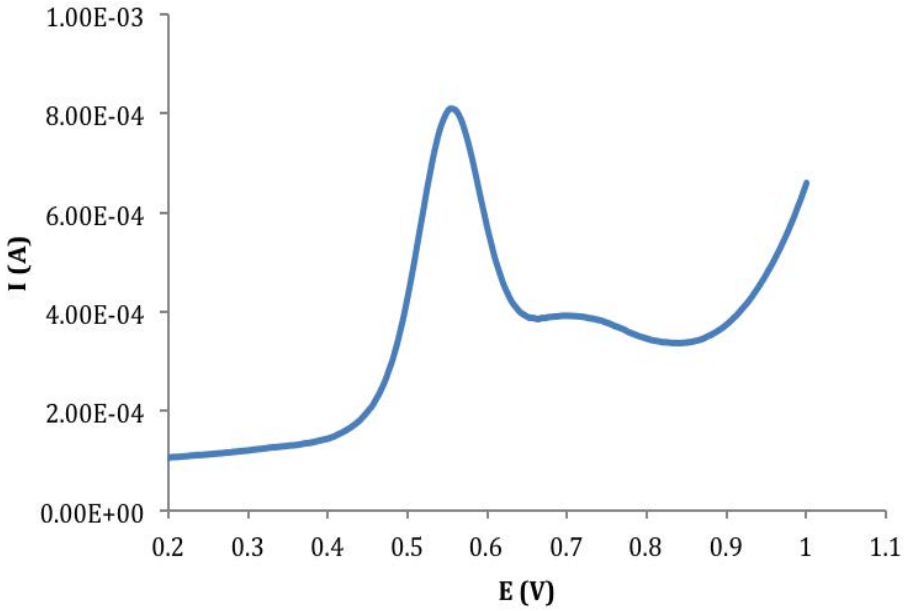

Figure S32. Cyclic voltammogram (a) and differential pulse voltammogram (b) for the aqua complex $\mathbf{8}^{2+}$ in water pH 8 (phosphate buffer) at 100 mV/s scan rate. Glassy carbon electrode is used as working electrode and the potential is measured *vs.* SCE.

5. Computational study

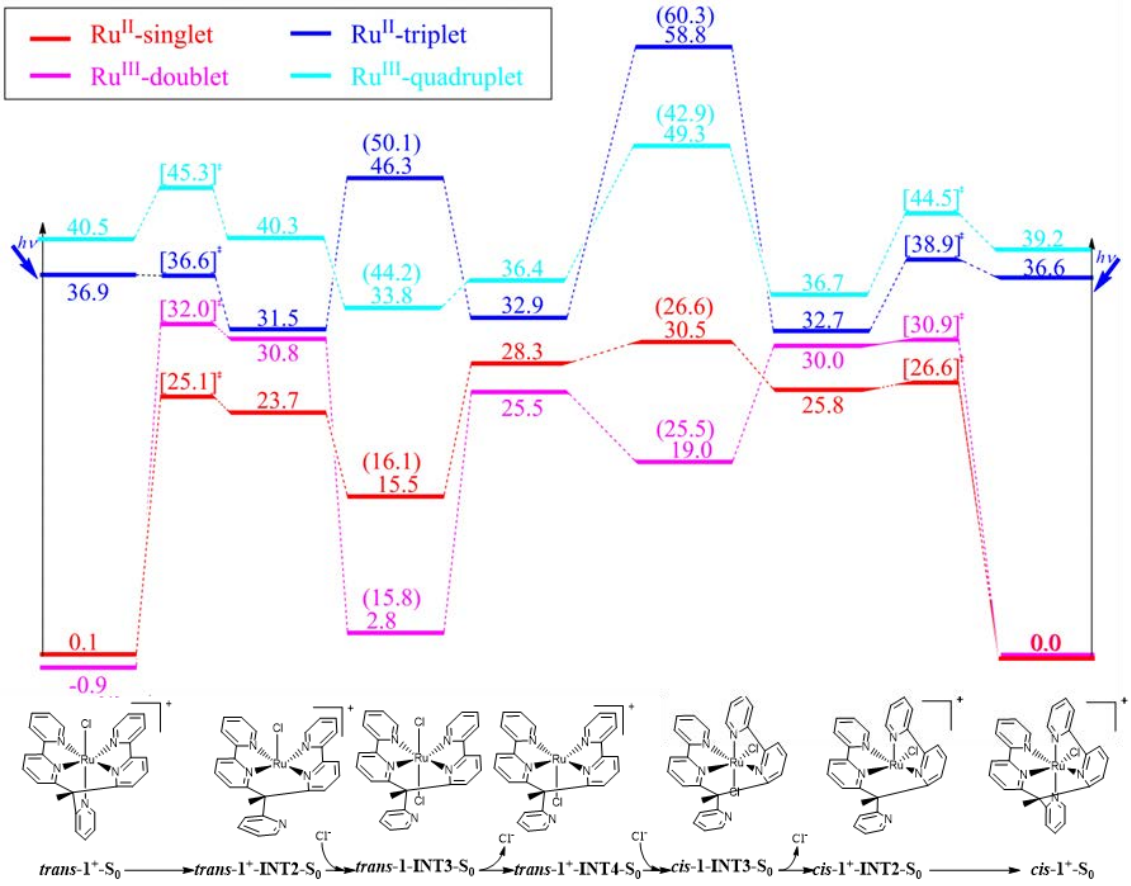

Figure S33. Energy diagram (B3LYPd3/TZVP-D95+~sdd//B3LYPd3/SVP~sdd) for the thermal and photoisomerization processes for $\mathbf{1}^{+}$ and $\mathbf{1}^{2+}$ in methanol. Red curve denotes the singlet spin surface, and blue curve denotes the triplet spin surface for Ru^{II}, whereas pink and cyan curves denote the doublet and quadruplet spin surfaces for Ru^{III}, respectively. All energies are calculated on the basis of *cis*-$\mathbf{1}^{+}$ and are eported in units of kcal/mol. All Gibbs energies are calculated relative to *cis*-$\mathbf{1}^{+}$ or *cis*-$\mathbf{1}^{2+}$ and reported in kcal/mol (transition state energies in brackets, and the energies of the corresponding intermediates bearing a methanol ligand instead of a chlorido in parentheses). S_0 = ground state.

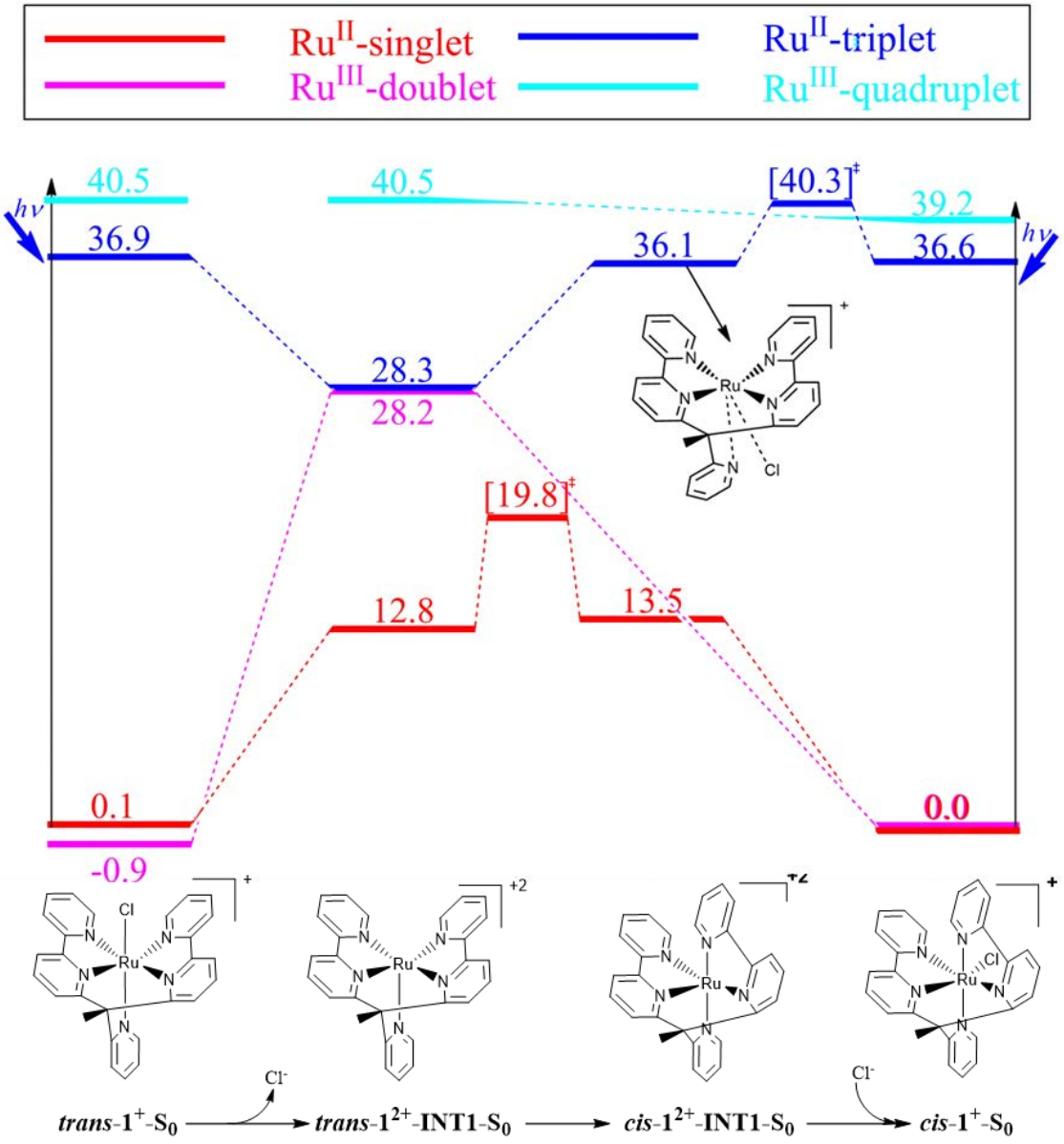

Figure S34. Energy diagram (B3LYPd3/TZVP-D95+~sdd//B3LYPd3/SVP~sdd) for the thermal and photo-induced isomerization processes for $\mathbf{1}^{+}$ and $\mathbf{1}^{2+}$ in methanol. Red curve denotes the singlet spin surface, and blue curve denotes the triplet spin surface for Ru^{II}, whereas pink and cyan curves denote the doublet and quadruplet spin surfaces for Ru^{III}, respectively. All Gibbs energies are calculated relative to *cis*-$\mathbf{1}^{+}$ or *cis*-$\mathbf{1}^{2+}$ and are reported in kcal/mol (transition state energies in brackets). S_0 = ground state.

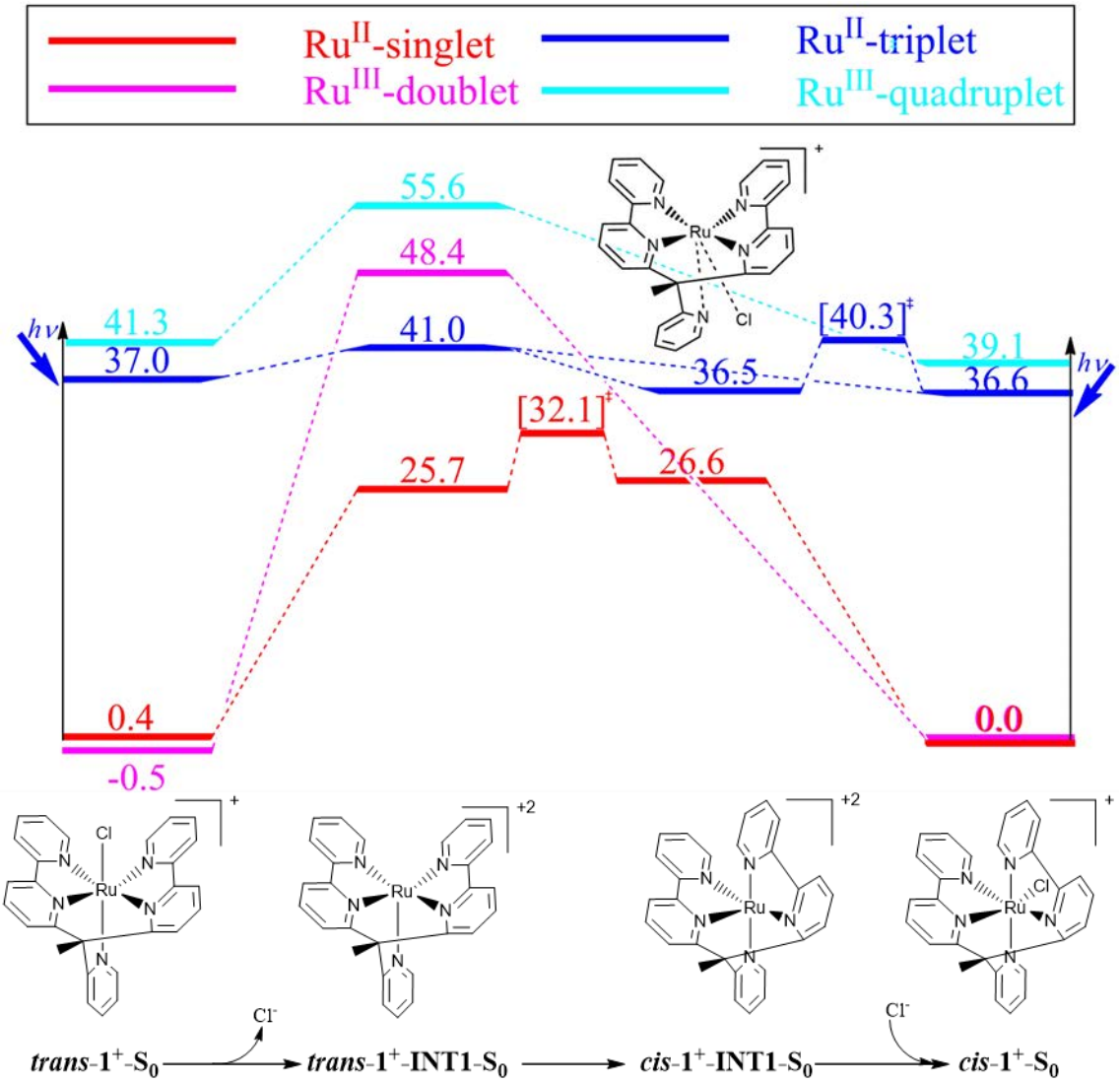

Figure S35. Energy diagram (B3LYPd3/TZVP-D95+~sdd//B3LYPd3/SVP~sdd) for the thermal and photo-induced isomerization processes for $\mathbf{1}^{+}$ and $\mathbf{1}^{2+}$ in DCM. Red curve denotes the singlet spin surface, and blue curve denotes the triplet spin surface for Ru^{II}, whereas pink and cyan curves denote the doublet and quadruplet spin surfaces for Ru^{III}, respectively. All Gibbs energies are calculated relative to *cis*-$\mathbf{1}^{+}$ or *cis*-$\mathbf{1}^{2+}$ and are reported in kcal/mol (transition state energies in brackets). S_0 = ground state.

The rest of computational details, can be found in the Supporting information of the published paper *DOI: 10.1021/acs.inorgchem.6b01755*.

6. References

[1] Hoang, T. N. Y.; Humbert-Droz, M.; Dutronc, T.; Guénée, L.; Besnard, C.; Piguet C. A *Inorg. Chem.* **2013**, *52*, 5570-5580.

PAPER B: Ru water oxidation catalysts based on py_5 ligands

Gil-Sepulcre, M.; Schilling, M.; Böhler, M.; Bozoglian, F; Bachmann, C.; Scherrer, D.; Fox, T.; Spingler, B.; Gimbert-Suriñach, C.; Alberto, R.; Bofill, R.; Sala, X.; Luber, S.; Richmond, C. J.; Llobet A. *ChemSusChem* **2017**, *10*, 4517-4525.

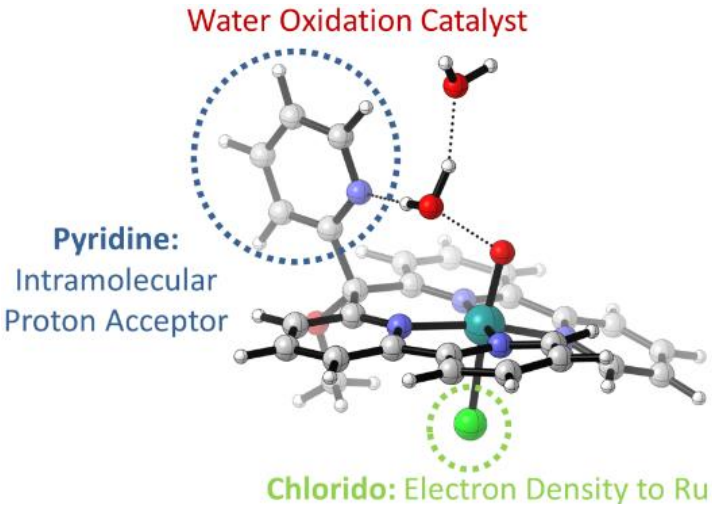

Abstract: Ru complexes containing the pentapyridyl ligand 6,6''-(methoxy(pyridin-2-yl)methylene)di-2,2'-bipyridine (L-OMe) of general formula *trans*-[Ru^{II}(X)(L-OMe-κ-N^5)]$^{n+}$ (X = Cl, n = 1, *trans*-**1**$^{+}$; X = H_2O, n = 2, *trans*-**2**$^{2+}$) have been isolated and characterized in solution (NMR, UV-Vis) and in the solid state by XRD. Both complexes suffer a series of substitution reactions at oxidation state II and III, when dissolved in aqueous triflic acid-trifluroethanol solutions that have been monitored by UV-vis spectroscopy and their corresponding rate constants reported. In particular, aqueous solutions of the Ru^{III}-Cl complex *trans*-[Ru^{III}(Cl)(L-OMe-κ-N^5)]$^{2+}$ (*trans*-**1**$^{2+}$) generates a family of Ru-aqua complexes namely *trans*-[Ru^{III}(H_2O)(L-OMe-κ-N^5)]$^{2+}$ (*trans*-**2**$^{3+}$), [Ru^{III}(H_2O)$_2$(L-OMe-κ-N^4)]$^{3+}$ (*trans*-**3**$^{3+}$) and [Ru^{III}(Cl)(H_2O)(L-OMe-κ-N^4)]$^{3+}$ (*trans*-**4**$^{2+}$). While complex *trans*-**4**$^{2+}$ is a powerful water oxidation catalyst, complex *trans*-**2**$^{3+}$ has only a moderate activity and *trans*-**3**$^{3+}$ is not a catalyst. Further, a parallel work has been carried out with related complexes but containing the methyl substituted ligand 6,6''-(1-pyridin-2-yl)ethane-1,1-diyl)di-2,2'-bipyridine (L-Me). The behavior of all these catalysts has been rationalized based on substitution kinetics, oxygen evolution kinetics, electrochemical properties and DFT calculations. The best catalysts, *trans*-**4**$^{2+}$, reach turnover frequencies of 0.71 s^{-1} using Ce(IV) as a sacrificial chemical oxidant with oxidative efficiencies above 95%.

III

Introduction

The oxidation of water to give molecular oxygen together with the reduction of water to give molecular hydrogen, are the two key reactions involved in the water splitting process. If the energy required to perform the reaction comes from sunlight, this process becomes a sustainable way of producing a renewable fuel that may replace the fossil fuels in a future energy economy.[1] Both reactions require the use of catalysts that activate the water molecule and allow the formation of new O-O and H-H bonds. In the particular case of the water oxidation half-reaction, mononuclear and dinuclear ruthenium-polypyridyl complexes have been described that are very fast and efficient catalysts for this reaction.[2] Among them, those complexes containing one or two anionic carboxylate groups, have shown to give the best results in terms of overpotential and turnover frequency, in some cases reaching values over one million turnover numbers.[3] The high efficiency of these catalysts is attributed to the synergistic effect of several factors; i) stabilization of Ru high oxidation states by high sigma donation of the carboxylate anionic ligands, ii) the possibility to form seven coordinated ruthenium species at high oxidation states, iii) formation of intramolecular hydrogen bonds between the Ru-OH and the carboxylate groups, the latter acting as an auxiliary base. Other crucial contributions from the ruthenium-polypyridinic complexes research are the mechanistic studies of the water oxidation reaction, which shed some light into the catalytic pathways that lead to the formation of molecular oxygen.[4] Indeed, the investigation of the mechanism of the reaction, including electrochemical, kinetic studies, detection of key intermediates as well as theoretical calculations, are essential for a rational design of new and better catalysts.

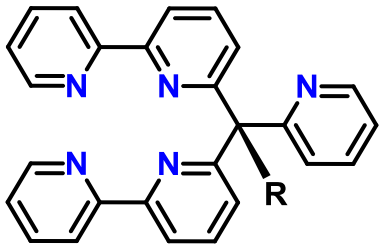

R = OH, L-OH
R = OMe, L-OMe
R = Me, L-Me

Chart 1. Ligands discussed in this work.

In this work, two new ruthenium complexes coordinated by the pentapyridine ligand 6,6’’-(methoxy(pyridin-2-yl)methylene)di-2,2'-bipyridine, L-OMe in Chart 1, are prepared. The two compounds differ in the sixth coordination ligand, which is either a chlorido ligand or an aquo ligand. A comprehensive kinetic analysis of the ligand-aquo

substitution reactions that generate the active species for each compound is described and their capacity to oxidize water into oxygen gas is evaluated. The kinetics and catalytic results are compared with those obtained for analogous complexes containing the methyl derivative ligand 6,6''-(1-pyridin-2-yl)ethane-1,1-diyl)di-2,2'-bipyridine, L-Me in Chart 1. Density functional Theory (DFT) calculations of intermediate species and key transition states support the experimental results.

Results and Discussion

Synthesis and structural characterization of complexes $\mathbf{1}^{+}$ and $\mathbf{2}^{2+}$

Complex [Ru(L-OMe)Cl]+, $\mathbf{1}^{+}$, was prepared from ligand L-OH shown in Chart 1, after methylation of the OH group and insitu complexation with $RuCl_3$ (Scheme 1). The reaction gave a 2:1 mixture of the *trans*-$\mathbf{1}^{+}$ and *cis*-$\mathbf{1}^{+}$ isomers that can be clearly identified in the ^{1}H NMR spectrum of the reaction crude mixture (Figure S2 in SI, here *trans* and *cis* refer to the relative disposition of the pyridine (in blue) and chlorido ligands as indicated in Scheme 1). A pure sample of the *trans*-$\mathbf{1}^{+}$ isomer was isolated in 35 % yield after column chromatography and recrystallization. A *trans* and *cis* mixture is also obtained for the related complex $\mathbf{1'}^{+}$ containing a methyl group instead of a methoxy group attached to the sp3 C atom of the pentapyridyl ligand (L-Me in Chart 1).[5] The Ru-aquo complex *trans*-$[Ru(L\text{-}OMe)(OH_2)]^{2+}$, *trans*-$\mathbf{2}^{2+}$, was prepared in 65 % yield from *trans*-$\mathbf{1}^{+}$ after reaction with $AgNO_3$ that removes the Cl^{-} ligand from the first coordination sphere and promotes aquotion (Scheme 1).

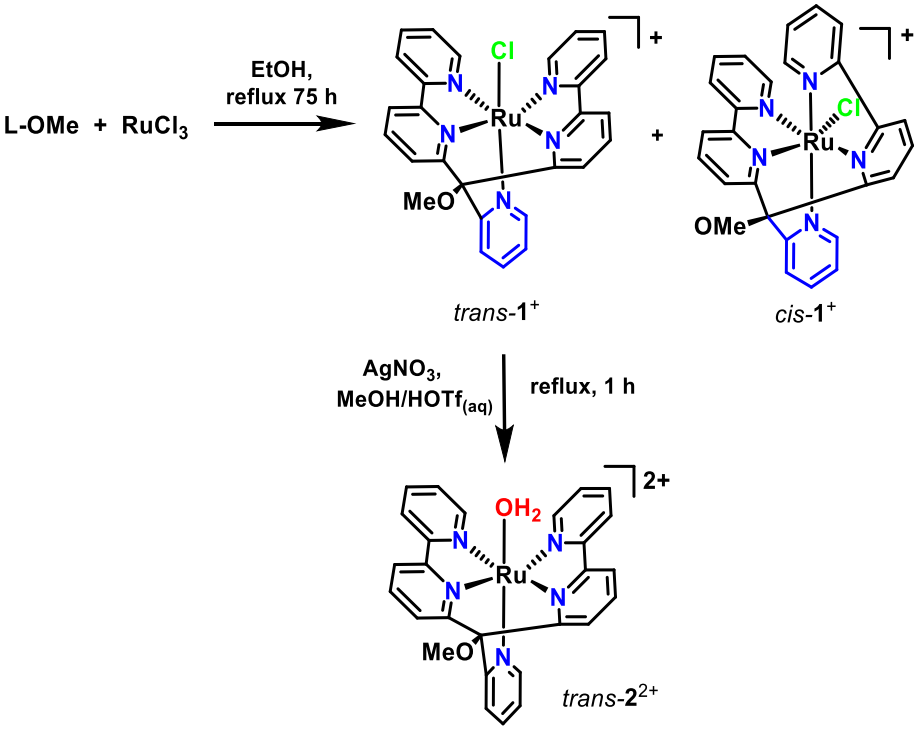

Scheme 1. Synthesis of complexes *trans*-**1**$^{+}$ and *trans*-**2**$^{2+}$ discussed in this work.

Complexes *trans*-**1**$^{+}$ and *trans*-**2**$^{2+}$ have been characterized by NMR, mass spectrometry and elemental analysis. The ^{1}H NMR spectra of both complexes show one single set of signals for the two bipyridyl groups, as expected according to the symmetry of the trans isomer. Good quality crystals, suitable for single crystal X-ray diffraction studies, were obtained for both complexes. Figure 1 shows the representative molecular structure of the chlorido complex *trans*-**1**$^{+}$. The Ru complex has a distorted octahedral geometry due to the steric constrains imposed by the pentadentate L-OMe ligand, resulting in a Cl-Ru-N_{pyr} angle of 170.0º. The rest of the bond distances and angles are within expected values for related octahedral ruthenium complexes containing polypyridine ligands.[5,6] It is interesting to observe that the angle between the two bipyridyl groups of L-OMe situated in the equatorial plane is 134.4º as opposed to the 180º expected for an ideal octahedron with no restraints between the bipyridyl ligands. This is due to constraints imposed by the sp^{3} carbon atom connecting the two bipyridyl groups. Similar structural characteristics are observed for the analogous aquo complex *trans*-**2**$^{2+}$ (Figure S10).

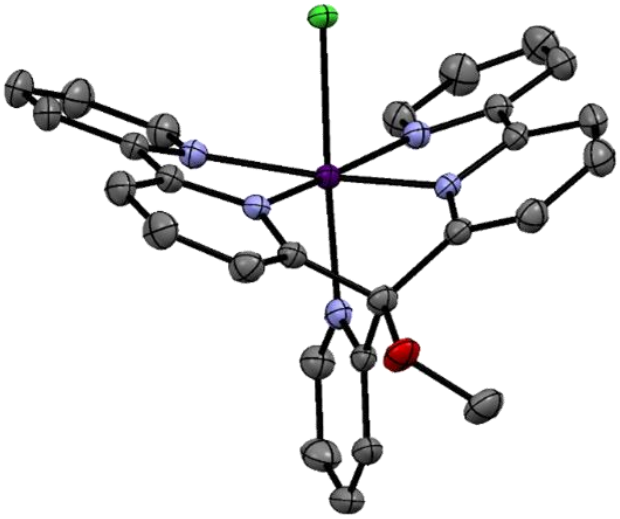

Figure 1. ORTEP representation of *trans*-**1**$^{+}$ at 50% probability level. The counter ions, solvent molecules and hydrogen atoms have been omitted for clarity. Colour code: C, grey; N, blue; O, red; Cl, green; Ru, purple.

DFT calculations were also carried out to complete the structural characterization of the complexes described, as well as to shed light into key intermediates and transition states involved in the catalytic cycle. Good structural agreement was found between structures obtained from geometry optimization with DFT using BP86[7]-D3[8]/def2-TZVP[9] and the crystallographic data. The M06-L[10] functional and the PBEh-3c method[11] (based on the PBE functional)[12] were also tested and gave similar results for the experimentally verifiable structures. Electronic energies were obtained with B3LYP[13](B3LYP-D3/def2-TZVP/COSMO)[14] and were practically identical to those obtained with PBE0 (PBE0-D3/def2-TZVP/COSMO) which has been recommended by Kang *et al.*[15] Unless otherwise noted, energies are reported as free energies consisting of electronic energies plus energy corrections from the solvation model (B3LYP-D3/COSMO) and thermal corrections obtained with the BP86 exchange-correlation functional (for details, see SI). We note that the complexes were modelled with the methoxy group being 'anti' to the pyridine fragment ('gauche' in crystal structures) because the rotational barrier for the isomerization was small and subsequent structures showed a preference for the 'anti' isomer.

The *trans* isomer of **1**$^{+}$ is approx. 1.0 kcal mol^{-1} more stable than its *cis* counterpart, which is in agreement with *trans*-**1**$^{+}$ being the major compound in the synthetic mixture, under the assumption that the reaction conditions lead to an

equilibrium mixture. For the oxidized isomers *trans*-**1**$^{2+}$ and *cis*-**1**$^{2+}$ we find a free energy difference of about 0.7 kcal mol^{-1}, which is in very good agreement with the experimental value as well as discussed below. Although such small computed energy differences in general need to be taken with caution, we note that said complexes show a high degree of structural similarity which supports a high level of error cancellation.

Low oxidation states: substitution and isomerization reactions

We studied the reactivity of complexes *trans*-**1**$^{+}$ and *trans*-**2**$^{2+}$ towards aquo substitution and oxidation reactions by time resolved UV-Visible spectroscopy. For fast processes ($t_{½}$ < 170 sec) stopped-flow techniques were employed. The rate constants were calculated using Reactlab Kinetics simulation software. Species distribution diagrams and simulated spectra were obtained with the same software. Cyclic voltammetry (CV) and Differential Pulse Voltammetry (DPV) techniques were used to study the redox properties of all the complexes described here. All potentials reported are given *vs*. the NHE electrode. In addition, we used Density Functional Theory (DFT) calculations to obtain theoretical redox potentials and key transition states to support our experimental results. Details about the experimental procedures and calculations are given in the supporting information (SI).

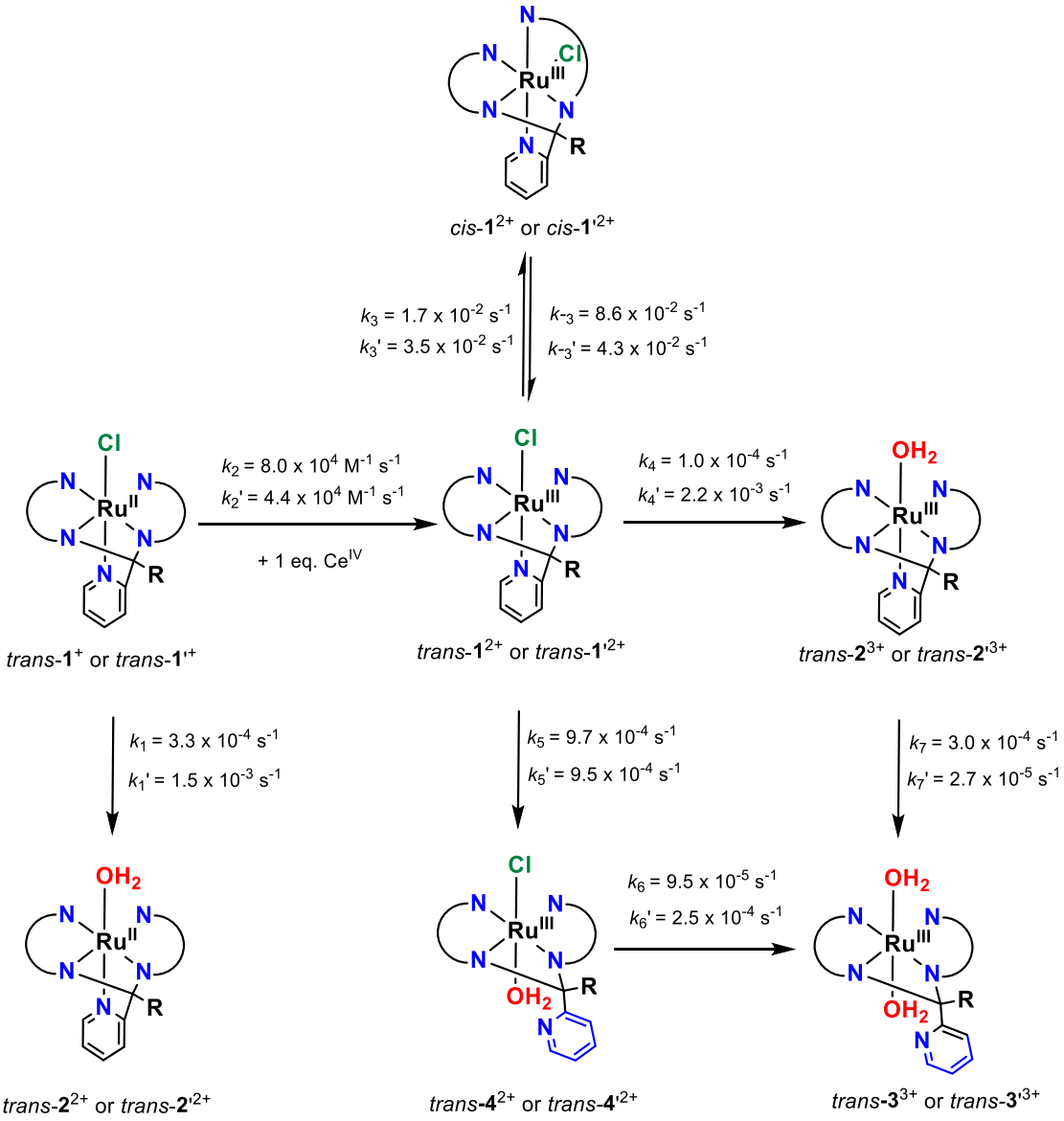

Scheme 2. Reaction pathways associated with *trans*-**1**$^{+}$ and *trans*-**1**'$^{+}$ containing the L-OMe and L-Me ligands, respectively. The latter complexes and their associated kinetic constants are denoted with a prime.

The kinetics of the conversion of the chlorido complex *trans*-**1**$^{+}$ to the aquo complex *trans*-**2**$^{2+}$ in aqueous 0.1 M trifluoromethansulfonic acid:trifluoroethanol solution (TfOH:TFE, 95:5) was studied using a 40 µM solution of *trans*-**1**$^{+}$ and monitored via UV-vis spectroscopy (Figure 2, left). TFE was used to increase the solubility of the complex. The final spectra matched that of isolated *trans*-**2**$^{2+}$ (Figure S9, SI). The substitution reaction is relatively slow, showing a pseudo-first order rate constant of k_1 = 3.3 x 10^{-4} s^{-1} and half time of $t_{½}$ = 35 min (see bottom left of Scheme 2). In sharp contrast, the same reaction for the analogue *trans*-**1**'$^{+}$ containing the L-Me ligand is one order of magnitude faster under the same conditions with a rate constant of k_1' = 1.5 x 10^{-3} s^{-1} and

half time of $t_{½}$ = 8 min (Figure 2, right). The chlorido to aquo substitution at oxidation state Ru(II) is also evident from CV experiments of *trans*-**1**$^{+}$ in an aqueous mixture of 0.1 M TfOH:TFE. The intensity of the Ru(III/II) redox couple of the chlorido complex *trans*-**1**$^{+}$ at $E_{1/2}$ = 0.93 V slowly decreases when the solution is left standing for 30 minutes, while a new redox couple at higher potential $E_{1/2}$ = 1.12 V appears. This value matches the potential of the Ru(III/II) couple for the isolated aquo complex *trans*-**2**$^{2+}$ (Figure S17-S18 in SI). Calculated Ru(III/II) redox potentials using DFT reproduce the experimental results well, giving values of 0.8 V (0.93 V experimental value) and 1.3 V (1.12 V experimental value) for the chlorido and aquo complexes, respectively (Figures S25-S26 in the SI).

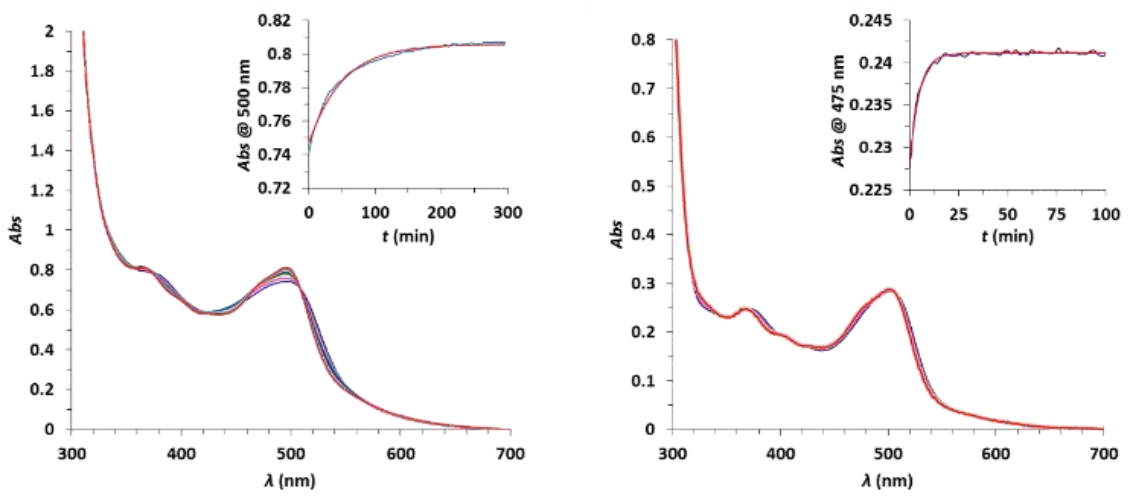

Figure 2. Evolution of UV-vis absorption spectra over time of a 40 μM solution of *trans*-**1**$^{+}$ (left) and *trans*-**1**'$^{+}$ (right) in 0.1 M TfOH solution containing 5% of TFE at 25 °C. The inset figures show the experimental kinetics profile at a specific wavelength (blue) and its mathematical fit (red).

We then explored the substitution reactions upon one electron oxidation of *trans*-**1**$^{+}$ with cerium (IV) ammonium nitrate (Ce(IV) hereafter). The fast outer sphere electron transfer reaction between Ce(IV) and *trans*-**1**$^{+}$ to give *trans*-**1**$^{2+}$ was followed by stopped-flow UV-Vis spectroscopy and fitted to a second order kinetic profile with a rate constant of k_2 = 8.0 x 10^{4} M^{-1} s^{-1} (Figure 3 and Scheme 2, center left). Following the formation of the oxidized complex *trans*-**1**$^{2+}$, a second slower process was observed in the stopped-flow experiment, which corresponds to the isomerization of *trans*-**1**$^{2+}$ to *cis*-**1**$^{2+}$ that remain in equilibrium as indicated in the top part of Scheme 2. The final distribution of species was calculated by means of ^{1}H NMR analysis of a solution of *trans*-**1**$^{+}$ after

oxidation with Ce(IV) and re-reduction with sodium ascorbate (Figure S13 in SI). The kinetic constants for this process were calculated to be k_3 = 1.7 x 10^{-2} s^{-1} and k_{-3} = 8.6 x 10^{-2} s^{-1}. A species distribution diagram is shown in Figure 3 indicating that the equilibrium is reached within a few seconds giving a final *trans-cis* mixture of *ca.* 9:1. A parallel isomerization process was observed for the methyl derivative *trans*-**1**'$^{+}$ but the final equilibrium gives a calculated distribution of *trans*-**1**'$^{2+}$ and *cis*-**1**'$^{2+}$ in 3:2 ratio and rate constants of k_3' = 3.5 x10^{-2} s^{-1} and k_{-3}' = 4.3 x 10^{-2} s^{-1} (Figure S12 and S14 in SI).

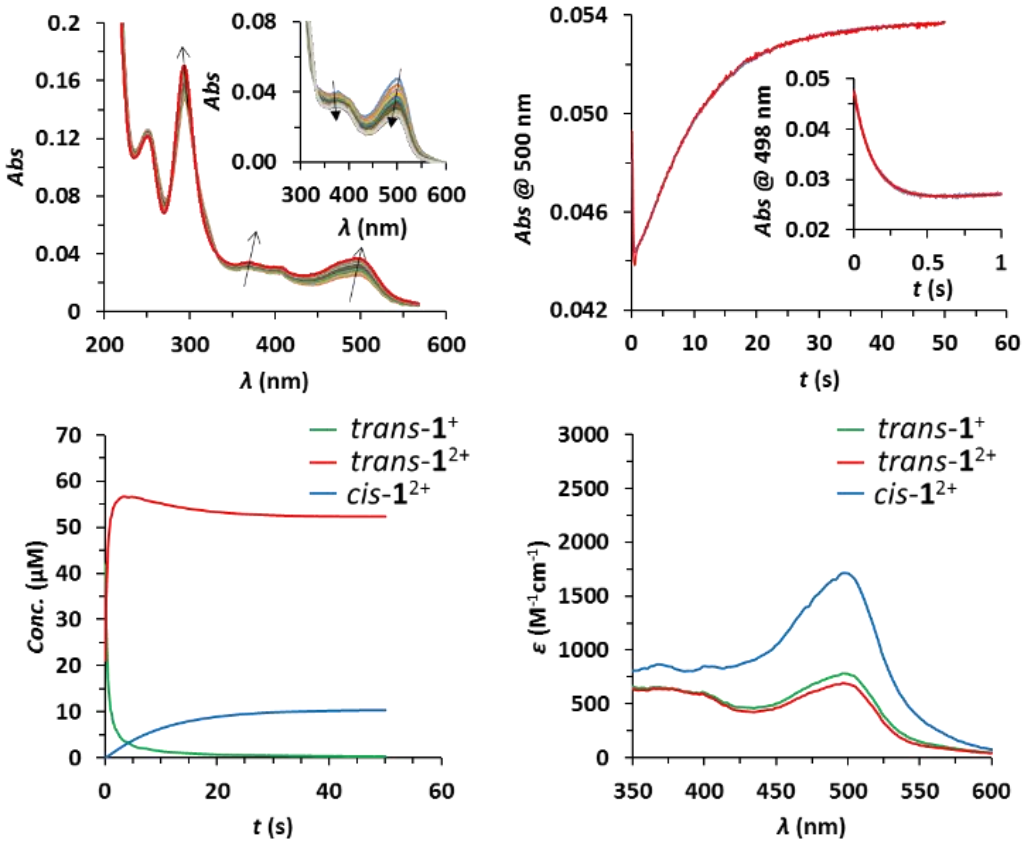

Figure 3. (Top) (Left) Evolution of stopped-flow UV-vis absorption spectra of a 63 μM solution of *trans*-**1**$^{+}$ with 1 equivalent of Ce(IV) in 0.1 M TfOH solution containing 5% of TFE at 25 °C for one minute. *Inset.* Evolution spectra of the first process (1 second) attributed to the oxidation of *trans*-**1**$^{+}$ to *trans*-**1**$^{2+}$. (Right) changes in the absorbance at 500 nm vs time for one minute (blue line) and its mathematical fit (red line). *Inset.* Changes in the absorbance at 498 nm vs time (blue line) and its mathematical fit (red line), during 1 second of reaction. **(Bottom)** (Left) calculated concentration distribution diagram vs time for the different species. (Right) calculated spectra for the proposed species in solution.

At longer oxidation reaction times, we observed a complex kinetics profile, which indicates that several processes are taking place in the mixture (Figure 4, top). As indicated in Scheme 2, the key intermediate species *trans*-**1**$^{2+}$ can undergo labile chlorido ligand substitution to give the Ru-aqua *trans*-**2**$^{3+}$ (Scheme 2, center right). Alternatively, it is possible that the aquo ligand replaces the pyridine giving rise to a trans chlorido-aquo-Ru complex with a dangling pyridine group (*trans*-**4**$^{2+}$ in Scheme 2, center bottom). The latter process is consistent with electrochemical results and DFT calculations obtained for trans-**1**'$^{2+}$, which demonstrated that the pyridine group in this type of complexes is prone to decoordination.[5] Indeed, cyclic voltammetry experiments of *trans*-**1**$^{+}$ in *dichloromethane* show an irreversible Ru(III/II) redox couple at E_{ox} = 1.11 V that gives rise to a new wave at $E_{1/2}$ = 0.53 V, associated with a trans-bis(chlorido) species with a pendant pyridine group as similarly observed for complex *trans*-**1**'$^{+}$ (Figure S19).[5] This process is favored by the release of strain upon pyridyl decoordination in both ligands L-OMe and L-Me.

The transient mono-aquo species *trans*-**2**$^{3+}$ and *trans*-**4**$^{2+}$, both evolve to the bis-aquo complex *trans*-**3**$^{3+}$ species after a second substitution (Scheme 2, bottom right). This process was studied independently for complex *trans*-**2**$^{3+}$, which could be prepared from the one-electron oxidation of *trans*-**2**$^{2+}$ with Ce(IV) (Figure 5). The mathematical fit gives pseudo-first order kinetic constant of k_7 = 3.0 x 10^{-4} s^{-1}. Cyclic voltammetry experiments in aqueous 0.1 M TfOH:TFE mixtures also show the formation of the bis(aquo) species *trans*-**3**$^{3+}$ with a characteristic Ru(III/II) couple at $E_{1/2}$ = 0.73 V, typical for this type of complexes (Figure 6 and Figures S17-S18 in SI).[16]

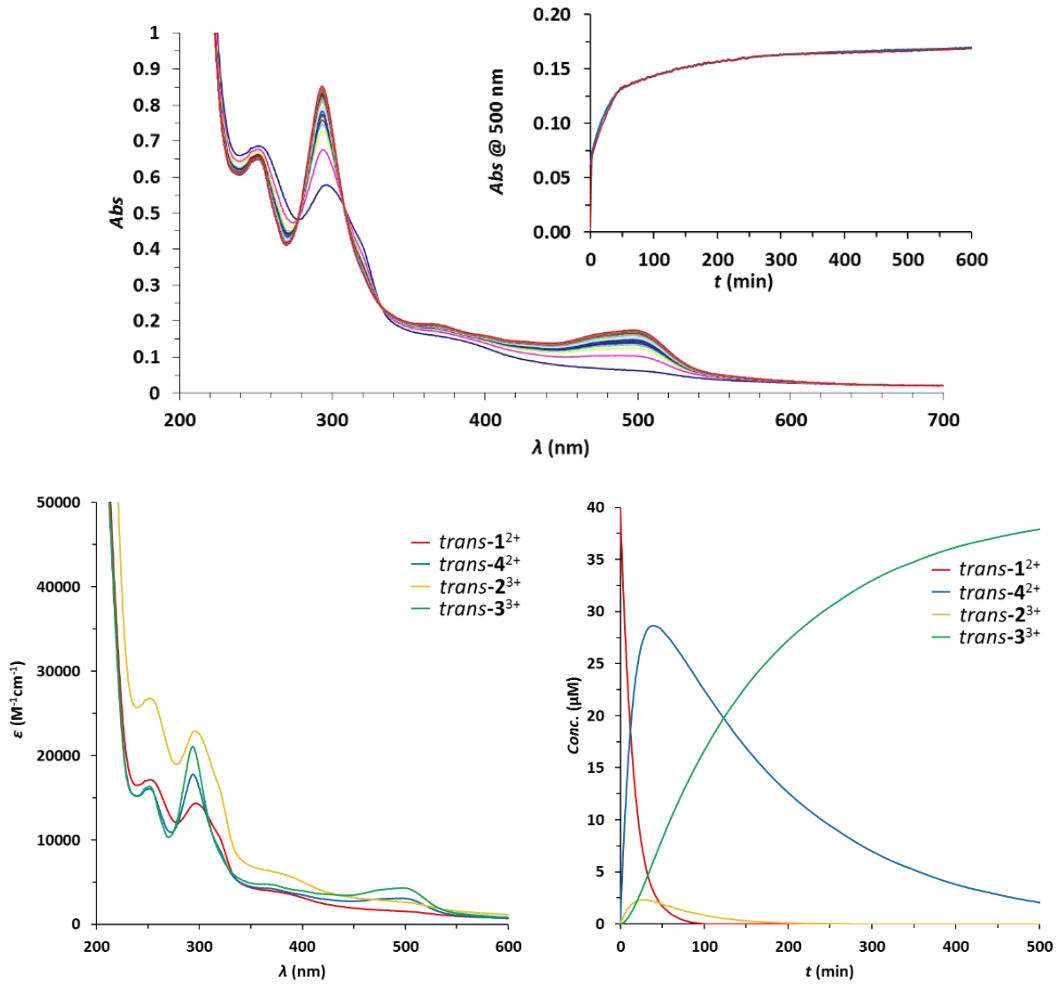

Figure 4 (Top) Evolution of UV-vis absorption spectra of a 40 μM solution of *trans*-**1**$^{+}$ with 1 equivalent of Ce(IV) in 0.1 M TfOH containing 5% TFE at 25 °C. *(inset)* Changes in abs. *vs*. t at 500 nm (blue line) and mathematical fit (red line). **(Bottom)** (Left) calculated spectra of the different species proposed in Scheme 2. (Right) calculated concentration distribution diagram *vs*. time for the different species.

The values of the remaining rate constants involved in the reaction sequence model indicated in Scheme 2 were calculated by fixing the values of k_1, k_2, k_3, k_{-3} and k_7 obtained independently as discussed above. Thus, k_5 and k_4, assigned to two competitive reactions from the *trans*-**1**$^{2+}$ intermediate to form the corresponding Ru-aqua species *trans*-**4**$^{2+}$ and *trans*-**2**$^{3+}$, give values of $k_5 = 9.7 \times 10^{-4}$ s^{-1} and $k_4 = 1.0 \times 10^{-4}$ s^{-1} respectively. Once the Ru^{III}-Cl complex, *trans*-**1**$^{2+}$, is formed then the formation of the Ru-H$_2$O-Cl is the dominant species. Finally, at longer timescales, the bis-aqua *trans*-**3**$^{3+}$ complex forms from *trans*-**4**$^{2+}$, with a rate constant of $k_6 = 9.5 \times 10^{-5}$ s^{-1}.

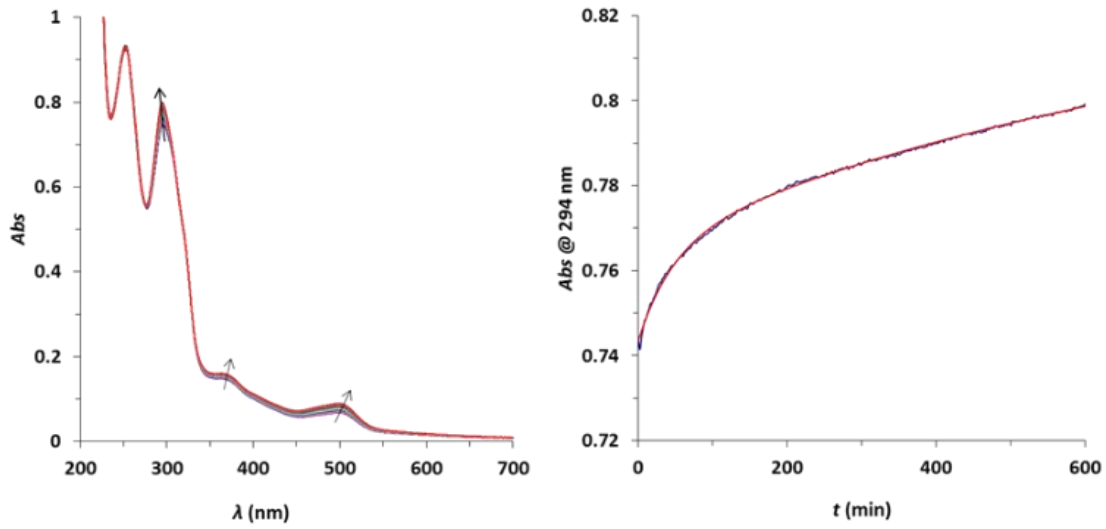

Figure 5 (Left) evolution of UV-vis absorption spectra at 25 °C of a 40 μM of *trans*-**2**$^{3+}$ in 0.1 M triflic acid solution containing 5% of TFE. (Right) changes in the absorbance at 294 nm vs time (blue line) and its mathematical fit (red line).

Figure 4 (bottom) shows the evolution of all the species derived from *trans*-**1**$^{2+}$ together with their respective UV-Vis calculated spectra. A comparison of the experimental UV-Vis spectrum of *trans*-**2**$^{3+}$ with its calculated spectrum shows a close match that gives a strong support to this reaction model (Figure S15 in SI). The same experiment and calculations were done for the methyl derivative *trans*-**1**'$^{2+}$ (Figure S16 in the SI). Although both complexes follow the same reaction scheme, the changes in kinetic constants have a dramatic effect on the relative distribution of species, particularly for the mono-aquo intermediates *trans*-**2**$^{3+}$ and *trans*-**4**$^{2+}$, both catalytically active species towards the water oxidation reaction. While the chlorido-aquo species *trans*-**4**$^{2+}$ is the major species in solution during the first minutes, the contribution of the *trans*-**2**$^{3+}$ is almost negligible (blue and yellow lines in Figure 4, respectively). For instance, we obtain a *trans*-**4**$^{2+}$:*trans*-**2**$^{3+}$ ratio of 92:8, 20 min after mixing *trans*-**1**$^{+}$ with Ce(IV). In contrast, an opposite trend is observed for the methyl derivative *trans*-**1**'$^{+}$, for which we observe a *trans*-**4**'$^{2+}$:*trans*-**2**'$^{3+}$ ratio of 26:74 at the same reaction time (Figure S16 in SI). These differences are crucial to understand the differentiated catalytic activity observed when the Ru-Cl complexes *trans*-**1**$^{+}$ and *trans*-**1**$^{+}$', that are not water oxidation catalysts but catalyst precursors, are dissolved in aqueous mixtures of TfOH:TFE.

DFT calculated standard reduction potentials are in qualitative agreement with the CV data. Reduction potentials for the redox couple of Ru(III/II) of 0.8 V (exp. 0.92 V) for *trans*-**1**$^{2+}$/*trans*-**1**$^{+}$ and 1.3 V (exp. 1.12 V) for *trans*-**2**$^{3+}$/*trans*-**2**$^{2+}$ were found. Although the thermodynamic tables of both complexes show virtually identical values (see Figures S25 and S27 in the SI), it is the association of water (and the displacement of pyridine) in which they differ, in agreement with the experimental description. The displacement of pyridine by a water molecule is predicted to be endergonic for both ligands with the ruthenium metal center in the oxidation states II or III. The associated free energies are 4 and 1 kcal mol^{-1} for L-OMe (*trans*-**1**$^{+}$), and 14 and 12 kcal mol^{-1} for L-Me (*trans*-**1**'$^{+}$), respectively. Reflecting the experimental observation, the displacement is consistently calculated to be more endergonic (by approx. 10 kcal mol^{-1}) for the complex with the L-Me ligand compared to the one with the L-OMe ligand.

High oxidation states: water oxidation catalysis

CV and DPV experiments of the Ru-aquo complex *trans*-**2**$^{2+}$ in an aqueous mixture of 0.1 M TfOH:TFE (95:5) show the redox couples Ru(III/II) at $E_{1/2}$ = 1.12 V, Ru(IV/III) at $E_{1/2}$ = 1.28 V and Ru(V/IV) at $E_{1/2} \approx$ 1.73 V, followed by a catalytic wave associated with water oxidation catalysis (Figure 6, red line). In the reverse scan in the CV, we also observe the characteristic Ru(III/II) redox couple at $E_{1/2}$ = 0.73 V associated with *trans*-**3**$^{3+}$, that is formed after oxidation (*vide supra*).

CV and DPV were also carried out, 15 minutes after the addition of Ce(IV) to a solution of *trans*-**1**$^{+}$ and is shown in the black traces in Figure 6. According to the previous kinetic analysis this generates a mixture of one Ru(III)-Cl complex and three Ru(III)-aqua complexes with the following ratios: *trans*-**1**$^{2+}$:*trans*-**2**$^{3+}$:*trans*-**3**$^{3+}$:*trans*-**4**$^{2+}$ of 5:1:1:10. Ru-aqua complexes *trans*-**2**$^{3+}$ and *trans*-**3**$^{3+}$ have been characterized independently and thus simplifies the assignment shown in Figure 6. The most interesting feature that is observed in the Figure is the 200 mV cathodic shift of the electrocatalytic wave with regard to that of *trans*-**2**$^{3+}$ (see the blue vertical lines in the DPV in Figure 6), and large enhancement of the catalytic current density under comparable conditions. This significant negative shift of the onset of the catalysis is a consequence of the higher electron density transmitted by the anionic chlorido ligand to Ru in *trans*-**4**$^{2+}$ as compared to the pyridyl group in *trans*-**2**$^{3+}$, that highly stabilizes Ru(V). The large enhancement in kinetics is associated with the dangling pyridyl ligand in *trans*-**4**$^{2+}$ that acts as base and

accepts a proton at the O-O bond formation step during the water nucleophilic attack as will be further discussed below. The contribution from *trans*-**2**$^{3+}$ in this case is negligible due to the much lower concentration and activity.

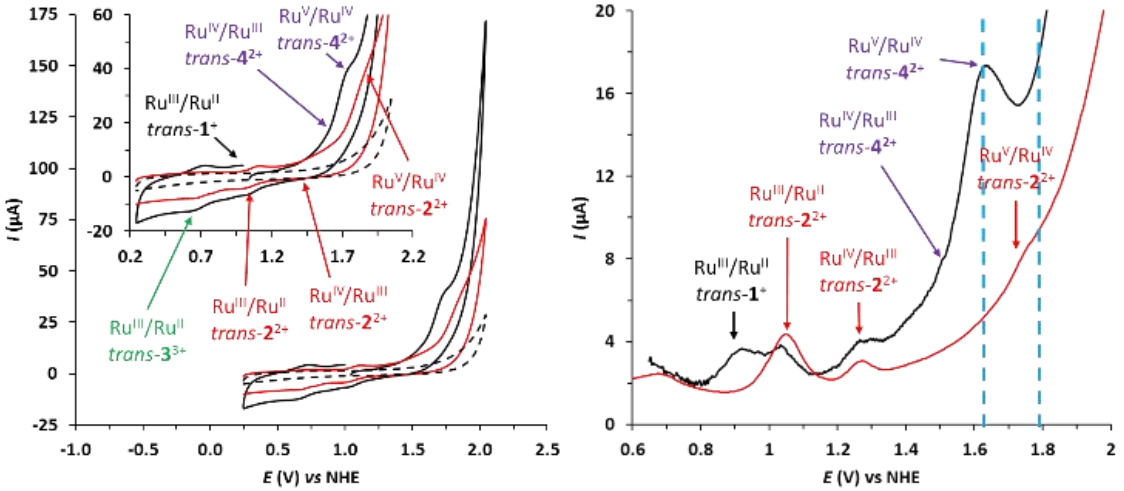

Figure 6. Cyclic Voltammograms (left) and Differential Pulse Voltammograms (right) of *trans*-**2**$^{2+}$ (solid red) and *trans*-**1**$^{+}$ measured 15 minutes after oxidation with 1 equivalent of Ce(IV) (solid black) in 0.1 M TfOH solution containing 5% of TFE. The addition of Ce(IV) generates four electroactive species in solution that are observed in the CV namely, *trans*-**1**$^{2+}$:*trans*-**2**$^{3+}$:*trans*-**3**$^{3+}$:*trans*-**4**$^{2+}$ in a 5:1:1:10 ratio; see text for details. The arrows indicated the assigned redox couple for the different species. Blue vertical lines in the DPV correspond the Ru(V)/Ru(IV) couple for *trans*-**2**$^{3+}$ and *trans*-**4**$^{2+}$, that is associated with water oxidation electrocatalysis. Dashed black correspond to a blank with no catalyst. Conditions: scan rate of 100 mV s^{-1}, [**Complex**] = 0.3 mM. Glassy Carbon disk as working electrode, Pt disk as counter electrode and Hg/$HgSO_4$ as reference electrode.

The same striking differences are observed in manometric experiments monitoring the oxygen evolution profiles obtained after chemically induced catalysis. Indeed, addition of 100 equivalents of Ce(IV) to a 1 mM complex solution (black and blue lines in Figure 7) shows that while the *trans*-**2**$^{2+}$ complex gives modest turnover numbers (TONs) of 8 and initial turnover frequency (TOFi) of 0.037 s^{-1}, the complex *trans*-**4**$^{2+}$ (generated by the addition of Ce(IV) to the Ru-Cl complex *trans*-**1**$^{+}$) gives 24 TONs that represents a 96% oxidative efficiency based on Ce(IV) with a TOFi = 0.71 s-1 (20 times faster; see Table 1). Lowering the catalyst concentration to 1 μM increases the TONs up to 168 but lowers the oxidative efficiency to 67% (Figure S22 in SI). A second and third subsequent additions of Ce(IV) to the catalytic mixture generated upon dissolving *trans*-**1**$^{+}$, shows that the system is still active with oxidative efficiencies higher

than 95% (Figure S23 in SI). However, the slopes of the catalytically generated oxygen over time decrease after each addition of Ce(IV). This is a phenomenon that is attributed to the increased concentration of nitrate ions in solution due to the successive addition of Ce(IV), as observed before for related catalytic systems.17 Another deactivation pathway that might be occurring is the conversion of *trans*-$\mathbf{1}^{+}$ to *trans*-$\mathbf{2}^{2+}$ in aqueous solutions at longer periods of time that we have shown to occur in the previous section. Indeed, when analogous manometry experiments using trans-1+ were performed a few minutes after catalyst mixing, the catalytic activity dropped to give similar results to those obtained for the Ru-aquo complex *trans*-$\mathbf{2}^{2+}$, in agreement with the kinetic analysis described in the previous section.

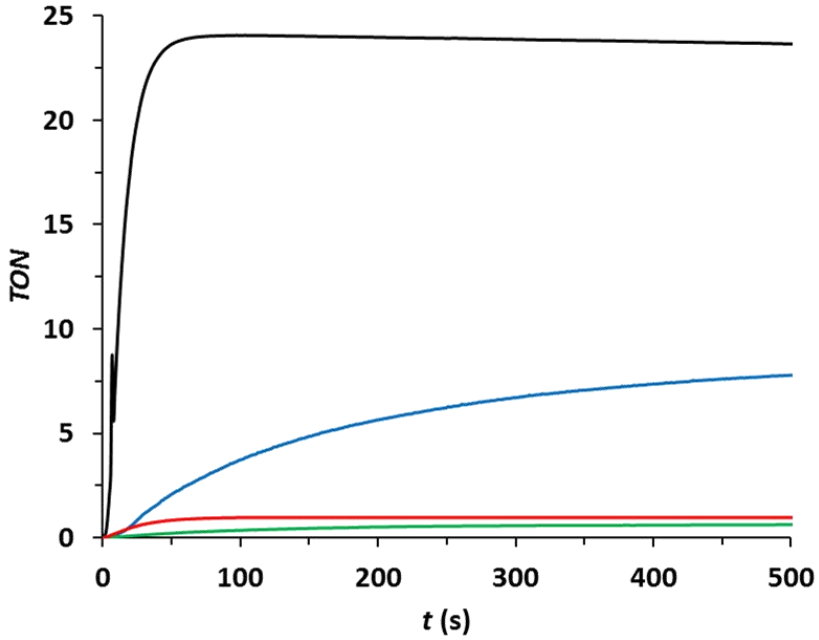

Figure 7. Oxygen evolution profile, given in turnover numbers (TON) *vs.* time for complex *trans*-$\mathbf{4}^{2+}$ (generated from the *in situ* addition of Ce(IV) to *trans*-$\mathbf{1}^{+}$; black line), *trans*-$\mathbf{2}^{2+}$ (blue line), *trans*-$\mathbf{2'}^{2+}$ (red line) and generated in situ from *trans*-$\mathbf{1'}^{+}$ (green line). Conditions: 1 mM catalyst or precursor catalyst in 0.1 M TfOH solution (pH 1) and 100 equivalents of Ce(IV) at 25 °C.

The coordination environment of complex *trans*-$\mathbf{2}^{2+}$, is reminiscent to that of $[(trpy)(bpy)Ru(H_2O)]^{2+}$, $\mathbf{5}^{2+}$, and $[(trpy)(Hbpp)Ru(H_2O)]^{2+}$, $\mathbf{6}^{2+}$, complexes (where trpy = 2,2':2",6'-terpyridine, bpy = 2,2'-bipyridine, Hbpp = 2,2'-(1Hpyrazole-3,5-diyl)dipyridine) in the sense that they are coordinated by five neutral pyridyl groups besides the critical aqua ligand. In agreement with this analogous coordination environment the Ru(V/IV) redox potential of *trans*-$\mathbf{2}^{2+}$, $\mathbf{5}^{2+}$ and $\mathbf{6}^{2+}$ (1.7-1.8V range) and

their catalytic water oxidation activities are similar.[4c,18] In sharp contrast the 20 times increase in rate and the nearly 100% oxidative efficiencies for *trans*-**4**$^{2+}$ as compared to *trans*-**2**$^{2+}$, is associated with the presence of both the coordinated chlorido group au lieu of the pyridyl group, in *trans*-**2**$^{2+}$ and in **5**$^{2+}$, and the presence of the dangling pyridyl moiety as mentioned earlier.

Table 1. Summary of catalytic performance of complexes *trans*-**4**$^{2+}$, *trans*-**2**$^{2+}$, *trans*-**1'**$^{+}$ and *trans*-**2'**$^{2+}$. Conditions: 1 mM catalyst in 0.1 M TfOH solution (pH 1) and 100 equivalents of Ce(IV) at 25 °C.

Complex	TON	Ox. Eff.[b] (%)	TOF_i[c] x10^3
trans-**4**$^{2+}$,[a]	24	96	710
trans-**2**$^{2+}$	8	32	37
trans-**1'**$^{+}$	0.67	2.7	4
trans-**2'**$^{2+}$	1	4	21

[a] Obtained from the addition of Ce(IV) to *trans*-**1**$^{+}$. [b] Ox. Eff. = oxygen efficiency = (measured mols O_2)/(theoretical mols O_2). Calculated from manometry and on-line mass spectrometry experiment. [c] Initial turnover frequencies in s^{-1}.

Interestingly, the related complex *trans*-**1'**$^{+}$, shows a completely different scenario. Oxygen evolution experiments after addition of Ce(IV) to solution of the chlorido *trans*-**1'**$^{+}$ and aquo *trans*-**2'**$^{2+}$ complexes both show a very poor catalytic activity with 1 TON or less (Figure 7 and Table 1). This result is consistent with the relative concentration of active species extracted from the species distribution diagram based on the substitution kinetics described earlier (see Figure S16 in the SI). Here the corresponding highly active chlorido-aquo complex *trans*-**4'**$^{2+}$ is a minor species in the mixture whereas the modestly active mono-aquo complex *trans*-**2'**$^{3+}$ is the major compound.

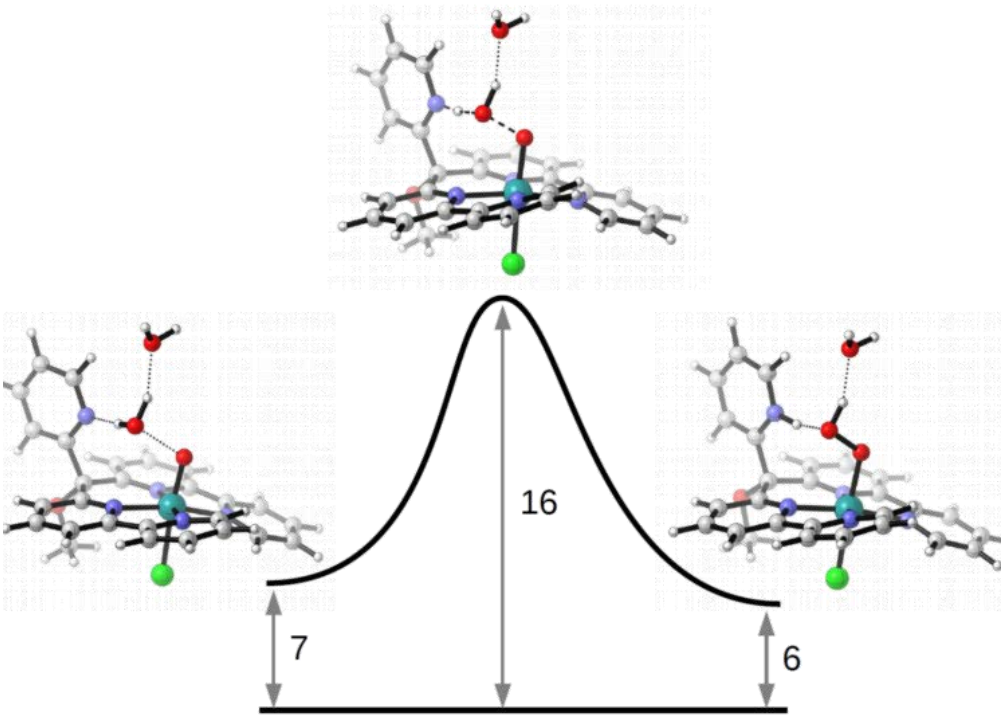

Figure 8. DFT calculated energy diagram of the nucleophilic attack of a water molecule to the Ru=O species derived from *trans*-**1**$^{+}$ to form a Ru-OOH species. The values are given in kcal mol^{-1} with respect to the separated reactants.

As previously mentioned the DFT calculated standard reduction potentials for the Ru(III/II) redox couple are in qualitative agreement with the CV data. In contrast to this, the computed reduction potentials for the Ru(IV/III) and Ru(V/IV) couples derived from *trans*-**2**$^{2+}$ are substantially higher than the ones obtained in CV measurements. This might be a failure of the implicit solvation model and may, for instance, be mitigated via a wider correlation of computed and experimentally determined redox potentials. Additionally, we note that test calculations using the DCOSMO-RS[19] and SMD[20] solvation models predict similar values. Despite the flaws in the above case, the calculated reduction potential of 1.8 V for the Ru(V/IV) couple of, [Ru(O)(Cl)(L-OMe-κ-N^4)]$^{+}$, is supported by the experimental value of 1.62 V (extracted from DPV in Figure 6) and validates at least qualitative statements regarding trends in activity. For *trans*-**2**$^{2+}$ a significantly higher reduction potential (600 mV shift) compared to the chlorido containing species is obtained (as can be expected from its higher charge, Figures S25-S26 in the SI).

Transition states energies for the WNA in the Ru(V) oxidation state for complexes with both ligand frameworks (L-OMe and L-Me) are practically identical. They are computed to be 16 and 14 kcal mol^{-1} with respect to the separated reactants for the OMe and Me

ligands, respectively (Figures 8 and S28). The transition states were modelled with an explicit solvent water molecule as the corresponding peroxido species could not be found otherwise. The role of the dangling pyridine as a proton acceptor can be observed in these structures. A similar transition state for the aquo complex with two explicit water molecules, where one water molecule would act as the base, could not be obtained. Modelling with more water molecules was not further pursued in this study.

Conclusions

A detailed kinetic study of the ligand substitution reactions of ruthenium complexes *trans*-**1**$^{+}$ and *trans*-**2**$^{2+}$ by water, in aqueous solution, reveal a multiple reaction sequence involving both the chlorido and one pyridyl group of the pentapyridyl ligand L-OMe. The same reactions are observed for related complexes *trans*-**1**'$^{+}$ and *trans*-**2**'$^{2+}$ containing the ligand L-Me. However, the differences on the kinetic constant values of the consecutive steps generate a distinct distribution of intermediate species for *trans*-**1**'$^{+}$ as compared to *trans*-**1**$^{+}$. Thus, for the L-OMe complex *trans*-**1**$^{+}$ the major species in solution during the first minutes is the chlorido-aquo complex *trans*-**4**$^{2+}$. In contrast, the aquo complex *trans*-**2**'$^{3+}$ is the most abundant species for *trans*-**1**'$^{+}$. These differences are responsible for dramatic changes in their water oxidation catalytic activity as observed by electrochemical, oxygen evolution experiments and DFT calculations. Our computational analysis suggests that the formation of the active *trans*-**4**$^{2+}$-type complex is the crucial step in the catalytic cycle and is mainly responsible for the different activities, since subsequent steps (PCETs, oxidations, WNA) show virtually identical free energies in both systems. This could be used as a handle to improve such catalysts. Complex *trans*-**4**$^{2+}$ is a fast catalyst that operates with TOF_i = 0.71 s^{-1} and produces 168 TON in the presence of 1000 equivalents of Ce(IV) as sacrificial agent. On the other hand, complexes *trans*-**2**$^{2+}$ and *trans*-**2**'$^{+}$ are poor catalysts producing less than 8 and 1 TONs respectively. Eventually, both catalysts evolve to the inactive bis(aquo) complexes *trans*-**3**$^{3+}$ and *trans*-**3**'$^{3+}$.[21] The difference in the catalytic performance of *trans*-**4**$^{2+}$ and *trans*-**2**$^{3+}$ is due to the chlorido ligand in *trans*-**4**$^{2+}$ that helps in lowering the redox potential to access Ru(V) that is the species responsible for electrocatalysis, and in the presence of the pendant pyridine group facilitates the O-O bond formation step, lowering the kinetic barrier at the water nucleophilic attack step.

Contribution

Marcos Gil-Sepulcre performed the electrochemical, spectroscopic and catalytic experiments and prepared the manuscript.

Acknowledgements

MINECO and FEDER (CTQ2016-80058-R, CTQ2015-64261-R, CTQ-2015-73028-EXP, SEV 2013-0319, ENE2016-82025-REDT, CTQ2016-81923-REDC) and AGAUR (2014-SGR-915). The authors thank the *University of Zurich*, the *URPP LightChEC* and the *Swiss National Science Foundation* (grant No. PP00P2_170667) for financial support for this work. Laurent Moser is also acknowledged for his assistance in the synthesis of complex $\mathbf{1}^{+}$.

References

[1] a) N. S. Lewis, *Science* **2016**, *351*, ad19201-aad19209. (b) S. Berardi, S. Drouet, L. Francàs, C. Gimbert-Suriñach, M, Guttentag, C. Richmond, T. Stoll, A. Llobet, A. *Chem. Soc. Rev.* **2014**, *43*, 7501-7519. (c) M. G. Walter, E. L. Warren, J. R. McKone, S. W. Boettcher, Q. Mi, E. A. Santori, N. S. Lewis. *Chem. Rev.* **2010**, *110*, 6446-6473.

[2] (a) P. Garrido-Barros, C. Gimbert-Suriñach, R. Matheu, S. Sala, A. Llobet, *Chem. Soc. Rev*. **2017**, *DOI: 10.1039/c7cs00248c*. (b) L. Tong, R. P. Thummel, *Chem. Sci*. **2016**, *7*, 6591-6603. (c) L. Francàs, R. Bofill, J. García-Antón, L. Escriche, X. Sala and A. Llobet, *Molecular Water Oxidation Catalysis: A Key Topic for New Sustainable Energy Conversion Schemes*, John Wiley & Sons Ltd, Chichester UK, 2014. (d) I. Romero, M. Rodríquez, C. Sens, J. Mola, M. R. Kollipara, L. Francàs, E. Mas-Marza, L. Escriche, A. Llobet, *Inorg. Chem.* **2008**, *47*, 1824-1834.

[3] (a) L. Duan, A. Fischer, Y. Xu, L. Sun, *J. Am. Chem. Soc.* **2009**, *131*, 10397-10399. (b) L. Duan, F. Bozoglian, S. Mandal, B. Stewart, T. Privalov, A. Llobet, L. Sun, *Nat. Chem.* **2012**, *4*, 418-423. (c) C. J. Richmond, R. Matheu, A. Poater, L. Falivene, J. Benet-Buchholz, X. Sala, L. Cavallo, A. Llobet, *Chem. Eur. J.* **2014**, *20*, 17282-17286. (d) R. Matheu, M. Z. Ertem, J. Benet-Buchholz, E. Coronado, V. Batista, X. Sala, A. Llobet, *J. Am. Chem. Soc.* **2015**, *137*, 10786-10795. (e) J. Creus, R. Matheu, I. Peñafiel, D. Moonshiram, P. Blondeau, J. Benet-Buchholz, J. García-Antón, X. Sala, C. Godard, A. Llobet, *Angew. Chem. Int. Ed*. **2016**, *55*, 15382-15386.

[4] (a) J. J. Concepcion, J. W. Jurss, J. L. Templeton, T. J. Meyer, *J. Am. Chem. Soc.*, 2008, **130**, 16462-16463. (b) J. J. Concepcion, M.-K. Tsai, J. T. Muckerman and T. J. Meyer, *J. Am. Chem. Soc.*, 2010, **132**, 1545-1557. (c) J. J. Concepcion, J. W. Jurss, M. R. Norris, Z. Chen, J. L. Templeton, T. J. Meyer, *Inorg. Chem.*, **2010**, *49*, 1277-1279. (d) A. Keidel, I. López, J. Staffa, U. Kuhlmann, F. Bozoglian, C. Gimbert-Suriñach, J. Benet-Buchholz, P. Hildebrandt, A. Llobet, *ChemSusChem* **2017, *10*, 551-561. (f)** F. Bozoglian, S. Romain, M. Z. Ertem, T. K. Todorova, C. Sens, J. Mola, M. Rodríguez, I. Romero, J. Benet-Buchholz, X. Fontrodona, C. J. Cramer, L. Gagliardi, A. Llobet, *J. Am. Chem. Soc.*, **2009**, *131*, 15176-15187.

[5] M. Gil-Sepulcre, J. Axelson, J. Aguiló, L. Solà, L. Francàs, A. Poater, L. Blancafort, J. Benet-Buchholz, G. Guirado, L. Escriche, A. Llobet, R. Bofill, X. Sala, *Inorg. Chem.* **2016**, *55*, 11216-11229.

[6] (a) S. Maji, I. Lopez, F. Bozoglian, J. Benet-Buchholz, A. Llobet, *Inorg. Chem.* **2013**, *52*, 3591-3593. (b) R. Zong, R. P. Thummel, *J. Am. Chem. Soc.* **2005**, *127*, 12802-12803. (d) M. Yagi, S. Tajima, M. Komi, H. Yamazaki, *Dalton Trans.* **2011**, *40*, 3802-3804.

[7] (a) A. D. Becke, *Phys. Rev. A* **1988**, *38*, 3098–3100 (b) J. P. Perdew, *Phys. Rev. B* **1986**, *33*, 8822–8824.

[8] S. Grimme, J. Antony, S. Ehrlich, H. Krieg, *J. Chem. Phys.* **2010**, *132*, 154104.

[9] F. Weigend, R. Ahlrichs, *Phys. Chem. Chem. Phys.* **2005**, *7*, 3297–3305.

[10] Y. Zhao, D. G. Truhlar, *JCP* **2006**, *125*, 194101.

[11] (a) J. P. Perdew, K. Burke, M. Ernzerhof, *Phys. Rev. Lett*. **1996**, *77*, 3865 (b) J. P. Perdew, M. Ernzerhof, K. Burke, *J. Chem. Phys.* **1996**, *105*, 9982.

[12] S. Grimme, J. G. Brandenburh, C. Bannwarth, A. Hansen, *J. Chem. Phys.* **2015**, *143*, 054107.

[13] (a) A. D. Becke, *J. Chem. Phys.* **1993**, *98*, 5648–5652 (b) C. Lee, W. Yang, R. G. Parr, *Phys. Rev. B* **1988**, *37*, 785–789.

[14] A. Klamt, G. Schüürmann, *J. Chem. Soc. Perkin Trans. 2* **1993**, *0*, 799–805.

[15] R. Kang, J. Yao, H. Chen, *JCTC* **2013**, *9*, 1872-1879.

[16] J. C. Dobson, T. J. Meyer, *Inorg. Chem.* **1988**, *27*, 3283-3291.

[17] A. C. Sander, S. Maji, L. Francas, T. Boehnisch, S. Dechert, A. Llobet, F. Meyer, *ChemSusChem* **2015**, *8*, 1697-1702.

[18] (a) D. J. Wasylenko, C. Ganesamoorthy, B. D. Koivisto, M. A. Henderson, C. P. Berlngette, *Inorg. Chem.* **2010**, *49*, 2202-2209. (b) D. J. Wasylenko, C. Ganesamoorthy, M. A. Henderson, B. D. Koivisto, H. D. Osthoff, C. P. Berlinguette, *J. Am. Chem. Soc.* **2010**, *132*, 16094-16106. (c) S. Roeser, P. Farràs, F. Bozoglian, M. Martínez-Belmonte, J. Benet-Buchholz, A. Llobet, *ChemSusChem* **2011**, *4*, 197-207. (d) M. Yoshida, S. Masaoka, J. Abe, K. Sakai, *Chem. Asian J.* **2010**, *5*, 2369-2378. (e) A. Kimoto, K. Yamauchi, M. Yoshida, S. Masaoke, K. Sakai, *Chem. Commun.* **2012**, *48*, 239-241.

[19] S. Sinnechker, A. Rajendran, A. Klamt, M. Diedenhofen, F. Neese, *J. Phys. Chem. A* **2006**, *110*, 2235-2245.

[20] A. V. Marenich, C. J. Cramer, D. G. Truhlar, *J. Phys. Chem. B* **2009**, *113*, 6378-6396.

[21] X. Sala, M. Z. Ertem, L. Vigara, T. K. Todorova, W. Chen, R. C. Rocha, F. Aquilante, C. J. Cramer, L. Gagliardi, A. Llobet, *Angew. Chem. Int. Ed.* **2010**, *49*, 7745-7747.

Supporting information

Ru water oxidation catalysts based on py_5 ligands

Table of Contents

1. Experimental Section

Materials

All general reagents and chemicals were used as purchased from Sigma-Aldrich, Fluka or Merck chemical companies without further purification unless otherwise stated. $RuCl_3$ was obtained from I^2CNS chemical company and used as purchased. Complex trans-**1**'$^{+}$, trans-**2**'$^{2+}$ and ligand L-OH were prepared according to the experimental procedure reported in the bibliography.[1,2] Cerium ammonium nitrate $Ce(NH_4)_2(NO_3)_6$ (CAN or Ce(IV) in the text) was purchased from Sigma-Aldrich (99.99%) and used without purification. THF was dried over Na/Benzophenone and stored under N_2. Air and moisture sensitive reactions were carried out under N_2 in oven-dried (120°C) glassware and monitored by TLC or HPLC. Evaporation of solvents *in vacuo* was done with a *Büchi Rotevapor R-134* at 40°C. Chromatography: neutral alox with the indicated solvent system. Thin layer chromatography (TLC): *Merck* TLC plates silica gel *60* on alox with the indicated solvent system; the spots were visualized in ambient light or under UV light (254 and 366 nm).

III

Instrumentation and measurements

NMR spectra were measured on a *Bruker AV-500* spectrometer and *Bruker 500 MHz* spectrometer equipped with cryoprobe. All the NMR experiments were performed at room temperature in corresponding deuterated solvents and using internal protons as reference.

High-resolution electrospray ionization mass spectra (HR-ESI-MS): *QExactive* (*Thermo Fisher Scientific*, Bremen, Germany) with a heated ESI source connected to a *Dionex Ultimate 3000* UHPLC system. Samples were dissolved in MeOH or H_2O at ca. 50 mg ml^{-1}; injection of 1 ml on-flow with an auto-sampler (mobile phase: MeOH + 0.1% HCOOH or CH_3CN/H_2O 2:8 + 0.1% HCOOH; flow rate 120 ml ml^{-1}); ion source parameters: spray voltage 3.0 kV, capillary temperature 320°C, sheath gas 5 l min^{-1}, s-lens RF level 55.0; full scan MS in alternating (+)/(–)-ESI mode; mass ranges 80–1200, 133–2000, or 200–3000 amu; resolution (full width half-maximum) 70000; automatic gain control (AGC) target 3.00 10^6; maximum allowed ion transfer time (IT) 30 ms; mass calibration <2 ppm accuracy for *m/z* 130.06619–1621.96509 in (+)-ESI and for *m/z* 265.14790–1779.96528 in (–)-ESI with *Pierce*® ESI calibration solutions (*Thermo*

Fisher Scientific, Rockford, USA); lock masses: ubiquitous erucamide (*m/z* 338.34174, (+)-ESI) and palmitic acid (*m/z* 255.23295, (–)-ESI).

Elemental analyses were performed on a *Leco CHNS-932* elemental analyzer.

Electrochemical measurements

Differential pulse voltammetry (DPV) and cyclic voltammetry (CV) were measured on a CHI660D potentiostat using a three-electrode cell. A glassy carbon (GC) working electrode (d = 3 mm) was employed while a Pt rod was used as counter electrode and $Hg/HgSO_4$ (K_2SO_4 sat) was used as reference electrode. Working electrodes were polished with 1 and 0.05 micron alumina paste, washed with distilled water and acetone and sonicated in acetone for 5 minutes before each measurement. DCM employed for electrochemical measurements was prepared with containing the necessary amount n-Bu_4NPF_6 ($TBAPF_6$) as supporting electrolyte to yield a 0.1 M ionic strength. CVs were typically recorded at a scan rate of 100 mV/s. DPVs were recorded with the following parameters: amplitude= 50 mV, step height=4 mV, pulse width= 0.05 s, pulse period= 0.5 s and sampling width= 0.0167 s.

Manometric and Online mass spectrometry measurements

The experiments were carried out with a Testo 521 differential pressure manometer, with an operating range of 1-100 hPa and an accuracy of within 0.5% of the measurement, coupled to thermostatted reaction vessels for dynamic monitoring of the headspace pressure above each reaction. In a typical experiment, 0.1 M triflic acid solution (TfOH, pH 1, 1.5 mL) was added to the reaction vessel containing a suspension of the catalyst under stirring and the equivalent volume added to the reference vessel. The pressures were equalised and a blank solution of TfOH (0.5 mL) was injected into the reference cell and an TfOH solution containing cerium(IV) ammonium nitrate (CAN, 1.33M, 150 µL) was then injected into the reaction vessel. Resulting a final concentration of catalyst = 1mM and concentration of CAN = 100 Mm. TOF values were calculated from the increase of TON in the initial 30 seconds after addition of oxidant.

Online mass spectrometry measurements were performed on a Pfeiffer Omnistar GSD 301C mass spectrometer, in the same conditions as the manometric measurements.

UV-vis spectra and kinetic studies

UV-Vis spectra were measured on a *Cary 50 UV-vis* spectrometer by *Varian Inc*. For oxidation and isomerization Kinetics presented in this work, a fast mixing stopped flow module Bio-Logic SFM300 with a cryostat Huber CC3-905 VPC and a fast JM TIDAS UV-Vis Diode Array spectrophotometer was employed.

Hydrolysis Kinetics (at oxidation state Ru(II)). Substitution studies were performed at various concentrations of complex *trans*-**1**$^{+}$ and *trans*-**1**'$^{+}$. In a typical experiment, a solution of Ru complex (800 µM) in trifluorethanol was added to a 0.1 M triflic acid solution and monitored during time. The absorption spectra were recorded at 25 ºC in a 1.0 cm path length quartz cell on a CARY 50-Bio from Agilent. Reactlab Kinetics software[3] was used to process the data and thus obtain the rate constant values.

Oxidation and isomerization Kinetics. Kinetic studies on the oxidation of 63 µM of *trans*-Ru^{II}-Cl, were performed using a fast mixing stopped flow module. In a typical experiment, a solution of Ru complex (70 µM) in 0.1 M triflic acid solution containing 5 % of trifluoroethanol was mixed with stoichiometric amounts of a solution of cerium(IV) ammonium nitrate in the same media (resulting in a final concentration of complex of 63 µM) and the changes in absorbance with time were monitored. For slow reactions ($t½$ > 170 sec) a Cary 50-Bio from Agilent was used. In a typical experiment, to a 2.375 mL solution of cerium(IV) ammonium nitrate (40 µM) in 0.1M triflic acid were added 125 µL of Ru^{II}-Cl or Ru^{II}-H_2O (800 µM) complex in trifluoroethanol, resulting in a final concentration of 40µM of complex. In all cases, the temperature was maintained at 25 ºC.

Kinetic constants were calculated by a global fitting using ReactLab Kinetics software. For the calculation of k_2, k_3 and k_{-3} we restricted the fitting solutions with the equilibrium constants calculated from ^{1}H NMR solutions after reaching the trans:cis equilibrium, after oxidation (K_{eq}(trans-**1**$^{+}$) = 0.1 and K_{eq}(trans-**1**'$^{+}$) = 0.8, see Figures S14-S15). The kinetic constants k_1 and k_7 were obtained by studying the independent processes with isolated samples of *trans*-**2**$^{2+}$ and *trans*-**2**$^{3+}$. Introducing the model in Scheme 2 in Reactlab Kinetics software and fixing in the previously calculated constants k_2, k_3, k_{-3} and k_7, we were able to fit k_4, k_5 and k_6. SVD analysis of the spectral data was used to obtain the significant components. A global fitting of the model was used to calculate the spectrum of the intermediate species and the change in concentration with time. Rate constants

were measured at 25 °C. Errors shown correspond to one-sigma of the models respect to experimental points.

Computational Methods

Calculations were carried out using the Turbomole software package[4] (version 7.0). Geometry optimizations and frequency analyses were performed employing (unrestricted) Kohn-Sham density functional theory with the BP86 exchange-correlation functional,[5,6] the def2-TZVP basis set[7] (with the corresponding effective core potential for Ru) and Grimme's D3 dispersion correction[8] (no Becke-Johnson damping).

Single-point electronic energies were obtained with B3LYP-D3[9,10]/def2-TZVP and the COSMO solvation model[11] (dielectric constant ε = 80 for water, default radii).

Calculations were sped-up by means of the Resolution-of-the-Identity approach (RI-J), with its corresponding basis set[12] and Multipole-Assisted-RI-J[13] (MARIJ). The error of both approximations was checked for selected molecules and found to be negligible.

Gibbs free-energy corrections were obtained from the normal mode analysis, based on the rigid-rotor, harmonic oscillator approximations, using the Turbomole module freeh at a pressure of 1 bar and a temperature of 298.15 K; no scaling factor was applied to the vibrational frequencies.

The Gibbs free energies were furthermore corrected for the change in standard state from 1 bar to 1 M (resp. 1 bar to 55.6 M for water). Deprotonations include the solvation free energy of a proton (but not its translational free energy) of 265.9 kcal mol^{-1};[14] reduction potentials are given relative to the standard hydrogen electrode (SHE) which was taken to be 4.28 V. The standard reduction potential was calculated as given below, where n is the number of electrons transferred, F is the Faraday constant, $\Delta G^{\circ}_{red}$the Gibbs free energy change in the reduction and $E^{\circ,abs.}_{SHE}$ the absolute potential of the SHE:

$$E^{\circ}_{red} = -\frac{\Delta G^{\circ}_{red}}{nF} - E^{\circ,abs.}_{SHE}.$$

Proton-coupled electron transfer reactions include the energy of half a hydrogen molecule[15] whose Gibbs free energy correction consists of the zero-point vibrational energy plus a thermal correction of 0.52 eV.[16] Larger basis sets (def2-TZVPP, def2-QZVP) were used to calculate single-point electronic energies but did not influence the

relative energies significantly. Free energies arising from spin multiplicity were neglected. Test calculations using the implicit solvation models DCOSMO-RS[17] and SMD[18] were done in Turbomole and Orca 4,[19] respectively.

Unless otherwise stated, the energies referred in the text are (Gibbs) free energies given in kcal mol^{-1}.

Synthesis of *trans*-$\mathbf{1}^{+}$ and *trans*-$\mathbf{2}^{2+}$

Synthesis of [Ru(L-OMe)Cl]Cl (*trans*-$\mathbf{1}^{+}$): In a Young flask Bpy_2PyOH (102 mg, 0.2 mmol) and NaH (60% dispersion in mineral oil, 42 mg, 0.96 mmol) were stirred in anhydrous THF (5.5 mL) for 30 min. Excess iodomethane (300 µL) was then added and the reaction mixture was stirred at 70°C in the sealed vessel for 15 h. The mixture was concentrated followed by addition of aq. NaOH (*ca.* 2 M) and DCM. The phases were separated and the aqueous phase extracted 3 times with DCM. The combined organic phases were dried over $MgSO_4$, filtered and concentrated. The crude ligand (105 mg), was then refluxed with $RuCl_3$ (48 mg, 0.2 mmol) in EtOH (10 mL) for 75 h followed by filtration through celite. The resulting deep red solution was concentrated to give the crude product. Purification by column chromatography (neutral alox, DCM/MeOH 1:0 - 9:1) followed by vapour diffusion (MeOH, Et_2O) yielded crystalline and pure [Ru(Bpy_2PyOMe)Cl]Cl (*trans*-$\mathbf{1}^{+}$). Yield: 32 mg (35%). ^{1}H-NMR (d_4-methanol, 500 MHz, 293 K): δ = 10.00 (d, J = 8.0 Hz, 2H, d_4), 9.12 (d, J = 8.0 Hz, 1H, e_4), 8.43 (d, J = 8.0 Hz, 2H, d_1), 8.32 (d, J = 8.0 Hz, 2H, h_3), 8.21 (d, J = 8.0 Hz, 2H, h_1), 8.12 (m, 4H, h_2/d_2), 7.97 (d, J = 8.0 Hz, 1H, e_1), 7.90 (d, J = 8.0 Hz, 1H, e_2), 7.81 (t, J = 8.0 Hz, 2H, d_3), 7.12 (t, J = 8.0 Hz, 2H, e_3), 4.31 (s, 3H, -OCH_3); ^{13}C-NMR (d4-methanol, 100 MHz): δ 162.0 (q_3), 160.3 (q_2), 160.1 (q_4), 158.8 (q_1), 157.9 (e_4), 155.0 (d_4), 140.0 (e_2), 139.5 (d_2), 137.9 (h_2), 127.0 (d_3), 126.2 (e_1), 124.9 (e_3), 124.2 (d_1), 123.1 (h_1), 122.7 (h_3), 93.4 (R_3*C*OMe), 59.5 (-O*C*H_3); ESI-MS: m/z = 568.05 (100%, $[M]^{+}$); 550.63 (5%, [M – Cl + OH]$^{+}$). Elemental Analysis (% found): C, 51.14; H, 3.56; N, 11.02. Calcd. for [Ru(Bpy_2PyOMe)Cl]Cl·H_2O: C 52.18, H 3.73, N 11.27.

Synthesis of [Ru(L-OMe)(H_2O)](ClO_4)$_2$ (*trans*-$\mathbf{2}^{2+}$): *trans*-$\mathbf{1}^{+}$ (40 mg, 0.066 mmol) was dissolved in a mixture of MeOH (4 mL) and 0.1 M $HOTf_{(aq)}$ (2 mL), $AgNO_3$ (22 mg, 0.132 mmol) was added and the deep reddish purple solution was heated to reflux for 1 h. The orange red reaction mixture was filtered through celite to remove the AgCl precipitate, excess $LiClO_4$ was added and the solution was left to stand at room

temperature. **NOTE OF CAUTION**: Perchlorate salts can be explosive and should be handled with care and preferably on a small scale. After 5 days, large (> 4mm) dark red crystals had precipitated from the solution. The mother liquor was decanted off and the crystals were washed with a little cold water before drying in air to give pure $[Ru(Bpy_2PyOMe)(H_2O)](ClO_4)_2$ (*trans*-$\mathbf{2}^{2+}$). Yield: 32 mg (65%). ^{1}H-NMR (d_4-methanol, 500 MHz, 293 K): δ = 10.10 (d, *J* = 5.5 Hz, 2H, d_4), 9.13 (d, *J* = 5.5 Hz, 1H, e_4), 8.59 (d, *J* = 7.8 Hz, 2H, d_1), 8.44 (d, *J* = 7.8 Hz, 2H, h_3), 8.29-8.21 (m, 6H, h_1, h_2, d_2), 7.96 (d, *J* = 8.0 Hz, 1H, e_1), 7.90 (m, 3H, d_3, e_2), 7.18 (t, *J* = 5.5 Hz, 2H, e_3), 4.31 (s, 3H, -OC*H*$_3$); ^{13}C-NMR (5:1 d3-acetone-D_2O, 100 MHz): δ 160.4 (q_3), 159.2 (q_2), 158.2 (q_4), 158.0 (e_4), 157.6 (q_1), 154.9 (d_4), 140.0 (d_2), 139.1 (e_2), 138.3 (h_2), 127.1 (d_3), 125.6 (e_1), 124.5 (e_3), 124.4 (d_1), 123.0 (h_1), 122.6 (h_3), 92.2 (R$_3$*C*OMe), 59.2 (-O*C*H$_3$); ESI-MS: m/z = 664.05 (25%, $[M - H_2O + MeOH + ClO_4]^+$); 650.04 (5%, $[M + ClO_4]^+$); 632.02 (23%, $[M - H_2O + ClO_4]^+$); 280.54 (100%, $[M - H_2O + MeOH]^{2+}$); 275.54 (24%, $[M]^{2+}$); 266.54 (12%, $[M - H_2O]^{2+}$); Elemental Analysis (% found): C, 41.04; H, 3.44; N, 8.65. Calcd. for $[Ru(BpyPyOMe)(H_2O)](ClO_4)_2 \cdot 2H_2O$: C, 41.28; H, 3.46; N, 8.92.

2. Characterization of complexes *trans*-$\mathbf{1}^+$ and *trans*-$\mathbf{2}^{2+}$

NMR

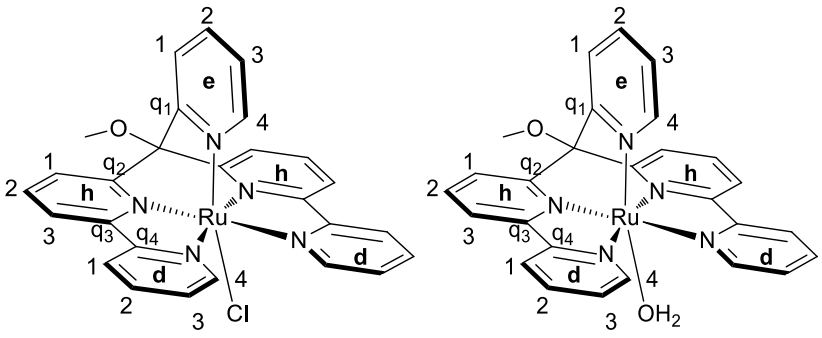

Figure S1. Schematic representation of the synthetized complexes *trans*-$\mathbf{1}^+$ (left) and *trans*-$\mathbf{2}^{2+}$ (right) and their ^{1}H-NMR and ^{13}C-NMR assignments (see Figures S4-S7).

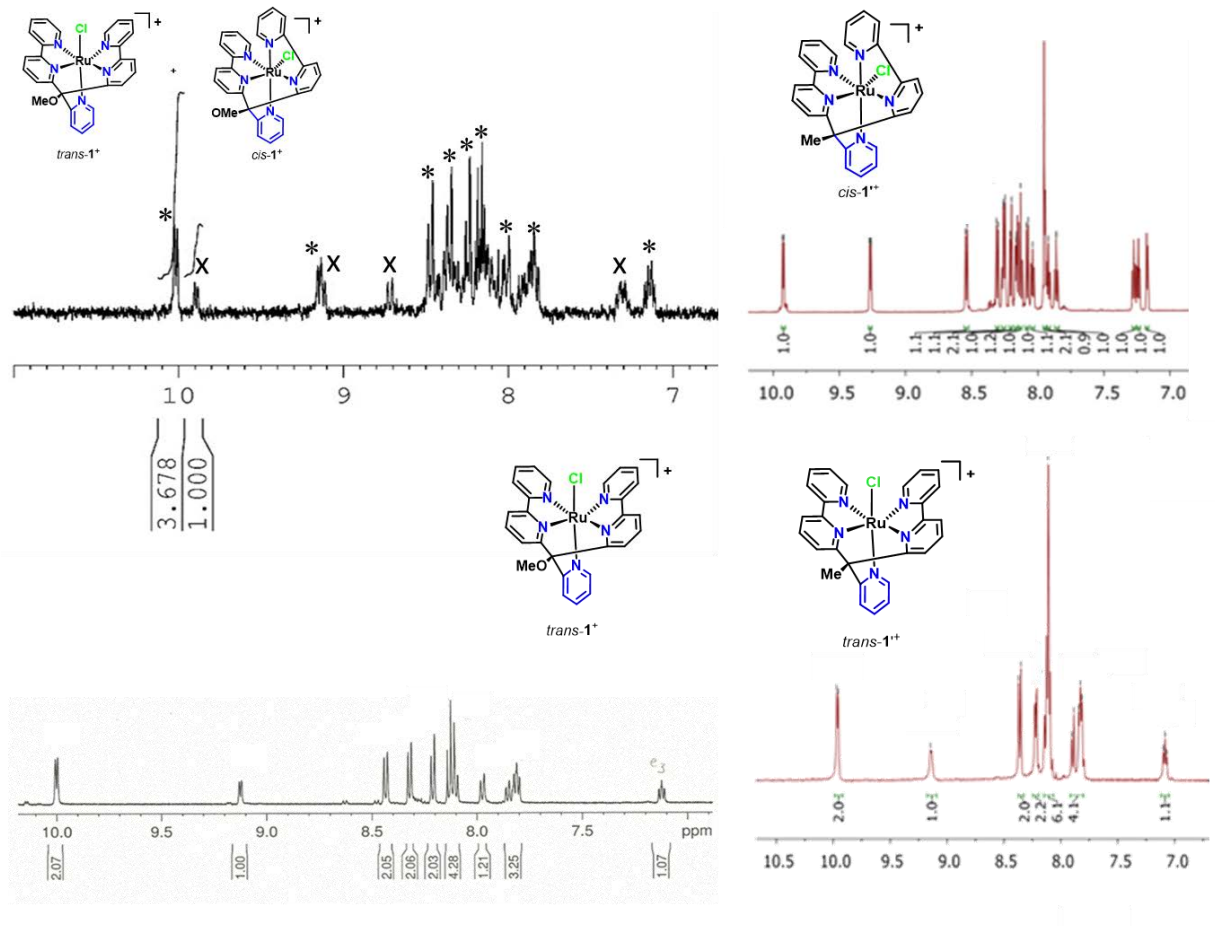

Figure S2. (Top left) ^{1}H-NMR (300 MHz, 293K, d_4-Methanol) spectra of crude *cis-trans* mixture of complex *trans*-**1**$^{+}$ before column chromatography. Resonances for *trans* and *cis* isomer are marked by (∗) and (X) respectively. (Top right) ^{1}H-NMR spectrum of complex *cis*-**1**'$^{+}$ (d_4-Nitromethane, 600 MHz, 25 ℃). (Bottom left) ^{1}H-NMR spectrum of complex *trans*-**1**$^{+}$ (d_4-Methanol, 500 MHz, 25 ℃). (Bottom right) ^{1}H-NMR spectrum of complex *trans*-**1**'$^{+}$ (d_4-Nitromethane, 400 MHz, 25 ℃).

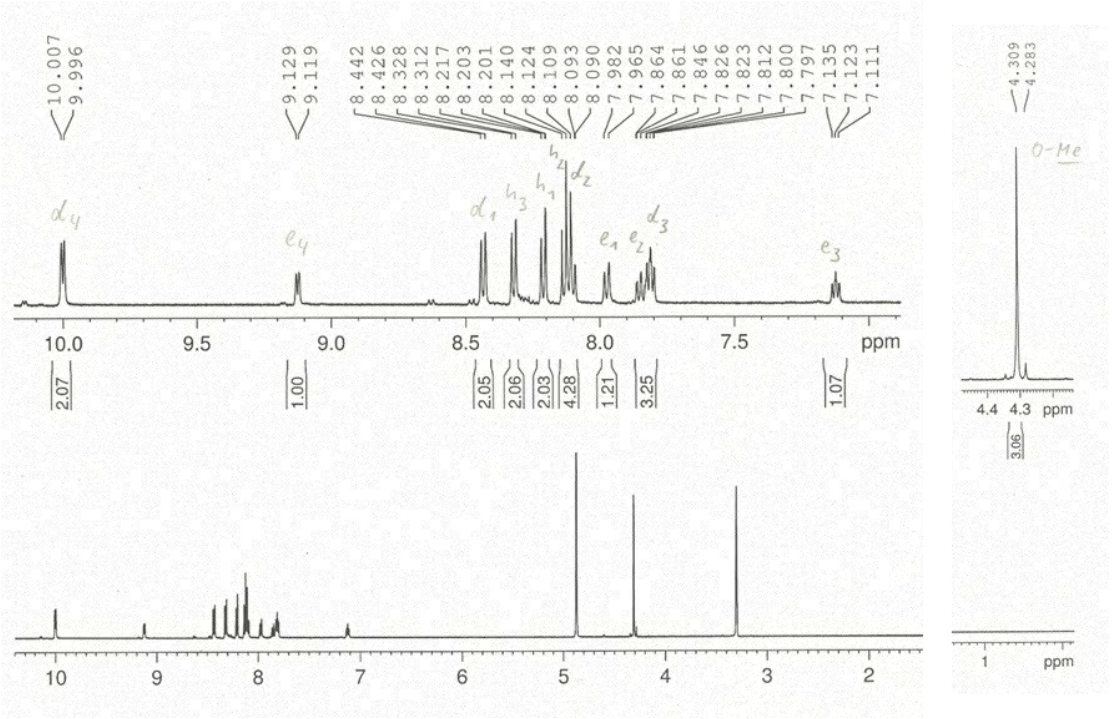

Figure S3. ^{1}H-NMR spectrum of complex *trans*-**1**$^{+}$ (d_4-methanol, 500 MHz, 25 ºC).

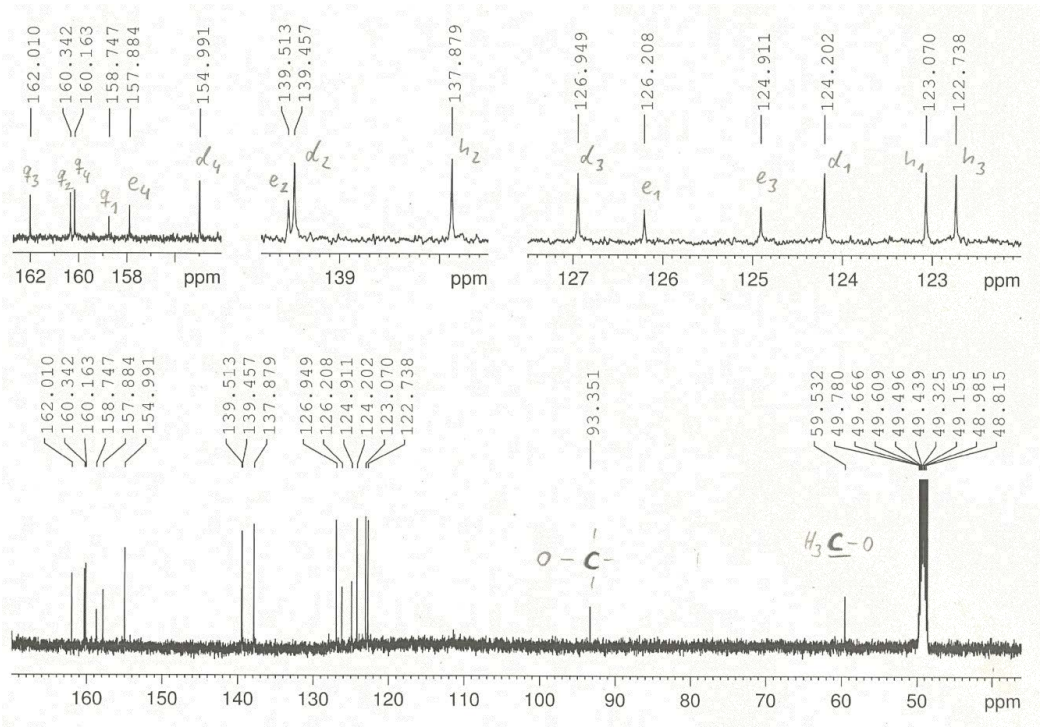

Figure S4. ^{13}C-NMR spectrum of complex *trans*-**1**$^{+}$ (d_4-methanol, 500 MHz, 25 ºC).

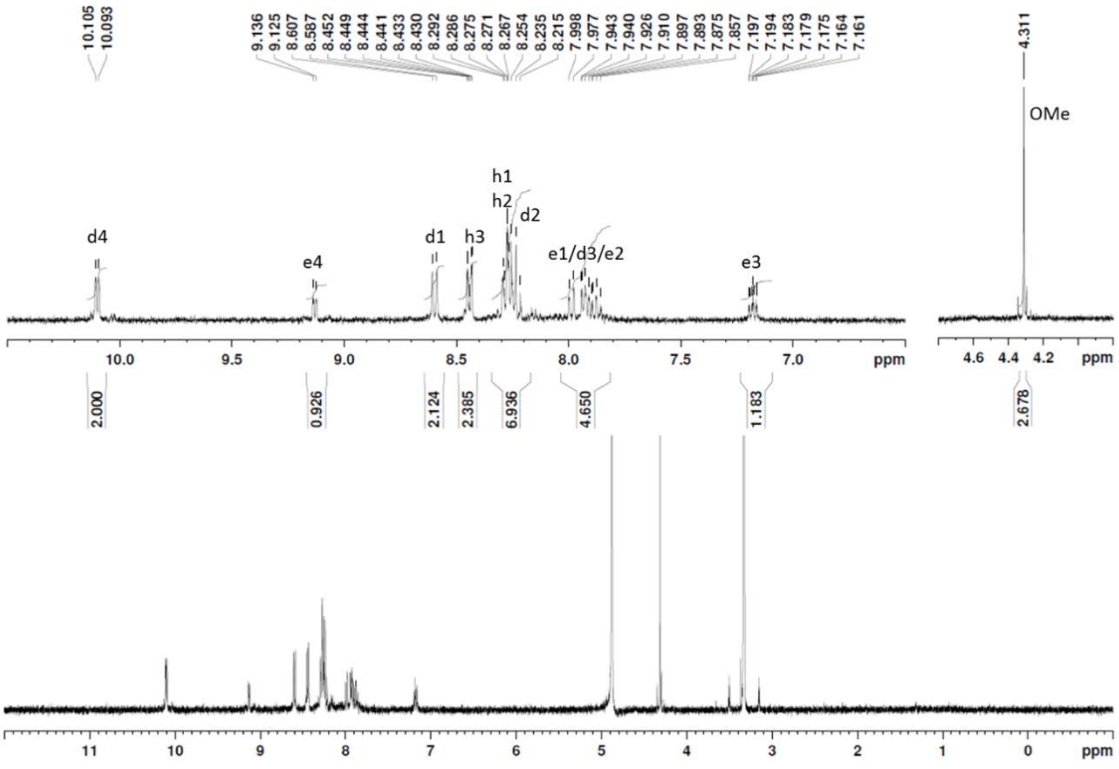

Figure S5. ^{1}H-NMR spectrum of complex *trans*-$\mathbf{2}^{2+}$ (d_4-methanol, 500 MHz, 25 ºC).

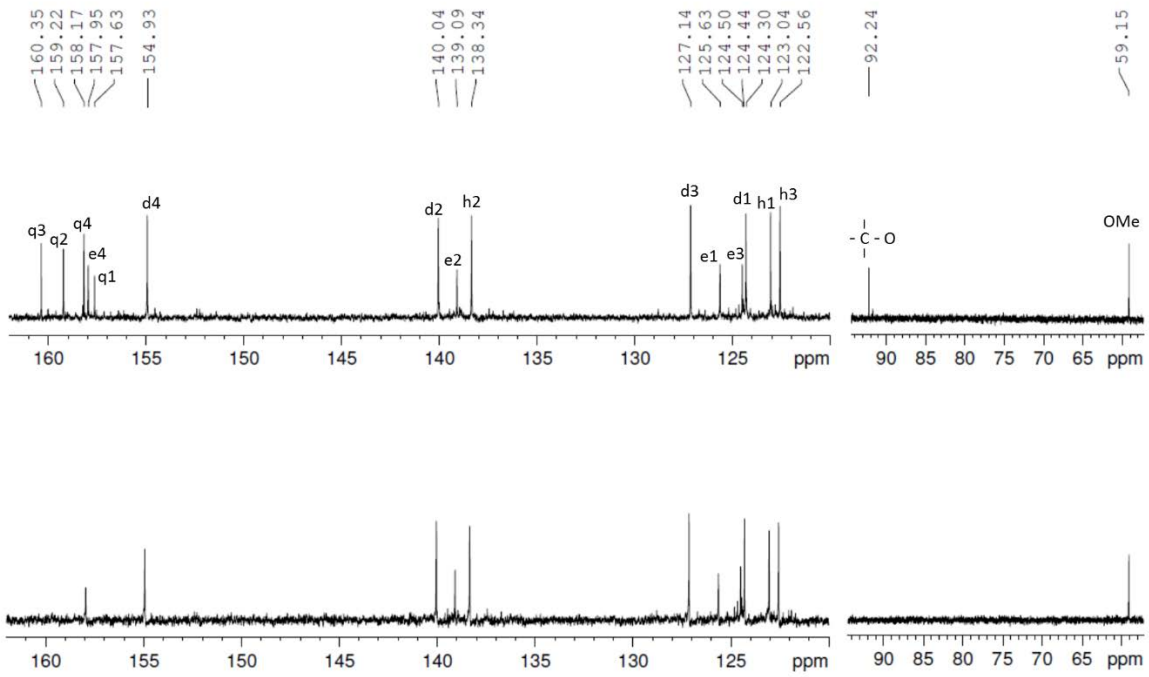

Figure S6. ^{13}C-NMR spectrum of complex *trans*-$\mathbf{2}^{2+}$ (d_4-methanol, 500 MHz, 25 ºC).

Mass spectrometry

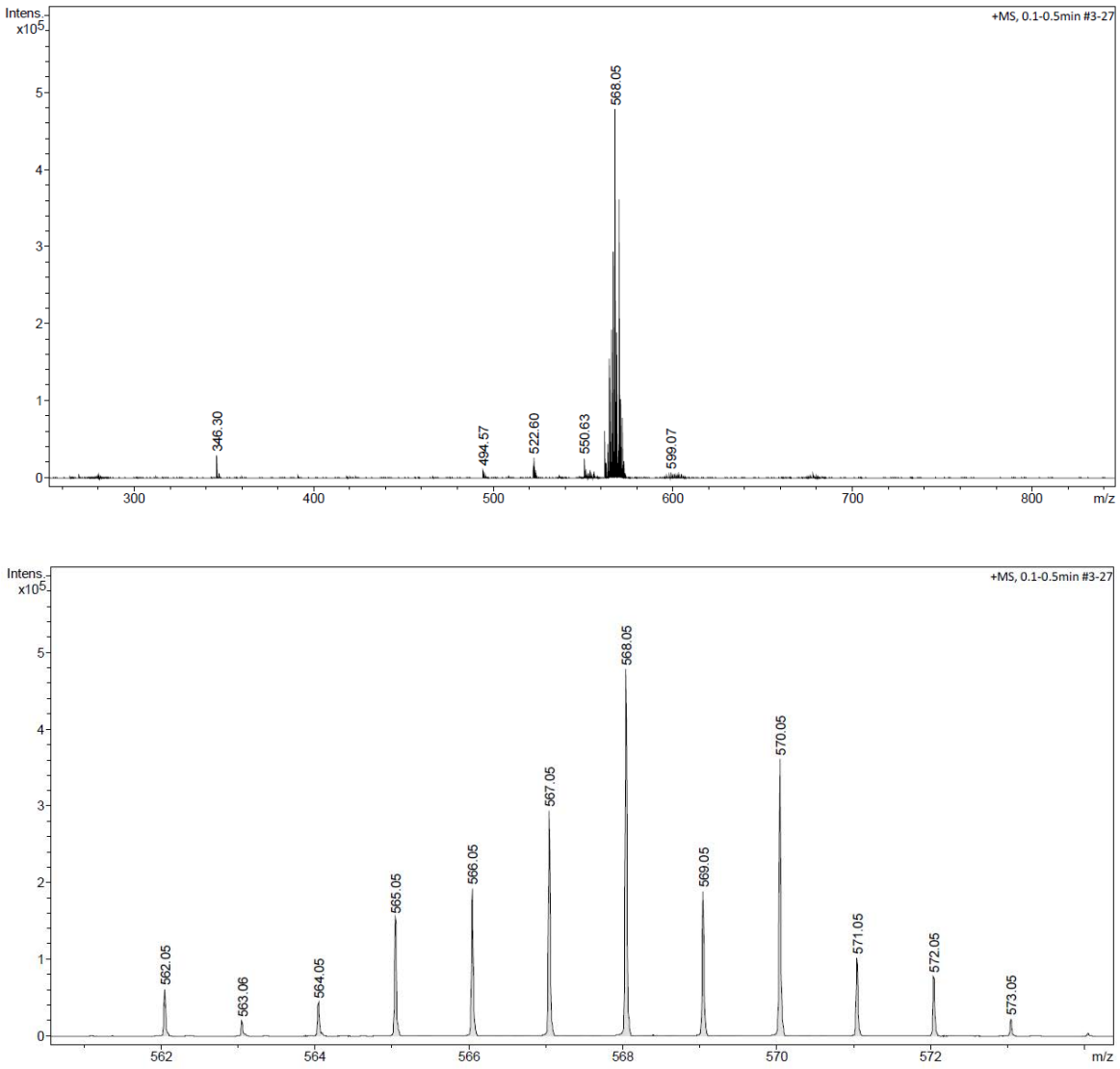

Figure S7. (+)-ESI-MS for compound *trans*-**1**$^{+}$.

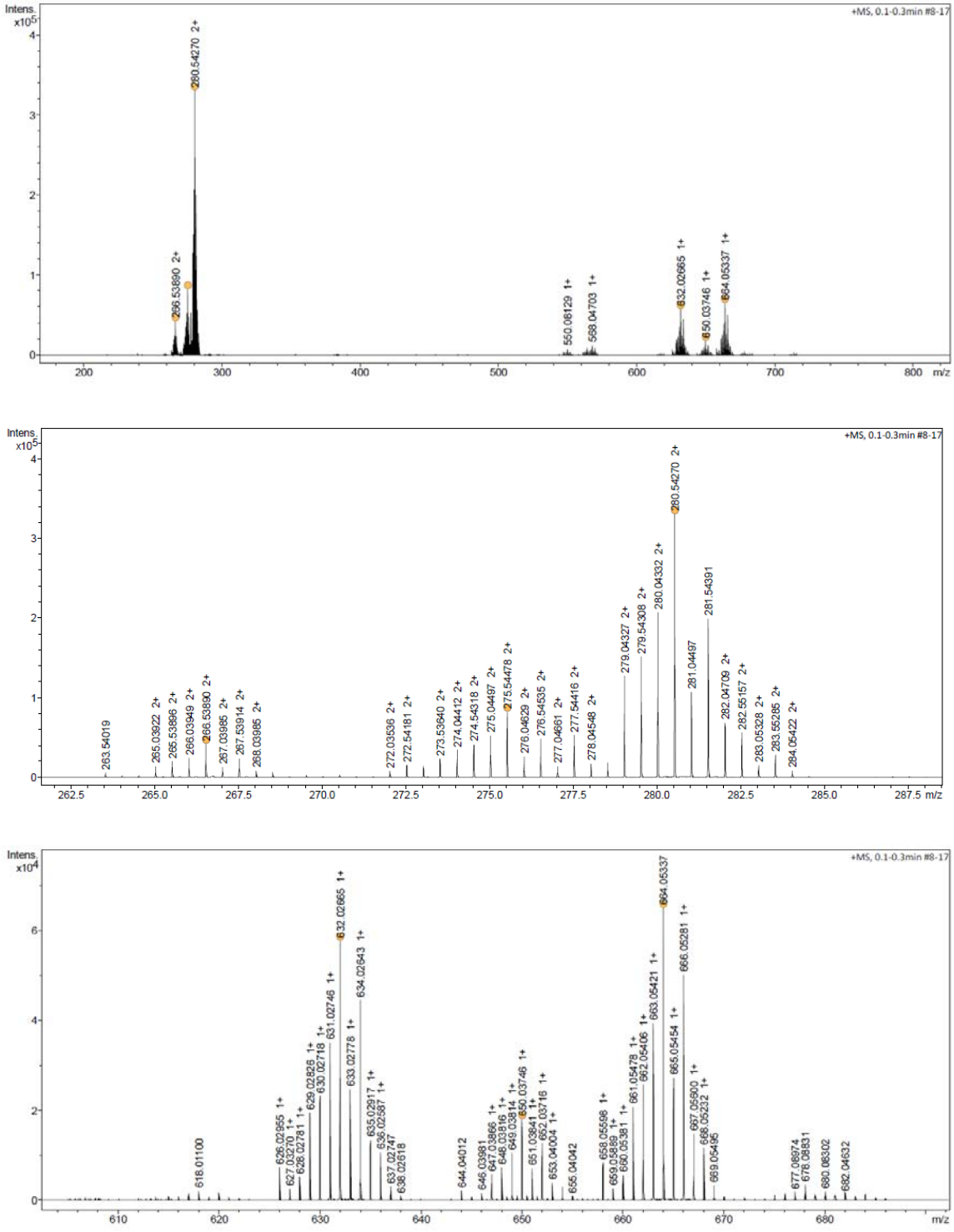

Figure S8. (+)-ESI-MS for compound trans-$\mathbf{2}^{2+}$. *m/z* = 664.05 (25%, $[M - H_2O + MeOH + ClO_4]^+$); 650.04 (5%, $[M + ClO_4]^+$); 632.02 (23%, $[M - H_2O + ClO_4]^+$); 280.54 (100%, $[M - H_2O + MeOH]^{2+}$); 275.54 (24%, $[M]^{2+}$); 266.54 (12%, $[M - H_2O]^{2+}$).

UV-Vis spectroscopy

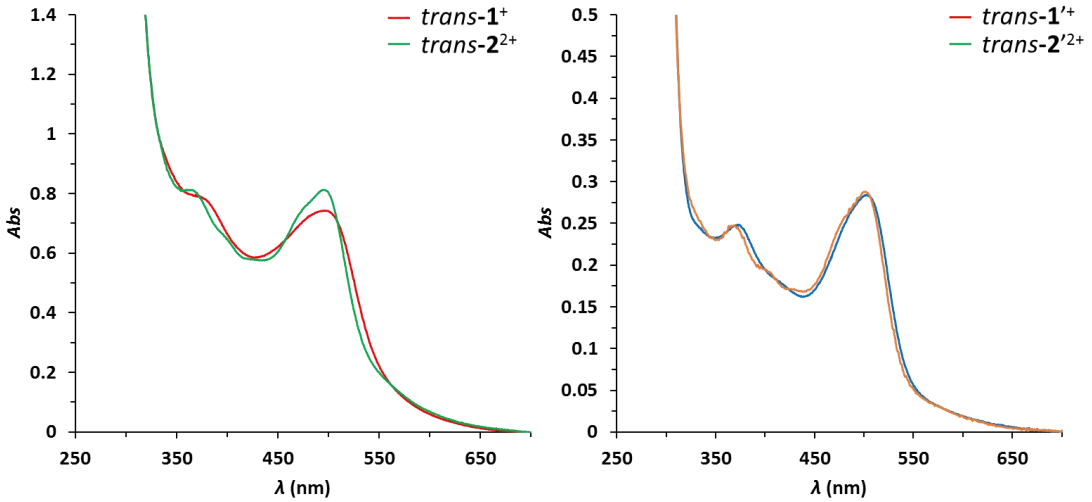

Figure S9. (Left) UV-vis absorption spectrum of *trans*-**1**$^{+}$ (red line) and *trans*-**2**$^{2+}$ (green line). (Right) UV-vis absorption spectrum of *trans*-**1'**$^{+}$ (blue line) and trans-**2'**$^{2+}$ (orange line). Conditions: 40 µM of complexes in 0.1 M TfOH solution containing 5% of TFE.

X-Ray Crystallography

X-ray Crystal structure determination: Crystallographic data for *trans*-**1**$^{+}$ and *trans*-**2**$^{2+}$ were collected at 183(2) K with Mo K_α radiation (λ = 0.7107 Å) that was graphite-monochromated on an *Oxford Diffraction CCD Xcalibur* system with a Ruby detector. Suitable crystals of *trans*-**1**$^{+}$ were grown by vapour diffusion (MeOH, Et_2O) and crystals of *trans*-**2**$^{2+}$ were grown by slow evaporation of a solution of *trans*-**2**$^{2+}$ in 0.1 M triflic acid solution / MeOH (2:1 by volume). Single crystals were covered with oil (*Infineum V8512*, formerly known as *Paratone N*), placed on a nylon loop that is mounted in a *CrystalCap Magnetic*™ (*Hampton Research*) and immediately transferred to the diffractometer. The program suite *CrysAlis*^{Pro} was used for data collection, multi-scan absorption correction and data reduction.[20] The structures were solved with direct methods using *SIR97*[22] and were refined by full-matrix least-squares methods on F^2 with *SHELXL-97*.[22] CCDC 1480864 and 1480863 contain the supplementary crystallographic data for this paper. The data can be obtained free of charge from *The Cambridge Crystallographic Data Centre* via .

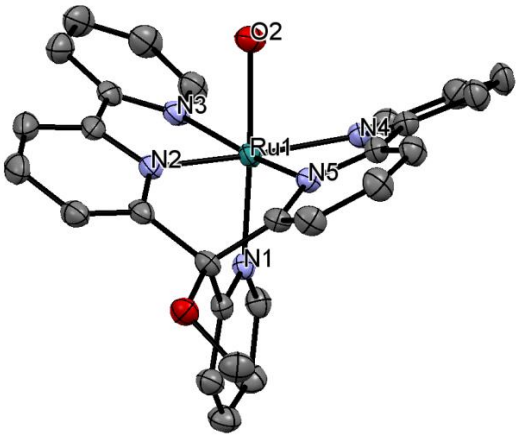

Figure S10. ORTEP representation of and *trans*-**2**$^{2+}$ at 50% probability level. The counter ions, solvent molecules and non-acidic hydrogen atoms have been omitted for clarity. Colour code: C, black; N, blue; O, red; Ru, light blue.

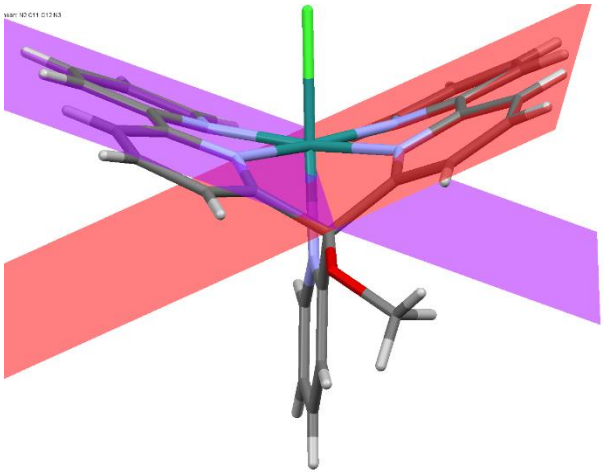

Figure S11. Picture showing the angle between the two bipyridine groups of L-OMe in *trans*-**1**$^{+}$ situated in the equatorial plane. This angle has a value of 134.4º as opposed to the 180º expected for an ideal octahedron

3. Kinetic studies

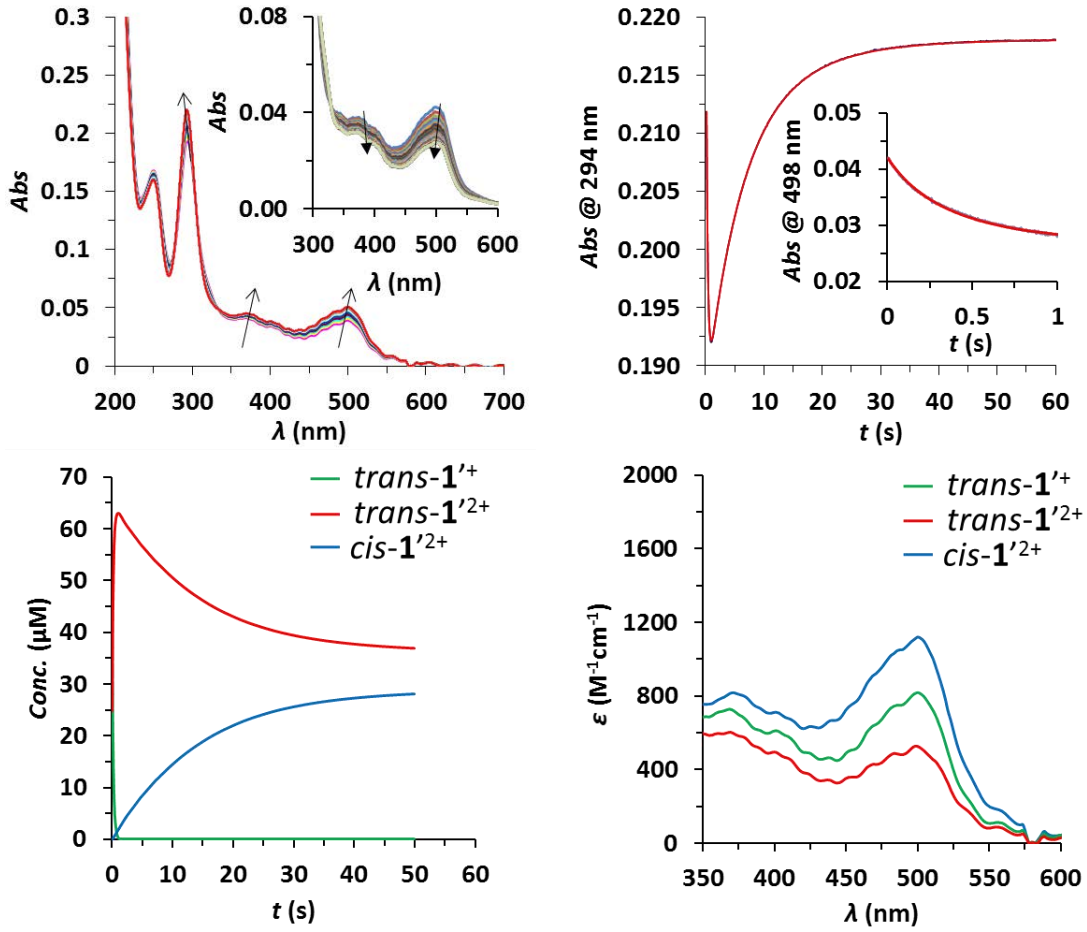

Figure S12. (Top) (Left) Evolution of stopped-flow UV-vis absorption spectra of a 63 μM solution of *trans*-**1**'$^{+}$ with 1 equivalent of Ce(IV) in 0.1 M TfOH solution containing 5% of TFE at 25 °C. *Inset* Evolution spectra of the first process (1 second) attributed to the oxidation of *trans*-**1**'$^{+}$ to *trans*-**1**'$^{2+}$. (Right) changes in the absorbance at 294 nm vs time (blue line) and its mathematical fit (red line). *Inset.* Changes in the absorbance at 498 nm vs time (blue line) and its mathematical fit (red line), during 1 second of reaction. **(Bottom)** (Left) calculated concentration distribution diagram vs time for the different species. (Right) calculated spectra for the proposed species in solution.

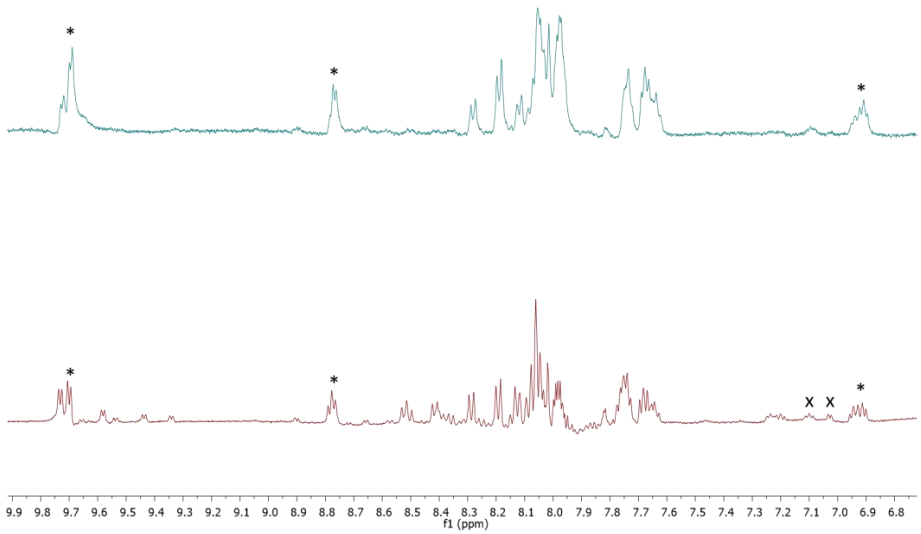

Figure S13. (Top) ^{1}H-NMR of *trans*-**1**$^{+}$ in a 0.1 M deuterated TfOH solution containing 20% of TFE. **(Bottom)** ^{1}H-NMR of *trans*-**1**$^{+}$ after oxidation with 1 equivalent of Ce(IV) in a 0.1 M deuterated triflic acid solution containing 20% of TFE followed by addition of sodium ascorbate as reducing agent (50 seconds after oxidation). (*) Signals of *trans*-**1**$^{+}$, (^{x}) Signals of *cis*-**1**$^{+}$. After oxidation (red spectrum), new signals associated with the cis isomer (^{x}) arise.

III

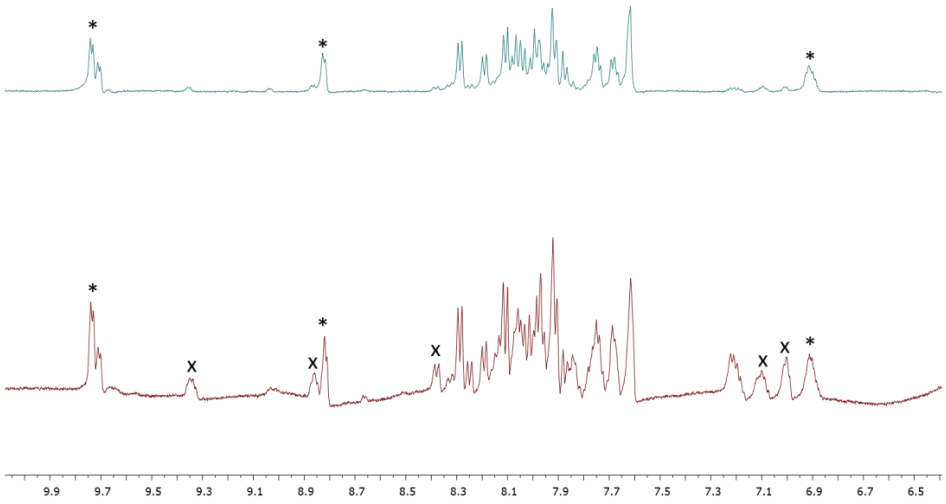

Figure S14. (Top) ^{1}H-NMR of *trans*-**1**'$^{+}$ in a 0.1 M deuterated TfOH solution containing 20% of TFE. **(Bottom)** ^{1}H-NMR of *trans*-**1**'$^{+}$ after oxidation with 1 equivalent of Ce(IV) in a 0.1 M deuterated triflic acid solution containing 20% of TFE followed by addition of sodium ascorbate as reducing agent (50 seconds after oxidation). (*) Signals of *trans*-**1**'$^{+}$; (^{x}) Signals of *cis*-**1**'$^{+}$. After oxidation (red spectrum), new signals associated with the cis isomer (^{x}) arise.

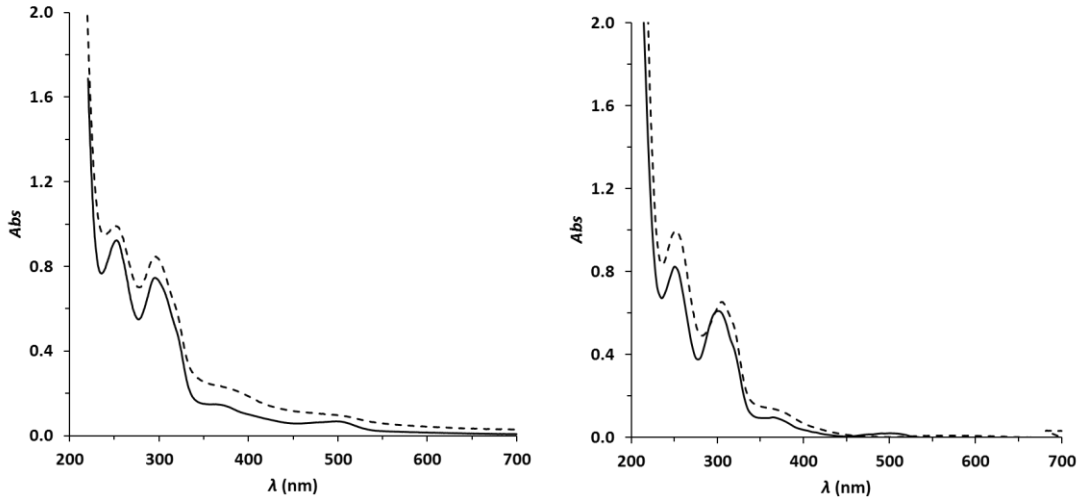

Figure S15. Comparison of experimental (solid line) and calculated (dashed line) spectra of *trans*-**2**$^{3+}$ (left) and *trans*-**2**'$^{3+}$ (right). Complexes *trans*-**2**$^{3+}$ and *trans*-**2**'$^{3+}$ were prepared by adding a solution of *trans*-**2**$^{2+}$ or *trans*-**2**'$^{2+}$ in TFE to a solution containing 1 equivalent of Ce(IV) in 0.1 M TfOH solution at 25 °C.

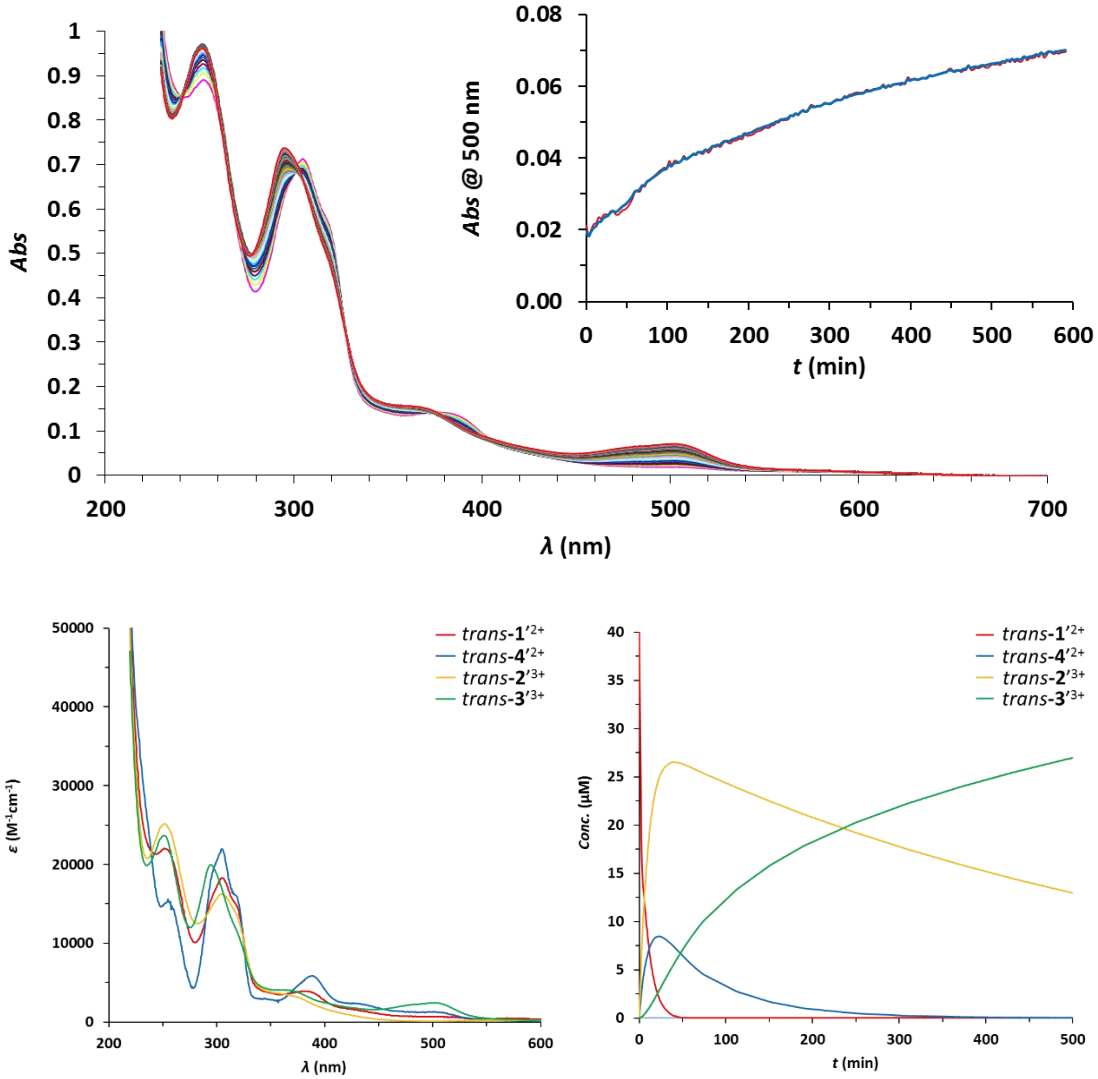

Figure S16. (Top) Evolution of stopped-flow UV-vis absorption spectra of a 40 μM solution of *trans*-**1**'$^{+}$ with 1 equivalent of Ce(IV) in 0.1 M TfOH solution containing 5% of TFE at 25 °C. (Inset) Changes in absorbance vs time at 500 nm (blue line) and fit (red line). **(Bottom)** (Left) calculated spectra of the different species proposed in Scheme 2. (Right) concentration distribution diagram vs time for the different species.

4. Electrochemistry

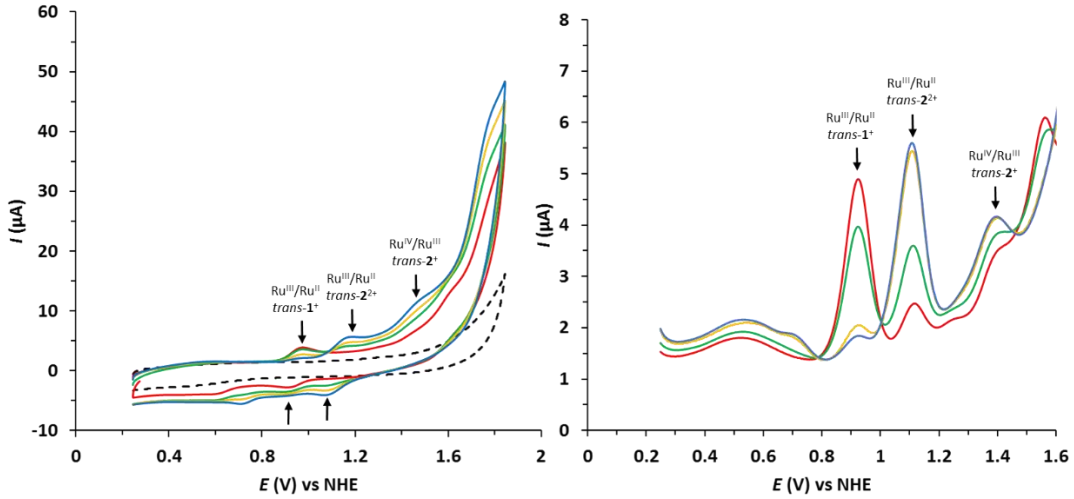

Figure S17. Cyclic Voltammograms (left) and Differential Pulse Voltammograms (right) of *trans*-**1**$^{+}$ at 2 min (solid red), 5 min (solid green), 15 min (solid yellow), 30 min (solid blue) and blank (dashed black) after addition of the complex to a mixture 0.1 M TfOH/TFE solvent mixture (3:1 by volume) with a scan rate of 100 mV s^{-1}. Conditions: [*trans*-**1**$^{+}$] = 0.5 mM.

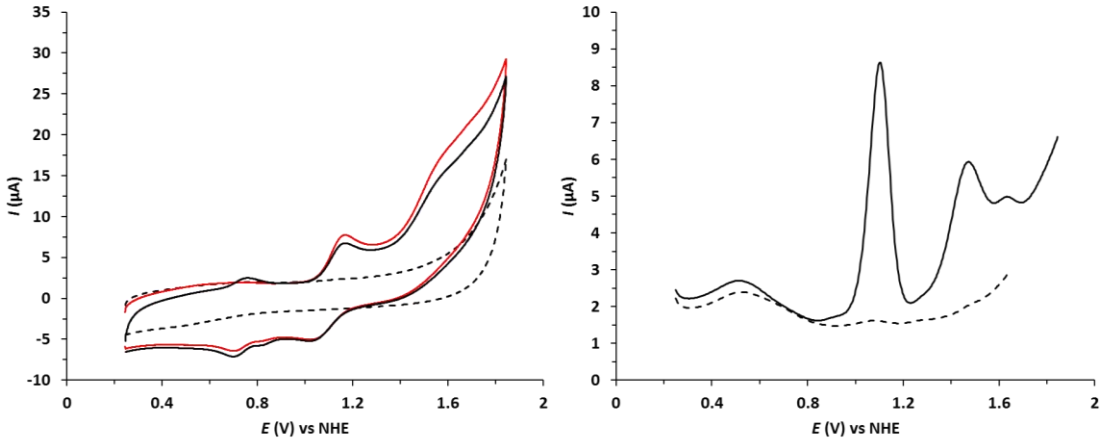

Figure S18. Cyclic Voltammograms (left) and Differential Pulse Voltammograms (right) of *trans*-**2**$^{2+}$; first scan (solid black); second scan (solid red); and blank electrolyte (dashed black) in 0.1 M TfOH/TFE solvent mixture (3:1 by volume) with a scan rate of 100 mV s^{-1}. Conditions: [*trans*-**2**$^{2+}$] = 0.5 mM.

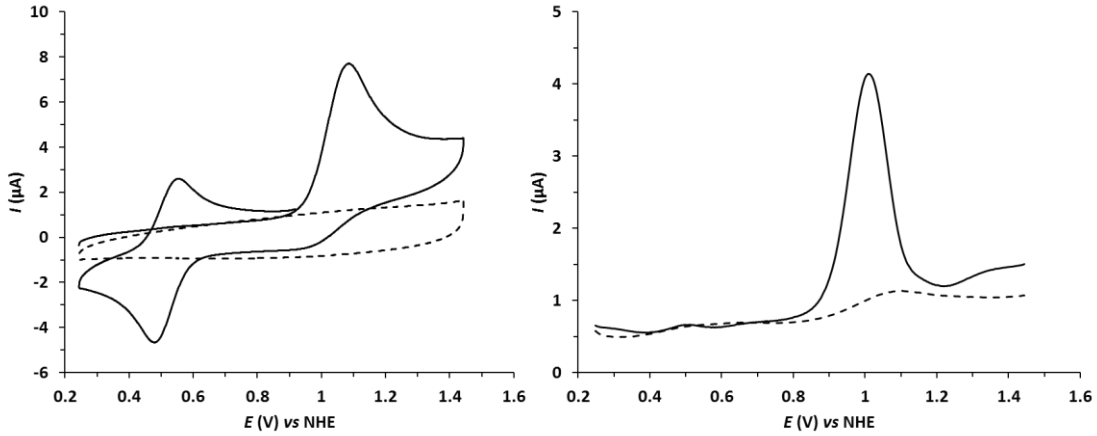

Figure S19. Cyclic Voltammograms (left) and Differential Pulse Voltammograms (right) of *trans*-**1**$^{+}$ (solid black) and blank electrolyte (dashed black) with a scan rate of 100 mV s^{-1}. Conditions: [*trans*-**1**$^{+}$] = 0.5 mM in 0.1 M $TBAPF_6$ in DCM.

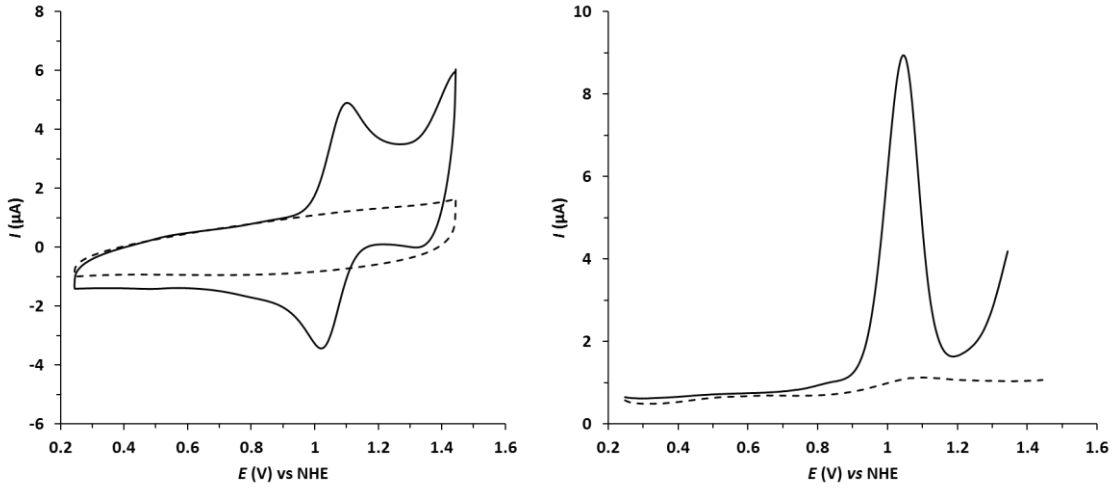

Figure S20. Cyclic Voltammograms (left) and Differential Pulse Voltammograms (right) of *trans*-**2**$^{2+}$ (solid black) and blank electrolyte (dashed black) with a scan rate of 100 mV s^{-1}.Conditions: [*trans*-**2**$^{2+}$] = 0.5 mM in 0.1 M $TBAPF_6$ in DCM.

5. Electrocatalysis

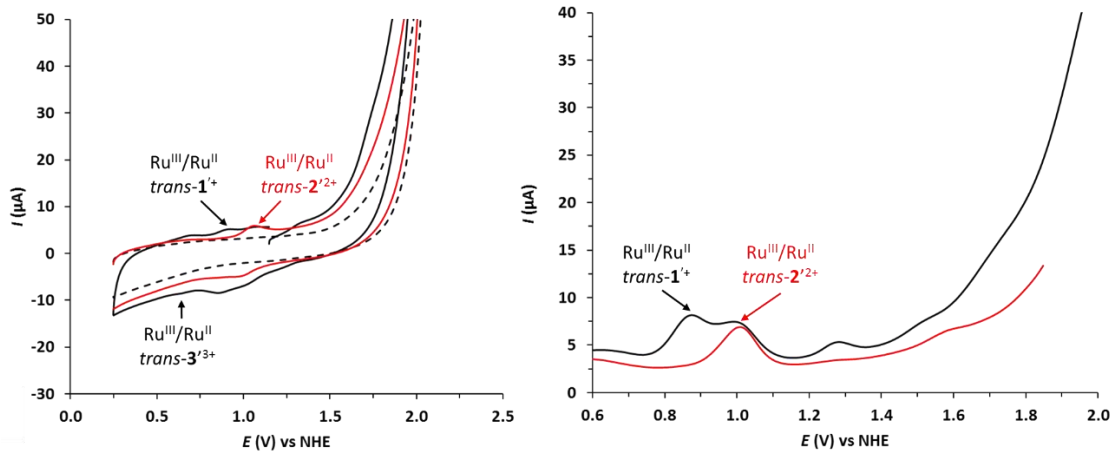

Figure S21. (Left) Cyclic Voltammograms (right) and Differential Pulse Voltammograms (right) of *trans*-**1**'$^{+}$ after oxidation with 1 equivalent of Ce(IV) and incubation during 20 min for generating the proposed species *trans*-**4**'$^{2+}$ (solid black), *trans*-**2**'$^{2+}$ (solid red) and blank (dashed black) in 0.1 M TfOH solution containing 5% of TFE. Conditions: Scan rate of 100 mV s^{-1}, [**Complex**] = 0.3 mM. GC as working electrode, Pt as counter electrode and $Hg/HgSO_4$ as reference electrode.

6. Catalysis with Ce(IV)

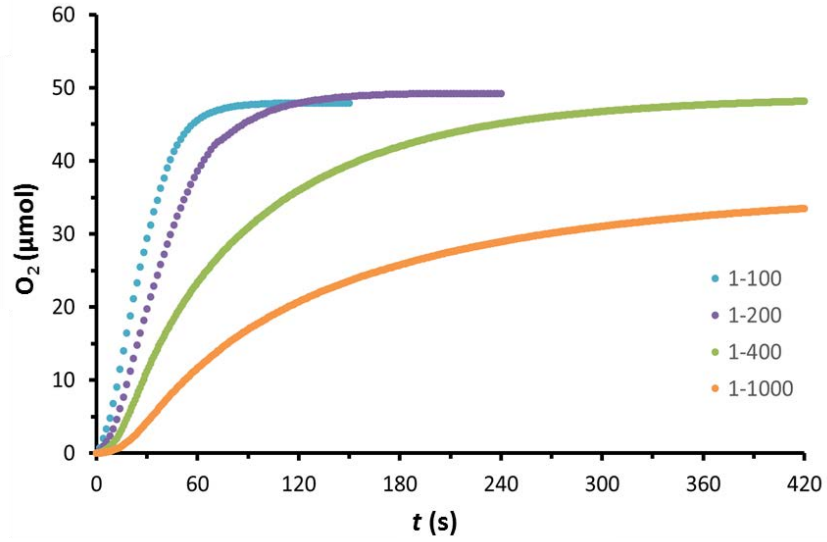

Figure S22. Oxygen evolution profiles after addition of Ce(IV) (111 mg, 0.2 mmol in 150 µL of 0.1 M triflic acid solution) to a suspension of *trans*-**1**$^{+}$, 2 µmol (dashed blue); 1 µmol (dashed purple); 0.5 µmol (solid green); and 0.2 µmol (solid orange) in 1.85 mL of 0.1 M TfOH solution.

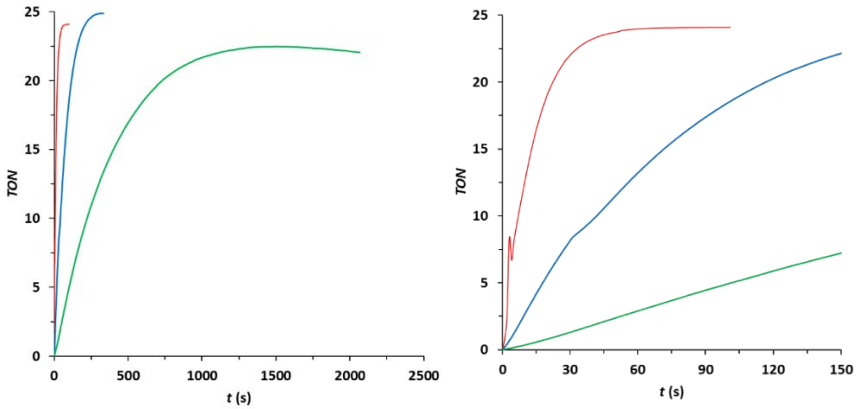

Figure S23. (Left) Monitoring of gas evolution *vs.* time for complex *trans*-**1**$^{+}$ during three consecutive additions of Ce(IV), first injection (red line), second injection (blue line) and third injection (green line). (Right) Zoom in 0-150 s region. Conditions: 1 mM catalyst in 0.1 M TfOH solution (pH 1) and 100 equivalents of CAN at 25 ºC.

7. Computational study

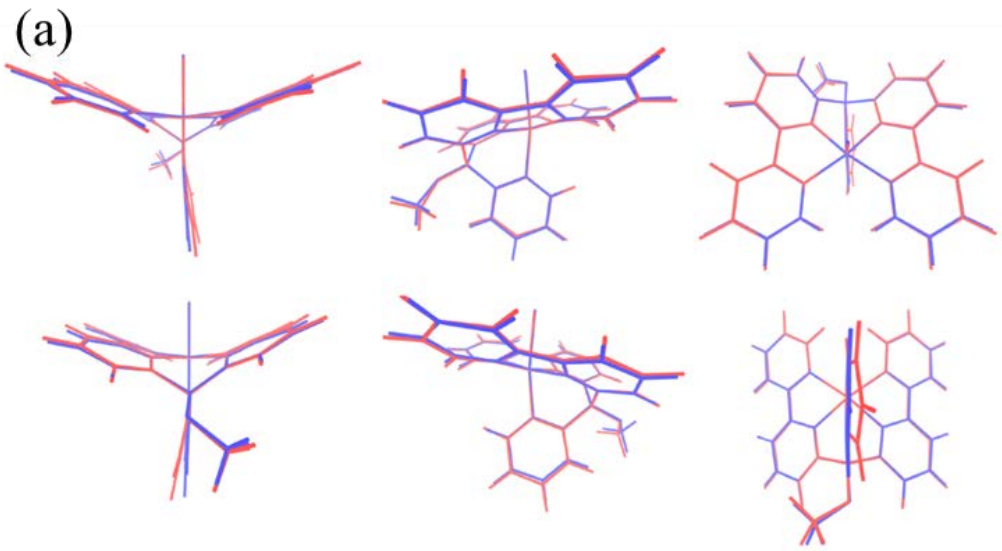

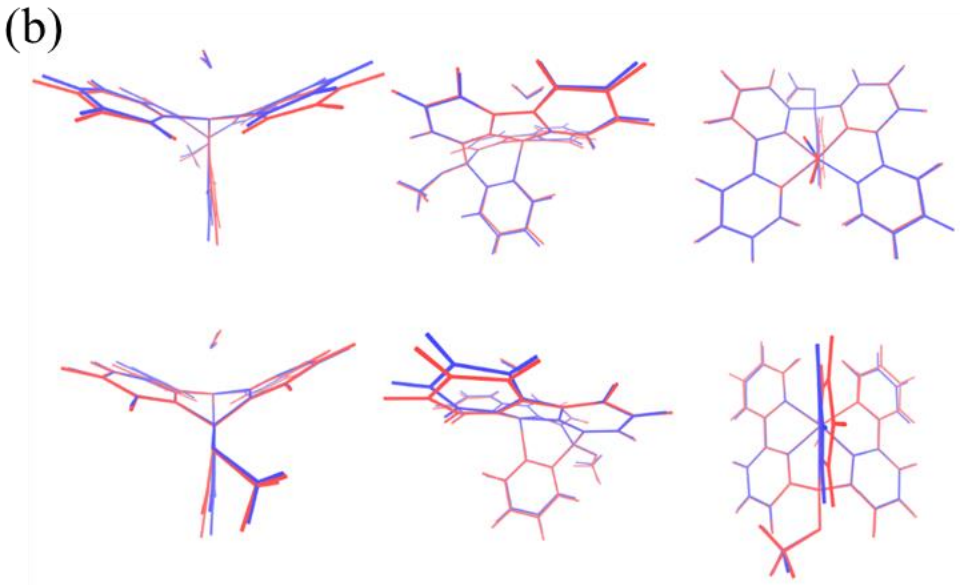

Figure S24. Different views of an overlay of a crystal structure with its calculated one using BP86-D3/def2-TZVP functional for: a) *trans*-**1**$^{+}$ and b) *trans*-**2**$^{2+}$. In both cases a 0.17 Å value for RMDS is obtained.

In the figures below N^{X}-Ru(Y)-OH_Z-Cl describes structure of the complex: X is the number of nitrogen atoms coordinated, Y the Ru oxidation state and Z the number of hydrogens on O (if present).

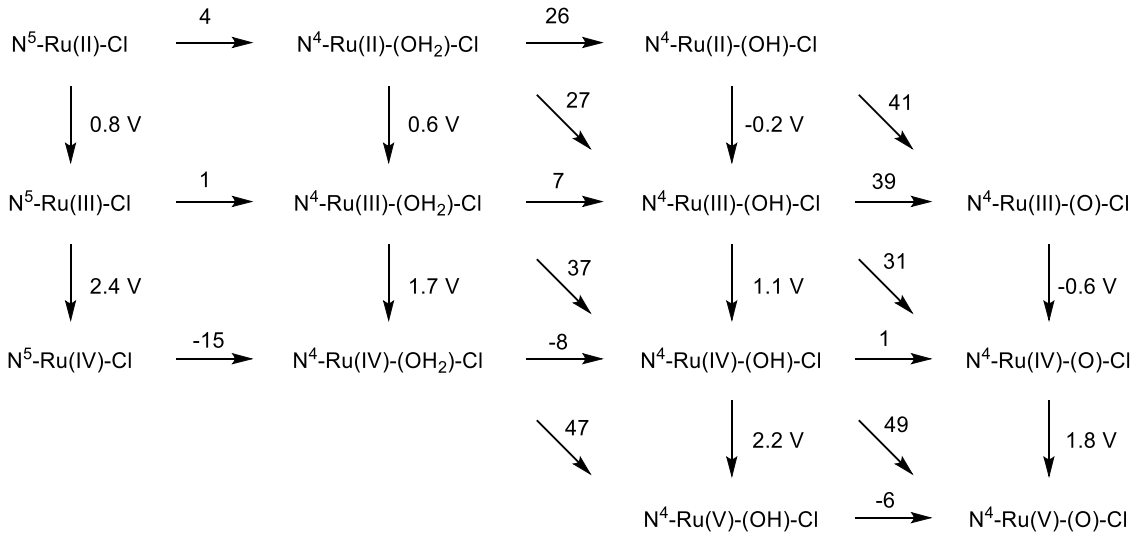

Figure S25. Redox potential (vertical arrows), water association (first horizontal arrow), deprotonations (second and third horizontal arrow) and PCETs (diagonal arrows) associated with the redox events involving complex *trans*-**1**$^{+}$. All energies are given in kcal mol^{-1} and redox potentials in Volt. Note that N^{4}-Ru(IV)-(OH_2)-Cl has a proton transferred from the O to the pyridine-N and is therefore N-H acidic.

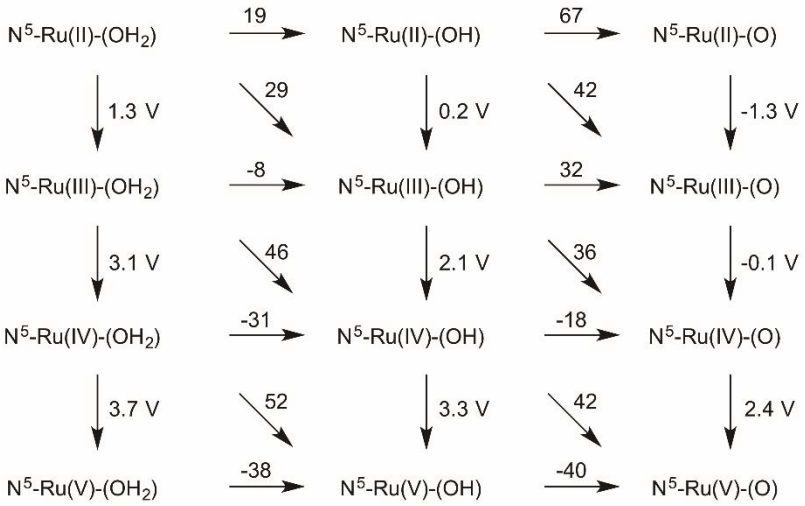

Figure S26. Redox potential (vertical arrows), deprotonations (horizontal arrows) and PCETs (diagonal arrows) associated with the redox events involving complex *trans*-**2**$^{2+}$. All energies are given in kcal mol^{-1} and redox potentials in Volt.

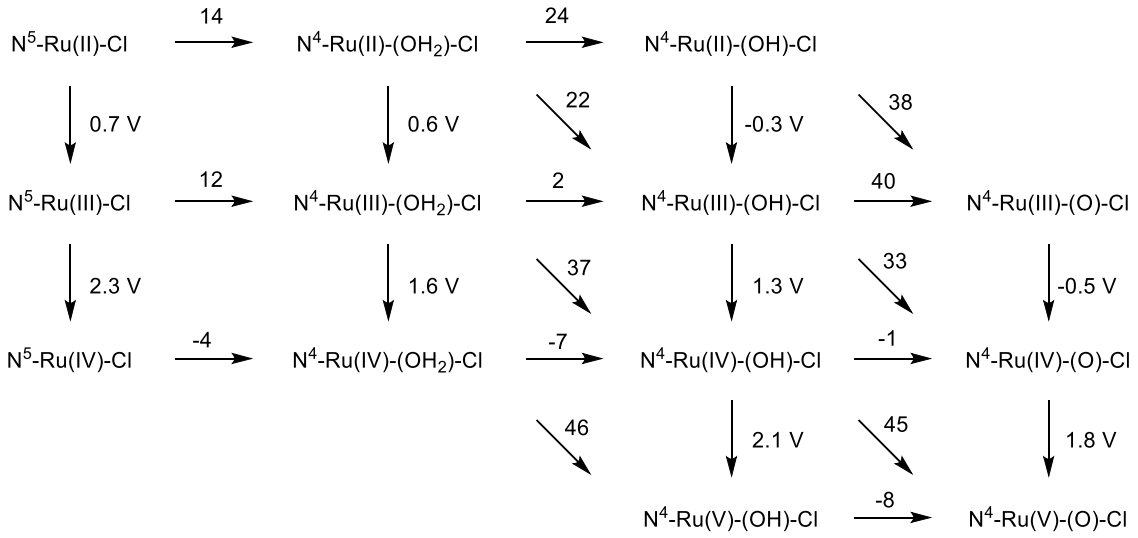

Figure S27. Redox potential (vertical arrows), water association (first horizontal arrow), deprotonations (second and third horizontal arrow) and PCETs (diagonal arrow) associated with the redox events involving complex *trans*-**1**'$^{+}$. All energies are given in kcal mol^{-1} and redox potentials in Volt. Note that N^4-Ru(IV)-(OH_2)-Cl has a proton transferred from the O to the pyridine-N and is therefore N-H acidic.

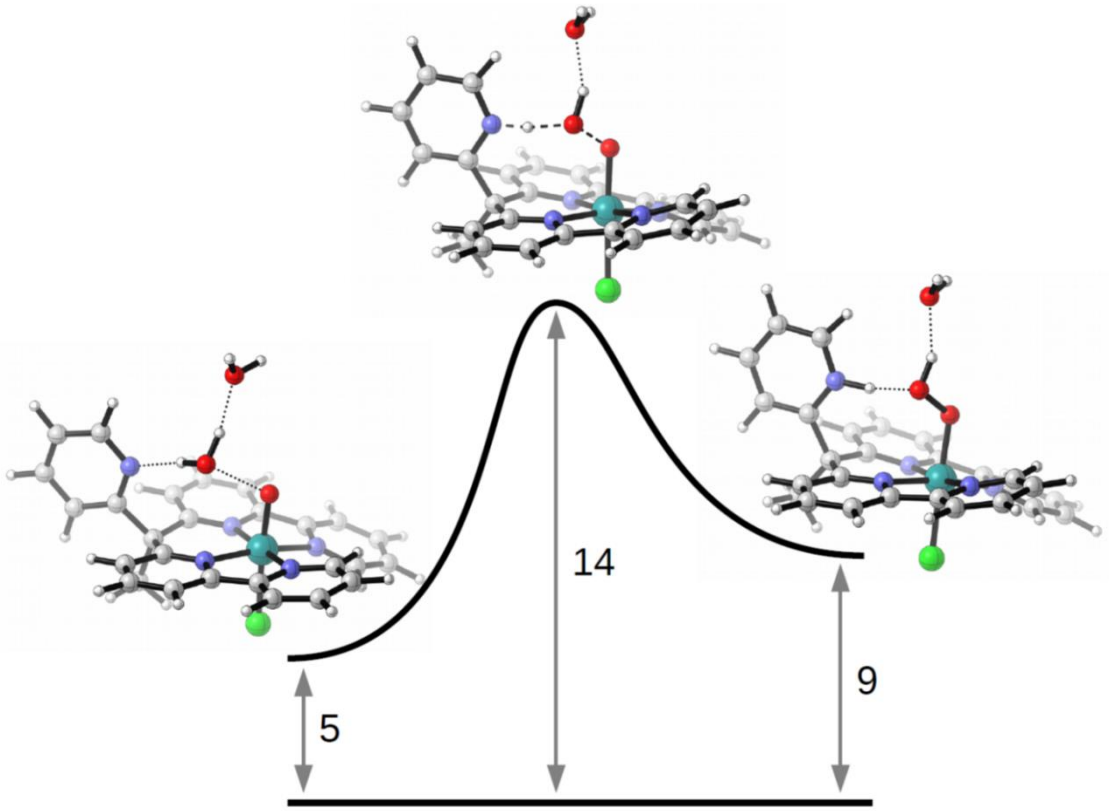

Figure S28. Structures calculated by means of DFT. Energy diagram of the nucleophilic attack of a water molecule to the Ru=O species derived from *trans*-**1**'$^{+}$ to form a Ru-OOH species. The values are given in kcal mol^{-1} with respect to the separated reactants.

8. References

[1] Gil-Sepulcre, M.; Axelson, J.; Aguiló, J.; Solà, L.; Francàs, L.; Poater, A.; Blancafort, L.; Benet-Buchholz, J.; Guirado, G.; Escriche, L.; Llobet, A.; Bofill, R.; Sala, X. *Inorg. Chem.* **2016**, *55*, 11216-11229.

[2] Bachmann, C.; Guttentag, M.; Spingler, B.; Alberto, R. *Inorg. Chem.*, **2013**, *52*, 6055-6061.

[3] ReactLab Kinetics 1.1 from Jplus Consulting Pty Ltd (8 Windsor Road, East Fremantle, WA 6158, Australia).

[4] Ahlrichs, R.; Bär, M.; Häser, M.; Horn, H.; Kölmel, C. *Chem. Phys. Lett*. **1989**, *162*, 165–169.

[5] Becke, A. D. *Phys. Rev. A* **1988**, *38*, 3098–3100.

[6] Perdew, J. P. *Phys. Rev. B* **1986**, *33*, 8822–8824.

[7] Weigend, F.; Ahlrichs, R. *Phys. Chem. Chem. Phys.* **2005**, *7*, 3297–3305.

[8] Grimme, S., Antony, J.; Ehrlich, S.; Krieg, H. *J. Chem. Phys.* **2010**, *132*, 154104.

[9] Becke, A. D. *J. Chem. Phys.* **1993**, *98*, 5648–5652.

[10] Lee, C.; Yang, C.; Parr, R. G. *Phys. Rev. B* **1988**, *37*, 785–789.

[11] Klamt, A.; Schüürmann, G. *J. Chem. Soc. Perkin Trans. 2* **1993**, *0*, 799–805.

[12] (a) Eichkorn, K.; Treutler, O.; Öhm, H.; Häser, M.; Ahlrichs, R. *Chem. Phys. Lett.* **1995**, *242*, 652–660. (b) Eichkorn, K.; Treutler, O.; Öhm, H.; Häser, M.; Ahlrichs, R. *Chem. Phys. Lett.* **1995**, *240*, 283–290. (c) Eichkorn, K.; Weigend, F.; Treutler, O.; Ahlrichs, R. *Theor. Chem. Acc.* **1997**, *97*, 119–124. (d) Weigend, F. *Phys. Chem. Chem. Phys.* **2006**, *8*, 1057–1065.

[13] Sierka, M.; Hogekamp, A.; Ahlrichs, R. *J. Chem. Phys.* **2003**, *118*, 9136–9148.

[14] (a) Tissandier, M. D.; Cowen, K. A.; Feng, W. Y.; Gundlach, E.; Cohen, M. H.; Earhart, A. D.; Coe, J. V. Tuttle, T. R. *J. Phys. Chem. A* **1998**, *102*, 7787–7794. (b) Kelly, C. P.; Cramer, C. J.; Truhlar, D. G. *J. Phys. Chem. B* **2006**, *110*, 16066–16081. (c) Marenich, A. V.; Ho, J.; Coote, M. L.; Cramer, C. J.; Truhlar, D. G. *Phys. Chem. Chem. Phys.* **2014**, *16*, 15068–15106.

[15] Nørskov, J. K.; Rossmeisl, J.; Logadottir, A.; Lindqvist, L.; Kitchin, J. R.; Bligaard, T.; Jónsson, H. *J. Phys. Chem. B* **2004**, *108*, 17886–17892.

[16] Piccinin, S.; Fabris, S. *Phys. Chem. Chem. Phys.* **2011**, *13*, 7666–7674.

[17] Sinnechker, S.; Rajendran, A.; Klamt, A.; Diedenhofen, M.; Neese, F. *J. Phys. Chem. A* **2006**, *110*, 2235-2245.

[18] Marenich, A. V.; Cramer, C. J.; Truhlar, D. G. *J. Phys. Chem. B* **2009**, *113*, 6378-6396.

[19] Neese, F. WIREs Comput Mol Sci **2012**, *2*, 73–78.

[20] CrysAlisPro Software system; Agilent Technologies, vers. 171.37 Oxford, UK, **2014**.

[21] Altomare, A.; Burla, M. C.; Camalli, M.; Cascarano, G. L; Giacovazzo, C.; Guagliardi, A.; Moliterni, A. G. G.; Polidori, G.; Spagna, R. J. *Appl. Cryst.*, **1999**, *32*, 115-119.

[22] Sheldrick, G. M. *Acta Cryst.*, **2008**, *A64*, 112-122.

CHAPTER IV

Synthesis of new Cu^{II} complexes bearing bipyridyl-diamidate ligands. Characterization and water oxidation catalysis.

New mononuclear Cu^{II} complexes containing a bipyridyl framework that incorporates a strong σ-donor amidate scaffold are developed and fully characterized in this work. The electrochemical properties and their catalytic behavior towards water oxidation (WO) are presented. The effect of the proximity of a pendant sulfonate group to the copper centre regarding the catalytic performance is also discussed in this chapter. Moreover, a detailed comparison with the most relevant Cu-based WO catalysts is also reported, showing how the introduction of σ-donor scaffolds coordinating the Cu centre can provoke a decrease of the overpotentials needed to perform WO catalysis.

PAPER C: Synthesis of new Cu^{II} complexes bearing bipyridyl-diamidate ligands. Characterization and water oxidation catalysis.

Gil-Sepulcre, M.; Garrido-Barros, P.; Bofill, R.; Sala. X.; Llobet, A. (*MS in preparation*)

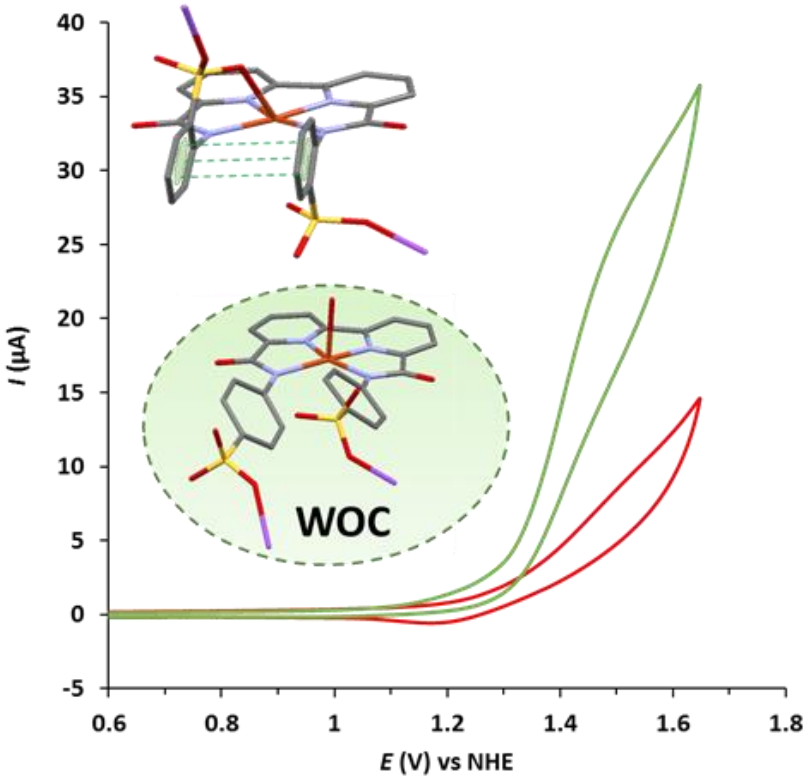

Abstract: Two new tetradentate ligands, 4,4'-(([2,2'-bipyridine]-6,6'-dicarbonyl)bis(azanediyl)) dibenzenesulfonic acid (*p*-L) and its homologue containing the sulfonate group at *ortho* position with respect to the amidate scaffold (*o*-L), have been synthesized. These new ligands have been used for the preparation of the complexes of general formula $[(L)Cu^{II}]^{2-}$ (L = *p*-L (**1**$^{2-}$); L = *o*-L (**2**$^{2-}$)), which have been fully characterized by X-ray diffraction and electrochemical techniques. At pH 11.4 only complex **1**$^{2-}$ exhibits a raise in the current associated with water oxidation (WO) at an overpotential of 835 mV confirmed by O_2-detection experiments during 1 hour of bulk electrolysis at 1.6 V vs. NHE. The comparison with other Cu-based catalysts reveals that strong σ-donor groups not only lower the Cu(III)/Cu(II) redox potential but also the overpotential for the WO reaction.

Introduction

Molecular water oxidation (WO) driven by transition metal complexes[1] is a promising and active field at present for its implication in the obtaining of solar fuels from water and sunlight.[2] In particular, developing an efficient and robust water splitting device using cheap and abundant non-noble metal catalysts is still a great challenge for the scientific community. Several first-row transition metal complexes such as iron[3], cobalt,[4] manganese[5] and copper[6] have been developed and tested towards WO, becoming a promising alternative to the extensively studied ruthenium[7] and iridium[8] catalysts. In particular, molecular copper-based complexes are relative new actors in this field and have become attractive candidates for WO catalysis during the last years due to their earth-abundance, relative easy synthesis and the available exhaustive studies on their coordination chemistry.

Mayer and co-workers first reported Cu(II) complexes bearing a simple 2,2'-bipyridine ligand, which were capable of oxidizing water into dioxygen.[9] Since this first work, the bipyridine moiety has been modified for its use in the synthesis of effective Cu(II) WO catalysts.[10] In these catalysts hydroxyl pendant groups were introduced, which were proposed to lower the overpotentials, facilitating the proton coupled electron transfer (PCET) process and stabilizing the key intermediates. Recently, Llobet and co-workers reported a family of new Cu(II) complexes that are capable to drastically downshift the overpotential until a value as low as 170 mV.[11] The key for the unprecedented overpotential achieved with these catalysts is the presence of four amidate groups in the ligand, which decrease the potential of the Cu(III)/Cu(II) couple necessary for performing WO. Furthermore, the non-innocent nature of the ligand allows the control of the overpotential by changing the substituents present in the aromatic rings.

Herein, we present the synthesis and full characterization of a new family of Cu^{II} complexes [(*p*-L)Cu]$(Na^+)_2$ (**1**$^{2-}$) and [(*o*-L)Cu]$(Na^+)_2$ (**2**$^{2-}$) containing two new tetra-anionic ligands 4,4'-(([2,2'-bipyridine]-6,6'-dicarbonyl)bis(azanediyl)) dibenzenesulfonic acid (*p*-L) and 2,2'-(([2,2'-bipyridine]-6,6'-dicarbonyl)bis(azanediyl))dibenzenesulfonic acid (*o*-L), which differ in the position of the sulfonate group with respect to the amide moiety. These complexes have been designed containing two negative coordinated amidate scaffolds to lower their overpotentials and enhance their WO catalytic activity. Furthermore, we also compare their electrochemical properties with those of related

homogeneous Cu(II) complexes and analyze the key factors that control their catalytic performance in WO.

Synthesis and characterization of ligands and complexes

The new ligands 4,4'-(([2,2'-bipyridine]-6,6'-dicarbonyl)bis(azanediyl)) dibenzenesulfonic acid (*p*-L) and 2,2'-(([2,2'-bipyridine]-6,6'-dicarbonyl)bis(azanediyl))dibenzenesulfonic acid (*o*-L) were synthetized *via* the reaction of the corresponding sulfanilic acid with [2,2'-bipyridine]-6,6'-dicarboxylic acid that has been previously converted into its acyl chloride form by reaction with $SOCl_2$ (Scheme 1). The ligands *p*-L and *o*-L were obtained as white powders in high yield (82 % and 85 %, respectively; a detailed description of their synthetic pathways can be found in the Supporting Information). Both ligands have been fully characterized by ^{1}H-NMR, ^{13}C-NMR and ESI-MS (Figures S1-13). It is interesting to note the 2 ppm downfield shift of the amide proton observed in the ^{1}H-NMR spectrum of *o*-L (vs *p*-L) due to the proximity of the sulfonate groups. Suitable crystals for X-ray diffraction analysis were also obtained for *o*-L by slow diffusion of EtOH in an aqueous solution of the ligand (Figure S16 and Table S1).

A schematic drawing of the synthetic route employed for the preparation of the complexes $\mathbf{1}^{2-}$ and $\mathbf{2}^{2-}$ is depicted in Scheme 1. Synthesis of $\mathbf{1}^{2-}$ involved the presence of $NaOH_{(aq.)}$ in MeOH as a base to deprotonate the amidate groups, which react with Cu(II) perchlorate to form the corresponding complex. The purification was carried out *via* evaporation of MeOH and crystallization by slow diffusion of acetone into the remaining aqueous solution, yielding $\mathbf{1}^{2-}$ as green crystals. A moderate yield (32%) was obtained, which could be related with the partial conversion of the Cu^{2+} precursor into copper oxide in basic media.[12] The same synthetic strategy was employed for the preparation of $\mathbf{2}^{2-}$, obtaining the desired product as a blue powder in a similar yield (25%). Both complexes were characterized by X-ray diffraction (Figure 1), UV-Vis spectroscopy (Figure 2) and mass spectrometry (Figures S14 and S15).

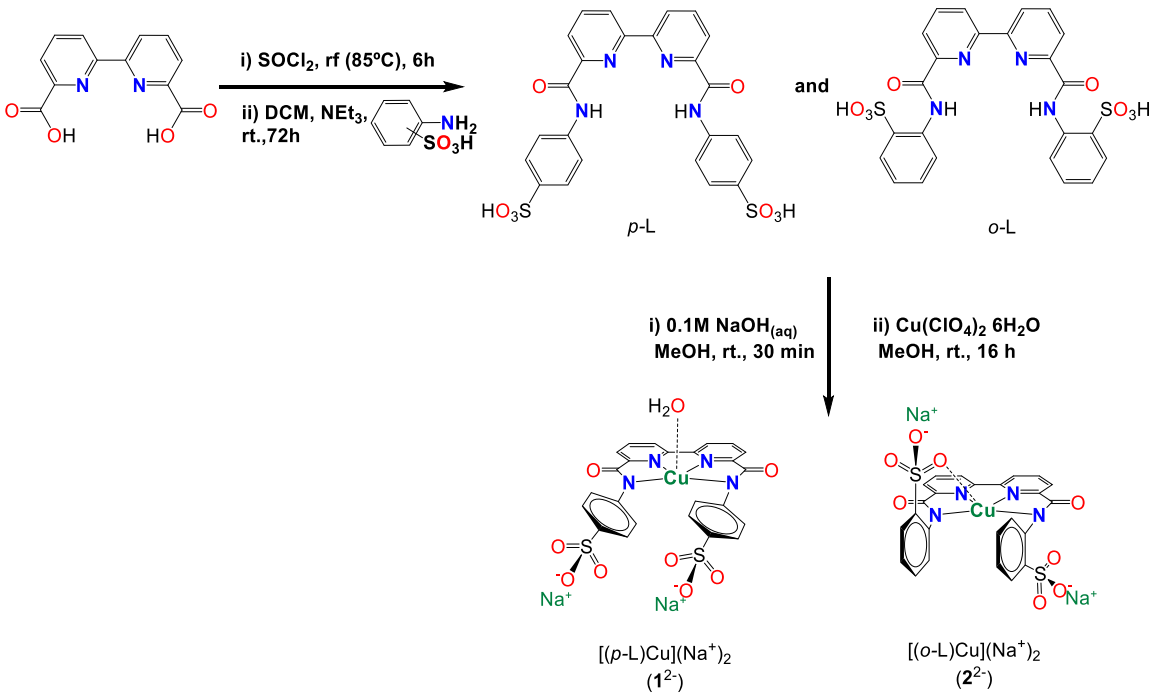

Scheme 1. Schematic drawing of the synthesis of ligands *p*-L and *o*-L and their corresponding Cu(II) complexes.

The X-Ray structure of complex $\mathbf{1}^{2-}$ (Figure 1, left, and Table S3) confirmed the presence of a Cu(II) metal centre with a distorted square planar geometry, with the four N donor atoms placed on the base of the pyramid and with the apical position occupied by a close O atom probably coming from one water molecule, with a Cu–O bond distance of 2.31 Å. All Cu–N_{bpy} distances are 1.95 Å and close to 2.0 Å for the Cu–N_{amide} bonds, thus manifesting a strong coordination to the metal centre. On the other hand, the rigidity of the *p*-L scaffold is made patent when observing the N_{amide}–Cu–N_{amide} (119.69º) and N_{bpy}–Cu–N_{bpy} (78.27º) angles, which are far from the ideal square planar geometry (90º).

Complex $\mathbf{2}^{2-}$ (Figure 1, right, and Table S2) also displays a distorted square planar geometry, showing similar Cu – N bond distances (1.95-2 Å) and N_{amide}–Cu–N_{amide} (120.78º) and N_{bpy}–Cu–N_{bpy} (78.49º) angles to those in $\mathbf{1}^{2-}$. However, some significant differences arise between $\mathbf{1}^{2-}$ and $\mathbf{2}^{2-}$. First, the apical position of $\mathbf{2}^{2-}$ is occupied by an oxygen atom coming from the sulfonate moiety (instead of the water molecule observed in $\mathbf{1}^{2-}$), with a Cu–O bond distance of 2.61 Å. Then, weak π-π stacking interactions at 3.77 Å between both phenyl groups take place.[13] It is also interesting to note that the disposition of the sulfonate moieties in *para* with respect to the amide moieties facilitates the formation of an interesting polymeric-type 2D framework connected through the sulfonate groups (Figure S17).

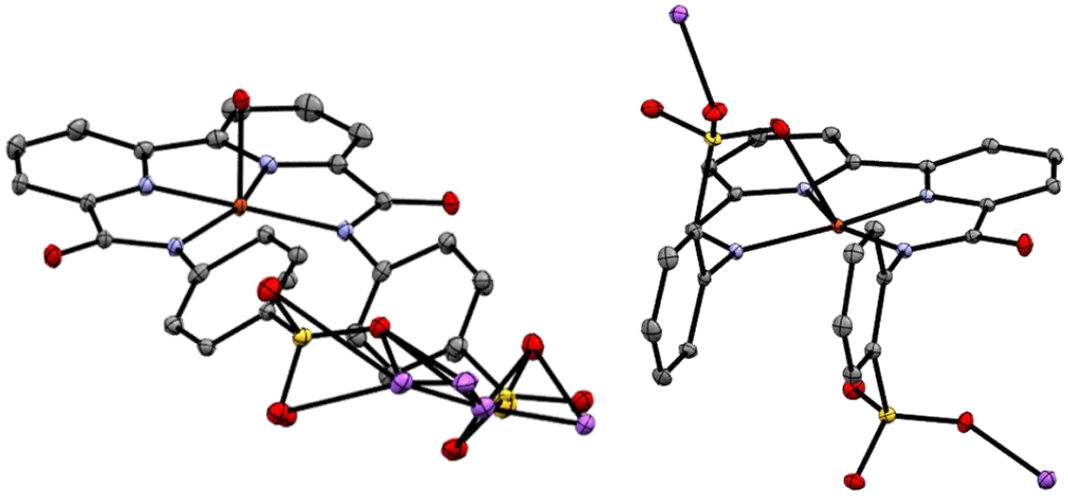

Figure 1. ORTEP representation of $\mathbf{1}^{2-}$ (left) and $\mathbf{2}^{2-}$ (right) at 50% probability level. The solvent molecules and hydrogen atoms have been omitted for clarity. Colour code: C, grey; N, blue; O, red; S, yellow; Na, purple; Cu, orange.

The UV-Vis spectra of $\mathbf{1}^{2-}$ and $\mathbf{2}^{2-}$ are presented in Figure 2. The spectra are typical for similar Cu(II) complexes,[6a,14] exhibiting intense absorption bands between 250-400 nm, corresponding to π-π* transitions of the ligands, and less intense absorptions in the visible region, with a maximum at 639 and 636 nm for $\mathbf{1}^{2-}$ and $\mathbf{2}^{2-}$, respectively, corresponding to MLCT and d-d transition bands.

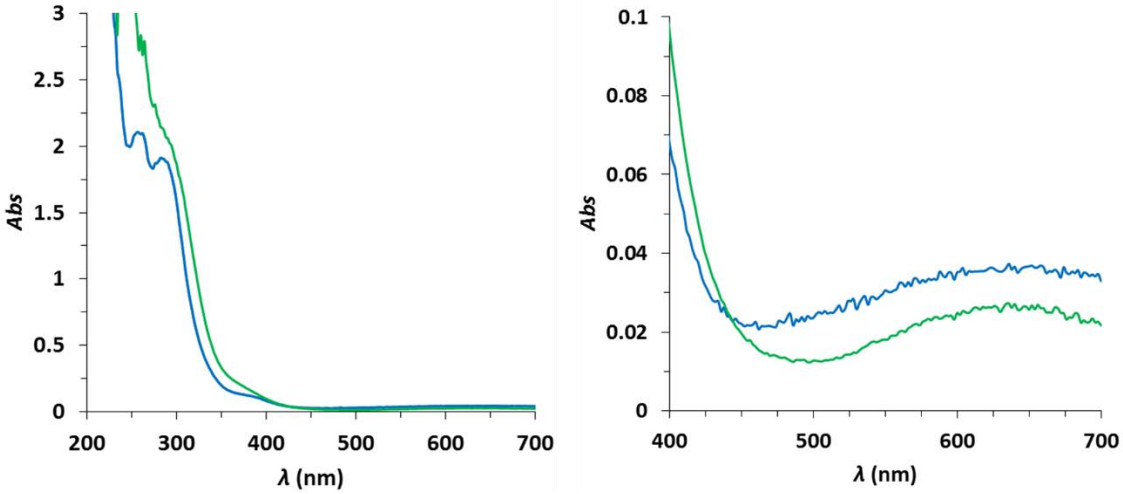

Figure 2. (Left) UV-vis spectra of $\mathbf{1}^{2-}$ (green line) and $\mathbf{2}^{2-}$ (blue line). **(Right)** UV-vis spectra enlargement of the visible region for both copper complexes. Conditions: [**complex**] = 0.1 mM in 0.1 M phosphate buffer (pH 11.4).

Electrochemical studies

The redox properties of both complexes were first investigated in DMF by electrochemical techniques. All the potentials presented in this work are referenced vs. NHE by adding 0.648 V to the measured potential (see Experimental Section for further details). Figure 3 shows the CVs for *p*-L, *o*-L, $\mathbf{1}^{2-}$ and $\mathbf{2}^{2-}$. The initial anodic scan for $\mathbf{1}^{2-}$ shows two irreversible electron transfer processes at E_{ap1} = 1.21 V and E_{ap2} = 1.42 V. In the case of $\mathbf{2}^{2-}$, these waves appear at $E_{ap1'}$ = 1.00 V and $E_{ap2'}$ = 1.19 V, thus showing a smaller shift (195 mV) between them compared to $\mathbf{1}^{2-}$ (210 mV). The presence of two anodic peaks has also been confirmed by DPV (Figure S18). These waves observed in organic media (DMF) were assigned respectively to the Cu(III)/Cu(II) electron transfer process and the ulterior oxidation of the coordinated ligand. As can be observed in Figure 3, the CV measurement of the free ligands exhibits an irreversible wave at E_{pa} = 1.29 V for *p*-L and $E_{pa'}$ = 1.24 V for *o*-L, therefore suggesting their non-innocent redox character. The difference observed in the E_{ap2} values (230 mV) between complexes $\mathbf{1}^{2-}$ and $\mathbf{2}^{2-}$ suggests that the ligand oxidation may occur in the phenyl moiety, in contrast with the similar values in the potentials which would be expected if the oxidation was centered in the similar bypyridyl rings. However, this option can not be completely ruled out. Formation of radical cations in phenyl moieties during water oxidation catalysis has been previously reported in the literature.[11]

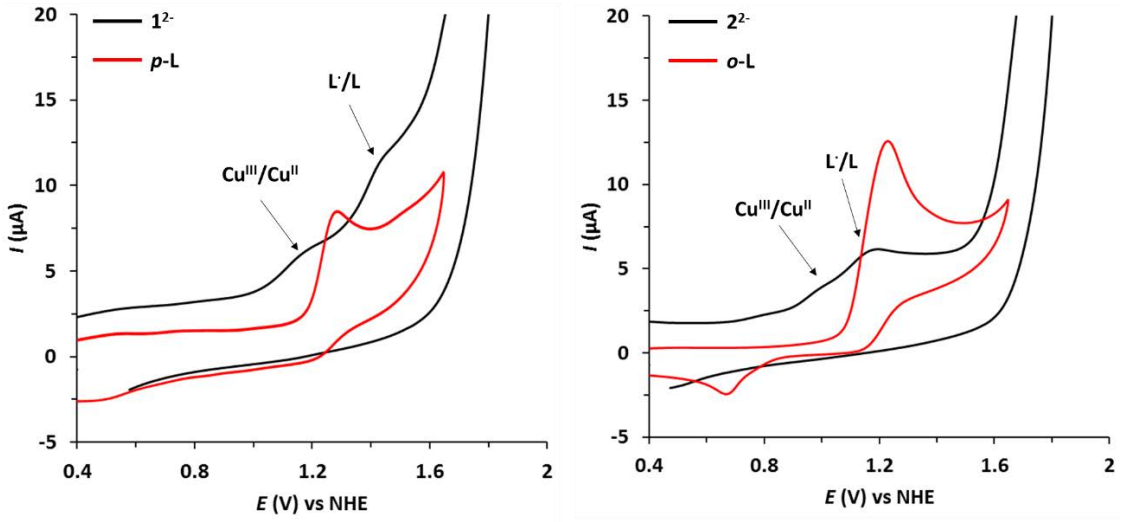

Figure 3. (**Left**) Cyclic Voltammograms of $\mathbf{1}^{2-}$ (black line) and *p*-L (red line). (**Right**) Cyclic Voltammograms of $\mathbf{2}^{2-}$ (black line) and *o*-L (red line). Conditions: scan rate of 100 mV/s, 1 mM of complex or ligand in DMF containing 0.1 M of TBAPF. Glassy Carbon

disk as working electrode, Pt disk as counter electrode and $Hg/HgSO_4$ as reference electrode.

The potentials of the Cu(III)/Cu(II) couples of complexes $\mathbf{1}^{2-}$ and $\mathbf{2}^{2-}$ were compared with those from related complexes.[11] Thus, $[(L1)Cu]^{2-}$ (L1= N_1,N_1'-(1,2-phenylene)bis(N_2-methyloxalamide), see Figure 7B below for a drawing of this complex) in MeCN shows this wave at 0.25 V vs. NHE, which is clearly lower respect to our complexes (1.21 V and 1.00 V vs. NHE for $\mathbf{1}^{2-}$ and $\mathbf{2}^{2-}$, respectively) due to the presence of a strong σ-donor tetra-anionic ligand.

In case of $\mathbf{1}^{2+}$, the first and second oxidation waves were found to be non-reversible in a scan rate window of 25-500 mV/s (Figure S19). In contrast, the waves of $\mathbf{2}^{2-}$ turned reversible at higher scan rates (Figure S20). A higher increase in the current of the second oxidation wave of $\mathbf{1}^{2-}$ with respect to $\mathbf{2}^{2-}$can be also appreciated. This behavior is probably related with a higher reactivity of complex $\mathbf{1}^{2-}$ respect to $\mathbf{2}^{2-}$, which after the formation of the highly reactive radical cation $[(p\text{-}L^{\bullet})Cu(III)]^{-}$ can oxidize DMF or residual H_2O present in the solvent, provoking an increase in the current, while in case of $\mathbf{2}^{2-}$ this radical anion might be more stable. The higher reactivity of $\mathbf{1}^{2-}$ suggests that it may be more promising for its application in WO catalysis.

On the other hand, in the corresponding cathodic scan of complex $\mathbf{1}^{2-}$, CVs showed the presence of one irreversible reduction wave at an E_{pc3} value of -0.35 V, whereas in the case of complex $\mathbf{2}^{2-}$ this irreversible redox event happened at an $E_{pc3'}$ value of -0.57 V (Figure S22). Both reduction processes can be assigned to the reduction of Cu(II) to Cu(I). The observed irreversible character of the Cu(II)/Cu(I) wave is highly consistent with the oxidation wave observed around E = 0.34 V in the corresponding anodic scan, which is related with the degradation of the complex, which releases Cu^{2+}. This behavior is also consistent with the CVs performed at slow scan rates (25 and 50 mV/s) between 0.6 and -0.9 V vs. NHE (Figure S22), where the Cu(II)/Cu(I) couple of the free Cu^{2+} ions is clearly observed after coming back from reductive potentials. This behavior can be related to the preferred tetrahedral geometry of Cu(I) complexes. Thus, the reduction of the square pyramidal Cu(II) complexes brings the need of Cu(I) to adopt a tetrahedral disposition, which is not allowed by the highly rigid planar ligand, thus finally provoking the breakage of the complex and subsequent release of Cu(I) ions.

Electrocatalytic measurements

In order to test the electrocatalytic activity of complexes $\mathbf{1}^{2-}$ and $\mathbf{2}^{2-}$, their electrochemical behavior was analyzed at different pH values (Figures S23-25). The experiments performed at pH 11.4 were repeated using a Boron Doped Diamond (BDD) electrode as working electrode, with the objective of avoiding the residual current derived from the oxidation of the glassy carbon electrode (Figure 4). Under basic conditions (pH 11.4), $\mathbf{1}^{2-}$ displays an irreversible oxidation wave at 1.38 V, and $\mathbf{2}^{2-}$ at 1.29 V according to DPV measurements (Figure 4). The experiments performed at different pH values showed the pH-independent character of this electron-transfer process. (Figure S26). This behavior suggests that the water molecule in $\mathbf{1}^{2-}$ that displays a contact (~2.3 Å) with the Cu centre according to its solid state structure is not coordinating the Cu in solution at the working pH values (7-11.4) and therefore PCET events are not observed. This is also in agreement with the similar redox potentials observed for both complexes, in contrast with the different values that would be expected between them if an aqua/hydroxo/oxo ligand was coordinating the copper centre in $\mathbf{1}^{2-}$.

For $\mathbf{1}^{2-}$, this redox event is followed by a steep rise in the current associated at the same time with an increase in the slope, which is tentatively assigned to electrocatalytic water oxidation. In contrast, no catalytic response is apparently observed for $\mathbf{2}^{2-}$ with respect to the blank.

IV

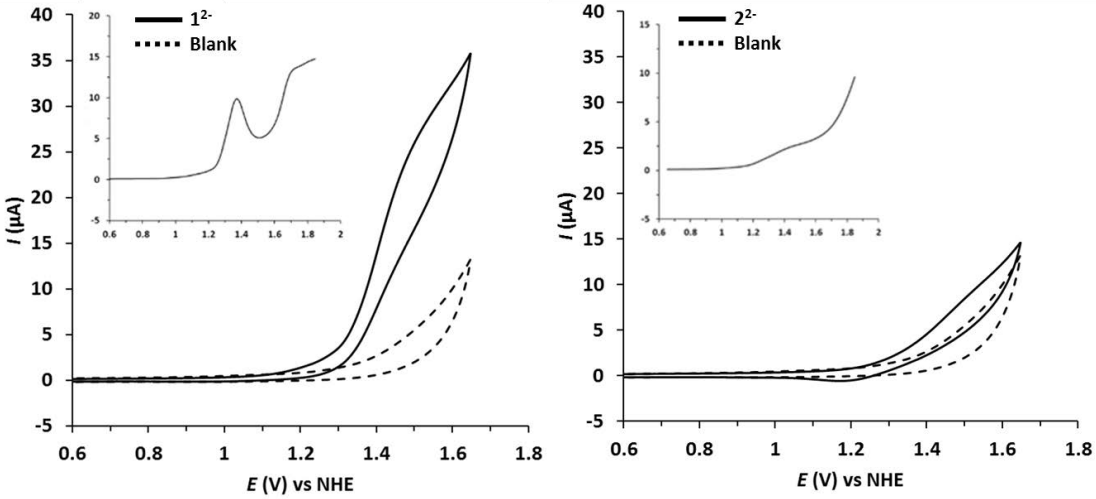

Figure 4. Cyclic Voltammograms of $\mathbf{1}^{2-}$ (left) and $\mathbf{2}^{2-}$ (right) in 0.1 M phosphate buffer pH 11.4. Black dashed line corresponds to a blank with no catalyst. (*Inset*) Differential Pulse Voltammograms for $\mathbf{1}^{2-}$ and $\mathbf{2}^{2-}$. Conditions: scan rate of 100 mV/s, [**Complex**] = 1 mM. BDD disk as working electrode.

The onset potential for the oxidation of the free ligands, 1.03 V for *o*-L and 1.05 V for *p*-L (Figure S28), suggests that the first oxidation process occurring in aqueous solution before the catalytic wave for $\mathbf{1}^{2-}$ (Figure 4, left) is a ligand-based oxidation to form a radical anion. The oxidation of a non-innocent redox ligand before the oxidation of Cu(II) to Cu(III) is also supported by previously detailed mechanistic studies performed with related Cu complexes.[15] Thus, the second oxidation wave can be therefore associated with the formation of Cu(III), together with the coordination or approximation of an hydroxide ligand onto Cu(III) and a raise in the current derived from the oxidation of water into dioxygen. All these processes are depicted in equations 1-3 below.

$$[(p\text{-L})Cu^{II}]^{2-} \rightarrow [(p\text{-L}^{\bullet})Cu^{II}]^{-} + 1e^{-} \quad (1)$$

$$[(p\text{-L}^{\bullet})Cu^{II}]^{-} \rightarrow [(p\text{-L}^{\bullet})Cu^{III}] + 1e^{-} \quad (2)$$

$$[(p\text{-L}^{\bullet})Cu^{III}] + OH^{-} \rightarrow [(p\text{-L}^{\bullet})Cu^{III}(OH)]^{-} \quad (3)$$

Oxygen evolution by $\mathbf{1}^{2-}$ and $\mathbf{2}^{2-}$ was investigated by using controlled potential electrolysis (CPE) at 1.6 V vs. NHE using a large surface area boron-doped diamond plate working electrode (~1.5 cm^2) with 1 mM catalyst buffer solutions. Oxygen was detected by using a Clark-type electrode and was monitored at three different pH values (7, 9 and 11.4). However, in strong agreement with the electrocatalytic waves observed in the respective CV measurements, no oxygen evolution above background was observed below pH 11.4 (Figures S29 and S30).

In the case of complex $\mathbf{1}^{2-}$, a steady formation of dioxygen was detected immediately after starting the CPE experiment at pH 11.4 (Figure 5, left). No significant induction time was observed in the catalytic curve, supporting the homogeneity of $\mathbf{1}^{2-}$, which is capable of oxidizing water into dioxygen with an overpotential of 835 mV according to DPV measurements (Figure 4, *inset*). Catalyst $\mathbf{1}^{2-}$ achieves a moderate activity towards water oxidation, and remains active for 100 min. A Faradic efficiency of 19 % was calculated at t = 60 min (Figure S31, left). This value manifests the presence of a deactivation process that competes with WO catalysis. CV measurements performed after the CPE experiment (Figure S32) confirm that a deactivation process of the catalyst is the main responsible for the low Faradaic efficiency and end of catalysis after 100 min (Figure S31, right).

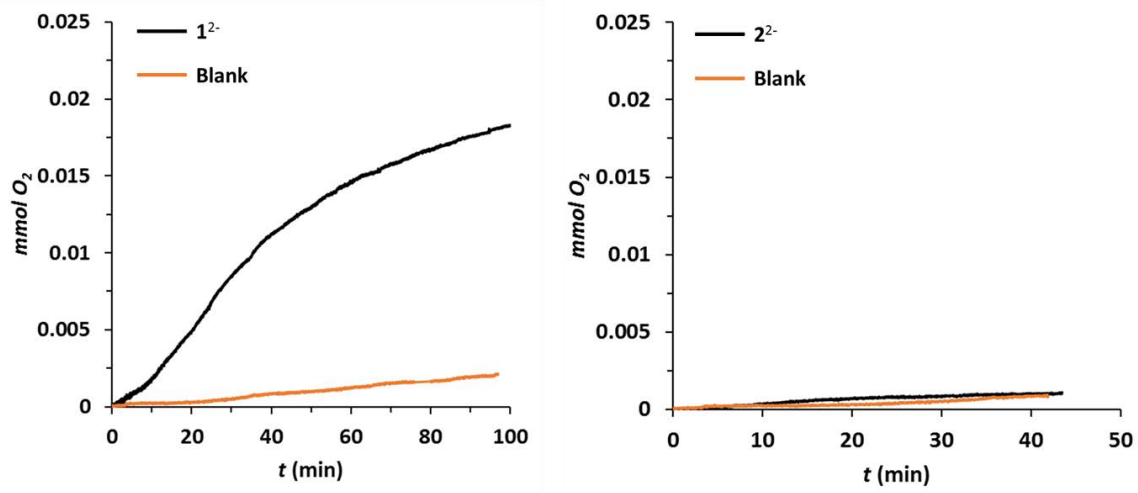

Figure 5. Oxygen evolution measurements given in mmol O_2 *vs.* time (min) for complexes $\mathbf{1}^{2-}$ (left) and $\mathbf{2}^{2-}$ (right) at 1.5 mM concentration using a Clark probe electrode during a CPE at 1.6 V vs. NHE in 0.1 M phosphate buffer pH 11.4. Blank data in the absence of complex is shown in orange. BDD plate as working electrode, Pt mesh as counter electrode and AgCl as reference electrode.

It is interesting to note that no higher amounts of oxygen compared to the blank were detected during the CPE with $\mathbf{2}^{2-}$ under the same conditions than $\mathbf{1}^{2-}$ (Figure 5, right), confirming that $\mathbf{2}^{2-}$ is not active towards water oxidation. The lack of reactivity of $\mathbf{2}^{2-}$ may be related with the presence of a sulfonate moiety at *ortho* position with respect to the amidate group, which could obstruct the approximation or coordination of OH^- onto the copper centre, thus impeding WO catalysis. This is in good agreement with the absence of current above the blank in the CV experiments performed at pH 11.4 (Figure 4 and Figures S25 and S27), and its X-ray structure, where an interaction between the sulfonate group and Cu^{2+} is observed (Figure 1, right).

To evaluate the stability and homogeneity of $\mathbf{1}^{2-}$ and $\mathbf{2}^{2-}$, several CV cycles (25) were performed on a 1 mM solution in 0.1 M phosphate buffer pH 11.4 (Figure 6). In the case of $\mathbf{1}^{2-}$, a decrease in the current of the electrocatalytic wave was observed during the cycles, probably due to the previously mentioned deactivation process. In contrast, $\mathbf{2}^{2-}$ experiences a slower decrease in the current, thus showing a better stability after oxidation to Cu(III).

Both electrodes were immersed in a new catalyst-free 0.1 M phosphate buffer pH 11.4 solution and CVs were registered (Figure 6, *insets*). In comparison with the blank

experiments, no catalytic response derived from the formation of active heterogeneous copper oxide materials on the surface of the BDD electrode was observed.

Glassy carbon electrodes subjected to catalytic water oxidation electrolysis during 20 minutes at 1.6 V vs. NHE with 1.5 mM solutions of complexes $\mathbf{1}^{2-}$ and $\mathbf{2}^{2-}$ were also analyzed by scanning electron microscopy (SEM) and energy dispersive X-ray spectroscopy (EDX), showing again no evidence of nanoparticles, film formation or copper-based heterogeneous materials over the surface (Figures S35-37). These results support the homogeneity of the catalytic active species.

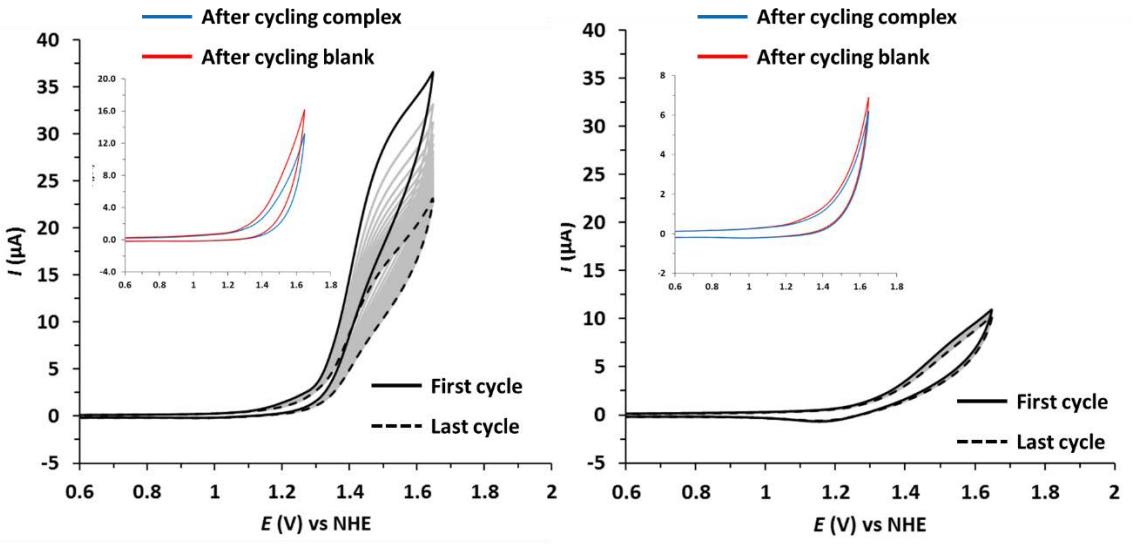

Figure 6. Evolution of CV profiles of $\mathbf{1}^{2-}$ (left) and $\mathbf{2}^{2-}$ (right) in 0.1 M phosphate buffer pH 11.4 after 25 cycles. (*Inset*) CV measurements with a BDD electrode that has performed the previous 25 cycles of the complex (blue line) or of a blank solution (red line) immersed in a freshly-prepared catalyst-free 0.1 M phosphate buffer pH 11.4. Conditions: scan rate of 100 mV/s, [**Complex**] = 1 mM. BDD as working electrode.

In addition, the possibility of a electrocatalytic response due to the presence of free Cu^{2+} was also discarded by comparing the CV of $Cu(ClO_4)_2$ in phosphate buffer at pH 11.4 with complexes $\mathbf{1}^{2-}$ and $\mathbf{2}^{2-}$(Figure S27). These tests revealed an onset potential similar to the blank and approximately 300 mV shifted towards higher potentials with respect to the electrocatalytic wave of $\mathbf{1}^{2-}$. It should be emphasized that $\mathbf{2}^{2-}$ does not show a raise in current density with respect to $Cu(ClO_4)_2$ or the blank.

In order to investigate the factors that affect the WO catalytic activity, the behavior of complexes $\mathbf{1}^{2-}$ and $\mathbf{2}^{2-}$ was compared with that of relevant catalysts previously reported in the literature. It is well known that mononuclear copper catalysts containing

macrocyclic or polypyridinic ligands usually undergo a series of electron transfer and/or PCET processes to achieve highly oxidized species capable of oxidizing water into dioxygen. Despite the fact that the pathway and the active species implicated in WO catalysis by Cu complexes is not always clear, recent publications have shed light on this matter,[6,15,16] showing how the active species is formed by consecutive one electron oxidations that can be either metal or ligand centered. Thus, WO by molecular Cu complexes can be mediated by different mechanisms, such as water nucleophilic attack (WNA), interaction of two M–O units (I2M) and single electron-transfer water nucleophilic attack (SET-WNA), all of them sharing in common the involvement of Cu(III) species. It is thus of fundamental importance to understand how to lower the potential of the Cu(III)/Cu(II) redox couple, since this is a requirement for obtaining low overpotentials close to the thermodynamic value of water oxidation. The effect of introducing anionic groups that can directly coordinate to the metal centre has proven to be very successful in order to decrease the overpotentials and improve the TOFs.[17,18]

Table 1 displays E^o Cu(III)/Cu(II) and overpotential values (η) for the WO reaction for $\mathbf{1}^{2-}$ and $\mathbf{2}^{2-}$ and a set of related Cu complexes (see Figure 7B for a drawing of these complexes) containing ligands of various anionic charges (n^-). In the case of complexes $\mathbf{1}^{2-}$ and $\mathbf{2}^{2-}$ (entries 1 and 2), E^o Cu(III)/Cu(II) are similar to the previous one reported by Mayer *et al.* for a Cu complex bearing a bipyridine ligand ([(bpy)$Cu(OH)_2$], Table 1, entry 3),[9] although between 50 and 100 mV lower, probably due to the slightly higher electron-donating character of the amidate group with respect to the hydroxo group. As a result, comparable overpotentials are observed for these complexes, 823 mV for $\mathbf{1}^{2-}$ and 750 mV for **[(bpy)$Cu(OH)_2$]**. In case of the complex **[(bpyalk)Cu]**, synthesized recently in our laboratory (entry 4), a reversible Cu(III)/Cu(II) redox couple is observed at 1.28 V (Figure S34). After scanning at cathodic potentials, an alkoxy group is substituted by an hydroxo ligand, forming [(bpyalk)Cu(OH)], down-shifting the onset potential and increasing the activity towards water oxidation. An overpotential of roughly 750 mV at 12 pH is achieved, which is in strong agreement with respect to other catalysts with $n^- = 2$.

In the case of the recently reported complex **[Cu(pyalk)$_2$]** (entry 5), the Cu(III)/Cu(II) electron transfer has been reported to be located at 1.26 V vs. NHE at pH 8, which is in concordance with the potential of the analogous complex **[(bpyalk)Cu].**[19] However, the ~240 mV reduction of the overpotential for the electrocatalytic wave of **[Cu(pyalk)$_2$]** and

the raise in the electrocatalytic current before the reported Cu(III)/Cu(II) redox potential suggests the formation of new species during catalysis, probably derived from the substitution of a pyalk unit by two hydroxo ligands, achieving therefore the typical overpotentials expected for catalysts with $n^- = 3$.

Table 1. Electrochemical data for complexes $\mathbf{1}^{2-}$ and $\mathbf{2}^{2-}$ and related Cu complexes described in the literature.

Entry[a]	Complex[b]	n^{-}[d]	*pH*	$E^o_{III/II}$ (V vs. NHE)	η (mV)[g]
1[tw]	$\mathbf{1}^{2-}$	2	11.4	1.35[e]	823
2[tw]	$\mathbf{2}^{2-}$	2	11.4	1.3	-
3[9]	$[(bpy)Cu(OH)_2]$	2	12.5	1.4[e]	~750
4[c]	[(bpyalk)Cu]	2	12	1.28	~750
5[19]	$[Cu(pyalk)_2]$	2-3[f]	10.4-13.3	1.26[f]	~520-580
6[10a,15]	$[(6,6'\text{-dhbp})Cu(OH_2)_2]$	3	12.4	1.0[e]	~540
7[14]	$[Cu(pim)]^-$	3	12	0.95[e]	~620
8[11]	$[(L1)Cu]^{2-}$	4	11.5	0.56	600
9[11]	$[(L2)Cu]^{2-}$	4	11.5	0.51	400
10[11]	$[(L3)Cu]^{2-}$	4	11.5	0.55	270
11[11]	$[(L4)Cu]^{2-}$	4	11.5	0.48	170

(a) tw stands for this work (b) bpy is 2,2'-bipyridine; dhbp is 6,6'-dihydroxy-2,2'-bpy; bpyalk is 2,2'-([2,2'-bipyridine]-6,6'-diyl)bis(propan-2-olate); pyalk is 2-pyridyl-2-propanoate; pim is 2-(2'-pyridyl)-imidazole; L1 is N_1,N_1'-(1,2-phenylene)bis(N_2-methyloxalamide); L2, L3 and L4 are derivatives of L1 containing different electron-donating groups (see figure 7B). (c) Unpublished results, electrochemical data available in the supporting information (Figure S34) (d) Negative charge of the ligand coordinated directly to the Cu centre, (e) The Cu(III)/(II) redox couple is proposed to appear under the electrocatalytic wave. (f) $E^o_{III/II}$ reported at pH 8 for $n^- = 2$. However, comparison with the analogous complex [(bpyalk)Cu] suggests the formation of new species during catalysis containing a ligand of $n^- = 3$. (g) Overpotential for WO catalysis measured by DPV for entries 1, 7-10 and from the half-peak potential of CVs for the rest.

In the case of **$[(6,6'\text{-dhbp})Cu(OH_2)_2]$** (entry 6), the introduction of two hydroxyl pendant groups in the bipyridyl ring provides a redox-accessible ligand framework which stabilizes the intermediates, thus lowering the overpotential until ~540 mV.[10a] Despite the fact that in the original report the authors suggested a first metal centered oxidation process at *ca.* 1 V vs. NHE,[10a] recent computational studies have demonstrated that the activation of the Cu(II) complex takes place in two consecutive PCET processes. A first ligand centred electron subtraction forming $[(6,6'\text{-dhbp}^{\bullet})Cu(OH)(OH_2)]$ followed by a

Cu(III)/Cu(II) oxidation forming [(6,6′-dhbp$^{\bullet}$)Cu(OH)$_2$] is a more reasonable pathway.[15] The stabilization of the intermediate [(6,6′-dhbp$^{\bullet}$)Cu(OH)(OH$_2$)] by PCET and the hydrogen bonding interactions with the alkoxy pendant groups explains the observed overpotentials typical of catalysts with $n^- = 3$.

The effect of introducing a third negative charge in the ligand has also a clear effect in the potential of the Cu(III)/Cu(II) couple of complex **[Cu(pim)]$^-$** (entry 7), decreasing down to values below 1.0 V. WO occurs at an overpotential ~620 mV based on the half-peak potential for the CV at pH 12, which is in strong agreement with the predicted overpotentials for complexes containing $n^- = 3$.[14]

Finally, a further down-shift of the E^o Cu(III)/Cu(II) for complexes bearing the tetradentate amidate acyclic ligands H$_4$LY (Y = 1-4) containing 4 negative charges can be observed (entries 8-11), corroborating the strong influence of coordinated negatively charged ligands to the copper centre.[11] However, due to the non-innocent redox character of the ligands, the overpotentials in these complexes can be either higher or lower than those of Cu complexes containing less negatively charged ligands. Therefore, η is strongly dependent on the nature of the substituents present in the aromatic ring. In the most favourable case (entry 11), the overpotential decreases until *ca.* 170 mV thanks to the introduction of two high electron-donating methoxy groups.

Figure 7 shows the correlation of E^o Cu(III)/Cu(II) and η (V) vs. the number of anionic charges (n^-) contained in the auxiliary ligands bonded to the metal centre for the catalysts studied in this work and related Cu complexes. As can be seen, the redox potential of the Cu(III)/Cu(II) couple decreases by roughly 250 - 400 mV per anionic charge depending on the nature of the anionic electron-donating group.

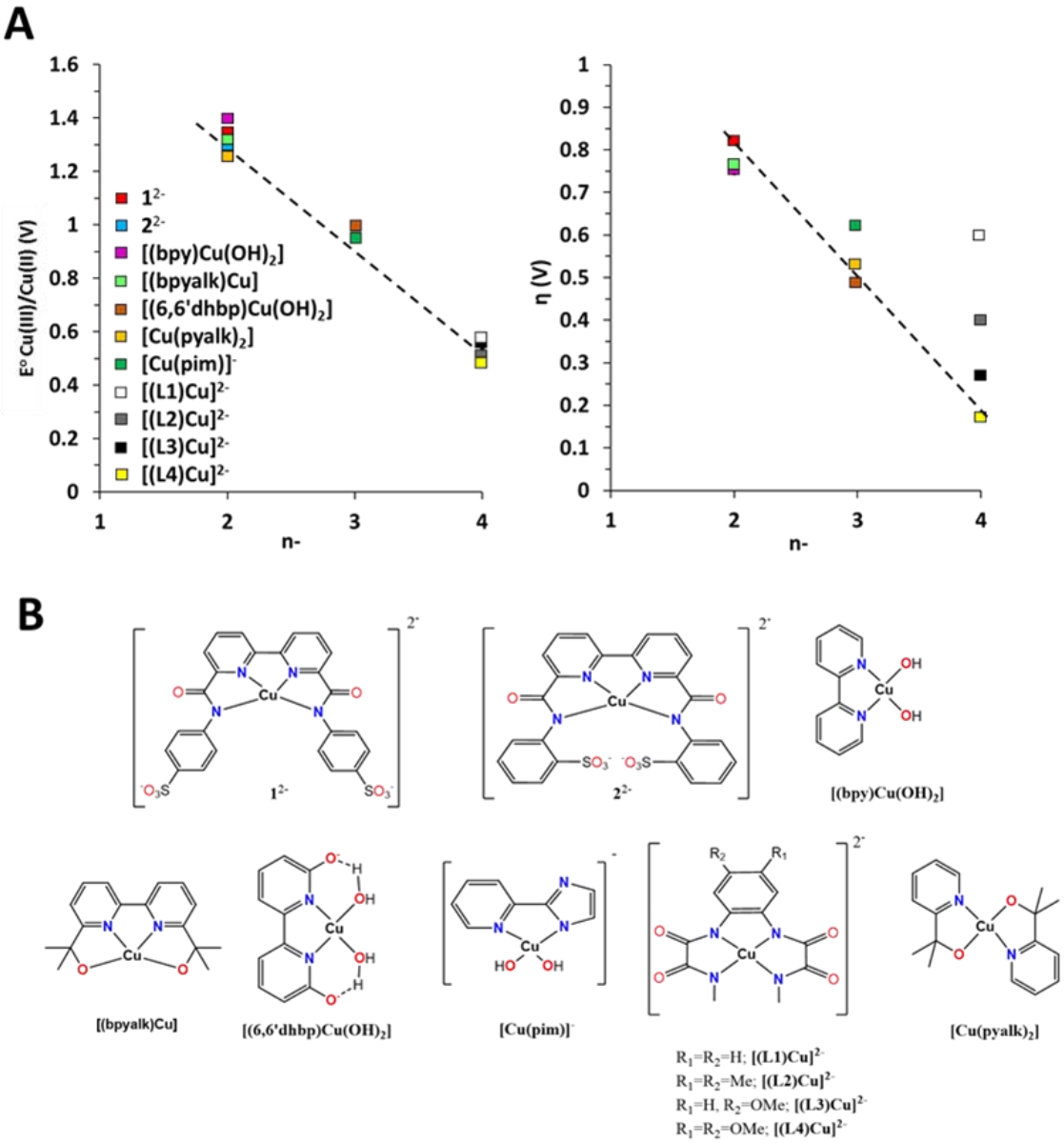

Figure 7. (**A**) Correlation between the number of anionic charges (n^-) contained in the ligands that are bonded to the Cu centre with the potential of Cu(III)/Cu(II) redox couple (Top left) and the reported overpotential for achieving electrocatalytic WO (Top right). (**B**) Drawing of the proposed structures in solution for all Cu complexes analyzed.

With regards to the overpotential trend, there is also a general decrease with increasing anionic charge of the ligands, although now a higher dependence on the particular reaction mechanism of each catalyst is also observed. Therefore, the accessibility to a Cu(III) species seems to be a limitation for being able to perform WO catalysis at low overpotentials, but this is not the only requirement, and thus the introduction of non-innocent redox ligands that are capable of helping the electron transfer processes can assist in this task.

Conclusions

New tetradentate bipyridine-based ligands containing strong electron-donating amidate groups have been synthetized and successful coordinated, forming their corresponding copper complexes. These complexes have been tested with regards their capacity of oxidizing water at basic pH. While $\mathbf{1}^{2-}$ operates under basic conditions with an overpotential of 835 mV, $\mathbf{2}^{2-}$ resulted to be inactive. The lack of reactivity of $\mathbf{2}^{2-}$ can be rationalized due to the *ortho* configuration of the sulfonate groups in the phenyl moieties, which blocks the imperative approximation of OH^- molecules during WO catalysis at basic pH. Finally, a comparison with related Cu complexes previously published shows that the introduction of ligands containing strong sigma donor groups coordinated directly to the metal centre play a key role in the stabilization of the Cu(III) species needed for achieving WO overpotentials as low as possible. Further experimental and computational work is in progress in our laboratory to develop a family of molecular copper-based catalysts in order to understand the factors that control their catalytic performance and achieve the design of improved molecular Cu-based WO catalysts.

Contribution

Marcos Gil-Sepulcre synthetized and characterized the new compounds, performed the electrochemical and catalytic experiments and prepared the manuscript.

References

[1] (a) Berardi, S.; Drouet, S.; Francas, L.; Gimbert-Surinach, C.; Guttentag, M.; Richmond, C.; Stoll, T.; Llobet, A. *Chem. Soc. Rev*. **2014**, *43*, 7501-7519. (b) Blakemore, J. D.; Crabtree R. H.; Brudvig G. W. *Chem. Rev*. **2015**, *115*, 12974-13005. (c) Kärkäs, M. D.; Verho, O.; Johnston, E. V.; Åkermark, B. *Chem. Rev*. **2014**, *114*, 11863-12001.

[2] Lewis, N. S. Science, 2016, 351, 19201-19209.

[3] (a) Okamura, M.; Kondo, M.; Kuga, R.; Kurashige, Y.; Yanai, T.; Hayami, S.; Praneeth, V. K. K.; Yoshida, M.; Yoneda, K.; Kawata, S.; Masaoka, S. *Nature*, **2016**, *530*, 465-468. (b) Ellis, W. C.; McDaniel, N. D.; Bernhard, S.; Collins, T. J. *J. Am. Chem. Soc*. **2010**, *132*, 10990-10991.

[4] (a) Wasylenko, D. J.; Ganesamoorthy, C.; Borau-Garcia, J.; Berlinguette, C. P. *Chem. Commun.* **2011**, *47*, 4249-4251; (b) Dogutan, D. K.; McGuire Jr, R.; Nocera, D. G. *J. Am. Chem. Soc.* **2011**, *133*, 9178-9180.

[5] Naruta, Y.; Sasayama, M.; Sasaki, T. *Angew. Chem., Int. Ed. Engl.* **1994**, *33*, 1839-1841.

[6] (a) Zhang, M.-T.; Chen, Z.; Kang, P.; Meyer T. *J. Am. Chem. Soc.* **2013**, *135*, 2048-2051; (b) Fu L.-Z.; Fang, T.; Zhou, L.-L.; Zhan, S.-Z. *RSC Adv.* **2014**, *4*, 53674-53680. (c) Pap, J. S.; Szyrwiel, L.; Srankó, D.; Kerner, Z.; Setner, B.; Szewczuk, Z.; Malinka W, *Chem. Commun*, **2015**, *51*, 6322-6324.

[7] (a)Duan, L.; Bozoglian, F.; Mandal, S.; Stewart, B.; Privalov ,T.; Llobet A.; Sun. L. *Nature Chemistry* **2012**, *4*, 418-423, (b) Matheu, R.; Ertem, M. Z.; Benet-Buchholz, J.; Coronado, E.; Batista, V. S.; Sala, X.; Llobet, A. *J. Am. Chem. Soc*. **2015**, *137*, 10786-10795.

[8] Rodriguez, G. M.; Gatto, G.; Zuccaccia, C.; Macchioni, A. *ChemSusChem* (DOI: 10.1002/cssc.201701818).

[9] Barnett, S. M.; Golderg, K. I.; Mayer, J. M. *Nature Chemistry* **2012**, *4*, 498-502.

[10] (a) Zhang, T.; Wang, C.; Liu, S.; Wang, J.-L.; Lin, W. *J. Am. Chem. Soc*. **2014**, *136*, 273-281 (b) Gerlach, D. L.; Bhagan, S.; Cruce, A. A.; Burks, D. B.; Nieto, I.; Truong, H. T.; Kelley, S. P.; Herbst-Gervasoni, C. J.; Jernigan, K. L.; Bowman, M. K.; Pan, S.; Zeller, M.; Papish, E. T. *Inorg. Chem.* **2014**, *53*, 12689-12698.

[11] Garrido-Barros, P.; Funes-Ardoiz, I.; Drouet, S.; Benet-Buchholz J.; Maseras F.; Llobet, A. *J. Am. Chem. Soc.* **2015**, *137*, 6758-6761.

[12] Beverskog, B.; Puigdomenech, I. *J. Electrochem. Soc.* **1997**, *144*, 3476-3483.

[13] Janiak, C. *J. Chem. Soc., Dalton Trans.* **2000**, *0*, 3885-3896.

[14] Stott, L. A.; Prosser, K. E.; Berdichevky, E. K.; Walsby, C. J.; Warren, J. J. *Chem. Commun.* **2017**, *53*, 651-654.

[15] Funes-Ardoiz, I.; Garrido-Barros, P.; Llobet, A.; Maseras, F. *ACS Catal.* **2017**, *7*, 1712-1719.

[16] Koepke, S. J.; Light, K. M.; VanNatta, P. E.; Wiley, K. M. *J. Am. Chem. Soc.* **2017**, *139*, 8586-8600.

[17] Gil-Sepulcre, M.; Schilling, M.; Böhler, M.; Bozoglian, F; Bachmann, C.; Scherrer, D.; Fox, T.; Spingler, B.; Gimbert-Suriñach, C.; Alberto, R.; Bofill, R.; Sala, X.; Luber, S.; Richmond, C. J.; Llobet A. ChemSusChem *(DOI:10.1002/cssc.201701747).*

[18] (a) Matheu, R.; Ertem, M. Z.; Gimbert-Suriñach, C.; Benet-Buchholz, J.; Sala, X.; Llobet, A. *ACS Catal.* **2017**, *7*, 6525-6532; (b) Tong, L.; Wang. Y.; Duan, L.; Xu, Y.; Cheng, X.; Fischer, A.; Ahlquist, M. S. G.; Sun, L. *Inorg. Chem.* **2012**, *51*, 3388-3398.

[19] Fisher, K. J.; Materna, K. L.; Mercado, B. Q.; Crabtree R. H.; Brudvig, G. W. *ACS Catal.* **2017**, *7*, 3384-3387.

Supporting Information

Synthesis of new Cu^{II} complexes bearing bipyridyl-diamidate ligands. Characterization and water oxidation catalysis.

Table of Contents

1. Experimental Section

Materials

All general reagents and chemicals were used as purchased from Sigma-Aldrich, Fluka and Merck chemical companies without further purification unless otherwise stated. The ligand precursor ([2,2'-bipyridine]-6,6'-dicarboxylic acid) was prepared according to the experimental procedure reported in the literature.[1] Air and moisture sensitive reactions were carried out under N_2 or Ar in oven-dried (120°C) glassware. Evaporation of solvents *in vacuo* was done with a *Büchi Rotevapor R-200* at 40°C.

Instrumentation and measurements

NMR spectra were measured on a *Bruker AV-500* and *Bruker 300 MHz* spectrometers. All NMR experiments were performed at room temperature in corresponding deuterated solvents and using internal protons as reference.

UV-Vis spectra were measured on a *Cary 50 UV-vis* spectrometer by *Varian Inc*.

Electrospray ionization mass spectra (ESI-MS) were performed on an *Agilent Technologies 6130-Quadrupole LC/MS* connected to an *Agilent Technologies HPLC-1200 series*. Samples were dissolved in MeOH or H_2O and injected directly with an auto-sampler.

Electrochemical measurements

Differential pulse voltammetry (DPV) and cyclic voltammetry (CV) were measured on a CHI660D potentiostat using a three-electrode cell. Glassy carbon (GC) or boron-doped diamond (BDD) (d = 3 mm) working electrodes were employed while a Pt rod/mesh was used as counter electrode and a $Hg/HgSO_4$ (K_2SO_4 sat.) or Ag/AgCl (KCl sat.) electrode was used as a reference electrode. Working electrodes were polished with 1 and 0.05 micron alumina paste, washed with distilled water and acetone and sonicated in acetone for 5 minutes before each measurement. DMF employed for electrochemical measurements was prepared containing the necessary amount of n-Bu_4NPF_6 ($TBAPF_6$) as supporting electrolyte to yield a 0.1 M ionic strength. CVs were typically recorded at different scan rates from 25 to 1000 mV/s. DPVs were recorded with the following parameters: amplitude= 50 mV, step height=4 mV, pulse width= 0.05 s. All redox

potentials in the present work are reported versus NHE by adding 0.648 V to the measured potential.

O_2 evolution experiments

Controlled Potential Electrolysis (CPE) experiments were performed at different potentials and different pH values to catalyze the water oxidation reaction by the complexes by using a two-compartment cell closed with a septum. As working electrode large surface BDD electrodes (rectangular shape with 1.5 cm^2 surface) were used together with a silver/silver chloride (KCl sat.) as a reference electrode. These ones were placed in one of the compartments that was filled with a 1 mM solution of the complex (phosphate buffer pH 7, borate buffer pH 9 or phosphate buffer pH 11.4, of 0.1 M ionic strength). In the other compartment, containing only the buffer solution, a mesh platinum counter electrode was used.

The oxygen evolution was monitored with an OXNP type Clark electrode in gas phase (from Unisense Company). The CPE was carried out using an IJ-Cambria CHI-660 potentiostat and was started as soon as the oxygen sensor signal was stable under air atmosphere. During the experiment, solutions of both compartments were vigorously stirred. Calibration of the oxygen sensor was performed after each experiment by adding known amounts of pure oxygen into the cell using a Hamilton syringe. The results of the water oxidation catalysis with the complexes were compared with blank experiments under the same conditions but in the absence of the complex. The Faradaic efficiency was determined according to the total charge passed during the CPE and the total amount of generated oxygen by taking into account that water oxidation is a 4 e^- oxidation process.

Synthesis of *p*-L and *o*-L

The general procedure for the synthesis of ligands *p*-L and *o*-L was adapted from the literature[2] as follows: 500 mg (2.05 mmol) of [2,2'-bipyridine]-6,6'-dicarboxylic acid were suspended in 20 mL of $SOCl_2$ and the mixture was refluxed at 85 ºC under a nitrogen atmosphere during 6 hours. After complete dissolution of the reactant, $SOCl_2$ was completely removed under vacuum, yielding a white powder corresponding to the corresponding acyl chloride derivative. The white solid was re-suspended in 40 mL of dry DCM and the temperature was decreased until 0 ºC using an ice bath. Then, a catalytic amount of NEt_3 was added dropwise and stirred for 10 minutes. Finally, a previously prepared solution of the corresponding sulfonated phenylamine (705.6 mg, 4.1 mmol) in

40 mL of dry DCM were added dropwise to the reaction volume and the mixture was vigorous stirred for 72 h at room temperature. The appearing solid consisted in the corresponding ligand (*p*-L or *o*-L), which was filtered and washed with DCM and Et_2O, yielding the desired product without further purification.

p-L

Yield: 931 mg, 1.68 mmol, 82%. ^{1}H-NMR (DMSO-d_6): δ [ppm] = 10.70 (H_4, s, 2H), 9.24 (H_1, dd, J= 7.3, 1.6 Hz, 2H), 8.30 ($H_{2\text{-}3}$, m, 4H), 7.90 (H_5, d, J= 8.7 Hz, 2H), 7.65 (H_6, d, J= 8.7 Hz, 2H). ^{13}C-NMR (DMSO-d_6): 162,9 (C_6), 153.9 (C_5), 150.0 (C_1), 144.7 (C_{10}), 139.8 (C_4), 138.6 (C_7), 126.5 (C_9), 125.3 (C_2), 123.7 (C_3), 120.4 (C_8). ESI-MS (MeOH) m/z negative mode: 553.0 [*p*-L -H^+]$^-$, 276.1 [*p*-L -$2H^+$]$^{2-}$.

o-L

Yield: 965 mg, 1.74 mmol, 85%. 1H-NMR (DMSO-d_6): δ [ppm] = 12.55 (H_4, s, 2H), 9.51 (H_1, dd, J= 7.3, 1.7 Hz, 2H), 8.67 (H_5, dd, J= 8.2, 1.1 Hz, 2H), 8.26 ($H_{2\text{-}3}$, m, 4H), 7.82 (H_8, dd, J= 7.7, 1.7 Hz, 2H), 7.43 (H_6, t, J= 1.2 Hz, 2H), 7.14 (H_7, td, J= 7.5, 1.2 Hz, 2H). ^{13}C-NMR (DMSO-d_6): 162,4 (C_6), 153.9 (C_5), 149.6 (C_1), 139.9 (C_4), 136.8 (C_{12}), 135.3 (C_7), 130.1 (C_9), 127.6 (C_8), 125.4 (C_2), 123.2 ($C_{1\text{-}2}$), 120.2 ($C_{3\text{-}7}$). ESI-MS (MeOH) m/z negative mode: 553.0 [*p*-L -H^+]$^-$, 276.1 [*p*-L -$2H^+$]$^{2-}$.

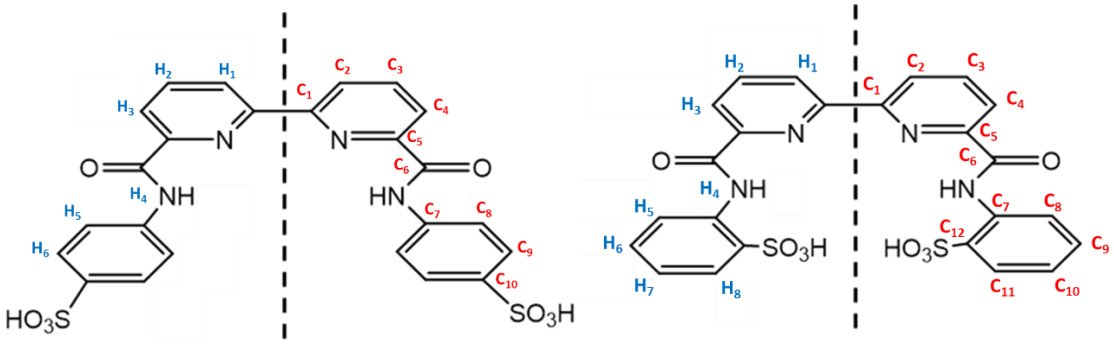

Figure S1: Schematic drawing of the two ligands synthetized in this work: *p*-L (left) and *o*-L (right) and their ^{1}H-NMR and ^{13}C-NMR assignments.

Synthesis of complexes 1^{2-} and 2^{2-}

The general procedure for the synthesis of the copper complexes was adapted from a previous work published.[3] 50 mg (0.09 mmol) of the corresponding ligand were suspended in 4 mL of MeOH and stired during 15 minutes. Afterwards, 3.6 mL (4 eq.) of 0.1 M $NaOH_{aq.}$ were added to the reaction mixture and vigorously stirred during 30 minutes at room temperature. After complete dissolution of the ligand, 33.3 mg (0.09 mmol) of copper perchlorate hexahydrate dissolved in 4 mL of MeOH were added dropwise to the mixture, which was allowed to react overnight (16 h) at room temperature. Then, the reaction mixture was filtrated through celite and MeOH was evaporated under vacuum, and the remaining solution was diffused with acetone, yielding the corresponding complexes.

Complex 1^{2-}

Yield: 19 mg, 0.03 mmol, 32% ESI-MS (MeOH) m/z negative mode: 636.0 $[M\text{-}Na^{+}]^{-}$, 614.0 $[M\text{-}Na^{+} + H^{+}]^{-}$.

Complex 2^{2-}

Yield: 15 mg, 0.02 mmol, 25%. ESI-MS (MeOH) m/z negative mode: 636.0 $[M\text{-}Na^{+}]^{-}$, 614.0 $[M\text{-}Na^{+} + H^{+}]^{-}$.

2. Spectroscopic Characterization

NMR and Mass Spectroscopy

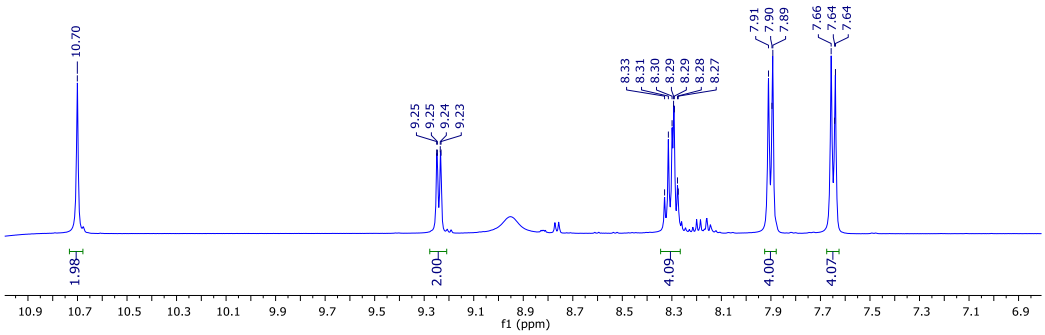

Figure S2. ^{1}H-NMR spectrum of the ligand *p*-L (DMSO-d_6, 500 MHz, 25 °C).

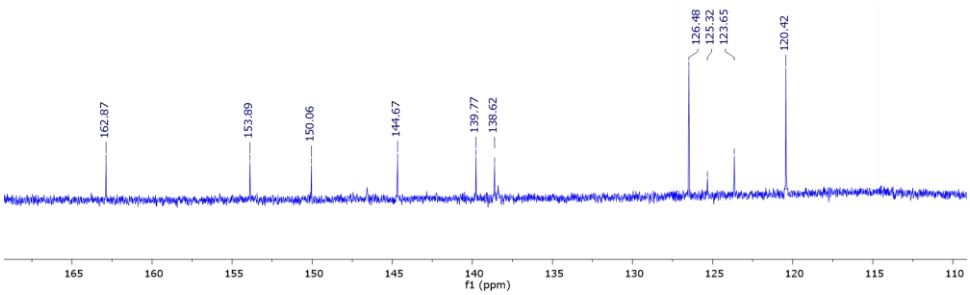

Figure S3. ^{13}C-NMR spectrum of the ligand *p*-L (DMSO-d_6, 500 MHz, 25 °C).

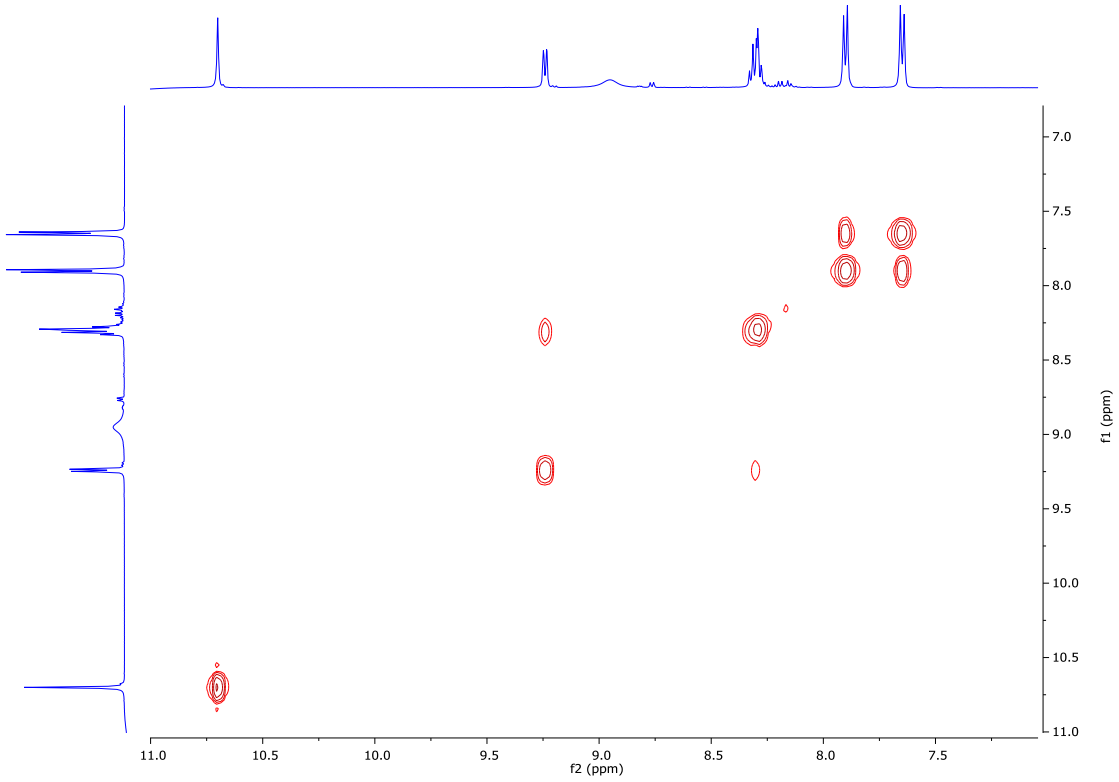

Figure S4. COSY spectrum of the ligand *p*-L (DMSO-d_6, 500 MHz, 25 °C).

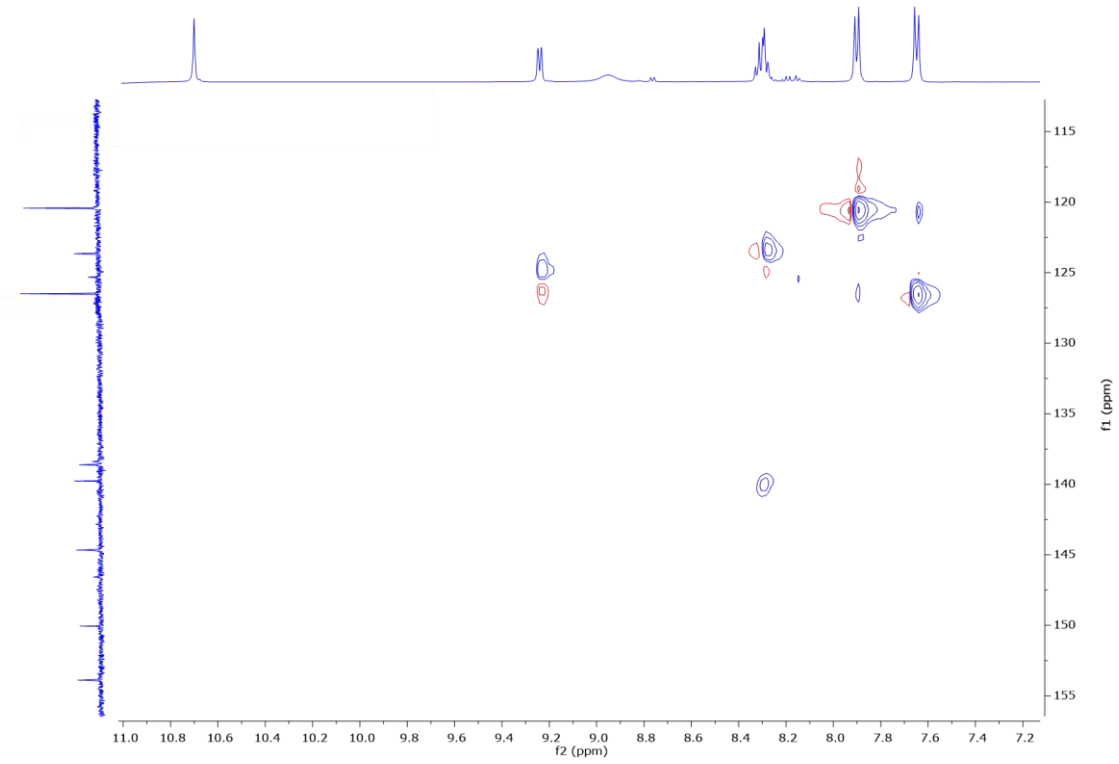

Figure S5. HSQC spectrum of the ligand *p*-L (DMSO-d_6, 500 MHz, 25 °C).

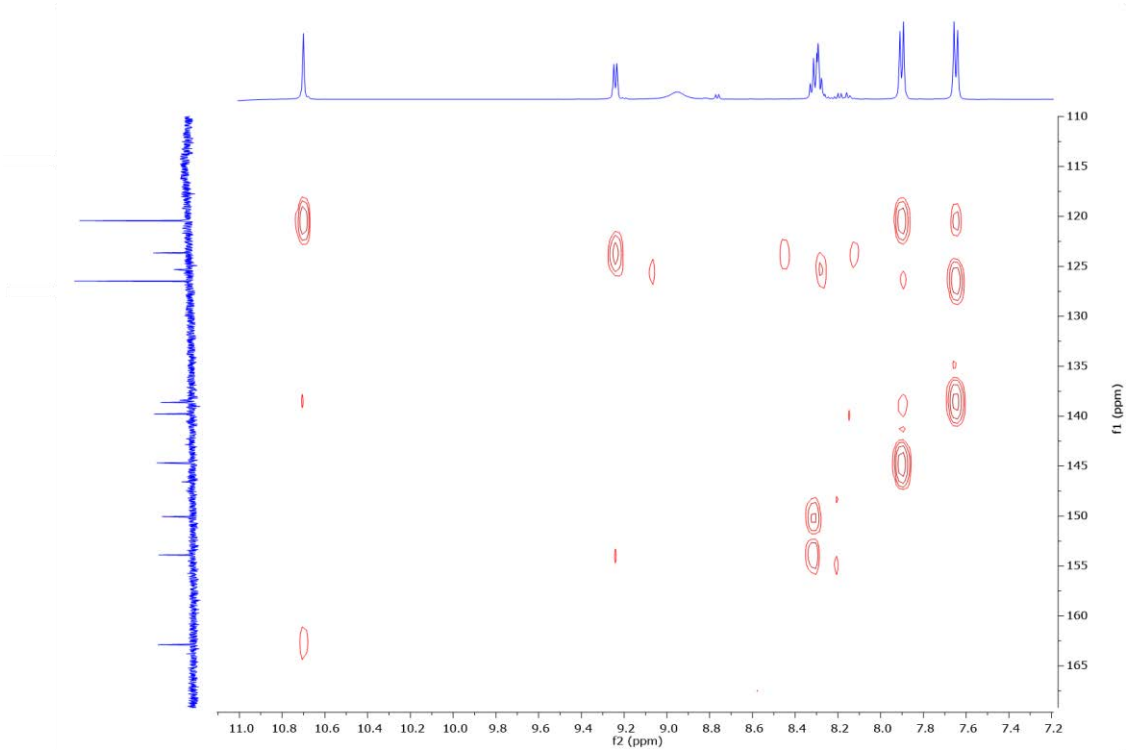

Figure S6. HMBC spectrum of the ligand *p*-L (DMSO-d_6, 500 MHz, 25 °C).

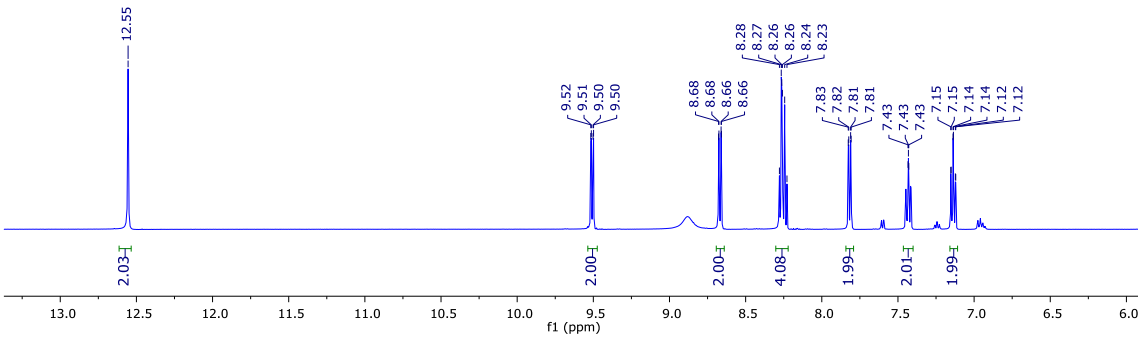

Figure S7. ^{1}H-NMR spectrum of the ligand *o*-L (DMSO-d_6, 300 MHz, 25 °C).

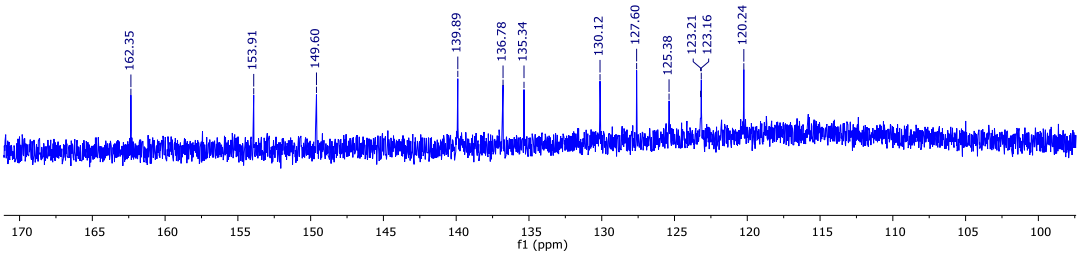

Figure S8. ^{13}C-NMR spectrum of the ligand *o*-L (DMSO-d$_6$, 500 MHz, 25 °C).

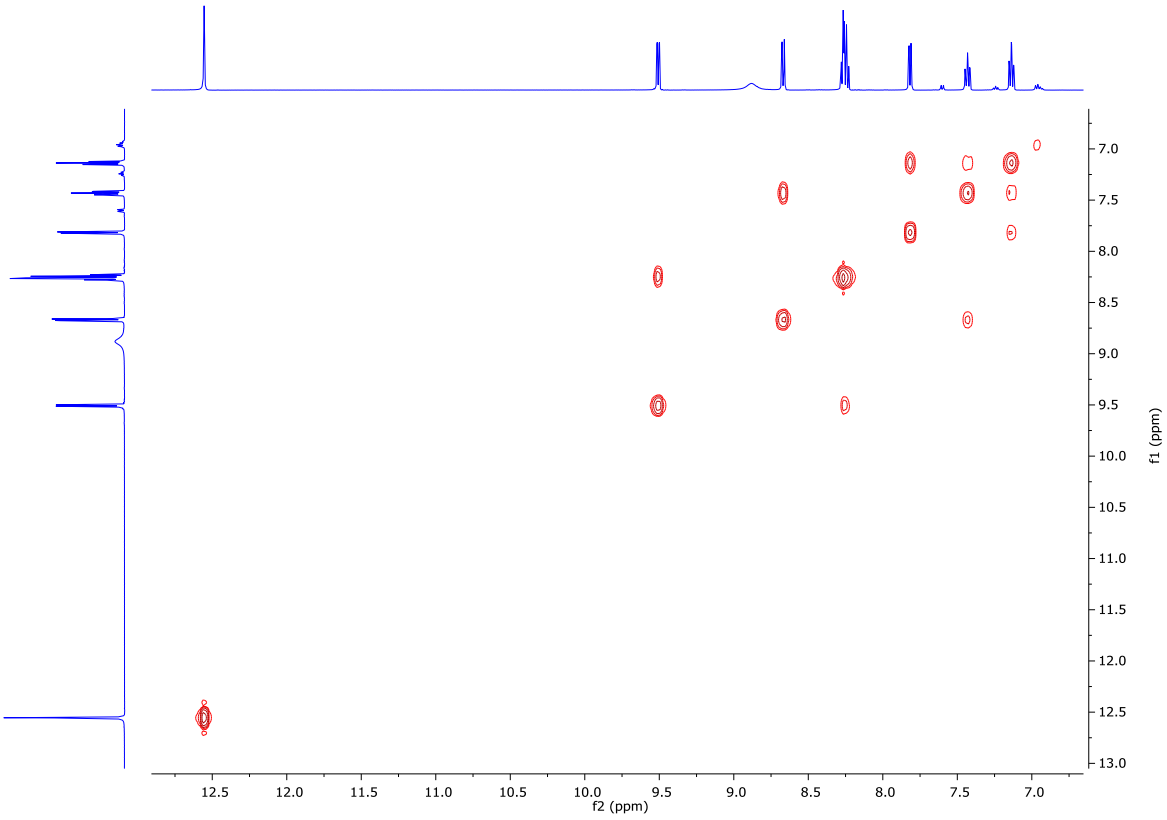

Figure S9. COSY spectrum of the ligand *o*-L (DMSO-d$_6$, 500 MHz, 25 °C).

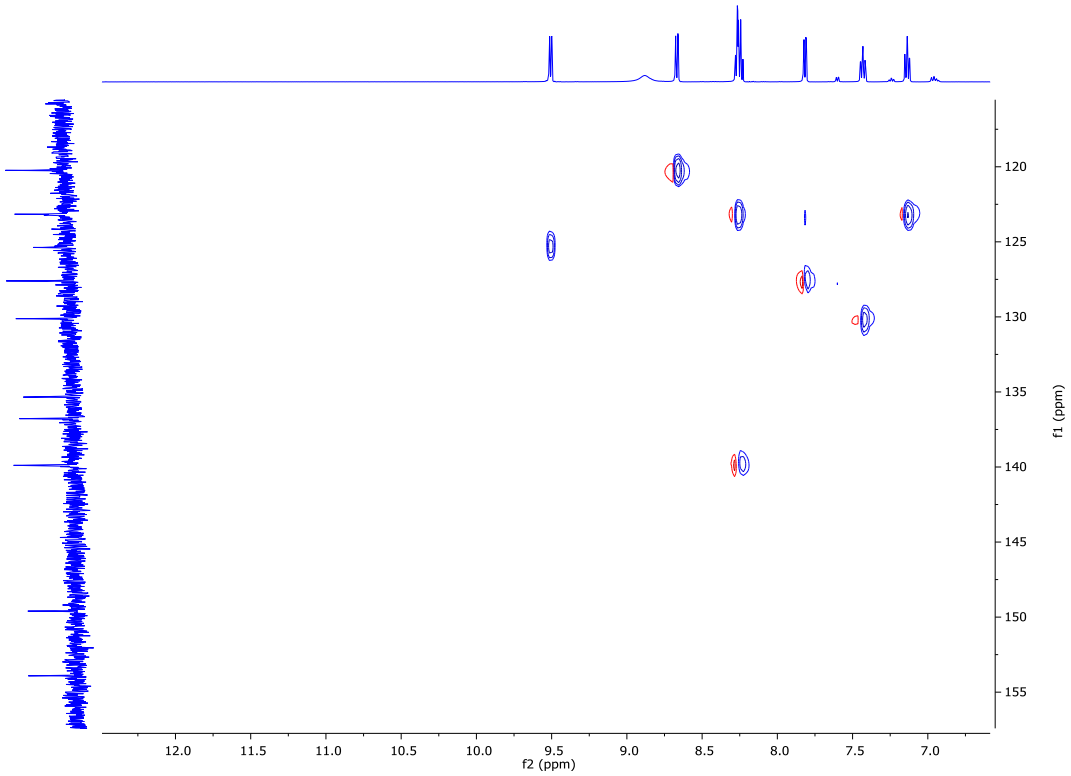

Figure S10. HSQC spectrum of the ligand *o*-L (DMSO-d_6, 500 MHz, 25 °C).

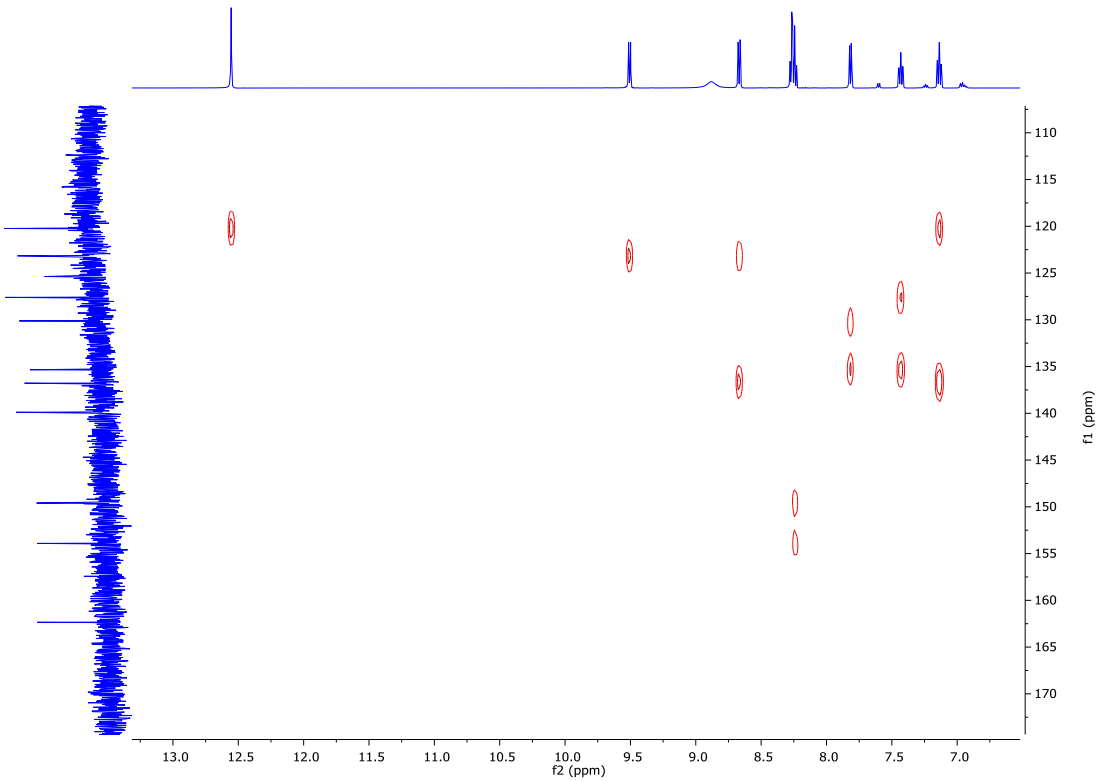

Figure S11. HMBC spectrum of the ligand *o*-L (DMSO-d_6, 500 MHz, 25 °C).

Mass-spectrometry

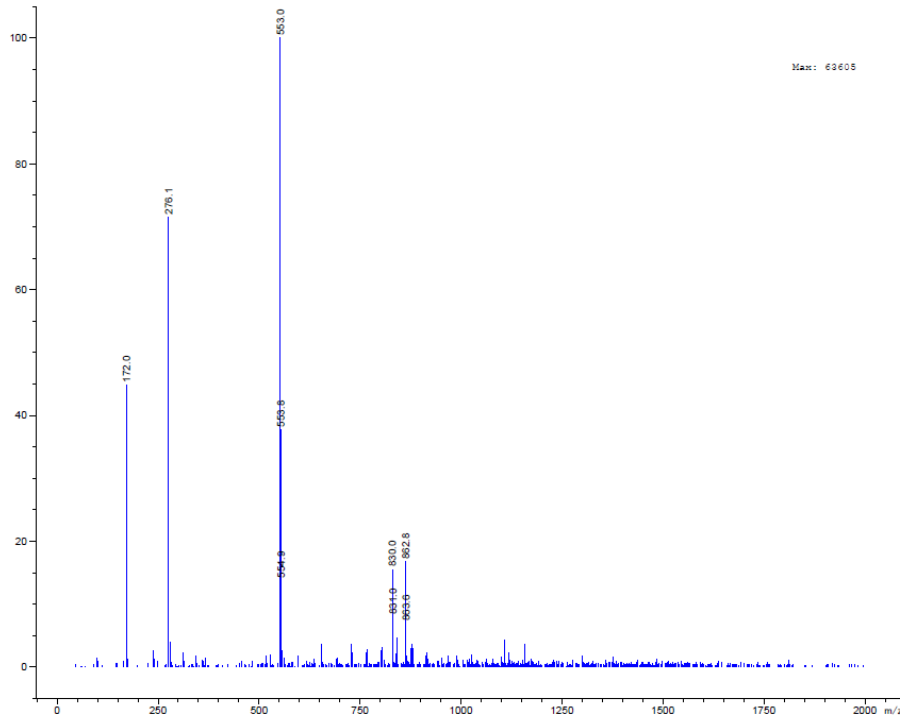

Figure S12. (-)-ESI-MS spectrum for the ligand *p*-L. m/z = 553.0 $[p\text{-L} -H^{+}]^{-}$; m/z = 276.1 $[p\text{-L} -2H^{+}]^{2-}$.

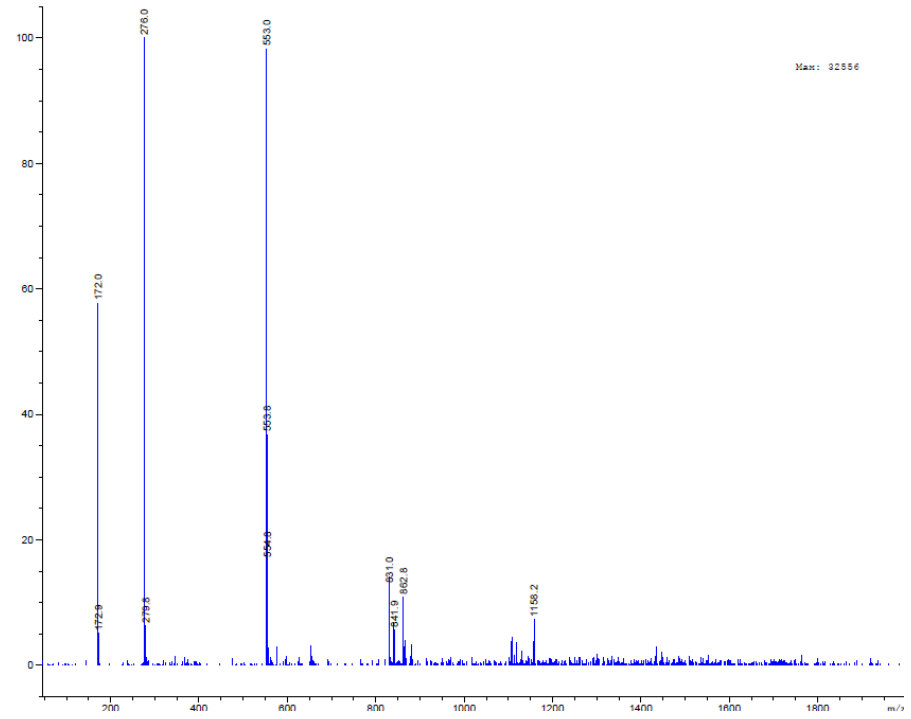

Figure S13. (-)-ESI-MS spectrum for the ligand *o*-L. m/z = 553.0 $[p\text{-L} -H^{+}]^{-}$; m/z = 276.1 $[p\text{-L} -2H^{+}]^{2-}$.

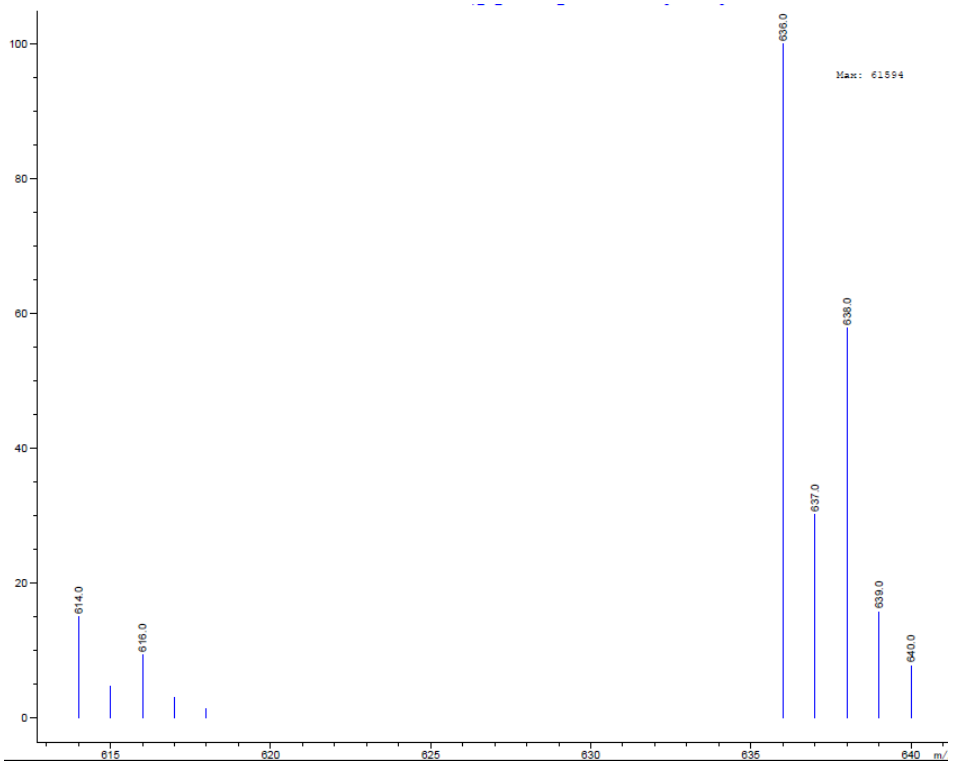

Figure S14. (-)-ESI-MS for $\mathbf{1}^{2-}$. m/z = 636.0 $[M\text{-}Na^{+}]^{-}$; m/z = 614.0 $[M\text{-}Na^{+} + H^{+}]^{-}$.

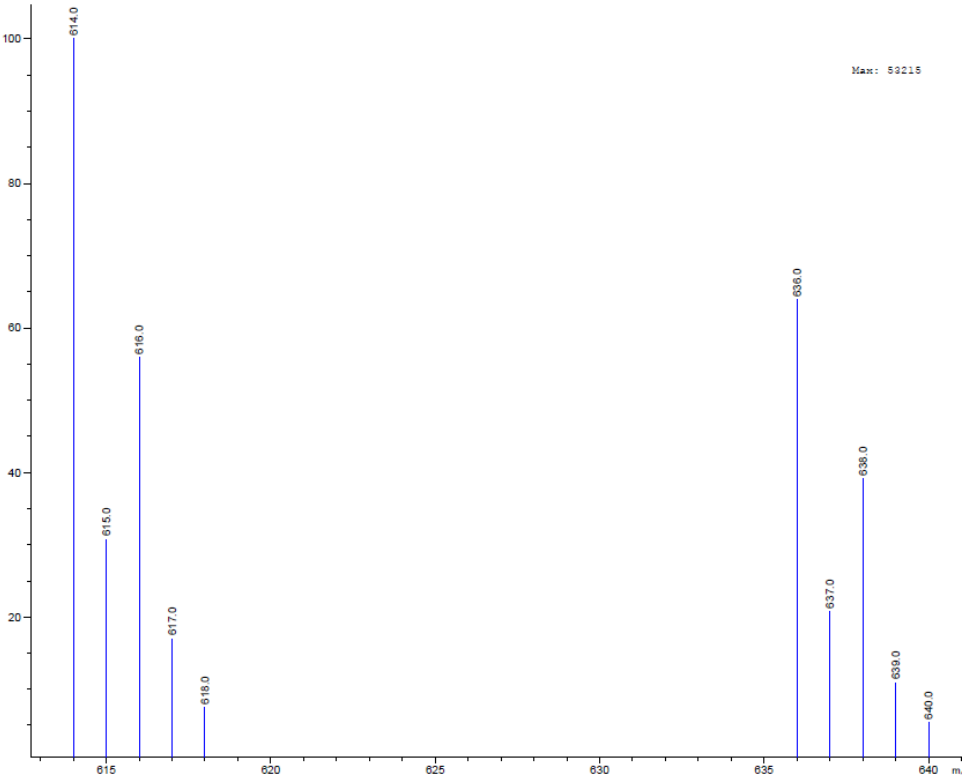

Figure S15. (-)-ESI-MS for $\mathbf{2}^{2-}$. m/z = 636.0 $[M\text{-}Na^{+}]^{-}$; m/z = 614.0 $[M\text{-}Na^{+} + H^{+}]^{-}$.

3. X-Ray Crystallography

Crystal preparation: Crystals of $\mathbf{1}^{2-}$, $\mathbf{2}^{2-}$and *p*-L were grown in water (by slow diffusion of acetone for $\mathbf{1}^{2-}$ and $\mathbf{2}^{2-}$, and EtOH for *o*-L). The crystals were selected using a Zeiss stereomicroscope using polarized light and prepared under inert conditions immersed in perfluoropolyether as protecting oil for manipulation.

Data collection: Crystal structure determinations for samples $\mathbf{1}^{2-}$, $\mathbf{2}^{2-}$and *o*-L were carried out using a Apex DUO Kappa 4-axis goniometer equipped with an APPEX 2 4K CCD area detector, a Microfocus Source E025 IuS using MoK$_\alpha$ radiation, Quazar MX multilayer Optics as monochromator and an Oxford Cryosystems low temperature device Cryostream 700 plus (T = -173 $^\circ$C). Full-sphere data collection was used with ω and φ scans. *Programs used:* Bruker Device: Data collection APEX-2[4], data reduction Bruker Saint[5] V/.60A and absorption correction SADABS[6].

Structure Solution and Refinement: Crystal structure solution was achieved using the computer program SHELXT[7]. Visualization was performed with the program SHELXle[8]. Missing atoms were subsequently located from difference Fourier synthesis and added to the atom list. Least-squares refinement on F^2 using all measured intensities was carried out using the program SHELXL 2015[9]. All non-hydrogen atoms were refined including anisotropic displacement parameters. **Comments to the structures:** Sample *o*-L: The asymmetric unit contains half a molecules of the organic salt. The main molecule shows *C*i-symmetry. $\mathbf{2}^{2-}$: The asymmetric unit contains one molecule of the Copper metal complex, two Sodium cations and eight molecules of water. $\mathbf{1}^{2-}$: The asymmetric unit contains one molecule of the metal complex, two sodium cations and 6.75 water molecules which are highly disordered (18 positions) The sulfoxide groups and the Sodium cations are disorder in three orientations with an approximated ratio of 33:33:33. One of the disordered sodium cations is additionally split in two positions (33:33:22:11). In the CIF-file a B-Alert related to D-H without acceptor is commented in relation to the water molecules: In this highly disordered structure there were 18 positions for 6.75 disordered water molecules and it was not possible to assign correctly all the corresponding hydrogen atom positions.

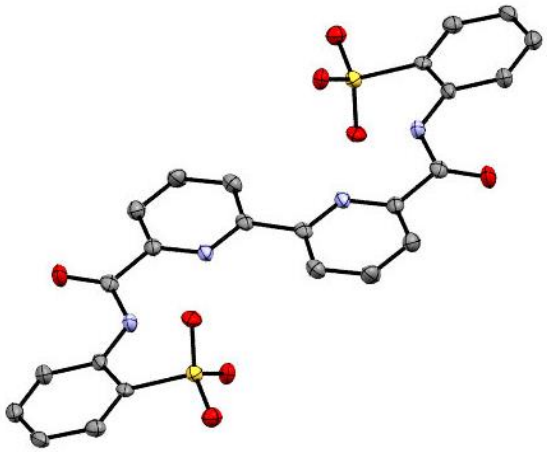

Figure S16. ORTEP representation of *o*-L at 50% probability level. The counter ions, solvent molecules and hydrogen atoms have been omitted for clarity. Colour code: C, grey; N, blue; O, red; S, yellow.

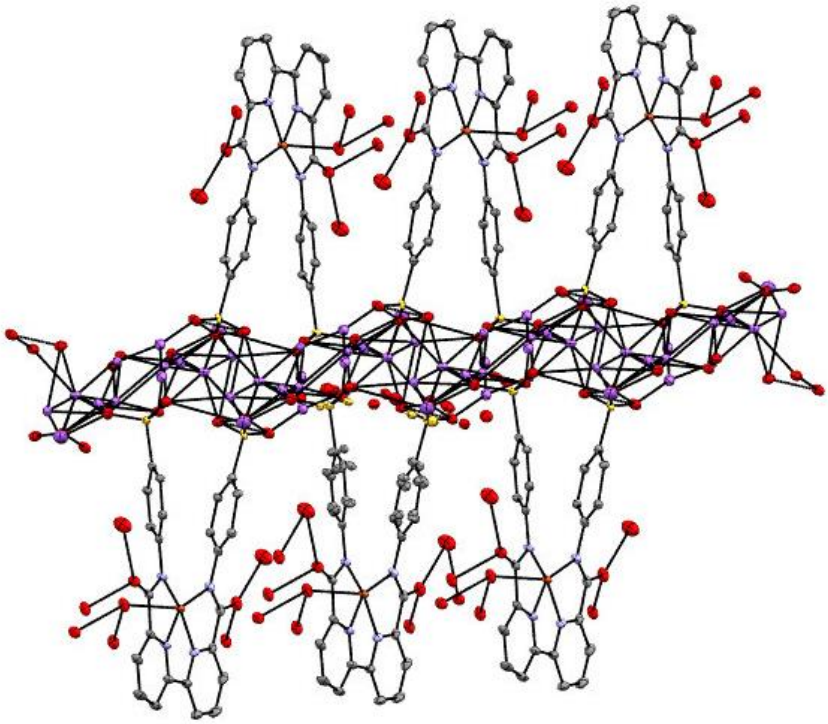

Figure S17. X-Ray structure representation of 2D polymeric framework of $\mathbf{1}^{2-}$. Colour code: C, grey; N, blue; O, red; S, yellow; Na, Purple; Cu, Orange.

Table S1. Crystal data and structure refinement for *o*-L.

Identification code	*o*-L	
Empirical formula	C36 H48 N6 O8 S2	
Formula weight	756.92	
Temperature	100(2) K	
Wavelength	0.71073 Å	
Crystal system	Monoclinic	
Space group	P2(1)/c	
Unit cell dimensions	a = 14.4650(14)Å	α= 90°.
	b = 8.5135(9)Å	β = 109.155(3)°.
	c = 15.7483(14)Å	γ = 90°.
Volume	1832.0(3) $Å^3$	
Z	2	
Density (calculated)	1.372 Mg/m^3	
Absorption coefficient	0.206 mm^{-1}	
F(000)	804	
Crystal size	0.30 x 0.05 x 0.05 mm^3	
Theta range for data collection	2.654 to 25.391°.	
Index ranges	-16<=h<=17,-6<=k<=10,-18<=l<=15	
Reflections collected	13699	
Independent reflections	3343[R(int) = 0.0878]	
Completeness to theta =25.391°	98.9%	
Absorption correction	Multi-scan	
Max. and min. transmission	0.990 and 0.541	
Refinement method	Full-matrix least-squares on F^2	
Data / restraints / parameters	3343/ 0/ 238	
Goodness-of-fit on F^2	0.999	
Final R indices [I>2sigma(I)]	R1 = 0.0493, wR2 = 0.1071	
R indices (all data)	R1 = 0.0942, wR2 = 0.1269	
Largest diff. peak and hole	0.314 and -0.474 e.$Å^{-3}$	

Table S2. Crystal data and structure refinement for $\mathbf{2}^{2-}$.

Identification code	$\mathbf{2}^{2-}$	
Empirical formula	C24 H30 Cu N4 Na2 O16 S2	
Formula weight	804.16	
Temperature	100(2) K	
Wavelength	0.71073 Å	
Crystal system	Monoclinic	
Space group	P2(1)/c	
Unit cell dimensions	a = 7.5982(3)Å	α = 90°.
	b = 17.2572(6)Å	β= 98.6877(10)°.
	c = 24.3433(9)Å	γ = 90°.
Volume	3155.4(2) $Å^3$	
Z	4	
Density (calculated)	1.693 Mg/m^3	
Absorption coefficient	0.934 mm^{-1}	
F(000)	1652	
Crystal size	0.40 x 0.10 x 0.05 mm^3	
Theta range for data collection	2.063 to 34.993°.	
Index ranges	-12<=h<=10,-24<=k<=27,-38<=l<=38	
Reflections collected	38704	
Independent reflections	13011[R(int) = 0.0346]	
Completeness to theta =34.993°	93.6%	
Absorption correction	Multi-scan	
Max. and min. transmission	0.955 and 0.798	
Refinement method	Full-matrix least-squares on F^2	
Data / restraints / parameters	13011/ 0/ 506	
Goodness-of-fit on F^2	1.073	
Final R indices [I>2sigma(I)]	R1 = 0.0423, wR2 = 0.0932	
R indices (all data)	R1 = 0.0556, wR2 = 0.0978	
Largest diff. peak and hole	1.087 and -0.796 e.$Å^{-3}$	

Table S3. Crystal data and structure refinement for $\mathbf{1}^{2-}$.

Identification code	$\mathbf{1}^{2-}$	
Empirical formula	C24 H27.50 Cu N4 Na2 O14.75 S2	
Formula weight	781.64	
Temperature	100(2) K	
Wavelength	0.71073 Å	
Crystal system	Triclinic	
Space group	P-1	
Unit cell dimensions	a = 7.1558(3)Å	α = 70.5590(10)°
	b = 12.3988(5)Å	β = 89.3240(10)°
	c = 18.4833(7)Å	γ = 80.6830(10)°
Volume	1524.44(11) $Å^3$	
Z	2	
Density (calculated)	1.703 Mg/m^3	
Absorption coefficient	0.961 mm^{-1}	
F(000)	801	
Crystal size	0.50 x 0.50 x 0.03 mm^3	
Theta range for data collection	1.762 to 33.916°.	
Index ranges	-11<=h<=11,-19<=k<=17,-28<=l<=28	
Reflections collected	34506	
Independent reflections	11681[R(int) = 0.0302]	
Completeness to theta =33.916°	94.6%	
Absorption correction	Multi-scan	
Max. and min. transmission	0.972 and 0.863	
Refinement method	Full-matrix least-squares on F^2	
Data / restraints / parameters	11681/ 1914/ 965	
Goodness-of-fit on F^2	1.120	
Final R indices [I>2sigma(I)]	R1 = 0.0452, wR2 = 0.1120	
R indices (all data)	R1 = 0.0544, wR2 = 0.1165	
Largest diff. peak and hole	0.936 and -0.564 $e.Å^{-3}$	

4. Electrochemistry

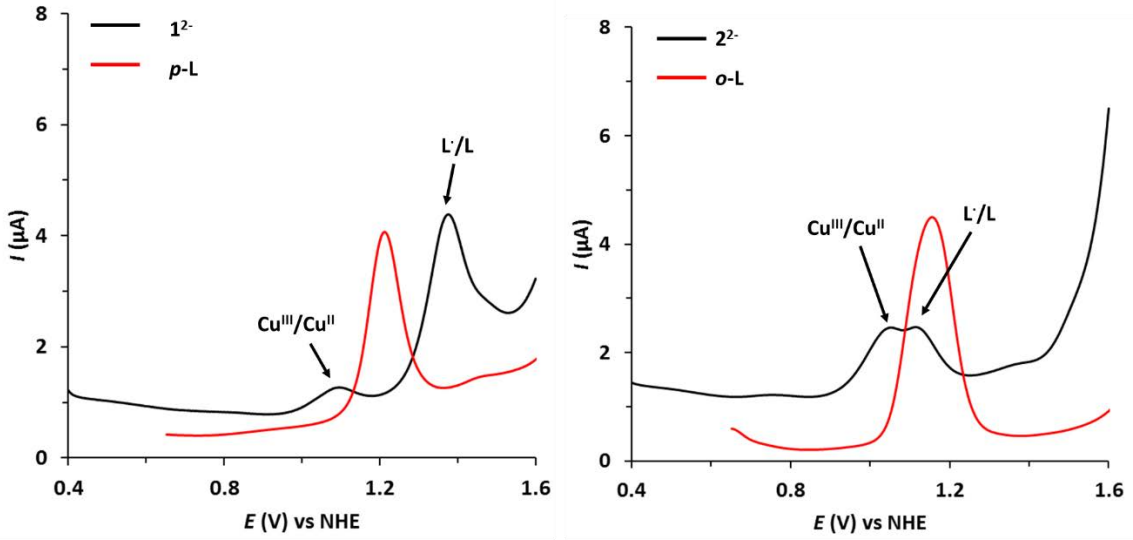

Figure S18. (**Left**) DPV experiments of $\mathbf{1}^{2-}$ (black line) and *p*-L (red line). (**Right**) DPV experiments of $\mathbf{2}^{2-}$ (black line) and *o*-L (red line). Conditions: 1 mM of ligand or complex in DMF containing 0.1 M of TBAPF. GC disk as working electrode.

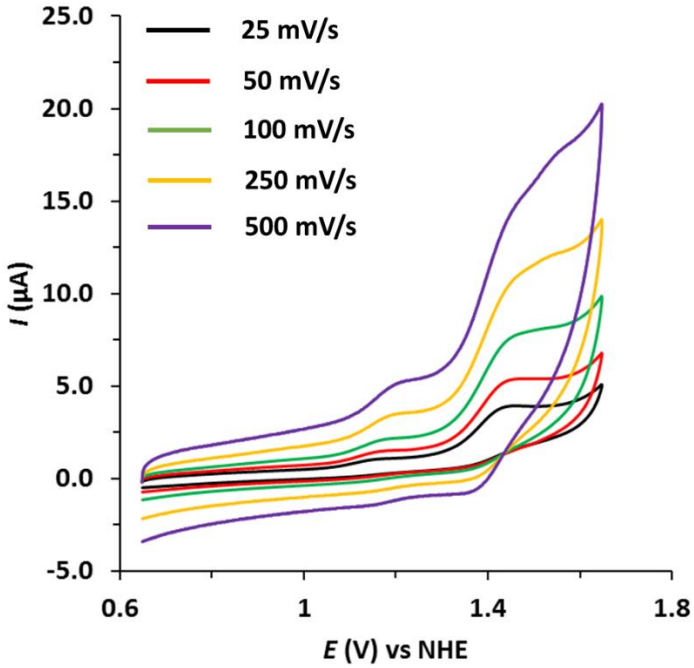

Figure S19. Cyclic Voltammograms of $\mathbf{1}^{2-}$ at different scan rates (25-500 mV/s). Conditions: 1 mM of complex in DMF containing 0.1 M of TBAPF. GC disk as working electrode.

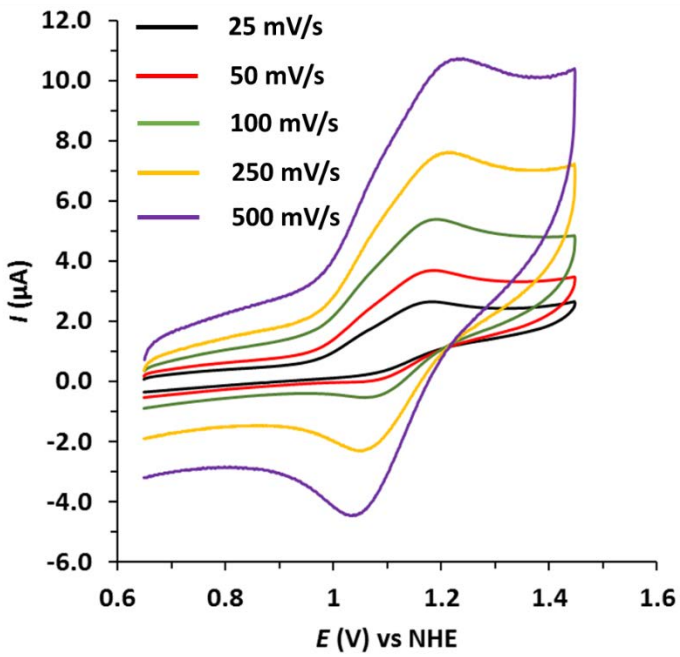

Figure S20. Cyclic Voltammograms of $\mathbf{2}^{2-}$ at different scan rates (25-500 mV/s). Conditions: 1 mM of complex in DMF containing 0.1 M of TBAPF. GC disk as working electrode.

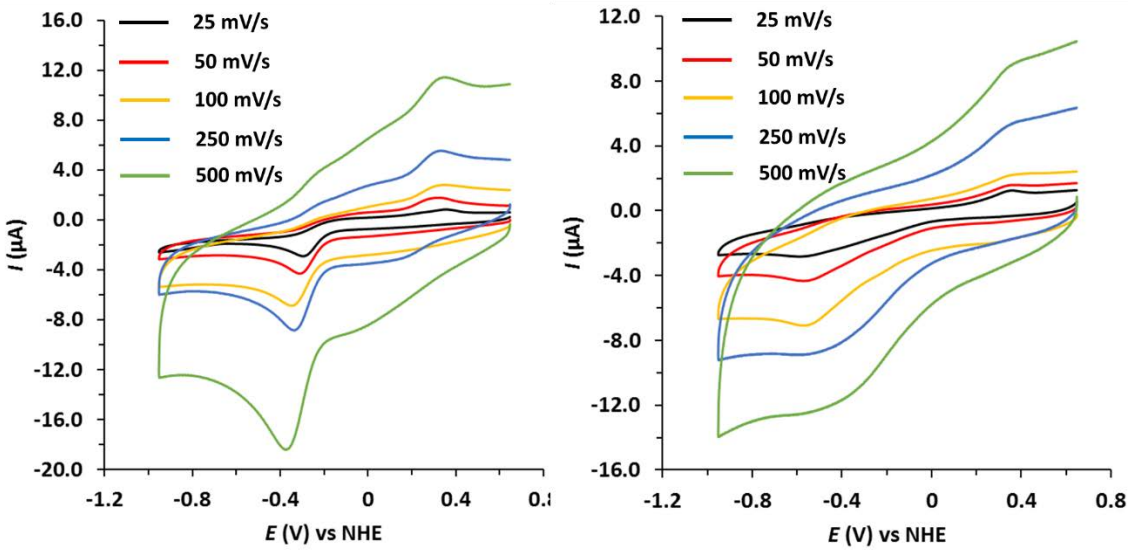

Figure S21. Cyclic Voltammograms of $\mathbf{1}^{2-}$ (left) and $\mathbf{2}^{2-}$ (right) at different scan rates (25-500 mV/s). Conditions: 1 mM of complex in DMF containing 0.1 M of $TBAPF_6$. GC disk as working electrode.

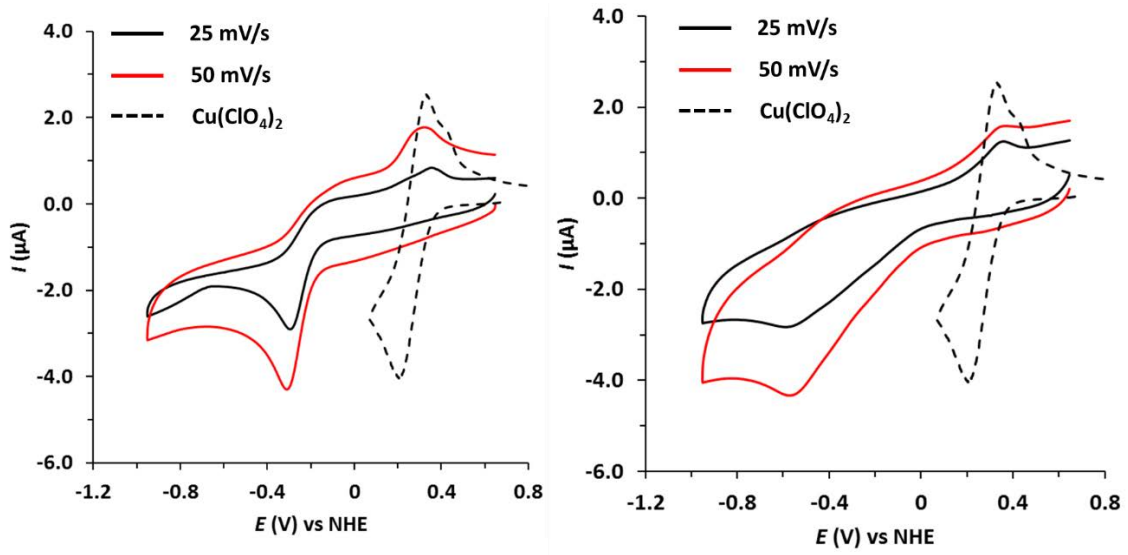

Figure S22. Cyclic Voltammograms of $\mathbf{1}^{2-}$ (left) and $\mathbf{2}^{2-}$ (right) at low scan rates (25-50 mV/s). Dashed black line corresponds to a blank solution containing 1 mM of $Cu(ClO_4)_2$ salt at 100 mV/s scan rate. Conditions: 1 mM of complex in DMF containing 0.1 M of TBAPF. GC disk as working electrode.

5. Electrocatalysis

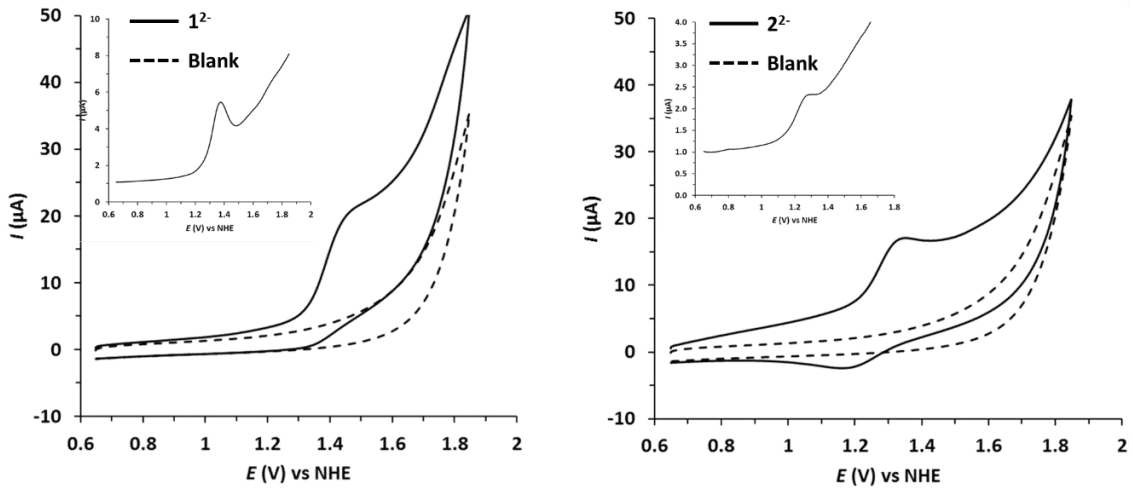

Figure S23. Cyclic Voltammograms of $\mathbf{1}^{2-}$ (left) and $\mathbf{2}^{2-}$ (right) in 0.1 M phosphate buffer pH 7.0. *Inset* Differential Pulse Voltammograms for $\mathbf{1}^{2-}$ and $\mathbf{2}^{2-}$. Dashed black line corresponds to a blank with no catalyst. Conditions: scan rate of 100 mV/s, [**Complex**] = 1 mM. GC as working electrode.

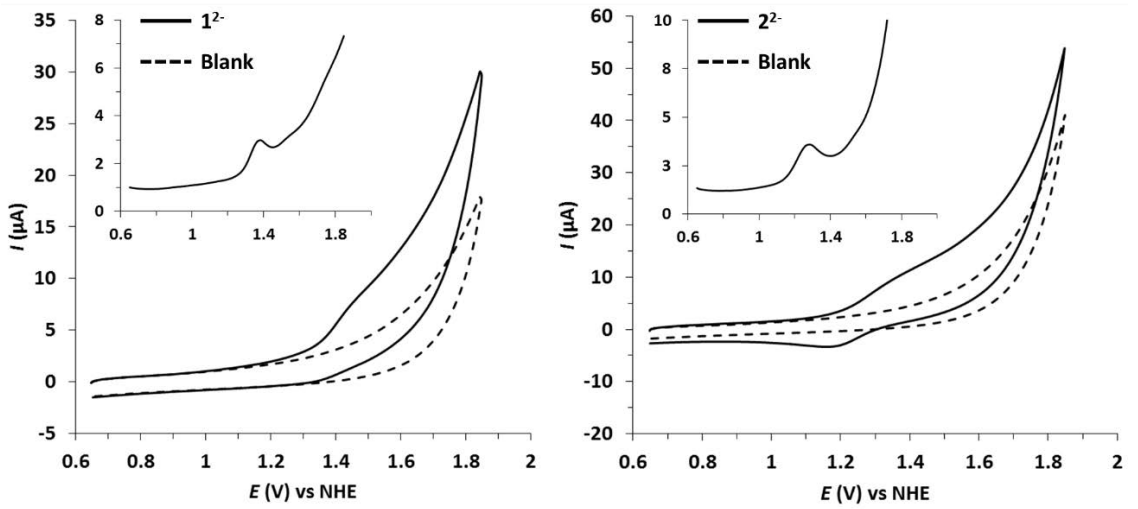

Figure S24. Cyclic Voltammograms of $\mathbf{1}^{2-}$ (left) and $\mathbf{2}^{2-}$ (right) in 0.1 M phosphate buffer pH 9.0. *Inset* Differential Pulse Voltammograms for $\mathbf{1}^{2-}$ and $\mathbf{2}^{2-}$. Dashed black line corresponds to a blank with no catalyst. Conditions: scan rate of 100 mV/s, [**Complex**] = 1 mM. GC disk as working electrode.

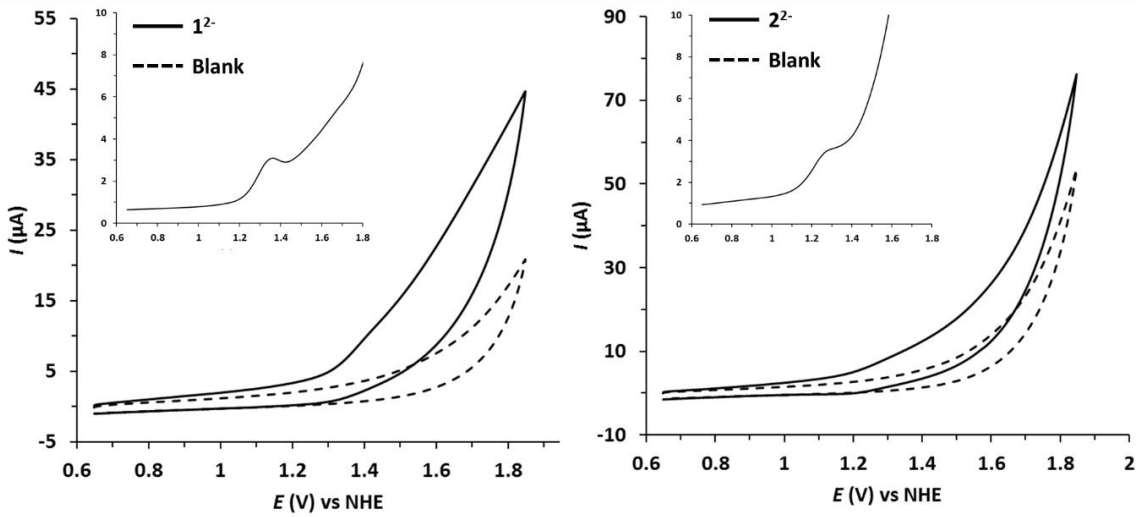

Figure S25. Cyclic Voltammograms of $\mathbf{1}^{2-}$ (left) and $\mathbf{2}^{2-}$ (right) in 0.1 M phosphate buffer pH 11.4. *Inset* Differential Pulse Voltammograms for $\mathbf{1}^{2-}$ and $\mathbf{2}^{2-}$. Dashed black line corresponds to a blank with no catalyst. Conditions: scan rate of 100 mV/s, [**Complex**] = 1 mM. GC as working electrode.

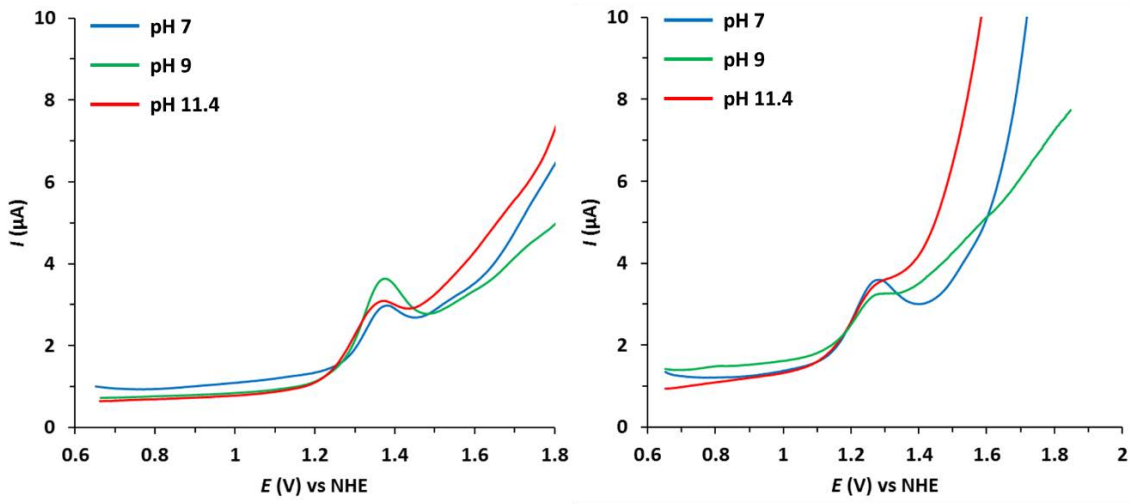

Figure S26. DPV experiments of $\mathbf{1}^{2-}$ (left) and $\mathbf{2}^{2-}$ (right), 1 mM concentration in phosphate buffers (pH 7.0, 9.0 and 11.4). GC as working electrode.

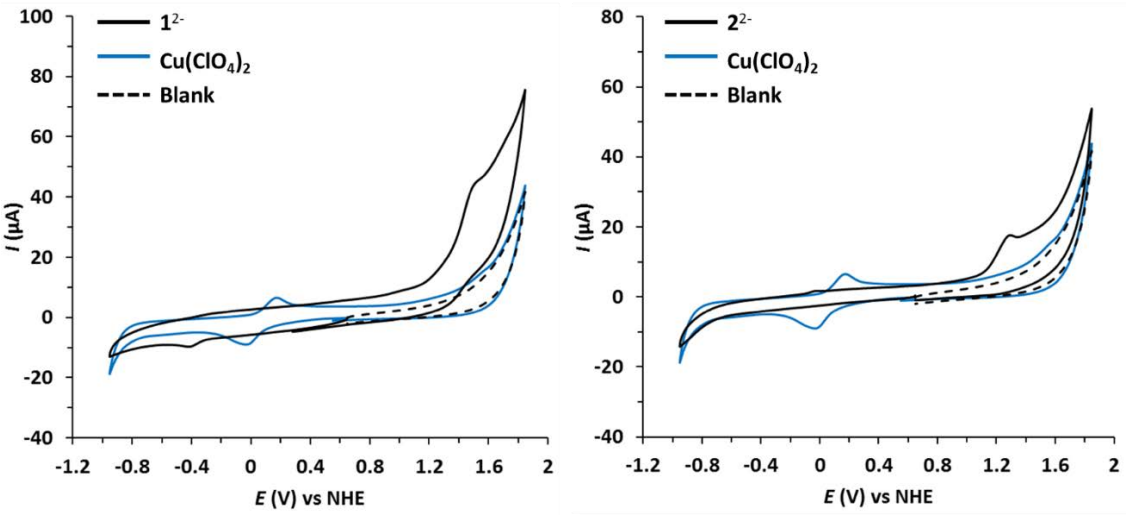

Figure S27. Cyclic Voltammograms of $\mathbf{1}^{2-}$ (left) and $\mathbf{2}^{2-}$ (right) in 0.1 M phosphate buffer pH 11.4, showing the electrocatalytic response of the complex (solid black line), $Cu(ClO_4)_2$ (solid blue line) and the blank (dashed line). Conditions: scan rate of 100 mV/s, [**Complex**] = 1 mM. BDD disk as working electrode.

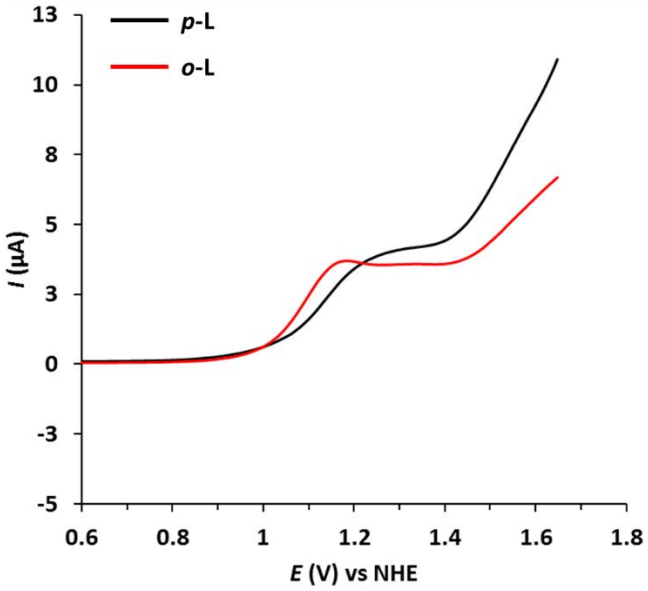

Figure S28. DPV experiments of *p*-L (black line) and *o*-L (red line) in 0.1 M phosphate buffer pH 11.4. [**Ligand**] = ~1 mM. BDD disk as working electrode.

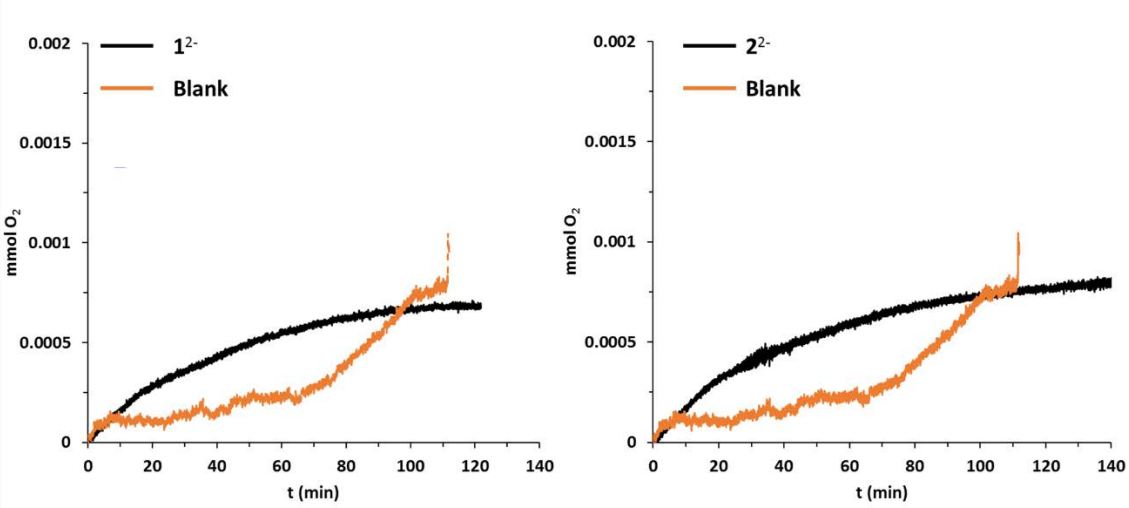

Figure S29. Oxygen evolution measurements given in mmol O_2 vs. time (min) for complexes $\mathbf{1}^{2-}$ (left) and $\mathbf{2}^{2-}$ (right) at 1.5 mM concentration using a Clark probe electrode during a CPE at 1.6 V vs. NHE in 0.1 M phosphate buffer pH 7. Blank data in the absence of complex is shown in orange. BDD plate as working electrode, Pt mesh counter electrode and AgCl as reference electrode.

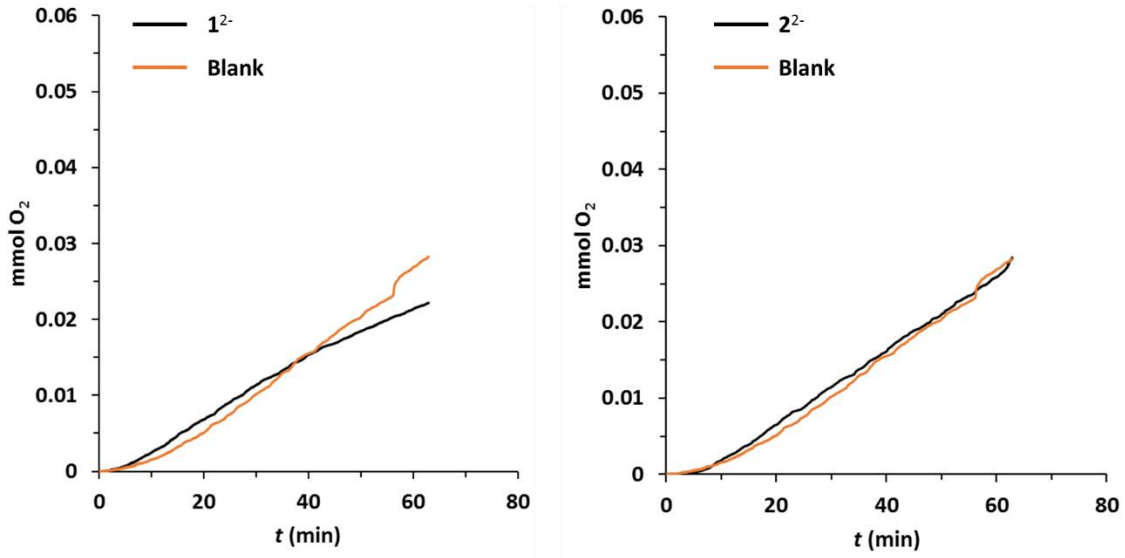

Figure S30. Oxygen evolution measurements given in mmol O_2 vs. time (min) for complexes $\mathbf{1}^{2-}$ (left) and $\mathbf{2}^{2-}$ (right) at 1.5 mM concentration using a Clark probe electrode during a CPE at 1.6 V vs. NHE in 0.1 M borate buffer pH 9. Blank data in the absence of complex is shown in orange. BDD plate as working electrode, Pt mesh counter electrode and AgCl as reference electrode.

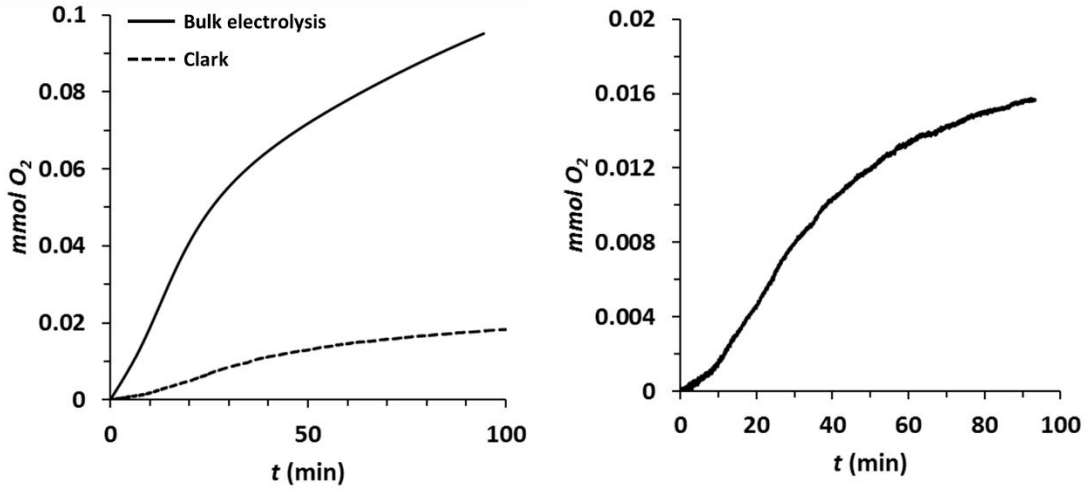

Figure S31. Comparison between current (expressed as mmol of O_2) obtained during the CPE experiment at 1.6 V vs. NHE in 0.1 M phosphate buffer pH 11.4 for complex $\mathbf{1}^{2-}$ and the number of mmol of O_2 detected by the Clark electrode (left). Evolution of O_2 detected during the CPE experiment by the Clark electrode with blank subtraction (right).

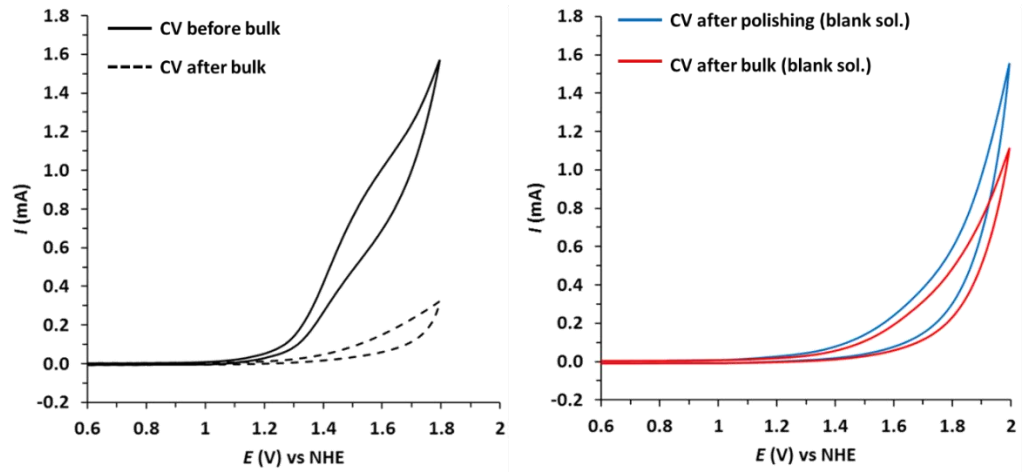

Figure S32. (Left) CV measurements for $\mathbf{1}^{2-}$ before (black solid line) and after (black dashed line) a CPE at 1.6 V during 95 min in 0.1 M phosphate buffer pH 11.4. **(Right)** Comparison of CVs of a blank solution after a CPE at 1.6 V during 95 min and the mechanically polished BDD electrode under a blank solution, showing no catalytic response due to the presence of heterogeneous materials deposited onto the surface of the electrode. Conditions: scan rate of 100 mV/s. BDD plate as working electrode, Pt mesh counter electrode and Ag/AgCl as reference electrode.

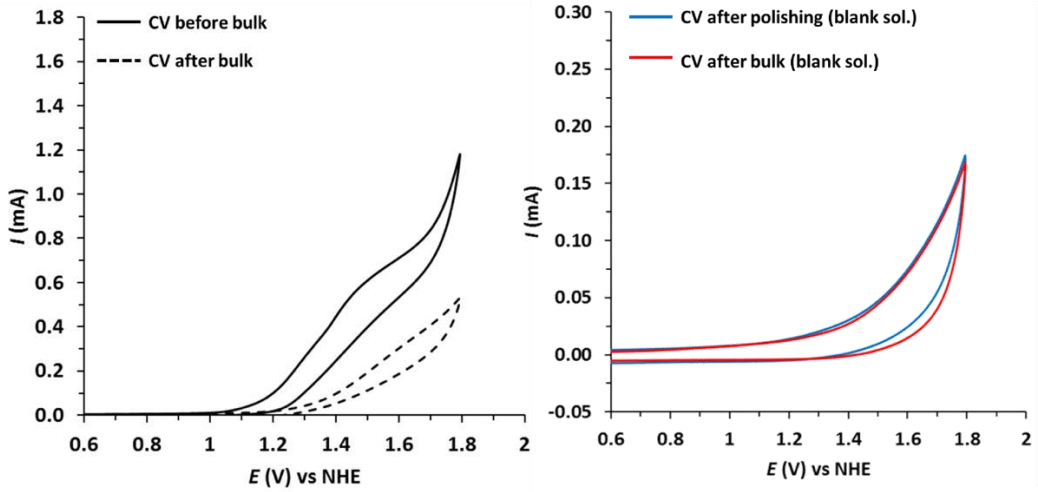

Figure S33. (Left) CV measurements of $\mathbf{2}^{2-}$ before (black solid line) and after (black dashed line) a CPE at 1.6 V during 45 min in 0.1 M phosphate buffer pH 11.4. **(Right)** Comparison of CVs of a blank solution after a CPE at 1.6 V during 95 min and of the mechanically polished BDD electrode under a blank solution, showing no catalytic response due to the presence of heterogeneous materials deposited onto the surface of the electrode. Conditions: scan rate of 100 mV/s. BDD plate as working electrode, Pt mesh counter electrode and AgCl as reference electrode.

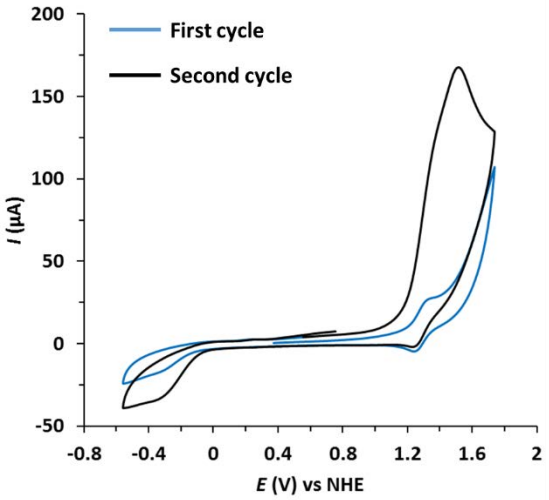

Figure S34. CV (left) and DPV (right) of **[(bpyalk)Cu]** in 0.1 M KNO_3 pH 12.05. Conditions: scan rate of 100 mV/s, [**Complex**] = 1 mM. GC as working electrode.

6. Scanning Electron Microscopy

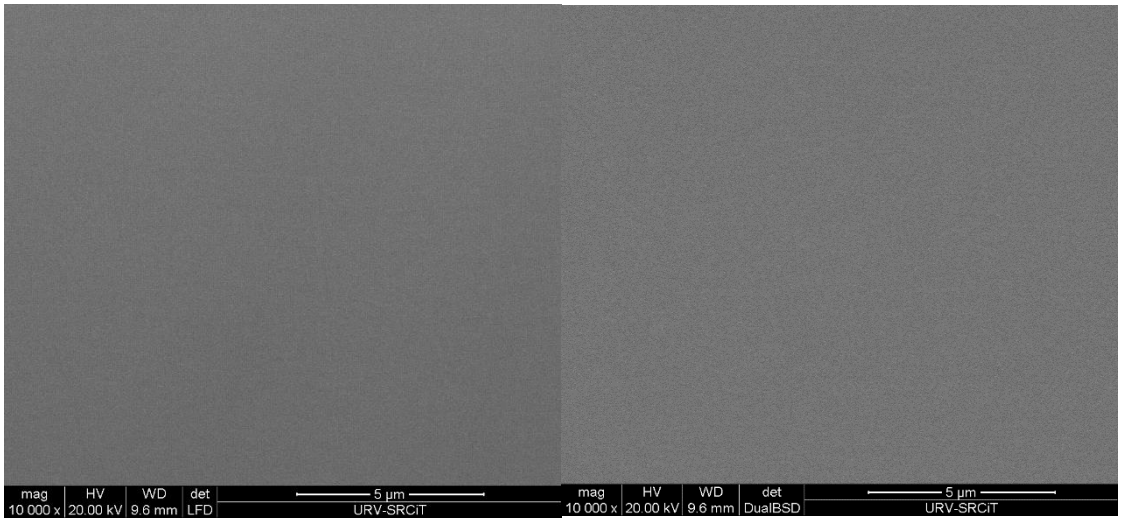

Figure S35. SEM micrographs (left) and corresponding back-scattered electron micrographs (right) of a glassy carbon electrode after a 20 minute electrolysis of $\mathbf{1}^{2-}$ (1.5 mM) in phosphate buffer pH 11.4 at 1.6 V vs. NHE. There is no appreciable presence of copper oxide nanoparticles or deposited materials on the electrode.

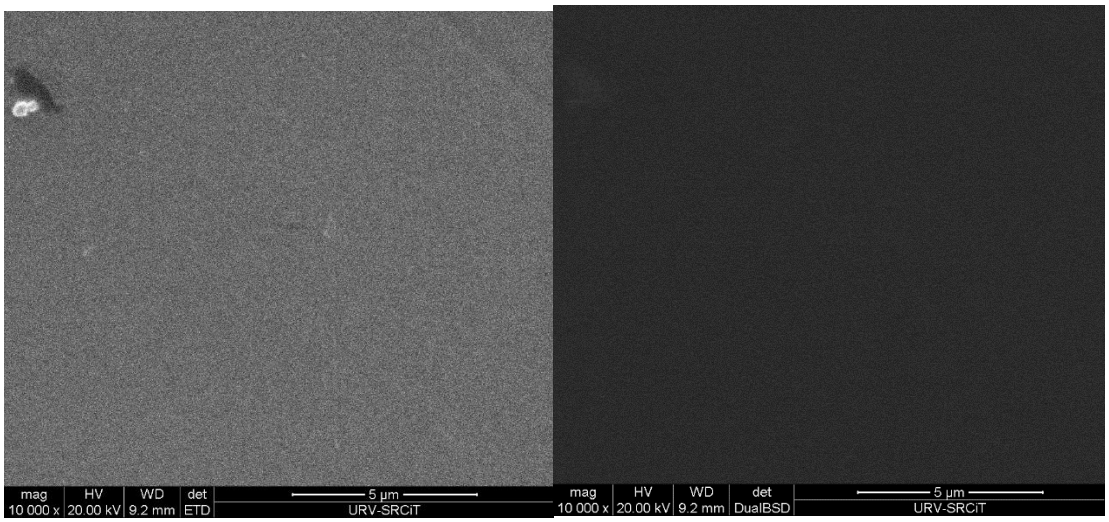

Figure S36. SEM micrographs (left) and corresponding back-scattered electron micrographs (right) of glassy carbon electrode after a 20 minute electrolysis of $\mathbf{2}^{2-}$ (1.5 mM) in phosphate buffer pH 11.4 at 1.6 V vs. NHE. There is no appreciable presence of copper oxide nanoparticles or deposited materials on the electrode.

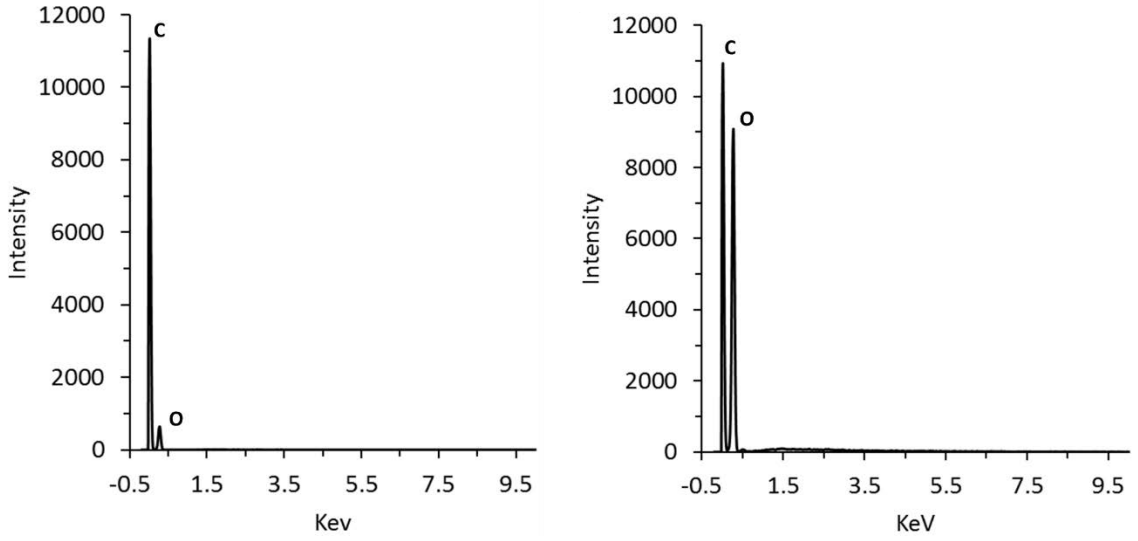

Figure S37. EDX spectra of the glassy carbon electrode after a 20 minute electrolysis of $\mathbf{1}^{2-}$(left) and $\mathbf{2}^{2-}$ (right) in phosphate buffer pH 11.4 at 1.6 V vs. NHE. There is no appreciable presence of copper on the surface of the electrode.

7. References

[1] Bozoklu, G.; Marchal, C.; Gateau, C.; Pécaut, J.; Imbert, D.; Mazzanti, M.; *Chem. Eur. J.* **2010**, *16*, 6159-6163.

[2] Shao, j.; Qiao, Y.-H.; Lin, H.; Lin, H.-K. *J. Lumin.* **2008**, *128*, 1985-1988.

[3] Garrido-Barros, P.; Funes-Ardoiz, I.; Drouet, S.; Benet-Buchholz J.; Maseras F.; Llobet, A. *J. Am. Chem. Soc.* **2015**, *137*, 6758-6761.

[4] Data collection with APEX II version v2013.4-1. Bruker (2007). Bruker AXS Inc., Madison, Wisconsin, USA.

[5] Data reduction with Bruker SAINT version V8.30c. Bruker (2007). Bruker AXS Inc., Madison, Wisconsin, USA.

[6] SADABS: V2012/1 Bruker (2001). Bruker AXS Inc., Madison, Wisconsin, USA. Blessing, Acta Cryst. **1995**, A51, 33-38.

[7] SHELXT; V2014/4 (Sheldrick 2014). Sheldrick, G.M. *Acta Cryst*. **2015**, A71, 3-8.

[8] SHELXle; C.B. Huebschle, G.M. Sheldrick & B. Dittrich; J. Appl. Cryst. **2011**, 44, 1281-1284.

[9] SHELXL; SHELXL-2014/7 (Sheldrick 2014). Sheldrick, G.M. *Acta Cryst*. **2015**, C71, 3-8.

CHAPTER V

Catalytic H_2 evolution with CoO, $Co(OH)_2$ and CoO(OH) NPs generated from a molecular polynuclear Co complex.

As we introduced in Chapter I, transition metal NPs supported in carbon materials are a promising option for developing efficient and robust proton reduction cathodes. In this work, we present the preparation and characterization of Co NPs electrodeposited onto glassy carbon electrodes arising from a molecular complex. The influence of the solvent on the size and nature of the nanoparticulated species formed are analyzed. Furthermore, a detailed catalytic study is presented, showing how the different species electrodeposited on the cathodes can affect the catalytic performance towards HER at basic pH.

This chapter consist in the following paper:

Gil-Sepulcre, M.; Gimbert-Suriñach, C.; Aguilà, D.; Velasco, V.; García-Antón, J.; Llobet, A.; Aromí, G.; Bofill, R.; Sala X. *Submitted*

PAPER D: Catalytic H_2 evolution with CoO, $Co(OH)_2$ and CoO(OH) NPs generated from a molecular polynuclear Co complex

Gil-Sepulcre, M.; Gimbert-Suriñach, C.; Aguilà, D.; Velasco, V.; García-Antón, J.; Llobet, A.; Aromí, G.; Bofill, R.; Sala X. *Submitted*

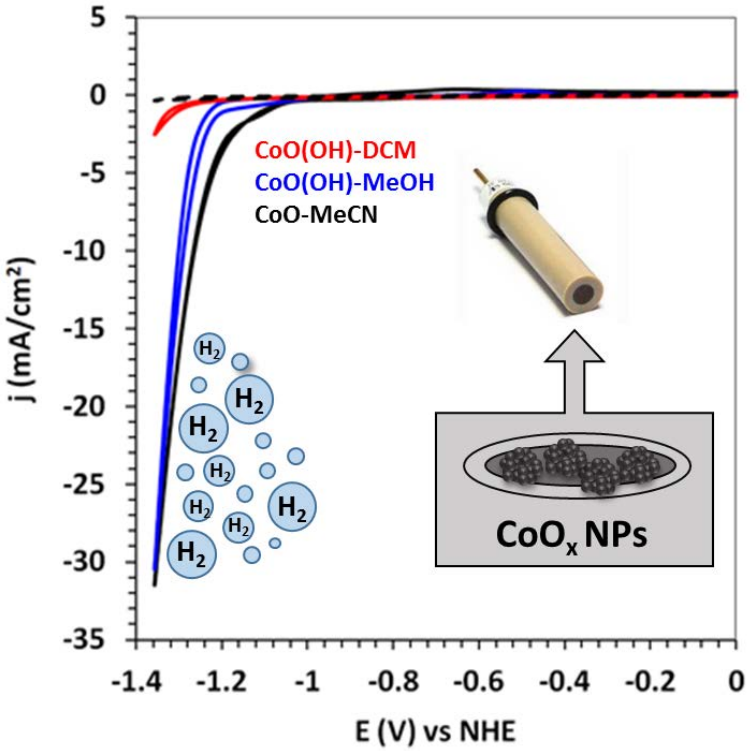

Abstract: Electrochemical water reduction by employing first row transition metal nanoparticles (NPs) constitutes a sustainable way for the generation of H_2. We have synthesized Co-based NPs from a molecular Co^{II}/Co^{III} precursor after its reductive decomposition at -1.86 V *vs.* NHE in different organic solvents. These NPs are able to electrochemically reduce water at pH 14. SEM, EDX and XPS analyses have allowed the determination of the chemical nature of the as-deposited NPs: CoO when using MeCN as solvent and CoO(OH) when employing either dichloromethane (DCM) or MeOH. After 2h of constant polarization at 10 $mA \cdot cm^{-2}$, the electrocatalytic activity of the NPs obtained in MeCN and DCM decreases, whereas for those obtained in MeOH increases. In this solvent, the overpotential is reduced by 215-220 mV and the specific current density is triplicated. Interestingly, during this activation process in MeOH the precursor CoO(OH) NPs are converted into $Co(OH)_2$. The implications of these results in the context of the current research in the field are also discussed.

Introduction

During the last decade, the struggle against global warming has been centred in attaining sustainable fuel generation systems. The generation of H_2 through the (photo)electrochemical reduction of protons is one of the most promising alternatives.[1] In this context, several transition metal nanoparticles (NPs) have been shown to be catalytically active in the hydrogen evolution reaction (HER),[2] from which cobalt, a relatively abundant 1st row transition metal, constitutes a good cheap candidate.[3]

Co, CoO and $Co(OH)_2$ NPs have been successfully tested as catalysts for the HER at pH 13-14. Further, Co NPs have been encapsulated within carbon shells, carbon nanotubes (CNTs) and carbon nanofibers (CNFs) with a varied range of activities (from -196 to -375 mV overpotentials at 10 $mA \cdot cm^{-2}$ -from now on η-) and good stability (5.5-10 h electrolysis).[3b,3c,4] Also, mixed Co/CoO NPs have been deposited on N-doped graphitic C[5] and Co NPs on N,S-doped C,[6] with decreased η values of -395 and -250 mV, respectively, which remarkably further decreases to -50 mV if the Co NPs are embedded inside a CoO matrix.[7] Finally, $Co(OH)_2$ NPs with variable sizes (from 1 to 30 nm) have also been successfully tested at neutral or slightly basic pH under different supports in photocatalytic hydrogen evolution.[8,9]

In the last few years, the *in-situ* formation of catalytically active metal and metal oxide/hydroxide NPs from the decomposition of molecular precursors under catalytic conditions has been indeed described. This is very common in redox catalysis where ligands and metal centres are exposed to oxidative/reductive stress. In the case related to water oxidation, the work of Spiccia and co-workers dealing with the formation of MnO_x NPs inside a Nafion matrix from a wide set of structurally diverse Mn-based complexes under photoelectrochemical catalytic conditions is particularly revealing.[10] The size and catalytic performance of the formed NPs is found to be highly dependent on the structure of the molecular precursor and thus on the nature of the ligands bonded to the Mn ion. For the particular case of Co ions, the *in-situ* formation of $Co(OH)_x$ and CoO_x NPs as the real active catalytic water oxidation species when starting from mononuclear Co complexes and from a Co polyoxometalate, respectively, has also been described.[11] Interestingly, formation of Co-derived NPs has also been observed under HER catalytic conditions at modest cathodic potentials (-0.75 V *vs.* NHE) in the presence of acid in acetonitrile.[3a]

In this work, CoO and CoO(OH) NPs have been obtained by decomposition in several organic solvents of the molecular Co^{II}/Co^{III} complex $[Co_8Na_4(L)_4(OH)_2(CO_3)_2(py)_{10}](BF_4)_2$ (**1**; py = Pyridine; L = 2,6-bis-(3-oxo-3-(2-hydroxyphenyl)-propionyl)-pyridine)[12] that are able to electrochemically form H_2 from water at pH 14. The NPs have been deposited onto the surface of a glassy carbon (GC) electrode after applying a potential of -1.86 V *vs.* NHE during 1 h in different solvents, and characterized by SEM, EDX, XPS and electrochemical techniques. The electrocatalytic properties of the as-deposited NPs and those of a new $Co(OH)_2$ phase generated under catalytic conditions have been analysed using the protocol for catalysts benchmarking recently reported by Jaramillo *et al.*[13] The implications of these results in the context of the current research in catalytic HER by Co-derived NPs are also discussed.

Results

Electrodeposition and characterization of Co-derived NPs

Two years ago, Aromí *et al.* described that the heptadentate ligand 2,6-bis-(3-oxo-3-(2-hydroxyphenyl)-propionyl)-pyridine (H_4L) reacts with Co(II) salts in strong basic conditions, yielding in the presence of atmospheric CO_2 the mixed Co^{II}/Co^{III} complex $[Co_8Na_4(L)_4(OH)_2(CO_3)_2(py)_{10}](BF_4)_2$ (**1**; py=pyridine) containing two trapped carbonate anions in very close proximity.[12] Given its unprecedented coordination features and the presence of 4 Co(II) and 4 Co(III) ions, we decided to study the potential applications of this complex in redox catalysis, specifically for the possible oxidative coupling of both trapped anions into a chemically interesting product. However, when studying its electrochemical features in acetonitrile (MeCN), two irreversible waves at -0.85 V and -1.50 V *vs.* NHE (-1.48 V and -2.13 V vs. Fc^+/Fc) and an irreversible oxidative wave near 0.35 V *vs.* NHE (-0.28 V vs. Fc^+/Fc) appeared, with a concomitant increase in their intensity upon performing several cyclic voltammetry (CV) cycles (Figure S16). This behaviour indicated that an irreversible chemical transformation of the electroactive species was taking place together with an increase of its available concentration at the electrode surface. This phenomenon could be related to an electrodeposition process on the surface of the GC electrode used for the measurements following the decomposition of **1** into bulk, nanoparticulated or layered Co-based materials. In fact, according to the literature, Co-based NPs able to electrochemically reduce water have already been reported to deposit at the electrode surface at modest cathodic potentials starting from a molecular Co(III) complex.[3a] Thus, we decided to test the possible deposition of Co-based

NPs active in HER catalysis after an electrolysis of our system at more negative potentials than those of the first and second irreversible waves, *i.e.*, at -1.16 V and -1.86 V *vs.* NHE, respectively. The optimum electrolysis time resulted to be 1 h, since no significant changes in the size of the NPs nor their electrocatalytic activity (see below) were detected at higher electrolysis times. The SEM micrographs of the surface of the GC electrodes obtained are shown in Figures S1 and S2, respectively. The presence of NPs containing heavy nuclei is clear from the back-scattered electron SEM micrographs (bright spots) in both cases, with average diameters of 65.5 ± 18.2 and 52.5 ± 15.7 nm after the treatment at -1.16 V and -1.86 V, respectively *vs.* NHE. Furthermore, the elemental analysis by EDX of the SEM data (Figure S9) indicated the presence of Co in both samples, thus confirming the formation of Co-based NPs under these conditions. Additionally, the formation of Co-derived NPs can be deduced from the gradual loss of colour intensity of the MeCN solution of **1** during its electrolysis at -1.86 V *vs.* NHE and the appearance of dispersed colloidal particles after 16 h (Figure S14). The depletion of the original complex from the solution is confirmed by the complete disappearance of the characteristic absorbance band at 218 nm of **1** after 16 h (Figure S15).

Since the NPs obtained at -1.86 V *vs.* NHE show smaller size and higher uniformity (lower standard deviation of the average diameter) compared to those formed at -1.16 V, we decided to focus our attention on the former conditions to carry out our morphological and catalytic studies. It seems reasonable to expect higher catalytic activities with smaller NPs and thus with larger surface areas. Thus, an analogous procedure at -1.86 V *vs.* NHE was carried out in the presence of other solvents in which **1** is also soluble, namely dichloromethane (DCM) and methanol (MeOH). The SEM analyses showed the formation of smaller Co-derived NPs now, with average diameters of 37.5 ± 10.1 and 32.0 ± 9.3 nm for DCM and MeOH, respectively (Figures S3 and S4). Again, the presence of the element Co in the samples was confirmed by EDX (Figure S10). Furthermore, the ability of the octanuclear clustered complex **1** to transform into small and isolated NPs is demonstrated when analysing the results obtained under analogous conditions using $CoCl_2$ salt as Co precursor (Figure S8), now producing Co-derived NP aggregates of 0.28-0.45 μm in size with significant size dispersion.

In order to characterize the chemical composition of the as deposited-Co-derived NPs in MeCN, DCM and MeOH, XPS analyses were carried out (Figures 1 and Figure S12). The Co 2p XPS spectrum of the sample obtained in MeCN shows two main peaks

at 780 and 796 eV accompanied by two broad satellite peaks at higher energies (786 and 802 eV), while for the samples obtained in DCM and MeOH the spectra are identical, basically showing only two main components at ca. 780.5 and 796 eV (Figure 1). The latter correspond to the Co $2p_{3/2}$ and Co $2p_{1/2}$ components, respectively,[14] while the satellite peaks indicate the presence of unpaired electrons in the sample, *i.e.*, of Co^{II} (d^7) atoms.[15] The O 1s XPS spectra, show a single band at 530.5 eV for the MeCN sample, which is shifted towards 531.4 eV for the DCM and MeOH cases (Figure S12, a). This shift towards higher energies is due to the presence of hydroxyl groups on the Co surface.[2,7,14,16] Thus, when taking all XPS data in consideration, it is clear that in MeCN we obtain CoO NPs. This is supported by the similarity of our Co 2p XPS spectrum with those of CoO previously reported[15] and by the presence of a band at *ca.* 530 eV for the O 1s XPS spectrum, as reported elsewhere.[7,14] In sharp contrast, in DCM and MeOH mixed oxy-hydroxide Co^{III} (d^6) NPs are obtained (CoO(OH) NPs) based on the almost complete absence of Co 2p satellite bands and the 780.5 eV value for the Co $2p_{3/2}$ transtion[17] as well as on the high energy shift of the O 1s band. The presence of CoO(OH) in the sample formed in DCM could be due either to the presence of a small fraction of water in DCM or to hydration processes provoked by air exposure prior to the XPS measurements. Regarding N and C XPS signals (Figure S12, b-c), the N 1s band found ca. 399 eV for all samples is typical of Co-N bonds or N-pyridyls,[4a-b,6] which originate from ligand L in precursor **1** during its electrodecomposition (a comparison of the N atomic percentage measured by XPS indicates that the amount of N of the samples is comprised between 8 and 15 % and thus is not negligible compared to the 0.7 % atomic percentage of the blank), and the C 1s band at ca. 284.2 eV is due to the GC electrode.[18] From now on in this work and for the sake of brevity, the three sets of NPs formed after 1h-electrolysis at -1.86 V vs. NHE will be named as CoO-MeCN, CoO(OH)-MeOH and CoO(OH)-DCM.

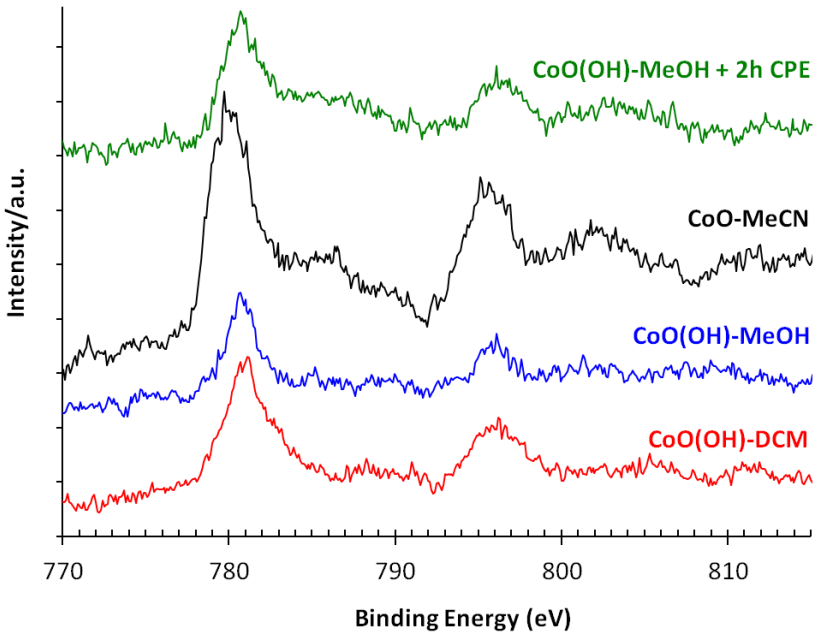

Figure 1. Co 2p XPS spectra for the Co-based NPs obtained from **1** in MeCN (black), DCM (red) and MeOH (blue) after a 1h-electrolysis at -1.86 V *vs.* NHE and from **1** in MeOH after a 1h-electrolysis at -1.86 V *vs.* NHE plus a 2h-CPE at 10 $mA \cdot cm^{-2}$ (green). Energies have been calibrated according to the C 1s band of graphite at 284.2 eV.

Electrocatalytic performance

The Co-derived NPs deposited on the surface of a rotating disk electrode (RDE) obtained in the three different solvents were characterized by rotating disk voltammetry (RDV) at pH 14 (Figure 2), where an intense irreversible catalytic current with onset potential at *ca.* -1.11, -1.15 and -1.20 V *vs.* NHE appears for CoO-MeCN, CoO(OH)-MeOH and CoO(OH)-DCM, respectively, with associated current densities of 1.27, 0.76 and 0.26 mA/cm^2. According to H_2-sensitive Clark electrode measurements, this process corresponds to the reduction of protons to generate H_2 with a Faradaic efficiency between 96% and 98% for all cases (Figure S22). From the experimental onset potential of the catalytic waves compared to the thermodynamic reduction potential $E(H^+/H_2)$ at pH 14 (-0.828 V *vs.* NHE), the MeCN, MeOH and DCM samples show an onset overpotential of -276 mV, -321 mV and -348 mV, respectively.

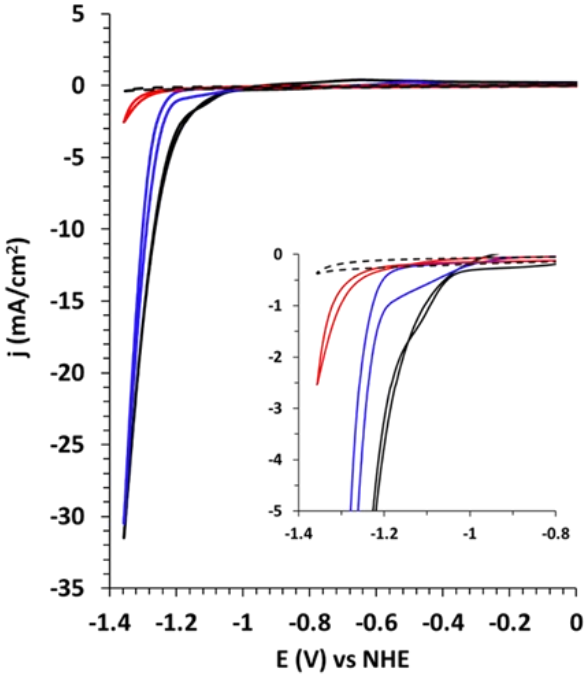

Figure 2. Representative rotating disk voltammograms of CoO(OH)-DCM (red), CoO(OH)-MeOH (blue) and CoO-MeCN (black). The non-functionalized RDE electrode (blank) is shown as a black dashed line. Conditions: N_2-Saturated 1 M NaOH solution, 0.01 V/s scan rate and 1600 rpm. Inset: zoomed view of the onset potential region.

A thorough electrochemical analysis of the behaviour of the Co-based NPs has been performed following the procedures described by Jaramillo *et al.*[13] Thus, the electrochemically active surface area (ECSA) of each modified RDE with Co-based NPs was estimated from its electrochemical double-layer capacitance (C_{dl}) by measuring the non-Faradaic capacitive current associated with double-layer charging (Figure S17). The roughness factor (RF) is calculated by dividing the estimated ECSA by the geometric area of the electrode. Furthermore, 30s-controlled current step-chronopotentiometry and chronoamperometry (Figure S19) and 2h-controlled current electrolysis (Figure S21) measurements have allowed us to determine the overpotential at a constant current density of 10 $mA \cdot cm^{-2}$ (η). This is a widely accepted benchmarking parameter for the catalytic activity of heterogeneous catalysts which corresponds to the approximate current density expected for a 10% efficient solar-to-fuel conversion photoelectrochemical cell under 1 sun illumination.[19] The NPs with lower η are CoO-MeCN (-435 mV), followed by CoO(OH)-MeOH (-465 mV) and finally by CoO(OH)-DCM (-504 mV). Interestingly, when the CoO-MeCN and CoO(OH)-DCM NPs are submitted to a 2h-controlled current electrolysis at a constant current density of 10 $mA \cdot cm^{-2}$ (Figure S21), the η steadily increases, particularly for CoO-MeCN, denoting the relative instability of both systems

under HER conditions. Effectively, XPS (Figure S13) and SEM analyses (Figures S6 and S7) show the lack of stability of both CoO-MeCN and CoO(OH)-DCM NPs after a 2h-controlled current electrolysis. For the former case, no Co-derived NPs are detected on the surface of the GC electrode, and for the latter the CoO(OH) composition of the NPs is maintained, although their concentration clearly decreases (less intense Co 2p signal and decrease of the Co atomic concentration from 1.61 % to 0.64 % according to XPS measurements, Figure S13) while at the same time the average diameter increases from 37.5 nm (Figure S3) to 77.7 nm (Figure S7).

In contrast, as shown in Figure 3a, the η of CoO(OH)-MeOH NPs clearly decreases over time. The superior activity of the resulting nanomaterial after electrolysis is also appreciated when comparing its RDV with that of the original CoO(OH) NPs in the same conditions (Figure 3b). A detailed electrocatalytic analysis of this "activated" system can be found in Figures S18, S20 and S23. The results corroborate its higher performance, with a decrease in η by 213 mV and a significant increase in the specific current density (j_s) at an overpotential of -480 mV, which is more than triplicated, from 174 to 596 mA·cm^{-2}.

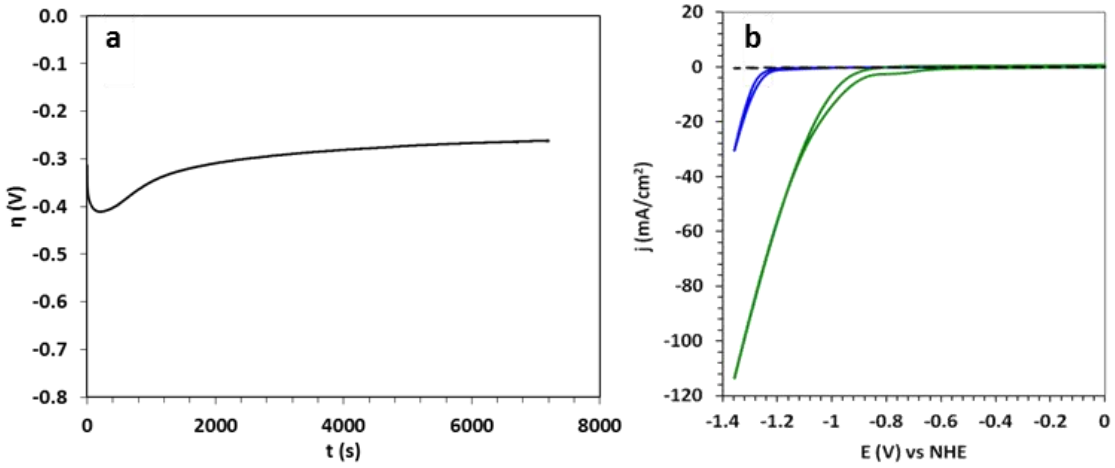

Figure 3. a) 2h-controlled current electrolysis in MeOH at 10 mA·cm^{-2} of CoO(OH)-MeOH; b) representative rotating disk voltammograms of CoO(OH)-MeOH at t=0 (blue) and after a 2h-controlled current electrolysis at 10 mA·cm^{-2} (green). The non-functionalized RDE electrode (blank) is shown as a dashed line. Conditions: N_2-Saturated 1 M NaOH solution, 0.01 V/s scan rate and 1600 rpm.

In order to better understand the nature of this "activated" system, the 2h-electrolized cathode was characterized by SEM (Figures S5 and S11) and XPS (Figure 1

and Figure S12). SEM images show an average diameter of 39.9 ± 16.4 nm, very close to the precursor CoO(OH) NPs before the activation (Figure S4).

Comparison of the Co 2p XPS spectra of the CoO(OH)-MeOH sample and its 2h-electrolyzed derivative shows the appearance of two satellite bands for the latter (Figure 1) and the presence of an O 1s XPS band at 531.2 eV in both samples (Figure S12, a). Thus, a reduction of the Co^{III} atoms to Co^{II} is taking place without losing hydroxyl groups. Therefore, we propose the formation of $Co(OH)_2$ NPs after the 2h activation process in MeOH. Indeed, the positions of the Co 2p main peaks at 780.7 and 796.5 eV as well as the overall shape of the spectrum are coincident with previous data reported for $Co(OH)_2$.[8,11a,15,17] Curiously, the low intensity shoulder at *ca.* 287.5 eV of its C 1s XPS spectrum (Figure S12, c) could be attributed to the presence of MeOH molecules coordinated onto the surface of the $Co(OH)_2$ NPs.[20]

Finally, the Tafel plots for all four Co-derived NPs and two blanks prepared in MeOH from $CoCl_2$ and $CoCl_2$ in the presence of H_4L are shown in Figure 4, in which it becomes clear the superior HER activity of the $Co(OH)_2$ NPs obtained after a 2h-CPE in MeOH (red line).

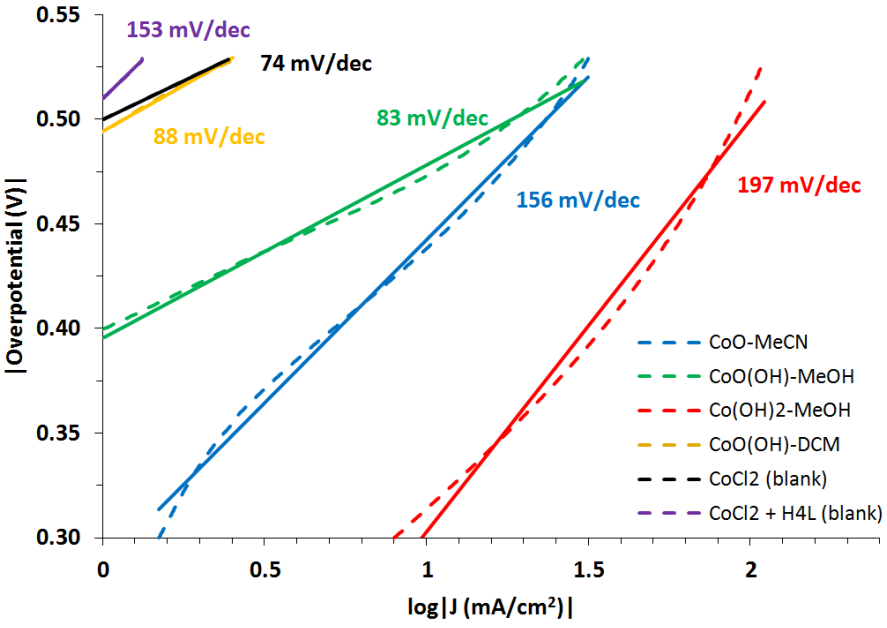

Figure 4. Tafel plots registered at pH 14 for the Co-based NPs synthesized in this work in different solvents and from $CoCl_2$ or $CoCl_2$ + H_4L in MeOH (blanks).

Discussion

A comparison of the physical and electrochemical properties of the Co-derived NPs formed from **1** in this work with those of the respective blanks prepared from $CoCl_2$ is shown in Table 1. In all cases, the NPs obtained in the blanks (entries 5-8) are one order of magnitude larger and less uniformly sized than their respective NPs formed from **1** (entries 1-3), showing the relevant role of the molecular precursor for its proper reduction into small Co-derived NPs. This result highlights the already reported role of metal complexes in allowing better control over *in-situ* electrodeposition processes than simple salts.[10b] Thus, the initial η ($\eta_{t=0}$) and the η value after 2h-electrolysis ($\eta_{t=2}$) are normally higher than the respective values for the NPs obtained from **1** (entries 1 *vs.* 5, 2 *vs.* 6 and 3 *vs.* 7) while the j_s values are between 1 and 3 orders of magnitude lower. Also, the presence of uncoordinated H_4L ligand in the $CoCl_2$ blank prepared in MeOH does not significantly alter the performance of the obtained NPs compared to the blank prepared in its absence (entries 7 and 8), thus pointing to the importance of starting from a precursor containing the ligand within its molecular scaffold.

The ECSA and RF values of our Co-based NPs are similar, assuming the one order of magnitude inherent accuracy of the RF measurements, while they are significantly lower -around three orders of magnitude- than those of Co electrodes previously benchmarked.[13] These results are consistent with the fact that in our case low concentrations of **1** are used for the NP electrodeposition (0.25 mM) compared to the much higher concentrations used in the literature (around 100 mM).[13] The low ECSA values combined with the high catalytic currents measured translate into particularly high specific current densities (j_s) in the HER when measured at an overpotential of -480 mV (entries 1-4, Table 1).

On the other hand, the CoO-MeCN and CoO(OH)-DCM NPs suffer from an increase in η over time (entries 1 and 2), specially in the former case. This decrease in the HER activity is more pronounced than that previously reported for the best metallic cathodes by Jaramillo *et al.*,[13] Furthermore, the XPS and SEM measurements performed after a 2h-CPE (Figures S6, S7 and Figure S13) have shown the instability of these nanoparticulated systems, probably due to the inability of MeCN and DCM to form stabilizing hydrogen bonds with the NPs (see below). However, despite this drawback, our Faradaic efficiencies are comprised in the 96-98% range, which stand out among the

normal ε values found for some of the best metal-based HER catalysts reported so far at pH 14.[13]

Contrastingly, CoO(OH)-MeOH NPs undergo a dramatic decrease in η over time while being converted into $Co(OH)_2$ NPs (entries 3 and 4), reaching a $\eta_{t=2}$ value as low as *ca.* -250 mV at pH 14. This overpotential is lower than that of other published Co-based NP systems under analogous conditions. Thus, Co NPs encapsulated in N-rich CNTs have shown an η of -375 mV at pH 14,[3b] whereas Co/CoO**Error! Bookmark not defined.**[4a] and Co NPs[4a] immobilized on N-doped and Co-N-doped C feature η values of -395 and -314 mV, respectively, at pH 13. Also, a similar η of -250 mV has been measured at pH 14 for Co NPs on N,S-doped C[6] and for trimetallic CoNiFe NPs.[13]

Table 1. Physical and electrochemical properties of the Co-derived NPs synthesized in this work onto the surface of a RDE electrode.

Entry	Co Precursor	Solvent	NP[a]	diameter (nm)[b]	ECSA[c]	RF[c]	Onset η (mV)[d]	$\eta_{t=0}$ (mV)[e]	$\eta_{t=2}$ (mV)[f]	j_s @ η= -480 mV (mA·cm^{-2})[g]	ε[h]
1	**1**	MeCN	CoO	52.5 ± 15.7	0.14 ± 0.02	1.14 ± 0.19	-276 ± 47	-435 ± 29	-669 ± 37	225 ± 30	96%
2	**1**	DCM	CoO(OH)	37.5 ± 10.1	0.08 ± 0.01	0.65 ± 0.11	-348 ± 28	-504 ± 20	-595 ± 12	20 ± 10	98%
3	**1**	MeOH	CoO(OH)	32.0 ± 9.3	0.15 ± 0.02	1.24 ± 0.18	-321 ± 78	-465 ± 98	-252 ± 16	174 ± 124	98%
4	CoO(OH)	MeOH	$Co(OH)_2$[i]	39.9 ± 16.4	0.15 ± 0.02	1.24 ± 0.18	-140 ± 74	-246 ± 20	n.d.	596 ± 216	98%
5	$CoCl_2$	MeCN	n.d.[j]	448 ± 146	0.14 ± 0.04	1.21 ± 0.06	-367 ± 80	-461 ± 97	n.d.	0.46 ± 0.28	n.d.
6	$CoCl_2$	DCM	n.d.	325 ± 280	0.08 ± 0.01	0.64 ± 0.09	-390 ± 60	-475 ± 70	n.d.	0.56 ± 0.31	n.d.
7	$CoCl_2$	MeOH	n.d.	283 ± 175	0.13 ± 0.02	1.07 ± 0.19	-398 ± 15	-515 ± 88	-679 ± 70	15 ± 14	n.d.
8	$CoCl_2$ + H_4L	MeOH	n.d.	n.d.	0.16 ± 0.02	1.24 ± 0.20	-406 ± 45	-544 ± 30	-572 ± 20	11 ± 8	n.d.

[a] Formed during 1h-electrolysis at -1.86 V *vs.* NHE at 1600 rpm and determined by XPS analyses. [b] Determined by SEM analyses. [c] Electrochemically-active surface area (ECSA) and roughness factor (RF) determined according to Jaramillo *et al.*[13] The double-layer capacitance of the systems has been calculated as the average of the absolute value of the slopes of their linear fits to the data shown in Figs. S13 and S16. [d] Onset overpotential of the electrocatytic wave estimated from RDV experiments. [e] Overpotential required for reaching a 10 mA·cm^{-2} current density. The values have been estimated from the 30 s step-chronopotentiometry and chronopotentiometry experiments. [f] Overpotential required for reaching 10 mA·cm^{-2} current density after a 2h-controlled current electrolysis experiment. [g] Specific current density (j_s) obtained by dividing the experimental current density (j, in mA·cm^{-2}) by the ECSA at an overpotential of -480 mV. [h] ε = faradaic efficiency. [i] The precursor are the CoO(OH) NPs obtained in MeOH after 1h-electrolysis of **1** at -1.86 V *vs.* NHE, which are then submitted to a 2h-CPE experiment at 10 mA·cm^{-2}. [j] n.d. = not determined.

Concerning the CoO(OH)-DCM NPs, it is difficult to rationalize why, having very similar size and RF values as those of CoO(OH)-MeOH (entries 2 and 3), they clearly possess lower HER catalytic activity and stability (*i.e.*, higher η -specially over time- and one order lower j_s value, and even higher $\eta_{t=0}$ than its $CoCl_2$ blank counterpart). This may be due in part to slower mass transport of H^+ into the NPs in the case of DCM, as suggested by Jaramillo *et al.* during the catalytic performance of metallic nanoporous films compared to non-nanoporous films made from the same metal.[13] Thus, the CoO(OH) NPs obtained in DCM may have a different structure than those synthesized in MeOH, probably because of the non-coordinating and non-hydrogen bonding abilities of DCM, which may lead to less stable NPs. In fact, previous studies with metallic NPs have demonstrated their morphology dependence with the nature/polarity of the solvent employed for their synthesis.[21] Furthermore, it is likely that the hydrogen binding abilities of MeOH -completely absent in DCM and MeCN- may play a key role in the stabilization of CoO(OH) NPs and their further conversion into the more active $Co(OH)_2$ NPs during the 2h-CPE. Contrastingly, the non-hydrogen binding abilities of both DCM and MeCN may be one of the reasons for the progressive deactivation of the CoO(OH)-DCM and CoO-MeCN NPs along time. Nonetheless, the amount of N and C coming from the ligand initially present in **1** or fragments of it within all Co derived NPs (see N 1s and C 1s XPS data of Figure S12b-c of the Supplementary Material) should not be ignored, since these elements may not only contribute to the formation of small and highly dispersed NPs but could also provide a stabilizing effect to the NPs during catalysis. However, an exact determination of the amount of C and N originating from **1** is not possible given the use of GC electrodes as supports and the presence of N in the supporting electrolyte ($TBAPF_6$) and in MeCN.

Finally, from the analysis of the Tafel plots (Figure 4) it also becomes obvious that the three more active systems (the ones on the right hand side of the graph) are those obtained from **1** in MeCN and MeOH (in fact, the activity of CoO(OH)-DCM is very close to that of the $CoCl_2$ blank obtained in MeOH). The slopes for CoO-MeCN, CoO(OH)-MeOH and $Co(OH)_2$ are close or above 100 mV/dec. Therefore, consistent with the literature,[22] the rate determining step (rds) for the HER reaction in our three most active systems must be the Volmer step, *i.e.*, the electrochemical H adsorption onto the NP surface. On the other hand, the crossing of the CoO-MeCN (blue line) and the CoO(OH)-MeOH (green line) curves confirms that the former is more active (higher *j*) at

an overpotential lower than *ca.* -520 mV, but that at overpotentials more negative than -520 mV the latter performs better in HER.

Conclusions

In this work, we have demonstrated that the molecular Co^{II}/Co^{III} complex **1** generates electrodeposited ~50 nm CoO or ~35 nm CoO(OH) NPs depending on the solvent employed (MeCN for the former, MeOH or DCM for the latter) from its decomposition at -1.86 V *vs.* NHE. The resulting cathodes, possessing low and comparable ECSA and RF values, catalyze the electrochemical reduction of water at pH 14 with distinctive specific activities (j_s) under the application of a -480 mV bias. The most active system at t=0 h is CoO-MeCN ($\eta_{t=0}$= -435 mV, j_s=225 mA·cm^{-2} at an overpotential of -480 mV). However, the CoO(OH)-MeOH NPs, with an initial catalytic activity very close to those of CoO-MeCN, become significantly more active after a 2h constant polarization process at 10 mA·cm^{-2} ($\eta_{t=2}$= -250 mV, j_s=596 mA·cm^{-2} at an overpotential of -480 mV). These activated NPs correspond to $Co(OH)_2$ according to XPS analysis, which show better HER performance than many Co-based NP systems published elsewhere under analogous conditions. Contrastingly, the HER activity steadily decreases for CoO-MeCN and CoO(OH)-DCM during a 2h-chronopotentiometry experiment at 10 mA·cm^{-2}. This decrease in activity is proposed to be mainly related to the inability of these solvents to form stabilizing hydrogen bonds with the NPs, in contrast to MeOH. Finally, the observed increase in H_2 evolution activity with increasing presence of hydroxyl groups in the series CoO(OH)<$Co(OH)_2$ observed during the 2h-chronopotentiometry in MeOH is in agreement with previous results in the literature.[8] However, further structural studies of the surfaces of both CoO(OH) systems obtained in DCM and MeOH are under way to fully understand their markedly different catalytic performance.

Experimental

All reagents used in the present work were obtained from Sigma Aldrich in reagent grade and were used without further purification. Reagent grade organic solvents were obtained from Scharlab and Panreac. Anhydrous $CoCl_2$ was supplied by Sigma Aldrich. NaOH was obtained from Panreac (99%), and milliQ quality grade water was employed. $[Co_8Na_4(L)_4(OH)_2(CO_3)_2(py)_{10}](BF_4)_2$ (**1**) was prepared as previously reported.[12]

UV-Vis spectroscopy was performed on a HP8453 spectrometer using 1 cm quartz cells. Scanning Electron Microscopy (SEM) and Energy-dispersive X-Ray Spectroscopy (EDX) analyses were performed using a JEOL JSM 6700F electron microscope working at 10 kV.

X-ray photoelectron spectroscopy (XPS) experiments were performed with a SPECS EA10P hemispherical analyser using a non-monocromated X-ray source (Al Kα line of 1486.6 eV and 300W). The direction of the X-ray source with respect to the sample was 90º and ultrahigh vacuum was maintained during the measurements, obtaining a residual pressure of 10^{-8} Pa. GC electrodes analysed by SEM and XPS were functionalized for 1h by applying a constant potential (-1.86 V or -1.16 V *vs.* NHE) to a solution of **1** (0.6 mg, 2 µmol) in the different solvents assayed. Afterwards, the GC surface was washed with distilled H_2O, MeCN and acetone. Then, a small section of the electrode was cut on a Mintom rotating saw (Struers) equipped with a metal cut-off wheel, washed again with distilled H_2O, acetone and Et_2O and dried over vacuum for 2h.

Electrochemical measurements were carried out on a Bio Logic Science Instrument SP-150 potentiostat and CHI660D potentiostat using a three-electrode cell. A glassy carbon (GC, 3 mm internal diameter) or a rotating disk electrode (RDE, 4 mm GC disk diameter) were employed as working electrodes, while a platinum wire was used as counter electrode and $Hg/HgSO_4$ or SCE were used as the reference electrodes. The solvents used for functionalization of the electrode (acetonitrile, methanol or dichloromethane) were prepared containing the necessary amount of n-Bu_4NPF_6 ($TBAPF_6$) as supporting electrolyte to yield a 0.1 M ionic strength. Electrodeposition of Co NPs was carried out in a 10 mL three electrode cell using RDE as working electrode, platinum as counter electrode and $Hg/HgSO_4$ as reference electrode. Before each functionalization, the RDE electrode was polished with 1 and 0.05 micron alumina suspension in distilled water, sonicated for 5 min in H_2O and washed with distilled water and acetone before each measurement. 1 mg (0.3 µmol) of **1** was sonicated in the 10 mL three electrode cell until complete solution in 3 mL of the corresponding organic solvent (MeCN, DCM or MeOH) containing 0.1 M of electrolyte ($TBAPF_6$). Subsequently, a constant potential of -1.86 V or -1.16 V *vs.* NHE was applied to the solution for 1 hour. Finally, the functionalized RDE electrode was washed with distilled H_2O, MeCN and acetone and dried over vacuum for 30 minutes before electrochemical measurements.

For the electrochemical characterization and catalytic experiments in HER, the cell was purged for 30 minutes with N_2 and was continuously bubbled during the measurements. The resistance of the cell (typically $R_u \sim 13\ \Omega$) was compensated at 85%. In the case of electrochemical capacitance measurements, linear sweep voltammetry (LSV) was performed in a potential window where there is a non-Faradaic current response as determined from cyclic voltammetry. This range is typically 0.1 V centred on the Open-circuit potential (OCP) for each electrode. The measurements were carried out by sweeping the potential across the selected potential range at 8 different scan rates (0.005, 0.01, 0.025, 0.05, 0.1, 0.2, 0.4, 0.8 V/s). The working electrode was held at the starting potential before beginning the next LSV experiment.

For Faradaic efficiency measurements, H_2 was quantified using a Unisense H_2-probe controlled by a Unisense Microprocessor Multimeter. Measurements were carried out in a U-compartment cell containing a functionalized GC electrode (3 mm diameter), a reference electrode (Ag/AgCl) and the hydrogen probe in the first compartment and a counter electrode in the second compartment, both separated by a frit and filled with 15 mL of NaOH solution (pH 14). For H_2 measurements, the solution was degassed with a N_2 flow for 30 minutes under vigorous stirring. The baseline was recorded for 20 minutes and a constant potential of -1.86 V *vs.* NHE was held at the working electrode containing Co NPs for 30 min. The increase in pressure of H_2 was monitored during this time, and from this the total amount of H_2 gas formed was determined. Finally, Faradaic efficiency was calculated by dividing the total amount of H_2 produced during the experiment by the theoretical amount calculated from the total charge passed in the bulk-electrolysis experiment.

Contribution

Marcos Gil-Sepulcre synthetized and characterized the CoO, $Co(OH)_2$ and CoO(OH) NPs, performed the catalytic experiments and prepared the manuscript.

Acknowledgements

Support from MINECO/FEDER (CTQ2015-64261-R and CTQ2016-80058-R) is gratefully acknowledged. M. G.-S. is grateful for the award of a PIF doctoral grant from UAB. J. G.-A. acknowledges the Serra Húnter Program. G. A., D. A. and V. V. thank the ERC for contracts under ERC Starting Grant StG-2010-258060 and the Generalitat de Catalunya for the prize ICREA Academia 2008 and 2013. We also thank the Servei de Microscopia Electrònica, Universitat Autònoma de Barcelona, for allocating instrument time.

References

[1] (a) Han, Z.; Eisenberg, R. *Acc. Chem. Res.* **2014**, *47*, 2537-2544; (b) Wang, M.; Han, K.; Zhang S.; Sun, L.; *Coord. Chem. Rev.* **2015**, *287*, 1-14; (c) Xu, Y.; Zhang, B.; *Cat. Sci. & Tech.* **2015**, *5*, 3084-3096; (d) Jiang, N.; You, B.; Sheng, M.; Sun, Y. *Angew. Chem. Int. Ed.* **2015**, *54*, 6251-6254; (e) You, B.; Jiang, N.; Sheng, M.; Bhushan, M. W. Sun, Y. *ACS Catal.* **2016**, *6*, 714-721; (f) You, B.; Liu, X.; Liu, X.; Sun, Y.; *ACS Catal.* **2017**, *7*, 4564-4570; (g) You, Y.; Sun, Y. *Adv. Energy Mater.* **2016**, *6*, 1502333.

[2] Fukuzumi, S.; Yamada, Y. *J. Mater. Chem.* **2012**, *22*, 24284-24296.

[3] (a) Anxolabéhère-Mallart, E.; Costentin, C.; Fournier, M.; Nowak, S.; Robert, M. Savéant, J.-M. *J. Am. Chem. Soc.* **2012**, *134*, 6104-6107; (b) Zou, X.; Huang, X. Goswami, A.; Silva, R.; Sathe, B. R.; Mikmekov, E.; Asefa, T. *Angew. Chem. Int. Ed.* **2014**, *53*, 4372-4376; (c) Zhang, E.; Xie, Y.; Ci, S.; Jia, J.; Cai, P.; Yia, L.; Wen, Z.; *J. Mat. Chem. A* **2016**, *4*, 17288-17298.

[4] (a) Wang, Y.; Nie, Y.; Ding, W.; Chen, S. G.; Xiong, K.; Qi, X. Q.; Zhang, Y.; Wang, J.; Wei, Z. D. *ChemComm.* **2015**, *51*, 8942-8945; (b) Su, H.; Wang, H.-H.; Zhang, B.; Wang, K.-X., Lin, X.-H.; Chenn, J.-S. *Nano Energy* **2016**, *22*, 79-86.

[5] Zhang, X.; Liu, R.; Zang, Y.; Liu, G.; Wang, G.; Zhang, Y.; Zhang, H.; Zhao, H. *ChemComm.* **2016**, *52*, 5946-5949.

[6] Deng, W.; Jiang, H.; Chen, C.; Yang, L.; Zhang, Y.; Peng, S.; Wang, S.; Tan, Y.; Ma, M.; Xie, Q. *ACS Appl. Mater. Interfaces* **2016**, *8*, 13341-13347.

[7] Liu, X.; Dong, C.; Dong, W.; Wang, X.; Yuan, X.; Huang, F. *RSC Adv.* **2016**, *6*, 38515-38520.

[8] Li, Z.; Wu, Y.; Lu, G. *Appl. Cat. B: Environm.* **2016**, *188*, 56-64.

[9] (a) Dang, H.; Dong, X.; Dong, Y.; Fan, H.; Qiu, Y.; *Mater. Lett.* **2015**, *138*, 56-59; (b) Wender, H.; Gonçalves, R. V.; Dias, C. S. B.; Zapata, M. J. M.; Zagonel, L. F.; Mendonça, E. C.; Teixeira, S. R.; Garcia, F. *Nanoscale*, **2013**, *5*, 9310-9316.

[10] (a) Hocking, R. K.; Brimblecombe, R., Chang, L.-Y.; Singh, A.; Cheah, M. H.; Glover, C.; Casey, W. H.; Spiccia, L. *Nat. Chem.* **2011**, *3*, 461-466; (b) Singh, A.; Hocking, R. K.; Chang, S. L.-Y.; George, B. M.; Fehr, M.; Lips, K.; Schnegg, A.; Spiccia, L. *Chem. Mater.* **2013**, *25*, 1098-1108.

[11] (a) Hong, D.; Jung, J.; Park, J.; Yamada, Y.; Suenobu, T.; Lee, Y.-M.; Nam, W.; Fukuzumi, S.; *Energy Environ. Sci.* **2012**, *5*, 7606–7616; (b) Stracke, J. J.; Finke, R. G. *J. Am. Chem. Soc.* **2011**, *133*, 14872-14875.

[12] Velasco, V.; Aguilà, D.; Barrios, L. A.; Borilovic, I.; Roubeau, O.; Ribas-Ariño, J.; Fumanal, M.; Teat, S. J.; Aromí, G. *Chem. Sci.* **2015**, *6*, 123-131.

[13] McCrory, C. C. L.; Jung, S.; Ferrer, I. M.; Chatman, S. M.; Peters, J. C.; Jaramillo, T. F.; *J. Am. Chem. Soc.* **2015**, *137*, 4347–4357.

[14] Indra, A.; Menezes, P. W.; Das, C.; Göbel, C.; Tallarida, M.; Schmeiβer, D.; Driess, M. *J. Mat. Chem. A* **2017**, *5*, 5171-5177.

[15] Biesinger, M. C.; Payne, B. P.; Grosvenor, A. P.; Lau, L. W. M.; Gerson, A. R.; Smart, R. St. C. *Appl. Surf. Sci.* **2011**, *257*, 2717-2730.

[16] Fester, J.; García-Melchor, M.; Walton, A. S.; Bajdich, M.; Li, Z.; Lammich, L.; Vojvodic, A.; Lauritsen, J. V. *Nat. Commun.* **2017**, *8: 14169*, 1-8.

[17] Yang, J.; Lu, H.; Martens, W. N.; Frost, R. L. *J. Phys. Chem. C* **2010**, *114*, 111-119.

[18] (a) Fang, L. J.; Wang, X. L.; Li, Y. H.; Liu, P.F.; Wang, Y. L.; Zeng, H. D.; Yang, H. G. *Appl. Catal B: Environ.* **2017**, *200*, 578-584; (b) Yue, X.; Yi, S.; Wang, R.; Zhang, Z.; Qiu. S. *Nat. Sci. Reports*, **2017**, *6: 22268*, 1-8.

[19] Walter, M. G.; Warren, E. L.; McKone, J. R.; Boettcher, S. W.; Mi, Q.L; Santori, E. A.; Lewis, N. S. *Chem. Rev.* **2010**, *110*, 6446-6473.

[20] Agegnehu, A. K.; Pan, C.-J.; Rick, J.; Lee, J.-F.; Su, W.-N.; Hwang, B.-J. *J. Mater. Chem.* **2012**, *22*, 13849-13854.

[21] Pelzer, K.; Vidoni, O.; Philippot, K.; Chaudret, B.; Collière, V. *Adv. Funct. Mater.* **2003**, *13*, 118-126.

[22] Zheng, Y.; Jiao, Y.; Jaroniec, M.; Qiao, S. Z. *Angew. Chem. Int. Ed.* **2015**, *54*, 52-65.

Supporting Information

Catalytic H_2 evolution with CoO, $Co(OH)_2$ and CoO(OH) NPs generated from a molecular polynuclear Co complex

Table of Contents

1. Scanning Electron microscopy

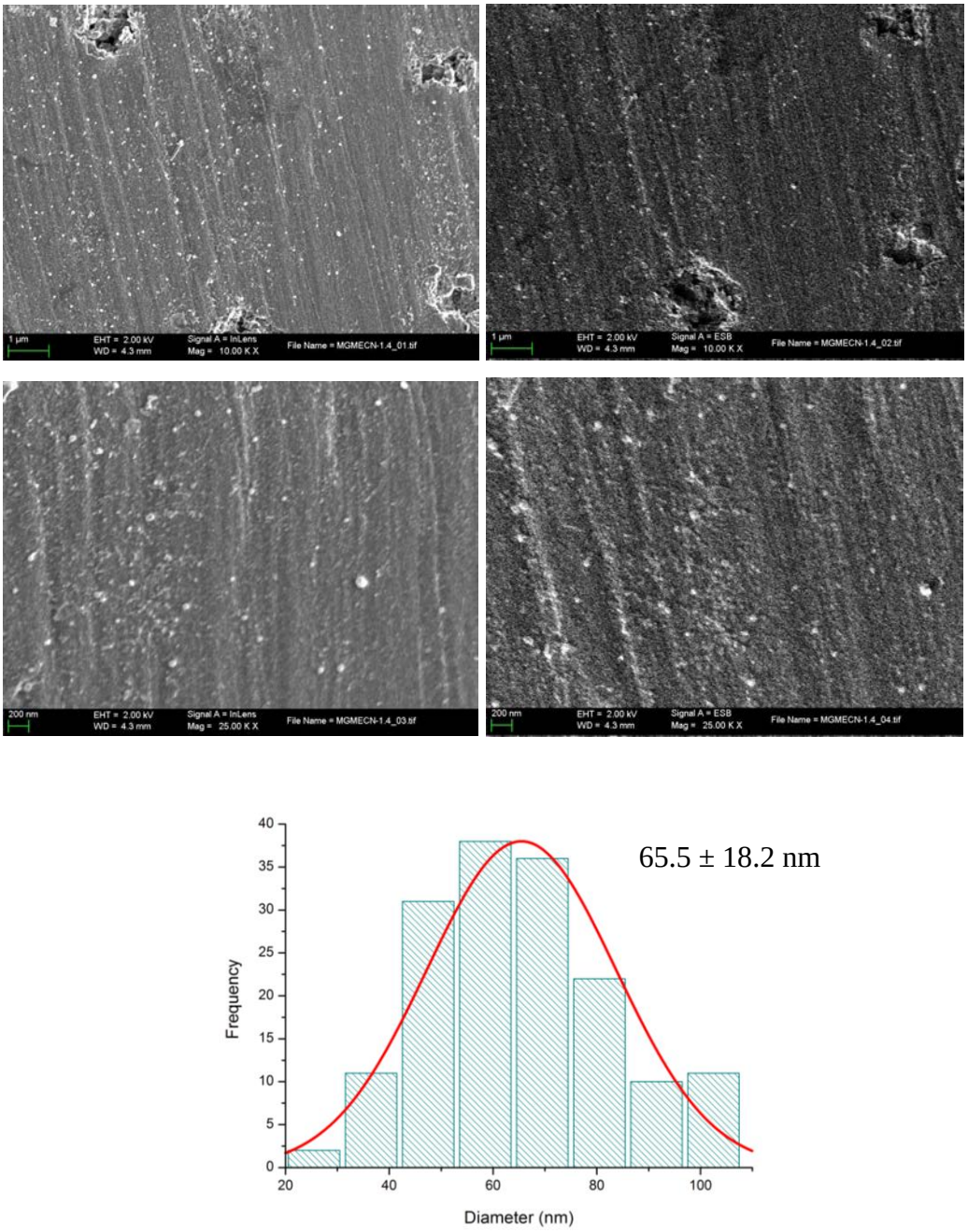

Figure S1. SEM micrographs (left) and corresponding back-scattered electron micrographs (right) of Co-based NPs obtained after a 1h-electrolysis of **1** in MeCN at -1.16 V *vs.* NHE. A size distribution histogram of the NPs is also shown.

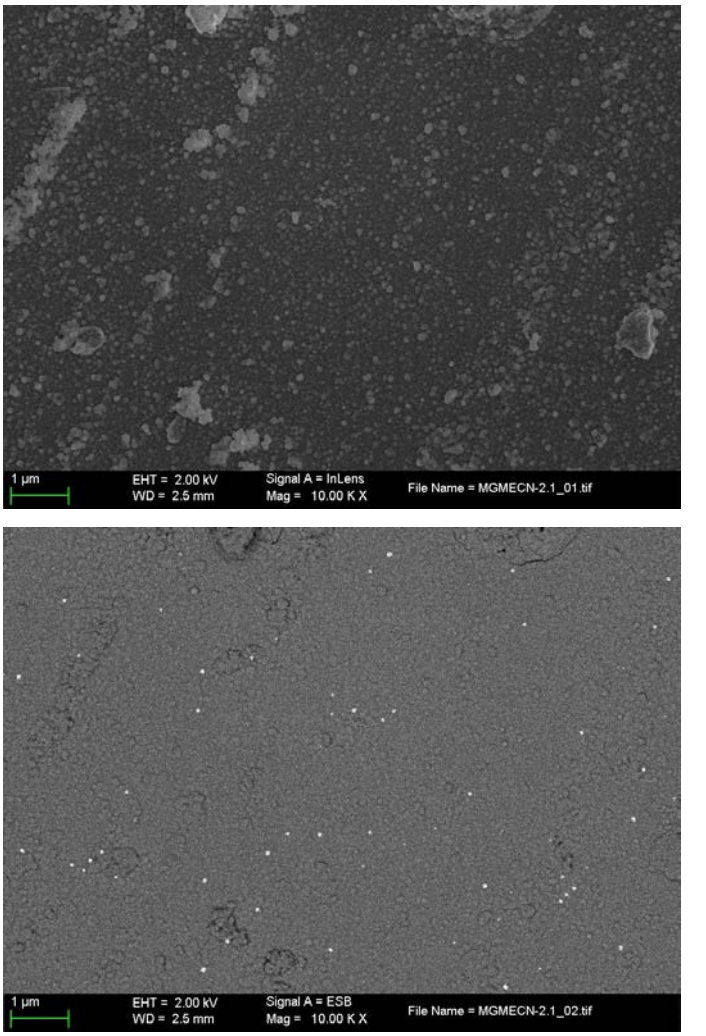

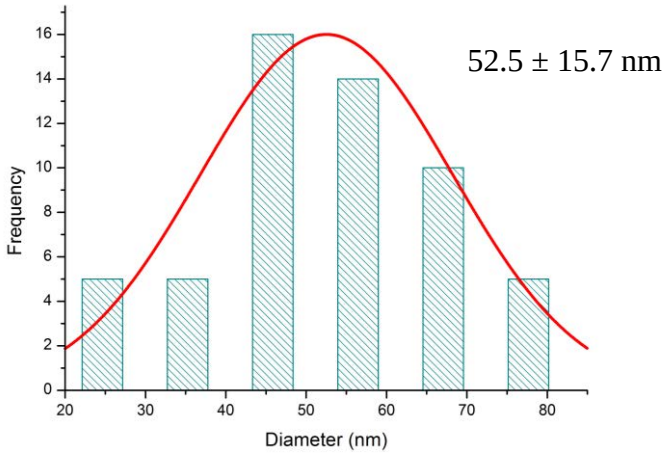

Figure S2. SEM micrographs (top) and corresponding back-scattered electron micrographs (bottom) of Co-based NPs obtained after a 1h-electrolysis of **1** in MeCN at -1.86 V *vs.* NHE. A size distribution histogram of the NPs is also shown

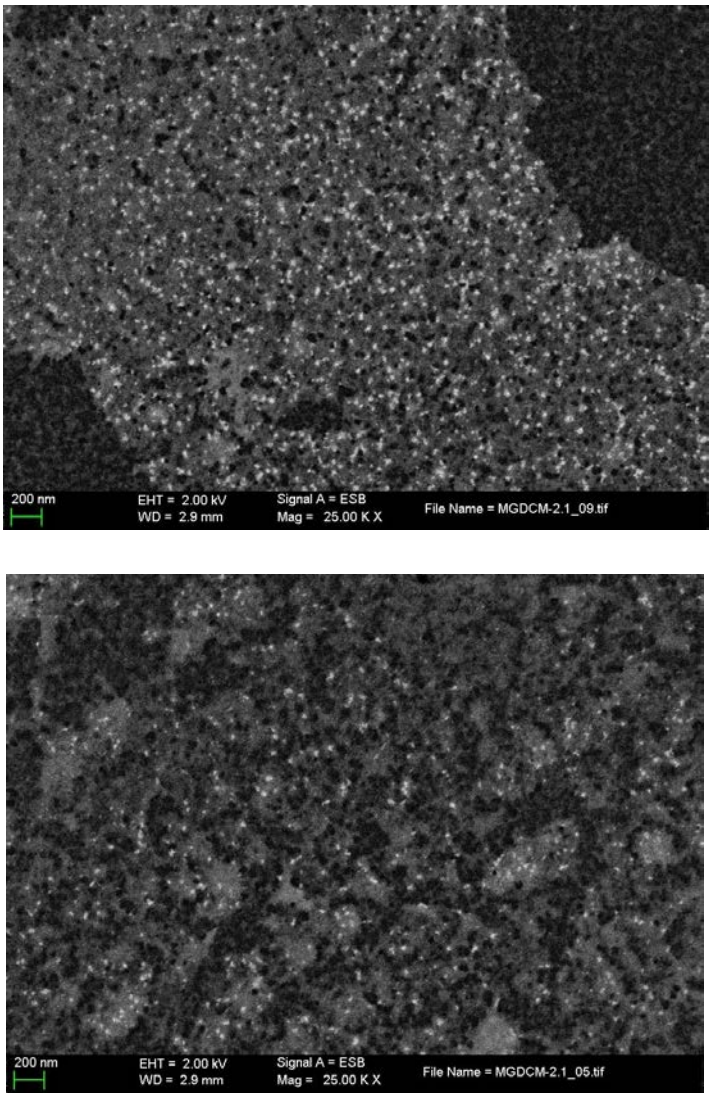

Figure S3. Back-scattered electron SEM micrographs of Co-based NPs obtained after a 1h-electrolysis of **1** in DCM at -1.86 V *vs.* NHE. A size distribution histogram of the NPs is also shown.

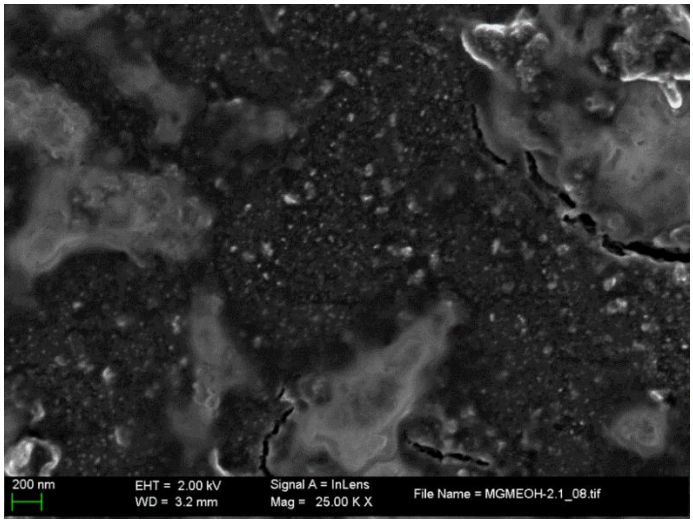

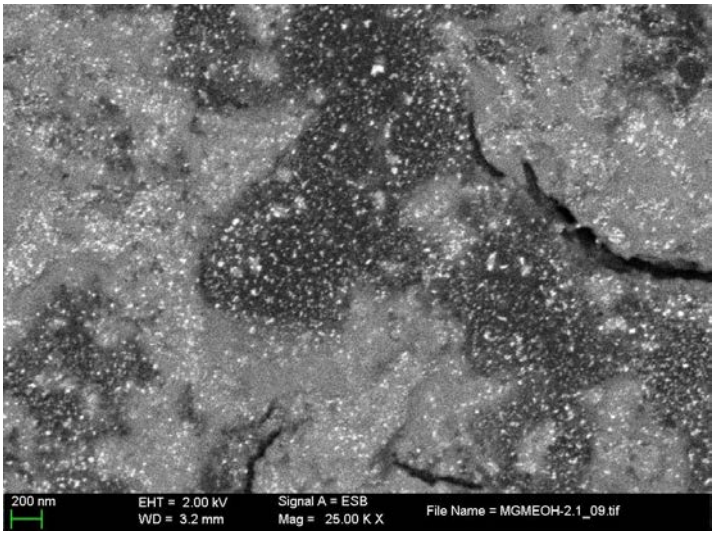

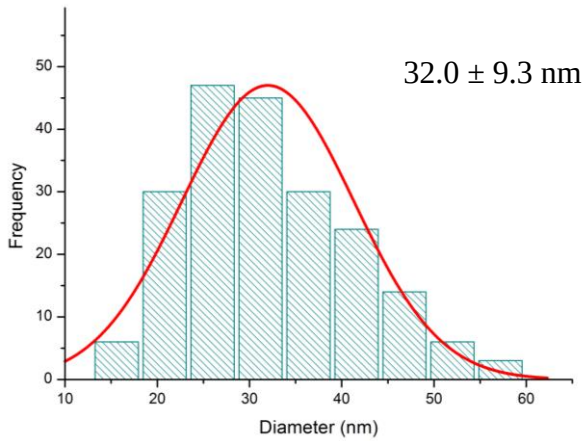

Figure S4. SEM (top) and corresponding back-scattered electron (bottom) micrographs of Co-based NPs obtained after a 1h-electrolysis of **1** in MeOH at -1.86 V *vs.* NHE. A size distribution histogram of the NPs is also shown.

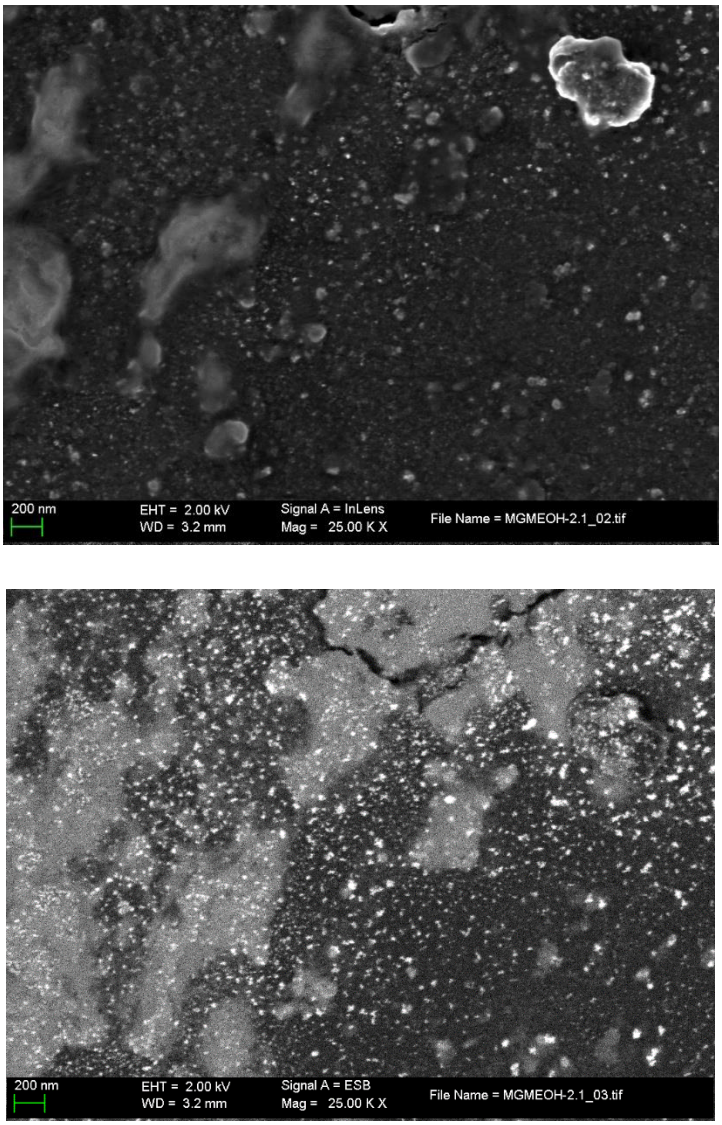

Figure S5. SEM (top) and corresponding back-scattered electron (bottom) micrographs of the $Co(OH)_2$ NPs formed after a 2h-chronopotentiometry at 10 $mA \cdot cm^{-2}$ in MeOH of CoO(OH)-MeOH. A size distribution histogram of the NPs is also shown.

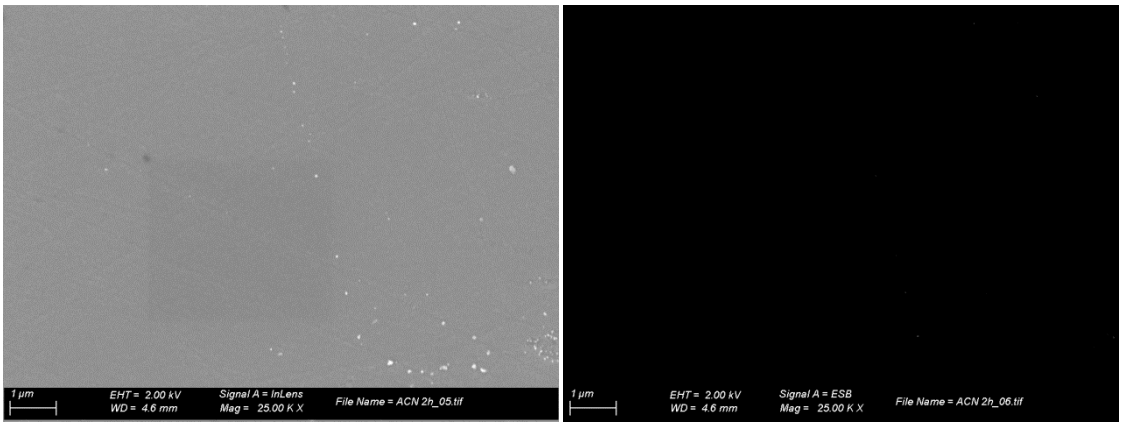

Figure S6. SEM (top) and corresponding back-scattered electron (bottom) micrographs of the CoO NPs after a 2h-chronopotentiometry at 10 mA·cm^{-2} in MeCN.

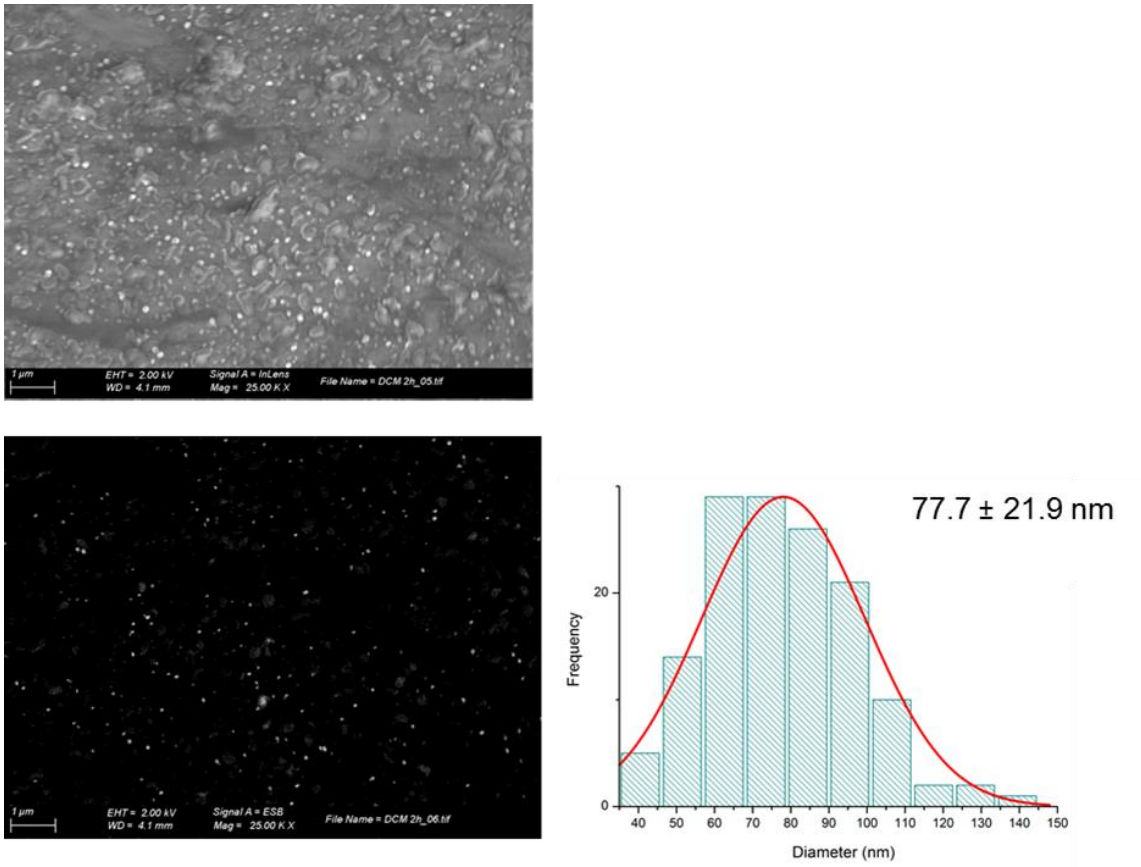

Figure S7. SEM (top) and corresponding back-scattered electron (bottom) micrographs of the CoO(OH) NPs after a 2h-chronopotentiometry at 10 mA·cm^{-2} in DCM. A size distribution histogram of the NPs is also shown.

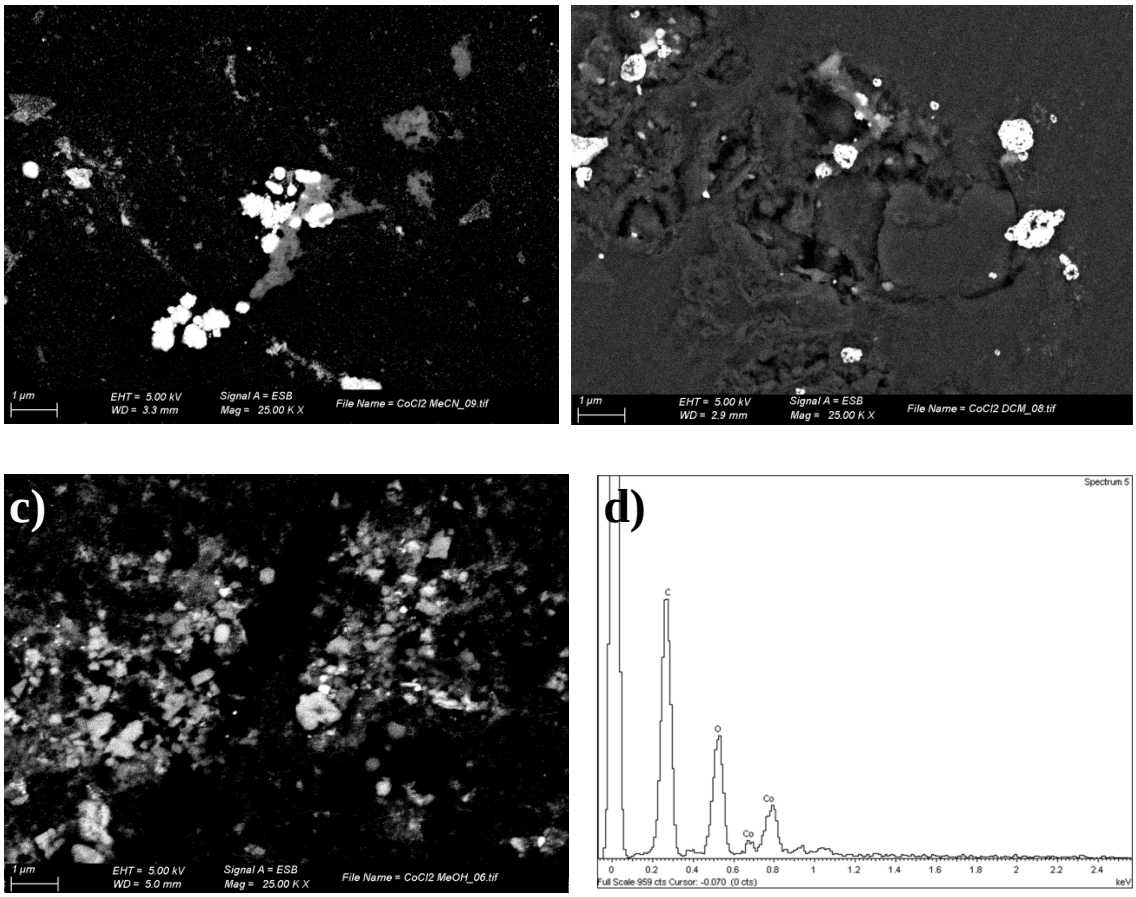

Figure S8. Back-scattered electron SEM micrographs of Co-based NPs obtained after a 1h-electrolysis of $CoCl_2$ in MeCN (a), DCM (b) and MeOH (c) at -1.86 V *vs.* NHE, and representative EDX analysis from SEM measurements of the of Co-based NPs obtained

2. Energy-Dispersive X-Ray spectroscopy

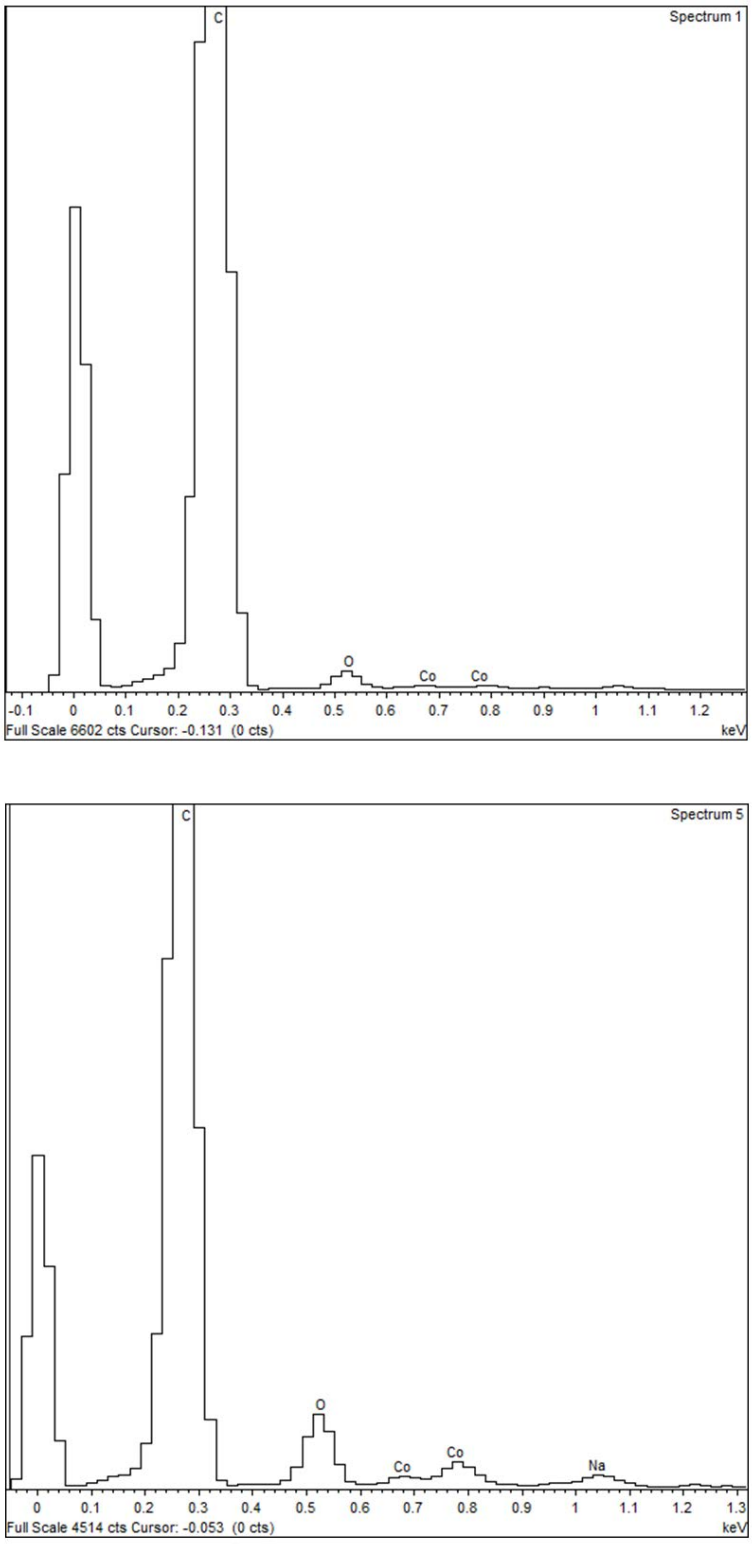

Figure S9. EDX analysis from SEM measurements of the of Co-based NPs obtained after a 1h-electrolysis of **1** in MeCN at -1.16 V *vs.* NHE (top) and -1.86 V *vs.* NHE (bottom).

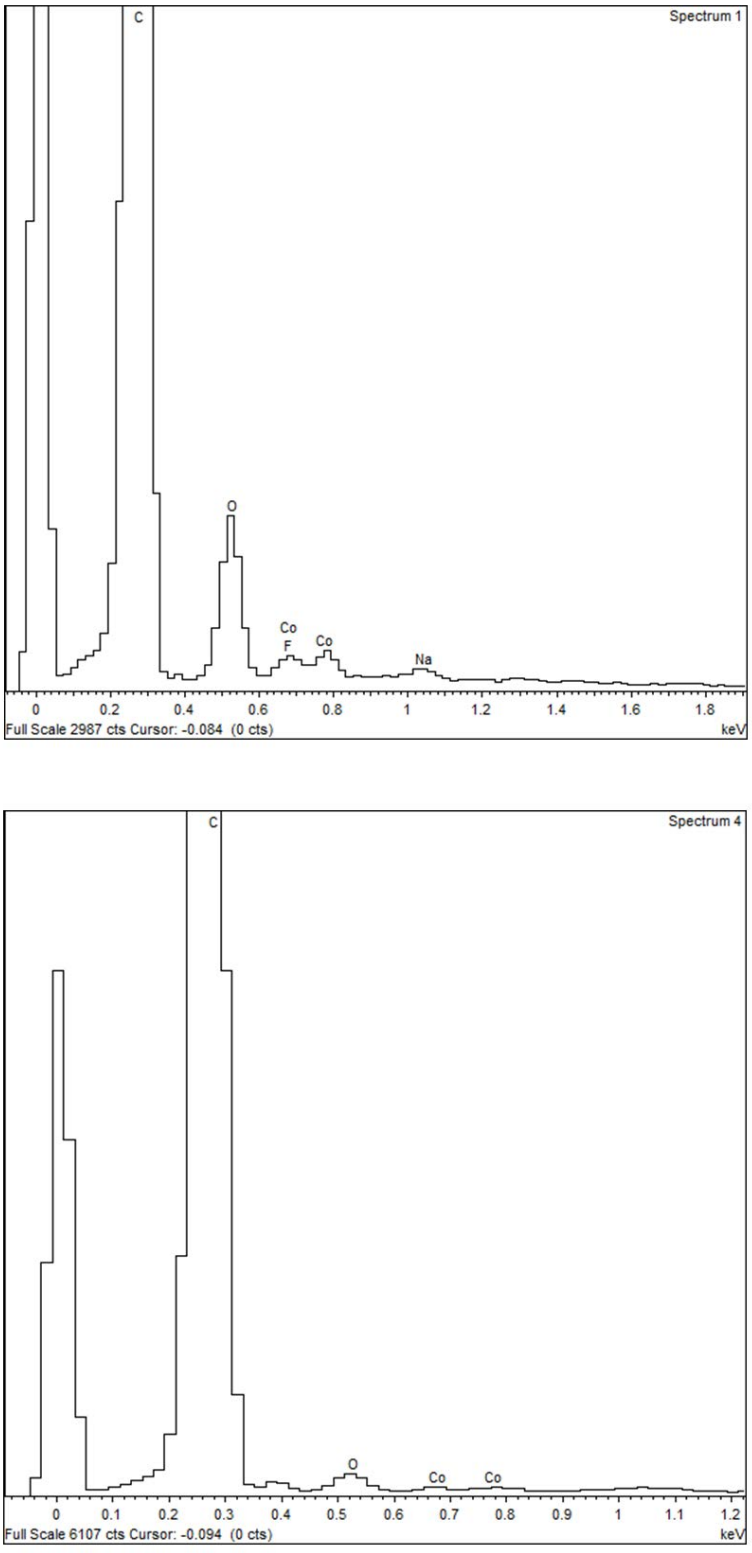

Figure S10. EDX analysis from SEM measurements of the of Co-based NPs obtained after a 1h-electrolysis at -1.86 V *vs.* NHE of **1** in DCM (top) and MeOH (bottom).

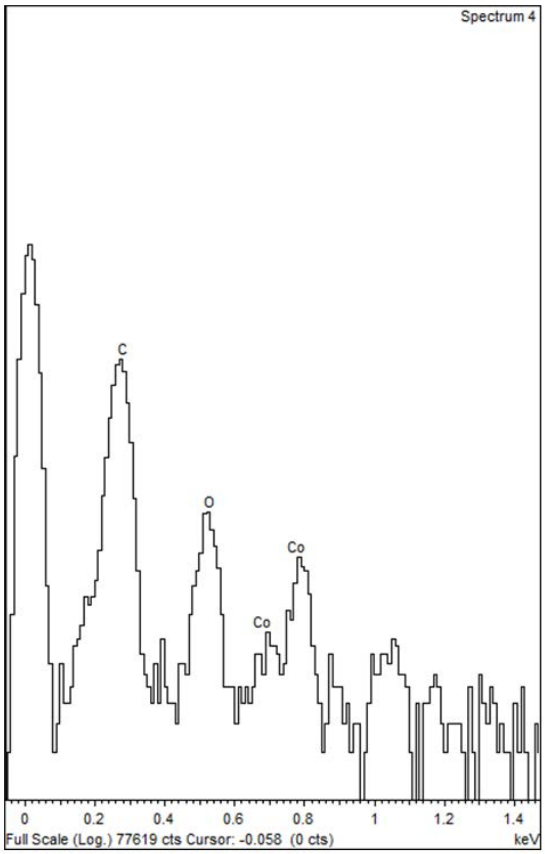

Figure S11. EDX analysis from SEM measurements of the Co-based NPs $Co(OH)_2$ NPs formed after a 2h-chronopotentiometry at 10 $mA \cdot cm^{-2}$ in MeOH of CoO(OH)-MeOH.

3. X-Ray spectroscopy

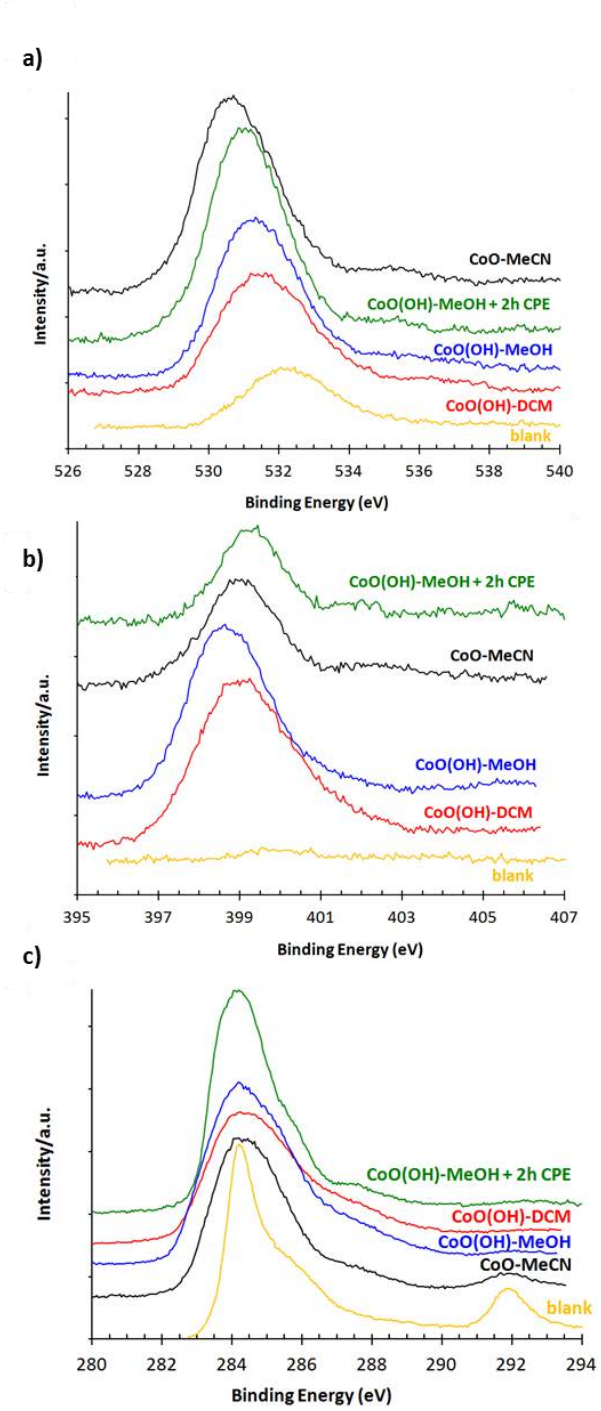

Figure S12. O 1s (a), N 1s (b) and C 1s (c) XPS spectra for the Co-based NPs obtained from **1** in MeCN, DCM and MeOH after a 1h-electrolysis at -1.86 V *vs.* NHE and from **1** in MeOH after a 1h electrolysis at -1.86 V *vs.* NHE plus a 2h-CPE at 10 $mA \cdot cm^{-2}$. The blank consists of a bare GC electrode. Please note that the small C 1s band at 292 eV for the blank is probably due to CF_2 contamination of the GC. Energies have been calibrated according to the C 1s band of graphite at 284.2 eV.

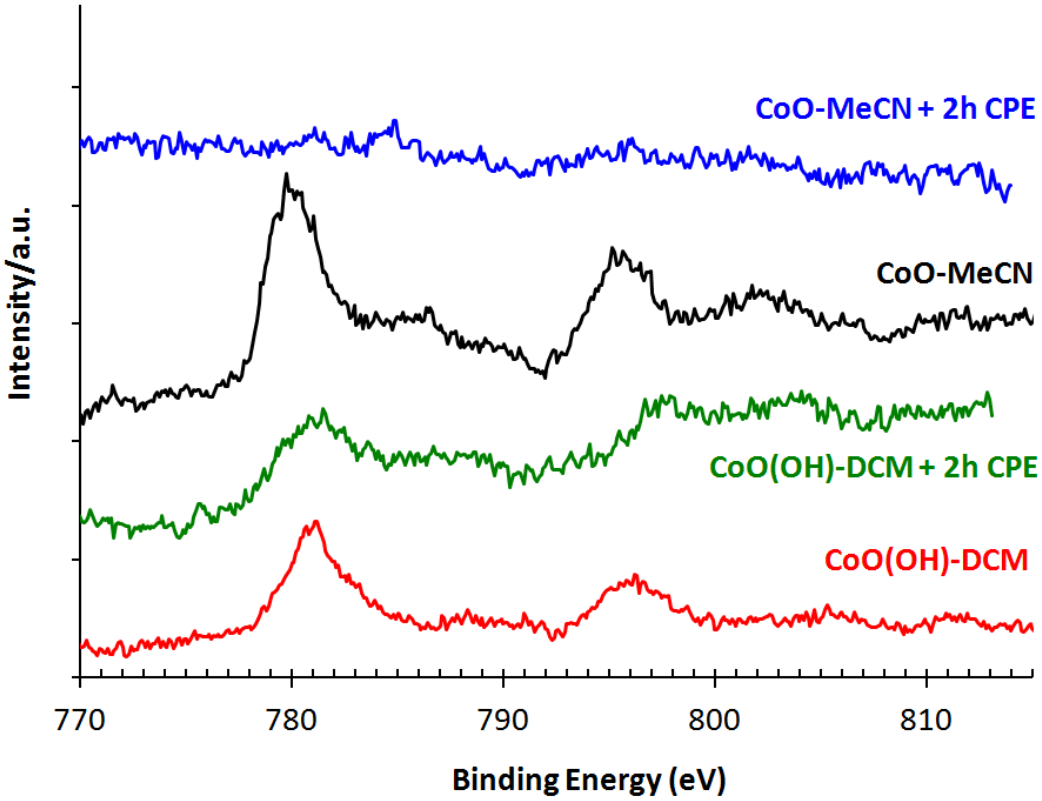

Figure S13. Co 2p XPS spectra for the Co-based NPs obtained from **1** in MeCN (black) and DCM (red) after a 1h-electrolysis at -1.86 V *vs.* NHE and from **1** in MeCN (blue) and DCM (green) after a 1h-electrolysis at -1.86 V *vs.* NHE plus a 2h-CPE at 10 $mA \cdot cm^{-2}$. Energies have been calibrated according to the C 1s band of graphite at 284.2 eV.

4. UV-Vis

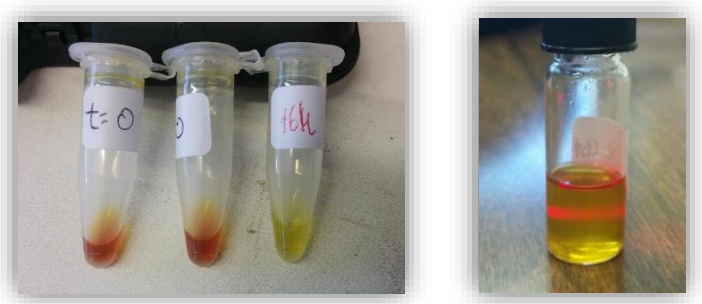

Figure S14. Left: photograph of samples taken from a MeCN solution of **1** after different electrolysis times at -1.86 V *vs.* NHE (from left to right: 0 min, 30 min and 16 h). Right: photograph of laser beam passing through the solution of a MeCN solution of **1** after 16 h of electrolysis at -1.86 V *vs.* NHE, showing the presence of colloidal particles in solution.

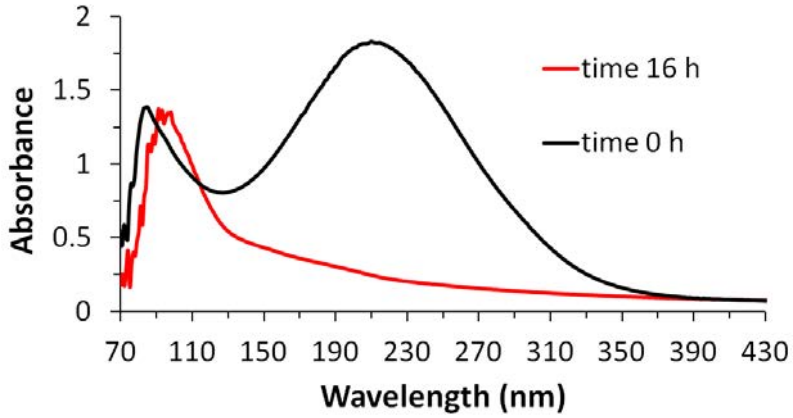

Figure S15. UV-vis spectra evolution of a solution of **1** in MeCN during electrolysis at -1.86 V *vs.* NHE.

5. Electrochemistry

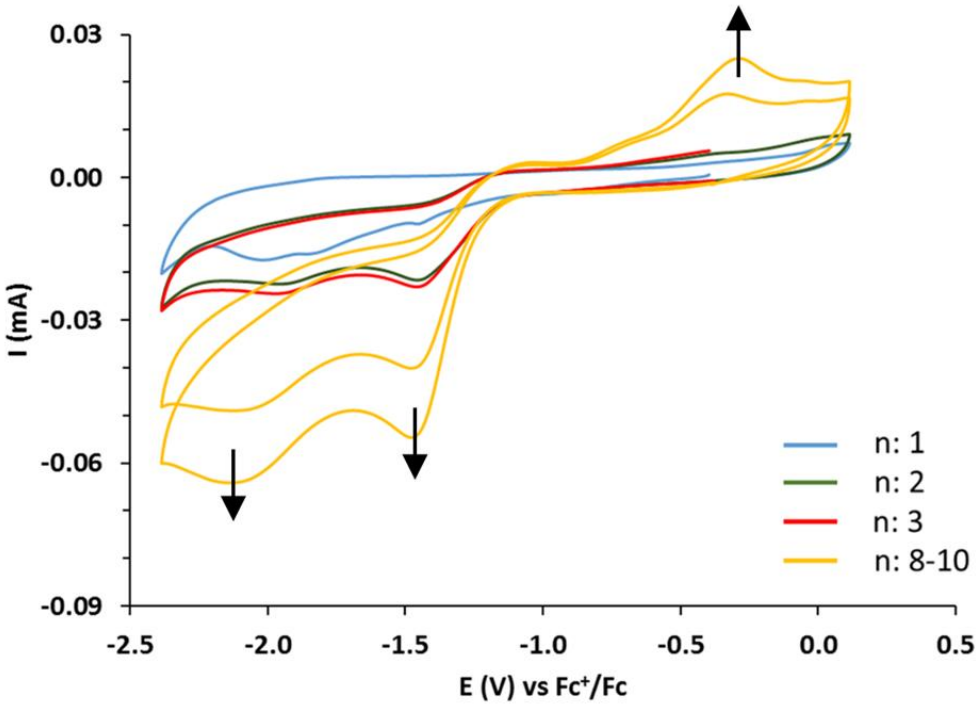

Figure S16. Cyclic voltammetry cycles of a 0.25 mM solution of $[Co_8Na_4(L)_4(OH)_2(CO_3)_2(py)_{10}](BF_4)_2$ (**1**) in acetonitrile (0.1 M $TBAPF_6$) at a 0.1 V/s scan rate. Working electrode: glassy carbon (GC) electrode. Arrows show growing intensity direction of new bands that appear along time.

Determination of Roughtness Factor

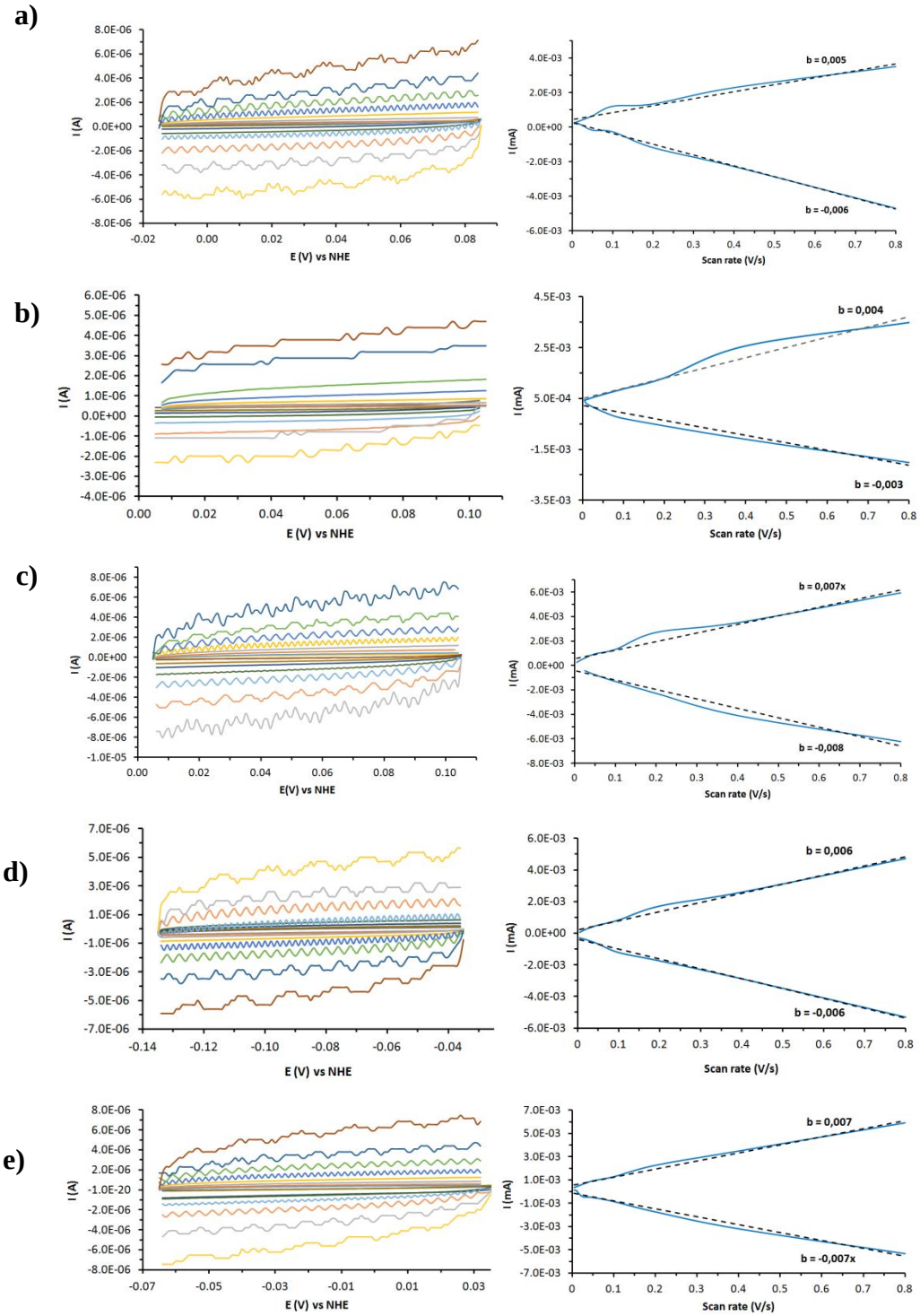

Figure S17. Left column: double-layer capacitance measurements for determining the ECSA of CoO-MeCN (a), CoO(OH)-DCM (b) and CoO(OH)-MeOH (c) and of the Co-derived NPs formed at -1.86 V *vs.* NHE during 1 h from $CoCl_2$ in MeOH (d) and $CoCl_2$ + H_4L in MeOH (e). Linear sweep voltammograms were measured in a non-Faradaic region of the voltammogram at the following scan rates: 0.01, 0.025, 0.050, 0.1, 0.2, 0.4 and 0.8 V/s. The working electrode was held at each potential vertex for 10 s before beginning the next sweep. All currents are assumed to be due to capacitive charging.

Right column: cathodic (negative slopes) and anodic (positive slopes) charging currents measured at 0.055 V (a,b,c), -0.09 V (d) or -0.02 V (e) *vs.* NHE plotted as a function of scan rate.

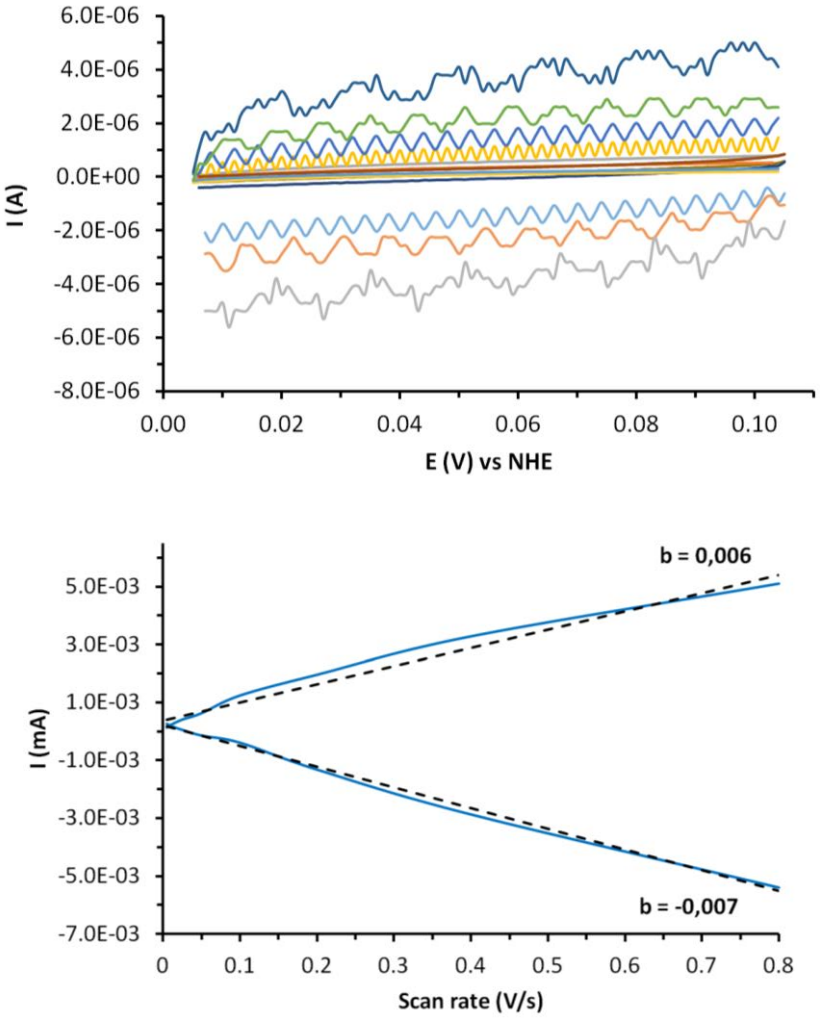

Figure S18. Top: double-layer capacitance measurements for determining the ECSA of the $Co(OH)_2$ NPs formed after a 2h-chronopotentiometry at 10 $mA \cdot cm^{-2}$ in MeOH of CoO(OH)-MeOH. Linear sweep voltammograms were measured in a non-Faradaic region of the voltammogram at the following scan rates: 0.01, 0.025, 0.050, 0.1, 0.2, 0.4 and 0.8 V/s. The working electrode was held at each potential vertex for 10 s before beginning the next sweep. All currents are assumed to be due to capacitive charging. Bottom: cathodic (negative slope) and anodic (positive slope) charging currents measured at 0.055 V *vs.* NHE plotted as a function of scan rate.

Electrocatalytic performance

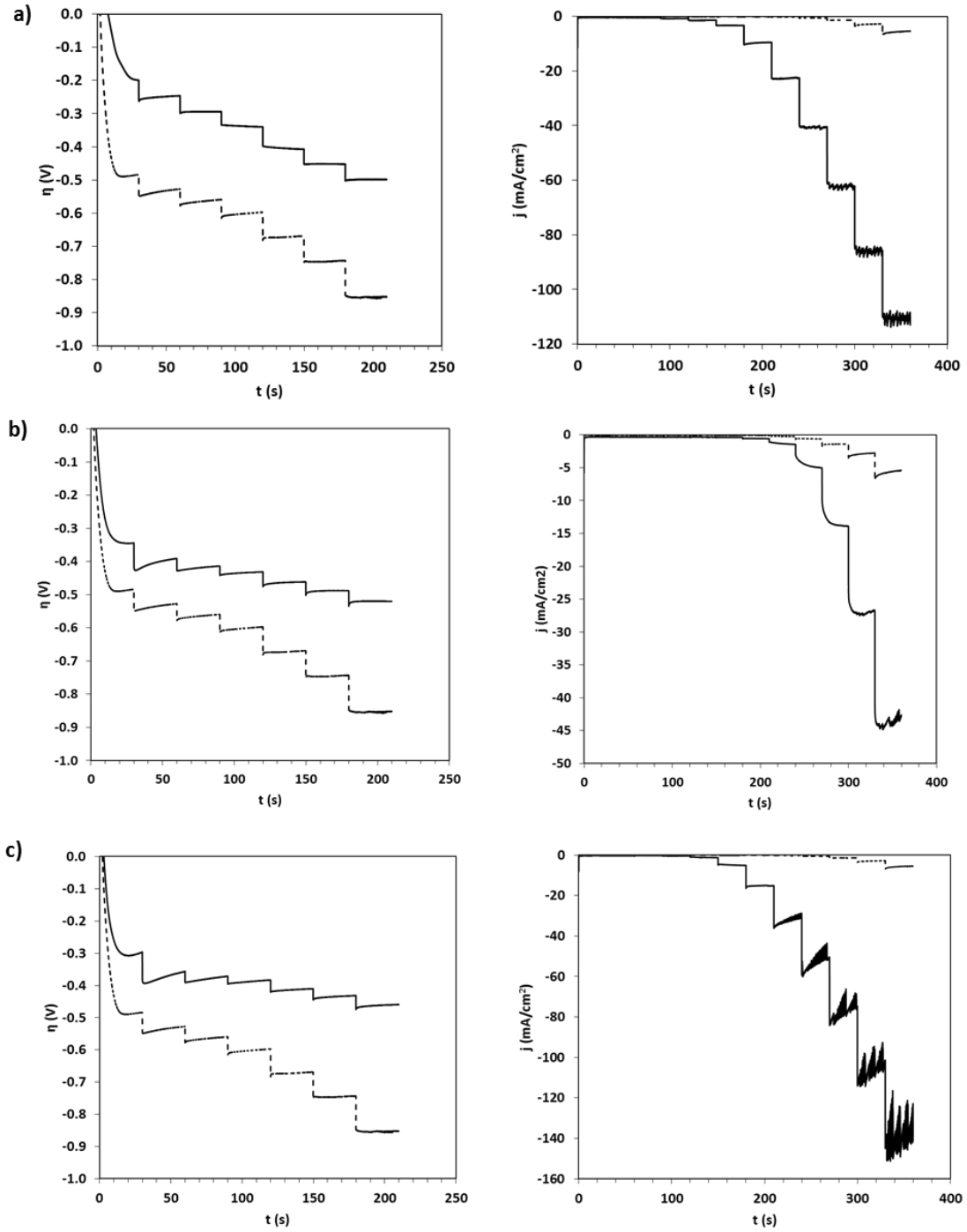

Figure S19. Chronopotentiometry (from 0.1 to 10 $mA \cdot cm^{-2}$, left) and chronoamperometry (from η= -190 to -680 mV, right) for CoO-MeCN (a), CoO(OH)-DCM (b) and CoO(OH)-MeOH (c). In this experiment, the current (left) or the potential (right) is held constant for 30 s, and the resulting potential-time or current-time profile should decay to a steady-state value at times > 2 s.

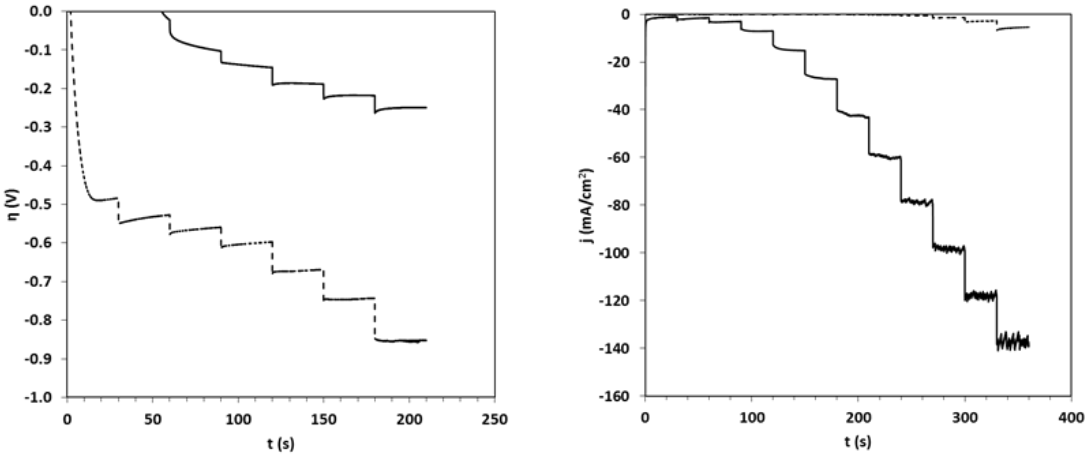

Figure S20. Chronopotentiometry (from 0.1 to 20 $mA \cdot cm^{-2}$, left) and chronoamperometry (from η= -190 to -680 mV, right) for the $Co(OH)_2$ NPs formed after a 2h-chronopotentiometry at 10 $mA \cdot cm^{-2}$ in MeOH of CoO(OH)-MeOH. In this experiment, the current (left) or the potential (right) is held constant for 30 s, and the resulting potential-time or current-time profile should decay to a steady-state value at times > 2 s.

Stability measurements

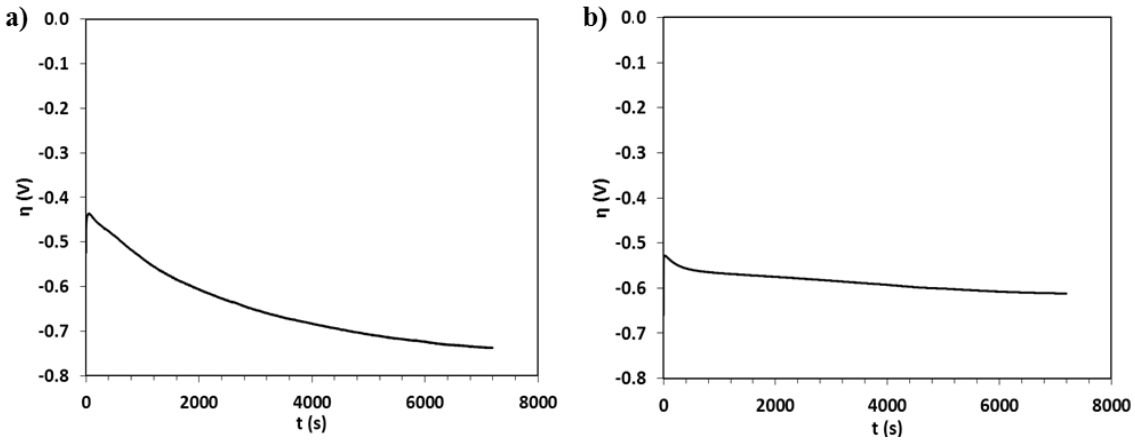

Figure S21. Controlled current electrolysis at 10 $mA \cdot cm^{-2}$ performed with CoO-MeCN (a) and CoO(OH)-DCM (b).

Faradaic efficiency

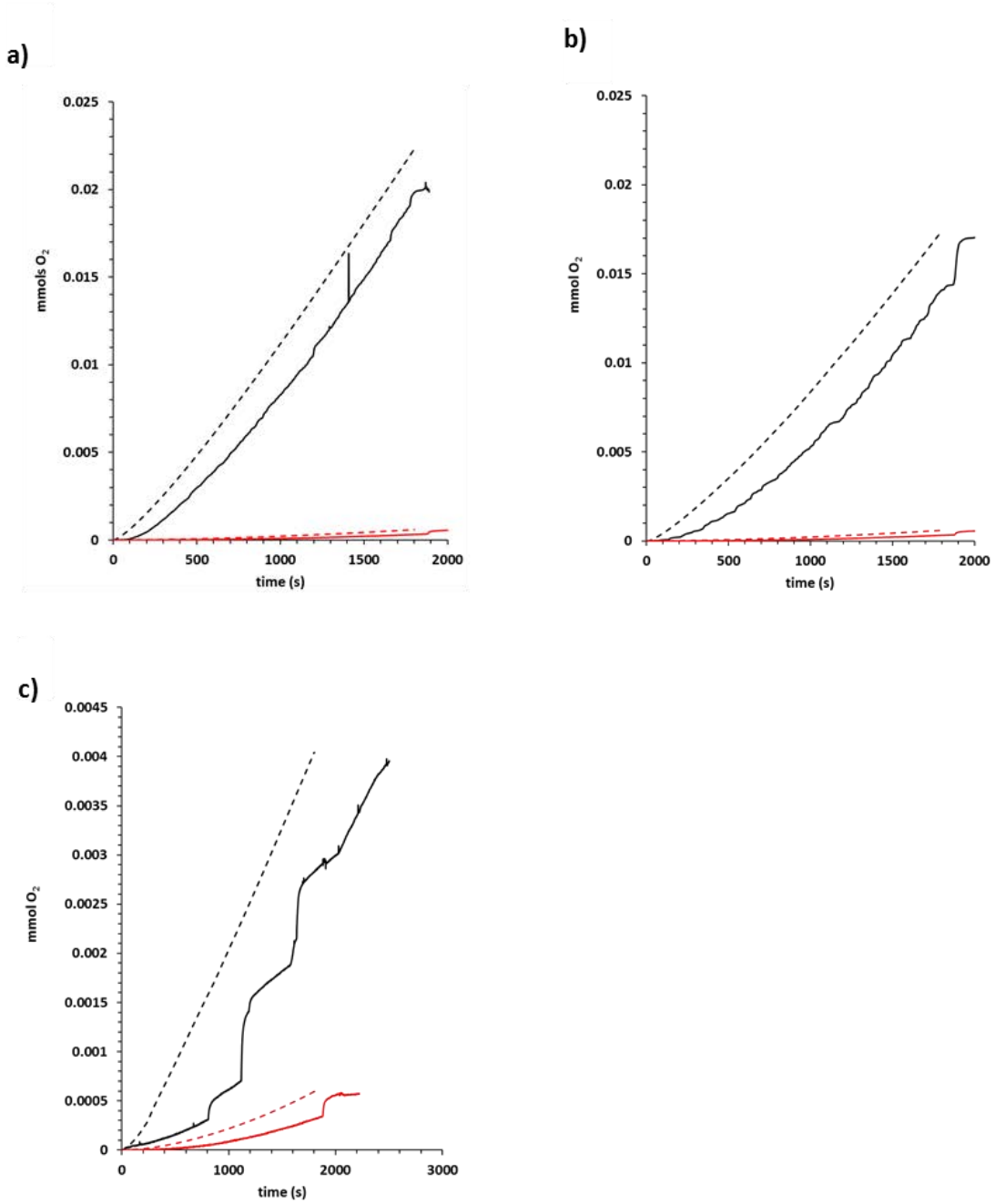

Figure S22. Faradaic efficiency determination from the comparison between the bulk electrolysis charge at η=-480 mV (dashed lines) and the H_2-sensitive Clark electrode signal (solid lines) for CoO-MeCN (a), CoO(OH)-DCM (b) and CoO(OH)-MeOH (c). Black lines correspond to the Co-derived NPs deposited onto GCE and red lines to the bare GC electrode.

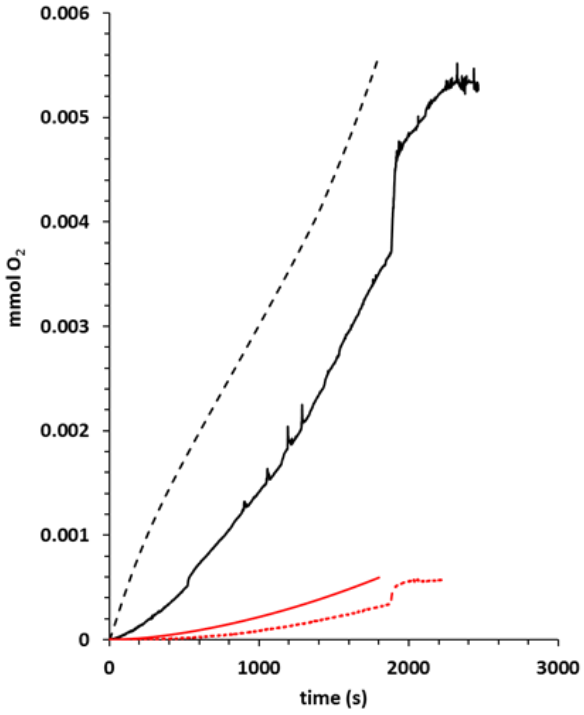

Figure S23. Faradaic efficiency determination from the comparison between the bulk electrolysis charge at η=-480 mV (dashed lines) and the H_2-sensitive Clark electrode signal (solid lines) for the $Co(OH)_2$ NPs formed after a 2h-chronopotentiometry at 10 $mA \cdot cm^{-2}$ in MeOH of CoO(OH)-MeOH (black lines) and bare GC electrode (red lines).

CHAPTER VI

General conclusions

Considering the general objectives proposed and the experimental results obtained, this thesis is summarized in this chapter.

Chapter III - A

✓ A new family of Ru(II) mononuclear complexes containing the pentadentate ligand 1-(2-pyridyl)-1,1-bis(6-2,2′-bipyridyl)ethane (**bpy2PYMe)** and its derivative containing a methyl substituent (**bpy(bpyMe)PYMe**), of general formula $[Ru^{II}(L)(X)]^{n+}$ (X = Cl, n = 1 and X = H_2O, n = 2), have been prepared and fully characterized by spectroscopic and electrochemical techniques.

✓ The NMR studies carried out have showed that when a solution of $[Ru^{II}$(**bpy2PYMe**)Cl$]^+$ (**1**$^+$) in MeOH is irradiated with light and/or warmed up a *cis-trans* equilibrium takes place. DFT calculations have been performed for fully understanding the mechanism of this isomerization, thus allowing the proposal of a dissociative mechanism in which a chloride and a pyridyl moiety decoordination leads to the *cis-trans* interconversion. This isomerization equilibrium can be avoided *via* the introduction of a methyl group in the pentadentate ligand, such as in **bpy(bpyMe)PYMe**, which increases the steric hindrance in the complex framework.

✓ When $[Ru^{II}$(**bpy2PYMe**)Cl$]^+$ (**1**$^+$) is oxidized to its Ru(III) state in DCM, a new κ-**N4-bis-Cl**$^+$ species is formed. This new compound is formed as result of the introduction of a Cl^- counterion inside the coordination sphere of Ru, thus displacing a pyridyl group. *Cis-trans* interconversion takes place again through the common intermediate κ-**N4-bis-Cl**$^+$ when the system comes back to Ru(II). The combination of electrochemical experiments and simulation through the *DigiSim 2.0 CV simulation software* have allowed us to build up the mechanism and calculate the kinetic and thermodynamic constants associated to the proposed isomeric equilibrium. DFT calculations performed on this system also strongly supports the proposed mechanism.

✓ A comparison of the electrochemical properties of the aquo complexes synthesized in this work with those of related Ru(II) complexes bearing pentadentate ligands (**PY4Im**) and (**PY5Me$_2$**) shows only a slight difference in the potential of the Ru(III)/Ru(II) and Ru(IV)/Ru(III) redox couples. Interestingly, the strong σ-donor character of the carbene ligand present in $[Ru^{II}$(**PY4Im**)$(H_2O)]^{2+}$ provokes a significant decrease of the acidy of its aquo group compared to the rest of aquo complexes, all containing a RuN_5O coordinative environment.

Chapter III – B

✓ Two new Ru(II) mononuclear complexes containing the pentadentate ligand 6,6''-(methoxy(pyridin-2-yl)methylene)di-2,2'-bipyridine (**L-OMe**) of general formula *trans*-[Ru^{II}(X)(L-OMe-κ-N^5)]$^{n+}$ (X = Cl, n = 1, *trans*-**1**$^{+}$; X = H_2O, n = 2, *trans*-**2**$^{2+}$) have been prepared and fully characterized by spectroscopic and electrochemical techniques.

✓ A detailed kinetic study of *trans*-**1**$^{+}$ and its analogous complex containing a Me substituent instead of OMe, *trans*-[Ru^{II}(**bpy2PYMe**)Cl]$^{+}$ (*trans*-**1**$^{'+}$), in aqueous solution at pH 1 is presented. Upon oxidation of Ru(II) to Ru(III), the new species containing an aquo (*trans*-**2**$^{3+}$ and *trans*-**2**$^{'3+}$), a chlorido and an aquo (*trans*-**4**$^{2+}$ and *trans*-**4**$^{'2+}$) and two aquo (*trans*-**3**$^{3+}$ and *trans*-**3**$^{'3+}$) ligands are formed, which are crucial for explaining the behavior of both complexes towards water oxidation (WO) catalysis.

✓ The set of complexes have also been tested in WO catalysis triggered by Ce(IV). The best catalyst is *trans*-**4**$^{2+}$, achieving a TOF of 0.71 s^{-1} and a TON of 168. The different catalytic performances between complexes containing aquo and/or chlorido ligands puts in evidence the important role of the chlorido ligand in the catalytic output.

✓ The differences on the values of the kinetic constant of the consecutive steps after oxidation with Ce^{IV} generate a distinct distribution of intermediate species for *trans*-**1'**$^{+}$ as compared to *trans*-**1**$^{+}$. Thus, for the L-OMe complex *trans*-**1**$^{+}$ the major species in solution during the first minutes is the chlorido-aquo complex *trans*-**4**$^{2+}$. In contrast, the aquo complex *trans*-**2**$^{'3+}$ is the most abundant species for *trans*-**1**$^{'+}$. These differences are responsible for the higher water oxidation catalytic activity of *trans*-**1**$^{+}$ as observed by the electrochemical analysis and oxygen evolution experiments and supported by DFT calculations.

✓ The chlorido ligand in the chlorido-aquo complex *trans*-**4**$^{2+}$ decreases the potential necessary to reach the Ru(V) state required for water oxidation, while the presence of a pendant pyridine group helps the O-O bond formation step, therefore decreasing the kinetic activation barrier of the reaction. These factors have been proposed to be responsible for the high catalytic performance of *trans*-**1**$^{+}$.

Chapter IV

- ✓ A new family of Cu(II) complexes have been synthetized bearing the new ligands 4,4'-(([2,2'-bipyridine]-6,6'-dicarbonyl)bis(azanediyl))dibenzenesulfonic acid ($\mathbf{1}^{2-}$) and its homologous with the sulfonate group at *orto* position with respect to the amidate group ($\mathbf{2}^{2-}$) and further characterized by X-ray diffraction, ESI-MS and electrochemical techniques.
- ✓ The catalytic properties of the complexes have been tested with regards to their ability to oxidize water into dioxygen, affording a moderate activity for the case of $\mathbf{1}^{2-}$. For $\mathbf{2}^{2-}$, the interaction of the sulfonate group with the copper centre is proposed as the cause of its lack of catalytic activity.

- ✓ The high overpotential necessary to oxidize water into dioxygen of $\mathbf{1}^{2-}$ has been proposed to be the main weak aspect of this complex. Accordingly, the high working potentials benefit its deactivation pathway after the formation of a radical anion.

- ✓ The absence of Cu heterogeneous materials deposited onto the electrodes according to SEM and EDX analyses confirm the molecular nature of these catalytic systems.

- ✓ The redox properties and WO catalytic performance of $\mathbf{1}^{2-}$ and $\mathbf{2}^{2-}$ have been compared with those of related Cu complexes previously reported in the literature. The use of tetra-anionic ligands coordinating directly to the Cu centre is a requirement to reach the reactive Cu(III) species needed for WO catalysis at low enough overpotentials.

Chapter V

- ✓ The formation Co-derived nanoparticles (NPs) from the molecular Co complex $[Co_8Na_4(L)_4(OH)_2(CO_3)_2(py)_{10}](BF_4)_2$ when submitted to reductive potentials in organic solvents has been demonstrated.

- ✓ The resulting functionalized electrodes have been further characterized by X-ray photoelectron spectroscopy (XPS), Scanning Electron Microscopy (SEM), Energy-dispersive X-Ray Spectroscopy (EDX) and electrochemical techniques.

- ✓ The influence of the solvent employed in the formation of the Co-derived NPs has been elucidated. XPS analysis of the systems have shown the formation of CoO NPs in MeCN and CoO(OH) NPs in DCM and MeOH.

- ✓ The comparison of the hydrogen evolution catalytic performance and the stability of the cathodes prepared in different solvents shows that cathodes prepared in MeOH are stable after long periods of catalysis, while a decrease in the loading of NPs takes place when DCM or MeCN are employed. Thus, a key role of MeOH in the stabilization of the CoO(OH) NPs due to its capability of forming hydrogen bonds has been proposed.

- ✓ The prepared cathodes are capable of electrochemically reducing water into hydrogen gas at pH 14, achieving high current densities with small total Co loading.

- ✓ The most active NPs in proton reduction catalysis are the CoO(OH) NPs formed in MeOH, which become "activated" after a 2 h constant polarization process at 10 mA/cm^2, generating afterwards $Co(OH)_2$ NPs with an optimized $\eta_{t=2}$ of -250 mV and a specific current density (j_s) of 596 $mA \cdot cm^{-2}$ at an overpotential of -480 mV.

VI

CHAPTER VII

Annexes

The following papers have been published during this PhD thesis and are closely related with the work carried out during this PhD. In the first work, a new $[Ru^{II}(bpy)]_2(\mu\text{-bimp})(\mu\text{- Cl})]^{2+}$ catalyst has been synthesized and its capacity as water oxidation (WO) and alkene epoxidation catalyst has been studied, resulting a good candidate for the latter with outstanding stereospecificity for *cis* and *trans* olefins. In the second work, the synthesis of a new family of Ru complexes containing N-heterocyclic carbene ligands is presented. This new family of complexes has been tested in WO and epoxidation catalysis, showing how the different auxiliary meridional and facial ligands affect their catalytic behavior. Finally, the third work is focused on the synthesis of two new Re complexes and their applications in CO_2 reduction catalysis. These new complexes incorporate an imidazolium group in the second coordination sphere, which not only modulates their redox properties and catalytic activity, but also alters mechanistic aspects of the catalysis.

Powerful Bis-facially Pyrazolate-Bridged Dinuclear Ruthenium Epoxidation Catalyst

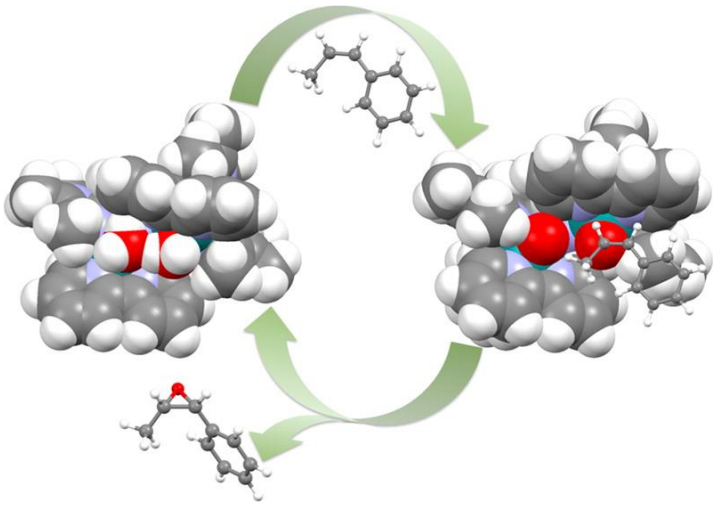

Aguiló, J.; Francàs, L.; Bofill, R,; **Gil-Sepulcre, M.**; García-Antón, J.; Poater, A.; Llobet, A.; Escriche, L.; Meyer, F.; Sala, X. *Inorg. Chem*. **2015**, *54*, 6782-6791.

Contribution

Marcos Gil-Sepulcre resynthesized the complexes and performed part of the epoxidation catalytic experiments.

Inorganic Chemistry

Article

pubs.acs.org/IC

Powerful Bis-facially Pyrazolate-Bridged Dinuclear Ruthenium Epoxidation Catalyst

Joan Aguiló,[†,‡] Laia Francàs,[‡] Roger Bofill,[†] Marcos Gil-Sepulcre,[†] Jordi García-Antón,[†,§] Albert Poater,[∥] Antoni Llobet,[†,‡] Lluís Escriche,*[,†] Franc Meyer,[⊥] and Xavier Sala*[,†]

[†]Departament de Química, Facultat de Ciències, Universitat Autònoma de Barcelona, Cerdanyola del Vallès, 08193 Barcelona, Spain

[‡]Institute of Chemical Research of Catalonia (ICIQ), Av. Països Catalans 16, 43007 Tarragona, Spain

[∥]Institut de Química Computacional i Catàlisi and Departament de Química, Universitat de Girona, Campus de Montilivi, 17071 Girona, Spain

[⊥]Institut für Anorganische Chemie, Georg-August-Universität, Tammannstrasse 4, 37077 Göttingen, Germany

Supporting Information

ABSTRACT: A new bis-facial dinuclear ruthenium complex, $\{[Ru^{II}(bpy)]_2(\mu\text{-bimp})(\mu\text{-Cl})\}^{2+}$, $\mathbf{2}^{2+}$, containing a hexadentate pyrazolate-bridging ligand (Hbimp) and bpy as auxiliary ligands has been synthesized and fully characterized in solution by spectrometric, spectroscopic, and electrochemical techniques. The new compound has been tested with regard to its capacity to oxidize water and alkenes. The *in situ* generated bis-aqua complex, $\{[Ru^{II}(bpy)(H_2O)]_2(\mu\text{-bimp})\}^{3+}$, $\mathbf{3}^{3+}$, is an excellent catalyst for the epoxidation of a wide range of alkenes. High turnover numbers (TN), up to 1900, and turnover frequencies (TOF), up to 73 min^{-1}, are achieved using PhIO as oxidant. Moreover, $\mathbf{3}^{3+}$ presents an outstanding stereospecificity for both *cis* and *trans* olefins toward the formation of their corresponding epoxides due to specific interactions transmitted by its ligand scaffold. A mechanistic analysis of the epoxidation process has been performed based on density functional theory (DFT) calculations in order to better understand the putative cooperative effects within this dinuclear catalyst.

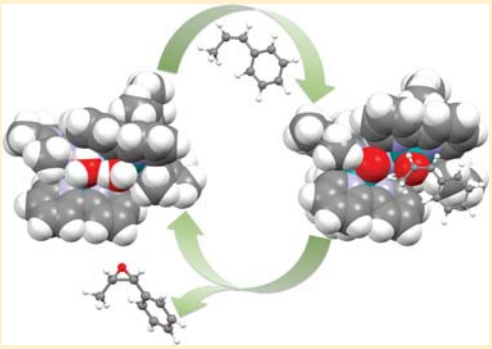

The epoxidation of olefins, a process of great industrial and economical importance, has historically constituted a great challenge for the organic synthetic chemists.[1,2] Epoxides constitute a family of essential chemicals, particularly for the synthesis of various polymers (polyglycols, polyamides, polyurethanes, etc.),[3,4] and fine chemicals, such as pharmaceuticals, food additives, or flavor and fragrance compounds.[5] For instance, propylene oxide monopolizes the epoxide chemical business with a yearly 8 million ton production and an expected annual increase of 5%.[6]

Enantioselective epoxidation of olefins and allylic alcohols is a chemical process of utmost industrial relevance. Numerous works by the Nobel laureate K. B. Sharpless with the Ti tartrate catalyst[7,8] or by H. Jacobsen with Mn^{III}−salen catalysts[9,10] have been proven efficient in this field. Thus, the Ti−tartrate catalyst consistently affords high enantioselectivities for widely different substrates thanks to a combination of stereoelectronic and steric factors, which leads to a concerted formation of both epoxide C−O bonds.[8] Concerning the Mn^{III}−(salen) catalysts, enantioselectivity is provoked by the presence of a chiral diimine bridge and of bulky groups at the 3,3′-positions of the salen ligand and the existence of π conjugation of the olefinic double bond.[9] In this case, epoxidation occurs by the direct attack of one of the C atoms of the C═C bond on the oxo ligand of a Mn(V)═O intermediate, generating a triplet radical species that would then collapse before or after rotating, thus generating the *cis* or the *trans* epoxide, respectively, depending on the relative height of the activation barriers for collapse and rotation.[10]

Ru complexes have also been proven to serve as excellent catalysts for redox transformations such as alcohol oxidation,[11−18] sulfoxidation,[19−22] water oxidation,[23−32] and epoxidation.[18,33−41] In all these cases, a Ru^{IV}═O or Ru^{V}═O group has been shown to be the active catalytic unit. Most of the literature related to redox catalysis using Ru complexes is based on mononuclear complexes, since they are generally easily accessible from a synthetic point of view. In sharp contrast, two powerful diruthenium epoxidation catalysts in terms of epoxide selectivity and substrate conversion have been recently reported by our research group.[42,43] In addition, these new catalysts display distinctive reactivity with regards to *cis* and *trans* alkenes. Both features are proposed to originate from a hydrogen bonding interaction between the second Ru^{IV}═O site and the substrate employed, together with steric effects.

Received: March 20, 2015
Published: June 29, 2015

DOI: 10.1021/acs.inorgchem.5b00641
Inorg. Chem. 2015, 54, 6782−6791

Our groups have extensive experience in the synthesis, characterization, and evaluation of the oxidative catalytic performance of dinuclear Ru complexes, most of them inspired by the well-known $\{[Ru^{II}(trpy)]_2(\mu\text{-bpp})(\mu\text{-Cl})\}^{2+}$ water oxidation catalyst.[44] Modifications around this paradigmatic compound, like the replacement of the trpy auxiliary ligands by facially coordinating scaffolds such as bpea or tpym, as well as the exchange of the bpp^- bridge by other tetradentate bridges, for instance, $pdz\text{-}dc^{2-}$, $pyr\text{-}dc^{3-}$, or pbl^- (see Chart 1 for a drawing of these ligands), and by bis-meridional hexadentate bridges, have been prepared, characterized, and catalytically evaluated.[42−48] The use of facial ligands such as bpea and tpym allowed an "up, down" relative orientation of the two Ru═O groups, which dramatically affects both the steric and electronic properties of these complexes as well as their final reactivity and water oxidation reaction mechanism.

Chart 1. Bridging and Auxiliary Ligands Discussed in This Work

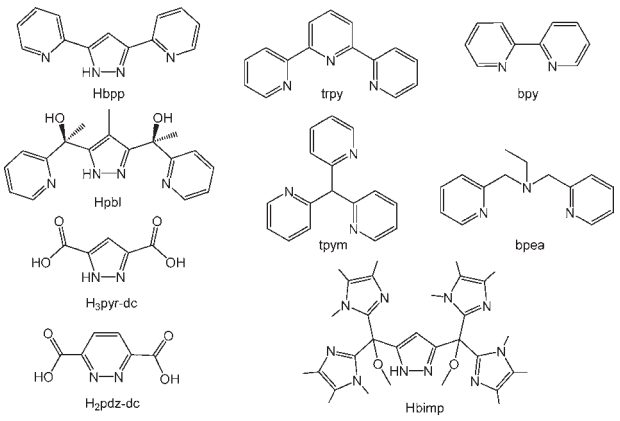

The use of a bis-facial bridging ligand to prepare dinuclear Ru catalysts for water oxidation or olefin epoxidation has not been attempted so far. Therefore, in order to explore the properties of this kind of system, herein we report the synthesis and spectroscopic and redox properties of a new dinuclear complex with formula $\{[Ru^{II}(bpy)]_2(\mu\text{-bimp})(\mu\text{-Cl})\}^{2+}$, $\mathbf{2}^{2+}$, and its bis-aqua derivative $\{[Ru^{II}(bpy)(H_2O)]_2(\mu\text{-bimp})\}^{3+}$, $\mathbf{3}^{3+}$ (bpy = 2,2′-bipyridine; bimp = 3,5-bis[bis(1,4,5-trimethyilmidazol-2-yl)-methoxymethyl]pyrazolate). The already reported $bimp^-$ ligand[49] will act as bridging and bis-facial coordinating ligand. Finally, the reactivity of $\mathbf{3}^{3+}$ toward the epoxidation of olefins and a theoretical study on its putative epoxidation mechanism are reported in this work.

RESULTS AND DISCUSSION

Synthesis and Structural Characterization of $\mathbf{2(PF_6)_2}$ and $\mathbf{3}^{3+}$. The synthetic strategy followed for the preparation of the respective μ-chloro and bis-aqua dinuclear complexes $\mathbf{2(PF_6)_2}$ and $\mathbf{3}^{3+}$ is depicted in Scheme 1.

Preparation of precursor **1** from $RuCl_3{\cdot}nH_2O$ involved the presence of sodium methoxide as a base to deprotonate the pyrazolic NH group of the Hbimp ligand. Because of the high solubility of **1** in the reaction media, the addition of diethyl ether was compulsory in order to precipitate the desired product as a green powder (see ESI-MS spectrum of **1** in Figure S1, Supporting Information). The reaction of **1** in the presence of LiCl, triethylamine, and 2,2′-bypyridine (2 equiv) ended up generating $\mathbf{2}^{2+}$ after overnight stirring at room temperature. The addition of water and 1 mL of a saturated aqueous solution of NH_4PF_6 yielded a violet powder corresponding to the desired complex, $\mathbf{2(PF_6)_2}$. The dissolution of $\mathbf{2(PF_6)_2}$ in a pH 1.0 aqueous solution (triflic acid 0.1 M) resulted in the generation of the bis-aqua complex $\mathbf{3}^{3+}$.

Scheme 1. Synthetic Pathway for the Preparation of $\mathbf{2(PF_6)_2}$ and $\mathbf{3}^{3+a}$

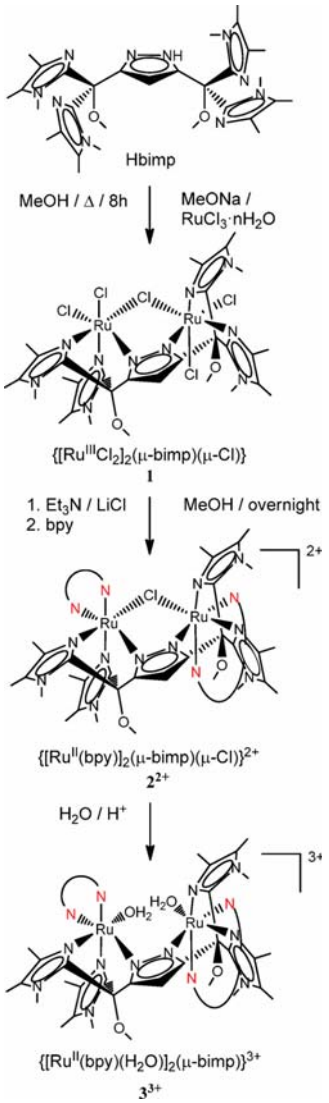

[a]2,2′-Bipyridine (Bpy) ligands have been represented schematically (red N atoms) for the sake of clarity.

Each tridentate unit of the hexadentate μ-$bimp^-$ ligand, given its configuration, can only coordinate in a facial fashion to an octahedral metal center. In addition, the μ-$bimp^-$ ligand can potentially generate the C_s (*cis*) and C_2 (*trans*) isomers depicted in Figure 1. The terms *cis* and *trans* indicate whether the two bipyridines are located both on the same side (*cis*) of or one above and one below (*trans*) the distorted plane formed by the pyrazolate ring, the Ru metal centers, and the chlorido bridge or the two coordinated aqua ligands.

Complex $\mathbf{2(PF_6)_2}$ has been characterized in acetone solution by NMR spectroscopy (Figure 2 and Figure S2, Supporting

DOI: 10.1021/acs.inorgchem.5b00641
Inorg. Chem. 2015, 54, 6782−6791

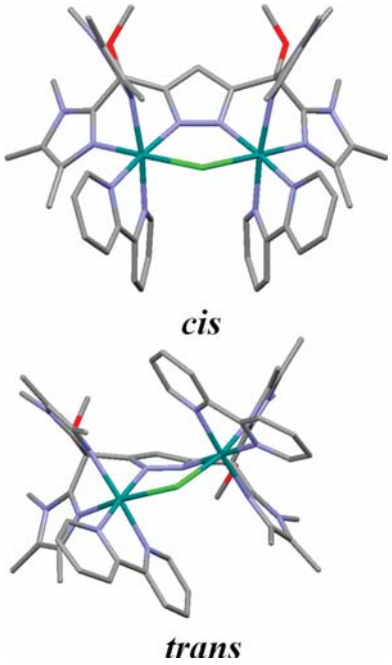

Figure 1. Mercury plot of the μ-Cl front view corresponding to the DFT calculated structures of *cis*- and *trans*-$\mathbf{2}^{2+}$. Atom color code: blue, nitrogen; light green, chlorine; dark green, ruthenium; light gray, carbon; red, oxygen. Hydrogen atoms have been omitted for clarity purposes.

Information) as well as by ESI-MS (Figure S4 in the Supporting Information).

The broad ^{1}H NMR signals of $\mathbf{2}^{2+}$ (Figure S2a, Supporting Information) show the paramagnetic character of the sample, probably due to the partial oxidation of $\mathbf{2}^{2+}$. This oxidation is avoided under the presence of a reducing agent (Zn amalgam), when significantly narrower peaks are observed (Figure S2b, Supporting Information). Figure 2 and Figure S2c−e, Supporting Information, display both ^{1}H and ^{13}C {^{1}H} 1D and 2D (COSY, HSQC, and HMBC) NMR spectra for $\mathbf{2}^{2+}$. From these spectra, the presence of a single isomer of $\mathbf{2}(\mathbf{PF_6})_2$ in solution could be deduced. However, the low solubility of the complex in the regular deuterated solvents and its above-mentioned ease of oxidation prevented the recording of a NOESY NMR spectrum. Therefore, the pyridine rings of each bpy and the four methyl groups bonded to the imidazole moieties could not be distinguished. For this reason, only a partial assignment of the ^{1}H (Figure 2, top) and ^{13}C resonances of $\mathbf{2}^{2+}$ could be accomplished (see the Experimental Section).

Density functional theory (DFT) calculations have been carried out in order to further extract structural and electronic information about the potential *cis*/*trans* isomers. These calculations show for the chlorido-bridged complex $\mathbf{2}^{2+}$ an energy value of 3.2 kcal/mol lower for the *trans* isomer compared with its *cis* counterpart (Figure 1 and Table S1, Supporting Information). When the same calculations were carried out for the corresponding *cis* and *trans*-bis-aqua complex $\mathbf{3}^{3+}$ (Figure 3 and Table S1, Supporting Information), the *cis*/*trans* energy gap increased to 8.2 kcal/mol, again demonstrating the higher thermodynamic stability of the *trans* isomer. Even though these energy differences are not large enough to totally discard the formation of the *cis* isomer under the reaction conditions, they are a good indication of the potential

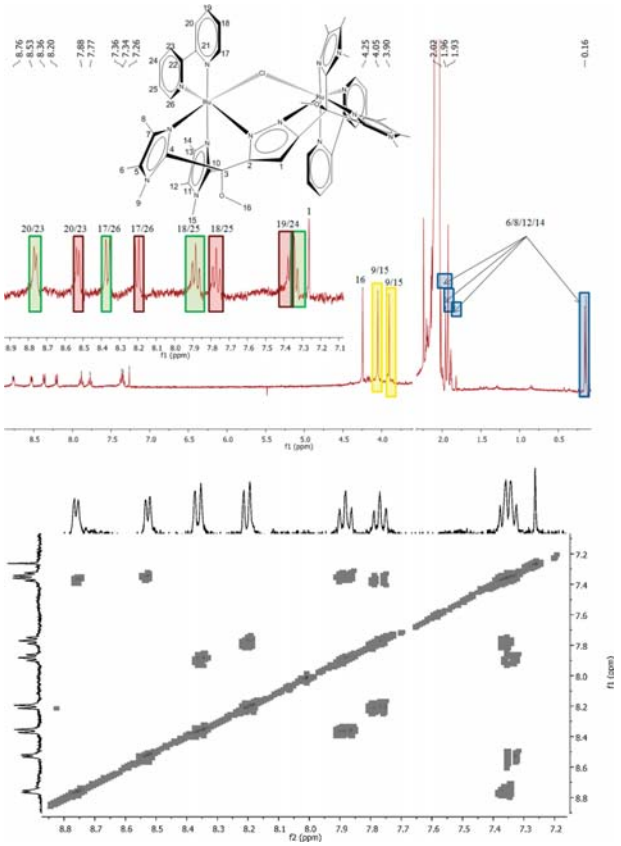

Figure 2. ^{1}H NMR spectra (400 MHz, 298 K, acetone-d_6) for $\mathbf{2}^{2+}$: 1D spectrum including partial assignment of signals (top) and 2D-COSY spectrum (bottom).

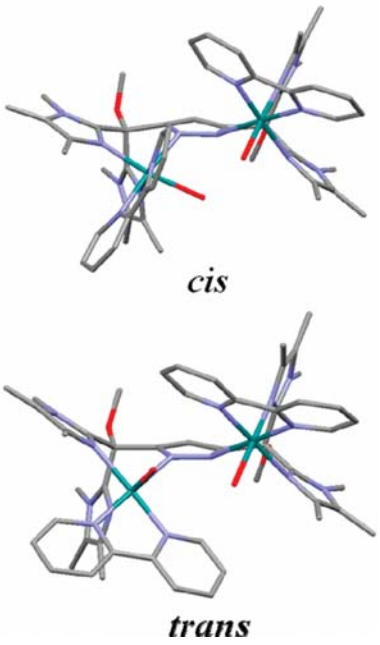

Figure 3. Mercury plot of the bis-H_2O front view corresponding to the DFT calculated structures of *cis*- and *trans*-$\mathbf{3}^{3+}$. Atom color code: blue, nitrogen; dark green, ruthenium; light gray, carbon; red, oxygen. Hydrogen atoms have been omitted for clarity purposes.

DOI: 10.1021/acs.inorgchem.5b00641
Inorg. Chem. 2015, 54, 6782−6791

formation of the *trans* compound given the isomeric purity of the obtained complex. Moreover, this hypothesis is further supported by the trends observed when performing a detailed comparison of the DFT-calculated structures for *cis*- and *trans*-$\mathbf{2}^{2+}$ (Figure S3, Supporting Information). Thus, for *cis*-$\mathbf{2}^{2+}$, we observe the presence of repulsive H···H interactions among the methyl groups, between the methoxy and the CH group of the pyrazole ring, and among the CH groups of the bpys, together with the absence of $\pi-\pi$ stacking interactions between the pyridine rings of neighboring bpys (torsion angle of 22.2°). In addition, significant tension within the *cis* complex exists, since the dihedral angle between the pyr rings of the same bpy is 27.0° and the Ru binding angles are far from ideal octahedral coordination. On the contrary, for *trans*-$\mathbf{2}^{2+}$ the repulsive H···H interactions are now abated (longer average H−H distances), while more favorable C···H interactions between the C atoms of the pyr rings and the H atoms of the methyl groups are observed (four interactions for the *trans* isomer compared with only one for the *cis* one). These data, together with a less tensioned conformation for the *trans* isomer (dihedral angle between pyr rings of the same bpy of only 16.3° and Ru binding angles a bit closer to ideal octahedral geometry), indicate a clear preference of $\mathbf{2}^{2+}$ for the *trans* configuration.

Electrochemical and Spectroscopic Characterization of $\mathbf{2}^{2+}$ and $\mathbf{3}^{3+}$. The cyclic voltammetry (CV) of $\mathbf{2}^{2+}$ in dichloromethane (DCM) (Figure S5a, Supporting Information) exhibits two reversible waves, also confirmed by differential pulse voltammetry (DPV) (Figure S5b, Supporting Information), which can be assigned to the following electrochemical reactions (the $bimp^-$ and the bpy ligands are not shown for the sake of clarity):

$$[Ru^{III}(\mu\text{-Cl})Ru^{II}]^{3+} + 1e^- \rightarrow [Ru^{II}(\mu\text{-Cl})Ru^{II}]^{2+} \quad (0.55\ \text{V vs SSCE}) \quad (1)$$

$$[Ru^{III}(\mu\text{-Cl})Ru^{III}]^{4+} + 1e^- \rightarrow [Ru^{III}(\mu\text{-Cl})Ru^{II}]^{3+} \quad (0.98\ \text{V vs SSCE}) \quad (2)$$

The electrochemical properties of $\mathbf{3}^{3+}$ have been investigated after its "*in situ*" generation in an acetone/water (pH 1.0, 0.1 M triflic acid) 1:9 mixture by using $\mathbf{2}^{2+}$ as a precursor (see Scheme 1 and the pH dependence of the DPV signals of the resulting complex in Figure S5c, Supporting Information, which confirms the "*in situ*" formation of the bis-aqua complex $\mathbf{3}^{3+}$). From the CV and DPV (Figure 4) measurements of $\mathbf{3}^{3+}$, a total of four waves can be observed. The first three can be tentatively assigned, taking into account previous results on related complexes,[25] to the following redox processes:

$$[HO{-}Ru^{III}(\mu\text{-bimp})Ru^{II}{-}OH_2]^{3+} + 1e^- + 1H^+ \rightarrow [H_2O{-}Ru^{II}(\mu\text{-bimp})Ru^{II}{-}OH_2]^{3+} \quad (0.27\ \text{V vs SSCE}) \quad (3)$$

$$[HO{-}Ru^{III}(\mu\text{-bimp})Ru^{III}{-}OH]^{3+} + 1e^- + 1H^+ \rightarrow [HO{-}Ru^{III}(\mu\text{-bimp})Ru^{II}{-}OH_2]^{3+} \quad (0.46\ \text{V vs SSCE}) \quad (4)$$

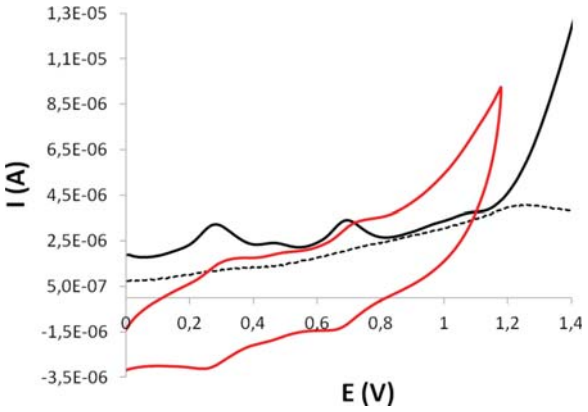

Figure 4. CV at 100 mV/s scan rate (red) and DPV (black) for the bis-aqua complex $\mathbf{3}^{3+}$ in acetone/water 1:9, pH 1.0 (0.1 M triflic acid). The DPV blank in the absence of catalyst is also shown (dashed line). A glassy carbon electrode was used as working electrode and the potential was measured vs SSCE. For further details, see Experimental Section.

$$[O{=}Ru^{IV}(\mu\text{-bimp})Ru^{III}{-}OH]^{3+} + 1e^- + 1H^+ \rightarrow [HO{-}Ru^{III}(\mu\text{-bimp})Ru^{III}{-}OH]^{3+} \quad (0.69\ \text{V vs SSCE}) \quad (5)$$

When the potential is increased further up to 1.4 V, a large anodic current is observed in the DPV that is associated with an additional complex oxidation with a concomitant electrocatalytic oxidation of water to dioxygen. For the case of a further one electron oxidation, this would be in agreement with eqs 6 and 7.

$$[O{=}Ru^{IV}(\mu\text{-bimp})Ru^{IV}{=}O]^{3+} + 1e^- + 1H^+ \rightarrow [O{=}Ru^{IV}(\mu\text{-bimp})Ru^{III}{-}OH]^{3+} \quad (\text{foot of the wave at 1.2 V vs SSCE}) \quad (6)$$

$$[O{=}Ru^{IV}(\mu\text{-bimp})Ru^{IV}{=}O]^{3+} + 2H_2O \rightarrow [H_2O{-}Ru^{II}(\mu\text{-bimp})Ru^{II}{-}OH_2]^{4+} + O_2 \quad (7)$$

Table 1 displays the $E_{1/2}$ values for $\mathbf{2}^{2+}$, $\mathbf{3}^{3+}$, and a set of related compounds containing the Hbpp ligand. The compounds have been classified depending on the σ-donor character of the coordinated N-donor ligand (pyridine < pyrazole ≈ imidazole < tertiary aliphatic amine) and the number of coordinated chlorido anions per Ru center (0 for the bis-aqua derivatives, 1/2 when a chlorido-bridge connects two Ru metal ions, or 1). Thus, a down-shift of $E_{1/2}$ is observed when comparing $\mathbf{2}^{2+}$ with $\{[Ru^{II}(trpy)]_2(\mu\text{-bpp})(\mu\text{-Cl})\}^{2+}$ (entry 2), in agreement with the higher σ-donor and lower π-acceptor capacity of the imidazole rings relative to the pyridines that are part of the trpy ligand and also present in the Hbpp ligand. The redox potentials of $\mathbf{2}^{2+}$ have also been compared with those of other bis-facial Ru dinuclear complexes (entries 3 and 4). With respect to the bpea complex (entry 3), both processes are anodically shifted by 180 and 260 mV, respectively, as a consequence of both the lower σ-donor and higher π-acceptor capacity of the imidazole rings in $\mathbf{2}^{2+}$ relative to the central tertiary aliphatic amine in the bpea ligand and the lower σ-donation power of the unique chlorido-bridged anion of $\mathbf{2}^{2+}$ in contrast to the two chlorido anions present in *trans*-

DOI: 10.1021/acs.inorgchem.5b00641
Inorg. Chem. 2015, 54, 6782−6791

Table 1. Redox Potentials in V (vs SSCE) at a 100 mV/s Scan Rate for 2^{2+}, 3^{3+}, and Related Ru Complexes

entry	complex	III,II/II,II	III,III/III,II	IV,III/III,III	IV,IV/IV,III	$N_{pyridine}$	$N_{pyrazole/imidazole}$	$N_{aliphatic\text{-}amine}$	Cl	ref
1	$\mathbf{2}^{2+a}$	0.55	0.98			2	3		1/2	*c*
2	$\{[Ru^{II}(trpy)]_2(\mu\text{-bpp})(\mu\text{-Cl})\}^{2+a}$	0.71	1.12			4	1		1/2	25
3	*trans*-$\{[Ru^{II}(bpea)(Cl)]_2(\mu\text{-bpp})\}^{+a}$	0.37	0.72			3	1	1	1	45
4	*trans*-$\{[Ru^{II}(tpym)(Cl)]_2(\mu\text{-bpp})\}^{+a}$	0.54	0.84			4	1		1	46
5	$\mathbf{3}^{3+b}$	0.27	0.46	0.69	1.20	2	3			*c*
6	*cis*-$\{[Ru^{II}(trpy)(H_2O)]_2(\mu\text{-bpp})\}^{3+b}$	0.59	0.65	0.88	1.10	4	1			25
7	*trans*-$\{[Ru^{II}(bpea)(H_2O)]_2(\mu\text{-bpp})\}^{3+b}$	0.21	0.43	0.61		3	1	1		45
8	*trans*-$\{[Ru^{II}(tpym)(H_2O)]_2(\mu\text{-bpp})\}^{3+b}$	0.54	0.75	1.18	1.52	4	1			46

[a] CH_2Cl_2 using $TBAPF_6$ (0.1 M) as electrolyte. [b] Aqueous solution at pH 1.0 (0.1 M triflic acid). [c] This work.

$\{[Ru^{II}(bpea)(Cl)]_2(\mu\text{-bpp})\}^{+}$. Interestingly, the redox potentials of $\mathbf{2}^{2+}$ are similar to those of the tpym chlorido complex (entry 4). While in the latter each Ru is coordinated to four pyridines, one pyrazolato, and one chlorido anion, in $\mathbf{2}^{2+}$ each Ru is bound to two pyridines, three imidazole/pyrazolato rings, and only half chlorido ligand. In consequence, the lower Cl^- content in $\mathbf{2}^{2+}$ might compensate the more pronounced σ-donating character of its imidazole and pyrazole rings, thus revealing the influence of both the N-ligands and the chlorido anions into the final $E_{1/2}$ values, and how this property is a perfect combination of both factors.

Concerning the bis-aqua species, a cathodic shift of the $E_{1/2}$ values of $\mathbf{3}^{3+}$ relative to those of *cis*-$\{[Ru^{II}(trpy)(H_2O)]_2(\mu\text{-bpp})\}^{3+}$ and *trans*-$\{[Ru^{II}(tpym)(H_2O)]_2(\mu\text{-bpp})\}^{3+}$ (entries 6 and 8) is observed, which can be explained again by the higher σ-donor and lower π-acceptor character of the imidazole rings compared with pyridines. Finally, similar $E_{1/2}$ values are observed for *trans*-$\{[Ru^{II}(bpea)(H_2O)]_2(\mu\text{-bpp})\}^{3+}$ (entry 7) and $\mathbf{3}^{3+}$. Thus, the presence in the bpea complex of a strong σ-donor (aliphatic tertiary amine) and three pyridines results in similar average donor/acceptor properties as combining two imidazoles, two pyridines and one pyrazole in $\mathbf{3}^{3+}$.

The UV−vis spectra of $\mathbf{2}^{2+}$ and $\mathbf{3}^{3+}$ have been recorded in acetone and acetone/water 8:2 (pH 1), respectively (Figure S6, Supporting Information). The region between 250 and 350 nm, usually displaying very intense bands due to the intraligand $\pi \rightarrow \pi^*$ transitions, could not be registered since it was out of the solvent window. With respect to the region between 350 and 550 nm, unsymmetrical broad metal-to-ligand charge transfer (MLCT) bands appear.[50,51] For the chlorido-bridged complex $\mathbf{2}^{2+}$, the MLCT bands are shifted to longer wavelengths due to the relative destabilization of the $d\pi$(Ru) levels provoked by the chlorido ligand compared with the aqua ligands.

Epoxidation Catalysis. Complex $\mathbf{3}^{3+}$ has been tested with regards to its ability to oxidize alkenes. The catalytic reactions have been carried out using a catalyst/substrate/oxidant/water ratio of 1:2000:4000:4000 after a 120 min mixing period of catalyst $\mathbf{2}^{2+}$ in the absence of substrate (see Experimental Section for further details), during which the excess of water ensures the generation of the oxidant PhIO species from $PhI(OAc)_2$[52] and of the bis-aqua derivative $\mathbf{3}^{3+}$ from its chloro counterpart $\mathbf{2}^{2+}$. This mixing period before substrate addition is crucial in order to improve the rate of the catalytic reaction. Scheme S1, Supporting Information, summarizes the set of reactions that take place during the catalytic epoxidation of alkenes for the proposed system. All products of each catalytic experiment have been identified by gas chromatography (GC)−mass spectrometry (MS) (see Figures S7−S10 in the Supporting Information for further details).

The catalytic activity of $\mathbf{3}^{3+}$ toward the epoxidation of alkenes has been initially tested and optimized for the oxidation of *cis*-β-methylstyrene, and its reaction progress monitored by GC and GC-MS. After that, six *cis*- and *trans*-olefins have been tested as substrates. All results from epoxidation catalysis are displayed in Table 2.

Table 2. Catalytic Performance of 3^{3+} in the Epoxidation of *cis*- and *trans*-Alkenes Using PhIO as Oxidant in DCE[a]

entry	alkene	conv. (%)[b]	selec. (%)[c]	TN/TOF_i[d]
1	*cis*-β-methylstyrene	>99	88	1760/73
2	*trans*-β-methylstyrene	50	80	800/21
3	*cis*-stilbene	>99	24	480/11
4	*trans*-stilbene	>99	14	280/4
5	*cis*-2-octene	95	100	1900/34
6	*trans*-2-octene	42	100	840/24
7	*cis*-2-hexene	93	100	1860/83
8	*trans*-2-hexene	58	100	1160/19
9	cyclooctene	95	65	1235/17

[a] Catalyst/substrate/oxidant/water ratio of 1:2000:4000:4000. See Experimental Section for further procedural details. [b] Substrate conversion = $\{[substrate]_{initial} - [substrate]_{final}\}/[substrate]_{initial} \times 100$. [c] Epoxide selectivity = $[epoxide]_{final}/\{[substrate]_{initial} - [substrate]_{final}\} \times 100$. [d] TN is the turnover number with regard to the total epoxide obtained. TOF_i is the initial turnover frequency expressed in epoxide cycles per minute (TN_i/min).

The system $\mathbf{3}^{3+}$ 0.85 mM/*cis*-β-methylstyrene 1.7 M/$PhI(OAc)_2$ 3.4 M/H_2O 3.4 M in 1,2-dichloroethane (DCE) renders 1.50 M *cis*-β-methylstyrene oxide, which represents a turnover number (TN) of 1760 with regard to the initial catalyst concentration after 90 min of reaction. The conversion of the initial substrate is total (>99%) after this time, and an epoxide selectivity of 88% is obtained. The activity of $\mathbf{3}^{3+}$ for the epoxidation of other alkenes is also very remarkable. For instance, the system $\mathbf{3}^{3+}$/*cis*-2-octene generates an impressive 1.62 M *cis*-2-octene oxide that represents a TN of 1900 with regard to the initial catalyst concentration with an initial turnover frequency (TOF_i) of 34.0 cycles per minute.

Although the results herein reported are difficult to compare with those of related complexes from the literature because the catalysts and oxidants used are substantially different, some conclusions can be drawn. First, as a general trend, the reported Ru mononuclear species in the literature show lower epoxide selectivities and substrate conversions.[53,54] And second, to our knowledge $\mathbf{3}^{3+}$ is more than 30 times faster than the best reported mononuclear Ru catalyst. Therefore, both figures suggest the existence of a potential cooperative effect between the two metal centers strategically situated in $\mathbf{3}^{3+}$ (see

DOI: 10.1021/acs.inorgchem.5b00641
Inorg. Chem. 2015, 54, 6782−6791

discussion below). Also, when compared with our recently reported Ru dinuclear catalysts,[42,43] $\mathbf{3}^{3+}$ performs better in the presence of aromatic *cis* substrates (e.g., higher conversion, selectivity, and TN and TOF_i values for *cis*-β-methylstyrene compared with the pdz-dc[42] and pyr-dc[43] counterparts, and for *cis*-stilbene higher conversion and TN figures compared with both previous catalysts and an even higher TOF_i value than its pdz-dc counterpart[42]).

A deeper look at Table 2 also shows that $\mathbf{3}^{3+}$ performs much better with substrates containing electron-donor groups than with those bearing electron-withdrawers. Thus, the best results are obtained for *cis*-2-octene and *cis*-2-hexene, whereas the poorest values are obtained for *trans*-stilbene, the latter also suffering from potential steric effects due to the bulkiness of its two phenyl rings. Also, the performance of $\mathbf{3}^{3+}$ in front of *cis*- and *trans*-β-methylstyrene, which could be seen as hybrids between the corresponding *cis*-/*trans*-stilbene and *cis*-/*trans*-2-octene/hexene substrates from a steric and electronic point of view, is indeed intermediate between the two extremes probably due to a combination of the two effects described above. Furthermore, the electronic effects are in agreement with the electrophilic character of the Ru^{IV}=O active site proposed in related works.[42,43] Also, the lower activity and selectivity of the catalyst toward *trans* substrates with regard to their related *cis* counterparts is worth mentioning (Table 2 and Figure 5, top). Given the nearly identical electronic nature of the *cis* and *trans* alkenes, the differential reactivity can only be due to distinctive interactions with the catalyst. To understand and rationalize the origin of this differentiated reactivity, we carried out DFT calculations of the energy and structure of the putative *cis*- and *trans*-O=Ru^{IV}–Ru^{IV}=O active species, which pointed to a higher thermodynamic stability for the *trans*-configuration (12.9 kcal/mol) compared with its *cis* counterpart (Figure 5, bottom, and Table S1, Supporting Information). Knowing the potential structure of the catalytic active species, it is clear that the aforementioned interactions may be a consequence of the high steric constrictions imposed by the cavity of the catalyst around the Ru^{IV}=O active sites. Thus, selectivity in favor of the *cis* or *trans* isomer of the substrate is determined by the ability of the alkene isomers to better fit into the reactive pocket of the catalyst (Figure 5, bottom).

Another interesting feature of the system studied in this work is the stereospecific nature of the catalytic process, since no *cis*/*trans* isomerization takes place for either the *cis*- or the *trans*-alkenes. This points toward a mechanism of either a concerted oxygen atom transfer from the Ru^{IV}=O active site to the double bond of the alkene (path I, Scheme 2) or a radical pathway where the C–C rotation of the generated radical is much slower than the ring closing that generates the final epoxide (path II1, Scheme 2).[55−59]

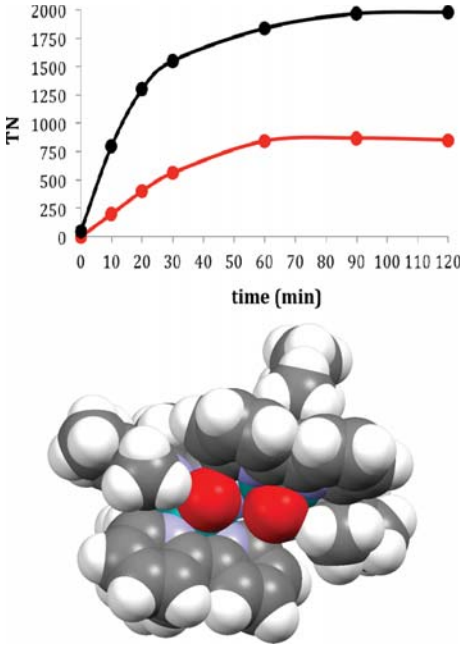

Figure 5. (top) Evolution of *cis*-β-methylstyrene oxide (black line) and *trans*-β-methylstyrene oxide (red line) when employing $\mathbf{3}^{3+}$ as catalyst. (bottom) Mercury spacefilling plot of the structure of the *trans*-O=Ru^{IV}–Ru^{IV}=O DFT-calculated state for catalyst $\mathbf{3}^{3+}$. Color code: oxygen, red; carbon, light gray; hydrogen, white; nitrogen, light blue; ruthenium, green.

Scheme 2. Proposed Stereoselective (I, II1) and Nonstereoselective (II2) Mechanisms for the Epoxidation of Alkenes by Ru^{IV}=O Species

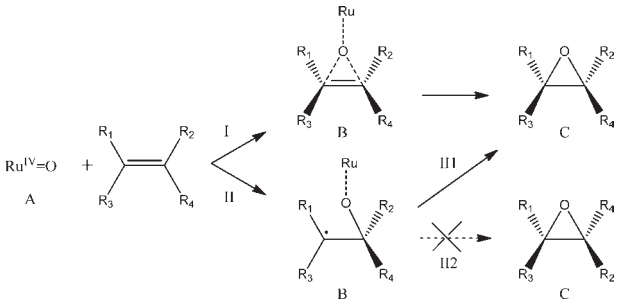

DFT calculations have been performed for $\mathbf{3}^{3+}$ in the presence of *cis*- and *trans*-β-methylstyrene, *cis*- and *trans*-stilbene, and *cis*- and *trans*-2-octene in order to quantify the energetics associated with the steric constraints that direct the epoxidation process (Table 3 and Figure S11 and Table S1, Supporting Information). The ground state multiplicity of all putative species was accurately evaluated, revealing that the initial bis-aqua species is a singlet, whereas the bis-oxo species is a quintuplet, and the presumed radical species present during the formation of the new C–O bond as well as the final epoxide species are triplets.

Table 3. Relative Energies in kcal/mol with Respect to Initial Substrate and Catalyst *trans*-$\mathbf{3}^{3+}$ of the Most Stable Epoxidation Pathway of the *cis* and *trans* Isomers of β-Methylstyrene, Stilbene and 2-Octene[a]

	A	TS(A →B)	B	TS(B→C)	C
cis-β-methylstyrene	0.0	21.0	11.5	11.6	0.3
trans-β-methylstyrene	0.0	23.1	12.6	12.7	0.3
cis-stilbene	0.0	23.5	5.1	13.8	−1.3
trans-stilbene	0.0	24.4	8.9	17.8	8.5
cis-2-octene	0.0	23.6			−5.1
trans-2-octene	0.0	29.2			−0.8

[a]A = *trans*-$\mathbf{3}^{3+}$ + substrate, B = radical intermediate, C = epoxide product bound to *trans*-$\mathbf{3}^{3+}$.

DOI: 10.1021/acs.inorgchem.5b00641
Inorg. Chem. 2015, 54, 6782−6791

The results obtained show that the rate-determining step (rds) of the whole process involves the interaction of the double bond of the alkene with one of the Ru=O groups that eventually will bond the O atom to the olefin (steps I or II, Scheme 2, and transition state (TS) (A → B), Figure S11 and Table S1, Supporting Information, and Table 3). However, the interaction of a Ru=O group with both carbon atoms of the olefin in a concerted way is not feasible, and thus all attempts collapse in a mono O···C interaction. This radical pathway is analogous to the one proposed for the [Mn^{III}(salen)Cl] catalyst[10] and differs fundamentally from the mechanism proposed for the Ti tartrate catalyst, where both epoxide C−O bonds are formed simultaneously.[8] Finally, the low stability of the radical species formed facilitates the formation of the final epoxide, except for the case of *cis*-2-octene, where its nonaromatic nature probably does not allow the localization of such radical intermediate, which could in turn be the reason why selectivity is as high as 100% (Table 2).

Interestingly, DFT calculations indicate that the transition state of this rds (TS(A → B)) is favored by 2.1, 0.9, and 5.6 kcal/mol for the *cis* isomer with respect to the *trans* substrate in the cases of *β*-methylstyrene, stilbene, and 2-octene, respectively (Table 3 and Table S1, Supporting Information), which could be an explanation for the higher observed experimental rates (TOF_i) for the *cis* substrates (Table 2).

Additionally, an analysis of the Ru=O···H distances lower than 3 Å in TS(A → B) for the reaction of *trans*-$\mathbf{3}^{3+}$ with both *cis* and *trans* substrates (Figures S12−S14, Supporting Information) shows that while for *trans*-*β*-methylstyrene three different H interactions between the oxo groups and the substrate exist (O1−CH, O1−CH_3, O2−CH_3; O1 being the epoxy-forming atom and O2 the second oxo group, not involved in O transfer), for *cis*-*β*-methylstyrene an additional O1−CH_3 interaction happens (Figure S12, Supporting Information). Analogously, for *trans*-stilbene three different H interactions between the oxo groups and the substrate exist (O1−CH_{arom}, O1−$CH_{olefinic}$, O2−$CH_{olefinic}$; O1 being the epoxy-forming atom and O2 the second oxo group), while for *cis*-stilbene an additional O2−CH interaction happens (there are two O1−$CH_{olefinic}$ interactions plus an O2−$CH_{olefinic}$ and an O2−CH_{arom} interaction, Figure S13, Supporting Information). In the two previous cases, those differences can only arise from the dissimilar orientation of the C=C bond as well as the different configuration of the *cis* vs *trans* substrates, thus demonstrating the more favored TS(A → B) for the substrate in *cis* configuration, which in turn may be in accordance with the lower calculated TS(A → B) energies (Table 3) and the higher experimental conversion, TN and TOF_i values (Table 2) reported above. At the same time, this could also explain the better performance of $\mathbf{3}^{3+}$ in front of aromatic *cis* substrates compared with its pdz-dc[42] and pyr-dc[43] counterparts. Concerning 2-octene, no clear differences among the Ru=O···H distances arise between the *cis* and *trans* substrate (four interactions of an average 2.5 Å distance, Figure S14, Supporting Information), although since in this case no clear mechanism has been envisaged by DFT calculations (attempts to detect states B and TS(B → C) have been unsuccessful, Table 3 and Table S1, Supporting Information), the explanation of the observed reactivity differences between the *cis* and *trans* substrate may not be as straightforward as in the two previous cases.

In short, in TS(A → B) the catalyst interacts with the substrate through the second Ru=O group, provoking intermolecular H-bond interactions with the aliphatic or aromatic substituents of the alkene or both. The latter phenomenon may be crucial for dictating the stereoselectivity of the catalyst. This second Ru=O group is situated in the cavity shown in Figure 5 (bottom), and in consequence the degree of interaction with a particular substrate will depend on the synergistic effect of combining the accommodation capacity of the substrate (steric effects) within the cavity with the substrate capacity to generate H-interactions with this second Ru=O group. This synergy between both Ru=O groups may also be responsible for the observed higher epoxidation rates and selectivities of $\mathbf{3}^{3+}$ compared with the already reported Ru mononuclear epoxidation catalysts.[41,43,60]

CONCLUSIONS

The *in situ* generated bis-aqua, bis-facial Ru dinuclear complex $\mathbf{3}^{3+}$ containing the hexadentate pyrazolate-bridging ligand $bimp^-$ is a catalyst with an impressive performance toward the epoxidation of a wide range of olefins. From the scope of the analyzed substrates, the following results can be pointed out: (a) *cis*-alkenes are epoxidized faster and in higher yields than their corresponding *trans* counterparts, (b) substrates containing electron-donor groups yield better results than those bearing electron-withdrawers because of the highly electrophilic character of the Ru^{IV}=O active sites, and (c) the catalytic system is stereospecific in nature, that is, no *cis*/*trans* isomerization takes place. We have also shown that a radical pathway where the C−C rotation of the generated radical is slower than the ring closing that generates the final epoxide is the likely mechanism for this transformation, at least for the cases of *β*-methylstyrene and stilbene. Also, the dinuclear complex $\mathbf{3}^{3+}$ in the form *trans*-O=Ru^{IV}−Ru^{IV}=O behaves stereoselectively probably due to the different role of the two Ru=O groups. While the first one is responsible for oxygen transfer, the second one appears to be involved in H interactions. The latter may also be influenced by the ligand architecture of the catalyst, thus generating a discriminating pocket for the incoming substrates. The combination of these factors renders $\mathbf{3}^{3+}$ one of the few examples of powerful stereoselective epoxidation catalysts that do not need the use of substrates with specific modifications.

EXPERIMENTAL SECTION

Materials. All reagents used in the present work were obtained from Aldrich Chemical Co. and were used without further purification. Reagent-grade organic solvents were obtained from Scharlab. $RuCl_3 \cdot 3H_2O$ was supplied by Alfa Aesar and was used as received. Synthesis and characterization of Hbimp ligand are reported in the literature.[49] All synthetic manipulations were routinely performed under nitrogen atmosphere using Schlenk tubes and vacuum-line techniques.

Instrumentation and Measurements. UV−vis spectroscopy was performed with an HP8453 spectrometer using 1 cm quartz cells. NMR spectroscopy was performed on a Bruker DPX 250 MHz, DPX 360 MHz or a DPX 400 MHz spectrometer. Samples were run in $CDCl_3$, CD_3CN, or acetone-d_6 with internal references. Electrospray ionization mass spectrometry (ESI-MS) experiments were carried out on an HP298s gas chromatography (GC-MS) system from the Servei d'Anàlisi Química of the Universitat Autònoma de Barcelona (SAQ-UAB). Cyclic voltammetry (CV) and differential pulse voltammetry (DPV) experiments were performed on an Ij-Cambria HI-660 potentiostat using a three-electrode cell. A glassy carbon electrode (2 mm diameter) was used as working electrode, a platinum wire as auxiliary electrode, and a sodium saturated calomel electrode (SSCE) as a reference electrode. Working electrodes were polished with 0.05 *μ*m alumina paste and washed with distillated water and acetone

DOI: 10.1021/acs.inorgchem.5b00641
Inorg. Chem. 2015, 54, 6782−6791

before each measurement. The complexes were dissolved in acetone, DCM, or acetone/water 1:9 containing the necessary amount of *n*-Bu_4NPF_6 ($TBAPF_6$) for the purely organic solvent cases or triflic acid pH 1.0 for the latter as supporting electrolyte to yield 0.1 M ionic strength solution. CV were recorded at a 100 $mV{\cdot}s^{-1}$ scan rate, and DPV were recorded using pulse amplitudes of 0.05 V, pulse widths of 0.05 s, sampling widths of 0.02 s, pulse periods of 0.1 s, and quiet times of 2 s. $E_{1/2}$ values reported in this work were estimated from CV experiments as the average of the oxidative and reductive peak potentials ($E_{p,a}$ + $E_{p,c}$)/2. Epoxidation catalytic experiments were performed as follows. First, a mixing period of 120 min was carried out by adding in a vial 1 mL of 1,2-dichloroethane (DCE) as solvent, 1.60 g (5.0 mmol) of (diacetoxyiodo)benzene ($PhI(OAc)_2$) as oxidant, 1 mmol of dodecane as internal standard, 1.8 mg (1.25×10^{-3} mmol) of catalyst $\mathbf{2}^{2+}$, and 90 μL (5.0 mmol) of water. This mixing period before substrate addition was observed to be key in order to improve the rate of the catalytic reaction. Then, the substrate (2.5 mmol) was added to the previous mixture, thus achieving a final volume of approximately 1.47 mL and the corresponding initial concentrations: catalyst, 0.85 mM; substrate, 1.7 M; dodecane, 0.68 M; $PhI(OAc)_2$, 3.4 M; water, 3.4 M. These concentrations correspond to a catalyst/substrate/oxidant/water ratio of 1:2000:4000:4000. Aliquots were taken every 5, 10, 15, 20, 25, or 30 min until completion of reaction. Each aliquot was filtered through a Pasteur pipet filled with Celite; after that diethyl ether was added in order to elute the organic compounds, and the filtrate was analyzed in an Agilent 6890N gas chromatograph (GC) coupled to a mass selective detector with ionization by electronic impact, or in an Agilent 6890 GC with a flame ionization detector (FID) detector using a HP5 column. The characterization of the reaction products was done by comparison with commercial products or by GC-MS spectrometry. GC conditions: initial temperature 40 °C for 10 min, ramp rate variable for each substrate (typically from 10 to 20°/min), final temperature 250 °C, injection temperature 220 °C, detector temperature 250 °C. Yield of epoxide and substrate conversion was calculated with regard to the initial concentration of substrate.

$$\text{substrate conversion} = \frac{\{[\text{substrate}]_{\text{initial}} - [\text{substrate}]_{\text{final}}\}}{[\text{substrate}]_{\text{initial}}} \times 100$$

$$\text{epoxide selectivity} = \frac{[\text{epoxide}]_{\text{final}}}{\{[\text{substrate}]_{\text{initial}} - [\text{substrate}]_{\text{final}}\}} \times 100$$

Computational Details. Density functional theory (DFT) calculations have been carried out with the Gaussian 09 set of programs,[61] using the BP86 functional of Becke and Perdew.[62−64] The electronic configuration of the molecular systems was described with the standard split-valence basis set with a polarization function of Ahlrichs and co-workers for H, C, N, O, and Cl (SVP keyword in Gaussian).[65] For Ru, we used the small-core, quasi-relativistic Stuttgart/Dresden effective core potential, with an associated valence basis set contracted (standard SDD keywords in Gaussian 09).[66−68] The geometry optimizations were performed without symmetry constraints, and the characterization of the located stationary points was performed by analytical frequency calculations.

The reported energies include solvent effects estimated with the polarizable continuous solvation model, PCM,[69,70] using DCE as a solvent, calculated through single point energy calculations on the BP86 geometries using the M06L functional[71] and the 6-311+G(d,p) basis set[72,73] for main group atoms.

Overall, the relative Gibbs energies reported in this work include energies computed using the M06L/6-311+G(d,p)//BP86/SVP method together with solvent effects obtained at the M06L/6-311+G(d,p) level and zero-point energies, thermal corrections, and entropy effects calculated at 298 K with the BP86/SVP method.

Synthetic Preparations. *{[$Ru^{III}Cl_2$]$_2$(μ-bimp)(μ-Cl)} [1].* A sample of Hbimp (0.382 mmol) was dissolved in 40 mL of dry methanol; then 1.8 mL of 0.2108 M MeONa (0.382 mmol) was added. The mixture was stirred at room temperature (RT) during 10 min, and 200 mg (0.765 mmol) of $RuCl_3{\cdot}3H_2O$ was added. The resulting solution was heated at reflux overnight while vigorous magnetic stirring was maintained. After this time, the volume was reduced in the rotary evaporator, and diethyl ether was added. The resulting solid was filtered and washed with diethyl ether. Yield: 336 mg (91%). ESI-MS (MeOH): m/z = 926.1 ($[M - 2Cl + MeO^-]^+$). Elemental analysis calcd for $C_{31}H_{43}Cl_5N_{10}O_2Ru_2$: C, 38.51; H, 4.49; N, 14.50. Found: C, 38.62; H, 4.50; N, 14.39.

{[Ru^{II}(bpy)]$_2$(μ-bimp)(μ-Cl)}(PF_6)$_2$ [2(PF_6)$_2$]. A mixture of 300 mg (0.311 mmol) of complex **1**, 39 mg (0.933) of LiCl, and 172.5 μL (1.244 mmol) of NEt_3 was dissolved in 90 mL of dry methanol. The mixture was stirred during 30 min, and then 96 mg (0.622 mmol) of bpy was added. The resulting solution was stirred overnight at RT. After this time, the crude was filtered, and 3 mL of NH_4PF_6 saturated aqueous solution and 30 mL of water were added to the filtrate. The volume was reduced until a violet precipitate appeared, which was filtered and washed with cold diethyl ether. Yield: 200 mg (45%). ^{1}H NMR (400 MHz, [D_6]acetone): δ = 8.76 (d, 2H, J = 5.20 Hz, H20 or H23), 8.53 (d, 2H, J = 5.20 Hz, H20 or H23), 8.36 (d, 2H, J = 7.30 Hz, H17 or H26), 8.20 (d, 2H, J = 7.30 Hz, H17 or H26), 7.88 (t, 2H, J = 8.90 Hz, J = 7.75 Hz, H18 or H25) 7.77 (t, 2H, J = 8.90 Hz, J = 7.75 Hz, H18 or H25), 7.36 (t, 2H, H19 or H24), 7.34 (t, 2H, H19 or H24), 7.26 (s, 1H, H1), 4.25 (s, 3H, H16), 4.05 (s, 3H, H9 or H15), 3.90 (s, 3H, H9 or H15), 2.02, 1.96, 1.93, 0.16.). ^{13}C{^{1}H} NMR (100 MHz, [D_6]acetone): δ = 161.57 (C21/22), 161.07 (C21/22), 157.32 (C20/23), 156.51 (C20/23), 154.86 (C2), 145.41 (C4/10), 143.32 (C4/10), 137.37 (C7/13), 136.06 (C7/13), 135.60, (C18/25), 134.53 (C18/25), 128.47 (C5/11), 126.66 (C19/24), 125.80 (C5/11), 124.30 (C17/24), 124.07 (C19/24), 122.88 (C17/24), 106.28 (C1), 85.35 (C3), 57.03 (C16), 33.05 (C9/15), 32.83 (C9/15), 13.62, 9.13, 8.67, 8.51. ESI-MS (MeOH): m/z = 1283.2 ($[M - PF_6]^+$). Elemental analysis calcd for $C_{51}H_{59}ClF_{12}N_{14}O_2P_2Ru_2$: C, 42.85; H, 4.16; N, 13.73. Found: C, 42.83; H, 4.20; N, 13.67.

■ ASSOCIATED CONTENT

Supporting Information

Additional spectroscopic, spectrometric, electrochemical, and computational (DFT) data. The Supporting Information is available free of charge on the ACS Publications website at DOI: 10.1021/acs.inorgchem.5b00641.

■ AUTHOR INFORMATION

Corresponding Authors

*Fax: + 34 93 581 24 77 E-mail: lluis.escriche@uab.cat. Homepage: www.seloxcat.wordpress.com.

*Fax: + 34 93 581 24 77 E-mail: xavier.sala@uab.cat. Homepage: www.seloxcat.wordpress.com.

Notes

The authors declare no competing financial interest.

§J.G.-A. is a Serra Húnter Fellow.

■ ACKNOWLEDGMENTS

Support form MINECO (Grants CTQ2011-26440, CTQ-2013-49075-R and CTQ2010-21532-C02-02) and the DFG (Grant Me1313/9-1) is gratefully acknowledged. J.A. is grateful for the award of a PIF doctoral grant from UAB. A.P. thanks the Spanish MINECO for the project CTQ2014-59832-JIN and the European Commission for a Career Integration Grant (No. CIG09-GA-2011-293900).

■ REFERENCES

(1) Sheldon, R. A. *J. Mol. Catal.* **1980**, *7*, 107−126.

(2) Joergensen, K. A. *Chem. Rev.* **1989**, *89*, 431−458.

(3) Cavani, F.; Teles, J. H. *ChemSusChem* **2009**, *2*, 508−534.

(4) Crivello, J. V. *J. Polym. Sci., Part A: Polym. Chem.* **2014**, *52*, 2934−2946.

DOI: 10.1021/acs.inorgchem.5b00641
Inorg. Chem. 2015, 54, 6782−6791

(5) Roberts, S. M., Whittall, J., Eds.*Regio- and Stereo-Controlled Oxidations and Reductions*; Catalysts for Fine Chemical Synthesis; John Wiley Sons, Ltd: Chichester, England, 2007, Vol. *5*.
(6) Nijhuis, T. A.; Makkee, M.; Moulijn, J. A.; Weckhuysen, B. M. *Ind. Eng. Chem. Res.* **2006**, *45*, 3447−3459.
(7) Woodard, S. S.; Finn, M. G.; Sharpless, K. B. *J. Am. Chem. Soc.* **1991**, *113*, 106−113.
(8) Finn, M. G.; Sharpless, K. B. *J. Am. Chem. Soc.* **1991**, *113*, 113−126.
(9) Jacobsen, H.; Cavallo, L. *Chem.—Eur. J.* **2001**, *7*, 800−807.
(10) Cavallo, L.; Jacobsen, H. *Angew. Chem., Int. Ed.* **2000**, *39*, 589−592.
(11) Bäckvall, J.-E.; Chowdhury, R. L.; Karlsson, U. *J. Chem. Soc., Chem. Commun.* **1991**, 473−475.
(12) Wang, G.-Z.; Andreasson, U.; Bäckvall, J.-E. *J. Chem. Soc., Chem. Commun.* **1994**, 1037−1038.
(13) Murahashi, S. I.; Naota, T. *Adv. Met.-Org. Chem.* **1994**, *3*, 225−253.
(14) Murahashi, S.-I.; Naota, T. *Zh. Org. Khim.* **1996**, *32*, 223−232.
(15) Friedrich, H. B. *Platinum Met. Rev.* **1999**, *43*, 94−102.
(16) Keene, F. R. *Coord. Chem. Rev.* **1999**, *187*, 121−149.
(17) Csjernyik, G.; Éll, A. H.; Fadini, L.; Pugin, B.; Bäckvall, J.-E. *J. Org. Chem.* **2002**, *67*, 1657−1662.
(18) Murahashi, S.-I., Ed.; *Ruthenium in Organic Synthesis*; Wiley-VCH: Weinheim, Germany, 2004.
(19) Mlodnicka, T.; James, B. R. *Catal. Met. Complexes* **1994**, *17*, 121−148.
(20) Huynh, M. H. V.; Witham, L. M.; Lasker, J. M.; Wetzler, M.; Mort, B.; Jameson, D. L.; White, P. S.; Takeuchi, K. J. *J. Am. Chem. Soc.* **2003**, *125*, 308−309.
(21) Hamelin, O.; Ménage, S.; Charnay, F.; Chavarot, M.; Pierre, J.-L.; Pécaut, J.; Fontecave, M. *Inorg. Chem.* **2008**, *47*, 6413−6420.
(22) Benet-Buchholz, J.; Comba, P.; Llobet, A.; Roeser, S.; Vadivelu, P.; Wiesner, S. *Dalton Trans.* **2010**, *39*, 3315−3320.
(23) Gersten, S. W.; Samuels, G. J.; Meyer, T. J. *J. Am. Chem. Soc.* **1982**, *104*, 4029−4030.
(24) Gilbert, J. A.; Eggleston, D. S.; Murphy, W. R., Jr.; Geselowitz, D. A.; Gersten, S. W.; Hodgson, D. J.; Meyer, T. J. *J. Am. Chem. Soc.* **1985**, *107*, 3855−3864.
(25) Sens, C.; Romero, I.; Rodríguez, M.; Llobet, A.; Parella, T.; Benet-Buchholz, J. *J. Am. Chem. Soc.* **2004**, *126*, 7798−7799.
(26) Zong, R.; Thummel, R. P. *J. Am. Chem. Soc.* **2005**, *127*, 12802.
(27) Tseng, H.-W.; Zong, R.; Muckerman, J. T.; Thummel, R. *Inorg. Chem.* **2008**, *47*, 11763−11773.
(28) Concepcion, J. J.; Jurss, J. W.; Templeton, J. L.; Meyer, T. J. *J. Am. Chem. Soc.* **2008**, *130*, 16462−16463.
(29) Sala, X.; Romero, I.; Rodriguez, M.; Escriche, L.; Llobet, A. *Angew. Chem., Int. Ed.* **2009**, *48*, 2842−2852.
(30) Xu, Y.; Åkermark, T.; Gyollai, V.; Zou, D.; Eriksson, L.; Duan, L.; Zhang, R.; Åkermark, B.; Sun, L. *Inorg. Chem.* **2009**, *48*, 2717−2719.
(31) Xu, Y.; Fischer, A.; Duan, L.; Tong, L.; Gabrielsson, E.; Åkermark, B.; Sun, L. *Angew. Chem., Int. Ed.* **2010**, *49*, 8934−8937.
(32) Duan, L.; Bozoglian, F.; Mandal, S.; Stewart, B.; Privalov, T.; Llobet, A.; Sun, L. *Nat. Chem.* **2012**, *4*, 418−423.
(33) Groves, J. T.; Quinn, R. *J. Am. Chem. Soc.* **1985**, *107*, 5790−5792.
(34) Bailey, C. L.; Drago, R. S. *J. Chem. Soc., Chem. Commun.* **1987**, 179−180.
(35) Stultz, L. K.; Binstead, R. A.; Reynolds, M. S.; Meyer, T. J. *J. Am. Chem. Soc.* **1995**, *117*, 2520−2532.
(36) Barf, G. A.; Sheldon, R. A. *J. Mol. Catal. A* **1995**, *102*, 23−39.
(37) Porter, M. J.; Skidmore, J. *J. Chem. Soc., Chem. Commun.* **2000**, 1215−1225.
(38) Arends, I. W. C. E.; Kodama, T.; Sheldon, R. A. *Top. Organomet. Chem.* **2004**, *11*, 277−320.
(39) Bhor, S.; Tse, M. K.; Klawonn, M.; Doebler, C.; Maegerlein, W.; Beller, M. *Adv. Synth. Catal.* **2004**, *346*, 263−267.
(40) Bäckvall, J.-E., Ed., *Modern Oxidation Methods*, 2nd ed.; Wiley-VCH Verlag GmbH & Co. KGaA: Wenheim, Germany, 2010.
(41) Serrano, I.; López, M. I.; Ferrer, I.; Poater, A.; Parella, T.; Fontrodona, X.; Solá, M.; Llobet, A.; Rodríguez, M.; Romero, I. *Inorg. Chem.* **2011**, *50*, 6044−6054.
(42) Di Giovanni, C.; Vaquer, L.; Sala, X.; Benet-Buchholz, J.; Llobet, A. *Inorg. Chem.* **2013**, *52*, 4335−4345.
(43) Di Giovanni, C.; Poater, A.; Benet-Buchholz, J.; Cavallo, L.; Solà, M.; Llobet, A. *Chem.—Eur. J.* **2014**, *20*, 3898−3902.
(44) García-Antón, J.; Bofill, R.; Escriche, L.; Llobet, A.; Sala, X. *Eur. J. Inorg. Chem.* **2012**, *30*, 4775−4789.
(45) Mola, J.; Dinoi, C.; Sala, X.; Rodriguez, M.; Romero, I.; Parella, T.; Fontrodona, X.; Llobet, A. *Dalton Trans.* **2011**, *40*, 3640−3646.
(46) Maji, S.; Vigara, L.; Cottone, F.; Bozoglian, F.; Benet-Buchholz, J.; Llobet, A. *Angew. Chem., Int. Ed.* **2012**, *124*, 6069−6072.
(47) Neudeck, S.; Maji, S.; López, I.; Meyer, S.; Meyer, F.; Llobet, A. *J. Am. Chem. Soc.* **2014**, *136*, 24−27.
(48) Sander, A. C.; Maji, S.; Francàs, L.; Böhnisch, T.; Dechert, S.; Llobet, A.; Meyer, F. *ChemSusChem* **2015**, *8*, 1697−1702, DOI: 10.1002/cssc.201403344.
(49) Müller, H.; Bauer-Siebenlist, B.; Csapo, E.; Dechert, S.; Farkas, E.; Meyer, F. *Inorg. Chem.* **2008**, *47*, 5278−5292.
(50) Takeuchi, K. J.; Thompson, M. S.; Pipes, D. W.; Meyer, T. J. *Inorg. Chem.* **1984**, *23*, 1845−1851.
(51) Rodríguez, M.; Romero, I.; Llobet, A. *Inorg. Chem.* **2001**, *40*, 4150−4156.
(52) In, J.-H.; Park, S.-E.; Song, R.; Nam, W. *Inorg. Chim. Acta* **2003**, *343*, 373−376.
(53) Sala, X.; Santana, N.; Serrano, I.; Plantalech, E.; Romero, I.; Rodríguez, M.; Llobet, A.; Jansat, S.; Gómez, M.; Fontrodona, X. *Eur. J. Inorg. Chem.* **2007**, 5207−5214.
(54) Serrano, I.; Sala, X.; Plantalech, E.; Rodríguez, M.; Romero, I.; Jansat, S.; Gómez, M.; Parella, T.; Stoeckli-Evans, H.; Solans, X.; Font-Bardia, M.; Vidjayacoumar, B.; Llobet, A. *Inorg. Chem.* **2007**, *46*, 5381−5389.
(55) Srinivasan, K.; Michaud, P.; Kochi, J. K. *J. Am. Chem. Soc.* **1986**, *108*, 2309−2320.
(56) Zona, T. A.; Goodman, J. L. *J. Am. Chem. Soc.* **1995**, *117*, 5879−5880.
(57) Baciocchi, E.; Boschi, T.; Cassioli, L.; Galli, C.; Jaquinod, L.; Lapi, A.; Paolesse, R.; Smith, K. M.; Tagliatesta, P. *Eur. J. Org. Chem.* **1999**, 3281−3286.
(58) Muray, E.; Illa, O.; Castillo, J. A.; Alvarez-Larena, A.; Bourdelande, J. L.; Branchadell, V.; Ortuno, R. M. *J. Org. Chem.* **2003**, *68*, 4906−4911.
(59) Kumar, D.; de Visser, S. P.; Shaik, S. *Chem.—Eur. J.* **2005**, *11*, 2825−2835.
(60) Poater, A.; Falivene, L.; Cavallo, L.; Llobet, A.; Rodríguez, M.; Romero, I.; Solá, M. *Chem. Phys. Lett.* **2013**, *577*, 142−146.
(61) Frisch, M. J.; Trucks, G. W.; Schlegel, H. B.; Scuseria, G. E.; Robb, M. A.; Cheeseman, J. R.; Scalmani, G.; Barone, V.; Mennucci, B.; Petersson, G. A.; Nakatsuji, H.; Caricato, M.; Li, X.; Hratchian, H. P.; Izmaylov, A. F.; Bloino, J.; Zheng, G.; Sonnenberg, J. L.; Hada, M.; Ehara, M.; Toyota, K.; Fukuda, R.; Hasegawa, J.; Ishida, M.; Nakajima, T.; Honda, Y.; Kitao, O.; Nakai, H.; Vreven, T.; Montgomery, J. A., Jr.; Peralta, J. E.; Ogliaro, F.; Bearpark, M.; Heyd, J. J.; Brothers, E.; Kudin, K. N.; Staroverov, V. N.; Kobayashi, R.; Normand, J.; Raghavachari, K.; Rendell, A.; Burant, J. C.; Iyengar, S. S.; Tomasi, J.; Cossi, M.; Rega, N.; Millam, J. M.; Klene, M.; Knox, J. E.; Cross, J. B.; Bakken, V.; Adamo, C.; Jaramillo, J.; Gomperts, R.; Stratmann, R. E.; Yazyev, O.; Austin, A. J.; Cammi, R.; Pomelli, C.; Ochterski, J. W.; Martin, R. L.; Morokuma, K.; Zakrzewski, V. G.; Voth, G. A.; Salvador, P.; Dannenberg, J. J.; Dapprich, S.; Daniels, A. D.; Farkas, O.; Foresman, J. B.; Ortiz, J. V.; Cioslowski, J.; Fox, D. J. *Gaussian 09*, revision A.1; Gaussian, Inc.: Wallingford, CT, 2009.
(62) Becke, A. *Phys. Rev. A* **1988**, *38*, 3098−3100.
(63) Perdew, J. P. *Phys. Rev. B* **1986**, *33*, 8822−8824.
(64) Perdew, J. P. *Phys. Rev. B* **1986**, *34*, 7406−7406.

DOI: 10.1021/acs.inorgchem.5b00641
Inorg. Chem. 2015, 54, 6782−6791

(65) Schaefer, A.; Horn, H.; Ahlrichs, R. *J. Chem. Phys.* **1992**, *97*, 2571−2577.
(66) Haeusermann, U.; Dolg, M.; Stoll, H.; Preuss, H. *Mol. Phys.* **1993**, *78*, 1211−1224.
(67) Kuechle, W.; Dolg, M.; Stoll, H.; Preuss, H. *J. Chem. Phys.* **1994**, *100*, 7535−7542.
(68) Leininger, T.; Nicklass, A.; Stoll, H.; Dolg, M.; Schwerdtfeger, P. *J. Chem. Phys.* **1996**, *105*, 1052−1059.
(69) Barone, V.; Cossi, M. *J. Phys. Chem. A* **1998**, *102*, 1995−2001.
(70) Tomasi, J.; Persico, M. *Chem. Rev.* **1994**, *94*, 2027−2094.
(71) Zhao, Y.; Truhlar, D. G. *J. Chem. Phys.* **2006**, *125*, 194101.
(72) Hehre, W. J.; Ditchfield, R.; Pople, J. A. *J. Chem. Phys.* **1972**, *56*, 2257−2261.
(73) Hariharan, P. C.; Pople, J. A. *Theor. Chim. Acta* **1973**, *28*, 213−222.

DOI: 10.1021/acs.inorgchem.5b00641
Inorg. Chem. 2015, 54, 6782−6791

Mononuclear ruthenium compounds bearing N-donor and N-heterocyclic carbene ligands: structure and oxidative catalysis

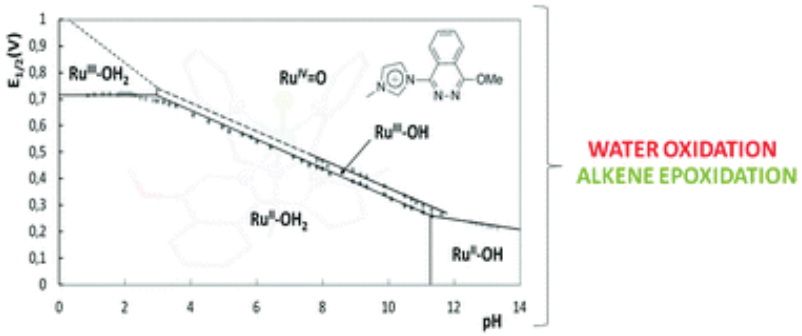

Liu, H.; **Gil-Sepulcre, M.**; Francàs, L.; Nolis, P.; Parella, T.; Benet-Buchholz, J.; Fontrodona, X.; García-Antón, J.; Romero, N.; Llobet, A.; Escriche, L.; Bofill, R.; Sala, X. *Dalton Trans.* **2017**, *46*, 2829-2843.

Contribution

Marcos Gil-Sepulcre resynthetized the complexes and performed their electrochemical characterization as well as the catalytic water oxidation experiments.

Dalton Transactions

PAPER

View Article Online
View Journal | View Issue

Cite this: *Dalton Trans.*, 2017, **46**, 2829

Mononuclear ruthenium compounds bearing N-donor and N-heterocyclic carbene ligands: structure and oxidative catalysis†

Hai-Jie Liu,[a] Marcos Gil-Sepulcre,[a] Laia Francàs,[b] Pau Nolis,[c] Teodor Parella,[c] Jordi Benet-Buchholz,[b] Xavier Fontrodona,[d] Jordi García-Antón,[a] Nuria Romero,[a] Antoni Llobet,[a,b] Lluís Escriche,*[a] Roger Bofill*[a] and Xavier Sala*[a]

Received 14th December 2016,
Accepted 25th January 2017

DOI: 10.1039/c6dt04729g

rsc.li/dalton

A new CNNC carbene-phthalazine tetradentate ligand has been synthesised, which in the reaction with [Ru(T)Cl_3] (T = trpy, tpm, bpea; trpy = 2,2′;6′,2″-terpyridine; tpm = tris(pyrazol-1-yl)methane; bpea = *N*,*N*-bis(pyridin-2-ylmethyl)ethanamine) in MeOH or iPrOH undergoes a C–N bond scission due to the nucleophilic attack of a solvent molecule, with the subsequent formation of the mononuclear complexes *cis*-[Ru(PhthaPz-OR)(trpy)X]$^{n+}$, [Ru(PhthaPz-OMe)(tpm)X]$^{n+}$ and *trans*,*fac*-[Ru(PhthaPz-OMe)(bpea)X]$^{n+}$ (X = Cl, *n* = 1; X = H_2O, *n* = 2; PhthaPz-OR = 1-(4-alkoxyphthalazin-1-yl)-3-methyl-1*H*-imidazol-3-ium), named **1a**$^{+}$/**2a**$^{2+}$ (R = Me), **1b**$^{+}$/**2b**$^{2+}$ (R = iPr), **3**$^{+}$/**4**$^{2+}$ and **5**$^{+}$/**6**$^{2+}$, respectively. Interestingly, regulation of the stability regions of different Ru oxidation states is obtained by different ligand combinations, going from **6**$^{2+}$, where Ru(III) is clearly stable and mono-electronic transfers are favoured, to **2a**$^{2+}$/**2b**$^{2+}$, where Ru(III) is almost unstable with regard to its disproportionation. The catalytic performance of the Ru–OH_2 complexes in chemical water oxidation at pH 1.0 points to poor stability (ligand oxidation), with subsequent evolution of CO_2 together with O_2, especially for **4**$^{2+}$ and **6**$^{2+}$. In electrochemically driven water oxidation, the highest TOF values are obtained for **2a**$^{2+}$ at pH 1.0. In alkene epoxidation, complexes favouring bi-electronic transfer processes show better performances and selectivities than those favouring mono-electronic transfers, while alkenes containing electron-donor groups show better performances than those bearing electron-withdrawing groups. Finally, when *cis*-β-methylstyrene is employed as the substrate, no *cis*/*trans* isomerization takes place, thus indicating the existence of a stereospecific process.

Introduction

N-Heterocyclic carbenes (NHCs) are neutral compounds featuring a divalent C atom that possesses six electrons in its valence shell and is inserted into an N-heterocycle. NHCs are excellent ligands for transition metal ions (M), forming rather strong M–C bonds and often stable complexes under ambient conditions.[1] Transition metal complexes containing NHCs have found multiple applications in important catalytic transformations, such as hydrogenation, transfer hydrogenation, water reduction and water oxidation.[2]

When designing catalysts for redox processes, controlling the oxidative power, the accessibility and stability of the oxidation states involved in the catalytic cycle is of paramount importance for the selectivity of the catalysed reaction. In general, in the presence of electron-donating ligands (such as carbenes) high oxidation states of the central metal ion will be stabilised, and hence its redox potentials decrease,[3] thus facilitating oxidative catalytic processes. Additionally, when a water molecule is directly coordinated to the metal centre, the redox properties of the complex will be affected by proton exchange. The successive 1e^{-} oxidations taking place are accompanied by a sequential loss of protons favoured by the enhanced acidity

[a]*Departament de Química, Facultat de Ciències, Universitat Autònoma de Barcelona, 08193 Cerdanyola del Vallès, Barcelona, Catalonia, Spain.*
E-mail: roger.bofill@uab.cat, lluis.escriche@uab.cat, xavier.sala@uab.cat; Fax: +34 93 581 24 77
[b]*Institute of Chemical Research of Catalonia (ICIQ), Av. Països Catalans 16, 43007 Tarragona, Catalonia, Spain*
[c]*Servei de Ressonància Magnètica Nuclear, Facultat de Ciències, Universitat Autònoma de Barcelona, 08193 Cerdanyola del Vallès, Barcelona, Catalonia, Spain*
[d]*Serveis Tècnics de Recerca, Edifici P-II, Campus Montilivi, Universitat de Girona, 17071 Girona, Catalonia, Spain*

†Electronic supplementary information (ESI) available: Spectroscopic (NMR, UV-Vis), spectrometric (ESI-MS), electrochemical (CV, DPV, bulk electrolysis, Pourbaix diagrams), catalytic (manometries) and structural (X-ray diffraction) data. CCDC 1522633 and 1522634. For ESI and crystallographic data in CIF or other electronic format see DOI: 10.1039/c6dt04729g

of the bonded aqua ligand. This phenomenon, known as proton coupled electron transfer (PCET), allows transition metals to achieve high oxidation states quite easily, since the successive loss of protons – going from the aqua to the hydroxo and finally oxo ligand – allows the maintenance of the total charge of the complex.[4] In addition, the σ and π donation of the oxo ligand present at high oxidation states further stabilises high oxidation states at the metal centre. Thus, promising examples of water oxidation catalysis have been reported within the last 6 years with Ir[5] and Ru[6] NHC complexes, most of which are monometallic, although a few are multimetallic. Interestingly, during the past few years researchers have emphasised the distinctive and sometimes superior performance of bimetallic catalysts because of the possible cooperative interactions existing between both M–OH_2 active sites thanks to their relative disposition imposed by the bridging ligand.[7]

Furthermore, Ru NHC complexes have also found relevant applications in alkene epoxidation catalysis.[8] A remarkable example is the use of Ru–aqua complexes with an increasing number of NHC units that stabilise the Ru(IV)/Ru(III) redox potential to a much higher extent than the Ru(III)/Ru(II) one, thus favouring the disproportionation of the Ru(III) oxidation state. As a consequence, the Ru(IV)=O species becomes a powerful two-electron oxidant. This is interesting because it avoids radical reaction pathways associated with 1 electron oxidation processes,[9] and becomes particularly attractive for the olefin epoxidation reactions, since it will favour a concerted pathway that will generate a stereoselective product.[8]

Within this context, and given the feasible preparation of thermodynamically stable NHCs and the interest in using them as ligands in oxidative catalytic systems, we have synthesised and characterised a new tetradentate imidazolium precursor ligand (1,4-bis(1-methylimidazolium-1-yl)phthalazine; H_2**L1**$^{2+}$) and evaluated its effect on the electrochemical properties and oxidative catalytic activity of the corresponding Ru complexes obtained in combination with an additional auxiliary tri-*N*-dentate ligand such as the meridional ligand trpy, the facial ligand tpm and either the meridional or facial ligand bpea (trpy = 2,2′:6′,2″-terpyridine, tpm = tris(pyrazol-1-yl)methane, bpea = *N*,*N*-bis(pyridin-2-ylmethyl)ethanamine) (Chart 1). However, this new ligand H_2**L1**$^{2+}$ loses a carbene moiety upon reacting with Ru(III) precursors under reflux in MeOH or iPrOH, generating two new imidazolium precursor ligands 1-(4-alkoxyphthalazin-1-yl)-3-methyl-1*H*-imidazol-3-ium (PhthaPz-OR; R = Me, iPr), named, respectively, Me-H**L2**$^+$ and iPr-H**L2**$^+$ (see Chart 1). As a consequence, we have obtained the mononuclear complexes *cis*-[Ru(Me-**L2**)(trpy)X]$^{n+}$, *cis*-[Ru(iPr-**L2**)(trpy)X]$^{n+}$, [Ru(Me-**L2**)(tpm)X]$^{n+}$ and *trans*,*fac*-[Ru(Me-**L2**)(bpea)X]$^{n+}$ (X = Cl, n = 1; X = H_2O, n = 2), named, respectively, **1a**$^+$/**2a**$^{2+}$, **1b**$^+$/**2b**$^{2+}$, **3**$^+$/**4**$^{2+}$ and **5**$^+$/**6**$^{2+}$, which show interesting redox properties when employed in water oxidation and alkene epoxidation catalysis.

Results and discussion

Synthesis of the ligand H_2**L1**$^{2+}$

H_2**L1**$(Cl)_2$ and H_2**L1**$(PF_6)_2$ were obtained following a one-step nucleophilic attack of 1-methylimidazole to 1,4-dichlorophthalazine (dcp) in DMF (Scheme 1). The insolubility of H_2**L1**$(Cl)_2$ in DMF allowed the easy isolation of the ligand by simple filtration and subsequent washing with diethyl ether (yield 70%). Subsequent treatment of H_2**L1**$(Cl)_2$ with a NH_4PF_6 saturated solution in MeOH allowed the exchange of the chloride by the PF_6^- counterion (H_2**L1**$(PF_6)_2$).

Characterization of the ligand H_2**L1**$^{2+}$

NMR spectroscopy for **L1**$^{2+}$ has been carried out both in acetone-d_6 (H_2**L1**$(PF_6)_2$) and methanol-d_4 (H_2**L1**$(Cl)_2$). Both 1D (^{1}H, ^{13}C{^{1}H}) and 2D (HSQC and HMBC) experiments were necessary to characterise the structure of the ligand in solution (Fig. 1 and S1 in the ESI†). All resonances could be unambiguously assigned based on their integrals, multiplicity and the C_{2v} symmetry of the ligand in solution. For H_2**L1**$(PF_6)_2$, both H9 and H10 (or H9′ and H10′) display a doublet of doublets with a mirror effect, which is in agreement with the typical AA′BB′ (9 9′10 10′ in our case) pattern of this kind of systems,[10] as shown in the inset of Fig. 1. The singlet appearing at very low fields in acetone-d_6 (Fig. 1a) can be assigned to the imidazolic protons 6 and 6′ in accordance with the high electron-

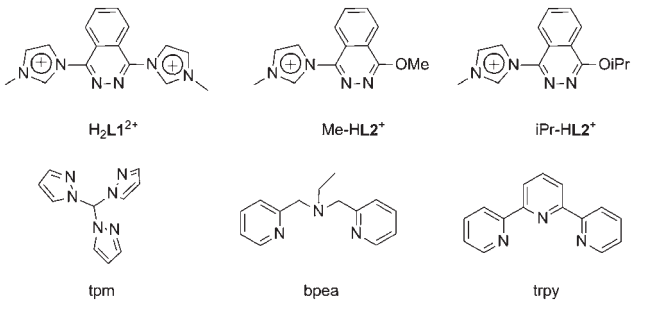

Chart 1 Drawing of the imidazolium precursor ligands (H_2**L1**$^{2+}$, Me-H**L2**$^+$, iPr-H**L2**$^+$) and the auxiliary tri-*N*-dentate ligands (tpm, bpea and trpy) used in this work.

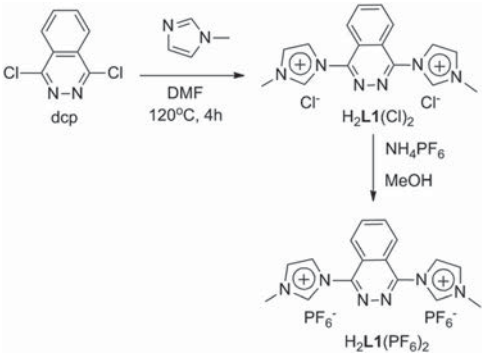

Scheme 1 Synthetic procedure for the synthesis of H_2**L1**$(Cl)_2$ and H_2**L1**$(PF_6)_2$.

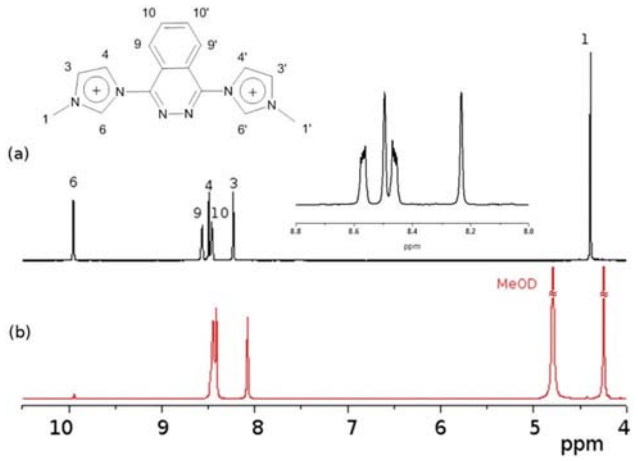

Fig. 1 600 MHz ^{1}H NMR spectrum of H_2**L1**$(PF_6)_2$ in acetone-d_6 (a) and of H_2**L1**$(Cl)_2$ in MeOD (b). Inset: Zoomed image of the aromatic region of H_2**L1**$(PF_6)_2$. Note the sharp decrease in the intensity of the acidic protons H6 when recorded in MeOD due to fast exchange with the solvent.

withdrawing effect of the two heteroatoms present in the α position, as previously reported for similar ligands.[11] However, the integral of this resonance at 9.9 ppm sharply decreases (up to only 5% of the expected value) when the ^{1}H NMR spectrum of H_2**L1**$(Cl)_2$ is recorded in methanol-d_4 (Fig. 1b), showing the fast exchange rate of these acidic protons with a protic solvent.

Suitable crystals for X-ray diffraction analysis were obtained by slow diffusion of diethyl ether into a solution of H_2**L1**$(PF_6)_2$ in acetone (Fig. 2). It is worth mentioning that the steric congestion of both five membered rings with the central phthalazine moiety (especially protons H6′–H9′ and H4–H9, at 2.40–2.45 Å) place the three scaffolds in different planes, with the left-side imidazole ring 42.5° below the phthalazine plane and the right-side imidazole ring 44.3° above (Fig. 2). The ORTEP plot for the cationic moiety of H_2**L1**$^{2+}$ and the acquisition and crystallographic data for H_2**L1**$(PF_6)_2$ can be found in Fig. S2 and Table S1 in the ESI,† respectively.

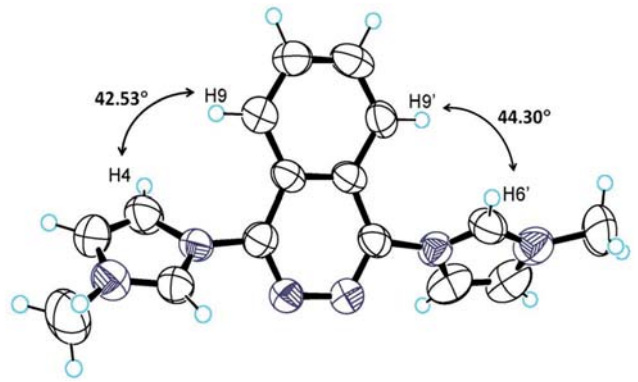

Fig. 2 ORTEP plot of the crystal structure of H_2**L1**$^{2+}$. The hydrogen atoms at closer distances have been labelled, and the angles between the plane of two imidazoles and the phthalazine scaffold are included. Color code: nitrogen, violet; carbon, black; hydrogen, blue.

Reaction of H_2**L1**$^{2+}$ with [Ru(T)Cl_3] (T = trpy, tpm, bpea). Breakage of ligand H_2**L1**$^{2+}$ and synthesis of complexes **1a**$^+$/**2a**$^{2+}$, **1b**$^+$/**2b**$^{2+}$, **3**$^+$/**4**$^{2+}$ and **5**$^+$/**6**$^{2+}$

Following synthetic strategies previously reported by our group[7b,10,12] 2 molar equivalents of [Ru^{III}(T)Cl_3] (T = trpy, tpm, bpea) were mixed with H_2**L1**$^{2+}$, triethylamine (Et_3N) as the reducing agent and LiCl to ensure the presence of a labile site in the generated complexes, and refluxed in MeOH for 16 h. After hot filtration, addition of a few drops of a saturated aqueous solution of NH_4PF_6 to the crude solution and partial solvent evaporation under vacuum, a brown precipitate appeared in all cases. However, despite the expected bimetallic species with the general formula [Ru^{II}_2(T)$_2$(μ-Cl)(μ-**L1**)]$^{3+}$ or [Ru^{II}_2(T)$_2$(Cl)$_2$(μ-**L1**)]$^{2+}$, when the obtained compounds were subjected to ^{1}H NMR analysis, their integrals matched those of a mononuclear Ru complex (see, for example, the ^{1}H NMR spectrum shown in Fig. S3 in the ESI† for the mononuclear compound obtained after reflux of [Ru^{III}(trpy)Cl_3] with H_2**L1**$(Cl)_2$ in MeOH, where the sum of the integrals of the aromatic protons is a multiple of 17 instead of the expected number of 30 for a dinuclear complex).

As a consequence, although H_2**L1**$^{2+}$ shows excellent stability in air and also dissolves in acetone or methanol at room temperature, it decomposes when refluxed overnight in methanol, thus pointing to the replacement of one imidazole ring of H_2**L1**$^{2+}$ by a methoxy group due to the nucleophilic attack of the solvent (Scheme S1 in the ESI† and Chart 1). Similar phenomena have already been reported by other authors when using related tetradentate CNNC or tridentate CNN ligands under similar conditions.[13] Then, isopropanol, with increased steric hindrance compared to methanol, was also tested as the solvent for the coordination of H_2**L1**$^{2+}$ to Ru. However, the same process occurred, with decomposition of the tetradentate ligand and formation of a mononuclear complex (Scheme 2). As a result, the new ligands PhthaPz-OMe (Me-H**L2**$^+$) and PhthaPz-OiPr (iPr-H**L2**$^+$) have been obtained from H_2**L1**$^{2+}$ (Chart 1 and Scheme S1†), which can only act as CN bidentate ligands towards Ru. The breakage of H_2**L1**$^{2+}$ can also be explained from an electronic point of view, since when H_2**L1**$^{2+}$ coordinates to the first electrophilic Ru ion, there is a flow of electron-density from the ligand to the metal centre and, therefore, the nucleophilic attack of a MeOH or iPrOH solvent molecule becomes still more favourable.

As a consequence, due to the breakage of H_2**L1**$^{2+}$ under the conditions used, we adjusted the [Ru^{III}(T)Cl_3] : H_2**L1**$^{2+}$ molar ratio to 1.5 : 1 in order to maximise the yield of formation of the Ru mononuclear species. Therefore, complexes **1a**$^+$ (*cis*-[Ru^{II}(Me-**L2**)(trpy)Cl]PF_6), **1b**$^+$ (*cis*-[Ru^{II}(iPr-**L2**)(trpy)Cl]PF_6), **3**$^+$ ([Ru^{II}(Me-**L2**)(tpm)Cl]PF_6) and **5**$^+$ (*trans*,*fac*-[Ru^{II}(Me-**L2**)(bpea)Cl]PF_6) were obtained in good yields. The subsequent synthesis of the corresponding aqua complexes involved the presence of $AgBF_4$ in acetone/H_2O, which promotes the decoordination of the chlorido ligand by formation of an AgCl

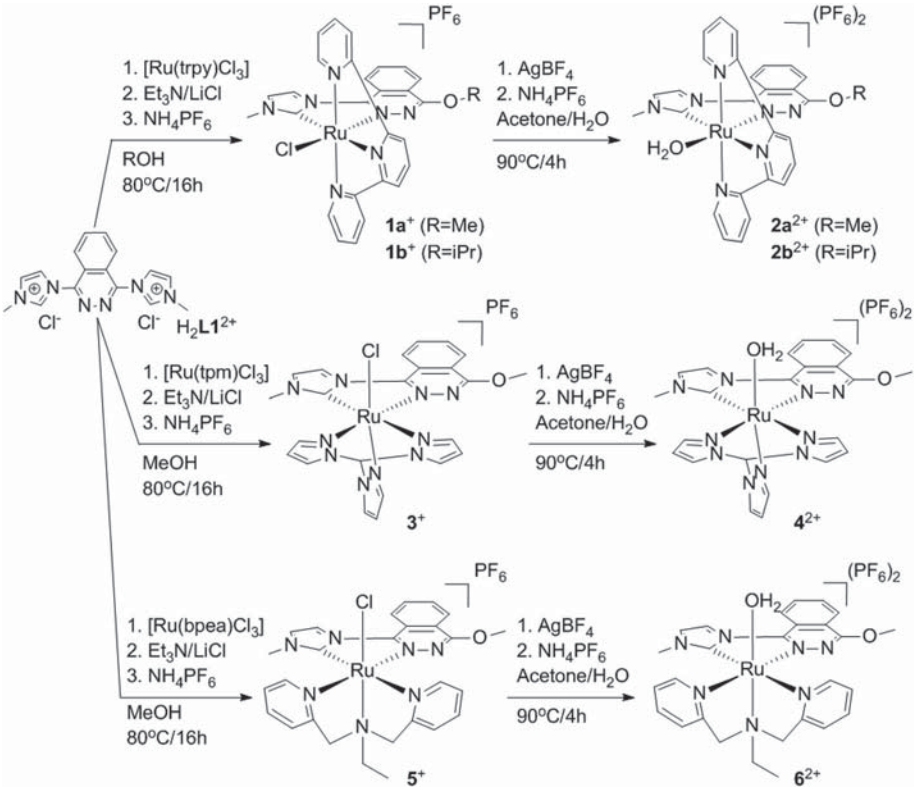

Scheme 2 Synthetic procedures used for the synthesis of $\mathbf{1a}^{+}/\mathbf{2a}^{2+}$, $\mathbf{1b}^{+}/\mathbf{2b}^{2+}$, $\mathbf{3}^{+}/\mathbf{4}^{2+}$ and $\mathbf{5}^{+}/\mathbf{6}^{2+}$. Note the breakage of $H_2\mathbf{L1}^{2+}$ when refluxed in MeOH or iPrOH.

precipitate and allows the coordination of a water molecule. After AgCl filtration, acetone was slowly evaporated under vacuum. The counter ion could be easily exchanged from BF_4^- to PF_6^- by adding excess NH_4PF_6(aq) into the aqueous solution, obtaining the whole set of Ru–aqua complexes [Ru(R-H**L2**)(T)(H_2O)][$(PF_6)_2$ (R = Me, T = trpy, $\mathbf{2a}^{2+}$; R = iPr, T = trpy, $\mathbf{2b}^{2+}$; R = Me, T = tpm, $\mathbf{4}^{2+}$; R = Me, T = bpea, $\mathbf{6}^{2+}$) as red (or brown) precipitates in yields ranging from 35 to 68% (Scheme 2).

Structural characterisation of complexes $\mathbf{1a}^{+}/\mathbf{2a}^{2+}$, $\mathbf{1b}^{+}/\mathbf{2b}^{2+}$, $\mathbf{3}^{+}/\mathbf{4}^{2+}$ and $\mathbf{5}^{+}/\mathbf{6}^{2+}$

All mononuclear complexes have been characterised by spectroscopic (1D and 2D NMR) and spectrometric (ESI-MS) techniques and by elemental analysis (EA).

In the ^{1}H NMR spectrum of $\mathbf{1a}^{+}$ (Fig. 3), the loss of the "ABBA" spin–spin coupling pattern perfectly agrees with the reduced symmetry of $H_2\mathbf{L1}^{2+}$ after nucleophilic decomposition. Furthermore, the two singlets integrating three protons each at 4.78 and 3.47 ppm can be assigned to the methyl group of the intact imidazole ring and the methyl group of the new methoxy substituent formed, respectively. Additional ^{13}C NMR and 2D-NMR spectra allowed full assignment of all resonances (see Fig. S4 in the ESI†).

As expected, a similar ^{1}H NMR spectrum to $\mathbf{1a}^{+}$ was obtained for $\mathbf{1b}^{+}$. However, now the singlet at 3.47 ppm assigned to the methoxy substituent in $\mathbf{1a}^{+}$ is replaced by a doublet and a septuplet (at 1.09 and 4.54 ppm, integrating six and one protons, respectively) due to the presence of the isopropoxy substituent (Fig. S5a in the ESI†). Furthermore, the integrity and purity of $\mathbf{1a}^{+}$ and $\mathbf{1b}^{+}$ were confirmed by EA and ESI-MS (Fig. S8a and b in the ESI†).

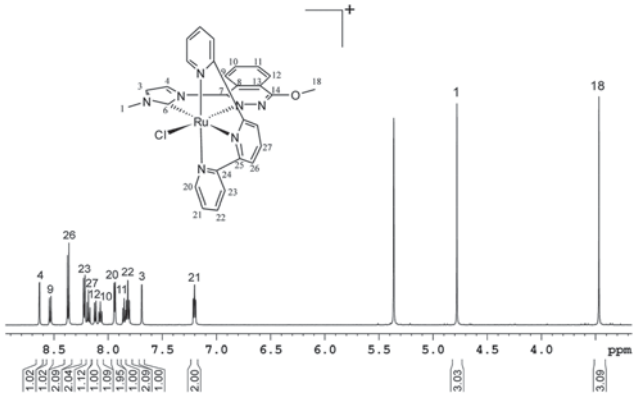

Fig. 3 600 MHz ^{1}H NMR spectrum of $\mathbf{1a}^{+}$ in CD_2Cl_2 and its corresponding proton assignment.

The chlorido compounds $\mathbf{1a}^{+}$ and $\mathbf{1b}^{+}$ display C_s symmetry in solution, with the symmetry plane passing through the PhthaPz-OMe ($\mathbf{1a}^{+}$) and PhthaPz-OiPr ($\mathbf{1b}^{+}$) ligand, the Ru centre, the chlorido ligand and carbons C(27) ($\mathbf{1a}^{+}$) or C(28) ($\mathbf{1b}^{+}$) of the trpy ligand, interconverting the two sides of the

molecule. Thus, with respect to the relative position of the chlorido ligand in relation to the Ru carbene bond, both the *cis* and *trans* isomers could be formed either for $\mathbf{1a}^+$ or $\mathbf{1b}^+$. However, only one isomer was obtained in the reaction crude for both $\mathbf{1a}^+$ and $\mathbf{1b}^+$, as determined by ^{1}H NMR (Fig. 3 and S5a†). 2D ROESY NMR spectra were then obtained to identify the *cis* or *trans* nature of the obtained compounds. As shown in Fig. 4, in the case of $\mathbf{1b}^+$ (see Fig. S5e† for the ROESY NMR spectra of the aromatic region of $\mathbf{1b}^+$) strong interactions were observed between the isopropyl group and H24, H27 and H28 of the trpy ligand as well as between the methyl group of the imidazole ring and H21 of the trpy ligand, which clearly allow the identification of the *cis* disposition of the $\mathbf{1b}^+$ complex. The same conclusion could be extracted from the ROESY NMR spectra of $\mathbf{1a}^+$ (Fig. S4e†), and therefore the only obtained isomer is also *cis* in nature. Again, additional ^{13}C NMR and 2D-NMR spectra allowed full assignment of all resonances of $\mathbf{1b}^+$ (Fig. S5 in the ESI†).

With regard to $\mathbf{3}^+$, due to the C_3 symmetry of the tpm ligand and its characteristic facial coordination mode, no isomeric mixtures are expected. This has been corroborated by its ^{1}H NMR spectrum (Fig. S6a†). The lack of symmetry of $\mathbf{3}^+$ (C_1 group) converts the whole set of protons in different resonances, and a complex spectrum is obtained. The assignment of each resonance to a single proton and carbon was carried out by 2D NMR experiments (HSQC, HMBC, ROESY and TOCSY), while the integrity and purity of $\mathbf{3}^+$ were confirmed by EA and ESI-MS (see Fig. S6 and S8c, respectively, in the ESI†).

Concerning $\mathbf{5}^+$, due to the flexibility of the tridentate bpea ligand, able to potentially coordinate the Ru metal ion either facially or meridionally,[14] seven diastereomers could be potentially formed when combining bpea with the non-symmetric bidentate CN ligand Me-**L2** (Fig. 5).[15] The notation *fac* and *mer* refers to the facial or meridional disposition of the bpea ligand, respectively, whereas *up* and *down* indicate the relative orientation of the ethyl group of bpea with regard to the chlorido ligand upon coordination. In the *fac* complexes, the *cis*/*trans* notation refers to the position of the chlorido ligand with respect to the aliphatic N atom of the bpea ligand, while in the

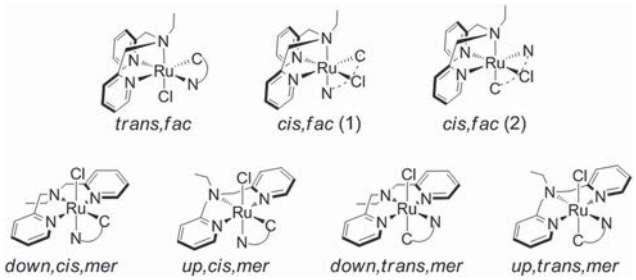

Fig. 5 Possible diastereomers for $\mathbf{5}^+$. The Me-**L2** ligand is represented as a CN connector for the sake of clarity.

mer cases the *cis*/*trans* notation refers to the position of the chlorido ligand with respect to the carbene atom of Me-**L2**. Both steric and electronic interactions between the ligands coordinated to the Ru metal ion play a key role in the formation of the synthetically obtainable isomeric mixture. However, in the synthesis of $\mathbf{5}^+$, only the *trans*,*fac* isomer is formed (see below). Hydrogen bonding interactions between the protons α to the pyridylic nitrogens of bpea and the chlorido ligand dramatically stabilise the *trans*,*fac* conformation, lowering the energy of the system. This strong stabilisation of the *trans*,*fac* isomer has already been reported and thoroughly studied by means of theoretical DFT calculations for similar Ru-based systems,[16] and the predominance of these hydrogen-bonding interactions over other factors for stabilising and selectively obtaining the *trans*,*fac* isomer in a series of related complexes has already been established by several research groups.[17] Furthermore, the preference of bpea for the facial coordination upon heating (thermodynamic conditions) has also been reported.[14]

Effectively, the *trans*,*fac* nature of the $\mathbf{5}^+$ complex was confirmed by selective NOESY NMR experiments, whose key interactions unambiguously revealed its stereoisomeric nature (Fig. S7e in the ESI†). Thus, interactions between H1 and H20–H21 and between H18 and H34 are observed, confirming its *trans*,*fac* configuration. As a consequence, analogously to what happened with $\mathbf{3}^+$, no symmetry is observed in its ^{1}H NMR spectrum (Fig. 6). Finally, the assignment of each resonance to

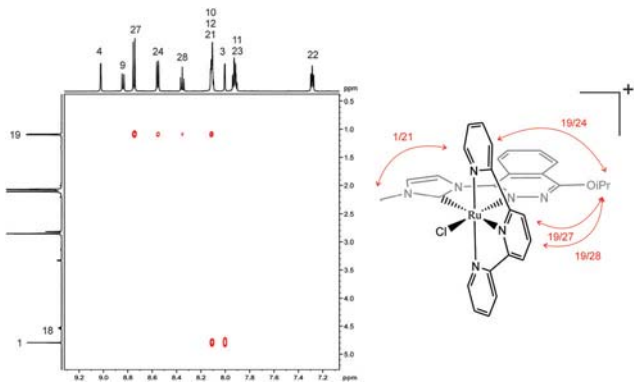

Fig. 4 Expanded area of 2D ROESY NMR spectrum of $\mathbf{1b}^+$ in acetone-d_6 and schematic drawing of the observed interactions.

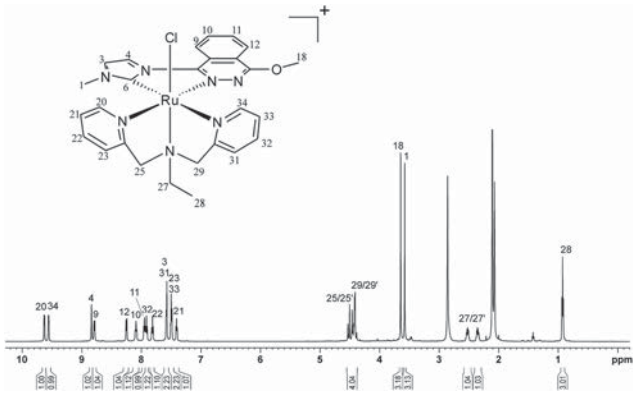

Fig. 6 600 MHz ^{1}H NMR spectrum of $\mathbf{5}^+$ in acetone-d_6 and its corresponding proton assignment.

a single proton and carbon was carried out by 2D NMR experiments (HSQC, ROESY), while the integrity and purity of $\mathbf{5}^+$ were confirmed by EA and ESI-MS (see Fig. S7 and S8d, respectively, in the ESI†).

Suitable crystals for X-ray diffraction analysis of $\mathbf{5}^+$ were obtained by slow diffusion of diethyl ether into a solution of the complex in methanol (Fig. 7), and a selection of the more relevant bond distances and angles is reported in Table S2.† An ORTEP plot for the cationic moiety of this complex as well as that corresponding to its unit cell can be found in Fig. S9 of the ESI.† Thus, $\mathbf{5}^+$ crystallises in a small unit cell containing one PF_6^- anion and one independent complex molecule. Additionally, a complete description of the acquisition and crystallographic data can be found in Table S3 of the ESI.†

The Ru(II) ion adopts a distorted octahedral geometry with bond distances and angles that resemble those of analogous complexes reported in the previous literature.[15b,18] The Ru carbene bond distance (1.962 ± 0.004 Å) is shorter than the Ru–N bonds, which range between 2.0 and 2.1 Å. The N1–Ru–Cl (171.63° ± 0.10°), N2–Ru–Cl (94.92° ± 0.12°) and N3–Ru–Cl (90.90° ± 0.11°) bond angles clearly confirm the facial coordination of bpea to Ru. In addition, the Ru–Cl bond appears *trans* to the aliphatic N atom of bpea, confirming again the *trans*,*fac* nature of $\mathbf{5}^+$. Furthermore, the imidazole and the phthalazine rings do not lie exactly on the same plane. Instead, there is a torsion angle of 10.6° ± 0.7°. However, this angle is obviously shorter with regard to the one observed for the free ligand, which is around 43° (Fig. 2). The methoxy group is nearly on the same plane of the phthalazine skeleton, since the observed torsion angle C18–O–C14–N5 is only 1.9° ± 0.6°. Finally, the N1–Ru–N3 and N1–Ru–N2 angles are, respectively, 81.15° ± 0.14° and 81.68° ± 0.15°, away from the 90° angle for an ideal octahedral geometry, due to the formation of two five-membered rings when bpea coordinates to the central Ru ion. In addition, clear hydrogen-bonding interactions are observed between the pyridyl protons of bpea on C20 and C34 and the chlorido ligand (2.68–2.71 Å). This electronic interaction is responsible for the strong stabilisation of the *trans*,*fac* configuration of $\mathbf{5}^+$, as stated before.[16,17]

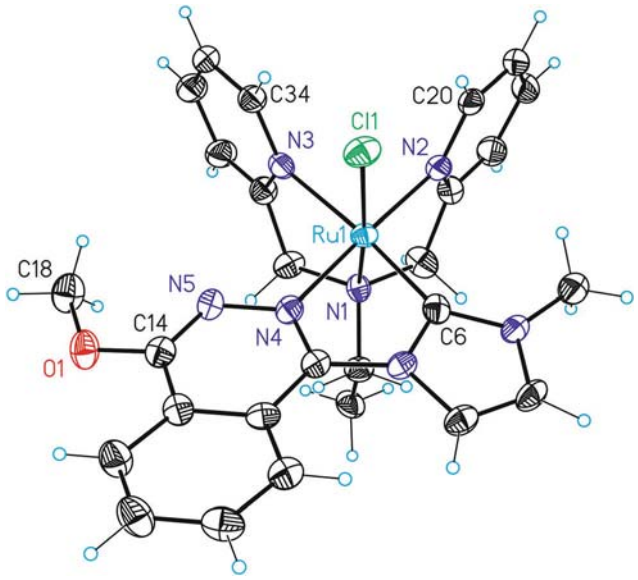

Fig. 7 ORTEP plot of the crystal structure of the cationic part of $\mathbf{5}^+$. Color code: ruthenium, blue; nitrogen, violet; oxygen, red; chlorine, green; carbon, black; hydrogen, blue. Atoms appearing in Table S2† or throughout the text have been labelled accordingly.

Replacement of the chlorido ligand by a water molecule in this family of complexes induces significant chemical shift displacements. This is exemplified by the $\mathbf{1a}^+/\mathbf{2a}^{2+}$ ^{1}H NMR comparison shown in Fig. S10,† where mainly protons close to these monodentate ligands such as H22, H26 and H27 are affected. Similar displacements of the chemical shifts were obviously observed for the very similar $\mathbf{1b}^+/\mathbf{2b}^{2+}$ couple, and both complexes maintain their *cis* conformation after the coordination of the aqua ligand (see Fig. S11 and S12,† respectively, for a full NMR assignment of all proton and carbon resonances of $\mathbf{2a}^{2+}$ and $\mathbf{2b}^{2+}$).

Complexes $\mathbf{4}^{2+}$ and $\mathbf{6}^{2+}$ also maintain their original conformation in solution after chloride displacement, as can be deduced from the NMR spectra shown in Fig. S13 and S14 in the ESI,† respectively. Furthermore, the integrity and purity of all four aqua complexes were confirmed by EA and ESI-MS (Fig. S15 in the ESI†).

Electrochemical and spectrophotometric characterisation of complexes $\mathbf{1a}^+/\mathbf{2a}^{2+}$, $\mathbf{1b}^+/\mathbf{2b}^{2+}$, $\mathbf{3}^+/\mathbf{4}^{2+}$ and $\mathbf{5}^+/\mathbf{6}^{2+}$

CV and DPV techniques have been used to determine the electrochemical properties of all complexes. The CVs of complexes $\mathbf{1a}^+$, $\mathbf{1b}^+$, $\mathbf{3}^+$ and $\mathbf{5}^+$ in dichloromethane are depicted in Fig. S16 in the ESI.† All chlorido complexes exhibit a single reversible wave corresponding to the Ru^{III}/Ru^{II} process. The redox potentials *vs.* SCE are very close for $\mathbf{1a}^+$ (0.79 V) and $\mathbf{1b}^+$ (0.78 V) given the high structural and chemical similarity of Ru in both meridional complexes, while a clear downshift of $E_{1/2}$ is observed for the facial derivatives $\mathbf{3}^+$ (0.71 V) and $\mathbf{5}^+$ (0.68 V). This is in agreement with the higher σ-donating and lower π-acceptor capacity of both the pyrazolyl rings ($\mathbf{3}^+$) and the aliphatic N ($\mathbf{5}^+$) with regard to the pyridyl units of the trpy scaffold. The observed decrease in the redox potentials lies within a 70–110 mV range and is in agreement with previous results obtained for analogous Ru carbene complexes containing trpy or bpea.[15b]

The redox behaviour of the four Ru–OH_2 complexes has been extensively investigated in aqueous media and their redox potentials and pK_a values are summarised in Table 1, together with those of related aqua complexes containing the bpy ligand instead of the carbene bidentate scaffold for the sake of comparison.

At pH 1, a single reversible wave corresponding to the Ru^{III}–OH_2/Ru^{II}–OH_2 process is observed for all aqua complexes (black lines in Fig. S17, S19, S21 and S22 in the ESI†), in which again a cathodic shift of $E_{1/2}$ (110–130 mV) takes place when introducing the facial ligands (entries 3 and 4 *vs.* entries 1 and

Table 1 Redox potentials (V) *vs.* SCE and pK_a values of complexes $\mathbf{2a}^{2+}$ to $\mathbf{6}^{2+}$ and related aqua complexes where the carbene bidentate scaffold has been replaced by bpy

Entry		$E_{1/2}^{III/II}$ pH 1[a]	$E_{1/2}^{IV/III}$ pH 7[b]	$E_{1/2}^{III/II}$	$\Delta E_{1/2}$ [c]	$E_{1/2}^{IV/II}$ [d]	$E_{1/2}^{V/IV}$	pK_{a_1}	pK_{a_2}	Ref.
1	$\mathbf{2a}^{2+}$	0.74	0.52	0.49	0.03	0.50	1.29	3.0	11.5	[e]
2	$\mathbf{2b}^{2+}$	0.73	0.51	0.48	0.03	0.49	—	2.8	11.0	[e]
3	$\mathbf{4}^{2+}$	0.62	—	0.35	—	—	1.33	1.8	11.2	[e]
4	$\mathbf{6}^{2+}$	0.61	0.52	0.32	0.20	0.42	1.28	1.2	11.7	[e]
5	$[Ru(trpy)(bpy)(OH_2)]^{2+}$	0.81	0.62	0.49	0.13	0.55	—	1.7	9.7	19
6	$[Ru(tpm)(bpy)(OH_2)]^{2+}$	0.70	0.71	0.40	0.31	0.55	—	1.9	10.8	20
7	$[Ru(bpea)(bpy)(OH_2)]^{2+}$	0.70	0.46	0.34	0.12	0.40	—	1.2	11.1	21

[a] 0.1 M triflic acid. [b] Phosphate buffer solution (μ = 0.1 M). [c] $\Delta E_{1/2} = (E_{1/2}^{IV/III} - E_{1/2}^{III/II})$. [d] Calculated as $(E_{1/2}^{IV/III} + E_{1/2}^{III/II})/2$. [e] This work.

2, Table 1), following the same trend observed for the Ru–aqua complexes bearing bpy instead of the bidentate carbene ligand (entries 5–7, Table 1).

At neutral pH, two very close redox processes separated by only 30 mV can be observed for $\mathbf{2a}^{2+}$ and $\mathbf{2b}^{2+}$, corresponding to the Ru^{IV}–O/Ru^{III}–OH and Ru^{III}–OH/Ru^{II}–OH_2 processes (red lines in Fig. S17 and S19†), thus making the stability region of the Ru(III) species very small ($\Delta E_{1/2}$ = 30 mV, Table 1). The decrease in the stability region of Ru(III) when introducing carbene ligands into Ru polypyridilic complexes has already been described,[8,15b] which can be confirmed in our case when comparing with the $\Delta E_{1/2}$ value for $[Ru(trpy)(bpy)(OH_2)]^{2+}$ (130 mV, Table 1). This tendency, however, can be reversed when replacing the trpy ligand in $\mathbf{2a}^{2+}$ and $\mathbf{2b}^{2+}$ by the facial aliphatic ligand bpea (Fig. S22†), since the higher σ-donating and lower π-acceptor capacity of bpea provoke a stabilisation of the Ru(III) state[21] (lowering the $E_{1/2}^{III/II}$ potential by 160–170 mV while keeping $E_{1/2}^{IV/III}$ unaltered, entries 1, 2 and 4, Table 1). Consequently, $\Delta E_{1/2}$ is 200 mV for $\mathbf{6}^{2+}$. Unfortunately, for the tpm derivative $\mathbf{4}^{2+}$ the Ru^{IV}–O/Ru^{III}–OH process could not be detected (Fig. S21†). The absence of the Ru(IV/III) redox couple in CV experiments is quite common for aqua complexes and is due to slow heterogeneous electron-transfer kinetics from the solution to the electrode surface.[22] Finally, the effect of the higher σ-donating character of the carbene ligand compared to bpy is evidenced when comparing the $E_{1/2}^{III/II}$ values of $\mathbf{4}^{2+}$ and $[Ru(tpm)(bpy)(OH_2)]^{2+}$ (cathodic shift of 50 mV, entries 3 and 6, Table 1). The simultaneous removal of protons and electrons (PCET processes) taking place for the four aqua-complexes can be observed in their Pourbaix diagrams (Fig. 8 and S20†), which allows the measurement of their pK_{a_1} (Ru^{III}–OH_2) and pK_{a_2} (Ru^{II}–OH_2) values. Thus, the aqua groups of $\mathbf{6}^{2+}$ (bpea) and $\mathbf{4}^{2+}$ (tpm) for the Ru(III) state are more acidic than those corresponding to their meridional (trpy) counterparts (pK_{a_1} values of 1.2 and 1.8 *vs.* 3.0–2.8, Table 1), while no significant differences are observed among the pK_{a_2} values. Finally, higher acidities are observed for their non-carbene analogues (lower pK_{a_1} and especially pK_{a_2} values, entries 5–7, Table 1), given the lower σ-donating character of bpy compared to the carbene bidentate ligand.

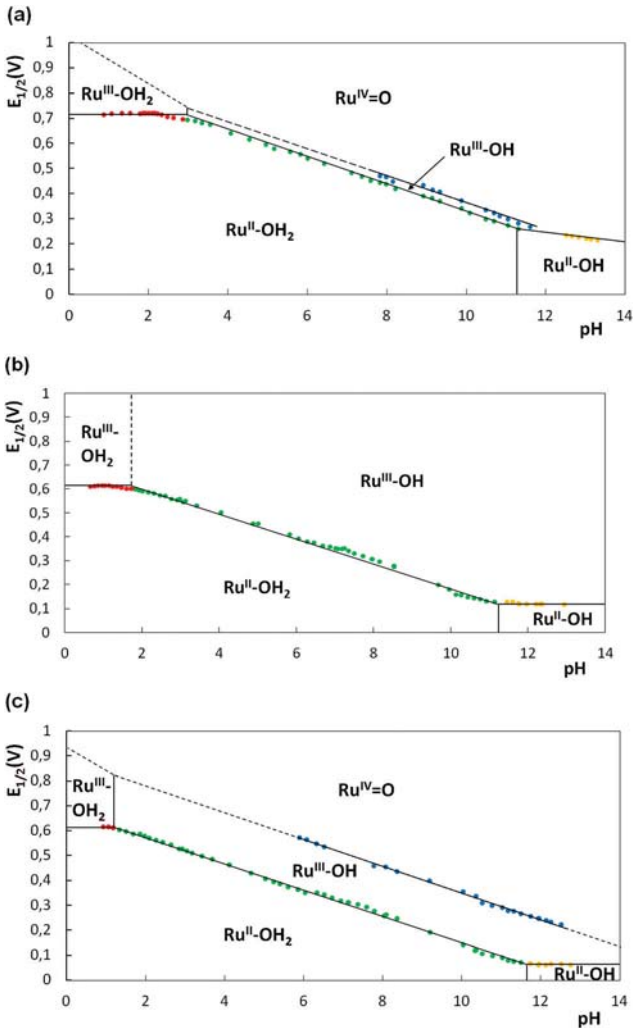

Fig. 8 Plot of $E_{1/2}$ *vs.* pH (Pourbaix diagram) for complexes $\mathbf{2a}^{2+}$ (a), $\mathbf{4}^{2+}$ (b) and $\mathbf{6}^{2+}$ (c). The pH/potential regions of stability for the various oxidation states and their dominant proton compositions are indicated by using abbreviations such as Ru^{II}–OH_2, for example, for $[Ru^{II}(Me\text{-}\mathbf{L2})(OH_2)(T)]^{2+}$ (T = trpy, tpm, bpea). The vertical lines in the various *E*/pH regions show the pK_a values.

Also, in order to confirm the correspondence of all observed redox waves to mono-electronic electrochemical processes, bulk electrolysis experiments were carried out at pH 4.9 for the aqua complexes (Fig. S18 in the ESI†). Thus, for $\mathbf{2a}^{2+}$ at 0.75 V *vs.* SCE (just after the predicted potential of the second redox wave) a value of 2.06 electrons per complex molecule was obtained (Fig. S18a†), while for $\mathbf{4}^{2+}$ at 0.6 V (after the potential of the unique redox wave was observed) a value of 0.97 electrons per molecule was obtained (Fig. S18b†). Finally, the stability of the Ru^{III}–OH species and the stepwise mono-electronic nature of both $Ru^{III/II}$ and $Ru^{IV/III}$ processes have been confirmed for $\mathbf{6}^{2+}$, since after applying a potential of 0.57 V *vs.* SCE (just after the expected potential of the first redox process), a value of 0.91 electrons per molecule was obtained (Fig. S18c†), while when the potential was set at 0.75 V, 1.87 electrons were transferred per molecule (Fig. S18d†). In summary, from an electronic point of view all aqua complexes favour mono-electronic transfers between Ru(II), Ru(III) and Ru(IV). However, for $\mathbf{2a}^{+}$ and $\mathbf{2b}^{+}$ their tendency for a bielectronic $Ru^{IV/II}$ process is very similar to the one electron transfer process $Ru^{IV/III}$, whereas in all the other cases the 1 electron transfer process is clearly favoured, as evidenced when comparing their respective $E_{1/2}^{IV/II}$ and $E_{1/2}^{IV/III}$ values (Table 1).

The UV-vis spectra of the eight complexes described in this work have been recorded in methanol and are displayed in Fig. S23 in the ESI.† Two regions can be observed in all cases: one region between 260 nm and 350 nm (or 325 nm for $\mathbf{5}^{+}/\mathbf{6}^{2+}$) with very intense bands due to intra ligand π–π* transitions, and a second one between 350 nm (or 325 nm for $\mathbf{5}^{+}/\mathbf{6}^{2+}$) and 550 nm, where typical broad unsymmetrical metal-to-ligand charge transfer (MLCT) bands appear, which could be tentatively assigned to Ru(dπ)–N ligand(π*) transitions.[19,21] Also, the electronic nature of the monodentate ligand influences to some extent the energies of the transitions involving Ru d orbitals. Thus, the MLCT bands for the Ru–aqua complexes are blue-shifted with regard to those of their Ru–Cl counterparts due to the relative stabilisation of the Ru(dπ) levels provoked by the almost non-π-donor character of the aqua ligand.

Electrochemical and chemical water oxidation by complexes $\mathbf{2a}^{2+}$, $\mathbf{2b}^{2+}$, $\mathbf{4}^{2+}$ and $\mathbf{6}^{2+}$

The capacity of the aqua complexes to oxidise water into dioxygen was initially tested electrochemically. For this purpose, the CVs of $\mathbf{2a}^{2+}$, $\mathbf{4}^{2+}$ and $\mathbf{6}^{2+}$ were recorded in aqueous solution at pH 1.0 until redox potentials were high enough to reach the oxidation states potentially able to oxidise water. Accordingly, a large electrocatalytic wave above 1.4 V *vs.* SCE corresponding to the oxidation of water to dioxygen was observed in all cases (see below).

In order to obtain kinetic information about the catalytic process, a "foot of the wave analysis" (FOWA)[23] was carried out to calculate the apparent rate constant k_{obs}. For this purpose we followed the equations adopted for water oxidation recently reported by some of us.[24] Thus, under catalytic conditions, eqn (1) is operative:

$$\frac{i}{i_p^0} = \frac{8.96\sqrt{\frac{RT}{F\nu}k_{obs}}}{1+\exp\left[\frac{F}{RT}\left(E_{PQ}^0 - E\right)\right]} \quad (1)$$

where E_{PQ}^0 is the standard potential for the catalysis-initiating redox couple (which corresponds to the pH independent $Ru^{V}O/Ru^{IV}O$ wave, observed at 1.29 V for $\mathbf{2a}^{2+}$, at 1.33 V for $\mathbf{4}^{2+}$ and at 1.28 V for $\mathbf{6}^{2+}$ according to the DPVs shown in Fig. S24 in the ESI† and shown in Table 1), i is the CV current intensity in the presence of the substrate, i_p^0 is the peak current intensity of a one-electron redox process of the catalyst (we approximate this current to the current associated with the Ru^{III}/Ru^{II} couple), F is the Faradaic constant, and ν is the scan rate and R is 8.314 J mol^{-1} K^{-1}, thus allowing the extraction of k_{obs}. As an example, Fig. 9 shows the CV of a 0.69 mM solution of $\mathbf{4}^{2+}$ at pH 1.0 (Fig. 9a) and the plot of i/i_p^0 *vs.* $1/\{1+\exp[(F/RT)(E_{PQ}^0 - E)]\}$ (Fig. 9b) as well as the dependence of k_{obs} on the catalyst concentration (Fig. 9b, inset). Identical studies have been performed for $\mathbf{2a}^{2+}$ and $\mathbf{6}^{2+}$, which can be found in Fig. S25 in the ESI.†

In all cases, the largest slope at the very beginning of the catalytic process (which translates to the foot of the wave in the original CVs) gives the value of k_{obs}, which is independent of the catalyst concentration, indicating the existence of a water nucleophilic attack (WNA) mechanism.[25] Moreover, under the used electrocatalytic scheme, k_{obs} is equivalent to the maximum turnover frequency (TOF_{max}) that a catalyst molecule can operate the water oxidation reaction when the applied potential tends to infinite.[23] At pH 1.0, the obtained k_{obs} values (expressed in s^{-1}) follow the trend $\mathbf{2a}^{2+}$ (0.570) > $\mathbf{6}^{2+}$ (0.051) > $\mathbf{4}^{2+}$ (0.015).

Finally, the relationship between the turnover frequency TOF and the overpotential (η), defined as the difference between the applied potential E and the thermodynamic potential of the catalysed reaction E_{AC}^0, in this case water

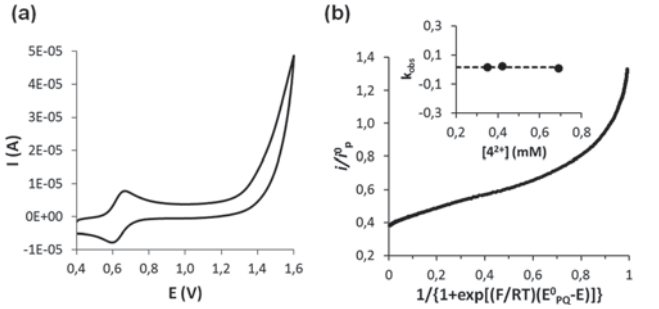

Fig. 9 Background corrected CV of a 0.68 mM solution of $\mathbf{4}^{2+}$ in 0.1 M aqueous triflic acid (pH 1.0) at 100 mV s^{-1} scan rate (a), and "foot of the wave analysis" of $\mathbf{4}^{2+}$ by plotting i/i_p^0 *vs.* $1/\{1+\exp[(F/RT)(E_{PQ}^0 - E)]\}$ (b). Inset: Plot of different k_{obs} values extracted from the "foot of the wave analysis" at each concentration (the dotted line represents the trend of the k_{obs} values).

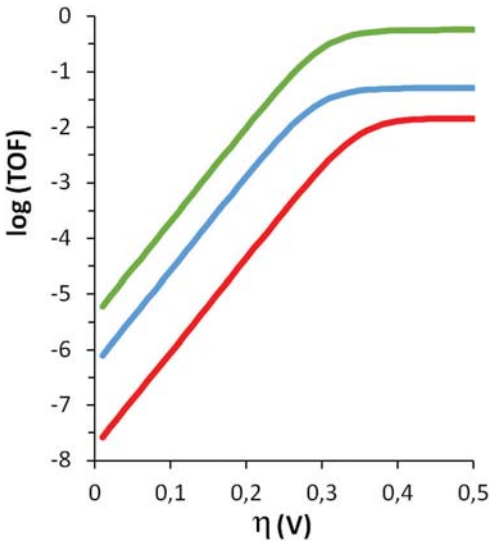

Fig. 10 Catalytic Tafel plots for $\mathbf{2a}^{2+}$ (green), $\mathbf{4}^{2+}$ (red) and $\mathbf{6}^{2+}$ (blue) at pH 1.0.

oxidation, is governed by eqn (2), whose logarithms for all three aqua compounds at pH 1.0 are plotted in Fig. 10 (catalytic Tafel plots).

$$\mathrm{TOF} = \frac{k_{\mathrm{obs}}}{1 + \exp\left[\frac{F}{RT}\left(E^0_{\mathrm{PQ}} - E^0_{\mathrm{AC}} - \eta\right)\right]} \qquad (2)$$

Fig. 10 shows how the higher value of E^0_{PQ} for $\mathbf{4}^{2+}$ (1.33 V, Table 1) translates in lower turnover frequencies when η is low (red line before reaching the plateau, when η makes the TOF reach its maximum and equals k_{obs}). Also, the higher performance of $\mathbf{2a}^{2+}$ (green line) is evident, in concordance with the higher k_{obs} values deduced by the "foot of the wave analysis". However, it should be noted that the kinetic parameters for catalytic reactions derived from electrochemical measurements depend on various details of the experimental procedures, and therefore values from different studies should be compared carefully.[26]

The four aqua complexes were also tested as chemically triggered water oxidation catalysts in the presence of Ce(IV) as the sacrificial oxidant. The total gas evolved was manometrically measured (Fig. S26 in the ESI†) and its composition in terms of the $O_2:CO_2$ ratio was analysed by means of on-line mass spectrometry (Fig. S27†). In the presence of 100 equivalents of Ce(IV) at pH 1, $\mathbf{4}^{2+}$ generated more gas (≈ 15 mBar) after 30 min of reaction than the other three complexes (Fig. S26†). In general, only considering the amount of generated gas, facial complexes are superior to their meridional counterparts. However, when the composition of the generated gases is analysed by on-line MS (Fig. S27†), $\mathbf{4}^{2+}$ has the lowest $O_2:CO_2$ ratio (1 : 5.5), followed by $\mathbf{6}^{2+}$, with a 1 : 1.4 ratio, while the $O_2:CO_2$ ratio is much higher for $\mathbf{2a}^{2+}$ and $\mathbf{2b}^{2+}$ (1 : 0.6). Therefore, despite being poor, the stability of the meridional trpy-based complexes $\mathbf{2a}^{2+}/\mathbf{2b}^{2+}$ is clearly higher than that of their facial (tpm or bpea) counterparts $\mathbf{4}^{2+}/\mathbf{6}^{2+}$, which easily get oxidised under the harsh reaction conditions of chemical water oxidation by Ce(IV) at pH 1.0. This is clearly reflected in Fig. S28,† where the profile of O_2 evolution of the four aqua complexes has been compared. Therefore, taking into account the volume of the vial (16.04 mL) and the amount of catalyst used (2.0 μmol), the turnover numbers (TN) at 298 K for $\mathbf{2b}^{2+}$ and $\mathbf{2a}^{2+}$ (2.39 and 2.17, respectively) are higher than those of $\mathbf{6}^{2+}$ (1.63) and $\mathbf{4}^{2+}$ (0.75). Moreover, this behaviour is consistent with the results obtained during the electrochemically triggered water oxidation at pH 1.0, with the highest TOF value corresponding to the trpy derivatives ($\mathbf{2a}^{2+}/\mathbf{2b}^{2+}$) and the lowest one to the tpm complex ($\mathbf{4}^{2+}$).

Catalyst–catalyst intermolecular oxidative degradation involving Ru^{IV}=O species[27] or the direct degradation of the complexes by the highly oxidant Ce(IV) species are considered as the potential origin of the evolved CO_2. In our system, the only relevant differences between the four evaluated complexes are the tridentate ligands employed. Therefore, tpm and bpea (both containing aliphatic carbon atoms prone to be easily oxidised under the harsh catalytic conditions employed) quickly decompose, generating large amounts of CO_2 that arise from ligand oxidation. Given that a great number of robust water oxidation catalysts containing the trpy ligand have been reported,[28] the observed evolution of CO_2 from $\mathbf{2a}^{2+}/\mathbf{2b}^{2+}$ clearly reflects a relative weakness of the PhthaPz-OR family of ligands under oxidative conditions.

Alkene epoxidation by complexes $\mathbf{2a}^{2+}$, $\mathbf{2b}^{2+}$, $\mathbf{4}^{2+}$ and $\mathbf{6}^{2+}$

Complexes $\mathbf{2a}^{2+}$, $\mathbf{2b}^{2+}$, $\mathbf{4}^{2+}$ and $\mathbf{6}^{2+}$ have been tested with regard to their ability to chemically oxidise alkenes. The catalytic reactions have been carried out using a catalyst : substrate : oxidant : water ratio of 1 : 1000 : 2000 : 2000 after a 120 min mixing period of the catalysts in the absence of the substrate (see the Experimental section for further details), during which the excess of water ensures the generation of the oxidant PhIO species from $PhI(OAc)_2$.[12,29] This mixing period before substrate addition is crucial in order to improve the rate of the catalytic reaction. Scheme S2† summarises the set of reactions that take place during the catalytic epoxidation of alkenes for the proposed systems. All products of each catalytic experiment have been identified by GC-MS, and all gathered results are shown in Table 2. For instance, the system: 1.7 mM of $\mathbf{2a}^{2+}$, 1.7 M of *cis*-β-methylstyrene, 3.4 M of $PhI(OAc)_2$, and 3.4 M of H_2O in 1,2-dichloroethane (DCE, entry 2) gives 1.42 M of *cis*-β-methylstyrene oxide in 525 minutes, which represents a TN value of 840 and a TOF value of 1.6 min^{-1}, and since the conversion of the initial substrate is complete the selectivity in the epoxide formation is 84%.

Similar figures are obtained for both trpy-based aqua-complexes ($\mathbf{2a}^{2+}/\mathbf{2b}^{2+}$) on the one hand and for both facial derivatives ($\mathbf{4}^{2+}/\mathbf{6}^{2+}$) on the other. Also, when comparing both sets of catalyst pairs, a clearly higher epoxidation capacity (higher conversion and selectivity) is observed for $\mathbf{2a}^{2+}/\mathbf{2b}^{2+}$ compared to $\mathbf{4}^{2+}/\mathbf{6}^{2+}$. For example, styrene $\mathbf{2a}^{2+}$ yields a 42% conversion (entry 1), while $\mathbf{4}^{2+}$ and $\mathbf{6}^{2+}$ only reach 23 and 21%

Table 2 Catalytic performance of $\mathbf{2a}^{2+}$ to $\mathbf{6}^{2+}$ in the epoxidation of *cis*- and *trans*-alkenes using PhIO as the oxidant in DCE[a]

Cat.	Entry	Alkene	Conv.[b] (%)	Selec.[c] (%)	TN/TOF[d]
$\mathbf{2a}^{2+}$	1	Styrene	42	46	194/0.8
	2	*cis*-β-Methylstyrene	>99	84[e]	840/1.6
	3	*trans*-Stilbene[f]	>99	68	680/1.3
	4	Cyclooctene	>99	93	930/1.9
$\mathbf{2b}^{2+}$	5	Styrene	29	66	191/1.1
	6	*cis*-β-Methylstyrene	>99	82[e]	816/1.3
	7	*trans*-Stilbene[f]	>99	60	596/1.1
	8	Cyclooctene	99	96	946/2.2
$\mathbf{4}^{2+}$	9	Styrene	23	26	60/0.5
	10	*cis*-β-Methylstyrene	97	56[e]	545/0.4
	11	*trans*-Stilbene[f]	90	16	148/0.3
	12	Cyclooctene	>99	76	756/0.3
$\mathbf{6}^{2+}$	13	Styrene	21	13	27/0.1
	14	*cis*-β-Methylstyrene	99	69[e]	687/0.7
	15	*trans*-Stilbene[f]	91	15	136/0.2
	16	Cyclooctene	>99	94	940/0.4

[a] Catalyst : substrate : oxidant : water ratio of 1 : 1000 : 2000 : 2000. See the Experimental section for further details. [b] Substrate conversion = {[substrate]initial − [substrate]final}/[substrate]initial × 100. [c] Epoxide selectivity = [epoxide]final/{[substrate]initial − [substrate]final} × 100. [d] TN is the turnover number with regard to the total epoxide obtained. TOF is the turnover frequency expressed in epoxide cycles per minute (TN min^{-1}). [e] *cis*-Epoxide. [f] DCE volume is 5 mL.

conversion, respectively (entries 9 and 13), and selectivity for $\mathbf{2b}^{2+}$ is 66% (entry 5) while it is only 26% and 13% for $\mathbf{4}^{2+}$ and $\mathbf{6}^{2+}$, respectively. Also, for *cis*-β-methylstyrene selectivities above 80% are obtained for $\mathbf{2a}^{2+}$ and $\mathbf{2b}^{2+}$ (entries 2 and 6), while for $\mathbf{4}^{2+}$ and $\mathbf{6}^{2+}$ they are below 60% and 70%, respectively (entries 10 and 14), and for *trans*-stilbene complete conversion and selectivities above 60% are obtained for $\mathbf{2a}^{2+}$ and $\mathbf{2b}^{2+}$ (entries 3 and 7), while for $\mathbf{4}^{2+}$ and $\mathbf{6}^{2+}$ conversion is around 90% and selectivity is close to 15% (entries 11 and 15). This behaviour can be rationalised on the basis of the electronic nature of the two pairs of complexes. Thus, while for $\mathbf{2a}^{2+}$/$\mathbf{2b}^{2+}$ bi-electronic transfers between the Ru(II) and Ru(IV) species are thermodynamically almost as favourable as the mono-electronic processes (Ru(III) stability region is minimal with regard to its disproportionation, Fig. 8a and S20†), for $\mathbf{4}^{2+}$/$\mathbf{6}^{2+}$ clearly mono-electronic processes take place (Fig. 8b and c). It is well known that catalysts favouring bi-electronic processes drive epoxidation reactions to concerted pathways and mono-electronic ones drive them to radical mechanisms, the latter usually ending up reducing the selectivity of the whole process by the generation of a wide set of by-products (Scheme S3†).[8,15b,30] Therefore, the existence of bi-electronic processes for $\mathbf{2a}^{2+}$/$\mathbf{2b}^{2+}$ could explain the higher selectivity observed with regard to their mono-electronic counterparts $\mathbf{4}^{2+}$ and $\mathbf{6}^{2+}$. Also, together with these electronic arguments, other conceivable reasons for the reduced epoxidation capacity of $\mathbf{4}^{2+}$/$\mathbf{6}^{2+}$ may arise due to the chemical nature of their facial ligands, since tpm and bpea are prone to be oxidised under oxidative conditions (they possess aliphatic C atoms), and their steric bulkiness may also hinder the interaction between the substrates and the catalyst active site. Interestingly, different results have been obtained with related Ru–N_5C complexes containing the same auxiliary trpy or bpea ligands but the smaller NHC ligand *N*-methyl-*N*′-2-pyridylimidazolium, where the bpea-containing complex yields higher selectivity in front of styrene and higher conversion efficiency and selectivity towards *trans*-stilbene than its corresponding trpy-complex.[15b] Therefore, these results demonstrate again the dramatic influence of the electronic and steric properties of the carbene ligand on the catalytic performance of the Ru complexes.

Table 2 also shows that the studied aqua complexes perform much better with substrates containing electron-donor groups than with those bearing electron-withdrawing substituents, indicating the strong electrophilic character of the Ru^{IV}=O group in all cases. Therefore, the best results are gathered for cyclooctene (entries 4, 8, 12 and 16) whereas the poorest values are obtained for styrene (entries 1, 5, 9 and 13) and *trans*-stilbene (entries 3, 7, 11 and 15), the latter also suffering from potential steric effects due to the bulkiness of its two phenyl rings.

Finally, another interesting feature observed is the stereo-specific nature of the catalytic epoxidation process. For the whole set of aqua complexes when *cis*-β-methylstyrene is employed as the substrate no *cis*/*trans* isomerisation takes place. Therefore, for $\mathbf{4}^{2+}$/$\mathbf{6}^{2+}$ ring closure must be faster than C–C rotation for the radical intermediates proposed to be formed (Scheme S3,† top), while for $\mathbf{2a}^{2+}$/$\mathbf{2b}^{2+}$ the stereo-specificity could be explained on the basis of the proposed concerted bi-electronic oxene insertion into the double bond (Scheme S3,† bottom).

Conclusions

A new tetradentate imidazolium precursor ligand has been synthesised and fully characterised by NMR and X-ray diffraction analysis. This ligand decomposes in nucleophilic solvents at high temperatures due to C–N bond cleavage, generating a bidentate NHC-phthalazine scaffold (R-**L2**) during the synthesis of the corresponding four Ru chlorido and aqua complexes $[Ru(R\text{-}\mathbf{L2})(T)X]^{n+}$ (X = Cl, n = 1, X = H_2O, n = 2; R = Me, iPr; T = trpy, tpm, bpea), which have been fully characterised electronically and spectroscopically.

Modulation of the thermodynamic stability in aqueous media of the Ru(III) oxidation state has been observed for the four aqua compounds. Thus, while for $\mathbf{4}^{2+}$/$\mathbf{6}^{2+}$ (T = tpm/bpea) the Ru(III) state is clearly stable at moderately high potentials and they increase their oxidation state from Ru(II) through mono-electronic processes ($\Delta E_{1/2}$ = 200 mV for the latter), for the trpy-based complexes $\mathbf{2a}^{2+}$/$\mathbf{2b}^{2+}$ the Ru(III) state is almost unstable with regard to its disproportionation ($\Delta E_{1/2}$ = 30 mV). This divergence in the electronic behaviour has direct implications in the epoxidation capacity of alkenes with $PhI(OAc)_2$, since the higher conversion and selectivity observed for $\mathbf{2a}^{2+}$/$\mathbf{2b}^{2+}$ can be rationalised on the basis of the existence of bi-electronic transfers that avoid the generation of radical intermediates of high energy that could reduce the selectivity of the

whole process. Additionally, the absence of *cis*/*trans* isomerisation in all cases – therefore leading to stereospecific epoxidation processes – may be explained on the basis of either a concerted bi-electronic process ($\mathbf{2a}^{2+}$/$\mathbf{2b}^{2+}$) or a radical mechanism in which the ring closure is much faster than C–C rotation ($\mathbf{4}^{2+}$/$\mathbf{6}^{2+}$).

We have also shown that the four aqua complexes are moderately unstable during catalytic water oxidation triggered by Ce(IV) addition due to ligand oxidation under the harsh conditions employed, especially those containing aliphatic carbon atoms ($\mathbf{4}^{2+}$/$\mathbf{6}^{2+}$). Also, under electrochemically triggered conditions $\mathbf{2a}^{2+}$ is the fastest catalyst at pH 1.0.

In conclusion, in this work we have evidenced that it is possible to modulate the electronic and catalytic properties of Ru NHC complexes by using different auxiliary meridional or facial *N*-tridentate ligands.

Experimental section

Materials and instrumentation

All reagents used in the present work were obtained from Sigma Aldrich Chemical Co. and were used without further purification. Reagent-grade organic solvents were obtained from Scharlab. $RuCl_3{\cdot}3H_2O$ was supplied by Alfa Aesar. The starting ligands tri(1*H*-pyrazol-1-yl)methane (tpm) and *N*,*N*-bis(pyridin-2-ylmethyl)ethanamine (bpea) were prepared as described in the literature.[31,32] The synthetic manipulations were routinely performed under a nitrogen atmosphere using a Schlenk flask and vacuum-line techniques.

UV-vis spectroscopy was carried out with a HP8453 spectrometer using 1 cm quartz cells. NMR spectroscopy was performed on a Bruker DPX 250 MHz, DPX 360 MHz, Avance-II 400 MHz, DPX 500 MHz or a Avance-II 600 MHz spectrometer. Samples were run in MeOD, DCM-d_2 or acetone-d_6 with internal references. Elemental analyses were performed using a Carlo Erba CHMS EA-1108 instrument from the Chemical Analysis Service of the Universitat Autònoma de Barcelona (SAQ-UAB). Electrospray ionisation Mass Spectrometry (ESI-MS) experiments were performed on an HP298s gas chromatography (GC-MS) system from the SAQ-UAB. Cyclic voltammetry and differential pulse voltammetry experiments were performed on a Bio Logic Science Instrument SP-150 potentiostat using a three-electrode cell. A glassy carbon electrode (7 mm diameter) was employed as the working electrode while a platinum wire as the auxiliary electrode and a SCE as the reference electrode. Working electrodes were polished with 0.05 micron alumina paste and washed with distilled water and acetone before each measurement. The complexes were dissolved in acetonitrile, methanol or dichloromethane solutions of 0.1 M ionic strength containing the necessary amount of *n*-Bu_4NPF_6 (TABH) as the supporting electrolyte. For electrochemical analysis performed in water, the complexes were dissolved in pH 1 triflic acid solution or solutions of phosphate buffer for other pH values, with a 0.1 M ionic strength. The pH values were increased or reduced by adding drops of 0.1 M NaOH solution or the pH 1 triflic acid solution. $E_{1/2}$ values here presented were estimated from CV experiments from the average of the oxidative and reductive peak potentials ($E_{p,a}$ + $E_{p,c}$)/2. For the epoxidation catalytic studies, experiments were performed as follows. First, mixing for a period of 120 min was carried out by adding in a vial 1 mL of 1,2-dichloroethane (DCE) as the solvent, 1.60 g (5.0 mmol) of (diacetoxyiodo) benzene ($PhI(OAc)_2$) as the oxidant, 1 mmol of 1,1′-biphenyl as the internal standard, 2.5×10^{-3} mmol of catalyst ($\mathbf{2a}^{2+}$ to $\mathbf{6}^{2+}$) and 90 μL (5.0 mmol) of water. This mixing period before substrate addition was observed to be important in order to improve the rate of the catalytic reaction. Then, the substrate (2.5 mmol) was added to the previous mixture, achieving a final volume of approx. 1.47 mL and the corresponding initial concentrations: catalyst, 1.7 mM; substrate, 1.7 M; biphenyl, 0.68 M; $PhI(OAc)_2$, 3.4 M; water, 3.4 M. These concentrations correspond to a catalyst : substrate : oxidant : water ratio of 1 : 1000 : 2000 : 2000. Aliquots were taken every 5, 10, 15, 20, 25 or 30 min until completion of the reaction. Each aliquot was filtered through a Pasteur pipette filled with Celite; after that diethyl ether was added in order to elute the organic compounds and the filtrate was analysed in an HP 5890 PACKARD SERIES II Gas Chromatograph (GC) coupled to a mass selective detector with ionisation by electronic impact. The characterisation of the reaction products was carried out by comparison with commercial products or by GC-MS spectrometry. GC conditions: initial temperature 40 °C for 10 min, ramp rate variable for each substrate (typically from 10 °C min^{-1} to 20 °C min^{-1}), final temperature 250 °C, injection temperature 220 °C, detector temperature 250 °C. Yield of epoxide and substrate conversion were calculated with regard to the initial concentration of the substrate.

$$\text{Substrate conversion} = \{[\text{substrate}]_{\text{initial}} - [\text{substrate}]_{\text{final}}\}/[\text{substrate}]_{\text{initial}} \times 100.$$

$$\text{Epoxide selectivity} = [\text{epoxide}]_{\text{final}}/\{[\text{substrate}]_{\text{initial}} - [\text{substrate}]_{\text{final}}\} \times 100.$$

On-line manometry measurements were performed on a Testo 521 differential pressure manometer with an operating range of 1 to 100 hPa and a measurement accuracy of 0.5%, coupled to thermostatted reaction vessels for dynamic monitoring of the headspace pressure above each reaction. On-line monitoring of the gas evolution was carried out on a Pfeiffer Omnistar GSD 301C mass spectrometer. Typically, a degassed vial of 16.04 mL containing 1.5 mL of a 1.33 mM solution of the catalysts in 0.1 M triflic acid was connected to a capillary tubing apparatus. Subsequently, 0.5 mL of an Ar degassed solution of 400 mM $(NH_4)_2Ce^{IV}(NO_3)_6$ in 0.1 M triflic acid (100 equiv.) were injected by using a Hamilton gastight syringe, and the reaction was dynamically monitored at 25 °C. A response ratio of 1 : 2 was observed when equal concentrations of dioxygen and carbon dioxide were injected, which was used for the calculation of their relative concentrations.

X-ray crystal structure determination

Crystals of H_2**L1**$^{2+}$ were grown by slow diffusion of diethyl ether into a solution of H_2**L1**$(PF_6)_2$ in acetone. Crystals of **5**$^+$ were prepared by slow diffusion of diethyl ether into a solution of **5**$^+$ in methanol.

Structure solution and refinement were performed using SHELXTL. The crystal data parameters of H_2**L1**$^{2+}$ and **5**$^+$ are listed in Tables S1 and S3.† The structures of H_2**L1**$^{2+}$ and **5**$^+$ were analysed using the programs ORTEP and Mercury. All information related to the structures can be found in the deposited CIF-files.

Synthetic preparations

1,4-Bis(1-methylimidazolium-1-yl)phthalazine dichloride (H_2L1(Cl)$_2$). To an evacuated Schlenk flask a mixture of 1,4-dichlorophthalazine (dcp) (990 mg, 0.5 mol) and 1-methylimidazole (2.050 g, 3 mol) was dissolved into 2 ml of DMF. The mixture was stirred under a nitrogen atmosphere at 120 °C for 4 hours. A white precipitate appeared in the reaction crude, which was filtered off, washed with DMF and diethyl ether and dried under vacuum. Yield: 1.26 g (70%). ^{1}H-NMR (600 MHz, acetone-d$_6$, 298 K) δ 9.95 (s, 2H, H6, H6′), 8.57 (dd, 2H, J_{9-10} = 6.2, 3.0 Hz, H9, H9′), 8.50 (s, 2H, H4, H4′), 8.46 (dd, 2H, J_{10-9} = 6.3, 3.0 Hz, H10, H10′), 8.23 (s, 2H, H3, H3′), 4.39 (m, 6H, H1). ^{13}C-NMR (151 MHz, acetone-d$_6$, 298 K) δ 150.65 (C7), 138.44 (C6), 136.50 (C10), 125.28 (C3), 124.16 (C9), 124.08 (C8), 123.57 (C4), 36.84 (C1). Elemental analysis (% found): C, 52.98; H, 4.49; N, 23.09. Calcd for $C_{16}H_{16}Cl_2N_6$: C, 52.90; H, 4.44; N, 23.14.

***cis*-[Ru^{II}(Me-L2)(trpy)Cl]PF$_6$ (1a(PF$_6$)).** [Ru(trpy)Cl$_3$] (130 mg, 0.3 mmol), 1,4-bis(1-methylimidazolium-1-yl)phthalazine dichloride (H_2**L1**$(Cl)_2$) (73 mg, 0.2 mmol) and LiCl (38 mg, 0.9 mmol) were mixed in a round bottom flask and dry methanol (20 mL) was added as the solvent. Triethylamine (121 mg, 166 μL, 1.2 mmol) was added to the solution and the mixture was refluxed at 65 °C for 16 hours. After cooling to room temperature, the reaction crude was filtered through Celite® to remove the black solid formed and then 20 drops of saturated aqueous NH_4PF_6 solution were added to the filtrate. The solution was concentrated under vacuum until about 10 mL, when a brown precipitate appeared. The precipitate was filtered off, washed with diethyl ether and dried under vacuum. Yield: 62 mg (41%). ^{1}H-NMR (600 MHz, CD_2Cl_2, 298 K) δ 8.63 (d, 1H, J_{4-3} = 2.4 Hz, H4), 8.53 (d, 1H, J_{9-10} = 8.7 Hz, H9), 8.37 (d, 2H, J_{26-27} = 8.1 Hz, H26), 8.22 (d, 2H, J_{23-22} = 8.0 Hz, H23), 8.18 (t, 1H, $J_{27-26,26'}$ = 8.1 Hz, H27), 8.12 (d, 1H, J_{12-11} = 8.1 Hz, H12), 8.07 (td, 1H, $J_{10-9,11}$ = 7.8 Hz, J_{10-12} = 1.1 Hz, H10), 7.94 (d, 2H, J_{20-21} = 5.3 Hz, H20), 7.85 (t, 1H, $J_{11-10,12}$ = 7.6 Hz, H11), 7.82 (t, 2H $J_{22-21,23}$ = 7.8 Hz, H22), 7.69 (d, 1H J_{3-4} = 2.4 Hz, H3), 7.20 (td, 2H, $J_{21-20,22}$ = 6.5 Hz, J_{21-23} = 1.1 Hz, H21), 4.78 (s, 3H, H1), 3.47 (s, 3H, H18). ^{13}C-NMR (151 MHz, CD_2Cl_2, 298 K) δ 200.66 (C6), 158.75 (C24), 158.43 (C14), 156.51 (C20), 155.50 (C25), 151.45 (C7), 136.59 (C22), 135.43 (C27), 133.91 (C10), 132.29 (C11), 126.88 (C21), 125.83 (C3), 124.51 (C12), 122.95 (C23), 121.16 (C26), 121.00 (C8), 120.20 (C9), 119.51 (C13), 118.77 (C4), 54.61 (C18), 38.15 (C1). UV/vis (methanol): λ_{max}, nm (ε, M^{-1} cm^{-1}) = 281 (11 988), 313 (14 247), 413 (4700), 475 (4332). ESI-MS (MeOH): m/z = 610.1 ([M − PF$_6$]). Elemental analysis (% found): C, 44.58; H, 3.10; N, 12.95. Calcd for $C_{28}H_{23}ClF_6N_7OPRu$: C, 44.54; H, 3.07; N, 12.99.

***cis*-[Ru^{II}(iPr-L2)(trpy)Cl]PF$_6$ (1b(PF$_6$)).** [Ru(trpy)Cl$_3$] (130 mg, 0.3 mmol), 1,4-bis(1-methylimidazolium-1-yl)phthalazine dichloride (H_2**L1**$(Cl)_2$) (73 mg, 0.2 mmol) and LiCl (38 mg, 0.9 mmol) were mixed in a round bottom flask and dry isopropanol (20 mL) was added as the solvent. Triethylamine (121 mg, 166 μL, 1.2 mmol) was added to the solution and the mixture was refluxed at 83 °C for 16 hours. After cooling to room temperature, the reaction crude was filtered through Celite® to remove the black solid formed and 20 drops of saturated aqueous NH_4PF_6 were added to the filtrate. The solvent was then totally removed in a rotary evaporator and the brown solid obtained was redissolved in isopropanol. The mixture was filtered through Celite® and isopropanol was removed from the filtrate under vacuum until about 10 mL was left. During this process a brown precipitate appeared, which was filtered off, washed with diethyl ether and dried under vacuum. Yield: 55 mg (35%). ^{1}H-NMR (600 MHz, acetone-d$_6$, 298 K) δ 9.02 (d, 1H J_{4-3} = 2.4 Hz, H4), 8.84 (d, 1H, J_{9-10} = 9.0 Hz, H9), 8.75 (d, 2H, J_{27-28} = 8.1 Hz, H27), 8.57 (d, 2H, J_{24-23} = 15.8 Hz, H24), 8.35 (t, 1H, $J_{28-27,27'}$ = 8.1 Hz, H28), 8.11 (m, 4H, J_{21-22} = 7.2 Hz, H21; J_{12-11} = 4.8 Hz, H12; $J_{10-9,11}$ = 9.0 Hz, H10), 8.00 (d, 1H, J_{3-4} = 2.4 Hz, H3), 7.92 (m, 3H, H11, H23), 7.29 (ddd, 1H, $J_{22-21,23,24}$ = 7.0, 5.6, 1.2 Hz, H22), 4.79 (s, 3H, H1), 4.54 (sept, 1H, J_{18-19} = 6.2 Hz, H18), 1.09 (d, 1H, J_{19-18} = 6.2 Hz, H19). ^{13}C-NMR (151 MHz, acetone-d$_6$, 298 K) δ 200.91 (C6), 159.08 (C25), 157.41 (C14), 156.82 (C21), 155.61 (C26), 151.44 (C7), 136.70 (C23), 135.48 (C28), 133.82 (C10), 132.09 (C11), 126.85 (C22), 126.03 (C3), 124.30 (C12), 123.13 (C24), 121.64 (C27), 121.28 (C8), 120.94 (C9), 119.61 (C13), 119.14 (C4), 70.79 (C18), 37.48 (C1), 20.96 (C19). UV/vis (methanol): λ_{max}, nm (ε, M^{-1} cm^{-1}) = 276 (11 315), 314 (14 616), 413 (5036), 479 (3889). ESI-MS (MeOH): m/z = 638.1 ([M − PF$_6$]). Elemental analysis (% found): C, 46.07; H, 3.52; N, 12.49. Calcd for $C_{30}H_{27}ClF_6N_7OPRu$: C, 46.01; H, 3.48; N, 12.52.

[Ru^{II}(Me-L2)(tpm)Cl]PF$_6$ (3(PF$_6$)). [Ru(tpm)Cl$_3$] (130 mg, 0.3 mmol), 1,4-bis (1-methylimidazolium-1-yl)phthalazine dichloride (H_2**L1**$(Cl)_2$) (73 mg, 0.2 mmol) and LiCl (38 mg, 0.9 mmol) were mixed in a round bottom flask and dry methanol (20 mL) was added as the solvent. Triethylamine (121 mg, 166 μL, 1.2 mmol) was added to the solution and the mixture was refluxed at 65 °C for 16 hours. After cooling to room temperature, the reaction crude was filtered through Celite® to remove the black solid formed and 20 drops of saturated aqueous NH_4PF_6 were added to the filtrate. The methanolic solution was concentrated in a rotary evaporator until about 10 mL and a brown precipitate was obtained. The precipitate was filtered off, washed with diethyl ether and dried under vacuum. Yield: 88 mg (60%). ^{1}H-NMR (600 MHz, acetone-d$_6$, 298 K) δ 9.66 (s, 1H, H24), 8.88 (d, 1H, J_{4-3} = 2.3 Hz, H4), 8.87 (d, 1H, J_{9-10} = 8.6 Hz, H9), 8.68 (d, 1H, J_{20-21} = 1.6 Hz, H20),

8.57 (d, 1H, J_{31-32} = 2.3 Hz, H31), 8.52 (d, 1H, J_{22-21} = 2.2 Hz, H22), 8.47 (d, 1H, J_{33-32} = 1.7 Hz, H33), 8.46 (d, 1H, J_{26-27} = 2.5 Hz, H26), 8.39 (d, 1H, J_{12-11} = 8.0 Hz, H12), 8.20 (t, 1H, $J_{10-9,11}$ = 7.3 Hz, H10), 8.07 (t, 1H, $J_{11-10,12}$ = 7.6 Hz, H11), 7.64 (d, 1H, J_{3-4} = 2.3 Hz, H3), 6.89 (d, 1H, J_{28-27} = 1.9 Hz, H28), 6.74 (t, 1H, $J_{21-20,22}$ = 2.3 Hz, H21), 6.67 (t, 1H, $J_{32-31,33}$ = 2.4 Hz, H32), 6.33 (t, 1H, $J_{27-26,28}$ = 2.4 Hz, H27), 4.16 (s, 3H, H18), 3.73 (s, 3H, H1). ^{13}C-NMR (151 MHz, acetone-d_6, 298 K) δ 205.44 (C6), 157.87 (C14), 151.40 (C7), 149.12 (C33), 146.71 (C28), 146.66 (C20), 134.70 (C26), 133.97 (C31), 133.75 (C10), 132.43 (C22), 132.27 (C11), 124.89 (C3), 124.34 (C12), 121.57 (C8), 121.28 (C9), 120.17 (C13), 119.63 (C4), 108.41 (C32), 108.27 (C27), 107.51 (C21), 76.77 (C24), 55.04 (C18), 36.27 (C1). UV/vis (methanol): λ_{max}, nm (ε, M^{-1} cm^{-1}) = 302 (7799), 410 (4745). ESI-MS (MeOH): m/z = 591.1 ([M − PF_6]). Elemental analysis (% found): C, 37.60; H, 3.05; N, 18.99. Calcd for $C_{23}H_{22}ClF_6N_{10}OPRu$: C, 37.53; H, 3.01; N, 19.03.

***trans*,*fac*-[Ru^{II}(Me-L2)(bpea)Cl]PF_6 (5(PF_6)).** [Ru(bpea)Cl_3] (130 mg, 0.3 mmol), 1,4-bis(1-methylimidazolium-1-yl)phthalazine dichloride (H_2**L1**$(Cl)_2$) (73 mg, 0.2 mmol) and LiCl (38 mg, 0.9 mmol) were mixed in a round bottom flask and dry methanol (20 mL) was added as the solvent. Triethylamine (121 mg, 166 μL, 1.2 mmol) was added to the solution and the mixture was refluxed at 65 °C for 16 hours. After cooling to room temperature, the reaction crude was filtered through Celite® to remove the black solid formed and 20 drops of saturated aqueous NH_4PF_6 were added to the filtrate. The methanolic solution was concentrated in a rotary evaporator until about 10 mL was left and a brown precipitate appeared. The precipitate was filtered, washed with diethyl ether and dried under vacuum. Yield: 68 mg (45%). ^{1}H-NMR (600 MHz, acetone-d_6, 298 K) δ 9.63 (d, 1H, J_{20-21} = 5.3 Hz, H20), 9.56 (d, 1H, J_{34-33} = 5.0 Hz, H34), 8.84 (d, 1H, J_{4-3} = 2.0 Hz, H4), 8.79 (d, 1H, J_{9-10} = 8.3 Hz, H9), 8.25 (d, 1H, J_{12-11} = 8.0 Hz, H12), 8.12 (t, 1H, $J_{10-9,11}$ = 7.5 Hz, H10), 7.97 (t, 1H, $J_{11-10,12}$ = 7.6 Hz, H11), 7.92 (t, 1H, $J_{32-31,33}$ = 7.3 Hz, H32), 7.82 (t, 1H, $J_{22-21,23}$ = 7.4 Hz, H22), 7.58 (m, 2H, J_{3-4} = 2.3 Hz, J_{31-32} = 7.3 Hz, H3, H31), 7.50 (m, 1H, $J_{23-22,33-32,34}$ = 7.3 Hz, H23, H33), 7.41 (t, 1H, $J_{21-20,22}$ = 6.5 Hz, H21), 4.52–4.42 (m, 4H, H25, H29), 3.65 (s, 3H, H18), 3.58 (s, 3H, H1), 2.53 (m, 1H, $J_{27-27',28}$ = 13.8, 6.8 Hz, H27), 2.35 (m, 1H, $J_{27'-27,28}$ = 13.7, 6.8 Hz, H27′), 0.91 (m, 3H, H28). ^{13}C-NMR (151 MHz, acetone-d_6, 298 K) δ 204.97 (C6), 161.42 (C20), 160.02 (C34), 158.07 (C14), 151.65 (C24), 150.15 (C13), 149.42 (C30), 136.55 (C32), 125.73 (C22), 133.74 (C10), 131.47 (C11), 125.00 (C3), 124.30 (C12), 123.63 (C21), 123.13 (C33), 121.52 (C8), 121.01 (C23), 120.70 (C9), 120.64 (C31), 119.44 (C7), 118.85 (C4), 67.49 (C25), 66.09 (C29), 61.96 (C27), 53.89 (C18), 35.45 (C1), 7.98 (C28). UV/vis (methanol): λ_{max}, nm (ε, M^{-1} cm^{-1}) = 299 (5226), 434 (5612). ESI-MS (MeOH): m/z = 604.1 ([M − PF_6]). Elemental analysis (% found): C, 43.37; H, 3.94; N, 13.05. Calcd for $C_{27}H_{29}ClF_6N_7OPRu$: C, 43.29; H, 3.90; N, 13.09.

***cis*-[Ru^{II}(Me-L2)(trpy)(OH_2)](PF_6)$_2$ (2a(PF_6)$_2$). 1a$^+$** (120 mg, 0.16 mmol) was dissolved in a mixture of acetone and water (acetone : water = 1 : 3, 40 mL). $AgBF_4$ (109 mg, 0.56 mmol) was added into the solution, which was then refluxed at 90 °C for 4 hours. After cooling to room temperature, the reaction crude was filtered through Celite® to remove the black solid formed. The red-brown solution was concentrated under vacuum until about 20 mL was left, followed by centrifugation (10 000 rpm, 10 min) to remove the potential colloidal silver still remaining. To the clear red solution 20 drops of saturated aqueous NH_4PF_6 solution were added and the precipitate formed was filtered off, washed with diethylether and dried under vacuum. Yield: 91 mg (65%). ^{1}H-NMR (600 MHz, acetone-d_6, 298 K) δ 9.01 (d, 1H, J_{4-3} = 2.4 Hz, H4), 8.80 (d, 2H, J_{26-27} = 7.4 Hz, H26), 8.78 (d, J_{9-10} = 8.7 Hz, H9), 8.62 (d, 2H, J_{23-22} = 8.0 Hz, H23), 8.44 (t, 2H, $J_{27-26,26'}$ = 8.1 Hz, H27), 8.19 (d, 2H, J_{20-21} = 5.0 Hz, H20), 8.12 (t, 1H, $J_{10-9,11}$ = 8.7 Hz, H10), 8.04–8.00 (m, 4H, H12, H3, H22), 7.91 (t, 1H, $J_{11-10,12}$ = 7.5 Hz, H11), 7.37 (m, 2H, H21), 4.56 (s, 3H, H1), 3.46 (s, 3H, H18). ^{13}C-NMR (151 MHz, acetone-d_6, 298 K) δ 200.62 (C6), 159.47 (C24), 158.01 (C14), 157.82 (C20), 156.41 (C25), 153.08 (C7), 138.22 (C22), 137.65 (C27), 134.20 (C10), 132.83 (C11), 127.53 (C21), 126.29 (C3), 124.05 (C12), 123.85 (C23), 122.38 (C26), 121.12 (C9), 120.90 (C8), 119.57 (C14), 119.21 (C3), 54.43 (C18), 36.55 (C1). UV/vis (methanol): λ_{max}, nm (ε, M^{-1} cm^{-1}) = 275 (12 189), 309 (13 040), 388 (4338), 467 (4474). ESI-MS (MeOH): m/z = 594.1 ([M − 2PF_6 + 1]). Elemental analysis (% found): C, 38.14; H, 2.89; N, 11.06. Calcd for $C_{28}H_{25}F_{12}N_7O_2P_2Ru$: C, 38.11; H, 2.86; N, 11.11.

***cis*-[Ru^{II}(iPr-L2)(trpy)(OH_2)](PF_6)$_2$ (2b(PF_6)$_2$). 1b$^+$** (120 mg, 0.15 mmol) was dissolved in a 40 mL mixture of acetone and water (1 : 3). $AgBF_4$ (109 mg, 0.56 mmol) was then added to the solution, which was then refluxed at 90 °C for 4 hours. After cooling to room temperature, the reaction crude was filtered through Celite® to remove the silver chloride formed. The brown filtrate was then concentrated in a rotary evaporator until about 20 mL, followed by centrifugation (10 000 rpm, 10 min) to remove the remaining solids. To the clear red solution 20 drops of a saturated aqueous NH_4PF_6 solution were added. The brown precipitate formed was filtered off, washed with diethyl ether and dried under vacuum. Yield: 91 mg (65%). ^{1}H-NMR (600 MHz, acetone-d_6, 298 K) δ 9.03 (d, 1H, J_{4-3} = 2.4 Hz, H4), 8.84 (d, 2H, J_{27-28} = 6.7 Hz, H27), 8.81 (d, 1H, J_{9-10} = 8.7 Hz, H9), 8.63 (d, 2H, J_{24-23} = 8.0 Hz, H24), 8.50 (t, 1H, $J_{28-27,27'}$ = 8.1 Hz, H28), 8.23 (dd, 2H, $J_{21-22,23}$ = 10.5, 5.6 Hz, H21), 8.13 (t, 1H, $J_{10-9,11}$ = 8.5 Hz, H10), 8.10 (d, 1H, J_{12-11} = 8.7 Hz, H12), 8.06–8.01 (m, 3H, H3, H23), 7.93 (t, 1H, $J_{11-10,12}$ = 7.6 Hz, H11), 7.38 (ddd, 1H, $J_{22-21,23,24}$ = 7.0, 5.6, 1.2 Hz, H22), 4.58 (s, 3H, H1), 4.49 (dt, 1H, $J_{18-19,19'}$ = 12.3, 6.2 Hz, H18), 1.07 (d, 6H, J_{19-18} = 6.2 Hz, H19). ^{13}C-NMR (151 MHz, acetone-d_6, 298 K) δ 200.66 (C6), 159.47 (C25), 157.96 (C21), 157.31 (C14), 156.32 (C26), 152.73 (C7), 138.23 (C23), 137.53 (C28), 134.05 (C10), 132.74 (C11), 127.63 (C22), 126.16 (C3), 124.24 (C12), 123.77 (C24), 122.47 (C27), 121.15 (C8), 121.07 (C9), 119.80 (C13), 119.62 (C4), 70.98 (C18), 36.39 (C1), 20.90 (C19). UV/vis (methanol): λ_{max}, nm (ε, M^{-1} cm^{-1}) = 280 (12 006), 311 (14 895), 392 (4700), 463 (4220). ESI-MS (MeOH): m/z = 622.1 ([M − 2PF_6 + 1]). Elemental analysis (% found): C, 39.63; H, 3.24; N, 10.74. Calcd for $C_{30}H_{29}F_{12}N_7O_2P_2Ru$: C, 39.57; H, 3.21; N, 10.77.

[Ru^{II}(Me-L2)(tpm)(OH_2)](PF_6)$_2$ (4(PF_6)$_2$). 3^+ (120 mg, 0.16 mmol) was dissolved in a 40 mL mixture of acetone and water (1 : 3). $AgBF_4$ (109 mg, 0.56 mmol) was added into the solution that was then refluxed at 90 °C for 4 hours. After cooling to room temperature, the reaction crude was filtered through Celite® to remove the silver chloride formed. The brown filtrate was then concentrated in a rotary evaporator until about 20 mL, followed by centrifugation (10 000 rpm, 10 min) in order to remove the remaining solids. To the clear red solution 20 drops of saturated aqueous NH_4PF_6 solution were added. The red precipitate formed was filtered off, washed with diethyl ether and dried under vacuum. Yield: 76 mg (55%). ^{1}H-NMR (600 MHz, acetone-d_6, 298 K) δ 9.90 (s, 1H, H24), 8.99 (d, 1H, J_{4-3} = 2.4 Hz, H4), 8.97 (d, 1H, J_{9-10} = 8.5 Hz, H9), 8.83 (d, 1H, J_{20-21} = 1.7 Hz, H20), 8.72 (d, 1H, J_{31-32} = 2.9 Hz, H31), 8.67 (d, 1H, J_{22-21} = 2.7 Hz, H22), 8.58 (d, 1H, J_{33-32} = 2.0 Hz, H33), 8.53 (d, 1H, J_{26-27} = 5.5 Hz, H26), 8.47 (d, 1H, J_{12-11} = 8.1 Hz, H12), 8.29 (dd, 1H, $J_{10-9,11}$ = 8.2, 7.7 Hz, H10), 8.17 (t, 1H, $J_{11-10,12}$ = 7.7 Hz, H11), 7.74 (d, 1H, J_{3-4} = 2.3 Hz, H3), 6.85 (m, $J_{21-20,22}$ = 2.4 Hz, J_{28-27} = 2.2 Hz, H21, H28), 6.80 (t, 1H, $J_{32-31,33}$ = 2.5 Hz, H32), 6.34 (t, 1H, $J_{27-26,28}$ = 2.5 Hz, H27), 4.20 (s, 3H, H18), 3.74 (s, 1H, H1). ^{13}C-NMR (151 MHz, acetone-d_6, 298 K) δ 200.22 (C6), 158.58 (C14), 152.76 (C7), 148.70 (C33), 148.04 (C28), 147.06 (C20), 135.74 (C26), 134.89 (C31), 134.17 (C10), 133.64 (C22), 133.40 (C11), 125.84 (C3), 124.48 (C12), 122.02 (C9), 121.75 (C8), 120.96 (C13), 120.61 (C4), 109.06 (C32), 108.69 (C27), 108.04 (C21), 76.61 (C24), 55.38 (C18), 36.65 (C1). UV/vis (methanol): λ_{max}, nm (ε, M^{-1} cm^{-1}) = 295 (8297), 392 (5315). ESI-MS (MeOH): m/z = 575.1 ([M − 2PF_6 + 1]). Elemental analysis (% found): C, 32.02; H, 2.81; N, 16.19. Calcd for $C_{23}H_{24}F_{12}N_{10}O_2P_2Ru$: C, 31.99; H, 2.80; N, 16.22.

***trans*,*fac*-[Ru^{II}(Me-L2)(bpea)(OH_2)](PF_6)$_2$ (6(PF_6)$_2$).** 5^+ (120 mg, 0.16 mmol) was dissolved in a 40 mL mixture of acetone and water (1 : 3). $AgBF_4$ (109 mg, 0.56 mmol) was then added into the solution, which was refluxed at 90 °C for 4 hours. After cooling to room temperature, the reaction crude was filtered through Celite® to remove the silver chloride formed. The red-brown solution was concentrated in a rotary evaporator until about 20 mL, followed by centrifugation (10 000 rpm, 10 min) to remove the remaining solids. To the clear red solution 20 drops of saturated aqueous NH_4PF_6 solution were added. The precipitate formed was filtered off, washed with diethyl ether and dried under vacuum. Yield: 96 mg (68%). ^{1}H-NMR (600 MHz, acetone-d_6, 298 K) δ 8.99 (d, 1H, J_{4-3} = 2.4 Hz, H4), 8.96 (d, 1H, J_{34-33} = 5.3 Hz, H34), 8.93 (m, 2H, H20, H9), 8.36 (d, 1H, J_{12-11} = 8.1 Hz, H12), 8.23 (t, 1H, $J_{10-9,11}$ = 7.7 Hz, H10), 8.08 (t, 1H, $J_{11-10,12}$ = 7.6 Hz, H11), 7.99 (td, 1H, $J_{32-33,31}$ = 7.8, J_{32-34} = 1.4 Hz, H32), 7.88 (td, 1H, $J_{22-23,21}$ = 7.4, J_{22-20} = 1.7 Hz, H22), 7.72 (d, 1H, J_{3-4} = 2.4 Hz, H3), 7.67 (d, 1H, J_{31-32} = 7.9 Hz, H31), 7.57 (m, 1H, H33), 7.55 (d, 1H, J_{23-22} = 7.9 Hz, H23), 7.50 (t, 1H, $J_{21-22,20}$ = 6.6 Hz, H21), 4.57–4.40 (m, 4H, H25, H29), 3.71 (s, 3H, H1), 3.65 (s, 3H, H18), 2.40 (m, 1H, $J_{27-27',28}$ = 9.2, 5.0 Hz, H27), 2.30 (m, 1H, $J_{27'-27,28}$ = 9.2, 5.0 Hz, H27′), 0.91 (t, 3H, $J_{28-27,27'}$ = 7.0 Hz, H28). ^{13}C-NMR (151 MHz, acetone-d_6, 298 K) δ 202.85 (C6), 161.20 (C24), 159.56 (C30), 158.81 (C14), 151.85 (C7), 149.37 (C20), 147.67 (C34), 137.42 (C32), 136.72 (C22), 134.06 (C10), 132.67 (C11), 125.82 (C3), 124.41 (C12), 124.30 (C21), 123.78 (C33), 121.63 (C8), 121.54 (C23), 121.49 (C31), 121.35 (C9), 120.47 (C13), 119.89 (C4), 67.89 (C25), 67.29 (C29), 62.80 (C27), 54.19 (C18), 35.89 (C1), 7.97 (C28). UV/vis (methanol): λ_{max}, nm (ε, M^{-1} cm^{-1}) = 299 (5810), 423 (5753). ESI-MS (MeOH): m/z = 586.1 ([M − 2PF_6]). Elemental analysis (% found): C, 37.06; H, 3.60; N, 11.15. Calcd for $C_{27}H_{31}F_{12}N_7O_2P_2Ru$: C, 36.99; H, 3.56; N, 11.19.

Acknowledgements

Support from MINECO (CTQ2011-26440, CTQ2015-64261-R, CTQ2016-80058-R and CTQ2015-64436-P) is gratefully acknowledged. M. G.-S. is grateful for the award of a PIF doctoral grant from UAB. J. G.-A. acknowledges the Serra Húnter Program. We also thank the Servei de Ressonància Magnètica Nuclear, Universitat Autònoma de Barcelona, for allocating instrument time.

Notes and references

1 W. A. Herrmann and C. Köcher, *Angew. Chem., Int. Ed. Engl.*, 1997, **36**, 2162.
2 (*a*) M. N. Hopkinson, C. Richter, M. Schedler and F. Glorious, *Nature*, 2014, **510**, 485; (*b*) S. Kaufhold, L. Petermann, R. Staehle and S. Rau, *Coord. Chem. Rev.*, 2015, **304–305**, 73.
3 A. Dovletoglou, S. A. Adeyemi and T. J. Meyer, *Inorg. Chem.*, 1996, **35**, 4120.
4 (*a*) X. Sala, S. Maji, R. Bofill, J. García-Antón, L. Escriche and A. Llobet, *Acc. Chem. Res.*, 2014, **47**, 504; (*b*) M. Dakkach, M. I. López, I. Romero, M. Rodríguez, A. Atlamsan, T. Parella, X. Fontrodona and A. Llobet, *Inorg. Chem.*, 2010, **49**, 7072; (*c*) T. J. Meyer and M. H. V. Huynh, *Inorg. Chem.*, 2003, **42**, 8140.
5 (*a*) R. Lalrempuia, N. D. McDaniel, H. Müller-Bunz, S. Bernhard and M. Albrecht, *Angew. Chem., Int. Ed.*, 2010, **49**, 9765; (*b*) A. Petronilho, M. Rahman, J. A. Woods, H. Al-Sayyed, H. Müller-Bunz, J. M. Don MacElroy, S. Bernhard and M. Albrecht, *Dalton Trans.*, 2012, **41**, 13074; (*c*) A. Petronilho, J. A. Woods, S. Bernhard and M. Albrecht, *Eur. J. Inorg. Chem.*, 2014, 708; (*d*) Z. Codolà, J. M. S. Cardoso, B. Royo, M. Costas and J. Lloret-Fillol, *Chem. – Eur. J.*, 2013, **19**, 7203; (*e*) A. Volpe, A. Sartorel, C. Tubaro, L. Meneghini, M. Di Valentin, C. Graiff and M. Bonchio, *Eur. J. Inorg. Chem.*, 2014, 665; (*f*) I. Corbucci, A. Petronilho, H. Müller-Bunz, L. Rocchigiani, M. Albrecht and A. Macchioni, *ACS Catal.*, 2015, **5**, 2714.
6 (*a*) Z. Chen, J. J. Concepcion and T. J. Meyer, *Dalton Trans.*, 2011, **40**, 3789; (*b*) R. Staehle, L. Tong, L. Wang, L. Duan, A. Fischer, M. S. G. Ahlquist, L. Sun and S. Rau, *Inorg. Chem.*, 2014, **53**, 1307.

7 (*a*) L. Francàs, R. Bofill, J. García-Antón, L. Escriche, X. Sala and A. Llobet, Ru-Based Water Oxidation Catalysts, in *Molecular Water Oxidation Catalysts: A Key Topic for New Sustainable Energy Conversion Schemes*, ed. A. Llobet, John Wiley & Sons, Ltd, 2014, pp. 29–50; (*b*) J. García-Antón, R. Bofill, L. Escriche, A. Llobet and X. Sala, *Eur. J. Inorg. Chem.*, 2012, 4775; (*c*) N. Planas, G. J. Christian, E. Mas-Marza, X. Sala, X. Fontrodona, F. Maseras and A. Llobet, *Chem. – Eur. J.*, 2010, **16**, 7965–7968; (*d*) L. Mognon, S. Mandal, C. E. Castillo, J. Fortage, F. Molton, G. Aromí, J. Benet-Buchhlolz, M.-N. Collomb and A. Llobet, *Chem. Sci.*, 2016, **7**, 3304.

8 (*a*) E. Masllorens, M. Rodríguez, I. Romero, A. Roglans, T. Parella, J. Benet-Buchholz, M. Poyatos and A. Llobet, *J. Am. Chem. Soc.*, 2006, **128**, 5306; (*b*) L. Vaquer, P. Miró, X. Sala, F. Bozoglian, E. Masllorens, J. Benet-Bucholz, X. Fontrodona, T. Parella, I. Romero, A. Roglans, M. Rodríguez, C. Bo and A. Llobet, *ChemPlusChem*, 2013, **78**, 235.

9 (*a*) F. R. Keene, *Coord. Chem. Rev.*, 1999, **187**, 121; (*b*) T. J. Meyer, *J. Electrochem. Soc.*, 1984, **131**, 221C.

10 J. Aguiló, A. Naeimi, R. Bofill, H. Mueller-Bunz, A. Llobet, L. Escriche, X. Sala and M. Albrecht, *New J. Chem.*, 2014, **38**, 1980.

11 (*a*) J. Van Veldhuizen, J. Campbell, R. Giudici and A. Hoveyda, *J. Am. Chem. Soc.*, 2005, **127**, 6877; (*b*) B. J. Truscott, R. Klein and P. T. Kaye, *Tetrahedron Lett.*, 2010, **51**, 5041.

12 J. Aguiló, L. Francàs, R. Bofill, M. Gil-Sepulcre, J. García-Antón, A. Poater, A. Llobet, L. Escriche, F. Meyer and X. Sala, *Inorg. Chem.*, 2015, **54**, 6782.

13 (*a*) C. Chen, H. Y. Qiu, W. Z. Chen and D. Q. Wang, *J. Organomet. Chem.*, 2008, **693**, 3273; (*b*) J. S. Ye, X. M. Zhang, W. Z. Chen and S. Shimada, *Organometallics*, 2008, **27**, 4166; (*c*) X. L. Liu and W. Z. Chen, *Organometallics*, 2012, **31**, 6614; (*d*) B. Tong, J. Qiang, Q. Mei, H. Wang and Q. Zhang, *Inorg. Chem. Commun.*, 2012, **17**, 113.

14 J. Mola, I. Romero, M. Rodríguez, F. Bozoglian, A. Poater, M. Solà, T. Parella, J. Benet-Buchholz, X. Fontrodona and A. Llobet, *Inorg. Chem.*, 2007, **46**, 10707.

15 (*a*) M. Dakkach, T. Parella, A. Atlamsani, I. Romero and M. Rodríguez, *Adv. Synth. Catal.*, 2011, **353**, 231; (*b*) M. Dakkach, A. Atlamsani, T. Parella, I. Romero and M. Rodríguez, *Inorg. Chem.*, 2013, **52**, 5077.

16 L. Vaquer, J. De Tovar, J. García-Antón, A. Llobet and X. Sala, *Inorg. Chem.*, 2013, **52**, 4985.

17 (*a*) X. Sala, A. Poater, A. Von Zelewsky, T. Parella, X. Fontrodona, I. Romero, M. Solà, M. Rodríguez and A. Llobet, *Inorg. Chem.*, 2008, **47**, 8016; (*b*) J. S. Ye, X. M. Zhang, W. Z. Chen and S. Shimada, *Organometallics*, 2008, **27**, 4166.

18 F. Laurent, E. Plantalech, B. Donnadieu, A. Jiménez, F. Hernández, M. Martínez-Ripoll, M. Biner and A. Llobet, *Polyhedron*, 1999, **18**, 3321.

19 K. J. Takeuchi, M. S. Thompson, D. W. Pipes and T. J. Meyer, *Inorg. Chem.*, 1984, **23**, 1845.

20 A. Llobet, P. Doppelt and T. J. Meyer, *Inorg. Chem.*, 1988, **27**, 514.

21 M. Rodríguez, I. Romero and A. Llobet, *Inorg. Chem.*, 2001, **40**, 4150.

22 (*a*) J. C. Dobson and T. J. Meyer, *Inorg. Chem.*, 1988, **27**, 3283; (*b*) G. E. Cabaniss, A. A. Diamantis, W. R. Murphy, R. W. Linton and T. J. Meyer, *J. Am. Chem. Soc.*, 1985, **107**, 1845.

23 C. Costentin, S. Drouet, M. Robert and J.-M. Savéant, *J. Am. Chem. Soc.*, 2012, **134**, 11235.

24 R. Matheu, S. Neudeck, F. Meyer, X. Sala and A. Llobet, *ChemSusChem*, 2016, **9**, 3361.

25 R. Matheu, M. Z. Ertem, J. Benet-Buchholz, E. Coronado, V. S. Batista, X. Sala and A. Llobet, *J. Am. Chem. Soc.*, 2015, **137**, 10786.

26 E. S. Rountree, B. D. McCarthy, T. T. Eisenhart and J. L. Dempsey, *Inorg. Chem.*, 2014, **53**, 9983.

27 L. Francàs, X. Sala, E. Escudero-Adan, J. Benet-Buchholz, L. Escriche and A. Llobet, *Inorg. Chem.*, 2011, **50**, 2771.

28 J. Aguiló, L. Francàs, H. J. Liu, R. Bofill, J. García-Antón, J. Benet-Buchholz, A. Llobet, L. Escriche and X. Sala, *Catal. Sci. Technol.*, 2014, **4**, 190.

29 J.-H. In, S.-E. Park, R. Song and W. Nam, *Inorg. Chim. Acta*, 2003, **343**, 373.

30 (*a*) L. K. Stultz, R. A. Binstead, M. S. Reynolds and T. J. Meyer, *J. Am. Chem. Soc.*, 1995, **117**, 2520; (*b*) W.-H. Fung, W.-Y. Yu and C.-M. Che, *J. Org. Chem.*, 1998, **63**, 7715.

31 D. L. Reger, T. C. Grattan, K. J. Brown, C. A. Little, J. J. S. Lamba, A. L. Rheingold and R. D. Sommer, *J. Organomet. Chem.*, 2000, **607**, 120.

32 S. Pal, M. K. Chan and W. H. Armstrong, *J. Am. Chem. Soc.*, 1992, **114**, 6398.

Electrocatalytic CO_2 Reduction by Imidazolium-Functionalized Molecular Catalysts.

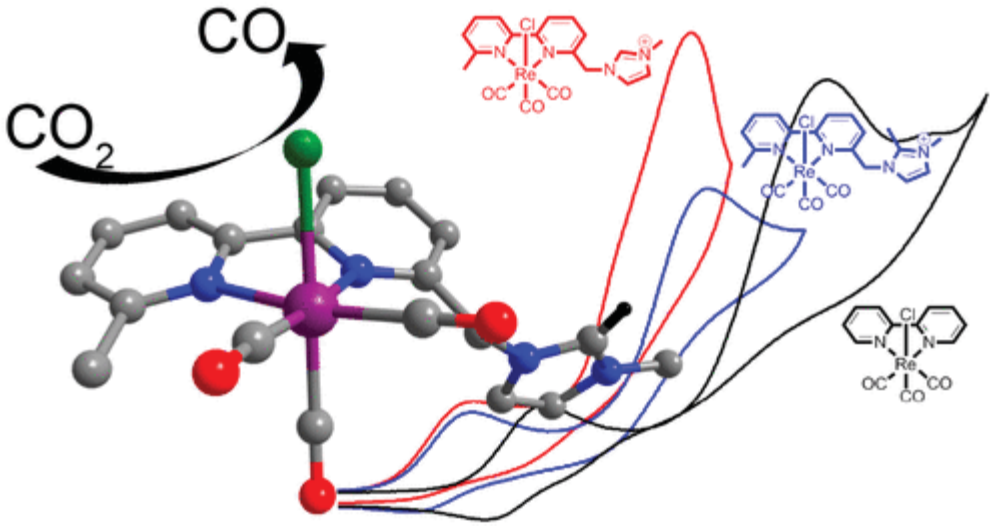

Sung, S.; Kumar, D.; **Gil-Sepulcre, M.**; Nippe, M.; *J. Am. Chem. Soc.*, **2017**, *139*, 13993-13996.

Contribution

Marcos Gil-Sepulcre helped in the design and performance of the bulk electrolysis experiments.

JACS
JOURNAL OF THE AMERICAN CHEMICAL SOCIETY

Communication

pubs.acs.org/JACS

Electrocatalytic CO_2 Reduction by Imidazolium-Functionalized Molecular Catalysts

Siyoung Sung,[†] Davinder Kumar,[†,‡] Marcos Gil-Sepulcre,[§] and Michael Nippe*[,†]

[†]Department of Chemistry, Texas A&M University, 3255 TAMU, College Station, Texas 77843, United States

[‡]School of Chemistry and Biochemistry, Thapar University, Patiala, Punjab 147004, India

[§]Departament de Química, Facultat de Ciències, Universitat Autònoma de Barcelona, Cerdanyola del Vallès, 08193 Barcelona, Catalonia, Spain

Supporting Information

ABSTRACT: We present the first examples of CO_2 electro-reduction catalysts that feature charged imidazolium groups in the secondary coordination sphere. The functionalized Lehn-type catalysts display significant differences in their redox properties and improved catalytic activities as compared to the conventional reference catalyst. Our results suggest that the incorporated imidazolium moieties do not solely function as a charged tag but also alter mechanistic aspects of catalysis.

The development of selective electrocatalysts for the reduction of carbon dioxide (CO_2) to yield C_1 products such as CO ($2e^-$), HCHO ($4e^-$), CH_3OH ($6e^-$), and CH_4 ($8e^-$) or higher C_n products would allow for a broad utilization of CO_2 as a C_1 feedstock.[1] However, the typically high energy barriers for the direct reduction of CO_2 on electrode or semiconductor surfaces necessitate reduction potentials significantly more negative than the corresponding thermodynamic CO_2 reduction potentials. The development of improved electrocatalysts which can lower overpotential requirements while maintaining appropriate catalytic rates and selectivity is therefore a key challenge toward future solar-driven CO_2 conversion technologies.[2]

Molecular catalysts are an attractive option due to the high degree of tunability of electronic and geometric parameters which allows for systematic reactivity studies that can lead to new catalyst design guidelines. For example, electron density at the reactive metal ion is readily tunable via incorporation of electron-withdrawing or -donating groups into the ligand backbone, which results in positively or negatively shifted redox potentials, respectively.[3] However, lowering electron density at the reactive transition metal ion does allow for less negative reduction potentials only at the cost of significantly decreased catalytic activity.[4]

More recently, focus has been given to tuning molecular electro-reduction catalysts via incorporation of functional groups into the secondary coordination sphere of transition metal complexes. Relevant examples include the incorporation of steric bulk[5] and incorporation of functional groups as proton relays and/or facilitators for substrate binding via hydrogen-bonding interactions, as well as intermediate stabilization.[6] Very recently, positively charged ammonium groups have also shown to improve electrocatalytic CO_2 reduction by metal porphyrin complexes.[7]

Our work is inspired by reports of efficient direct CO_2 reduction in ethyl-methyl-imidazolium (EMIM)-based ionic liquids on electrode materials[8] as well as by homogeneous catalysts.[9] We hypothesized that the incorporation of charged, slightly acidic, and redox-active imidazolium groups into the secondary coordination sphere of molecular complexes may provide alternative routes to tune redox potentials as well as allow for synergistic intramolecular interactions between reactive metal sites, imidazolium, and CO_2 substrate molecules. To test our hypothesis we functionalized the CO_2 electro (and photo)-reduction catalyst system based on $Re(bpy)(CO)_3Cl$ which was first discovered by Lehn et al.[10] and has been subject of detailed mechanistic studies.[11] Here, we present the first evaluation of imidazolium-functionalized CO_2 electro-reduction catalysts. We utilized precatalyst $\{Re[bpyMe(ImMe)](CO)_3Cl\}PF_6$ (**1PF$_6$**) (Figure 1) and compared its redox properties and catalytic activity to those of unfunctionalized $Re(bpy)(CO)_3Cl$ (**3**). To evaluate the possible involvement of the imidazolium C2−H bond of **1PF$_6$** during catalysis, we expanded our studies to include $\{Re[bpyMe(ImMe_2)](CO)_3Cl]PF_6$ (**2PF$_6$**) which is devoid of aforementioned C−H bond.

The functionalized complexes **1PF$_6$** and **2PF$_6$** were obtained as described in the Supporting Information. The molecular structures of **1**$^+$ and **2**$^+$ (Figure 1, Tables S1 and S2) feature octahedral Re(I) ions with Re−N, Re−C_{eq}, Re−C_{ax}, and Re−Cl distances of 2.206[3] Å (**2**$^+$: 2.224[6] Å), 1.916[5] Å (**2**$^+$: 1.925[9] Å), 1.924(5) Å (**2**$^+$: 1.993(9) Å), and 2.485(1) Å (**2**$^+$: 2.462(2) Å), respectively, which are comparable to those reported for related $Re(CO)_3Cl$ complexes.[12] Importantly, the structure of **1PF$_6$** features close proximity between imidazolium C2−H groups and Re-bound chloride ions of a neighboring molecule which likely indicates hydrogen-bonding like or electrostatic interactions between them in the solid state.[13] Binding between imidazolium moieties and anions in a C2−H···X$^-$ fashion has been broadly utilized for the sensing of anions in solution.[14] We therefore suggest that similar C2−H···X$^-$ interactions have also to be considered in solutions of **1PF$_6$** and may include *intramolecular* C2−H···Cl$^-$ as well as C2−H···

Received: July 23, 2017
Published: September 18, 2017

DOI: 10.1021/jacs.7b07709
J. Am. Chem. Soc. 2017, 139, 13993−13996

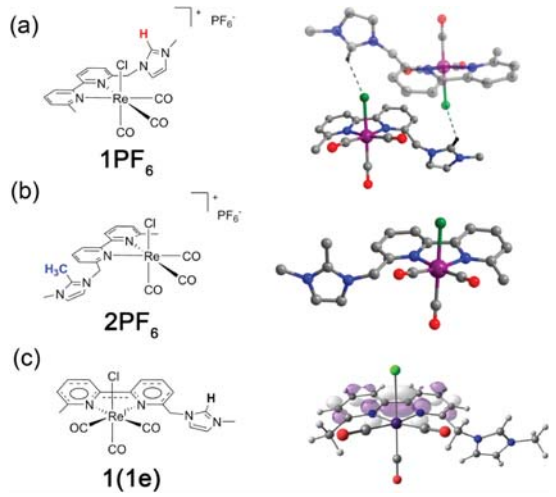

Figure 1. Molecular structures of (a) $\mathbf{1}^+$ and (b) $\mathbf{2}^+$ and (c) HOMO of calculated neutral species **1(1e)** (S = 1/2). Color code: purple = Re, green = Cl, red = oxygen, blue = nitrogen, gray = carbon). Hydrogen atoms (other than imidazolium C–H, shown in black), counter-anion(s), and co-crystallized solvent molecules have been omitted for clarity.

CO_2^- and C2–H···OH_2 interactions (*vide infra*) during catalysis.

The cyclic voltammograms (CVs) of $\mathbf{1}^+$, $\mathbf{2}^+$, and **3** recorded in CH_3CN under Ar (Figure S2) display initial redox couples at −1.65, −1.65, and −1.74 V, respectively (Table S3). The ∼100 mV positive shift in $E_{1/2}$ for the initial redox couple for $\mathbf{1}^+$ and $\mathbf{2}^+$ as compared to **3** is a likely consequence of the positive charge introduced by the imidazolium moiety. Reversibility of the initial redox couples of $\mathbf{1}^+$ and $\mathbf{2}^+$ becomes more apparent at faster scan rates (Figure 2). It is well established that the first 1e$^-$ reduction of **3** yields $[Re(I)(bpy^{\bullet-})(CO)_3Cl]^-$ which features a bipyridine based radical species. Importantly, the cationic ligands employed in $\mathbf{1}^+$ and $\mathbf{2}^+$ feature not only a redox-active bpy moiety but also a redox-active imidazolium group which could potentially be reduced by one electron to yield a neutral radical species.[15]

We thought to investigate the origin of the first 1e$^-$ reduction observed for $\mathbf{1}^+$ via computational methods using density functional theory (see Supporting Information). Importantly, the highest occupied molecular orbital (HOMO) of the 1e$^-$ reduced species **1(1e)** (S = 1/2) is exclusively centered on the π^* system of the bipyridine moiety (Figure 1c). No contributions from the imidazolium unit to the HOMO are observed. We therefore assign the initial reduction of $\mathbf{1}^+$ and $\mathbf{2}^+$ to the 1e$^-$ reduction of the bipyridine moiety which parallels the initial redox behavior of unfunctionalized **3**. The altered reversibility of the initial redox couples for $\mathbf{1}^+$ and $\mathbf{2}^+$ is therefore likely the result of accelerated Cl^- dissociation rates. Simulations of the CV profiles at varying scan rates according to an EC mechanism (Figure S3) suggests a ∼5.4 times faster chloride dissociation rate for $\mathbf{1PF_6}$ than for $\mathbf{2PF_6}$. We suggest that intramolecular C2–H···Cl^- interactions may allow for faster dissociation of Cl^- from the one-electron-reduced species **1(1e)** (Figure 2). Electrostatic and C4,5-H···Cl^- interactions may contribute to the faster Cl^- dissociation observed for $\mathbf{2PF_6}$ as compared to **3**. It is also important to note that this stands in contrast to reports for **3** in neat EMIM-based ionic liquids for which two 1e$^-$ reductions can precede Cl^- dissociation.[16] Consequently, we argue that the *intramolecular* incorporation of imidazolium moieties allows for distinct chemistry as compared to *intermolecular* imidazolium–catalyst systems. The diffusion coefficients of $\mathbf{1}^+$, $\mathbf{2}^+$, and **3** are similar as judged by DOSY NMR spectroscopy (Figures S4–S6) and rotating disk electrode voltammetry (Figures S7–S9), which suggests that *(i)* $\mathbf{1}^+$ is not dimeric in solution and *(ii)* diffusional behavior is not significantly affected by functionalization.

The activities of all complexes toward electrocatalytic reduction of CO_2 were investigated using identical conditions in CO_2 saturated CH_3CN solutions (Figure 3). Functionalized

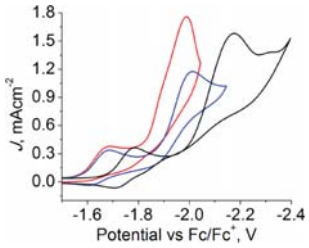

Figure 3. CVs of 1.0 mM $\mathbf{1}^+$ (red), $\mathbf{2}^+$ (blue), and **3** (black) recorded at 100 mV s^{-1} under CO_2 in CH_3CN (0.1 M NBu_4PF_6).

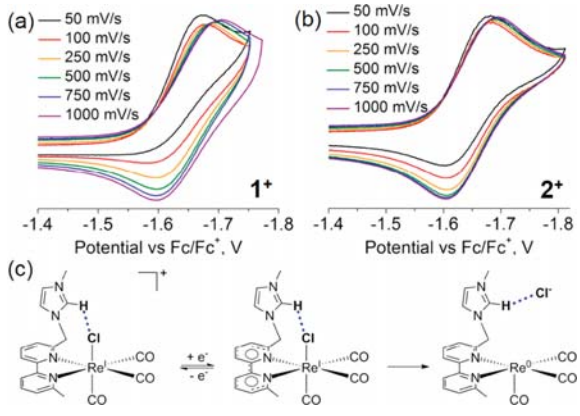

Figure 2. (a, b) Scan rate dependence of initial reduction of $\mathbf{1}^+$ and $\mathbf{2}^+$ under Ar (normalized current ($I/\nu^{-1/2}$) shown). (c) Proposed imidazolium-promoted Cl^- dissociation in $\mathbf{1}^+$ upon 1e$^-$ reduction.

complexes $\mathbf{1}^+$ and $\mathbf{2}^+$ exhibit comparable reductive current enhancement following the initial 1e$^-$ reduction event under CO_2. Most notably, the current enhancement occurs at significantly less negative potentials as compared to reference complex **3**. Catalytic half-wave potentials (Table S3) of reductive current enhancements of $\mathbf{1}^+$ and $\mathbf{2}^+$ are ∼170 and 140 mV less negative than that of **3**. The ratios of catalytic peak currents (i_{cat}) and initial peak currents (i_p; peak current of the initial 1e$^-$ reduction under Ar at the same scan rate) are also given in Table S3.[4a,17] Interestingly, for $\mathbf{1}^+$ we find a i_{cat}/i_p ratio of 4.7 which is higher than the one observed for **3** (4.4), even though the corresponding catalytic potential is significantly more positive than that of **3**. However, for complex $\mathbf{2}^+$, we observe smaller i_{cat}/i_p (3.5) as compared to **3**. We also note that the potential differences between the initial 1e$^-$ reduction and onset (or half-wave) potential of catalysis is much smaller for $\mathbf{1}^+$ (ΔE = 100 mV) as compared to $\mathbf{2}^+$ (150 mV) and **3** (180 mV) at a given scan rate. The latter observation (ΔE) further

DOI: 10.1021/jacs.7b07709
J. Am. Chem. Soc. 2017, 139, 13993–13996

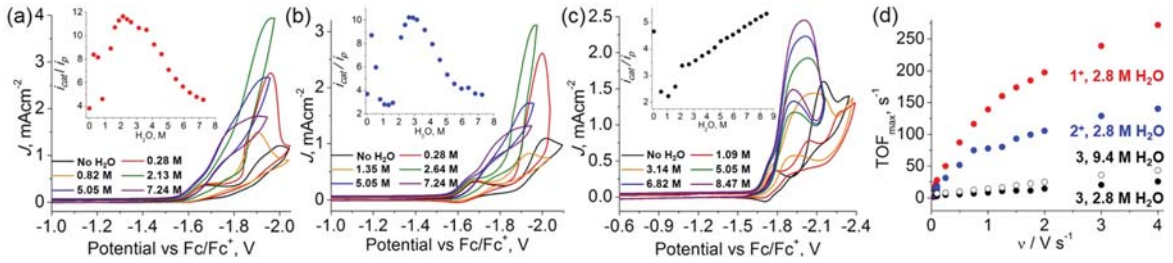

Figure 4. Effect of $[H_2O]$ on catalytic response under CO_2 by (a) $\mathbf{1}^+$, (b) $\mathbf{2}^+$, and (c) **3** at 100 mV s^{-1}. Insets display i_{cat}/i_p values over various $[H_2O]$. (d) Scan rate dependence of TOF_{max} (according to eq 1) for $\mathbf{1}^+$ (red), $\mathbf{2}^+$ (blue), and **3** (black). All CVs were recorded in a CH_3CN solution of 1.0 mM catalyst, 0.1 M NBu_4PF_6 under CO_2.

supports the hypothesis that Cl^- dissociation after $1e^-$ reduction is accelerated for $\mathbf{1}^+$, while the former (i_{cat}/i_p) may indicate synergistic effects of the C2−H group in $\mathbf{1}^+$ for CO_2 reduction catalysis, leading to higher current densities.

Although CO_2 itself can act as an oxide acceptor during catalysis,[11a] the addition of a proton source can facilitate the two-electron and two-proton reduction of CO_2 to CO and we decided to utilize H_2O as a proton source. CVs of $\mathbf{1}^+$, $\mathbf{2}^+$, and **3** were recorded under CO_2 with cumulative addition of H_2O. Ratios of i_{cat} over i_p were plotted versus concentration of H_2O and are presented in insets of Figure 4. Both imidazolium-functionalized catalysts show similar current responses to the addition of H_2O. Catalytic currents of $\mathbf{1}^+$ and $\mathbf{2}^+$ drastically increase upon addition of a small amounts of H_2O, which results in significant increase in i_{cat}/i_p values from ∼4 to 9 at a low H_2O concentration (0.28 M). Interestingly, the catalytic currents decrease up to ∼1 M H_2O and increase again upon further addition of H_2O displaying the highest i_{cat}/i_p values (∼12 and 10 for $\mathbf{1}^+$ and $\mathbf{2}^+$, respectively) at 2−3 M H_2O. The catalytic currents start to decrease gradually at concentrations higher than 3 M H_2O. It should also be noted that catalytic half-wave potentials gradually shift to more positive potentials as the H_2O concentration increases. At high $[H_2O]$, catalytic onset potentials are close to those where the initial $1e^-$ reduction was observed. In general, $\mathbf{1}^+$ exhibits higher i_{cat}/i_p values and faster positive potential shifts than $\mathbf{2}^+$ as $[H_2O]$ increases.

The unusual i_{cat}/i_p dependence on $[H_2O]$ observed for $\mathbf{1}^+$ and $\mathbf{2}^+$ contrasts the classical behavior obtained for **3**, which shows a linear increase of i_{cat}/i_p with increasing $[H_2O]$. These findings suggest that the mechanism for CO_2 reduction by $\mathbf{1}^+$ and $\mathbf{2}^+$ is significantly altered as compared to unfunctionalized **3** and also dependent on $[H_2O]$. While the origins of these mechanistic changes for $\mathbf{1}^+$ and $\mathbf{2}^+$ are subject of ongoing studies, we highlight that similar proton source dependence of i_{cat}/i_p has been reported recently for manganese bipyridyl tricarbonyl catalysts containing pendant methoxy groups.[6f] Here the presence of secondary coordination sphere R_2O groups was implicated in $R_2O\cdots HO(O)C-Mn$ interactions which allowed for easier C−OH bond cleavage. It is reasonable to assume that for $\mathbf{1}^+$ C−H···$^-$O(O)C−Re and/or C−H···OH_2···OH(O)C−Re interactions are also implicated during catalysis. Complex $\mathbf{2}^+$ on the other hand, could only feature potential interactions involving the C4−H and C5−H groups. However, these would be expected to be weaker than hydrogen bonding via C2−H moieties in $\mathbf{1}^+$.[18] This important difference is a likely cause for the differences in catalytic activity and selectivity between $\mathbf{1}^+$ and $\mathbf{2}^+$ as will be discussed in detail.

In an effort to obtain rate estimates for CO_2 reduction we studied the catalytic response at varying scan rates at the optimized $[H_2O]$ of 2.8 M. The obtained i_{cat}/i_p values were used to estimate TOF_{max} values according to eq 1.[19] We found

$$i_{cat}/i_p = 4.484\sqrt{\frac{RT}{F}}\sqrt{TOF_{max}}\,\nu^{-1/2} \quad (1)$$

that scan rate independence is nearly reached at scan rates of 4 V s^{-1} (Figure 4d). Although scan rate independence could not completely be achieved, it is clear that complex $\mathbf{1}^+$ operates at higher rates than $\mathbf{2}^+$. However, $\mathbf{2}^+$ shows significantly higher rates than parent complex **3**.

Controlled potential electrolysis (CPE) experiments were performed for all catalysts for 1 h in the presence of 2.8 or 9.4 M H_2O (Supporting Information) and the headspace after CPE was analyzed by gas chromatography (GC). CO was the only detectable reduction product after all CPE experiments. At 2.8 M H_2O, $\mathbf{1}^+$ consumes the largest charge with the highest faradaic efficiency generating the most CO among the three catalysts (Figure 5). We note that the charge consumed by $\mathbf{1}^+$ in 2.8 M H_2O is nearly twice as much as the charge consumed by **3**. $\mathbf{2}^+$ also consumes ∼1.5 times more charge than **3** with comparable faradaic efficiency. However, $\mathbf{1}^+$ as well as $\mathbf{2}^+$ show a gradual decrease in current over time (Figures S24 and S29). CVs recorded immediately after CPE experiments display the characteristic initial one-electron reductions of the complexes but a substantial decrease in the catalytic current (Figures S23 and S28). Resaturation of the solutions with CO_2 did not restore the high initial catalytic currents. As such, CO_2 substrate depletion or deactivation of catalysts[20] likely do not contribute to decrease in catalytic currents. These findings suggest that the

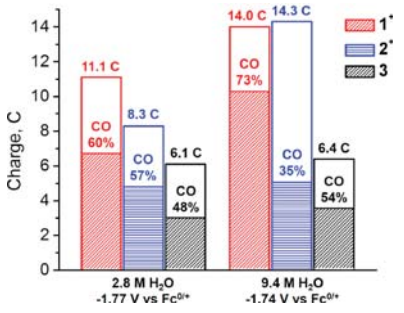

Figure 5. Results from CPE experiments at $[H_2O]$ = 2.8 and 9.4 M for 1.0 mM $\mathbf{1}^+$, $\mathbf{2}^+$, and **3**. Each column represents charge consumed by the respective catalyst. The shaded areas represent charge used for CO generation.

DOI: 10.1021/jacs.7b07709
J. Am. Chem. Soc. 2017, 139, 13993−13996

consumption of protons during electrolysis at low H_2O concentrations causes the decreased catalytic activity. CPE experiments were also performed at 9.4 M H_2O, in which reference complex **3** exhibits a higher i_{cat}/i_p value. Interestingly, $\mathbf{1}^+$ shows significantly improved catalytic performance in CPE experiments while **3** does not show any noticeable improvements. In fact, not only does the higher H_2O concentration increase the rate for $\mathbf{1}^+$ but also results in improved faradaic efficiency as well as longevity of the catalyst (Figures S37–S41). CVs recorded after CPE experiments show no obvious reduction in the catalytic current (Figure S38). However, $\mathbf{2}^+$, devoid of the C2–H moiety, exhibits the lowest faradaic efficiency (35%) among the three catalysts at 9.4 M H_2O although it consumes as much charge as $\mathbf{1}^+$. The observed faradaic efficiencies are in good agreement with previous results for Lehn-type catalyst systems in CH_3CN (61%;[21] 46%[22]).

Taken together, our results show that the incorporation of *intramolecular* imidazolium groups into CO_2 electro-reduction catalysts results in beneficial effects for catalysis. The differences in rate and selectivity between $\mathbf{1}^+$ and $\mathbf{2}^+$ point to the potentially crucial role of the C2–H bond of the imidiazolium moiety. To the best of our knowledge, this constitutes the first report of successfully utilizing *intramolecular* imidazolium groups to improve electrocatalysis. Computational results suggest that the redox-active imidazolium group does not interfere with the initial bipyridine-based reduction event. Detailed studies of the catalytic mechanism and potential imidazolium substrate interactions are currently underway.

■ ASSOCIATED CONTENT

Supporting Information

The Supporting Information is available free of charge on the ACS Publications website at DOI: 10.1021/jacs.7b07709.

Experimental and computational details, including Figures S1–S51 and Tables S1–S4 (PDF)
X-ray crystallographic data for $\mathbf{1PF_6}$ (CIF)
X-ray crystallographic data for $\mathbf{2PF_6}$ (CIF)

■ AUTHOR INFORMATION

Corresponding Author

*nippe@chem.tamu.edu

ORCID

Michael Nippe: 0000-0003-1091-4677

Notes

The authors declare no competing financial interest.

■ ACKNOWLEDGMENTS

M.N. is grateful to the TAMU Chemistry Department for start-up funds and financial support by the Welch Foundation (A-1880). We thank Dr. Julien Panetier for fruitful discussions.

■ REFERENCES

(1) (a) Dubois, M. R.; Dubois, D. L. *Acc. Chem. Res.* **2009**, *42*, 1974. (b) Benson, E. E.; Kubiak, C. P.; Sathrum, A. J.; Smieja, J. M. *Chem. Soc. Rev.* **2009**, *38*, 89. (c) Schneider, J.; Jia, H.; Muckerman, J. T.; Fujita, E. *Chem. Soc. Rev.* **2012**, *41*, 2036. (d) Costentin, C.; Robert, M.; Saveant, J.-M. *Chem. Soc. Rev.* **2013**, *42*, 2423. (e) Qiao, J.; Liu, Y.; Hong, F.; Zhang, J. *Chem. Soc. Rev.* **2014**, *43*, 631. (f) Grice, K. A.; Kubiak, C. P. *Adv. Inorg. Chem.* **2014**, *66*, 163.

(2) (a) Lewis, N. S.; Crabtree, G.; Nozik, A. J.; Wasielewski, M. R. *Basic Research Needs for Solar Energy Utilization*; U.S. Department of Energy, 2005. (b) Lewis, N. S.; Nocera, D. G. *Proc. Natl. Acad. Sci. U. S. A.* **2006**, *103*, 15729.

(3) (a) Johnson, B. A.; Maji, S.; Agarwala, H.; White, T. A.; Mijangos, E.; Ott, S. *Angew. Chem., Int. Ed.* **2016**, *55*, 1825. (b) Sun, Y.; Bigi, J. P.; Piro, N. A.; Tang, M. L.; Long, J. R.; Chang, C. J. *J. Am. Chem. Soc.* **2011**, *133*, 9212.

(4) (a) Smieja, J. M.; Kubiak, C. P. *Inorg. Chem.* **2010**, *49*, 9283. (b) Nippe, M.; Khnayzer, R. S.; Panetier, J. A.; Zee, D. Z.; Olaiya, B. S.; Head-Gordon, M.; Chang, C. J.; Castellano, F. N.; Long, J. R. *Chem. Sci.* **2013**, *4*, 3934.

(5) Sampson, M. D.; Kubiak, C. P. *J. Am. Chem. Soc.* **2016**, *138*, 1386.

(6) (a) Costentin, C.; Robert, M.; Savéant, J.-M.; Tatin, A. *Proc. Natl. Acad. Sci. U. S. A.* **2015**, *112*, 6882. (b) Agarwal, J.; Shaw, T. W.; Schaefer, H. F.; Bocarsly, A. B. *Inorg. Chem.* **2015**, *54*, 5285. (c) Neri, G.; Aldous, I. M.; Walsh, J. J.; Hardwick, L. J.; Cowan, A. J. *Chem. Sci.* **2016**, *7*, 1521. (d) Seu, C. S.; Appel, A. M.; Doud, M. D.; DuBois, D. L.; Kubiak, C. P. *Energy Environ. Sci.* **2012**, *5*, 6480. (e) Schmeier, T. J.; Dobereiner, G. E.; Crabtree, R. H.; Hazari, N. *J. Am. Chem. Soc.* **2011**, *133*, 9274. (f) Ngo, K. T.; McKinnon, M.; Mahanti, B.; Narayanan, R.; Grills, D. C.; Ertem, M. Z.; Rochford, J. *J. Am. Chem. Soc.* **2017**, *139*, 2604.

(7) Azcarate, I.; Costentin, C.; Robert, M.; Saveant, J.-M. *J. Am. Chem. Soc.* **2016**, *138*, 16639.

(8) (a) Rosen, B. A.; Salehi-Khojin, A.; Thorson, M. R.; Zhu, W.; Whipple, D. T.; Kenis, P. J. A.; Masel, R. I. *Science* **2011**, *334*, 643. (b) Medina-Ramos, J.; Pupillo, R. C.; Keane, T. P.; DiMeglio, J. L.; Rosenthal, J. *J. Am. Chem. Soc.* **2015**, *137*, 5021.

(9) Grills, D. C.; Matsubara, Y.; Kuwahara, Y.; Golisz, S. R.; Kurtz, D. A.; Mello, B. A. *J. Phys. Chem. Lett.* **2014**, *5*, 2033.

(10) (a) Hawecker, J.; Lehn, J.-M.; Ziessel, R. J. *J. Chem. Soc., Chem. Commun.* **1983**, 536. (b) Hawecker, J.; Lehn, J. M.; Ziessel, R. *Helv. Chim. Acta* **1986**, *69*, 1990.

(11) (a) Sullivan, B. P.; Bolinger, C. M.; Conrad, D.; Vining, W. J.; Meyer, T. J. J. *J. Chem. Soc., Chem. Commun.* **1985**, 1414. (b) Wong, K.-Y.; Chung, W.-H.; Lau, C.-P. *J. Electroanal. Chem.* **1998**, *453*, 161. (c) Hayashi, Y.; Kita, S.; Brunschwig, B. S.; Fujita, E. *J. Am. Chem. Soc.* **2003**, *125*, 11976. (d) Fujita, E.; Muckerman, J. T. *Inorg. Chem.* **2004**, *43*, 7636. (e) Riplinger, C.; Sampson, M. D.; Ritzmann, A. M.; Kubiak, C. P.; Carter, E. A. *J. Am. Chem. Soc.* **2014**, *136*, 16285.

(12) (a) Machan, C. W.; Chabolla, S. A.; Kubiak, C. P. *Organometallics* **2015**, *34*, 4678. (b) Manbeck, G. F.; Muckerman, J. T.; Szalda, D. J.; Himeda, Y.; Fujita, E. *J. Phys. Chem. B* **2015**, *119*, 7457. (c) Coe, B. J.; Foxon, S. P.; Pilkington, R. A.; Sánchez, S.; Whittaker, D.; Clays, K.; Depotter, G.; Brunschwig, B. S. *Organometallics* **2015**, *34*, 1701.

(13) Thomas, J.-L.; Howarth, J.; Hanlon, K.; McGuirk, D. *Tetrahedron Lett.* **2000**, *41*, 413.

(14) Xu, Z.; Kim, S. K.; Yoon, J. *Chem. Soc. Rev.* **2010**, *39*, 1457.

(15) Robillard, G.; Devillers, C. H.; Kunz, D.; Cattey, H.; Digard, E.; Andrieu, J. *Org. Lett.* **2013**, *15*, 4410.

(16) Grills, D. C.; Matsubara, Y.; Kuwahara, Y.; Golisz, S. R.; Kurtz, D. A.; Mello, B. A. *J. Phys. Chem. Lett.* **2014**, *5*, 2033.

(17) Chabolla, S. A.; Dellamary, E. A.; Machan, C. W.; Tezcan, F. A.; Kubiak, C. P. *Inorg. Chim. Acta* **2014**, *422*, 109.

(18) Caballero, A.; White, N. G.; Beer, P. D. *CrystEngComm* **2014**, *16*, 3694.

(19) (a) Costentin, C.; Drouet, S.; Robert, M.; Saveant, J. M. *Science* **2012**, *338*, 90. (b) Costentin, C.; Drouet, S.; Robert, M.; Savéant, J.-M. *J. Am. Chem. Soc.* **2012**, *134*, 11235. (c) Roy, S.; Sharma, B.; Pécaut, J.; Simon, P.; Fontecave, M.; Tran, P. D.; Derat, E.; Artero, V. *J. Am. Chem. Soc.* **2017**, *139*, 3685.

(20) (a) Costentin, C.; Saveant, J.-M. *ChemElectroChem* **2014**, *1*, 1226. (b) Rountree, E. S.; McCarthy, B. D.; Eisenhart, T. T.; Dempsey, J. L. *Inorg. Chem.* **2014**, *53*, 9983. (c) Benson, E. E.; Kubiak, C. P. *Chem. Commun.* **2012**, *48*, 7374.

(21) Liyanage, N. P.; Dulaney, H. A.; Huckaba, A. J.; Jurss, J. W.; Delcamp, J. H. *Inorg. Chem.* **2016**, *55*, 6085.

(22) Machan, C. W.; Chabolla, S. A.; Yin, J.; Gilson, M. K.; Tezcan, F. A.; Kubiak, C. P. *J. Am. Chem. Soc.* **2014**, *136*, 14598.

DOI: 10.1021/jacs.7b07709
J. Am. Chem. Soc. 2017, 139, 13993–13996